Advanced Electrochemical Platforms for Selective and Simultaneous Detection of Emerging Pollutants

Thesis Submitted in Partial Fulfilment of the Requirements
for the Award of the Degree of

DOCTOR OF PHILOSOPHY

by

CHANDRA BHAN

Department of Chemical Engineering
Indian Institute of Technology Guwahati
Assam-781039, INDIA

December 2025

DEDICATION

To my parents and family—

my guiding light,
my strength in struggle,
and my joy in success.

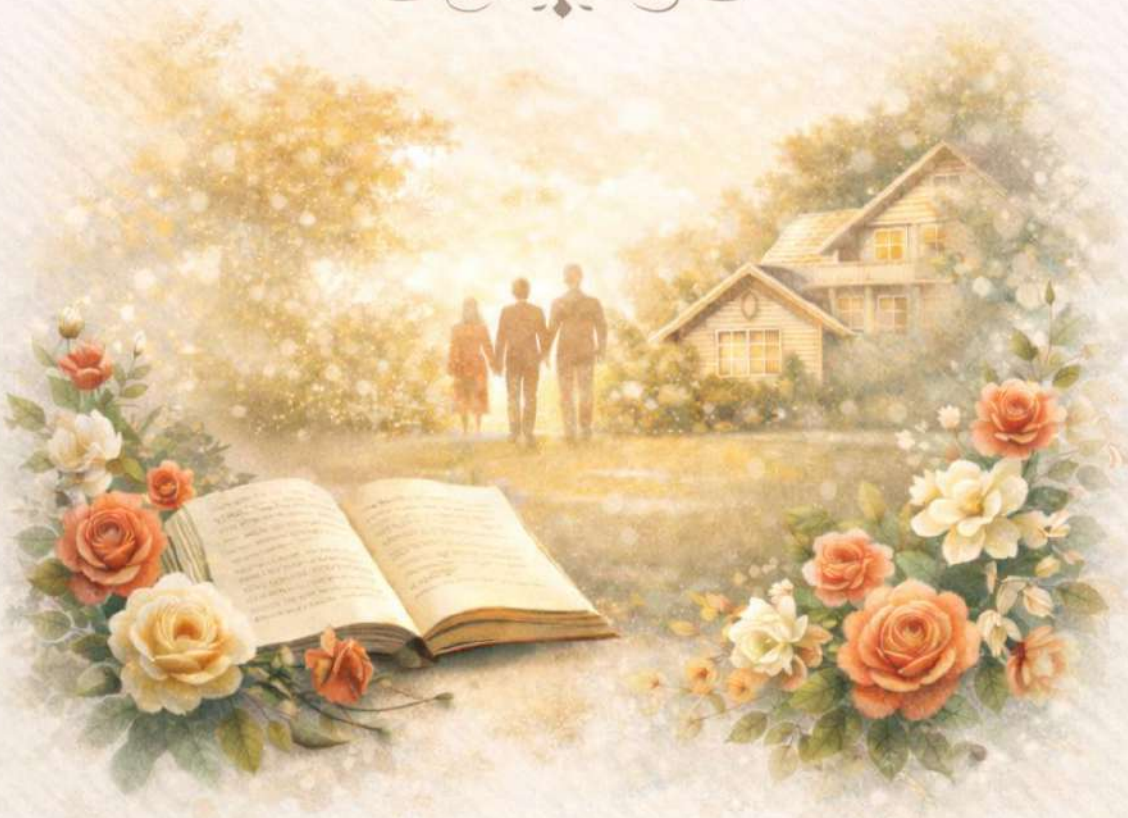

DEPARTMENT OF CHEMICAL ENGINEERING
INDIAN INSTITUTE OF TECHNOLOGY GUWAHATI
GUWAHATI – 781039
ASSAM, INDIA

DECLARATION

I hereby declare that the work embodied in this thesis, entitled **"Advanced Electrochemical Platforms for Selective and Simultaneous Detection of Emerging Pollutants"**, is the outcome of original investigations carried out by me at the Indian Institute of Technology Guwahati, Assam, INDIA – 781039, under the supervision of Prof. Animes Kumar Golder, Department of Chemical Engineering, IIT Guwahati. This thesis is submitted to Indian Institute of Technology Guwahati for the award of the degree of Doctor of Philosophy.

In accordance with standard academic practice, due acknowledgements have been made wherever the work presented is based on the contributions or findings of other researchers.

Chandra Bhan
Roll no.: 196107104
Department of Chemical Engineering
Indian Institute of Technology Guwahati
Guwahati, Assam, INDIA

DEPARTMENT OF CHEMICAL ENGINEERING
INDIAN INSTITUTE OF TECHNOLOGY GUWAHATI
GUWAHATI – 781039
ASSAM, INDIA

CERTIFICATE

This is to certify that the thesis entitled **"Advanced Electrochemical Platforms for Selective and Simultaneous Detection of Emerging Pollutants"** submitted by Mr. Chandra Bhan to Indian Institute of Technology Guwahati, India, for the award of the degree of Doctor of Philosophy, has been carried out by him under my guidance and supervision.

We further certify that the work embodied in this thesis is an original contribution of the candidate and has not been submitted, either in part or in full, to any other university or institute for the award of any degree or diploma.

Animes Kumar Golder
(Thesis Supervisor)
Professor
Department of Chemical Engineering
Indian Institute of Technology Guwahati
Guwahati – 781039
Assam, INDIA

Acknowledgement

It gives me immense pleasure to acknowledge the invaluable contributions of many individuals and institutions who made this doctoral journey possible.

First and foremost, I express my deepest gratitude to **Prof. Animes Kumar Golder** for his constant encouragement, insightful guidance, and generous freedom to explore research independently. His constructive criticism and thought-provoking suggestions at various stages of my work have been instrumental in shaping the direction and quality of this thesis.

I am fortunate to have had the support of my Doctoral Committee members, **Prof. Bishnupada Mandal** (chairman), **Prof. Nageswara Rao Peela**, and **Prof. Chandan Mukherjee**, whose critical evaluation and constructive feedback were invaluable in refining my research and keeping me on track throughout my PhD journey. Their insightful suggestions and encouragement significantly enhanced the scientific depth and clarity of this work.

I am also sincerely grateful to my thesis examiners, **Prof. Saptarshi Majumdar** (Indian Institute of Technology Hyderabad, India) and **Prof. Fabiana V. Fonseca** (Federal University of Rio de Janeiro, Brazil), for their thorough evaluation of my doctoral thesis. Their expert comments, critical observations, and valuable recommendations greatly strengthened the quality, rigor, and overall presentation of this research.

I extend my heartfelt thanks to the members of the Viva Voce Committee, **Prof. Bishnupada Mandal**, **Prof. Saptarshi Majumdar**, **Prof. Chandan Das**, and **Prof. Bhubaneswar Mandal**, for their time, insightful questions, and constructive suggestions during the viva voce examination. Their thoughtful assessment and encouraging feedback contributed significantly to improving the final form of this thesis.

I gratefully acknowledge the support of **Prof. Subrata Kumar Majumder**, Head, Department of Chemical Engineering, IIT Guwahati, for providing the necessary facilities and a conducive research environment. My appreciation also extends to the former Heads of the Department, **Prof. Anugrah Singh** and **Prof. Kaustubha Mohanty**, to the faculty and staff members of the Department of Chemical Engineering, and the Central Instrument Facility (CIF) at IIT Guwahati. The world-class instrumentation facilities at CIF were critical in conducting this research. I sincerely acknowledge the timely assistance of the Department of Chemical Engineering, IIT Guwahati, staff for their technical help and constant support.

I owe my sincere thanks to my lab seniors, Dr. Smruti Ranjan Dash, Dr. Paulomi Bose, Dr. Anirban Chowdhury, Dr. Swagata Patra, Dr. Daisy Das, and Dr. Sourav Maity for sharing their experience and for their continuous support in lab activities. I also thank my lab mates

and colleagues Dr. Ravi, Mr. Pramod Madhukar Gawal, Mr. Mrinal Kanti Dolai, Mr. Biswajit Bhattacharjya, Mr. Shuvam Bhowmick, Mr. Srijan Acharya, Dr. Anil Kumar, Mr. Bharat Bhushan Negi, Mr. Ajay Kumar Shakya, Ms. Gnana Sangeetha R, Mr. Joy Sriman Sarmah, Mr. Priyanuj Bania, Mr. Ayush Singh, and Mr. Suraj Kumar Yadav, for their cooperation, encouragement, and for creating a lively and motivating research environment.

A special word of gratitude is reserved for my friends, Dr. Ravi, Dr. Anil Kumar, and Dr. Sukhjeet Arora, whose support, patience, and unwavering belief in me have been a constant source of strength. Their encouragement and understanding gave me the resilience to persevere and complete this work.

This journey would have been impossible without the blessings, unconditional love, and constant support of my family. I dedicate my accomplishments to my father, **Shri Jagdish Prasad**, my mother, **Smt. Omvati Devi** and other family members, whose sacrifices and blessings have been the foundation of my strength.

Above all, I bow in reverence to the Almighty God for bestowing upon me the strength, health, and opportunities to accomplish this work. I am eternally grateful to God for granting me the courage to rise whenever I faltered and for blessing me with a loving family, supportive mentors, and wonderful friends.

Chandra Bhan
Roll no.: 196107104
Department of Chemical Engineering
Indian Institute of Technology Guwahati
Guwahati, Assam, INDIA

Abstract

Recent advances in the synthesis of nanostructures and nanomaterials have catalyzed transformative developments across multiple scientific domains. Among these, vertically aligned nanostructures (VANs) have attracted considerable attention due to their unique architectural features-such as high surface area and roughness, unimpeded charge transport, facile substrate penetration, large aspect ratio, and superior chemical stability. Specifically, their applications in the sensitive and selective detection of emerging pollutants in environmental matrices have gained increasing importance amid rising global consumption and release of these environmental noxious wastes. Such emerging environmental contaminants pose serious ecological and health risks due to their persistence and bioaccumulation potential.

In this doctoral study, phytochemicals from *Citrus limetta* and *Sechium edule* fruit extract were exploited to develop binder-based (dispersed nanostructures) and binder-free (direct growth of nanostructures) electrocatalytic platforms for detecting emerging pollutants, and bio-based VANs modified with CQDs using carbon-rich peel of *Sechium edule* for drug sensing.

To harness the potential of nanotechnology, both binder-based and binder-free electrochemical detection platforms must be strategically developed and tailored to specific sensing needs. With these aims, this work is structured into distinct sections, emphasizing the development of these platforms and their applications in detecting target analytes.

In the first part, phyto-analytic formation of Ag nanostructures (AgNSs) was carried out using the bio-extract of *Citrus limetta* for electrochemical sensing and quantifying ciprofloxacin (CFX). An average particle size of AgNSs was 43.5±3.9 nm. The effective surface area increased from 0.038 to 0.098 cm^2, and electrode kinetic resistance reduced from 3190 to 219 kΩ after the functionalization of AgNSs onto the bare glassy carbon electrode (GCE) surface. AgNSs/GCE showed the limit of detection (LOD) of 0.199 µM. The potential interferants could not alter the oxidation peak current during CFX detection, and only 12.38% reduction in the oxidation peak current was noted up to the 10^{th} reused cycles. The proposed AgNSs/GCE effectively detects CFX in real water samples, achieving nearly 100% recovery and results comparable to HPLC. However, rapid delamination of surface-embedded catalysts remained a limitation, reducing the sensor's life. Direct growth of catalysts can overcome this issue by eliminating the coating step and enhancing sensor stability.

To improve stability, this study documents on chemical-based synthesis of 1D surface vertically aligned ZnO nanorods directly grown on fluorine-doped tin oxide glass substrate (ZnO-VANRs/FTO) for the targeted electrochemical sensing of aniline. ZnO-VANRs/FTO

were 1.57±0.03 µm in length with high density. ZnO-VANRs/FTO electrode could increase the effective surface area from 0.154 to 0.384 cm^2 with about 86.85% reduction in charge transfer resistance compared to bare FTO. ZnO-VANRs/FTO electrode showed an LOD of 0.193 µM. The fabricated sensor was unprecedently selective towards aniline sensing, and potential interferents could not interfere with aniline sensing. However, the peak current was marginally decayed by 2.63 % up to the 6^{th} cycle. Moreover, ZnO-VANRs/FTO catalyzed sensing of aniline spiked in the environmental matrices, well conformed to liquid chromatography. Although the chemical synthesized VANs have proven effective for sensing, achieving bio-based growth of VANs on FTO remains a fundamentally challenging task.

A new bio-based route was successfully developed for synthesising hierarchical 2D ZnO VANs onto the FTO glass (ZnO-VANs(bio)/FTO) surface using *Sechium edule* fruit extract for targeted electrocatalytic sensing of p-Chloroaniline (p-CA). The morphological characterizations of ZnO-VANs(bio)/FTO showed the formation of vertical nanostructures with an average length of 820 nm. ZnO-VANs(bio)/FTO@pH7 electrode showed a decrease in electron transfer resistance from 7.78 to 3.02 MΩ with a 1.2-fold increase in effective surface area than FTO(bare). ZnO-VANs(bio)/FTO@pH7 exhibited remarkable electrocatalytic sensing of p-CA with LOD of 0.021 µM. Common interferents could not interfere with p-CA sensing, and only a 4.7% reduction in peak current was observed up to the 9^{th} cycle. ZnO-VANs(bio)/FTO@pH7 could efficiently sense p-CA in spiked water samples. Moreover, bioinspired VANs functionalized with carbon quantum dots derived from the remnant carbon-rich biomass could significantly enhance the sensor's performance.

This study reports bioinspired synthesis of 2D vertically aligned ZnO nanostructures onto FTO using *Sechium edule* fruit extract and its functionalization with carbon quantum dots (CQDs-ZnOVANs(bio)/FTO) fabricated using carbon-rich remnant peel. The functionalized platform was tested for electrocatalytic monitoring of norfloxacin (NFX). ZnOVANs(bio)/FTO modified with CQDs at deposition time of 1.5 min ($CQDs_{1.5}$-ZnOVANs(bio)/FTO) oriented vertically with an average length of 965.3 nm. The average particle size of CQDs was 4.7 nm. $CQDs_{1.5}$-ZnOVANs(bio)/FTO exhibited 63.1% enhancement in electroactive area with 34.6% decrement in charge transfer resistance compared to ZnOVANs(bio)/FTO. $CQDs_{1.5}$-ZnOVANs(bio)/FTO exhibited a detection limit of 0.0066 µM. The developed electrode exhibited excellent stability with only 8.1% reduction in peak response up to the 15^{th} reuse cycles. Common antibiotics could not interfere with NFX monitoring. $CQDs_{1.5}$-ZnOVANs(bio)/FTO could effectively monitor and quantify NFX spiked in environmental

samples, comparable to HPLC. Furthermore, the influence of morphological attributes (2D to 1D) of bio-based VANs were explored for electrochemical sensing applications.

This study highlights the development of nature-inspired 1D Bi_2S_3 vertically oriented nanorods on FTO glass (Bi_2S_3-VONs(nat)/FTO) using the bio-extract of *Sechium edule* for the detection of mancozeb (MCZ). Bi_2S_3 nanorods synthesized at 2.3 g of $Bi(NO_3)_3 \cdot 5H_2O$ and pH 3 (2.3Bi_2S_3-VONs(nat)/FTO@pH3) exhibit ~1.74±0.09 µm vertical length. 2.3Bi_2S_3-VONs(nat)/FTO@pH3 electrode exhibited 89.2% reduction in charge transfer resistance and 64.4% increase in effective surface area compared to FTO(bare). It exhibited an LOD of 0.0085 µM. Commonly used pesticides could not interfere with MCZ detection. Only a 16.4% reduction in peak current was observed up to the 30th run when the same sensing platform was reused. 2.3Bi_2S_3-VONs(nat)/FTO@pH3 could effectively detect MCZ spiked in the environmental matrices, which was comparable to HPLC. However, environmental matrices often contain multiple emerging pollutants, making simultaneous detection crucial. This strategy allows the sensor to distinguish overlapping signals, simultaneously quantify multiple analytes in a single run, and lower costs for the need of separate sensors.

Finally, the bio-based synthesis of Bi_2S_3-ZnO nanocomposites (Bi_2S_3-ZnO(bio)) was carried out using *Sechium edule* bio-extract for dual-analyte selective and simultaneous electrochemical monitoring of phenylbutazone (PBZ) and sulfamethoxazole (SMZ). Bi_2S_3-ZnO(bio) exhibited ZnO(bio) nanostructures embedded on the Bi_2S_3(bio) nanorods with an average rod length of 1409.7 nm. After immobilization of Bi_2S_3-ZnO(bio) onto the GCE (Bi_2S_3-ZnO(bio)/GCE), 94.6% reduction in charge transfer resistance and 63.2% rise in electroactive surface area were observed than bare/GCE. For simultaneous sensing, the Bi_2S_3-ZnO(bio)/GCE achieved LODs of 0.222 and 0.089 µM for PBZ and SMZ, respectively. The presence of common antibiotics could not interfere with the electrochemical sensing of PBZ and SMZ, and only a decrease in peak response of 12.9% for PBZ and 11.8% for SMZ was observed after 10 reuse cycles during the simultaneous sensing. The developed simultaneous sensing platform could efficiently detect and quantify PBZ and SMZ in real water samples.

Keywords: Phyto-analytic formation; Ag nanostructures; Electrocatalytic sensing of ciprofloxacin; 1D ZnO nanorods; FTO substrates; Electrochemical aniline sensing; Bio-based synthesis; 2D ZnO nanostructures; Electrochemical p-Chloroaniline sensing; Carbon quantum dots; Electrocatalytic norfloxacin monitoring; 1D Bi_2S_3 nanorods; Electrochemical mancozeb sensing; Bi_2S_3-ZnO nanocomposites; Simultaneous drug sensing; Square wave voltammetry; High selectivity; High sensitivity; Environmental pollutant monitoring

Table of Contents

CHAPTER 2: Materials and methodology

List of Figures

List of Tables

CHAPTER 1

Introduction, Literature Review, and Research Objectives

This chapter presents a comprehensive discussion on the electrochemical sensors and their ability to sense environmental emerging pollutants using directly growing (binder-free) and immobilizing (binder-based) diverse nanostructured materials on the working electrode surface. This chapter also documents the routes for synthesizing nanostructures and their utilization in the field of electrochemical sensors for sensing environmental pollutants using different electrochemical techniques. Additionally, this chapter provides a comprehensive framework and directions for the development of bioinspired vertically aligned nanostructures (VANs) on the surface of working electrode for point-of-care monitoring of target analytes.

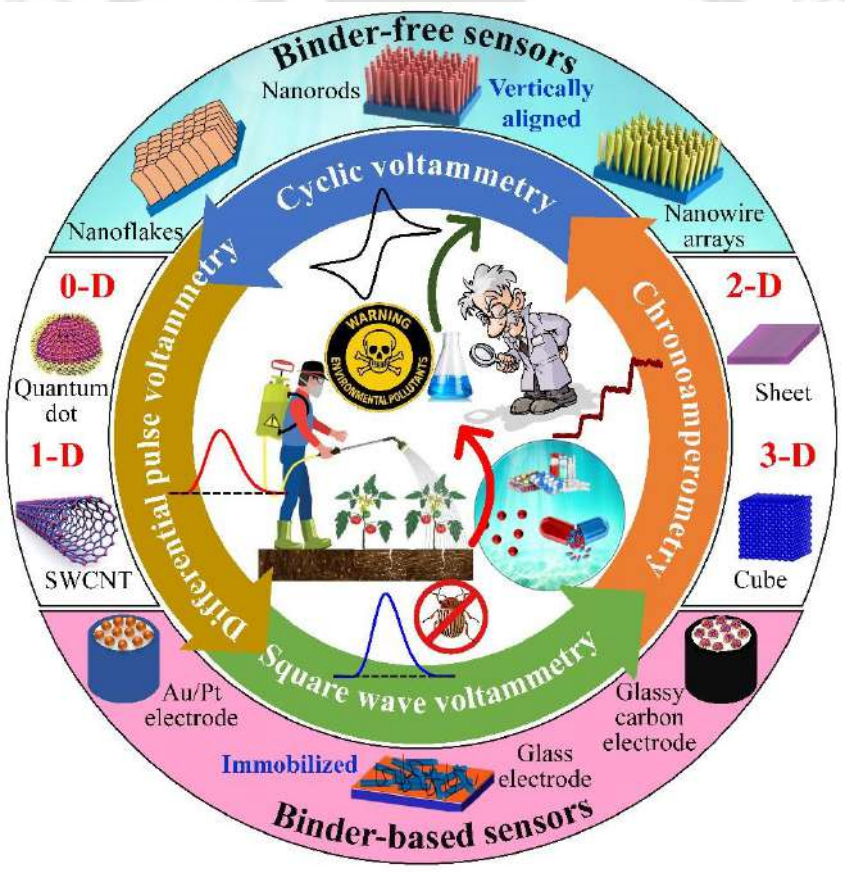

Chapter highlights

- Pathways for developing nature-inspired VANs for environmental noxious waste sensing
- Strategies for enhancing sensing performance through nanostructure functionalization
- Role of binder critically assessed for electrochemical environmental pollutant sensing
- Delineate pathways of future prospects in electrochemical emerging pollutants detection

1.1. Introduction

A huge number of synthetic pesticides are utilized to enhance agricultural productivity worldwide. The residual pesticide remnants pose a growing threat to human and environmental health. Pesticides encompass natural and synthetic compounds or mixtures utilized to manage, eradicate, control, prevent, or deter diseases, pests, insects, and weeds that pose a threat to plant growth (Pathak et al., 2022). These compounds are typically categorized based on their chemical composition, hazard level, mode of action, application method, and timing. Over the last many decades, the advent of chemical pesticides has substantially contributed to the significant increase in agricultural crop yields. Consequently, the global demand for pesticides has risen consistently and significantly since the mid-1940s, primarily due to commercial farming (Umapathi et al., 2022). However, the unregulated and extreme utilization of pesticides has contaminated food sources and led to pollution in the environment, agriculture, and aquatic systems (Sharma et al., 2019). In agriculture, several types of pesticides, for instance fungicides, insecticides, bactericides, and herbicides, are generally used to control pests and diseases. Pesticide residue can infiltrate the food chain via various pathways, including water, vegetables, fruits, processed food, soil, and air (Pradhan and Mailapalli, 2020). Fig. 1.1 demonstrates the pathways for pesticide residue to enter the food chain and their impacts on human health and our ecosystem. Farmers, who are directly exposed during handling and application, suffer the most. Pesticides applied to crops contaminate surface and groundwater through runoff and leaching. This polluted water affects aquatic life and re-enters the food chain, causing widespread toxicity. Plants absorb these pesticides, making the produce harmful for consumers. Consuming agricultural pesticides through diet could lead to chronic and acute health effects in humans, posing a significant public health concern, particularly in developing countries (Tudi et al., 2022). Agricultural pesticides have the potential to be cytotoxic, hepatotoxic, carcinogenic, endocrine, neurotoxic, teratogenic, developmental, reproductive, and mutagenic to human health (Kalyabina et al., 2021). To address this issue, regulatory authorities are continuously working to impose stringent laws and regulations to control pesticide pollution. However, developing highly efficient in-situ detection and determination of agricultural pesticides and their derivatives is a need of the hours to control pesticide pollution across the globe.

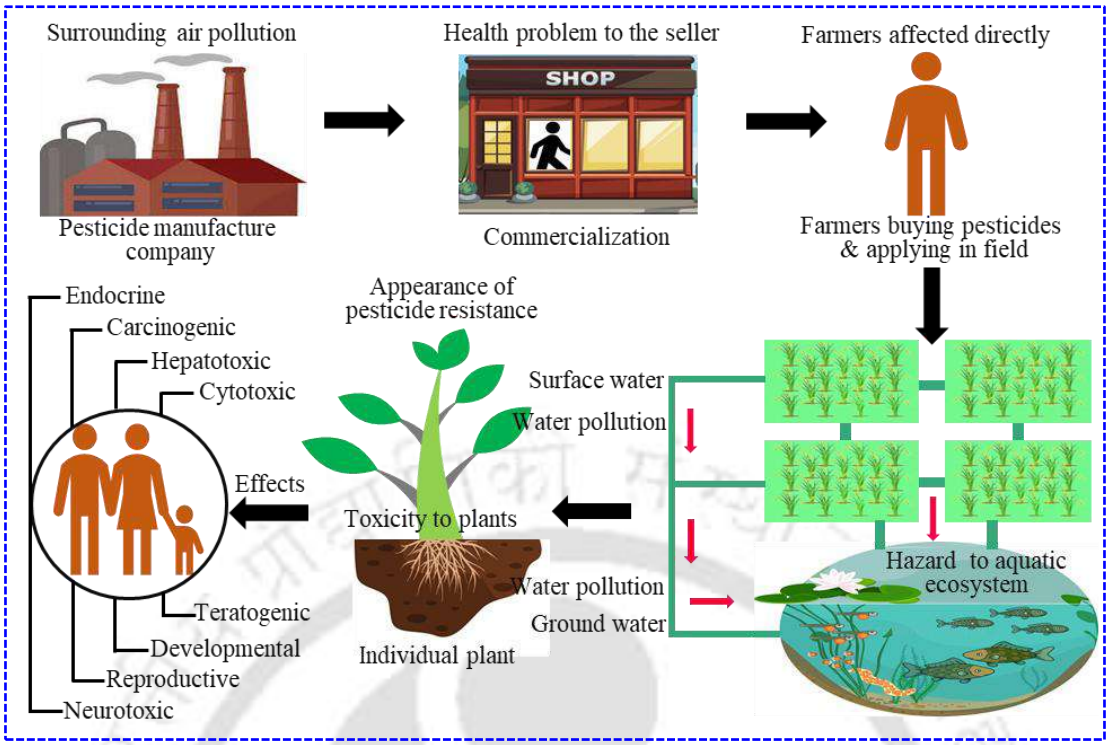

Figure 1.1: Pesticide residue enters the food chain through various pathways and their effects on the environment and human health.

Further, the increasing presence of pharmaceutically active compounds (PhACs) in the environment is an emerging global concern due to their potential impact on human health and ecosystems. Among the various PhACs, ciprofloxacin (CFX), phenylbutazone (PBZ), sulfamethoxazole (SMZ), and norfloxacin (NFX) are commonly used drugs that have been detected in water bodies and food supplies (Kaczala and E. Blum, 2016; Worboys and Toon, 2018). CFX, a fluoroquinolone antibiotic, is widely used in treating bacterial infections due to its broad-spectrum antimicrobial activity and effective penetration into tissues (Nejabatdoust et al., 2024). PBZ is a nonsteroidal anti-inflammatory drug extensively used for its anti-inflammatory and analgesic properties in human and veterinary medicine (Tesena et al., 2024). SMZ is a broad-spectrum antimicrobial agent frequently used to treat bacterial infections. NFX, also a fluoroquinolone antibiotic, is commonly utilized in the treatment of urinary tract and gastrointestinal infections due to its broad-spectrum antibacterial activity and favourable pharmacokinetics, including effective penetration into renal and prostatic tissues (Muungani and van Zyl, 2023). Despite their beneficial advantages, these PhACs have been found in aquatic environments (Fig. 1.2a), posing risks to aquatic organisms and potentially leading to the development of drug-resistant bacteria. Fig. 1.2b shows the existence of PhACs in groundwater and river water across the Ganges river basin in India and their ecological toxic

impacts (Ravi and Golder, 2025). The prolonged presence of PhACs in the environment, even at low concentrations, can lead to significant effects on human health, such as kidney damage, allergies, nausea, diarrhoea, vomiting, headache, disrupt aquatic ecosystems, blood disorders, thrombocytopenia, gastrointestinal issues, and exacerbate blood cell reduction (Borges et al., 2019; Pan et al., 2023). Therefore, detecting and determining PhACs in the environmental matrices due to their widespread use and environmental persistence is highly warranted.

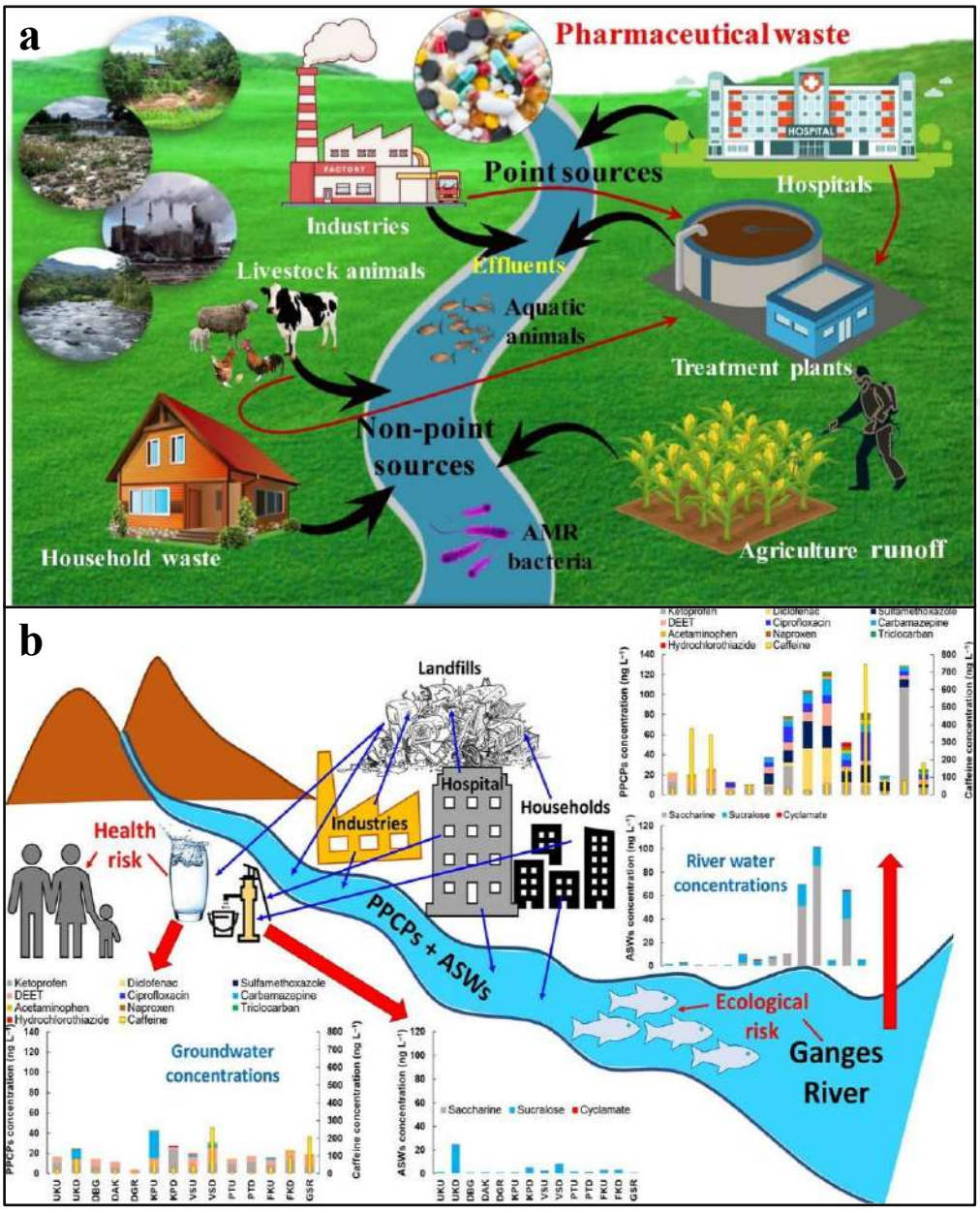

Figure 1.2: (a) Pathways of PhACs contamination from point and non-point sources to aquatic systems and (b) Presence of PhACs in groundwater and river water across the Ganges river basin, India, along with their associated ecological risks. Reprinted with permission from ref (Ravi and Golder, 2025) (copyright 2025 Elsevier).

Conventional analytical techniques, including liquid chromatography (Wang et al., 2023), gas chromatography (Granados-Povedano et al., 2023), fluorescence (Diop et al., 2023), high-performance liquid chromatography (HPLC) (Jafari and Ghani, 2023), mass chromatography (Chiang, 2008), and Raman spectroscopy (Yi et al., 2023), are employed for monitoring the existence of pesticides and pharmaceuticals in the environmental matrices. Though, these techniques needed sophisticated instrumentation and professionally accomplished individuals, triggering the high analysis cost, expensive instruments, operational complexities, time-consuming processes, and less accessible in certain situations. Additionally, these techniques necessitate labor-intensive sample preparation, preconcentration, and pretreatment processes before examining trace-level organic pollutants in environmental matrices. Therefore, these inherent limitations make them unsuitable for real-time or on-site determination of agricultural pesticide and pharmaceuticals residues in fields. However, the fabrication of highly effective, and economical devices for geographically independent and in-situ detection of pesticides and pharmaceuticals could be the key step in controlling the spreading of organic pollutants.

Electrochemical sensors exhibit significant potential of in-situ detecting and quantifying the specific analytes, including agricultural pesticides (He et al., 2023b; Li et al., 2023; Qiu et al., 2019; Zhou et al., 2023) and their intermediates (Castro et al., 2020), heavy metal ions (Q. Liang et al., 2023), and pharmaceutical drugs (Mohan et al., 2023). These sensors merited with cost-effectiveness, high selectivity, sensitivity, and potential to detect the target analytes at a low concentration. Additionally, the electrochemical sensor has the potential to reduce the need for conventional analytical techniques. The electrochemical sensor typically consists of three electrodes such as a working, reference, and counter electrode, and altogether submerged in an electrolyte media. When the target analyte is introduced into the solution, it interacts with the electroactive material modified on the functioning electrode surface, resulting in an alteration of the electrical signal that can be measured (Tanwar and Mathur, 2021). Past research is mostly attentive to sensing mechanisms and the development of recognition units. The working electrode development significantly receives less research focus. The physicochemical characteristics and microstructure of the working electrode contribute significantly to increasing the efficiency of the electrochemical sensor. As a minimum, three characteristics of the working electrode predominantly contribute to enhancing the performance of an electrochemical sensor, including the specific surface area, electric conductivity, and hydrophilicity. A high specific surface area of the base electrode can adapt large recognition units to increase response current during sensing and allow for real-time environmental

monitoring. A promoted charge transfer between the base electrode surface and electrolyte solution could be regulated by a high electric conductivity of the host electrode. For hydrophilic electrodes, it is crucial to have analytes in an aqueous solution, which provides prominent interaction of analytes with the electrode through surface wetting and enhances the sensor's sensitivity (Lee et al., 2014). The nanostructures inimitable characteristics could be exploited for designing the electrochemical sensor by targeting a higher sensitivity and lower detection limit for a desired analyte. Furthermore, the functionalization of nanoparticles (NPs) such as ZnO (Emin Çorman et al., 2023; Zhuang et al., 2023), CuO (Ali et al., 2023), NiO (Somasundaram et al., 2023), SnO_2 (AbdelHamid et al., 2023), Co_3O_4 (Arpitha et al., 2023), Fe_2O_3 (Wu et al., 2023), MnO_2 (Nguyen et al., 2023), Bi_2S_3 (Zhao et al., 2022), CdS (Hasheena et al., 2023), SnS_2 (Y. Liang et al., 2023), AgNPs (Ettadili et al., 2023), AuNPs (Abad-Gil et al., 2023), etc., on the native electrode surface might improve the performance of electrochemical sensor (binder-based) by several folds through facilitating an electrocatalytic reaction between the working electrode/nanostructure surface and target analytes. However, the embedded catalysts (not grown directly on the base electrode surface) are delaminated quickly during the course of sensing. It could deter repeatability and reproducibility. Moreover, the binder could potentially interfere with the electrochemical sensor, which could affect its sensing performance.

In recent research, the growth of vertically aligned nanostructure (VANs) on the surface of working electrode (fluorine-doped tin oxide (FTO)/Indium tin oxide (ITO) glass substrates) was performed, which significantly improved the performance of electrochemical sensors by several folds. They are merited with high specific surface area, maximum roughness, unimpeded electron transport characteristics, large aspect ratio, high chemical stability, and easy substrate penetration morphologies (Ahmad et al., 2017c, 2017b; Arsalan et al., 2022; Lin et al., 2023). Electrodes with a high surface area could have more number of active sites for the interaction between the electrode/nanostructure surface and analytes, enhancing its sensing performance by lowering the detection limit and increasing sensitivity. Additionally, the increased surface area of nanostructures can lead to a faster response time for the sensors, allowing for real-time environmental monitoring. The higher roughness of nanostructures provided more nucleation sites and unimpeded electron transport characteristics, allowing effective charge transmission between the electrode/nanostructure surface and electrolyte solution. Furthermore, forming VANs could remove the problem of delamination of nanostructure from the working electrode, the binder's need (decreasing the usage of environmentally hazardous chemicals), and the functionalization process of nanostructure on

the base electrode surface (Ahmad et al., 2017d). VANs nanostructure-based (binder-free) electrochemical sensors have promising prospects for detecting environmental pollutants (Ahmad et al., 2017e; Zhai et al., 2021). These sensors are highly sensitive, selective, and can detect trace amounts of target analytes in real-time with minimal interference from other environmental factors. Additionally, this type of sensor can be integrated into portable and handheld devices, allowing for on-site detection and determination of the targeted analyte. Overall, the prospects of binder-free electrochemical sensors are very promising by providing a fast, selective, cost-effective, and reliable method for monitoring and controlling pesticide use in agriculture, leading to improved environmental and human health outcomes.

This chapter provides a comprehensive discussion on the electrochemical sensors and their ability to sense environmental pollutants using directly growing (binder-free) and immobilizing (binder-based) diverse nanostructured materials on the host electrode surface. This chapter also documents the routes for synthesizing nanostructures and their utilization in the field of electrochemical sensors for sensing organic pollutants using different electrochemical techniques. Additionally, this chapter presents a comprehensive framework and directions for the development of bioinspired VANs on the surface of functioning electrode and integration with a smartphone-based portable electrochemical sensor for point-of-care monitoring of environmental noxious waste.

1.2. Types of electrochemical sensors detecting organic analytes

Electrochemical sensors provide real-time data on the system composition by connecting a recognition element (chemically selective layer) to an electrochemical transducer. It produces an electrical signal by reacting with the chemical solution, and the signal is proportional to the electrochemical species' concentration (Chen et al., 2019). An electrochemical sensor comprises three main components, the receptor (chemical recognition system) that binds the analyte, the analyte/sample/electroactive species, and the physicochemical transducer that changes the reaction into a computable electrical signal which could be sensed by an electrical instrumentation. These two combined parts, receptor and physicochemical transducer, form a working (sensing) electrode. The recognition unit is halted on the working electrode's surface. It is accountable for detecting the electrochemical species by the specific chemical reactions from which the transfer of charge occurs. Sometimes, reference and counter electrodes are also used for the electrical measurements. All three-electrode are enclosed in the sensor housing, filled with liquid electrolytes (Sharma et al., 2021). An electrochemical sensor has many

qualities with respect to the other sensors because the electrodes of the electrochemical sensor can detect an analyte with a very low recognition limit owed to acceptable reproducibility, good stability, and their wide range of linear responses (Beitollahi et al., 2020). Based on their operating mode, an electrochemical sensor can be classified into three main categories for instance, potentiometric, amperometric, and conductometric sensors.

1.2.1. Potentiometric sensors

Potentiometric sensors have undergone development for various real-world applications since the early 1930s. In this type of sensor, the electrode potential is determined by set-up local equilibrium on the sensor interface and the electroactive species' concentration is measured as a difference of potential between reference and working electrodes. Potentiometric sensors can be classified into three fundamental device types, for instance field effect transistors (FETs), coated wire electrodes (CWEs), and ion-selective electrodes (ISEs). Among these, ISEs behave as an indicator electrode, that can selectively measure the deed of a certain analyte. In a typical layout, ISEs contain working and reference electrodes. The potential of a working electrode is determined from its surroundings, though the potential of the reference electrode is established in a desired analysis solution. Dissolved ions concentration determines the potential difference between the two electrodes (reference and working), while the reference electrode potential remains constant (Bratov et al., 2010; Chaudhary et al., 2023). There are more than two dozen commercially available ISEs from different manufacturers such as Corning, Hitachi, Orion, Radiometer, Beckman, and many others. These sensors find applications in a broad range of areas, including the determination of anionic or cationic species and organic ions from several effluents.

The CWEs was initially presented by Freiser in the mid-1970s. In a typically CWEs, the conductor is coated with the thin layer of an ion-selective membrane, which is sensitive to a specific ion in an electrolyte media. The response current of CWEs and ISEs were almost same with respect of concentration range and detection limit. Additionally, it can be used in the wider range of applications, such as in the detection of heavy metal ions and organic analytes. Wang et al. (2015) developed a potentiometric sensor that can detect organophosphate pesticides with a limit of detection (LOD) of 3 µM in the concentrations range of 10-1000 µM (Wang et al., 2015).

It is mainly used to measure the analyte concentration by determining the variations in the potential difference between the reference and the working electrode at different concentrations of the analyte. To measure analytes concentration, the combination of ionic and

electric currents flowing in a closed circuit is essential. Nernst equation is employed to examine the electrochemical cell potential at any given pressure, temperature, and concentration of reactant. The signal of this type of sensor is based on Eq. 1.1 (Chang et al., 2004).

$$E = E^{\circ} \pm \left(\frac{RT}{nF}\right) \ln a_i \quad (1.1)$$

Where E, E^0, a_i, and n, are the potential (V), standard potential (V), activity of the analyte and total number of charges on the ion, respectively. The constants R, T, and F represent the gas constant (8.314 J $mol^{-1}.K^{-1}$), reaction temperature (K), and Faraday constant (96485 C mol^{-1}), respectively.

1.2.2. Amperometric sensors

Amperometric measurements involve measuring the flow of current (generated by the voltage applied between a reference and working electrode) of electroactive species in an electrochemical cell from the reduction or oxidation at a constant potential with respect to electroanalytical techniques. This type of measurement is known as voltammetry or voltammetric measurement, where the transfer of charge occurs. The initial instrumentation required for amperometric measurements is controlled-potential equipment, which includes an electrochemical cell with three (counter, reference, and working) electrodes fenced in the sensor housing filled with electrolyte. The base electrode is the site where the redox reaction takes place. The counter (auxiliary) electrode, typically constructed from a chemically inert, conductive material like graphite or platinum, completes the electrical circuit. The reference electrode provides the stable and constant potential concerning the base electrode. In addition to the electrodes, an appropriate supporting electrolyte solution is required to provide ions for the redox reaction to continue a constant ionic strength, abolish the effect of electromigration, and reduce the resistance of the solution (Chaudhary et al., 2023; Helm et al., 2010; Stetter and Li, 2008). Jo et al. (2014) developed an amperometric sensor with hollow gold/ruthenium nanoshells to detect ascorbic acid. The sensor showed a LOD of 2.2 µM and a sensitivity of 0.426 $\mu A \mu M^{-1} cm^{-2}$ (Jo et al., 2014).

Working electrodes and their modification with nanostructure strongly contribute in improving the amperometric sensors' performance, and various nanomaterials have been explored over the years to produce effective sensors. Historically, the development of electrochemical detection techniques of analytes began with the creation of dropping mercury electrode by Heyrovsky in the 1920s. Mercury electrode was popular due to their renewable surface, high reproducibility, and extended range of cathodic potential. However, the limited

anodic potential and toxicity of mercury have limited its use in environmental monitoring. In contrast, solid electrodes (such as platinum, gold, and nickel) fabricated from noble metals and carbon-based electrodes (such as carbon nanotubes, carbon paste, and glassy carbon) with immobilization of nanostructure using binder (Nafion, polyvinyl alcohol, chitosan, polyethylene glycol, and polystyrene) has become increasingly popular (Akhtar et al., 2022; Zhao et al., n.d.). It offers several advantages such as affordable, diverse potential window, minimum background current, and chemical inertness, making them suitable for in-situ detection and determination of analytes. Buledi et al. (2021) synthesized CuO nanostructure in a chemical growth route. Subsequently, the prepared nanostructure was functionalized onto a glassy carbon electrode (GCE) using Nafion (binder) to detect bentazone and mexacarbate pesticides simultaneously. The developed sensor showed the LOD of bentazone and mexacarbate were 0.008 and 0.0015 µM, respectively (Buledi et al., 2021).

Currently, researchers are directing their attention towards the direct growth of VANs of metal oxide/sulphide on the surface of a working electrode could provide a tunable interaction with the electroactive species due to unimpeded charge transmission kinetics and high surface area. Marie et al. (2015) projected a binder-free electrochemical glucose sensor constructed from VANs of ZnO incorporated into the ITO glass substrate. The diameter of the nanorods (hexagonal structure) was obtained in the range of 68-116 nm. The fabricated electrochemical sensor's sensitivity, LOD, and amperometric response were 10.911 $\mu A \mu M^{-1} cm^{-2}$, 0.22 µM, and 3 s, respectively (Marie et al., 2015). The progress of new and advanced electrode catalysts will continue to drive the progress of electroanalytical chemistry, leading to the formation of more efficient and sensitive electrocatalytic sensors for numerous applications, such as environmental pollutants detection, clinical diagnostics, and food quality control.

1.2.3. Conductometric sensors

In this type of sensor, the resistivity and conductivity are investigated in response to the concentration of analytes and the mobility of charged particles (ions or electrons) in the material. These sensors are non-specific (do not selectively detect a particular analyte) in nature. Additionally, conductometric sensors are unique in various applications, including biosensing and gas sensing, owing to cheap, insensitivity to light, ease of miniaturization, and simplicity (no need for reference anode). Aydin et al. (2023) fabricated a CuO nanostructured-based conductometric sensor for monitoring sweat loss with a LOD of 2850 µM (Aydın et al., 2023). Crispi and Neri (2022) developed the sensor using Al, Ca doped ZnO nanocomposite

for sensing formaldehyde in the air. The LOD of the sensor was 4.162 µM (Crispi and Neri, 2022).

1.3. Electrochemical techniques for sensing of environmental pollutants

Voltammetric electrochemical techniques are widely used in analytical chemistry for in-situ detection and quantification of various dissolved inorganic and organic constituents. In physical, biological, and inorganic chemistry, voltammetry is used to investigate the adsorption process of analytes on the support electrode's surface, the thermodynamic characteristics of solvated species, and the fundamentals of reduction and oxidation process of analytes, the reaction mechanism, electron transfer, and their kinetics. These studies can provide important information about the behaviour of molecules and ions in solution and help to elucidate the underlying chemical processes that occur in these systems. In addition, these techniques are also of interest for the electrocatalytic detection of environmental pollutants. The choice of voltammetric method depends on the nanostructure material functionalized onto the support electrode's surface, the applied potential function on the working electrode, and the type of analytes. Some of these voltammetric techniques are concisely described in the succeeding sections.

1.3.1. Cyclic voltammetry

In 1938, the cyclic voltammetry (CV) technique was initially introduced by Randles. It was the primary experimental method used to investigate the qualitative data of the electrochemical reactions. Additionally, it could provide information about the thermodynamic characteristics of redox event, chemical reactions of the redox couples, the kinetics of charge-transport events, and the fast detection of the redox potential of analytes. CV provides qualitative and quantitative data of electrochemical reactions between immobilized nanostructures on the functioning electrode's surface and analytes in electrolyte solution. This technique involves measuring the potential difference between the working and reference electrodes, while the current is assessed between the counter and reference electrodes. The electrolyte's operational stability limits the capacity of the potential. The resulting cyclic voltammogram is plotted as current versus potential (Elgrishi et al., 2018). The following Eqs. 1.2 and 1.3 determine the specific capacitance (Cs) (Chaudhary et al., 2023).

$$C = \frac{1}{m \times V \times V_s} \int_0^V I(V)dV \tag{1.2}$$

$$C_s = \frac{C}{m} \tag{1.3}$$

Where C, m, V, V_s, and IdV are the determined capacitance from Eq. 1.2, the material's active mass, potential range, scan rate, and area under the CV graph, respectively. Salaria et al. (2021) investigated the reductive behaviour of 2, 4, 6-trinitrotoluene using the CV technique. The modified Au electrode with PEG-coated cadmium sulphide (CdS/Au) displayed a remarkable sensitivity of 47.8 $\mu A \mu M^{-1} cm^{-2}$ and LOD of 0.00105 µM (Salaria et al., 2021).

1.3.1.1 Determination of electroactive surface area of working electrode

The effective surface area of the functioning electrode is calculated through CV at different scan rates using either K_3FeCN_6 (outer sphere) or $Ru[(NH_3)_6]Cl_3$ (inner sphere) as a standard probe in 0.1 M KCl electrolyte solution. Randles-Sevcik equation (Eq. 1.4) is used to estimate the electroactive surface area of the electrode (Elgrishi et al., 2018).

$$I_{Pa} = 0.4463\ C_0\ A_{eff}\ D^{1/2} n^{3/2} \upsilon^{1/2} \left(\frac{F^{3/2}}{R^{1/2}\ T^{1/2}}\right) \quad (1.4)$$

Where I_{pa} is the anodic peak current (A), C_0 is the concentration of a standard probe ($mol.cm^{-3}$), A_{eff} is the effective surface area of the host electrode (cm^2), n is the number of electron transfer in the redox events, D is the diffusion coefficient ($cm.s^{-1}$), and υ is the scan rate ($V.s^{-1}$). The significance of constants F, T, and R are the same as previously mentioned in section 2.1. At 298.15 K reaction temperature, the value of the term $\frac{F^{3/2}}{R^{1/2}\ T^{1/2}}$ of Eq. 1.4 can be written as 6.02×10^5 C $mol^{-1}.(C\ J^{-1})^{1/2}$ or 6.02×10^5 $(A.s\ mol^{-1})V^{-1/2}$ (where the unit of C and V are A.s and J C^{-1}, respectively), which gives Eq. 1.5 (Malode et al., 2020).

$$I_{Pa} = (2.69 \times 10^5)\ C_0\ A_{eff}\ D^{1/2} n^{3/2} \upsilon^{1/2} \quad (1.5)$$

Where the unit of the constant 2.69×10^5 is $(A.s\ mol^{-1})V^{-1/2}$. For the determination of A_{eff}, the slope of the linear plot I_{pa} vs. $\upsilon^{1/2}$ (obtained from CV) is determined by equating the Eq. 1.5 by assuming n = 1, and D = 8.43×10^{-6} $cm^2\ s^{-1}$ (for $Ru[(NH_3)_6]Cl_3$) or 7.60×10^{-6} $cm^2\ s^{-1}$ (for K_3FeCN_6).

1.3.1.2 Determination of electrochemical species adsorbed on the electrode

Free diffusion or adsorption of electrochemical species is examined by CV at different scan rates and fixed concentrations of targeted analyte in supporting electrolyte. In electrochemical systems where electron transfer procedures are reversible, which contain redox species freely diffusing in the supporting electrolyte. To determine an electrochemical adsorbed species on the electrode, the slope of the linear plot between peak current and scan rate (I_{pa} vs. υ, obtained from CV) is equated with Eq. 1.6 (Elgrishi et al., 2018).

$$I_{pa} = \frac{n^2F^2}{4RT} A_{eff}\, \upsilon\, \Gamma^* \quad (1.6)$$

Where Γ* is the surface coverage by the adsorption of electrochemical species (mol.cm^{-2}). The significance of I_{pa}, n, A_{eff}, υ, F, T, and R are the same as mentioned in the previous section.

1.3.1.3 Determination of ratio of electron and proton involved in electrochemical reaction

The ratio of electrons and protons participating in the electrochemical reaction is investigated by performing CV for sensing targeted analytes at various electrolyte pH and a constant scan rate. Nernstian equation (Eq. 1.7) has been used to calculate the ratio of electrons and protons by plotting a linear graph between the anodic peak potential (E_p) and pH (Manivannan et al., 2019). For the determination of the ratio of proton and electron ($\frac{m}{n}$), the slope of the linear plot between E_p vs. pH (obtained from CV) is equated with $-2.303\frac{mRT}{nF}$ (Eq. 1.7).

$$\frac{dE_p}{dpH} = -2.303\frac{mRT}{nF} \quad (1.7)$$

Where E_p is the anodic peak potential (V), m and n are the number of protons and electrons involved in the electrocatalytic reaction, respectively. The significance of constants F, T, and R are the same as aforementioned. Additionally, the value of the slope ($\frac{dE_p}{dpH}$) can be written as 29.58 and 59.17 mV pH^{-1} at the reaction temperature of 298.15 K by putting the value of the ratio of proton and electron ($\frac{m}{n}$) equal to 0.5 (indicating proton and electron participating in the ratio of 1:2) and 1 (indicating proton and electron participating in the ratio of 1:1), respectively. Therefore, the slope is very close to the values of 29.58 and 59.17 mV pH^{-1}, demonstrating that the proton and electron are involved in the ratio of 1:2 and 1:1 (equal number of proton and electron) during the electrochemical sensing reaction, respectively. In addition, the absence of a proton in the electrochemical reaction indicates no change in E_p with the changing pH of the supporting electrolyte.

1.3.1.4 Determination of the electrokinetic parameters for sensing target analyte

The electrokinetic parameters (number of electrons participating in the electrochemical reaction and heterogeneous reaction rate constant) are determined by recording CV at different scan rates and fixed concentration of the target analyte in the supporting electrolyte. The linear plot between the anodic peak current and square root of scan rate (I_{pa} vs. $\upsilon^{0.5}$) indicates

electrochemical reaction behaviour is diffusion control. Therefore, the Laviron equation (Eq. 1.8) is employed to determine the electrokinetic parameters of targeted analytes for the anodic peak and diffusion-controlled process (Li et al., 2019).

$$E_p = E^0 - \frac{2.303RT}{\alpha nF}\log\frac{RTk^0}{\alpha nF\upsilon_a} + \frac{2.303RT}{\alpha nF}\log\upsilon \quad (1.8)$$

Where E_p, E^0, υ, n, α, υ_a, and k^0 are the anodic peak potential (V), standard formal potential (V), scan rate (V s^{-1}), number of electrons involved in the electrochemical reaction, charge transfer coefficient, scan rate of anodic peak (V s^{-1}), and heterogeneous reaction rate constant (s^{-1}), respectively. The significance of constants F, T, and R are as aforementioned. The value of the n and k^0 is determined by equating the slope and intercept of the graph Ep vs. log υ with Eq. 1.8 by considering $\alpha = 0.5$, $\upsilon_a = 1$ V/s, when the value of E^0 is known. The value of E^0 can be investigated from the extrapolation of the graph between E_p vs. υ at scan rate zero ($\upsilon = 0$) in the origin.

1.3.1.5 Determination of LOD, LOQ, and sensitivity

The LOD, LOQ, and sensitivity of target analytes are determined by performing the CV or any other electrochemical sensing technique at the constant scan rate and different concentrations of targeted analytes in the supporting electrolyte. Eqs. 1.9 and 1.10 have been used to determine the LOD (µM) and LOQ (µM), respectively (Dash et al., 2018).

$$LOD = \frac{3S_d}{m} \quad (1.9)$$

$$LOQ = \frac{10S_d}{m} \quad (1.10)$$

Where m is the slope of the calibration curve (concentration of targeted analytes in µM vs. peak current in µA) in $\mu A \mu M^{-1}$ and S_d is the standard deviation of the blank run in µA. The sensitivity ($\mu A \mu M^{-1} cm^{-2}$) of the sensor is calculated by the ratio of the slope of the calibration curve (m) and electrochemical surface area obtained from the Randles-Sevcik equation (Eq. 1.5).

1.3.2. Linear sweep voltammetry

Linear sweep voltammetry (LSV) was first established in the 1950s by Jaroslav Heyrovský. This technique involves sweeping an applied linear potential ramp over a working electrode while simultaneously determining the resultant current. A signal creator generates a potential sweep linearly from the initial value (E_0) to the final value (E_f) at a consistent sweep rate (dE/dT), while the Potentiostat/Galvanostatic puts the potential wave to a desired working

electrode. Depending on the direction of the potential sweep, the sweep rate can be positive or negative. During the LSV, the resulting current produced from a redox event could be used to quantitatively measure the concentration of the target analytes in the electrolyte media (Aikens, 1983; Chaudhary et al., 2023). Ahmad et al. (2017) fabricated a nonenzymatic electrochemical sensor of Fe_2O_3-modified ZnO NRs/Ag for detecting nitrite using the LSV. The sensor exhibited the LOD of 0.015 µM and a sensitivity of 131.2 $\mu A \mu M^{-1} cm^{-2}$ within a concentration range of 1-1250 µM (Ahmad et al., 2017a).

1.3.3. Differential pulse voltammetry

This voltammetric technique was developed in the 1960s by Heyrovský and co-workers as a modification of the classic direct current polarography. Differential pulse voltammetry (DPV) is a highly sensitive technique that could differentiate various species and detect trace amounts of target analytes. It involves each constant potential pulse of a small amplitude (0.01 to 0.1) and the measurement of the resulting current at two points in time for each pulse. The current is assessed before and after each pulse, and the disparity between these two points is determined and graphically represented as a function of the base potential, which provides information about the sample's redox properties and the concentration of target analytes (Aikens, 1983; Wang et al., 1985). For instance, He et al. (2023) developed a PA-Cu-Co/GCE based sensor for the sensing of malathion using the DPV. The LOD of the developed sensor was found to be 0.3×10^{-6} µM in a wide concentration range of 0.5×10^{-6} to 5 µM (He et al., 2023a).

1.3.4. Square wave voltammetry

To overcome the limitations of traditional CV, which was limited in sensitive and peak separation. Square wave voltammetry (SWV) was first developed in 1966 by John L. Ramaley and William R. Krause and further improved by Oster Youngs and others (Aikens, 1983). This is a differential method which follows superimposition of a symmetrical square wave potential of constant amplitude on a base staircase potential (Fig. 1.3a) (Wang et al., 1985). In SWV, the current measurement is conducted at the end of every potential pulse. Pulses that align with the staircase ramp's direction are identified as forward pulses, whereas those oriented in the opposite direction are referred to as reverse pulses. In this technique, a graph is drawn between the mean potential of each waveform cycle and the current difference during forward and reverse cycles, resulting in a peak-shaped voltammogram (symmetric about the half-wave potential), as shown in Fig. 1.3b.

Additionally, net current is higher than the forward and reverse current. The peak potential in SWV corresponds to the formal standard potential (E_0) of the redox couple being analysed. This occurs due to the symmetry of the current function about the potential, allowing for precise determination of the peak potential and accurate measurement of the redox potential of the sample. It offers numerous advantages over alternative techniques, such as heightened sensitivity, minimal response time, decreased consumption of analytes, mitigated issues related to obstruction of the electrode's surface, and excellent peak separation, even in complex matrices, making it a valuable technique for in-situ detection and quantification of target analytes. Maji et al. (2023) developed an ultrasensitive sensor for determining glyphosate herbicides by SWV technique using FTO/rGO-H-gC_3N_4-$CuCo_2O_4$ nanocomposite. The sensor demonstrated that the LOD and sensitivity were 0.63×10^{-6} µM and 1.6×10^{-5} µAµM^{-1}, respectively. The fabricated sensor shows remarkable selectivity towards detecting other pesticides (malathion and chlorpyrifos), and practical applicability in real fruit samples (Maji et al., 2023). Malode et al. (2020) fabricated a MWCNT/Ca-ZnO/CPE based sensor for sensing carbendazim. The sensor exhibited LOD of 4.68×10^{-3} µM and LOQ of 1.75×10^{-2} µM in a wide range of 0.01 to 0.45 µM concentration. This study suggests that SWV is a better technique than DPV, LSV, and CV for detecting carbendazim in multiple samples (Malode et al., 2020).

1.3.5. Chronoamperometry

In chronoamperometry, the potential of an electrode is held constant while the current passing through the electrode is monitored as a function of time. This allows for the measurement of the rate of an electrocatalytic reaction at the electrode surface. During the experiment, a potential step is applied to the base electrode of an electrochemical cell, which causes a sudden change in the current passing through the electrode as a function of time. The current then gradually decreases as the electrochemical reaction proceeds at the electrode surface. The kinetics of electrocatalytic reactions can be determined by analysing the current-time curve. Dash et al. (2015) used this technique to determine ascorbic acid from biological entities using bio-based AgNPs immobilized on graphite paste (AgNPs/GPE) electrode. The LOD, sensitivity, and concentration range of the sensor were found to be 14.43 µM, 0.719 µAµ$M^{-1}cm^{-2}$, and 25-2000 µM, respectively (Dash et al., 2018).

1.3.6. Anodic stripping voltammetry

This is an electroanalytic technique where mercury is held toward negative potential electrode which reduce reduces the metal ions in the electrolyte media and a resulting amalgam is formed as a thin film on the electrode. After that, the analyte accumulates at the surface of the base electrode for a particular time, and electrode potential increases by re-oxidizing the electroactive species, which generates the resultant current signal. The amount of current obtained by anodic stripping voltammetry (ASV) is directly proportional to the analytes concentration in the electrolyte media (Aikens, 1983). Additionally, the resultant current also depends on the specific type of mercury electrode. Pei et al. (2014) developed a copper-based disposal sensor for electrochemical sensing of zinc in blood serum using an ASV technique. The sensor demonstrated a 0.14 μM LOD and sensitivity <1 $\mu A \mu M^{-1}$ (Pei et al., 2014).

Electrochemical sensors and their detection techniques are used to detect various analytes, including pharmaceutical drugs, heavy metals, agricultural pesticides, and their derivatives. Fig. 1.3c demonstrates the consumption (M.T.) and estimated demand (M.T.) of chemical pesticides in India during the years 2018-19 to 2023-24. The consumption of chemical pesticides gradually increased from 2018-19 to 2021-22 and slightly decreased during 2022-23, which could be due to the use of biopesticides (sustainable and eco-friendly). However, the estimated demand for chemical pesticides is higher than the consumption every year, which promotes the voluminous production of chemical pesticides in upcoming years. Fig. 1.3d illustrates the consumption of agricultural pesticides worldwide from 2015-2021. It is a fact that the used pesticides persist in the soil and water bodies for many years, increasing their concentration due to the continuous use of chemical pesticides. Therefore, emerging pesticide pollutants in the environment are essential owing to strict environmental protection acts and increased projected demand of chemical pesticides rather than consumption of pesticides due to the fast expansion of agriculture.

Similarly, pharmaceutical pollutants pose a growing environmental challenge. India, the third-largest producer of PhACs globally, has observed significant growth in its pharmaceutical sector, expanding to USD 42 billion in 2021, with projections of USD 65 billion by 2024 and USD 130 billion by 2030 (Fig. 1.3e). On a global scale, the pharmaceutical market is expected to expand from USD 1423.5 billion in 2021 to USD 2363.3 billion by 2030, a trend expected to further intensify PhACs-related pollution (Fig. 1.3f). Therefore, there is an urgent need to advance electrochemical sensing platforms to enable efficient, real-time monitoring of pesticide and pharmaceuticals pollutants in complex environmental matrices.

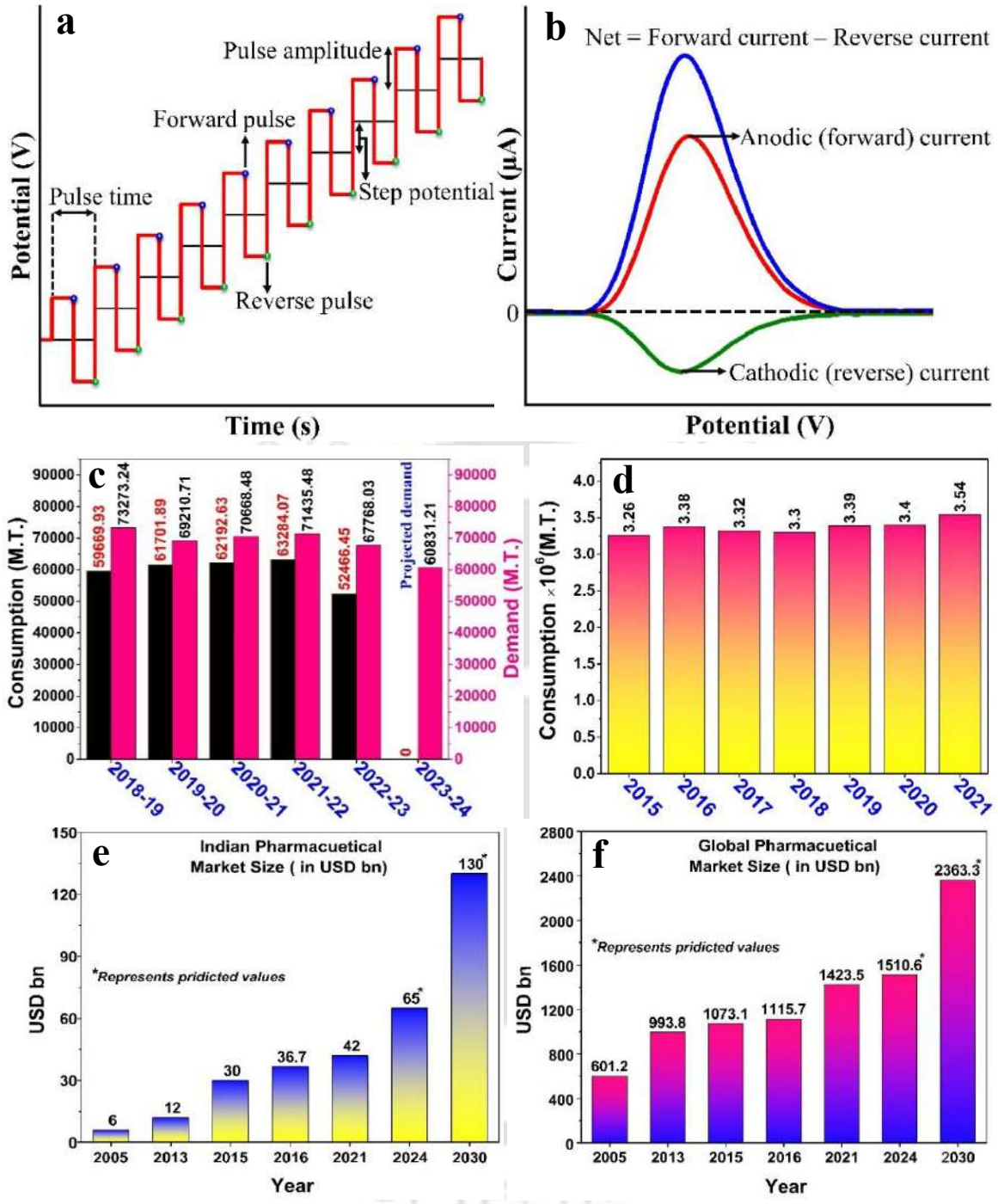

Figure 1.3: (a) Scheme of the excitation waveforms for SWV, (b) current signal in SWV (forward, reverse, and net current), resulting in the peak-shaped graph found by net current (forward current - revere current), (c) The consumption and estimated demand of chemical pesticides in India during 2018-19 to 2023-24 (Source: https://ppqs.gov.in/statistical-database), (d) The consumption of agricultural pesticides worldwide from 2015-2021 (Source: https://www.statista.com/statistics/1263077/global-pesticide-agricultural-use/), (e) Indian pharmaceuticals market revenue (in US$ billion), and (f) Global pharmaceuticals market revenue (in US$ billion) (Ravi and Golder, 2025).

1.4. Nanomaterials in improving sensing performance of organic analytes

Nanostructures have shown great potential in enhancing the sensing performance of electrochemical sensors owing to their unique physicochemical properties. The high surface area-to-volume ratio of nanostructures provides maximum docking sites per unit surface area of the functioning electrode, which could enhance the adsorption of target analytes and increase the sensitivity of the sensor. Moreover, nanostructures' optical, electrical, and magnetic properties can be adjusted by regulating their size, shape, and composition, making them highly suitable during the course of organic analytes sensing. Nanostructures can be classified based on their dimensions, for instance 0-D (quantum dots), 1-D (rods), 2-D (sheets), and 3-D (polycrystals). Finally, nanostructures can be used to enhance the stability and durability of the electrochemical sensor. The role of various types of nanostructure in the detection and determination of environmental noxious waste is briefly described in the following sections.

1.4.1. Metal nanostructures

Metal nanostructures have shown great potential as sensing platforms for detecting target analytes, including pesticides, pharmaceuticals, and heavy metal ions. Moreover, noble metal nanostructure-modified electrodes exhibited excellent electrocatalytic activity in compounds with slow redox processes and highly selectively bind the targeted analytes. Metal nanostructures merited with high catalytic activity due to their small size, resulting high surface area, which allows them to have a larger number of reactive sites and promotes faster reaction kinetics. They also exhibit unique electronic and optical properties that can be tweaked by changing their size, shape, composition, and have the potential for miniaturization into portable devices. Zahran et al. (2021) synthesized AgNPs in a chemical reduction method using natural reducing agents for instance dissolved organic matter (DOM-AgNPs), natural latex (NL-AgNPs), and mucilage (M-AgNPs). The synthesized AgNPs were immobilized on the GCE for electrocatalytic sensing of chlorpyrifos. The LOD of the DOM-AgNPs/GCE, NL-AgNPs/GCE, and M-AgNPs/GCE were 0.137, 0.087, and 4.91×10^{-5} µM within the linear range of 0.285-1.83, 0.114-1.19, and 0.114×10^{-3}-0.628×10^{-3} µM, respectively (Zahran et al., 2021). De Lima et al. (2016) fabricated chitosan stabilized AgNPs modified GCE for the sensitive electrochemical monitoring of pendimethalin and ethyl parathion pesticides in water, lettuce, and honey samples via SWV. The pendimethalin and ethyl parathion exhibited LOD of 0.036 and 0.04 µM within the working range of 0.07-2 and 0.04-8 µM, respectively (de Lima et al., 2016). Ranđelović et al. (2019) constructed an electrochemical sensor of the PtNPs-modified

multiwalled carbon nanotubes (MWCNTs) for the detection of clomazone pesticide in aqueous media by DPV. PtNPs were observed as light spots with a diameter up to 30 nm on the surface of MWCNTs. The fabricated sensor exhibited the LOD of 0.0016 µM in the concentration range of 0.0025-0.086 µM (Ranđelović et al., 2019). Özcan et al. (2021) synthesized AgNPs on fumed silica (FS@Ag) and immobilized them on the CPE to electrochemically detect the carbendazim in food and water samples. The prepared sensor demonstrated a LOD of 9.4×10^{-4} µM and a liner range of 0.05-3.0 µM (Özcan et al., 2021). Li et al. (2014) prepared PtNPs on carboxylic silica nanosheet (CSNS) and incorporated them on GCE using Nafion (binder) for sensitive determination of methyl parathion and carbaryl pesticides. The LOD of the fabricated sensor between the detection range of 1.0×10^{-6} to 1.0×10^{-2} µM were 5.52×10^{-7} and 5.65×10^{-7} µM for methyl parathion and carbaryl pesticide, respectively. The fabricated low-cost sensor showed good stability, sensitivity, and reproducibility (Li et al., 2014).

Fig. 1.5a illustrates the comparison in recent studies of the performance (LOD) of metal nanostructures for electrochemical sensing of environmental pollutants. Pt-CSNS/GCE exhibited good LOD (sensing of methyl parathion and carbaryl) in comparison to the M-AgNPs/GCE (chlorpyrifos), FS@Ag/CPE (carbendazim), Pt-MWCNT/GCE (clomazone), AgNPs/GCE (pendimethalin), AgNPs/GCE (ethyl parathion), NL-AgNPs/GCE (chlorpyrifos), and DOM-AgNPs/GCE (chlorpyrifos). Furthermore, M-AgNPs/GCE showed excellent LOD than NL-AgNPs/GCE and DOM-AgNPs/GCE for electrochemical sensing of chlorpyrifos pesticide (Fig. 1.5a).

1.4.2. Metal oxide nanostructures

Metal oxide nanostructures have gain substantial attention in the recent years owing to possessing distinctive properties and encouraging uses across various fields such as sensing, CO_2 conversion, wastewater treatment, etc. These nanostructures are synthesized using various techniques to achieve different morphological characteristics. The size, shape, stability, and high surface area of metal oxide nanostructure contribute to their remarkable properties, such as electrochemical, photochemical, electrical, and electronic. Metal oxide nanostructures such as ZnO, TiO_2, SnO_2, CuO, etc., have been successfully employed in developing electrochemical sensors for detecting environmental pollutants due to their fast electron transfer kinetics, catalytic activity, and various morphological characteristics. Further research in this area will undoubtedly yield new insights into the potential of these nanostructures and their applications. Ameen et al. (2017) synthesized cabbage-like ZnO nanostructures (C/ZnO NSs) in a hydrothermal route for in-situ detection and determination of resorcinol. The fabricated sensor

demonstrated the LOD of 5.89 µM and sensitivity of 1.98 $\mu A \mu M^{-1} cm^{-2}$ (Ameen et al., 2017). Ameen et al. (2015) synthesized hollow nanoglobules of ZnO in a sonochemical method for electrochemical sensing of piperidine using the CV technique. The sensor exhibited the LOD of 3.3 µM and a sensitivity of 0.059 $\mu A \mu M^{-1} cm^{-2}$ within 10 s of response time (Ameen et al., 2015a). Singh et al. (2015) compared the performance of ZnO and α-Fe_2O_3 nanoparticles by modifying the Au base electrode for electrochemical detection of p-Nitrophenol. The ZnO-modified Au electrode exhibited better LOD (0.8 µM) and sensitivity (16.7 $\mu A \mu M^{-1} cm^{-2}$) compared to α-Fe_2O_3 electrode (LOD of 3 µM and sensitivity of 2.06 $\mu A \mu M^{-1} cm^{-2}$) (Singh et al., 2015). Umar et al. (2008) fabricated a hydrazine electrochemical sensor using ZnO nanonails produced in a thermal evaporation technique. The sensor exhibited a sensitivity of 8.56 $\mu A \mu M^{-1} cm^{-2}$ and LOD of 0.2 µM (Umar et al., 2008). Zhao et al. (2014) fabricated a hydrazine sensor of ZnO nanowires synthesized in a hydrothermal route. The synthesized ZnO electrocatalyst was immobilized on the surface of the Au electrode by a printing-like process using Nafion as a binder. The sensor exhibited a sensitivity of 3.8 $\mu A \mu M^{-1} cm^{-2}$, LOD of 0.014 µM, and response time of 3 s within the linear concentration range of 3-562 µM (Zhao et al., 2014). Balram et al. (2020) synthesized 3D flower-like ZnO nanoparticles incorporated with functionalized MWCNTs in a sonochemical technique and modified them on screen-printed carbon electrode (SPCE) for electrochemical sensing of p-Nitrophenol. The developed sensor provided a sensitivity of 11.44 $\mu A \mu M^{-1} cm^{-2}$ and LOD of 0.013 µM in the linear concentration range of 0.06-100 µM (Balram et al., 2020). Daizy et al. (2021) prepared an electrochemical sensor of ZnO and molecularly imprinted polymer (MIP) functionalized GCE for selective detection of methyl parathion via the DPV technique. ZnO/MIP/GCE displayed a sensitivity of 0.571 $\mu A \mu M^{-1} cm^{-2}$ and LOD of 5×10^{-4} µM in the linear window of 0.005-10 µM (Daizy et al., 2021). Supraja et al. (2019) prepared a SnO_2 nanofibers-based electrochemical sensor to detect of atrazine in the water. The detection limit and sensitivity were 9.0×10^{-16} µM and 4.11 $\mu A \mu M^{-1} cm^{-2}$, respectively (Supraja et al., 2019). Khairy et al. (2018) fabricated an electrochemical sensor of NiO nanoplatelets modified screen-printed electrode for the detection of the parathion using the DPV technique. The detection limit of the parathion sensor was 0.024 µM (Khairy et al., 2018). Ganesan et al. (2023) synthesized hierarchical 3D microflowers of dysprosium vanadate ($DyVO_4$; represented as DyV) modifieds GCE (DyVMFs/GCE) for sensitive detection of organophosphate insecticide (fenitrothion), as shown in Fig. 1.4a. The developed sensor exhibited a LOD of 0.0014 µM and a sensitivity of 14.2 $\mu A \mu M^{-1} cm^{-2}$ with ~99 % recover in real samples including tomato (Fig. 1.4b), grapefruit (Fig. 1.4c), paddy grain (Fig. 1.4d), and potato (Fig. 1.4e) (Ganesan et al., 2023).

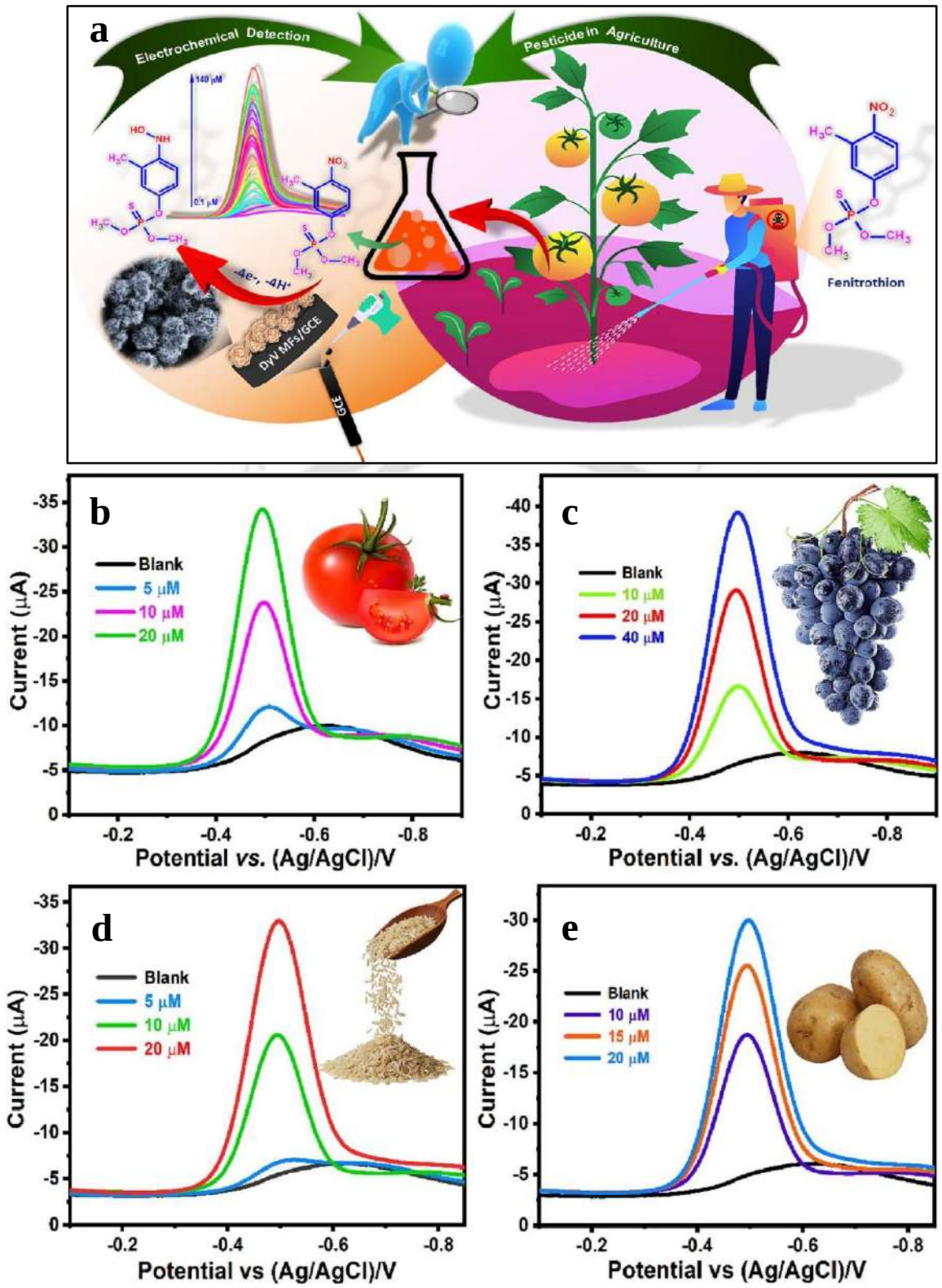

Figure 1.4: (a) Schematic illustration of electrochemical sensing of organophosphate insecticide (fenitrothion) using dysprosium vanadate ($DyVO_4$) modifieds GCE (DyVMFs/GCE), (b), (c), (d), and (e) are the DPV of fenitrothion insecticide spiked in tomato, grapefruit, paddy grain, and potato, respectively. Fig. 1.4 reprinted with permission from ref (Ganesan et al., 2023) (copyright 2023 Elsevier).

Fig. 1.5b demonstrates the noteworthy recent studies based on two essential sensing parameters i.e., LOD and sensitivity, of metal oxide nanostructures for the sensing of organic analytes. ZnO/MIP/GCE and ZnO/GCE exhibited excellent LOD and sensitivity for electrocatalytic sensing of methyl parathion and piperidine than the other reported sensors of various analytes, respectively. Furthermore, the ZnO/SPCE electrode illustrated better LOD in comparison to the ZnO/Au and α-Fe_2O_3/Au electrodes for electrochemical detection of p-Nitrophenol (Fig. 1.5b). Therefore, SPCE-functionalized metal oxide nanostructures revealed better sensing performance for electrochemical sensing of p-Nitrophenol than the Au-functionalized metal oxide nanostructures.

1.4.3. Metal sulphide nanostructures

Metal sulphide nanostructures are usually tiny particles made up of metal and sulphur atoms with exceptional characteristics (chemical and physical) owing to their size and shape, resulting in tailored to selectively detect specific analytes. The electrochemical sensing mechanism of metal sulphide nanostructures is based on the changes in the material's electrical characteristics upon exposure to the target analyte. These nanostructures have a variety of potential utilizations, for instance sensing, energy storage, and catalysis. Duan et al. (2019) constructed the $NiCo_2S_4$ modified GCE ($NiCo_2S_4$/GCE) based sensor for hydrazine detection. The sensor showed the LOD of 0.6 µM and a sensitivity of 0.179 $\mu A \mu M^{-1} cm^{-2}$. The practical utilization was found in tap water with a maximum recovery of 103.6% and relative standard deviation (RSD) of ~2.10-3.0% (Duan et al., 2019). Alshahrani et al. (2019) developed a sensor of CuS decorated carbon nanofragments (CuS-CNF) functionalized GCE for sensitive detection of hydroquinone and catechol. The sensor showed LOD of 0.293 µM (sensitivity 0.184 $\mu A \mu M^{-1} cm^{-2}$) and 0.259 µM (sensitivity 0.208 $\mu A \mu M^{-1} cm^{-2}$) for hydroquinone and catechol, respectively (Alshahrani et al., 2019). Rana et al. (2022) synthesized MoS_2 nanoparticles modified on the Au electrode's surface for hydrazine sensing. The sensor demonstrated sensitivity and LOD of 5.71 $\mu A \mu M^{-1} cm^{-2}$ and 0.196 µM, respectively (Rana et al., 2022). Liu et al. (2016) fabricated a Ni_3S_2 layer on the Ni (Ni_3S_2@Ni) foam-based 3D electrode for sensing of hydrazine. The presented electrode showed a sensitivity of 14.67 $\mu A \mu M^{-1} cm^{-2}$and LOD of 0.045 µM in the liner working range of 1-300 µM (Liu et al., 2016). Naik et al. (2021) developed an electrochemical sensor of ZnS/Au/MWCNT for sensitive detection of p-Nitrophenol using the LSV technique. The sensor exhibited a sensitivity of 0.808 $\mu A \mu M^{-1} cm^{-2}$, LOD of 0.03 µM and linear dynamic range of 10-150 µM (Naik et al., 2021). Shanmugam et al. (2022) developed SnS_2 anchored on the sulphur-doped graphitic carbon

nitride (SGCN) in an ultrasonic dispersion technique for electrochemical sensing of carbendazim in environmental matrices via DPV. The sensor exemplified the sensitivity of 0.137 $\mu A \mu M^{-1} cm^{-2}$, LOD of 0.03 µM, and linear response of 0.002-416 µM (Shanmugam et al., 2022). Mariyappan et al. (2021) fabricated an electrochemical sensor of Gd_2S_3 and rGO-functionalized GCE for sensing carbofuran in food and environment samples. The fabricated sensor exhibited LOD, sensitivity and linear dynamic range of 0.013 µM, 1.546 $\mu A \mu M^{-1} cm^{-2}$ and 0.001-1381 µM, respectively (Mariyappan et al., 2021). Selvi et al. (2023) developed an electrochemical sensor of polydopamine (PDA) functionalized WS_2 nanostructures in a co-precipitation method for sensitive determination of paraoxon ethyl pesticide. The developed electrochemical sensor exhibited 0.002 µM LOD and 0.31 sensitivity $\mu A \mu M^{-1} cm^{-2}$ (Selvi et al., 2023). He et al. (2020) formed nanoneedle arrays of $NiCo_2S_4$ on graphite carbon nanofiber film by a two-step hydrothermal route for selective detection of pyrimethanil fungicide. The electrochemical sensor displayed 0.02 µM LOD in the concentration range of 0.06-800 µM (He et al., 2020). Vilian et al. (2022) developed a reflux approach to prepare Mn-doped ZnS microspheres for the determination of carbendazim. The sensor displayed 3×10^{-5} µM LOD and 1.34 $\mu A \mu M^{-1} cm^{-2}$ sensitivity in the concentration range of 0.005-0.12 µM (Ezhil Vilian et al., 2022).

The LOD and sensitivity of metal sulphide nanostructures-based electrocatalytic sensors for sensing of agricultural pesticides and their derivatives are demonstrated in Fig. 1.5c. WS_2/PDA/SPCE (sensing of paraoxon ethyl) and SnS_2/SGCN/SPCE (sensing of carbendazim) electrode showed excellent LOD and sensitivity than the other reported electrodes of various analytes (Fig. 1.5c). Additionally, SPCE modified metal sulphide nanostructures exhibited better sensing performance in comparison to the GCE, Ni foam, and Au modified metal sulphide nanostructures.

1.4.4. Carbon materials

Carbon is the utmost fascinating element present on earth that captured attention due to its unique properties and versatility. Its ability to form various types of hybridization states (sp, sp^2, and sp^3) allows it to create a vast range of allotropes from graphite (soft material) to diamond (hard material) with potential applications. Recently, carbon-based nanostructures, such as graphene, graphene oxide (GO), reduced graphene oxide (rGO), and single and multiwalled carbon nanotubes (SWCNTs and MWCNTs) have been prepared, which expanded much consideration due to exceptional electronic, magnetic, optical, and physical characteristics. Overall, the excellent electrical conductivity, high surface area, and

biocompatibility of carbon-based nanomaterials make them promising candidates for a wide range of electrochemical sensing applications, and ongoing research in this field is expected to yield new and exciting discoveries in the coming years. Tanwar et al. (2023) formed graphene quantum dots (GQDs) via a hydrothermal route for sensitive detection of malathion by drop-casting GQDs on the GCE. The developed sensor demonstrated a LOD of 6.2×10^{-4} µM in the concentration range of 1-30 µM (Tanwar et al., 2023). Musameh et al. (2013) prepared carbon nanotube-modified GCE for ultrasensitive sensing of methyl parathion in aqueous solutions. The LOD of the developed sensor was estimated to be 0.001 µM (Musameh et al., 2013). Urbanová et al. (2017) developed GO-modified GCE for electrochemical sensing of thiamethoxam and imidacloprid insecticides. The proposed sensor exhibited LOD (between the linear dynamic response of 10-200 µM) for thiamethoxam and imidacloprid were 8.3 and 7.9 µM, respectively (Urbanová et al., 2017). Hu et al. (2023) studied the electrocatalytic behaviour of cellulose (C)/rGO/carbon fiber paper electrode (CFPE) towards ultra-selective determination of amitrole. The proposed sensor demonstrated the LOD of 0.244 µM between the linear dynamic response of 5-30 µM. Additionally, The RSD of repeatability and stability were 3.74 and 4.68%, respectively (Hu et al., 2023). Salehzadeh et al. (2016) fabricated an electrochemical sensor of MWCNTs modified GCE for simultaneously sensing fenitrothion and bifenox. The sensor showed a LOD of 0.08 µM and a concentration range of 0.2-60 µM for both pesticides, including fenitrothion and bifenox (Salehzadeh et al., 2016). Kulandaiswamy et al. (2019) developed S, N-doped graphene quantum dots (GQD) for electrocatalytic sensing of monocrotophos in water bodies. The proposed sensor exhibited a LOD of 0.025 µM and LOQ of 0.083 µM (Kulandaiswamy et al., 2020). Ilager et al. (2022) developed 2D graphene oxide sheets modified GCE for electrocatalytic sensing of carbendazim. The sensor revealed a LOD of 0.014 µM between the concentration range of 0.1-2500 µM (Ilager et al., 2022). Dash et al. (2021) prepared carbon dots (CDs) using *Psidium guajava* leaves waste via a hydrothermal route for electrocatalytic detection of chlorpyrifos by SWV technique. The proposed sensor exhibited a LOD of 0.0015 µM and a sensitivity of 1.30×10^{-3} $\mu A \mu M^{-1} cm^{-2}$ in the linear concentration range of 0.01-1 µM (Dash et al., 2022).

Fig. 1.5d shows the comparison of carbon materials-based sensors for the monitoring of agricultural pesticides. CDs/GCE demonstrated excellent LOD for electrocatalytic sensing of chlorpyrifos in comparison to the other reported sensors of different analytes, as illustrated in Fig. 1.5d. Moreover, CPE-rGO/B showed better LOD than GO/GCE and CTAB-rGO/SPCE for in-situ detection and determination of carbendazim.

1.4.5. Nanocomposites

The nanocomposite-based electrochemical sensors for environmental pollutants detection have gain significant attention in the recent years due to the synergistic effect of all metals, which results in enhanced sensing performance compared to sensors made of individual components. Nanocomposite merited with increased surface area, reactivity, and synergistic effect which allow faster and more efficient sensing of target analytes with high sensitivity and selectivity. Numerous studies have investigated the use of nanocomposites in the monitoring of environmental noxious waste. Kalia et al. (2024) presented a MoS2-rGO/Fe3O4 nanocomposite sensor in a microwave route for in-situ detection and determination of p-Nitrophenol via CV and DPV. The as prepared sensor illustrated the LOD of 0.8 µM and a sensitivity of 0.71 $\mu A \mu M^{-1} cm^{-2}$. The practical utilization was also investigated in DI, tap, and river water (Kalia et al., 2024). Trang et al. (2023) studied the effect of particle size and crystallinity of biogenic (Bio)-Ag/ZnO nanocomposite on the electrocatalytic determination of carbaryl. The proposed carbaryl sensor displayed a sensitivity of 0.03 $\mu A \mu M^{-1} cm^{-2}$ with a LOD of 0.27 µM between the concentration range of 0.25-100 µM (Le Nhat Trang et al., 2023). Disouza et al. (2023) synthesized ZnS/SnS_2/rGO heterostructure in a hydrothermal route, resulting provided a large electroactive surface area, more active sites, and a fast electron transfer rate. The fabricated sensor showed the LOD of 0.02 µM, sensitivity of 0.21 $\mu A \mu M^{-1} cm^{-2}$ and wide dynamic response of 0.01-2359 µM towards electrochemical sensing of maleic hydrazide in samples of water and potato (Disouza et al., 2023). Velmurugan et al. (2023) prepared a heterojunction of tungsten oxynitride (WON) and CuO via impregnation technique for electrochemical sensing of diuron herbicide. The sensitivity, LOD, and wide detection range of the proposed diuron sensor were 0.45 $\mu A \mu M^{-1} cm^{-2}$, 0.006 µM, and 0.01-764.4 µM, respectively (Velmurugan et al., 2023). Prathap et al. (2015) prepared a sensor of the nano-microstructure of CuO-MnO_2 for the sensing of lindane. The sensor exhibited LOD of 0.005 µM and a sensitivity of 0.12 $\mu A \mu M^{-1} cm^{-2}$ (Anu Prathap et al., 2015). Arumugam et al. (2023) constructed a nanocomposite of CeO_2 nanoparticles modified rGO (CeO_2 NPs/rGO) for electrochemical sensing of profenofos insecticide. The sensor provided the sensitivity of 2.63 $\mu A \mu M^{-1} cm^{-2}$ and LOD of 0.004 µM within the linear dynamic range of 0.01-170 µM (Arumugam et al., 2023). Alagarsamy et al. (2023) fabricated cerium molybdate covered boron doped (CMO/B) rGO modified GCE for ultrasensitive carbofuran pesticides sensing. The sensor displayed a LOD of 0.002 µM and a sensitivity of 4.06 $\mu A \mu M^{-1} cm^{-2}$ within the concentration range of 0.01-365 µM (Alagarsamy et al., 2023). Manavalan et al. (2020) formed a composite of ZnO nanostar and GO by the two-step microwave method. Subsequently,

nanocomposite functionalized on the SPCE for electrochemical sensing of methyl parathion. The fabricated sensor demonstrated the LOD of 0.0012 µM and a sensitivity of 16.5 $\mu A \mu M^{-1} cm^{-2}$ within the detection window of 0.03-670 µM (Manavalan et al., 2020). Lai et al. (2023) presented a Ce-MOF/MWCNTs/ZnO/GCE based sensor to determine carbendazim. The fabricated sensor exhibited a LOD of 0.013 µM (Lai et al., 2023). Kokulnathan et al. (2021) proposed the nanocomposite sensor of bismuth oxide/boron nitride (Bi_2O_3/h-BN) for flutamide monitoring. The sensor exhibited a LOD of 0.009 µM within a wide linear range of 0.04-87 µM (Kokulnathan et al., 2021).

Fig. 1.5e illustrates the sensing performance-based comparison in recent studies of nanocomposite for electrocatalytic sensing of organic analytes. In comparison to other nanocomposite-based electrodes for sensing of target analytes, ZnO/GO/SPCE and bio-Ag/ZnO NCs electrodes exhibited excellent LOD and sensitivity for electrochemical sensing of methyl parathion and carbaryl, respectively (Fig. 1.5e).

1.4.6. Green synthesized nanostructures

Green synthesized nanostructures have emerged as a promising alternate to conventionally synthesized nanoparticles for electrochemical sensing of environmental contaminats owing to their sustainability, low cost, non-toxicity and biocompatibility. Green synthesis involves the use of natural materials such as plant extracts, enzymes, bacteria, or fungi to reduce metal ions and form nanostructures, resulting in highly monodisperse nanostructures with well-defined shapes and sizes, which can enhance the electrochemical response. Kumar et al. (2017) synthesized MnO nanoparticles using *Syzygium aromaticum* (clove) extract. Subsequently, MnO nanoparticles were modified on the Au base electrode's surface with butyl carbitol acetate (BCA) in the ratio of 20:80 (BCA:MnO) for p-Nitrophenol monitoring. The proposed MnO/BCA/Au electrode exhibited the LOD of 15.65 µM and the sensitivity of 0.16 $\mu A \mu M^{-1} cm^{-2}$ (Kumar et al., 2017). Karuppiah et al. (2015) prepared bio-based AgNPs (by *Justicia glauca* leaf extract) functionalized rGO for the sensitive determination of nitrobenzene in wastewater. The AgNPs/rGO/GCE showed the LOD of 0.261 µM and a sensitivity of 0.84 $\mu A \mu M^{-1} cm^{-2}$ (Karuppiah et al., 2015). Shivakumar et al. (2020) prepared bio-based AgNPs by using *Eucalyptus* extract and modified them on the surface of GCE for sensing nitrobenzene by CV and DPV techniques. The AgNPs/GCE demonstrated a sensitivity of 2.26 $\mu A \mu M^{-1} cm^{-2}$ and LOD of 0.027 µM (between a linear range of 5-40 µM) (Shivakumar et al., 2020). Balasubramanian et al. (2018) synthesized AuNPs using tannic acid (TA) and immobilized on the GCE surface to detect the methyl parathion pesticides.

AuNPs/TA/GCE displayed the LOD of 0.011 µM, a sensitivity of 2.84 $\mu A \mu M^{-1} cm^{-2}$, and a linear working range of 0.033-167.7 µM (Balasubramanian et al., 2018a). Rajiv et al. (2022) prepared biogenic spherical Fe_3O_4 nanoparticles (size 34 nm) using *Artocarpus heterophyllus* seed extract. Further, synthesized Fe_3O_4 nanoparticles were modified on the surface of magnetic GCE for sensing carbofuran using CV and DPV technique in vegetable samples, compared with HPLC. Fe_3O_4/GCE showed the LOD of 0.01 µM in the linear dynamic range of 0.3-38.5 µM with a sensitivity of 6.53 $\mu A \mu M^{-1} cm^{-2}$ (Rajiv et al., 2022). Karthik et al. (2016) synthesized PtNPs using bio-extract of *Quercus glauca* leaves and modified on the GCE to examine electrocatalytic activity towards hydrazine in environmental samples via amperometric and CV technique. The as prepared PtNPs were spherical in morphology and 5-15 nm in size range. The proposed sensor showed LOD, sensitivity, and wide linear response of 0.007 µM, 1.7 $\mu A \mu M^{-1} cm^{-2}$, and 0.01-283 µM, respectively (Karthik et al., 2016). Abbas et al. (2019) synthesized green C@Cu nanoparticles in 3D pyramidal shape (C@3DPY/Cu) via a freeze-drying and carbonization method for simultaneous detection of phenolic pollutants including catechol, cresol, and p-Nitrophenol. The sensitivity of the catechol, cresol, and p-Nitrophenol were 0.08 (0.0041 µM), 0.07 (0.0038 µM), and 0.07 $\mu A \mu M^{-1} cm^{-2}$ (0.0019 µM), respectively (Abbas et al., 2019). Taqvi et al. (2022) synthesized $NiFe_2O_4$ nanoparticles via the green route using bio-extract of *Ixora coccinea* plant leaves. Subsequently, green synthesized $NiFe_2O_4$ nanoparticles were modified on the GCE ($NiFe_2O_4$/GCE) using Nafion as a binder for sensitive determination of pentachlorophenol. The green sensor exhibited LOD, LOQ, and linear working range of 0.0016, 0.005, and 0.01-90 µM, respectively (Taqvi et al., 2022). Puthalapattu et al. (2023) synthesized Fe_2O_3-CuO nanocomposite in a green route using Tulsi leaf extract. Subsequently, the prepared nanocomposite was immobilized on the GCE surface using Nafion for electrochemical sensing of amiprofos methyl herbicide in the soil and industrial waste. The developed sensor showed a LOD of 0.0214 µM (Puthalapattu et al., 2023).

Fig. 1.5f displays the important recent studies of green electrocatalysts of the LOD and sensitivity of electrochemical sensors for the detection of environmental noxious waste. C@3DPY/Cu demonstrates better LOD and sensitivity (sensing of p-Nitrophenol, cresol, and catechol) in comparison to the PtNPs/GCE (hydrazine), Fe_3O_4/GCE (carbofuran), AuNPs/TA/GCE (methyl parathion), AgNPs/GCE (nitrobenzene), AgNPs/rGO/GCE (nitrobenzene), and MnO/BCA/Au (p-Nitrophenol). In addition, AgNPs/GCE exhibited good LOD than AgNPs/rGO/GCE for electrochemical sensing of nitrobenzene, as shown in Fig. 1.5f.

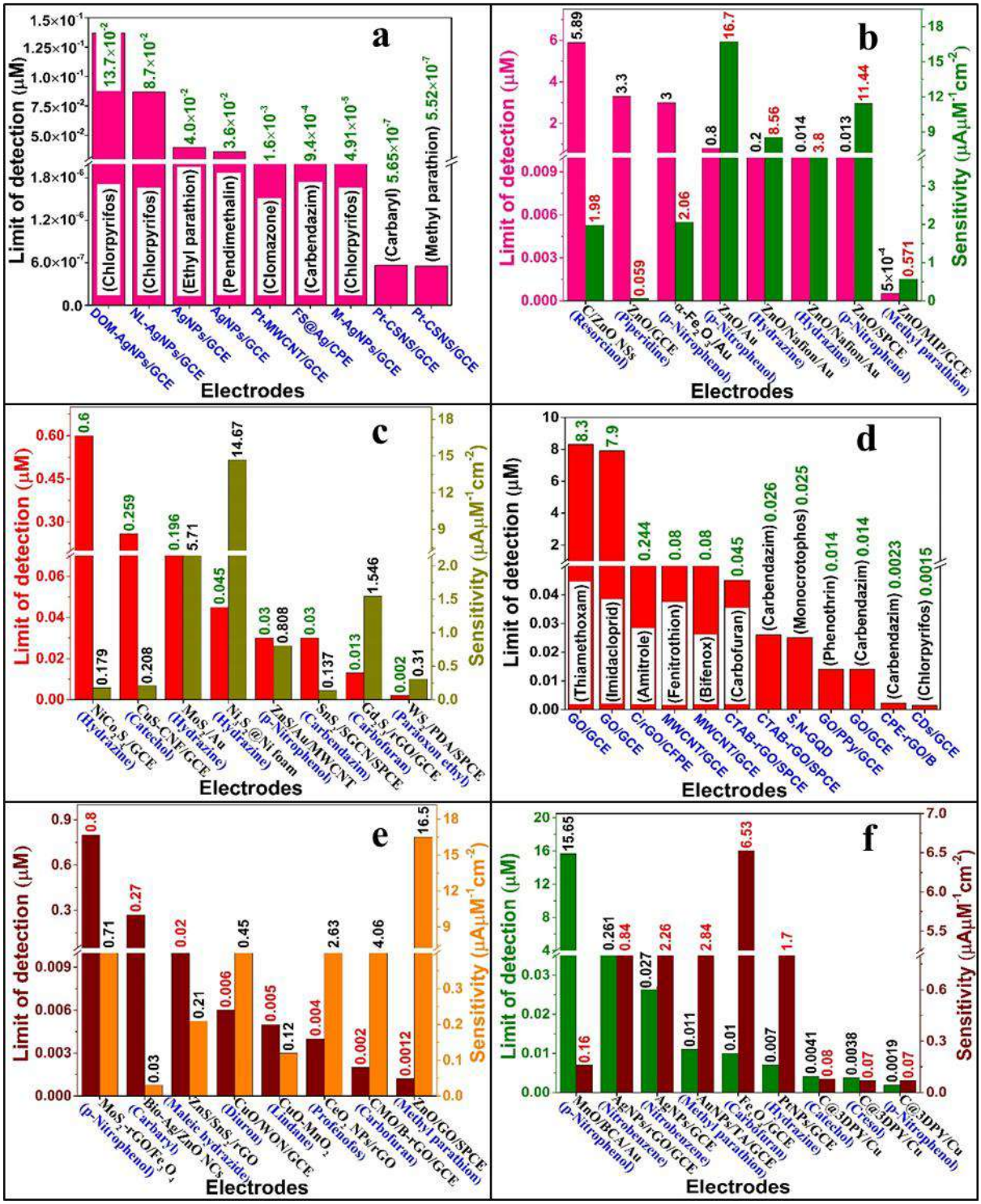

Figure 1.5: Sensing performance of (a) metal, (b) metal oxide, (c) metal sulphide, (d) carbon materials, (e) nanocomposites, and (f) green synthesized nanostructure-based electrodes for electrocatalytic sensing of agricultural pesticides and their intermediates. The analytes used in sensing studies are inserted in the round bracket of Figures (Figs. 1.5a and 1.5d) and x-axis labelling (Figs. 1.5b, 1.5c, 1.5e, and 1.5f) (Abbas et al., 2019; Akkarachanchainon et al., 2017; Alagarsamy et al., 2023; Alshahrani et al., 2019; Ameen et al., 2017, 2015a; Anu Prathap et

al., 2015; Arumugam et al., 2023; Balasubramanian et al., 2018a; Balram et al., 2020; Daizy et al., 2021; Dash et al., 2022; de Lima et al., 2016; Disouza et al., 2023; Duan et al., 2019; Hu et al., 2023; Ilager et al., 2022; Kalia et al., 2024; Karthik et al., 2016; Karuppiah et al., 2015; Kulandaiswamy et al., 2020; Kumar et al., 2017; Le Nhat Trang et al., 2023; Li et al., 2014; Liu et al., 2016; Manavalan et al., 2020; Mariyappan et al., 2021; Naik et al., 2021; Özcan et al., 2021; Rajiv et al., 2022; Rana et al., 2022; Ranđelović et al., 2019; Salehzadeh et al., 2016; Sant'Anna et al., 2020; Selvi et al., 2023; Shanmugam et al., 2022; Shivakumar et al., 2020; Singh et al., 2015; Tefera et al., 2018; Umar et al., 2008; Urbanová et al., 2017; Velmurugan et al., 2023; Zahran et al., 2021; Zhao et al., 2014).

Table 1.1 shows the synthesis methods and morphology of diverse nanostructures and their utilization in the electrochemical sensing of organic analytes using various electrochemical sensing techniques. In a nutshell, metal oxide-based (GCE/SnO_2/MPA/EDC-NHS/antibody) electrochemical sensor for sensing of atrazine exhibited the lowest LOD of 9.0×10^{-16} µM between the linear working range of 10^{-15}-1 µM than the other nanostructures-based sensor. Additionally, CDs/GCE demonstrated excellent sensitivity (1.30×10^{-3} $\mu A \mu M^{-1} cm^{-2}$ in the wide concentration range of 0.01-1 µM) for electrocatalytic sensing of chlorpyrifos by SWV technique in comparison to the other reported nanostructures-based sensors of different analytes (Table 1.1).

Table 1.1: Performance of nanostructure-based electrochemical sensor for detecting environmental noxious waste.

Electrodes	Morphology	Analytes	LOD (μM)	References
DOM-AgNPs/GCE	Spherical	Chlorpyrifos	0.137	Zahran et al., 2021
NL-AgNPs/GCE			0.087	
M-AgNPs/GCE			4.91×10^{-5}	
AgNPs/GCE	-	Pendimethalin	0.036	de Lima et al., 2016
		Ethyl parathion	0.04	
Pt-MWCNT/GCE	-	Clomazone	0.0016	Ranđelović et al., 2019
FS@Ag/CPE	Nanofiber	Carbendazim	9.4×10^{-4}	Özcan et al., 2021
Pt-CSNS/GCE	Sheet	Methyl parathion	5.52×10^{-7}	Li et al., 2014
		Carbaryl	5.65×10^{-7}	
C/ZnO NSs	Cabbage-like	Resorcinol	5.89	Ameen et al., 2017
ZnO/GCE	Hollow nanoglobules	Piperidine	3.3	Ameen et al., 2015a
ZnO/Au	-	p-Nitrophenol	0.8	Singh et al., 2015
α-Fe_2O_3/Au	-		3	
ZnO/Nafion/Au	Nanonails	Hydrazine	0.2	Umar et al., 2008
ZnO/Nafion/Au	Nanowires	Hydrazine	0.014	Zhao et al., 2014
ZnO/SPCE	3D flower-like	p-Nitrophenol	0.013	Balram et al., 2020
ZnO/MIP/GCE	Hollow spheres	Methyl parathion	5×10^{-4}	Daizy et al., 2021
GCE/SnO_2/MPA/EDC-NHS/Antibody	Nanofibers	Atrazine	9.0×10^{-16}	Supraja et al., 2019
NiO-SPEs	Nanoplatelets	Parathion	0.024	Khairy et al., 2018
DyVMFs/GCE	3D microflowers	Fenitrothion	0.0014	Ganesan et al., 2023
$NiCo_2S_4$/GCE	Porous sphere	Hydrazine	0.6	Duan et al., 2019
CuS-CNF/GCE	Nanoflake	Hydroquinone	0.293	Alshahrani et al., 2019
		Catechol	0.259	
MoS_2/Au	Flat sheet	Hydrazine	0.196	Rana et al., 2022
Ni_3S_2@Ni foam	Foam-like porous structure	Hydrazine	0.045	Liu et al., 2016
ZnS/Au/MWCNT	Nanospheres	p-Nitrophenol	0.03	Naik et al., 2021

SnS_2/SGCN/SPCE	Nano hexagons	Carbendazim	0.03	Shanmugam et al., 2022
Gd_2S_3/rGO/GCE	Rods	Carbofuran	0.013	Mariyappan et al., 2021
WS_2/PDA/SPCE	Nanosphere	Paraoxon ethyl	0.002	Selvi et al., 2023
$NiCo_2S_4$/GCNF	Nanoneedles	Pyrimethanil	0.02	He et al., 2020
Mn-doped ZnS	Microspheres	Carbendazim	3×10^{-5}	Ezhil Vilian et al., 2022
GQDs/GCE	Quantum dots	Malathion	6.2×10^{-4}	Tanwar et al., 2023
30 CNT/GCE	Nanotubes	Methyl parathion	0.001	Musameh et al., 2013
GO/GCE	Sheets	Thiamethoxam	8.3	Urbanová et al., 2017
		Imidacloprid	7.9	
C/rGO/CFPE	-	Amitrole	0.244	Hu et al., 2023
MWCNT/GCE	Nanotubes	Fenitrothion	0.08	Salehzadeh et al., 2016
		Bifenox		
S,N-GQD	Dots	Monocrotophos	0.025	Kulandaiswamy et al., 2020
GO/GCE	2D sheets	Carbendazim	0.014	Ilager et al., 2022
CDs/GCE	Dots	Chlorpyrifos	0.0015	Dash et al., 2022
CTAB-rGO/SPCE	Sheet-like	Carbofuran	0.045	Akkarachanchainon et al., 2017
		Carbendazim	0.026	
GO/PPy/GCE	Sheets	Phenothrin	0.014	Tefera et al., 2018
CPE-rGO/B	-	Carbendazim	0.0023	Sant'Anna et al., 2020
MoS_2-rGO/Fe_3O_4	Sheet-like	p-Nitrophenol	0.8	Kalia et al., 2024
ZnS/SnS_2/rGO	Spherical	Maleic hydrazide	0.02	Disouza et al., 2023
CuO/WON/GCE	Flowers	Diuron	0.006	Velmurugan et al., 2023
CuO-MnO_2	Flowers	Lindane	0.005	Anu Prathap et al., 2015
CeO_2 NPs/rGO	Rock like	Profenofos	0.004	Arumugam et al., 2023
CMO/B-rGO/GCE	-	Carbofuran	0.002	Alagarsamy et al., 2023
ZnO/GO/SPCE	3D nanostar	Methyl parathion	0.0012	Manavalan et al., 2020
Ce-MOF/MWCNTs/ZnO/GCE	Nanospheres	Carbendazim	0.013	Lai et al., 2023
Bi_2O_3/h-BN	Nanorods	Flutamide	0.009	Kokulnathan et al., 2021

MnO/BCA/Au	-	p-Nitrophenol	15.65	Kumar et al., 2017
AgNPs/rGO/GCE	Spherical	Nitrobenzene	0.261	Karuppiah et al., 2015
AgNPs/GCE		Nitrobenzene	0.027	Shivakumar et al., 2020
AuNPs/TA/GCE	Spherical	Methyl parathion	0.011	Balasubramanian et al., 2018a
Fe_3O_4/GCE	Spherical	Carbofuran	0.01	Rajiv et al., 2022
$NiFe_2O_4$/GCE	-	Pentachlorophenol	0.0016	Taqvi et al., 2022
PtNPs/GCE	Spherical	Hydrazine	0.007	Karthik et al., 2016
C@3DPY/Cu	3D pyramidal	Catechol	0.0041	Abbas et al., 2019
		Cresol	0.0038	
		p-Nitrophenol	0.0019	
Fe_2O_3-CuO/GCE	Spherical	Amiprofos methyl	0.0214	Puthalapattu et al., 2023
CuO NRs	Nanorods	Methyl Parathion	0.000289	Sakdarat et al., 2019
Nafion/CuO NWs-SWCNTs/GCE	Nanowires	Malathion	0.0003	Huo et al., 2014
Algal/SiO2-ZnO QDs/TEOS/ITO	Spherical	Acephate	10^{-6}	Pabbi and Mittal, 2017
Bi_2O_3/PGE	Pea-like	Diuron	0.0006	Annu et al., 2020
SnO_2 NPs-CGR-NF	-	Methyl parathion	5×10^{-8}	Zhou et al., 2013
		Carbofuran	5×10^{-7}	
NiO/GCE	-	Endosulfan	0.00017	Bakhsh et al., 2021b
NiO/GCE	Nanoseeds	Bentazone	0.0012	Bakhsh et al., 2021a
3D MoS_2NTs/GCE	3D nanotubes	Diethofencarb	1.197	Sinha et al., 2019
			2.356	
CuO-TiO_2 modified GCE	-	Methyl parathion	0.00459	Tian et al., 2018
AgNPs/GCE	Spherical	Ciprofloxacin	0.048	Meireles et al., 2024
CTN-Fe_3O_4/g-C_3N_4	-	Phenylbutazone	0.0013	Megalamani et al., 2023
g-C_3N_4/ZnO/GCE	Rod	Sulfamethoxazole	0.0066	Balasubramanian et al., 2018b

1.5. Methodology affecting functionality of nanostructured materials for organic analytes sensing

1.5.1. Hydrothermal method

The hydrothermal method is a simple and effective technique for the synthesis of high-quality metal oxide/sulphide nanostructure with controlled size and morphological characteristics. This process involves the use of an autoclave, which is a high-pressure vessel that can sustain a temperature and pressure differential across its length. In this technique, a precursor solution is heated with solvent (water) in the autoclave to a temperature above the boiling point of water under high pressure. This results in the formation of a supercritical fluid that can dissolve the precursors and promote the growth of nanostructures. The temperature gradient across the length of the autoclave is crucial in tuning the morphology and size of the nanostructures. This process can be difficult to prevent the formation of agglomerates or unwanted phases. This technique can synthesise single and multicomponent (heterojunction) metal oxide/sulphide nanostructures with high purity. The formation of VANs by the hydrothermal route is depicted in Fig. 1.8a. Haritha et al. (2023) utilized a facile hydrothermal route synthesized WS_2 nanosheets at 265 °C for 24 h. Afterwards, nanosheets of WS_2 were embedded on the GCE using Nafion (binder) for electrochemical monitoring of imidacloprid insecticide. The fabricated sensor exhibited the LOD of 0.28 µM and a sensitivity of 3.98 $\mu A \mu M^{-1} cm^{-2}$ (Haritha et al., 2023). Ahmad and Kim (2023) prepared MoS_2 flower-shaped nanostructures via a hydrothermal route for utilization in solar cell and p-Chlorophenol sensing. The MoS_2-based sensor showed a LOD of 0.39 µM and a sensitivity of 11.47 $\mu A \mu M^{-1} cm^{-2}$ (Ahmad and Kim, 2023).

Kokulnathan et al. (2023) developed a binder free electrochemical sensor of ZnO nanograins grown onto the carbon cloth in a hydrothermal method (90 °C for 3 h) for the determination of hydroxychloroquine. The LOD and sensitivity of the sensor were 0.09 µM and 0.279 $\mu A \mu M^{-1} cm^{-2}$, respectively (Kokulnathan et al., 2023). Khizir and Abbas (2021) formed VANs of TiO_2 on the FTO glass for biochemical sensing. The fabricated VANs demonstrate flower-shaped morphology with average diameter and depth of 25.48 nm and 22 µm, respectively (Khizir and Abbas, 2021). Cao et al. (2011) fabricated TiO_2 nanorods directly on the FTO glass substrate using a hydrothermal process for the application in UV sensors. This study showed that the length, diameter, and density could be changed with temperature, time, and initial reactant concentration. At optimum conditions (150 °C & 4 h), the nanorods exhibited a length of 6 µm with a diameter of 40-60 nm (Cao et al., 2011). FESEM images of

vertically aligned TiO_2 nanostructures on the FTO substrate at different precursor (titanium butoxide) concentrations, time, and temperature are illustrated in Figs. 1.6a-1.6h and EDX image of optimized TiO_2 nanostructures (4 % (v/v), 24 h, 150 °C) is shown in Fig. 1.6i. Abdelfatah and El-Shaer (2018) synthesized a vertically aligned submicron ZnO rod array on FTO glass via a hydrothermal technique using different mass concentrations of KOH. This study demonstrates that the diameter of a rod array depends on the mass concentration of KOH, and a small diameter ZnO rod array is more suitable in electronic photo applications (Abdelfatah and El-Shaer, 2018). Zhang et al. (2018) synthesized vertically aligned SnO_2 nanorod arrays onto the FTO glass in an acidic medium by the hydrothermal method for reaching high-performance perovskite solar cells (Zhang et al., 2018). Tang et al. (2016) incorporated vertically aligned Bi_2S_3 platelets onto the FTO glass substrate via the hydrothermal method. The synthesized platelets exhibited a length of 5 µm with a thickness range of 50 to 100 nm (Tang et al., 2016). Zheng et al. (2013) studied the effect of growth conditions (pH, time, temperature) of WO_3 nanorods over the ITO glass in a hydrothermal method. At optimal conditions (pH 2.4, 170 ° C, & 5 h), the prepared nanorods showed an average diameter of 70 nm, length of 0.9 µm, and density of 4.1 × 109 rods/cm^2 (Zheng et al., 2013). Jiang et al. (2017) synthesized a 2D vertically aligned MoS_2/WS_2 nanosheet (thickness 2-10 nm) on the ITO glass via a facile hydrothermal process (Jiang et al., 2017).

1.5.2. Co-precipitation method

The co-precipitation method is a chemical synthesis technique that is widely used to prepare high-purity and uniform nanostructure with an exact stoichiometry. This process involves the mixing of one or more water soluble divalent or trivalent metal ions in an aqueous medium, which reacts to form one or more water-soluble salts that precipitate out of the solution, followed by drying and grinding (Fig. 1.8b) (Kritika and Roy, 2022). The resulting nanostructures can have a wide range of compositions, structures, and uniform properties, making this technique useful in various applications, including electrocatalytic sensing, and electrochemical or photochemical reduction of CO_2 into various useful products. Zhang et al. (2022) formed nanobelt arrays of $NiCo_2O_4$ on the nickel using a co-precipitation method to detect the glucose via electrochemical sensing. The synthesized nanobelt array-based sensor exhibited a sensitivity of 5 and 0.727 $\mu A \mu M^{-1} cm^{-2}$ between the linear range of 0.9-67.2 µM and 67-1373 µM, respectively. The response time and LOD of the sensor were 4 s and 0.9 µM, respectively (Zhang et al., 2020). Nallusamy and Sujatha (2021) synthesized Co_3O_4

nanoparticles by the co-precipitation method for electrochemical determination of cholesterol in blood samples (Nallusamy and Sujatha, 2021).

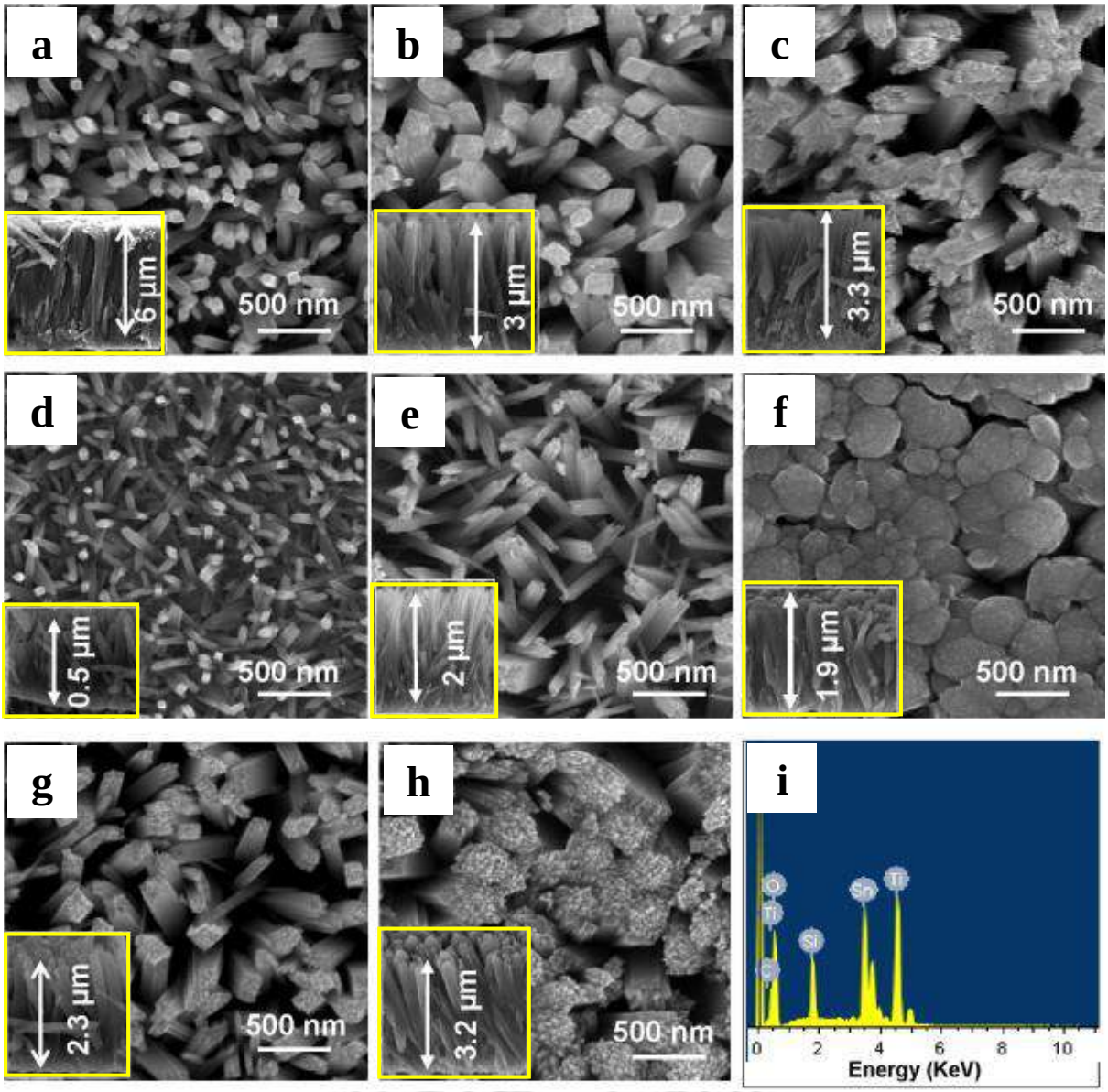

Figure 1.6: FESEM images of VANs of TiO_2 on the FTO glass at different precursor (titanium butoxide) concentrations, time, and temperature (a) 2 % (v/v), 4 h, 150 °C, (b) 2 % (v/v), 8 h, 150 °C, (c) 2 % (v/v), 24 h, 150 °C, (d) 2 % (v/v), 4 h, 120 °C, (e) 2 % (v/v), 4 h, 180 °C, (f) 4 % (v/v), 4 h, 150 °C, (g) 4 % (v/v), 16 h, 150 °C, (h) 4 % (v/v), 24 h, 150 °C, and (i) EDX image of 4 % (v/v), 24 h, 150 °C. The cross-sectional view of each image is inserted in the corresponding image. Reprinted with permission from ref (Cao et al., 2011) (copyright 2011 Elsevier).

1.5.3. Chemical growth method

The chemical growth method represents a straightforward and low-temperature approach compared to the hydrothermal method for synthesising metal oxide/sulphide nanostructures with controlled sizes and shapes. In this method, a reducing agent is added to the metal precursor, resulting in the reduction of the metal precursor to metal ions and the formation of a metal-based nanostructure under controlled conditions. The formation of 1D surface VANs of ZnO onto the FTO glass via an aqueous chemical growth route is illustrated in Fig. 1.8c. Mali et al. (2013) successfully synthesized VANs of ZnO on the FTO glass by an aqueous chemical growth method at a refluxed temperature of 95 °C for 5 h. The morphology of the 1-D ZnO nanorods was very suitable for fast electron transfer with the high surface area owing to the vertical alignment of nanorods. The fabricated rods exhibited an average diameter of 55-65 nm with a length of 2.1 μm (Mali et al., 2013).

1.5.4. Microwave-assisted method

The microwave method for nanoparticle formation involves the use of microwave irradiation to carry out chemical reactions. In this method, the reaction mixture is exposed to microwave radiation at a specific frequency and power for a predetermined amount of time. The microwave energy is used to heat the reaction mixture rapidly, which leads to faster and more efficient reactions. Microwave-assisted synthesis includes shorter reaction times, higher yields, and better control over the size and morphology of the nanostructures, which is particularly important for large-scale production. The synthesis of nanostructures by the microwave-assisted method is depicted in Fig. 1.8d. Borowska et al. (2023) presented a microwave-assisted route for SeNPs using yeast extract as a non-toxic capping and reducing agent. The biomolecules presented in the yeast extract were responsible for synthesising SeNPs. The variation in the size of SeNPs depends on the synthesis conditions, and their size increased in simulated gastric juice but returned to the initial value after the addition of simulated intestinal juice (Borowska et al., 2023). Dash et al. (2021) synthesized PtNPs decorated graphene nanocomposite in a microwave-assisted method (900 W for 300 s) by phytochemicals present in leaves extract of *Psidium guajava* for electrochemical sensing of dipyrone drug and its metabolites. The fabricated sensor exhibited the LOD of 0.142 μM and a sensitivity of 0.820 $\mu A \mu M^{-1} cm^{-2}$ within the linear working range of 1-100 μM (Dash et al., 2021).

1.5.5. Electrochemical deposition method

In this method, metal ions are reduced at the working electrode's surface by applying potential, leading to the formation of the nanostructure (Fig. 1.8e). The nanostructure size, shape, and composition can be tweaked by regulating the parameters of the electrochemical deposition process, such as the applied potential, current density, and electrolyte composition. Higher voltages and current densities typically lead to faster deposition rates and larger nanostructures. The major setback of this process is the need for specialized equipment and the difficulty of controlling the size distribution of the nanostructures. Chaure (2017) incorporated VANs of the CdO nanowire array with high density on the ITO glass substrate by the electrodeposition route. The fabricated nanowire arrow exhibited a length of 2.5 µm with a diameter of 50 nm (Chaure, 2017). Wang et al. (2010) investigated the impact of $ZnSO_4$ concentration on the phase change of VANs of ZnO from rod-like to plate-like via an electrochemical deposition route. The morphology of VANs of ZnO onto FTO substrate at different $ZnSO_4$ concentrations is shown in Figs. 1.7a-1.7h (Wang et al., 2010).

1.5.6. Sol-gel method

This method is very useful for the fabrication of metal oxide/sulphide and their composite nanostructures. It involves the hydrolysis of metal alkoxide precursors with water or alcohol in the presence of acid or base followed by condensation, leading to the formation of a gel-like substance that can be dried/sintered and processed into a powder/dense ceramic. Additionally, the sol (colloidal structure) could be deposited as a thin film on the substrate via spin/dip coating or precipitate in the powder form by grinding followed by calcination. The gel (porous structure) is converted into aerogel, xerogel, and cryogel by supercritical, thermal, and freeze drying, respectively (Fig. 1.8f) (Parashar et al., 2020; Valverde Aguilar, 2019). Furthermore, the calcination of powder (>500 °C) is essential to remove any remaining organic species and obtain a fine crystalline powder. Alsalme and Alsaeedi (2023) synthesized 2D $MoSe_2$ nanostructures via sol-gel technique for electrochemical monitoring of hydrazine using LSV and CV techniques. The $MoSe_2$-modified GC electrode exhibited the LOD of 0.091 µM with a sensitivity of 0.68 $\mu A \mu M^{-1} cm^{-2}$ (Alsalme and Alsaeedi, 2023).

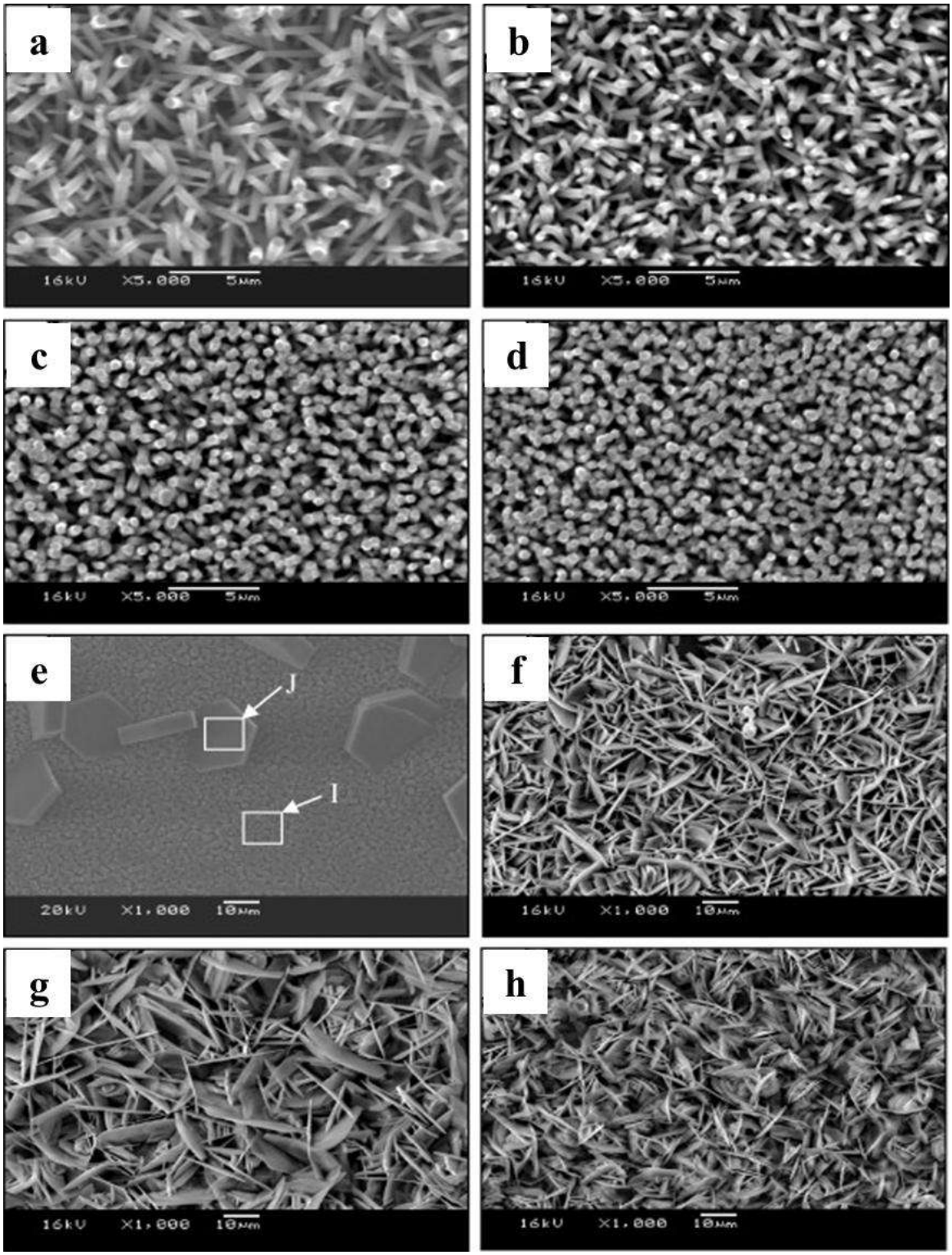

Figure 1.7: FESEM images of VANs of ZnO onto FTO substrate at different $ZnSO_4$ concentrations (a) 0.3 mM, 5 h, 80 °C, (b) 0.36 mM, 5 h, 80 °C, (c) 0.48 mM, 5 h, 80 °C, (d) 0.54 mM, 5 h, 80 °C, (e) 0.6 mM, 5 h, 80 °C, (f) 1.2 mM, 5 h, 80 °C, (g) 1.8 mM, 5 h, 80 °C, and (h) 3 mM, 5 h, 80 °C. Images a-d, e, and f-h depict rods, a mixture of rods and plates, and plates, respectively. Reprinted with permission from ref (Wang et al., 2010) (copyright 2010 Elsevier).

1.5.7. Microplasma-based method

In this method, a facile and portable dielectric barrier discharge reactor is used to synthesize metal oxide/sulphide nanostructures consisting of a double-layer cylinder with an open hollow quartz tube (the reaction took place within the outer cylinder), a copper wire, and a copper rod. The copper rod covered with the substrate (carbon cloth) was placed in the quartz inner tube and the copper wire was tightly wrapped on the outside of the tube. The copper wire (anode) and copper rod (cathode) are connected to the A.C. power source and a microplasma (bright blue) is observed in the reactants (Fig. 1.8g) (Chen et al., 2021). In this technique, microplasma is used to break down precursor molecules into atoms or smaller molecules, which then recombine to form nanostructured materials. The major setback of this process is the need for a stable and reproducible plasma source. He et al. (2022) prepared an ultra-thin 3D CuO nanosheet onto the copper form by the microplasma-based technique at ambient temperature and pressure for 10 min. The developed electrode revealed good electrocatalytic activity for glucose sensing, with a LOD of 0.53 μM (S/N = 30) and sensitivity of 7477 $\mu A \mu M^{-1} cm^{-2}$ between the linear range of 2-6 μM. Additionally, It provided a promising approach for fabricating ultra-thin CuO nanosheets and highlighted their potential utilization in electrochemical sensing (He et al., 2022). This synthesis technique is particularly advantageous owing to its ability to provide precise control over reaction parameters, including pressure and temperature, resulting in uniform and high-density nanostructures essential for sensing of organic analytes. Moreover, its versatility in accommodating a wide range of materials enables the fabrication of nanostructures with tailored properties for specific applications.

1.5.8. Vapour solid deposition method

This method involves the deposition of a vaporized precursor material into a reaction chamber containing a solid substrate, which acts as a nucleation site for nanostructure growth. The precursor molecules condense onto the solid substrate, and the nanostructure grows by adding more precursor molecules (Fig. 1.8h). The size and morphology of the nanostructure can be controlled by adjusting the temperature, pressure, concentration of precursor, type of substrate, and the distance between the precursor source and the solid substrate. This process can be performed using a variety of techniques, such as chemical vapour deposition (CVD) (Medina-Llamas et al., 2023), physical vapour deposition (PVD) (GangaReddy and Reddy, 2023), and atomic layer deposition (ALD) (Tseng et al., 2023). The major setback of this process is time-consuming. Tseng et al. (2023) fabricated a 3D binder-free electrode by the ALD of ZnO-TiO_2 nanocomposite for lithium-ion batteries (Tseng et al., 2023).

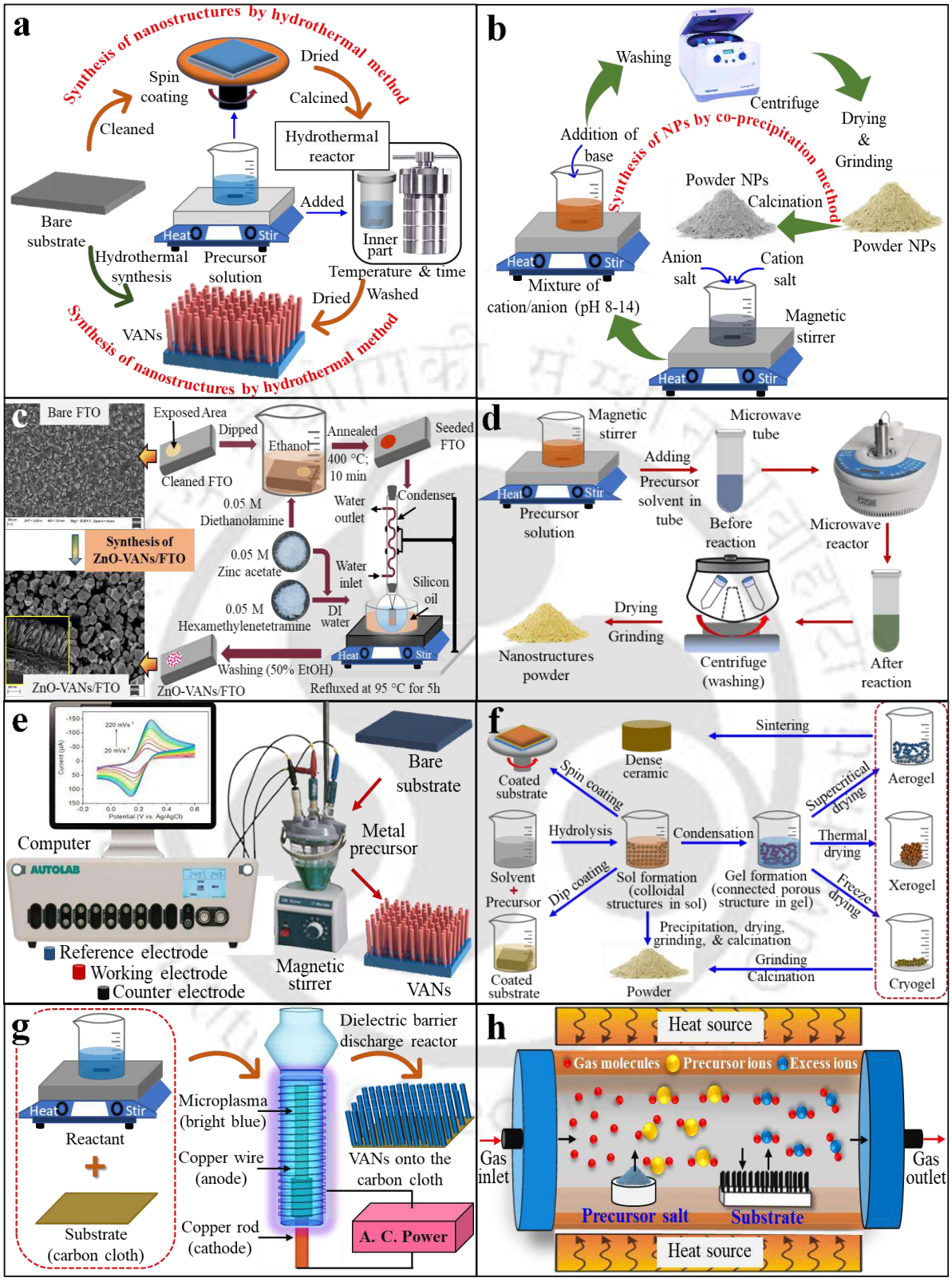

Figure 1.8: A comprehensive overview of various methods for nanostructure formation, including (a) Hydrothermal route for the formation of VANs, (b) Co-precipitation methodology, (c) Aqueous chemical growth of 1D surface VANs of ZnO on FTO substrate, (d) Microwave-assisted synthesis, (e) Electrodeposition of VANs onto the surface of a bare

substrate, (f) Sol-gel processing methodology, (g) Microplasma-based synthesis of VANs, and (h) Chemical vapour deposition route for the growth of nanostructures onto the substrate surfaces.

1.5.9. Bio-based synthesis method

Nowadays, bio-based synthesis of nanostructures has gained significant attention due to various advantages over conventional methods. The use of plant/microorganism extract in nanostructure synthesis not only reduces the environmentally hazardous chemicals, high pressure, and energy requirements but also offers several other benefits such as cost-effectiveness, simplicity, more sustainability, and an eco-friendly approach. Additionally, the bio-based method unusually avoids the use of separate reducing, stabilizing, and capping agents as the conventional method. The plant extracts contain a variety of phytochemicals, such as carbohydrates, proteins, aldehydes, polyphenols, vitamins, organic acids, polysaccharides, amides, alkaloids, ketones, flavonoids, terpenoids, etc., which can act as reducing and stabilizing agents for nanostructure synthesis. The steps included in the formation of nanostructures are nucleation, accumulation, stabilizing and capping. Bio-based synthesis of nanostructures is affected by factors such as temperature, salt concentration, pH, centrifugation, and incubation period (Fig. 1.9). Moreover, the bio-based development of nanostructures with high biocompatibility, low toxicity, unique properties and functions, making them suitable for various applications, including electrochemical sensing, energy storage devices, and drug recovery. The generalized bio-based synthesis route of the nanostructure using bio-extract of plant/microorganism is depicted in Fig. 1.9. Zokhtareh et al. (2023) synthesized Fe_3O_4 nanoparticles of spherical shape (average size 22.49 nm) using *S. ebulus* leaves extract. Afterwards, synthesized nanoparticles with graphene nanosheets were immobilized onto GCE (GR/Fe_3O_4NPs/GCE) for sensing of metronidazole. The fabricated sensor exhibited the LOD of 2.3×10^{-5} µM (Zokhtareh et al., 2023). Beheshtian et al. (2023) synthesized CuO nanoparticles in a green route (80 °C, 24 h) using bio-extract of *Malva sylvestris* as a capping and reducing agent. Dash et al. (2018) prepared AgNPs by the bio-based route using microwave irradiation to detect ascorbic acid from biological entitie. The fabricated electrode exhibited a LOD of 14.63 µM with a sensitivity of 0.719 $\mu A \mu M^{-1} cm^{-2}$ (Dash et al., 2018). Dash et al. (2020) fabricated an electrochemical sensor of Ag@Pt core-shell nanoparticles to detect Pb (II) from the environmental water samples. The fabricated sensor exhibited a high sensitivity of 307.26 $\mu A \mu M^{-1} cm^{-2}$ with a LOD of 0.8 µM (Dash et al., 2020). Wicaksono et al. (2022) successfully synthesized ZnO nanoparticles using orange peel extract for detection of

formaldehyde. Electrochemical studies showed an enhanced electron transfer rate on ZnO modified graphite paste electrode (ZnO NPs/GPE) than bare GPE. The sensor demonstrated a limit of detection of <18 µM and high selectivity for formaldehyde over ethanol (Wicaksono et al., 2022). Chowdhury et al. (2023) developed a bio-based route for the synthesis of 1D Bi_2S_3 nanorods using bio-extract of *Sechium edule* fruit for electrochemical reduction of CO_2 to formate. The nanorods of Bi_2S_3 showed the maximum faradaic efficiency of 92.3 % in 1h of reaction. Fig. 1.10 demonstrated the FETEM (Fig. 1.10a-1.10c), HRTEM (Fig. 1.10d), and SAED (inserted in Fig. 1.10c) images of 1D Bi_2S_3 nanorods (Chowdhury et al., 2023).

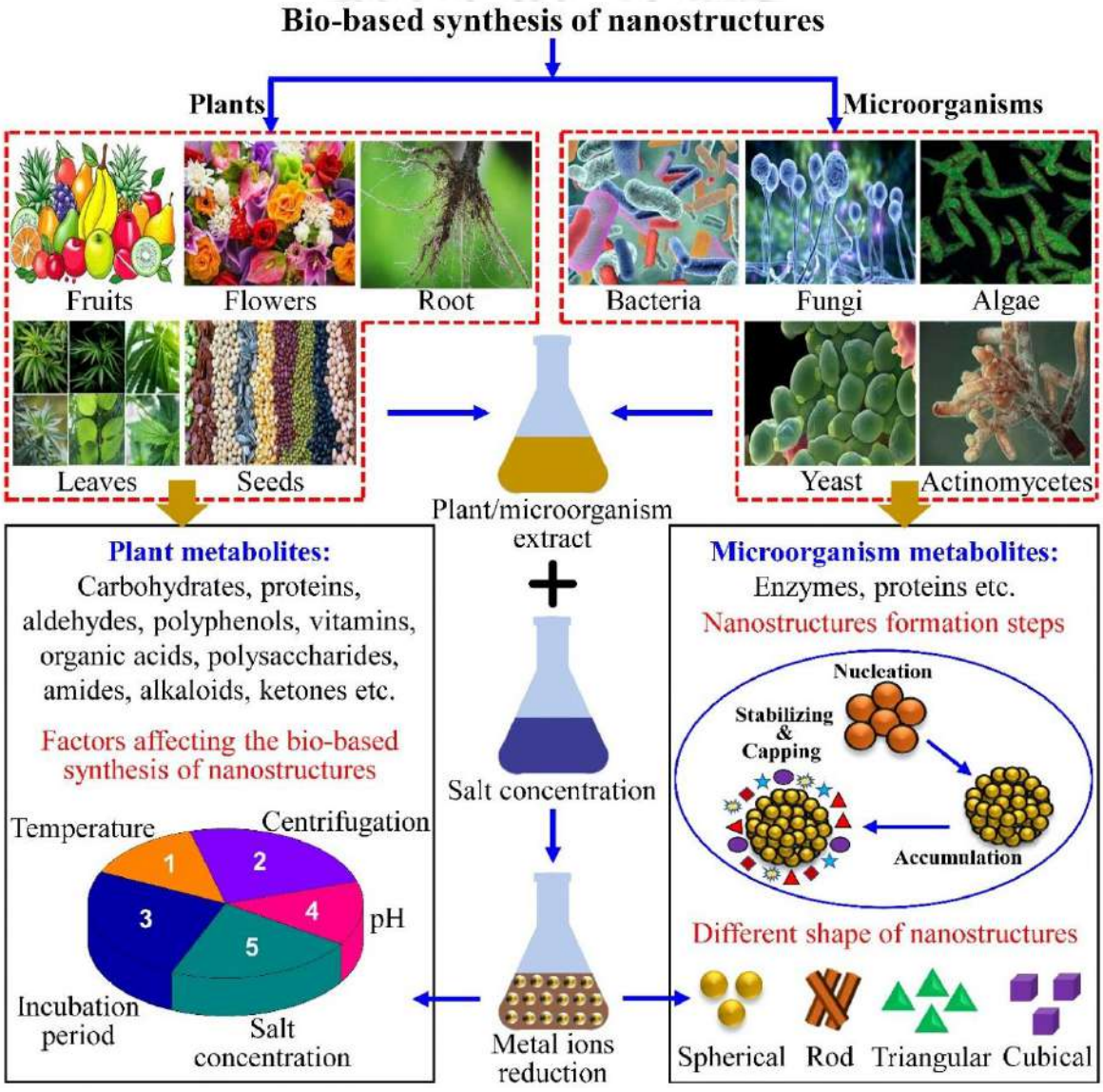

Figure 1.9: Schematic illustration of bio-based synthesis of nanostructures using phytochemicals present in the bio-extract of plant/microorganism.

In conclusion, green synthesis of the nanostructure is a promising approach that offers several benefits. It can lead to the development of new and innovative homogeneous nanostructures with better physicochemical properties than those synthesized using other methods. Nevertheless, the overall benefits of green synthesis methods outweigh their drawbacks, making them an attractive alternative to conventional methods for electrochemical sensing of environmental pollutants.

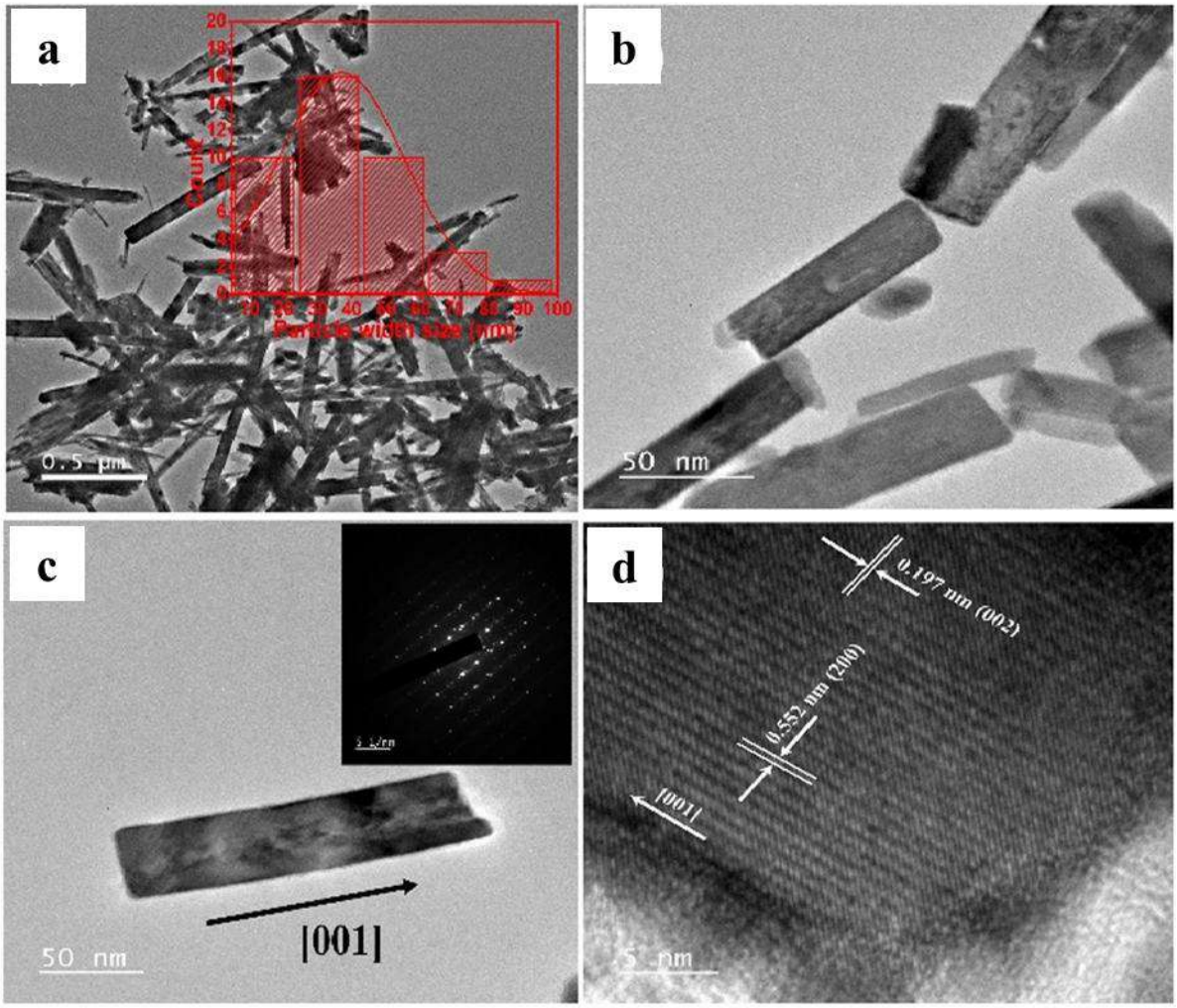

Figure 1.10: (a-c) and (d) are FETEM and HRTEM micrographs of 1D Bi_2S_3 nanorods synthesized via a bioinspired route using bio-extract of *Sechium edule* fruit, respectively. The SAED pattern of a single Bi_2S_3 nanorod is inserted in Fig. 1.10c. Reprinted with permission from ref (Chowdhury et al., 2023) (copyright 2023 Elsevier).

This review provided a comprehensive coverage of the synthesis method of VANs on the surface of substrate and powder nanostructures (the main focus on the development of VANs) of diverse shapes by conventional and bio-based methods. The potential applications of diverse

shape nanostructures are in various fields, including electrochemical sensors, wastewater treatment, hydrogen generation, and CO_2 reduction (Fig. 1.11). In the case of electrochemical sensors, nanostructures could utilize by the direct growth of VANs (binder-free) or immobilizing nanostructures (binder-based) on the support electrode for sensing of targeted analytes.

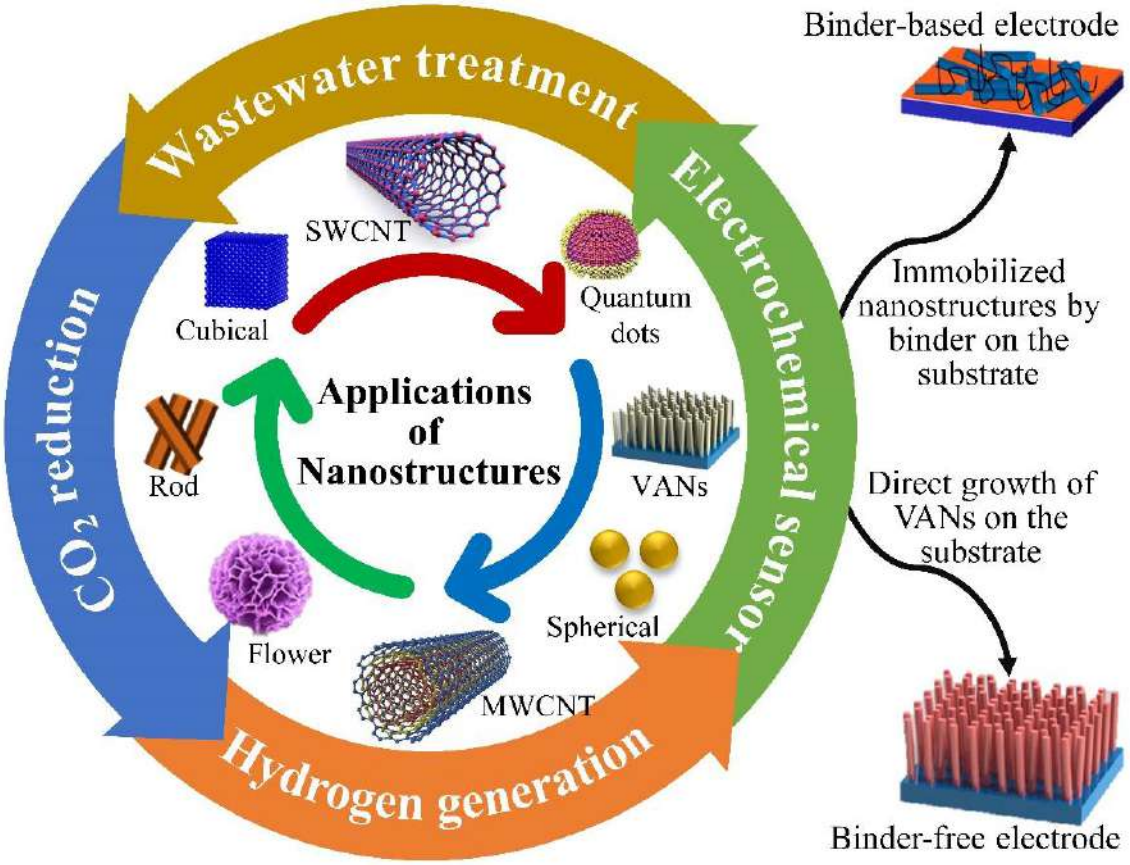

Figure 1.11: Potential applications of diverse shape nanostructures in various fields.

1.6. Binder-based and binder-free electrocatalytic sensing platform for organic analytes

1.6.1. Binder-based electrocatalytic sensing

A binder-based electrochemical sensor uses a binder to hold electrocatalytic materials (nanostructure of metal/metal oxide/metal sulphide) on the surface of the base electrode (glassy carbon, graphite paste, screen printed, boron-doped, gold electrode, platinum electrode etc.). The binder acts as a matrix that supports the electrocatalytic materials and facilitates their electrocatalytic reactions with the target analyte (pesticides, pharmaceuticals, heavy metal ions, etc.). The common binder used to bind the nanostructure on the functioning electrode's surface

is Nafion, polyvinyl alcohol (PVA), chitosan, polyethylene glycol (PEG), or polystyrene (PS), which is compatible with the electrocatalytic material and the electrolyte solution. Binder-based electrochemical sensors are commonly used in environmental monitoring, biomedical fields, and medicinal diagnostics. Alwael et al. (2023) proposed an electrochemical sensor of AuNPs functionalized onto the GCE using Nafion as a binder for monitoring parathion pesticides in water. The fabricated sensor showed the LOD of 6.06×10^{-4} µM and LOQ of 2.0×10^{-3} µM (Alwael et al., 2023). Baksh et al. (2020) presented an electrochemical sensor of NiO nanostructures functionalized on the GCE surface via Nafion (binder) for quantifying carbofuran in vegetables. The sensor revealed the LOD of 0.5 µM within the linear dynamic response of 5.0-305 µM (Baksh et al., 2020). Goswami and Mahanta (2021) formed Fe_3O_4-PANI nanocomposite functionalized on the GCE using chitosan (binder) by the drop-casting method for 2,4-dichlorophenoxyacetic acid monitoring. The sensitivity and LOD of the sensor evaluated by the chronoamperometry response were 4.62×10^{-7} $\mu A\mu M^{-1}cm^{-2}$ and 0.21 µM, respectively (Goswami and Mahanta, 2021). Fig. 1.12a despite the Fe_3O_4-PANI nanocomposite immobilized by chitosan as a binder on the GCE surface for electrocatalytic sensing of 2,4-dichlorophenoxyacetic acid. Kumar et al. (2022) synthesized Ce-TiO_2@rGO nanocomposite in a hydrothermal route and functionalized on the GCE using the drop-casting technique for sensing p-Nitroaniline by CV and DPV. The modified electrode displayed sensitivity, LOD, and a linear working range of 49.12 $\mu A\mu M^{-1}cm^{-2}$, 0.35 µM, and 0.1-1.5 µM, respectively (Kumar et al., 2022).

1.6.2. Binder-free electrocatalytic sensing

A binder-free electrochemical sensor does not require a binder to immobilize the electrocatalytic materials (directly grown VANs) onto the functioning electrode's surface for electrochemical sensing of environmental noxious waste. Ahmad et al. (2017) fabricated a stable binder-free sensor of vertically grown 1D surface ZnO nanorods on the FTO substrate to detect p-nitroaniline. The binder-free sensor demonstrated the LOD of 0.5 µM and a sensitivity of 10.18 $\mu A\mu M^{-1}cm^{-2}$ (Ahmad et al., 2017d). Liu et al. (2010) developed a hydrazine sensor of carbon-incorporated ZnO (C@ZnO) nanorods array directly formed on an inert alloy support via the immersion-calcination method. The C@ZnO/Alloy based sensor showed excellent sensitivity of 9.4 $\mu A\mu M^{-1}cm^{-2}$ and LOD of 0.1 µM (Liu et al., 2010). Khan et al. (2019) developed VANs of ZnO on the FTO substrate in a chemical method for electrochemical sensing of piperidine. ZnO/FTO electrode exhibited sensitivity, LOD, and linear piperidine concentration range of 0.53 $\mu A\mu M^{-1}cm^{-2}$, 0.06 µM, and 0.1-200 µM,

respectively (Khan et al., 2019). Ahmad et al. (2014) displayed a hydrazine electrochemical sensor of directly growing VANs of ZnO on Ag substrate via an aqueous route. The sensor presented a LOD, high sensitivity, and linear range of 0.0039 µM, 59.18 $\mu A \mu M^{-1} cm^{-2}$, and 0.001-60 µM, respectively (Ahmad et al., 2014). Ahmad et al. (2017) presented binder free hydrazine sensing electrode of directly growing 1D surface VANs of ZnO on the Ag substrate by the low-temperature solution method. The as-fabricated electrochemical sensor revealed the LOD of 0.005 µM, sensitivity of 105.5 $\mu A \mu M^{-1} cm^{-2}$, and linear working range up to 98.6 µM with excellent long-term stability (Ahmad et al., 2017e). Zhai et al. (2021) synthesized Ag-doped ZnO nanorods on the ITO substrate via a hydrothermal method towards highly sensitive electrochemical sensing of phosphothioate pesticides. The proposed sensor exhibited a LOD of 0.010 µM within the linear working range from 0.0500-700 µM (Zhai et al., 2021). Wang et al. (2020) synthesized 1D surface VANs of Ag-doped ZnO on the graphene oxide-functionalized GCE surface via an electrochemical deposition route for monitoring of carbamate pesticide in foodstuffs. The fabricated sensor revealed the LOD of 0.34×10^{-3} µM by DPV technique with excellent long-term stability and higher selectivity (Wang et al., 2020).

Cyclic voltammograms of p-nitroaniline sensing demonstrated that the binder-free (VANs of ZnO on FTO substrate) sensor could provide a higher peak current as compared to the binder-based (immobilized ZnO nanorods on FTO substrate) sensor due to the more favourable active morphology of VANs, easy substrate penetration morphology, and high specific surface area (Fig. 1.12b). Figs. 1.12c and 1.12d demonstrate the possible electrocatalytic sensing mechanism of p-nitroaniline and hydrazine over directly growing 1D surface VANs of ZnO on FTO and Ag substrates, respectively. Fig. 1.12e displayed the electrochemical sensing of ciprofloxacin using mixed copper-iron metal oxides nanostructures/reduced graphene oxide nanocomposite.

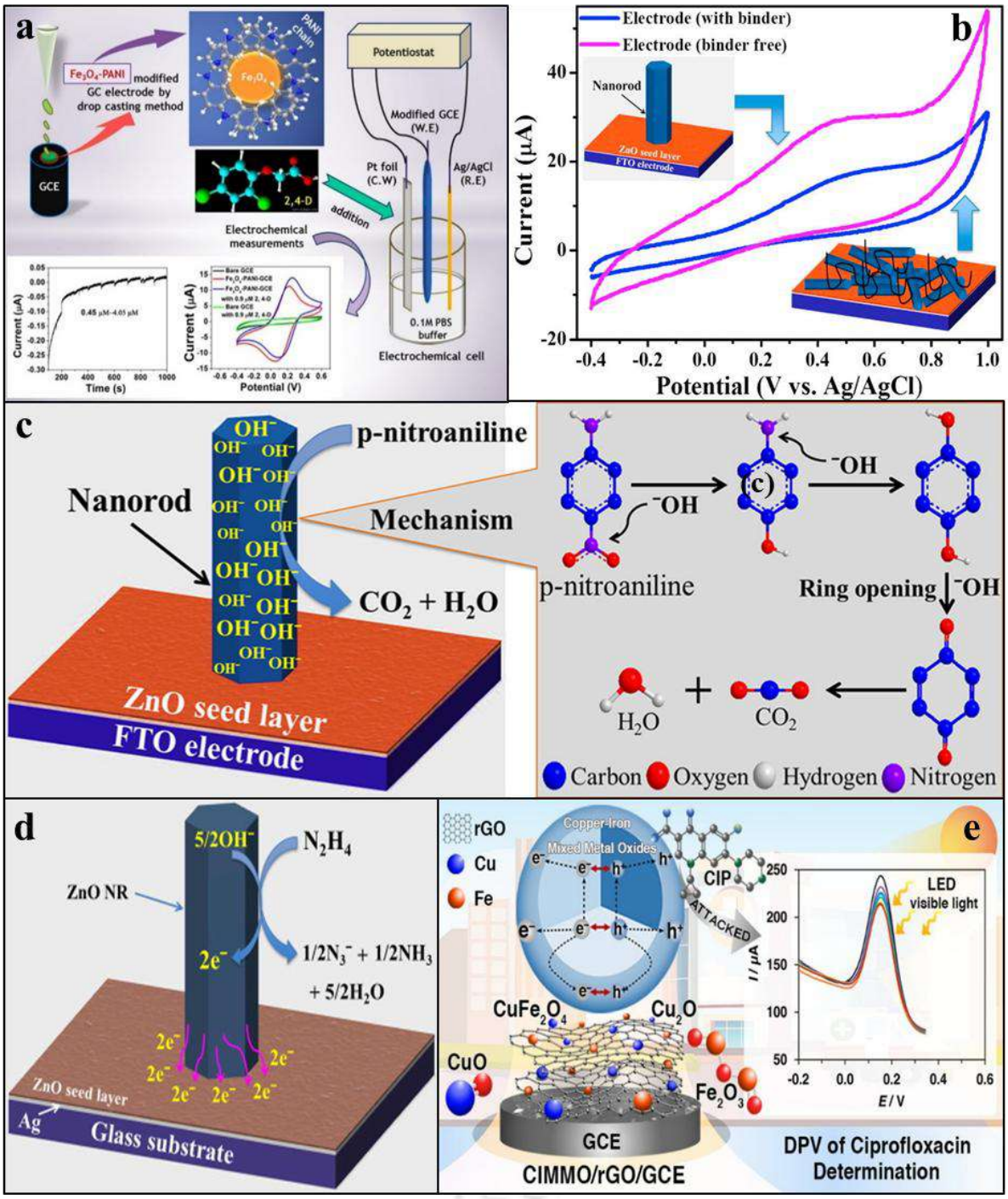

Figure 1.12: (a) Schematic illustration of Fe_3O_4-PANI nanocomposite immobilized onto the GCE with a binder (chitosan) by the drop-casting method for electrocatalytic sensing of 2,4-Dichlorophenoxyacetic acid, (b) Electrochemical sensing of p-nitroaniline using a binder-free (VANs of ZnO on FTO) and binder-based (immobilized ZnO nanorods on FTO) sensor by CV technique, (c), and (d) schematic illustration of the possible electrocatalytic sensing mechanism of p-nitroaniline and hydrazine over directly growing 1D surface VANs of ZnO on FTO and Ag substrate, respectively, and (e) Electrochemical sensing of ciprofloxacin using mixed

copper-iron metal oxides nanostructures/reduced graphene oxide nanocomposite. Fig. 1.12a is reprinted with permission from ref (Goswami and Mahanta, 2021), which is an open-access article distributed under the Creative Commons Attribution License (CC-BY-NC-ND 4.0., ACS, https://creativecommons.org/licenses/by-nc-nd/4.0/). Fig. 1.12b and 1.12c are reprinted with permission from ref (Ahmad et al., 2017d) (copyright 2017 Elsevier). Fig. 1.12d is reprinted with permission from ref (Ahmad et al., 2017e) (copyright 2017 Elsevier). Fig. 1.12e is reprinted with permission from ref (Chuiprasert et al., 2024), which is an open-access article distributed under the Creative Commons Attribution License (CC-BY 4.0., ACS, https://creativecommons.org/licenses/by/4.0/.).

Fig. 1.13 and Table 1.2 demonstrate the sensing performance of binder-free and binder-based sensors for electrochemical sensing of environmental pollutants. Binder-free sensors, namely ZnO/Ag and ZnO/FTO exhibited better LOD than the binder-based sensors, including ZnO/Nafion/Au and ZnO/GCE for electrochemical sensing of hydrazine and piperidine, respectively (Fig. 1.13). Additionally, Ag-doped ZnO/GO/GCE binder-free senor exhibited excellent LOD in comparison to CMO/B-rGO/GCE binder-based sensor for electrochemical detection of carbamate pesticides (Table 1.2). Binder-free sensors showed better LOD than binder-based sensors due to their more favourable active surface morphology of nanostructures (high specific surface area). The binder could block catalytic active sites, forming a dense and inhomogeneous film of immobilized nanostructures via drop casting/spin coating. It could also increase the cost of electrode fabrication. However, the reported method for the growth of VANs (binder-free sensors) on the surface of the support electrode may involve aggressive chemicals that are not environmentally benign. The bio-based development of VANs on the surface of support electrodes and their application in the electrochemical sensing of environmental noxious waste is highly warranted.

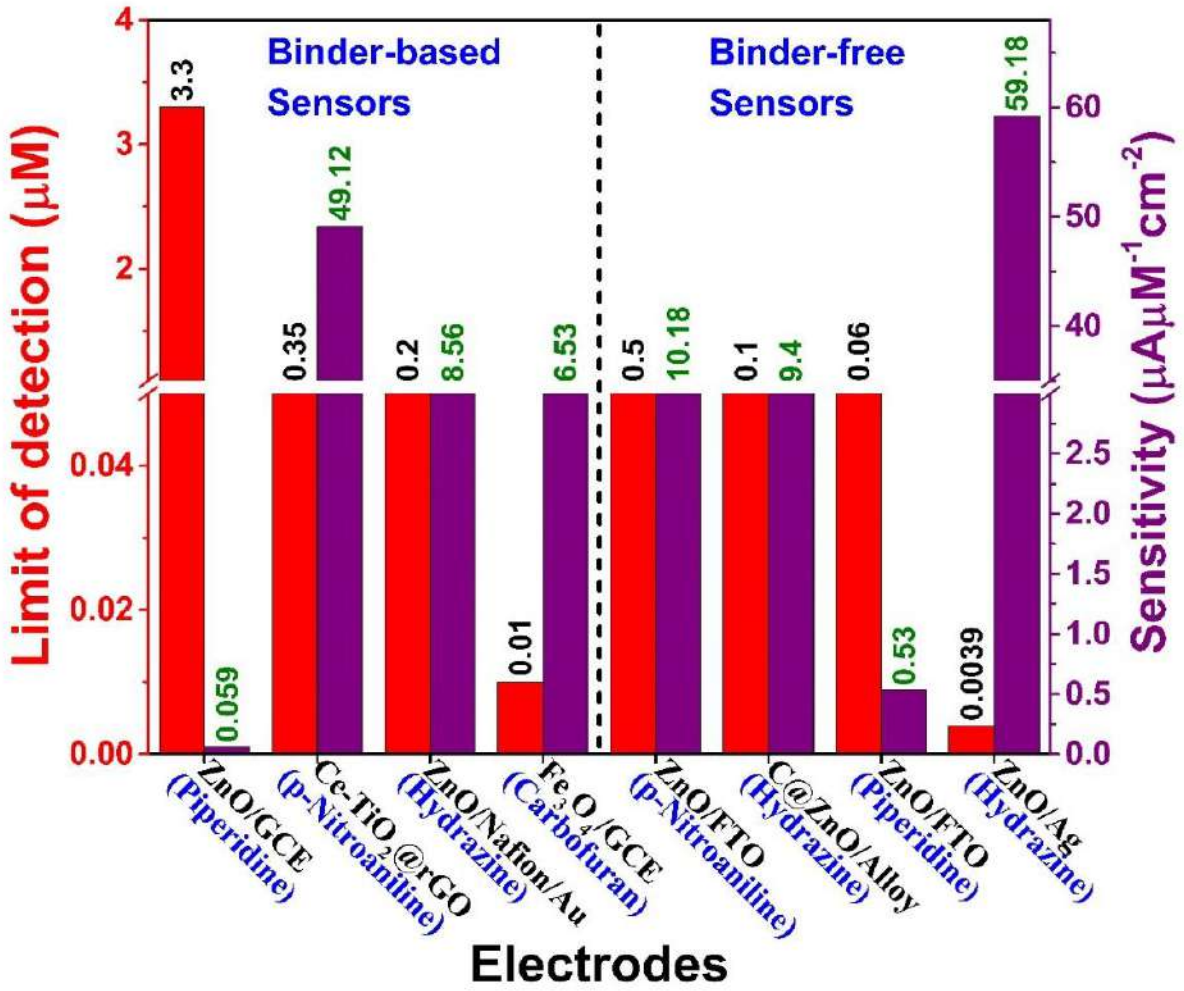

Figure 1.13: Comparison of sensing performance of binder-based and binder-free sensors for electrochemical sensing of organic analytes. The analytes used in sensing studies are in brackets of the x-axis labelling (Ahmad et al., 2017d, 2014; Ameen et al., 2015a; Khan et al., 2019; Kumar et al., 2022; Liu et al., 2010; Rajiv et al., 2022; Umar et al., 2008).

Table 1.2: Comparison of sensing performance of binder-free and binder-based electrochemical sensors for sensing environmental pollutants.

Electrode	Sensor type	Analytes	LOD (μM)	Sensitivity ($\mu A \mu M^{-1} cm^{-2}$)	Ref.
AgNRs/GCE	Binder-free	Aniline	0.1	4.56	Das et al., 2024
NPG/GCE	Binder-based		0.5	-	Wan et al., 2023
NP-Au			0.5	-	Lee et al., 2017
BND			0.29	-	Li et al., 2021
ZnO/FTO	Binder-free	p-Nitroaniline	0.5	10.18	Ahmad et al., 2017d
Ce/TiO_2/rGO	Binder-based		0.35	49.12	Kumar et al., 2022
C@ZnO/Alloy	Binder-free	Hydrazine	0.1	9.4	Liu et al., 2010
ZnO/Ag			0.004	59.18	Ahmad et al., 2014
ZnO/Ag			0.005	105.5	Ahmad et al., 2017e
ZnO/Nafion/Au	Binder-based		0.2	8.56	Umar et al., 2008
Au/SWCNHs/GCE			1.1	-	Zhao et al., 2016
SnO_2/CeO_2/GCE			0.179	81	Mohammad et al., 2021
ZnO@CoNi/LDH-NCDs			0.2	13.040	Zhang et al., 2023
ChAc-ZnO NS/Au			0.4	2.66	Kaur et al., 2022
CuO	Binder-free	H_2O_2	-	0.03	Jia et al., 2008
ZnO@ZIF-8/ITO			3	0.0047	Mei et al., 2022
3.5-NH_3-PM	Binder-based		0.25	31.3	Candia-Onfray et al., 2021
ZnO-Cu_xO/GCE			7.3	0.504	Jain et al., 2022
ZnO/FTO	Binder-free	Piperidine	0.06	0.53	Khan et al., 2019
ZnO/GCE	Binder-based		3.3	0.059	Ameen et al., 2015a
ZnO/GCE			9.4	0.238	Ameen et al., 2015b
Ag-doped ZnO/GO/GCE	Binder-free	Carbamate	0.34×10^{-3}	-	Wang et al., 2020
CMO/B-rGO/GCE	Binder-based		0.002	4.06	Alagarsamy et al., 2023

1.7. Knowledge gap and thesis objectives

The pollutants of emerging nature are major concerns of environmental scientist as their long-term health and ecological consequences are unknown to a large extent. The presence of pesticides, their intermediates, and pharmaceutical residues in the environment poses significant environmental and health risks due to their toxicity, persistence, and potential bioaccumulation. Long-term exposure to such pollutants can lead to chronic illnesses, endocrine disruption, antibiotic resistance, and carcinogenic effects. The existence of organic analytes in the environmental matrices can be monitored by conventional analytical techniques, such as chromatographic and spectroscopic. However, these techniques require adept personnel, arduous procedures, costly reagents, and extended sample preparation. Therefore, the development of an alternative cost-effective electrochemical sensing platform is highly warranted for detecting and determining organic analytes in environmental matrices.

Electrochemical sensors exhibit significant potential of in-situ detection and determination of the selective analytes, including agricultural pesticides and their intermediates, pharmaceuticals, and heavy metal ions. Simultaneous electrochemical sensing of organic analytes enhances real-time data integration and facilitates the correlation of multiple variables. Moreover, it is cost-effective, eliminating the need for separate sensors for each analyte, thereby reducing equipment and maintenance costs. Electrochemical sensors merited with cost-effectiveness, high selectivity, sensitivity, and potential to detect the target analytes at a low concentration. Additionally, the electrochemical sensor has the potential to reduce the need for conventional analytical techniques. Furthermore, the functionalization of nanostructures on the working electrode surface might improve the performance of the electrochemical sensor (binder-based) by several folds through facilitating an electrocatalytic reaction between the working electrode/nanostructure surface and target analytes. However, the embedded catalysts (not grown directly on the base electrode surface) are delaminated quickly during the course of sensing. It could deter repeatability and reproducibility. Moreover, the binder could potentially interfere with the electrochemical sensor, which could affect its sensing performance.

In recent research, the growth of VANs on the working electrode's surface was performed, which significantly enhanced the performance of electrochemical sensors by several folds. They are merited with high specific surface area, maximum roughness, unimpeded electron transport characteristics, large aspect ratio, high chemical stability, and easy substrate penetration morphologies. Kinetic electrodes with a high surface area could have

more active sites for the interaction between the electrode/nanostructure surface and analytes, enhancing its sensing performance by lowering the detection limit and increasing sensitivity. Additionally, the increased surface area of nanostructures can lead to a faster response time for the sensors, allowing for real-time environmental monitoring. The higher roughness of nanostructures provided more nucleation sites and unimpeded electron transport characteristics, allowing effective charge transmission between the electrode/nanostructure surface and electrolyte solution. Furthermore, forming VANs could remove the problem of delamination of nanostructure from the working electrode, the binder's need, and the functionalization process of nanostructure on the base electrode surface. VANs nanostructure-based (binder-free) electrochemical sensors have promising prospects for detecting environmental pollutants. These sensors are highly sensitive, selective, and can detect trace amounts of target analytes in real time with minimal interference from other environmental factors. However, the reported approaches for the formation of VANs involve chemical-based methodologies. Therefore, the development of a bioinspired approach for the synthesis of VANs on FTO substrate and their application in the electrochemical sensor for detecting environmental noxious waste is highly warranted.

The source of bio-extract was selected considering factors like availability, reducing substance contents, economic importance, growth characteristics, etc. The northeastern states of India are the hub for tropical plants that are a potential source of reducing and capping agents that can be used for effective and ecological approaches for synthesizing nanoparticles. Two groups of plants have been selected such as *Sechium edule* and *Citrus limetta*. It has been reported that the *Sechium edule* fruits contain abundant amounts of reducing analytes, including ascorbic acid (0.294 mg/g on the dry basis), amino acids (12.9 mg/g on the dry basis), flavonoids (19.3 mg/g on the dry basis), and polyphenols. *Citrus limetta* fruits are rich sources of citric acid, polyphenolic compounds, flavonoids, etc. The phytochemicals present in the bio-extracts of *Sechium edule* and *Citrus limetta* fruit have been exploited for the growth and formation of stable nanostructures. Furthermore, utilizing natural extracts can reduce the production costs of nanostructures compared to synthetic chemicals used in traditional methods.

Based on the above knowledge gaps, the following objectives are taken into considerations:

- Phyto-analytic formation of Ag nanostructures for targeted electrocatalytic sensing of ciprofloxacin (**Chapter 3**)

- Synthesis of ZnO nanorods aligned in a vertical configuration for targeted electrochemical detection of aniline (**Chapter 4**)
- Development of bio-based hierarchical vertically aligned 2D ZnO nanostructures for ultra-selective electrochemical sensing of p-Chloroaniline (**Chapter 5**)
- Bioinspired synthesis of vertically aligned 2D surface ZnO nanostructures modified with carbon quantum dots for electrocatalytic sensing of norfloxacin (**Chapter 6**)
- Development of vertically oriented 1D Bi_2S_3 surface nanorods for ultra-selective electrochemical sensing of mancozeb (**Chapter 7**)
- Dual-analyte selective electrochemical detection of phenylbutazone and sulfamethoxazole using bio-engineered Bi_2S_3-ZnO nanocomposites (**Chapter 8**)

1.8. Organization of the thesis

CHAPTER 1: Introduction and background of the work

This chapter provides an in-depth overview of electrochemical sensors for detecting agricultural pesticides and pharmaceuticals using binder-free and binder-based sensors of various nanomaterials to enhance sensing performance. The chapter also outlines various synthesis methods for these nanomaterials and their application across different electrochemical techniques. Furthermore, it presents a comprehensive framework for developing bioinspired VANs on functional electrodes, aimed at advancing point-of-care monitoring of target analytes.

CHAPTER 2: Materials and methodology

This chapter presents the experimental methodologies employed in this doctoral work, including the chemical and bioinspired synthesis of nanostructures. It also details the reagents used and the instrumentation for characterizing nanostructures and target analytes. This chapter also describes the general theory and detailed instructions of all the electrochemical experiments involved in this study.

CHAPTER 3: Phyto-analytic formation of Ag nanostructures for targeted electrocatalytic sensing of ciprofloxacin

This chapter provides the formation of phyto-analytic Ag nanostructures (AgNSs) using plant bioactives present in the bio-extract of *Citrus limetta*. The phytochemicals in the bio-extract could leverage the formation of AgNSs. Subsequently, the AgNSs were immobilized

onto the surface of a GCE using Nafion as a binder for electrochemical sensing of ciprofloxacin (CFX) via the SWV technique. The real-world implementation of the proposed electrochemical sensing platform was investigated in the environmental matrix by SWV and compared with the HPLC.

CHAPTER 4: ZnO nanorods aligned in a vertical configuration for targeted electrochemical detection of aniline

This chapter demonstrates the synthesis of 1D surface vertically aligned nanorods (VANRs) of ZnO on the FTO using a chemical growth method for electrochemical sensing of aniline via the SWV technique. This reusable electrode exhibits a high surface area and enhanced charge transport characteristics, while also mitigating the rapid delamination of nanostructures from the electrode surface. The fabricated electrode demonstrated remarkable stability, repeatability, and selectivity, even in the coexistence of interferants. To demonstrate the practical applicability of the fabricated electrode, aniline was detected and determined in tap and river water samples and compared with the HPLC.

CHAPTER 5: Bio-based vertically aligned hierarchical 2D ZnO nanostructures for ultra-selective electrochemical sensing of p-Chloroaniline

This chapter presents the synthesis of hierarchical 2D VANs of ZnO onto the surface of FTO glass via a bioinspired route using the bio-extract of *Sechium edule* fruit for targeted electrocatalytic sensing of p-Chloroaniline (p-CA). This reusable sensor could eliminate the quick delamination of catalysts from the electrode surface. Furthermore, the practical applications of the fabricated sensor were examined to detect and determine p-CA in the environmental matrix.

CHAPTER 6: Bioinspired synthesis of vertically aligned 2D surface ZnO nanostructures modified with carbon quantum dots for electrocatalytic sensing of norfloxacin

This chapter documents vertically aligned 2D surface ZnO nanostructures on FTO using the bio-extract of *Sechium edule* fruit. The leftover peel of the fruit is utilized to prepare carbon quantum dots. Subsequently, 2D VANs of ZnO were modified with carbon quantum dots for electrochemical sensing of norfloxacin (NFX) in tap and river water samples using the SWV technique. This reusable electrochemical sensing platform enhanced the developed sensor's performance and eliminated the rapid delamination of catalysts from the electrode surface.

CHAPTER 7: Nature-inspired vertically oriented 1D Bi_2S_3 surface nanorods for ultra-selective electrochemical sensing of mancozeb

This chapter displays the development of nature-inspired 1D surface vertically oriented nanostructures (VONs) of Bi_2S_3 on the surface of FTO using bio-extract of *Sechium edule* for highly selective electrochemical detection and determination of mancozeb (MCZ) by SWV. This study also aims to address the shortcoming of the rapid detachment of nanomaterials from the surface of kinetic electrodes by optimizing Bi_2S_3 VONs synthesis and electrochemical sensing parameters to maintain consistent sensitivity and selectivity. Moreover, the high surface area and unimpeded charge transfer characteristics of the VONs significantly contribute to enhancing the sensor's sensitivity and selectivity. The selectivity of the developed sensor was investigated in the presence of potential interferants, including chlorpyrifos, carbendazim, malathion, thiram, ziram, and profenofos. The practical applicability of the proposed sensing platform for MCZ detection and quantification was examined using tap water, river water, agricultural runoff, and wastewater and compared with the HPLC.

CHAPTER 8: Dual-analyte selective electrochemical detection of phenylbutazone and sulfamethoxazole using bio-engineered Bi_2S_3-ZnO Nanocomposites

Herein, we have synthesized a bio-based Bi_2S_3-ZnO nanocomposites using the phytochemicals present in the bio-extract of *Sechium edule* fruit. These phytochemicals could facilitate the development of a stable Bi_2S_3-ZnO nanocomposite. Subsequently, the bio-based synthesized Bi_2S_3-ZnO nanocomposite was functionalized onto the surface of GCE using a Nafion binder for the individual and simultaneous electrocatalytic sensing of phenylbutazone (PBZ), sulfamethoxazole (SMZ) through SWV technique. The practical applicability of the proposed simultaneous sensing platform was tested in the tap and river water samples. To the best of our knowledge, this is the first report detailing the bio-based synthesis and comprehensive characterizations of the Bi_2S_3-ZnO nanocomposite, along with its utilization as an electrocatalyst for the individual and simultaneous sensing of PBZ and SMZ using SWV. Additionally, this is the first study to report the simultaneous electrochemical sensing of PBZ and SMZ.

CHAPTER 9: Conclusions and scopes for future studies

This chapter presents the key findings of the study and highlights its significant outcomes. Based on insights gained during the research, suggestions and recommendations for future work are also provided.

References

Abad-Gil, L., Gismera, M.J., Sevilla, M.T., Procopio, J.R., 2023. Electrochemical sensing platform with gold nanoparticles capped by PDDA for benzyl alcohol determination. Microchim. Acta 190, 115. https://doi.org/10.1007/s00604-023-05690-6

Abbas, W., Akhtar, N., Liu, Q., Li, T., Zada, I., Yao, L., Naz, R., Zhang, W., Mazhar, M.E., Zhang, D., Ma, D., Gu, J., 2019. Facilely green synthesis of 3D nano-pyramids Cu/carbon hybrid sensor electrode materials for simultaneous monitoring of phenolic compounds. Sensors Actuators B Chem. 282, 617–625. https://doi.org/10.1016/j.snb.2018.11.114

Abdelfatah, M., El-Shaer, A., 2018. One step to fabricate vertical submicron ZnO rod arrays by hydrothermal method without seed layer for optoelectronic devices. Mater. Lett. 210, 366–369. https://doi.org/10.1016/j.matlet.2017.09.064

AbdelHamid, A., Elgamouz, A., Khanfer, M., Kawde, A.-N., 2023. COVID-19 chloroquine drug detection using novel, highly sensitive SnO_2-based electrochemical sensor. Arab. J. Chem. 16, 104674. https://doi.org/10.1016/j.arabjc.2023.104674

Ahmad, K., Kim, H., 2023. Hydrothermally grown MoS_2-flowers as low cost counter electrode material for dye sensitized solar cell and electrode modifier for electrochemical sensing of 4-Chlorophenol. Mater. Sci. Eng. B 295, 116563. https://doi.org/10.1016/j.mseb.2023.116563

Ahmad, R., Ahn, M., Hahn, Y., 2017a. A highly sensitive nonenzymatic sensor based on Fe_2O_3 nanoparticle coated ZnO nanorods for electrochemical detection of nitrite. Adv. Mater. Interfaces 4, 1–9. https://doi.org/10.1002/admi.201700691

Ahmad, R., Bhat, K.S., Ahn, M.-S., Hahn, Y.-B., 2017b. Fabrication of a robust and highly sensitive nitrate biosensor based on directly grown zinc oxide nanorods on a silver electrode. New J. Chem. 41, 10992–10997. https://doi.org/10.1039/C7NJ02526B

Ahmad, R., Tripathy, N., Ahn, M.-S., Bhat, K.S., Mahmoudi, T., Wang, Y., Yoo, J.-Y., Kwon, D.-W., Yang, H.-Y., Hahn, Y.-B., 2017c. Highly Efficient Non-Enzymatic Glucose Sensor Based on CuO Modified Vertically-Grown ZnO Nanorods on Electrode. Sci. Rep. 7, 5715. https://doi.org/10.1038/s41598-017-06064-8

Ahmad, R., Tripathy, N., Ahn, M.-S., Hahn, Y.-B., 2017d. Development of highly-stable binder-free chemical sensor electrodes for p-nitroaniline detection. J. Colloid Interface Sci. 494, 300–306. https://doi.org/10.1016/j.jcis.2017.01.099

Ahmad, R., Tripathy, N., Ahn, M.-S., Hahn, Y.-B., 2017e. Highly stable hydrazine chemical sensor based on vertically-aligned ZnO nanorods grown on electrode. J. Colloid Interface

Sci. 494, 153–158. https://doi.org/10.1016/j.jcis.2017.01.094

Ahmad, R., Tripathy, N., Jung, D.-U.-J., Hahn, Y.-B., 2014. Highly sensitive hydrazine chemical sensor based on ZnO nanorods field-effect transistor. Chem. Commun. 50, 1890. https://doi.org/10.1039/c3cc48197b

Aikens, D.A., 1983. Electrochemical methods, fundamentals and applications. J. Chem. Educ. 60, A25. https://doi.org/10.1021/ed060pA25.1

Akhtar, K., Ahmed Baig, J., Gul Kazi, T., Sirajuddin, Imran Afridi, H., Naz Talpur, F., Bakhsh Solangi, I., Samaijo, S., 2022. Novel fluoride selective voltammetric sensing method by amino phenylboronic acid-zirconium oxide nanoparticles modified gold electrode. Microchem. J. 174, 107073. https://doi.org/10.1016/j.microc.2021.107073

Akkarachanchainon, N., Rattanawaleedirojn, P., Chailapakul, O., Rodthongkum, N., 2017. Hydrophilic graphene surface prepared by electrochemically reduced micellar graphene oxide as a platform for electrochemical sensor. Talanta 165, 692–701. https://doi.org/10.1016/j.talanta.2016.12.092

Alagarsamy, S., Sundaresan, R., Chen, S.-M., Rasu, R., Mohammed, M.A., 2023. An ultrasensitive carbamate pesticide detection sensor based on metal molybdate encapsulated with boron doped reduced graphene oxide nanocomposite. Colloids Surfaces A Physicochem. Eng. Asp. 673, 131830. https://doi.org/10.1016/j.colsurfa.2023.131830

Ali, M.Y., Knight, D., Howlader, M.M.R., 2023. Nonenzymatic electrochemical glutamate sensor using copper oxide nanomaterials and multiwall carbon nanotubes. Biosensors 13, 237. https://doi.org/10.3390/bios13020237

Alsalme, A., Alsaeedi, H., 2023. Fabrication of selective and sensitive hydrazine sensor using sol-gel synthesized $MoSe_2$ as efficient electrode modifier. Crystals 13, 161. https://doi.org/10.3390/cryst13020161

Alshahrani, L.A., Miao, L., Zhang, Y., Cheng, S., Sathishkumar, P., Saravanakumar, B., Nan, J., Gu, F.L., 2019. 3D-flower-like copper sulfide nanoflake-decorated carbon nanofragments-modified glassy carbon electrodes for simultaneous electrocatalytic sensing of co-existing hydroquinone and catechol. Sensors 19, 2289. https://doi.org/10.3390/s19102289

Alwael, H., Al-Sedran, S.H., Oubaha, M., Asiri, N.A.A., Bashammakh, A.S., Alharthy, A.S., Albassami, N.A., Abduljabbar, T.N., Mohammed, G.I., Nassef, H.M., Bahaidarah, E.A., Alhogbi, B.G., El-Shahawi, M.S., 2023. Probe –integrated electrochemical sensing platform for measuring trace levels of parathion pesticides residues in water using Au-nanoparticles anchored Nafion nano composite modified glassy carbon electrode. J. Food

Compos. Anal. 124, 105649. https://doi.org/10.1016/j.jfca.2023.105649

Ameen, S., Akhtar, M.S., Seo, H.-K., Shin, H.S., 2015a. An electrochemical sensing platform based on hollow mesoporous ZnO nanoglobules modified glassy carbon electrode: Selective detection of piperidine chemical. Chem. Eng. J. 270, 564–571. https://doi.org/10.1016/j.cej.2015.02.052

Ameen, S., Akhtar, M.S., Shin, H.S., 2015b. Spindles shaped ZnO modified glassy carbon electrode for the selective monitoring of piperidine. Mater. Lett. 148, 188–191. https://doi.org/10.1016/j.matlet.2015.02.049

Ameen, S., Kim, E.-B., Akhtar, M.S., Shin, H.S., 2017. Electrochemical detection of resorcinol chemical using unique cabbage like ZnO nanostructures. Mater. Lett. 209, 571–575. https://doi.org/10.1016/j.matlet.2017.08.100

Annu, Raja, A.N., Singh, K., Halve, A.K., Jain, R., 2020. Fabrication of bismuth oxide-modified pencil graphite sensors for monitoring the hazardous herbicide diuron. Nanoscale Adv. 2, 3404–3410. https://doi.org/10.1039/D0NA00394H

Anu Prathap, M.U., Sun, S., Wei, C., Xu, Z.J., 2015. A novel non-enzymatic lindane sensor based on CuO–MnO_2 hierarchical nano-microstructures for enhanced sensitivity. Chem. Commun. 51, 4376–4379. https://doi.org/10.1039/C5CC00024F

Arpitha, S.B., Kumara Swamy, B.E., Shashikumara, J.K., 2023. An efficient electrochemical sensor based on ZnO/Co_3O_4 nanocomposite modified carbon paste electrode for the sensitive detection of hydroquinone and resorcinol. Inorg. Chem. Commun. 152, 110656. https://doi.org/10.1016/j.inoche.2023.110656

Arsalan, M., Saddique, I., Baoji, M., Awais, A., Khan, I., Shamseldin, M.A., Mehrez, S., 2022. Novel Synthesis of Sensitive Cu-ZnO Nanorod–Based Sensor for Hydrogen Peroxide Sensing. Front. Chem. 10, 932985. https://doi.org/10.3389/fchem.2022.932985

Arumugam, B., Muthulakshmi, L., Ramaraj, S.K., 2023. Enhanced selective detection of insecticide profenofos with aid of a novel CeO_2 NPs/rGO nanocomposite using bacterial derived bioflocculant polymer as reducing agent. J. Environ. Chem. Eng. 11, 109149. https://doi.org/10.1016/j.jece.2022.109149

Aydın, R., Akkaya, A., Kahveci, O., Şahin, B., 2023. Nanostructured CuO thin-film-based conductometric sensors for real-time tracking of sweat loss. ACS Omega 8, 20009–20019. https://doi.org/10.1021/acsomega.3c02232

Bakhsh, H., Buledi, J.A., Ghumro, T., Khand, N.H., Ameen, S., Solangi, A.R., Sherazi, S.T.H., Shah, Z.-H. ul H., 2021a. Sodium dodecyl sulfate stabilized NiO nanoseeds: A potential procedure for ultra-sensitive determination of bentazone in vegetables. J. Mater. Sci.

Mater. Electron. 32, 15917–15929. https://doi.org/10.1007/s10854-021-06143-7

Bakhsh, H., Buledi, J.A., Khand, N.H., Junejo, B., Solangi, A.R., Mallah, A., Sherazi, S.T.H., 2021b. NiO nanostructures based functional none-enzymatic electrochemical sensor for ultrasensitive determination of endosulfan in vegetables. J. Food Meas. Charact. 15, 2695–2704. https://doi.org/10.1007/s11694-021-00860-7

Baksh, H., Buledi, J.A., Khand, N.H., Solangi, A.R., Mallah, A., Sherazi, S.T., Abro, M.I., 2020. Ultra-selective determination of carbofuran by electrochemical sensor based on nickel oxide nanoparticles stabilized by ionic liquid. Monatshefte für Chemie - Chem. Mon. 151, 1689–1696. https://doi.org/10.1007/s00706-020-02704-4

Balasubramanian, P., Balamurugan, T.S.T.S.T., Chen, S.-M.M., Chen, T.-W.W., Sharmila, G., Yu, M.-C.C., 2018a. One-step green synthesis of colloidal gold nano particles: A potential electrocatalyst towards high sensitive electrochemical detection of methyl parathion in food samples. J. Taiwan Inst. Chem. Eng. 87, 83–90. https://doi.org/10.1016/j.jtice.2018.03.014

Balasubramanian, P., Settu, R., Chen, S.-M., Chen, T.-W., 2018b. Voltammetric sensing of sulfamethoxazole using a glassy carbon electrode modified with a graphitic carbon nitride and zinc oxide nanocomposite. Microchim. Acta 185, 396. https://doi.org/10.1007/s00604-018-2934-z

Balram, D., Lian, K.-Y., Sebastian, N., 2020. Ultrasound-assisted synthesis of 3D flower-like zinc oxide decorated fMWCNTs for sensitive detection of toxic environmental pollutant 4-nitrophenol. Ultrason. Sonochem. 60, 104798. https://doi.org/10.1016/j.ultsonch.2019.104798

Beitollahi, H., Tajik, S., Garkani Nejad, F., Safaei, M., 2020. Recent advances in ZnO nanostructure-based electrochemical sensors and biosensors. J. Mater. Chem. B 8, 5826–5844. https://doi.org/10.1039/D0TB00569J

Borges, R.S., Palheta, I.C., Ota, S.S.B., Morais, R.B., Barros, V.A., Ramos, R.S., Silva, R.C., Costa, J. da S., Silva, C.H.T.P., Campos, J.M., Santos, C.B.R., 2019. Toward of Safer Phenylbutazone Derivatives by Exploration of Toxicity Mechanism. Molecules 24, 143. https://doi.org/10.3390/molecules24010143

Borowska, M., Jiménez-Lamana, J., Bierla, K., Jankowski, K., Szpunar, J., 2023. A green and fast microwave-assisted synthesis of selenium nanoparticles and their characterization under gastrointestinal conditions using mass spectrometry. Food Chem. 417, 135864. https://doi.org/10.1016/j.foodchem.2023.135864

Bratov, A., Abramova, N., Ipatov, A., 2010. Recent trends in potentiometric sensor arrays—A

review. Anal. Chim. Acta 678, 149–159. https://doi.org/10.1016/j.aca.2010.08.035

Buledi, J.A., Buledi, P.A., Batool, M., Solangi, A.R., Mallah, A., Ameen, S., Palabiyik, I.M., Maleh, H.K., 2021. Exploring electrocatalytic proficiencies of CuO nanostructure for simultaneous determination of bentazone and mexacarbate pesticides. Appl. Nanosci. 11, 1889–1902. https://doi.org/10.1007/s13204-021-01864-x

Candia-Onfray, C., Bollo, S., Yáñez, C., Escalona, N., Marco, J.F., Menéndez, N., Salazar, R., Recio, F.J., 2021. Nanostructured Fe-N-C pyrolyzed catalyst for the H_2O_2 electrochemical sensing. Electrochim. Acta 387, 138468. https://doi.org/10.1016/j.electacta.2021.138468

Cao, C., Hu, C., Wang, X., Wang, S., Tian, Y., Zhang, H., 2011. UV sensor based on TiO_2 nanorod arrays on FTO thin film. Sensors Actuators B Chem. 156, 114–119. https://doi.org/10.1016/j.snb.2011.03.080

Castro, S.V.F., Silva, C. V., Stefano, J.S., Richter, E.M., Munoz, R.A.A., 2020. Voltammetric determination of traces of 4-Chloroaniline in antiseptic samples on a cathodically-treated boron-doped diamond electrode. J. Electroanal. Chem. 877, 2–8. https://doi.org/10.1016/j.jelechem.2020.114500

Chang, C.-N., Cheng, H.-B., Chao, A.C., 2004. Applying the Nernst equation to simulate redox potential variations for biological nitrification and denitrification processes. Environ. Sci. Technol. 38, 1807–1812. https://doi.org/10.1021/es021088e

Chaudhary, M., Kumar, A., Devi, A., Singh, B.P., Malhotra, B.D., Singhal, K., Shukla, S., Ponnada, S., Sharma, R.K., Vega-Olivencia, C.A., Tyagi, S., Singhal, R., 2023. Prospects of nanostructure-based electrochemical sensors for drug detection: a review. Mater. Adv. 4, 432–457. https://doi.org/10.1039/D2MA00896C

Chaure, S., 2017. Synthesis and characterization of vertically aligned cadmium oxide nanowire array. J. Mater. Sci. Mater. Electron. 28, 1832–1836. https://doi.org/10.1007/s10854-016-5733-5

Chen, K., Chou, W., Liu, L., Cui, Y., Xue, P., Jia, M., 2019. Electrochemical sensors fabricated by electrospinning technology: An overview. Sensors 19, 3676. https://doi.org/10.3390/s19173676

Chen, Y., Yang, L., Tang, X., Zhang, Y., He, Z., Liu, Y., Jiang, X., Xiong, X., 2021. Microplasma synthesis of $Ni(OH)_2$ nanoflake array on carbon cloth as an efficient nonenzymatic sensor for glucose. Ionics (Kiel). 27, 2739–2745. https://doi.org/10.1007/s11581-021-04067-0

Chiang, J., 2008. Simultaneous derivatization and extraction of anilines in waste water with dispersive liquid–liquid microextraction followed by gas chromatography–mass

spectrometric detection. Talanta 75, 70–75. https://doi.org/10.1016/j.talanta.2007.10.036

Chowdhury, A., Bhan, C., Rao Peela, N., Kumar Golder, A., 2023. A simple template-free bioinspired route of 1D Bi_2S_3 nanorods synthesis for electrochemical CO_2 reduction to formate. J. Ind. Eng. Chem. 127, 138–148. https://doi.org/10.1016/j.jiec.2023.06.055

Chuiprasert, J., Srinives, S., Boontanon, N., Polprasert, C., Ramungul, N., Karawek, A., Boontanon, S.K., 2024. Ciprofloxacin Electrochemical Sensor Using Copper–Iron Mixed Metal Oxides Nanoparticles/Reduced Graphene Oxide Composite. ACS Omega 9, 23172–23183. https://doi.org/10.1021/acsomega.3c06705

Crispi, S., Neri, G., 2022. Development of a conductometric sensor based on Al,Ca-doped ZnO for the detection of formaldehyde. Sensors 22, 7465. https://doi.org/10.3390/s22197465

Daizy, M., Ali, M.R., Bacchu, M.S., Aly, M.A.S., Khan, M.Z.H., 2021. ZnO hollow spheres arrayed molecularly-printed-polymer based selective electrochemical sensor for methyl-parathion pesticide detection. Environ. Technol. Innov. 24, 101847. https://doi.org/10.1016/j.eti.2021.101847

Das, D., Bhan, C., Mukherjee, C., Golder, A.K., 2024. Improved selectivity of electrochemical aniline sensing using one-dimensional silver nanorods with high aspect ratio synthesized by ascorbic acid assisted method. Anal. Chim. Acta 1310, 342697. https://doi.org/10.1016/j.aca.2024.342697

Dash, S.R., Bag, S.S., Golder, A.K., 2022. Carbon Dots Derived from Waste Psidium Guajava Leaves for Electrocatalytic Sensing of Chlorpyrifos. Electroanalysis 34, 1141–1149. https://doi.org/10.1002/elan.202100344

Dash, S.R., Bag, S.S., Golder, A.K., 2021. Bio-inspired PtNPs/Graphene nanocomposite based electrocatalytic sensing of metabolites of dipyrone. Anal. Chim. Acta 1167, 338562. https://doi.org/10.1016/j.aca.2021.338562

Dash, S.R., Bag, S.S., Golder, A.K., 2020. Synthesis of highly structured spherical Ag@Pt core-shell NPs using bio-analytes for electrocatalytic Pb(II) sensing. Sensors Actuators B Chem. 314, 128062. https://doi.org/10.1016/j.snb.2020.128062

Dash, S.R., Bag, S.S., Golder, A.K., 2018. Synergized AgNPs formation using microwave in a bio-mediated route: Studies on particle aggregation and electrocatalytic sensing of ascorbic acid from biological entities. J. Electroanal. Chem. 827, 181–192. https://doi.org/10.1016/j.jelechem.2018.09.023

de Lima, C.A., Santana, E.R., Piovesan, J.V., Spinelli, A., 2016. Silver nanoparticle-modified electrode for the determination of nitro compound-containing pesticides. Anal. Bioanal. Chem. 408, 2595–2606. https://doi.org/10.1007/s00216-016-9367-5

Diop, N.A., Diouf, D., Bodian, E.H.T., Faye, C., Bakhoum, J.-P., Thiare, D.D., Diaw, P.A., Gaye-Seye, M.D., Coly, A., Le Jeune, B., Giamarchi, P., 2023. High sensitivity on-site early warning system monitoring of pesticides by photo-induced fluorescence. Anal. Chim. Acta 1250, 340969. https://doi.org/10.1016/j.aca.2023.340969

Disouza, F.P.D., Ruspika, S., Chen, S.-M., Balaji, R., Meena Devi, J., Peng, J.-Y., Irudaya Jothi, A., 2023. Synergetic effect of ZnS: SnS_2/reduced graphene oxide heterostructures for electrochemical detection of carcinogenic pollutant maleic hydrazide. Microchem. J. 193, 109087. https://doi.org/10.1016/j.microc.2023.109087

Duan, C., Dong, Y., Sheng, Q., Zheng, J., 2019. A high-performance non-enzymatic electrochemical hydrazine sensor based on $NiCo_2S_4$ porous sphere. Talanta 198, 23–29. https://doi.org/10.1016/j.talanta.2019.01.081

Elgrishi, N., Rountree, K.J., McCarthy, B.D., Rountree, E.S., Eisenhart, T.T., Dempsey, J.L., 2018. A Practical Beginner's Guide to Cyclic Voltammetry. J. Chem. Educ. 95, 197–206. https://doi.org/10.1021/acs.jchemed.7b00361

Emin Çorman, M., Cetinkaya, A., Armutcu, C., Uzun, L., Ozkan, S.A., 2023. Designing of ZnO nanoparticles oriented interface imprinted electrochemical sensor for fluoxetine detection. Bioelectrochemistry 152, 108411. https://doi.org/10.1016/j.bioelechem.2023.108411

Ettadili, F.E., Aghris, S., Laghrib, F., Farahi, A., Bakasse, M., Lahrich, S., El Mhammedi, M.A., 2023. Electrochemical detection of ornidazole in commercial milk and water samples using an electrode based on green synthesis of silver nanoparticles using cellulose separated from Phoenix dactylifera seed. Int. J. Biol. Macromol. 242, 124995. https://doi.org/10.1016/j.ijbiomac.2023.124995

Ezhil Vilian, A.T., Hwang, S.-K., Lee, M.J., Huh, Y.S., Han, Y.-K., 2022. Manganese-doped zinc sulfide microspheres for improved electrocatalytic sensing ability toward carbendazim in food samples. Microchem. J. 175, 107204. https://doi.org/10.1016/j.microc.2022.107204

Ganesan, M., Keerthika Devi, R., Chen, S.-M., Ravi, S.K., 2023. Sustainable synthesis of hierarchical dysprosium vanadate 3D-micro flowers for electrochemical evaluation of organophosphate pesticide in food samples. Chem. Eng. J. 466, 143111. https://doi.org/10.1016/j.cej.2023.143111

GangaReddy, K., Reddy, M.V.R., 2023. Physical vapour deposition of Zn^{2+} doped NiO nanostructured thin films for enhanced selective and sensitive ammonia sensing. Mater. Sci. Semicond. Process. 154, 107198. https://doi.org/10.1016/j.mssp.2022.107198

Goswami, B., Mahanta, D., 2021. Fe_3O_4-polyaniline nanocomposite for non-enzymatic electrochemical detection of 2,4-Dichlorophenoxyacetic acid. ACS Omega 6, 17239–17246. https://doi.org/10.1021/acsomega.1c00983

Granados-Povedano, M., Domínguez, I., Egea-González, F., Garrido Frenich, A., Arrebola, F.J., 2023. Unified method for target and non-target monitoring of pesticide residues in fruits and fruit juices by gas chromatography-high resolution mass spectrometry. Foods 12, 739. https://doi.org/10.3390/foods12040739

Haritha, V.S., Sarath Kumar, S.R., Rakhi, R.B., 2023. WS_2-nanosheet-modified electrodes as an efficient electrochemical sensing platform for the nonenzymatic detection of the insecticide imidacloprid. ACS Omega 8, 8695–8702. https://doi.org/10.1021/acsomega.2c08077

Hasheena, M., Ratnamala, A., Noorjahan, M., Deepthi Reddy, G., Chandra Babu Naidu, K., 2023. Electrochemical sensor for detection of dopamine and tyrosine using CdS–C quantum dots modified electrode. J. Appl. Electrochem. 53, 571–583. https://doi.org/10.1007/s10800-022-01794-8

He, C., Yan, R., Gao, X., Xue, Q., Wang, H., 2023a. Non-enzymatic electrochemical malathion sensor based on bimetallic Cu-Co metal-organic gels modified glassy carbon electrode. Sensors Actuators B Chem. 385, 133697. https://doi.org/10.1016/j.snb.2023.133697

He, C., Yan, R., Xue, Q., Li, S., Wang, H., 2023b. Electrochemical malathion sensors based on phytic acid-doped polyaniline and overoxidized polyaniline nanorods. J. Mater. Sci. 58, 1200–1213. https://doi.org/10.1007/s10853-022-08052-4

He, Y., Wu, T., Wang, J., Ye, J., Xu, C., Li, F., Guo, Q., 2020. A sensitive pyrimethanil sensor based on porous $NiCo_2S_4$/graphitized carbon nanofiber film. Talanta 219, 121277. https://doi.org/10.1016/j.talanta.2020.121277

He, Z., Tang, X., Zhang, Y., Yu, H., Zou, Z., Huang, K., Xue, K., Xiong, X., 2022. Rapid preparation of 3D ultra-thin CuO nanosheets by dielectric barrier discharge microplasma for non-enzymatic detection of glucose. Catal. Letters 152, 3517–3525. https://doi.org/10.1007/s10562-022-03931-6

Helm, I., Jalukse, L., Leito, I., 2010. Measurement uncertainty estimation in amperometric sensors: A tutorial review. Sensors 10, 4430–4455. https://doi.org/10.3390/s100504430

Hu, H., Wu, S., Wang, C., Wang, X., Shi, X., 2023. Electrochemical behaviour of cellulose/reduced graphene oxide/carbon fiber paper electrodes towards the highly sensitive detection of amitrole. RSC Adv. 13, 1867–1876. https://doi.org/10.1039/D2RA07662D

Huo, D., Li, Q., Zhang, Y., Hou, C., Lei, Y., 2014. A highly efficient organophosphorus pesticides sensor based on CuO nanowires–SWCNTs hybrid nanocomposite. Sensors Actuators B Chem. 199, 410–417. https://doi.org/10.1016/j.snb.2014.04.016

Ilager, D., Malode, S.J., Shetti, N.P., 2022. Development of 2D graphene oxide sheets-based voltammetric sensor for electrochemical sensing of fungicide, carbendazim. Chemosphere 303, 134919. https://doi.org/10.1016/j.chemosphere.2022.134919

Jafari, Z., Ghani, M., 2023. Magnetic carbonized cellulose-MIL 101(Fe) composite as a sorbent for magnetic solid phase extraction of selected organophosphorus pesticides combined with high performance liquid chromatography-ultraviolet detection. Talanta Open 7, 100212. https://doi.org/10.1016/j.talo.2023.100212

Jain, S., Chakraborty, A., Sharma, B., Sarma, T.K., 2022. Cu^{2+} Ion Doping-Induced Self-Assembled ZnO-Cu_xO Nanostructures for Electrochemical Sensing of Hydrogen Peroxide and p -Nitrophenol. ACS Appl. Nano Mater. 5, 11973–11983. https://doi.org/10.1021/acsanm.2c03073

Jia, W., Guo, M., Zheng, Z., Yu, T., Wang, Y., Rodriguez, E.G., Lei, Y., 2008. Vertically Aligned CuO Nanowires Based Electrode for Amperometric Detection of Hydrogen Peroxide. Electroanalysis 20, 2153–2157. https://doi.org/10.1002/elan.200804299

Jiang, X., Sun, B., Song, Y., Dou, M., Ji, J., Wang, F., 2017. One-pot synthesis of MoS_2/WS_2 ultrathin nanoflakes with vertically aligned structure on indium tin oxide as a photocathode for enhanced photo-assistant electrochemical hydrogen evolution reaction. RSC Adv. 7, 49309–49319. https://doi.org/10.1039/C7RA10762E

Jo, A., Kang, M., Cha, A., Jang, H.S., Shim, J.H., Lee, N.-S., Kim, M.H., Lee, Y., Lee, C., 2014. Nonenzymatic amperometric sensor for ascorbic acid based on hollow gold/ruthenium nanoshells. Anal. Chim. Acta 819, 94–101. https://doi.org/10.1016/j.aca.2014.02.017

Kaczala, F., E. Blum, S., 2016. The Occurrence of Veterinary Pharmaceuticals in the Environment: A Review. Curr. Anal. Chem. 12, 169–182. https://doi.org/10.2174/1573411012666151009193108

Kalia, S., Kumar, R., Sharma, R., Kumar, S., Singh, D., Singh, R.K., 2024. Two-dimensional layered rGO-MoS_2 heterostructures decorated with Fe_3O_4 nanoparticles as an electrochemical sensor for detection of para-nitrophenol. J. Phys. Chem. Solids 184, 111719. https://doi.org/10.1016/j.jpcs.2023.111719

Kalyabina, V.P., Esimbekova, E.N., Kopylova, K. V., Kratasyuk, V.A., 2021. Pesticides: formulants, distribution pathways and effects on human health – a review. Toxicol.

Reports 8, 1179–1192. https://doi.org/10.1016/j.toxrep.2021.06.004

Karthik, R., Sasikumar, R., Chen, S.-M., Govindasamy, M., Kumar, J.V., Muthuraj, V., 2016. Green synthesis of platinum nanoparticles using extract and its electrochemical oxidation of hydrazine in water samples. Int. J. Electrochem. Sci. 11, 8245–8255. https://doi.org/10.20964/2016.10.62

Karuppiah, C., Muthupandi, K., Chen, S.-M., Ali, M.A., Palanisamy, S., Rajan, A., Prakash, P., Al-Hemaid, F.M.A., Lou, B.-S., 2015. Green synthesized silver nanoparticles decorated on reduced graphene oxide for enhanced electrochemical sensing of nitrobenzene in waste water samples. RSC Adv. 5, 31139–31146. https://doi.org/10.1039/C5RA00992H

Kaur, A., Chakraborty, U., Chauhan, M., Sharma, R., Kaur, G., Chaudhary, G.R., 2022. Choline acetate modified ZnO nanostructure as efficient electrochemical sensor for hydrazine detection. Electrochim. Acta 419, 140384. https://doi.org/10.1016/j.electacta.2022.140384

Khairy, M., Ayoub, H.A., Banks, C.E., 2018. Non-enzymatic electrochemical platform for parathion pesticide sensing based on nanometer-sized nickel oxide modified screen-printed electrodes. Food Chem. 255, 104–111. https://doi.org/10.1016/j.foodchem.2018.02.004

Khan, R., Periyayya, U., Kim, G.C., Lee, I.-H., 2019. Fabrication of ultra-sensitive piperidine chemical sensor with a direct grown well-aligned ZnO nanorods on FTO substrate as a working electrode. Solid State Sci. 97, 105986. https://doi.org/10.1016/j.solidstatesciences.2019.105986

Khizir, H.A., Abbas, T.A.-H., 2021. Hydrothermal growth and controllable synthesis of flower-shaped TiO_2 nanorods on FTO coated glass. J. Sol-Gel Sci. Technol. 98, 487–496. https://doi.org/10.1007/s10971-021-05531-z

Kokulnathan, T., Vishnuraj, R., Wang, T.-J.J., Kumar, E.A., Pullithadathil, B., 2021. Heterostructured bismuth oxide/hexagonal-boron nitride nanocomposite: A disposable electrochemical sensor for detection of flutamide. Ecotoxicol. Environ. Saf. 207, 111276. https://doi.org/10.1016/j.ecoenv.2020.111276

Kokulnathan, T., Wang, T.-J., Murugesan, T., Anthuvan, A.J., Kumar, R.R., Ahmed, F., Arshi, N., 2023. Structural growth of zinc oxide nanograins on carbon cloth as flexible electrochemical platform for hydroxychloroquine detection. Chemosphere 312, 137186. https://doi.org/10.1016/j.chemosphere.2022.137186

Kritika, Roy, I., 2022. Therapeutic applications of magnetic nanoparticles: Recent advances.

Mater. Adv. 3, 7425–7444. https://doi.org/10.1039/D2MA00444E

Kulandaiswamy, A.J., Sharma, N., Nesakumar, N., Kailasam, K., Rayappan, J.B.B., 2020. S,N-GQDs enzyme mimicked electrochemical sensor to detect the hazardous level of monocrotophos in water. Electroanalysis 32, 971–977. https://doi.org/10.1002/elan.201900447

Kumar, N., Sharma, A., Tiwari, D.C., Tomar, R., 2022. Hydrothermally synthesized polycrystalline Ce-TiO_2@rGO compound for sensing of para-nitroaniline. Bull. Mater. Sci. 45, 87. https://doi.org/10.1007/s12034-022-02673-w

Kumar, V., Singh, K., Panwar, S., Mehta, S.K., 2017. Green synthesis of manganese oxide nanoparticles for the electrochemical sensing of p-nitrophenol. Int. Nano Lett. 7, 123–131. https://doi.org/10.1007/s40089-017-0205-3

Lai, H., Ming, P., Liu, Y., Wang, S., Zhou, Q., Zhai, H., 2023. MWCNTs and ZnO-based Ce-MOF nanocomposites as enhanced sensing platform for electrochemical detection of carbendazim in Chinese traditional herbs samples. Microchim. Acta 190, 281. https://doi.org/10.1007/s00604-023-05869-x

Le Nhat Trang, N., Thi Nguyet Nga, D., Tufa, L.T., Tran, V.T., Hung, T.-T., Ngoc Phan, V., Pham, T.N., Hoang, V.-T., Le, A.-T., 2023. Unveiling the effect of crystallinity and particle size of biogenic Ag/ZnO nanocomposites on the electrochemical sensing performance of carbaryl detection in agricultural products. RSC Adv. 13, 8753–8764. https://doi.org/10.1039/D3RA00399J

Lee, K.-T., Liu, D.-M., Liang, Y.-Y., Matsushita, N., Ikoma, T., Lu, S.-Y., 2014. Porous fluorine-doped tin oxide as a promising substrate for electrochemical biosensors—demonstration in hydrogen peroxide sensing. J. Mater. Chem. B 2, 7779–7784. https://doi.org/10.1039/C4TB01191K

Lee, K.-U., Tran, T.H., Kim, S.H., Shin, H.-J., 2017. Fabrication of nanoporous gold thin films on glass substrates for amperometric sensing of aniline. J. Alloys Compd. 713, 132–137. https://doi.org/10.1016/j.jallcom.2017.04.173

Li, C.-P., Fan, S., Yin, C., Zhang, N., Du, S., Zhao, H., 2014. Carboxylic silica nanosheet–platinum nanoparticle modified glass carbon electrodes for pesticide detection. Anal. Methods 6, 1914–1921. https://doi.org/10.1039/C3AY42305K

Li, J., Wang, Q., Liu, Y., Jiang, Z., Liu, J., Li, H., Yuan, X., 2021. Boron/nitrogen co-doped diamond electrode for highly efficient electrochemistry detection of aniline. Funct. Diam. 1, 135–142. https://doi.org/10.1080/26941112.2021.1939170

Li, K., Li, Y., Wang, L., Yang, L., Ye, B., 2019. Study the voltammetric behavior of 10-

Hydroxycamptothecin and its sensitive determination at electrochemically reduced graphene oxide modified glassy carbon electrode. Arab. J. Chem. 12, 2732–2739. https://doi.org/10.1016/j.arabjc.2015.05.014

Li, W., Wang, P., Chu, B., Chen, X., Peng, Z., Chu, J., Lin, R., Gu, Q., Lu, J., Wu, D., 2023. A highly-sensitive sensor based on carbon nanohorns@reduced graphene oxide coated by gold platinum core–shell nanoparticles for electrochemical detection of carbendazim in fruit and vegetable juice. Food Chem. 402, 134197. https://doi.org/10.1016/j.foodchem.2022.134197

Liang, Q., Xiao, W., Zhang, C., Zhu, D., Wang, S.-L., Tian, S.-Y., Long, T., Yue, E.-L., Wang, J.-J., Hou, X.-Y., 2023. MOFs-based Fe@YAU-101/GCE electrochemical sensor platform for highly selective detecting trace multiplex heavy metal ions. Talanta 259, 124491. https://doi.org/10.1016/j.talanta.2023.124491

Liang, Y., Zhang, Lingyu, Wang, H., Cai, X., Zhang, Li, Xu, Y., Yao, C., Si, W., Huang, Z., Shi, G., 2023. Fabrication of a novel electrochemical sensor based on tin disulfide/multi-walled carbon nanotunbes-modified electrode for rutin determination in natural vegetation. Arab. J. Chem. 16, 104613. https://doi.org/10.1016/j.arabjc.2023.104613

Lin, Y.-H., Sivakumar, C., Balraj, B., Murugesan, G., Nagarajan, S.K., Ho, M.-S., 2023. Ag-decorated vertically aligned ZnO nanorods for non-enzymatic glucose sensor applications. Nanomaterials 13, 754. https://doi.org/10.3390/nano13040754

Liu, J., Li, Y., Jiang, J., Huang, X., 2010. C@ZnO nanorod array-based hydrazine electrochemical sensor with improved sensitivity and stability. Dalt. Trans. 39, 8693. https://doi.org/10.1039/c0dt00258e

Liu, X., Li, Y., Chen, N., Deng, D., Xing, X., Wang, Y., 2016. Ni_3S_2@Ni foam 3D electrode prepared via chemical corrosion by sodium sulfide and using in hydrazine electro-oxidation. Electrochim. Acta 213, 730–739. https://doi.org/10.1016/j.electacta.2016.08.009

Maji, B., Sahoo, S.J., Rout, V., Barik, B., Behera, N., Dash, P., 2023. Highly Sensitive and Selective Nonenzymatic Sensing of Glyphosate Using FTO-Modified MOF-Derived $CuCo_2O_4$ Nanostructures Intercalated in Protonated-g-C_3N_4 and 3D-Graphene Oxide Sheets. Ind. Eng. Chem. Res. 62, 3477–3491. https://doi.org/10.1021/acs.iecr.2c04426

Mali, S.S., Kim, H., Patil, P.S., Hong, C.K., 2013. Chemically grown vertically aligned 1D ZnO nanorods with CdS coating for efficient quantum dot sensitized solar cells (QDSSC): a controlled synthesis route. Dalt. Trans. 42, 16961. https://doi.org/10.1039/c3dt51287h

Malode, S.J., Keerthi, P.K., Shetti, N.P., Kulkarni, R.M., 2020. Electroanalysis of Carbendazim

using MWCNT/Ca-ZnO Modified Electrode. Electroanalysis 32, 1590–1599. https://doi.org/10.1002/elan.201900776

Manavalan, S., Veerakumar, P., Chen, S.-M., Lin, K.-C., 2020. Three-dimensional zinc oxide nanostars anchored on graphene oxide for voltammetric determination of methyl parathion. Microchim. Acta 187, 17. https://doi.org/10.1007/s00604-019-4031-3

Manivannan, K., Sivakumar, M., Cheng, C.-C., Lu, C.-H., Chen, J.-K., 2019. An effective electrochemical detection of chlorogenic acid in real samples: Flower-like ZnO surface covered on PEDOT:PSS composites modified glassy carbon electrode. Sensors Actuators B Chem. 301, 127002. https://doi.org/10.1016/j.snb.2019.127002

Marie, M., Mandal, S., Manasreh, O., 2015. An electrochemical glucose sensor based on zinc oxide nanorods. Sensors 15, 18714–18723. https://doi.org/10.3390/s150818714

Mariyappan, V., Keerthi, M., Chen, S.-M., 2021. Highly selective electrochemical sensor based on gadolinium sulfide rod-embedded RGO for the sensing of carbofuran. J. Agric. Food Chem. 69, 2679–2688. https://doi.org/10.1021/acs.jafc.0c07522

Medina-Llamas, V.L., Fajardo-Díaz, J.L., Morelos-Gomez, A., Endo, M., López-Urías, F., Muñoz-Sandoval, E., 2023. Crystalline multilayer graphene nanoflakes synthesized by catalytic chemical vapor deposition using reduced nanostructured hematite as catalyst precursor and 1,2-Dichlorobenzene and benzylamine mixture as carbon source. Carbon N. Y. 203, 813–826. https://doi.org/10.1016/j.carbon.2022.12.033

Megalamani, M.B., Patil, Y.N., Nandibewoor, S.T., 2023. A novel CTN-Fe_3O_4/g-C_3N_4 modified green synthetic sensor for electro-sensing of phenylbutazone. Mater. Sci. Semicond. Process. 166, 107750. https://doi.org/10.1016/j.mssp.2023.107750

Mei, H., Xie, J., Li, Z., Lou, C., Lei, G., Liu, X., Zhang, J., 2022. Rational design of ZnO@ZIF-8 nanoarrays for improved electrochemical detection of H_2O_2. CrystEngComm 24, 1645–1654. https://doi.org/10.1039/D1CE01704G

Meireles, L.M., Silva, R.M., da Silva, R.C., Okumura, L.L., Moreira, R.P.L., Silva, T.A., 2024. Low-cost electrochemical sensor for ciprofloxacin antibiotic based on green-synthesized silver nanoparticles and carbon black. J. Solid State Electrochem. https://doi.org/10.1007/s10008-024-06033-y

Mohammad, A., Ehtisham Khan, M., Alarifi, I.M., Hwan Cho, M., Yoon, T., 2021. A sensitive electrochemical detection of hydrazine based on SnO_2/CeO_2 nanostructured oxide. Microchem. J. 171, 106784. https://doi.org/10.1016/j.microc.2021.106784

Mohan, B., Kumari, R., Virender, Singh, G., Singh, K., Pombeiro, A.J.L., Yang, X., Ren, P., 2023. Covalent organic frameworks (COFs) and metal–organic frameworks (MOFs) as

electrochemical sensors for the efficient detection of pharmaceutical residues. Environ. Int. 175, 107928. https://doi.org/10.1016/j.envint.2023.107928

Musameh, M., Notivoli, M.R., Hickey, M., Huynh, C.P., Hawkins, S.C., Yousef, J.M., Kyratzis, I.L., 2013. Carbon nanotube-web modified electrodes for ultrasensitive detection of organophosphate pesticides. Electrochim. Acta 101, 209–215. https://doi.org/10.1016/j.electacta.2012.11.030

Muungani, G., van Zyl, W.E., 2023. A $CaCuSi_4O_{10}$/GCE electrochemical sensor for detection of norfloxacin in pharmaceutical formulations. RSC Adv. 13, 12799–12808. https://doi.org/10.1039/D3RA01702H

Naik, S.S., Lee, S.J., Theerthagiri, J., Yu, Y., Choi, M.Y., 2021. Rapid and highly selective electrochemical sensor based on ZnS/Au-decorated f-multi-walled carbon nanotube nanocomposites produced via pulsed laser technique for detection of toxic nitro compounds. J. Hazard. Mater. 418, 126269. https://doi.org/10.1016/j.jhazmat.2021.126269

Nallusamy, S., Sujatha, K., 2021. Experimental analysis of nanoparticles with cobalt oxide synthesized by coprecipitation method on electrochemical biosensor using FTIR and TEM. Mater. Today Proc. 37, 728–732. https://doi.org/10.1016/j.matpr.2020.05.735

Nejabatdoust, A., Mirmiran, S.D., Salehzadeh, A., Masouleh, F.R., 2024. Effective Release of Ciprofloxacin and Rifampicin Antibiotics from Alginate-Chitosan Complex and Its Application Against Clinical Strains of Staphylococcus aureus. Bionanoscience 14, 532–546. https://doi.org/10.1007/s12668-023-01262-3

Nguyen, H.T.T., Chu, N.T.H., Le, H.T.T., 2023. Fabrication of screen-printed electrodes modified by hydrothermal MnO_2 microflowers and carbon for electrochemical sensors in copper ions detection. J. Chem. 2023, 1–13. https://doi.org/10.1155/2023/3855430

Özcan, A., Hamid, F., Özcan, A.A., 2021. Synthesizing of a nanocomposite based on the formation of silver nanoparticles on fumed silica to develop an electrochemical sensor for carbendazim detection. Talanta 222, 121591. https://doi.org/10.1016/j.talanta.2020.121591

Pabbi, M., Mittal, S.K., 2017. An electrochemical algal biosensor based on silica coated ZnO quantum dots for selective determination of acephate. Anal. Methods 9, 1672–1680. https://doi.org/10.1039/C7AY00111H

Pan, Z., Wei, Y., Guo, H., Liu, B., Sun, L., Lu, Z., Wei, X., Zhang, H., Chen, Y., Yang, W., 2023. Sensitive detection of sulfamethoxazole by an electrochemical sensing platform with a covalent organic framework in situ grown on polyaniline. Microporous

Mesoporous Mater. 348, 112409. https://doi.org/10.1016/j.micromeso.2022.112409

Parashar, M., Shukla, V.K., Singh, R., 2020. Metal oxides nanoparticles via sol–gel method: A review on synthesis, characterization and applications. J. Mater. Sci. Mater. Electron. 31, 3729–3749. https://doi.org/10.1007/s10854-020-02994-8

Pathak, V.M., Verma, V.K., Rawat, B.S., Kaur, B., Babu, N., Sharma, A., Dewali, S., Yadav, M., Kumari, R., Singh, S., Mohapatra, A., Pandey, V., Rana, N., Cunill, J.M., 2022. Current status of pesticide effects on environment, human health and it's eco-friendly management as bioremediation: A comprehensive review. Front. Microbiol. 13, 2833. https://doi.org/10.3389/fmicb.2022.962619

Pei, X., Kang, W., Yue, W., Bange, A., Heineman, W.R., Papautsky, I., 2014. Disposable copper-based electrochemical sensor for anodic stripping voltammetry. Anal. Chem. 86, 4893–4900. https://doi.org/10.1021/ac500277j

Pradhan, S., Mailapalli, D.R., 2020. Nanopesticides for pest control. pp. 43–74. https://doi.org/10.1007/978-3-030-33281-5_2

Puthalapattu, R.P., Punyasamudram, S., Bathinapatla, A., Venkata, N.K.P., Kanchi, S., 2023. Electrochemical non-enzymatic strategy with green synthesized Fe_2O_3_CuO nanocomposite for detection of amiprofos-methyl herbicide in industrial effluents and soils. Chem. Phys. Impact 6, 100195. https://doi.org/10.1016/j.chphi.2023.100195

Qiu, L., Lv, P., Zhao, C., Feng, X., Fang, G., Liu, J., Wang, S., 2019. Electrochemical detection of organophosphorus pesticides based on amino acids conjugated nanoenzyme modified electrodes. Sensors Actuators B Chem. 286, 386–393. https://doi.org/10.1016/j.snb.2019.02.007

Rajiv, P., Manikandan, R., Sangeetha, S., Vanathi, P., Dhanasekaran, S., 2022. Fabrication of biogenic iron oxide and their efficiency to detect carbofuran in vegetable samples. Inorg. Chem. Commun. 142, 109649. https://doi.org/10.1016/j.inoche.2022.109649

Rana, D.S., Thakur, N., Thakur, S., Singh, D., 2022. Electrochemical determination of hydrazine by using MoS_2 nanostructure modified gold electrode. Nanofabrication 7, e002. https://doi.org/10.37819/nanofab.007.190

Ranđelović, M.S., Momčilović, M.Z., Milićević, J.S., Đurović-Pejčev, R.D., Mofarah, S.S., Sorrel, C.C., 2019. Voltammetric sensor based on Pt nanoparticles suported MWCNT for determination of pesticide clomazone in water samples. J. Taiwan Inst. Chem. Eng. 105, 115–123. https://doi.org/10.1016/j.jtice.2019.10.013

Ravi, R., Golder, A.K., 2025. Photocatalytic and biological degradation processes to mineralize pharmaceutically active compounds and catalyst recovery: A review. Coord. Chem. Rev.

523, 216267. https://doi.org/10.1016/j.ccr.2024.216267

Sakdarat, P., Chongsuebsirikul, J., Phongphut, A., Klinthingchai, Y., Prichanont, S., Thanachayanont, C., Pungetmongkol, P., 2019. Copper Oxide Nanorods Pesticide Sensor For Methyl Parathion Detection, in: 2019 IEEE 19th International Conference on Nanotechnology (IEEE-NANO). IEEE, pp. 113–116. https://doi.org/10.1109/NANO46743.2019.8993676

Salaria, K., Mehta, N., Krishna, C., Mehta, S.K., 2021. Electrochemical detection of TNT using CdS nanoparticles via cyclic voltammetry and amperometry. Curr. Res. Green Sustain. Chem. 4, 100166. https://doi.org/10.1016/j.crgsc.2021.100166

Salehzadeh, H., Ebrahimi, M., Nematollahi, D., Salarian, A.A., 2016. Electrochemical study of fenitrothion and bifenox and their simultaneous determination using multiwalled carbon nanotube modified glassy carbon electrode. J. Electroanal. Chem. 767, 188–194. https://doi.org/10.1016/j.jelechem.2016.02.011

Sant'Anna, M.V.S., Carvalho, S.W.M.M., Gevaerd, A., Silva, J.O.S., Santos, E., Carregosa, I.S.C., Wisniewski, A., Marcolino-Junior, L.H., Bergamini, M.F., Sussuchi, E.M., 2020. Electrochemical sensor based on biochar and reduced graphene oxide nanocomposite for carbendazim determination. Talanta 220, 121334. https://doi.org/10.1016/j.talanta.2020.121334

Selvi, S.V., Prasannan, A., Alagumalai, K., Liang, S.-T., Hong, P.-D., 2023. Disposable tungsten sulfide framed polydopamine nanostructure modified sensor for non-enzymatic electrochemical detection of organophosphate pesticide. Colloids Surfaces A Physicochem. Eng. Asp. 677, 132418. https://doi.org/10.1016/j.colsurfa.2023.132418

Shanmugam, R., Ganesamurthi, J., Chen, T.-W., Chen, S.-M., Alagumalai, K., Alkahtani, J., Alwahibi, M.S., M., A.A., 2022. Synergetic combination of nano hexagons SnS_2/Sulfur substituted graphitic carbon nitride: Evaluation of electrochemical sensor for the agricultural pollutant in environmental samples. Chem. Eng. J. 431, 134174. https://doi.org/10.1016/j.cej.2021.134174

Sharma, A., Kumar, V., Shahzad, B., Tanveer, M., Sidhu, G.P.S., Handa, N., Kohli, S.K., Yadav, P., Bali, A.S., Parihar, R.D., Dar, O.I., Singh, K., Jasrotia, S., Bakshi, P., Ramakrishnan, M., Kumar, S., Bhardwaj, R., Thukral, A.K., 2019. Worldwide pesticide usage and its impacts on ecosystem. SN Appl. Sci. 1, 1446. https://doi.org/10.1007/s42452-019-1485-1

Sharma, P., Pandey, V., Sharma, M.M.M., Patra, A., Singh, B., Mehta, S., Husen, A., 2021. A review on biosensors and nanosensors application in agroecosystems. Nanoscale Res.

Lett. 16, 136. https://doi.org/10.1186/s11671-021-03593-0

Shivakumar, M., Dharmaprakash, M.S., Manjappa, S., Nagashree, K.L., 2020. Green synthesis of silver nanoparticles (SNPs)-modified electrode for electrochemical detection of nitrobenzene. J. Iran. Chem. Soc. 17, 893–900. https://doi.org/10.1007/s13738-019-01822-z

Singh, K., Kaur, A., Umar, A., Chaudhary, G.R., Singh, S., Mehta, S.K., 2015. A comparison on the performance of zinc oxide and hematite nanoparticles for highly selective and sensitive detection of para-nitrophenol. J. Appl. Electrochem. 45, 253–261. https://doi.org/10.1007/s10800-014-0762-3

Sinha, A., Huang, Y., Zhao, H., 2019. Preparation of 3D assembly of mono layered molybdenum disulfide nanotubules for rapid screening of carbamate pesticide diethofencarb. Talanta 204, 455–464. https://doi.org/10.1016/j.talanta.2019.06.040

Somasundaram, G., Balasubramanian, S., Vaiyapuri, T., Muthiah, S., Sivanesan, J.R., Nesakumar, N., Shanmugam, S., Gunasekaran, B.M., 2023. Electrochemical detection of 4-Nitrophenol using a screen-printed carbon electrode modified by rod-shaped nickel oxide nanoparticles. ChemistrySelect 8, e202204418. https://doi.org/10.1002/slct.202204418

Stetter, J.R., Li, J., 2008. Amperometric gas sensors a review. Chem. Rev. 108, 352–366. https://doi.org/10.1021/cr0681039

Supraja, P., Tripathy, S., Krishna Vanjari, S.R., Singh, V., Singh, S.G., 2019. Electrospun tin (IV) oxide nanofiber based electrochemical sensor for ultra-sensitive and selective detection of atrazine in water at trace levels. Biosens. Bioelectron. 141, 111441. https://doi.org/10.1016/j.bios.2019.111441

Tang, C., Zhang, Y., Su, J., Wang, C., Sun, R., Zhang, J., Li, G., 2016. Synthesis and photocatalytic properties of vertically aligned Bi_2S_3 platelets. Solid State Sci. 51, 24–29. https://doi.org/10.1016/j.solidstatesciences.2015.11.004

Tanwar, S., Mathur, D., 2021. Graphene-based nanocomposites as sensing elements for the electrochemical detection of pesticides: a review. J. Solid State Electrochem. 25, 2145–2159. https://doi.org/10.1007/s10008-021-04990-2

Tanwar, S., Sharma, A., Mathur, D., 2023. A graphene quantum dots–glassy carbon electrode-based electrochemical sensor for monitoring malathion. Beilstein J. Nanotechnol. 14, 701–710. https://doi.org/10.3762/bjnano.14.56

Taqvi, S.I.H., Solangi, A.R., Buledi, J.A., Khand, N.H., Junejo, B., Memon, A.F., Ameen, S., Bhatti, A., Show, P.-L., Vasseghian, Y., Karimi-Maleh, H., 2022. Plant extract-based

green fabrication of nickel ferrite ($NiFe_2O_4$) nanoparticles: An operative platform for non-enzymatic determination of pentachlorophenol. Chemosphere 294, 133760. https://doi.org/10.1016/j.chemosphere.2022.133760

Tefera, M., Tessema, M., Admassie, S., Iwuoha, E.I., Waryo, T.T., Baker, P.G.L., 2018. Electrochemical determination of phenothrin in fruit juices at graphene oxide-polypyrrole modified glassy carbon electrode. Sens. Bio-Sensing Res. 21, 27–34. https://doi.org/10.1016/j.sbsr.2018.09.003

Tesena, P., Vinijkumthorn, R., Preuksathaporn, T., Piyakul, P., Chotikaprakal, T., Sirireugwipas, R., Wong-aree, K., Prapaiwan, N., 2024. Evaluation of gastrointestinal tract lesions and serum malondialdehyde levels after repeated oral administration of phenylbutazone in horses. Vet. Res. Commun. 48, 2343–2355. https://doi.org/10.1007/s11259-024-10415-y

Tian, X., Liu, L., Li, Y., Yang, C., Zhou, Z., Nie, Y., Wang, Y., 2018. Nonenzymatic electrochemical sensor based on CuO-TiO_2 for sensitive and selective detection of methyl parathion pesticide in ground water. Sensors Actuators B Chem. 256, 135–142. https://doi.org/10.1016/j.snb.2017.10.066

Tseng, G.-W., Lin, P.-C., Wang, C.-L., Wang, C.-C., Kei, C.-C., 2023. Development of three-dimensional flexible binder-free core-dual shell electrodes via atomic layer deposition of synergistic metal oxide nanocomposites for lithium-ion batteries. Appl. Surf. Sci. 614, 156177. https://doi.org/10.1016/j.apsusc.2022.156177

Tudi, M., Li, Hairong, Li, Hongying, Wang, L., Lyu, J., Yang, L., Tong, S., Yu, Q.J., Ruan, H.D., Atabila, A., Phung, D.T., Sadler, R., Connell, D., 2022. Exposure routes and health risks associated with pesticide application. Toxics 10, 335. https://doi.org/10.3390/toxics10060335

Umapathi, R., Ghoreishian, S.M., Sonwal, S., Rani, G.M., Huh, Y.S., 2022. Portable electrochemical sensing methodologies for on-site detection of pesticide residues in fruits and vegetables. Coord. Chem. Rev. 453, 214305. https://doi.org/10.1016/j.ccr.2021.214305

Umar, A., Rahman, M.M., Kim, S.H., Hahn, Y.-B., 2008. Zinc oxide nanonail based chemical sensor for hydrazine detection. Chem. Commun. 7345, 166–168. https://doi.org/10.1039/B711215G

Urbanová, V., Bakandritsos, A., Jakubec, P., Szambó, T., Zbořil, R., 2017. A facile graphene oxide based sensor for electrochemical detection of neonicotinoids. Biosens. Bioelectron. 89, 532–537. https://doi.org/10.1016/j.bios.2016.03.039

Valverde Aguilar, G., 2019. Introductory chapter: A brief semblance of the sol-gel method in research, in: Sol-Gel Method - Design and Synthesis of New Materials with Interesting Physical, Chemical and Biological Properties. IntechOpen, pp. 1–6. https://doi.org/10.5772/intechopen.82487

Velmurugan, S., Anupriya, J., Chen, S.-M., Hahn, Y.-B., 2023. Efficient lock-in CuO/WON heterostructures tailored for highly sensitive electrochemical detection of hazardous herbicide diuron in fruit juices and aqua region. Sensors Actuators B Chem. 375, 132920. https://doi.org/10.1016/j.snb.2022.132920

Wan, Q., Li, J., Liu, Z., Han, L., Huang, S., Wang, Z., 2023. Fabrication of Nanoporous Gold via an Improved Solid-Phase Method for Non-Enzymatic Detection of Aniline. Metals (Basel). 13, 754. https://doi.org/10.3390/met13040754

Wang, C., Song, Q., Liu, X., Zhu, X., 2020. Development of Electrochemical Sensor Based on Graphene Oxide Electrode Modified by Silver-Doped ZnO Nanorods for Detection of Carbamate Pesticide in Food. Int. J. Electrochem. Sci. 15, 5623–5631. https://doi.org/10.20964/2020.06.74

Wang, J., Luo, D.B., Farias, P.A.M., Mahmoud, J.S., 1985. Adsorptive stripping voltammetry of riboflavin and other flavin analogs at the static mercury drop electrode. Anal. Chem. 57, 158–162. https://doi.org/10.1021/ac00279a039

Wang, J., Yokokawa, M., Satake, T., Suzuki, H., 2015. A micro IrO potentiometric sensor for direct determination of organophosphate pesticides. Sensors Actuators B Chem. 220, 859–863. https://doi.org/10.1016/j.snb.2015.05.115

Wang, L., Liu, G., Zou, L., Xue, D., 2010. Phase evolution from rod-like ZnO to plate-like zinc hydroxysulfate during electrochemical deposition. J. Alloys Compd. 493, 471–475. https://doi.org/10.1016/j.jallcom.2009.12.129

Wang, Q., Wang, M., Jia, M., She, Y., Wang, J., Zheng, L., Abd El-Aty, A.M., 2023. Development of a specific and sensitive method for the detection of glyphosate pesticide and its metabolite in tea using dummy molecularly imprinted solid-phase extraction coupled with liquid chromatography-tandem quadrupole mass spectrometry. J. Chromatogr. A 1705, 464209. https://doi.org/10.1016/j.chroma.2023.464209

Wicaksono, W.P., Fadilla, N.I., Zamar, A.A., Fadillah, G., Anugrahwati, M., Anas, A.K., Kadja, G.T.M., 2022. Formaldehyde electrochemical sensor using graphite paste-modified green synthesized zinc oxide nanoparticles. Inorg. Chem. Commun. 143, 109729. https://doi.org/10.1016/j.inoche.2022.109729

Worboys, M., Toon, E., 2018. Phenylbutazone (Bute, PBZ, EPZ): one drug across two species.

Hist. Philos. Life Sci. 40, 27. https://doi.org/10.1007/s40656-018-0191-4

Wu, S., Xiong, W., Li, H., 2023. Insights into the Fe oxidation state of sphere-like Fe_2O_3 nanoparticles for simultaneous Pb^{2+} and Cu^{2+} detection. J. Alloys Compd. 934, 167863. https://doi.org/10.1016/j.jallcom.2022.167863

Yi, X., Yuan, Z., Yu, X., Zheng, L., Wang, C., 2023. Novel microneedle patch-based surface-enhanced raman spectroscopy sensor for the detection of pesticide residues. ACS Appl. Mater. Interfaces 15, 4873–4882. https://doi.org/10.1021/acsami.2c17954

Zahran, M., Khalifa, Z., A-H Zahran, M., Abdel Azzem, M., 2021. Abiotic sensor for electrochemical determination of chlorpyrifos in natural water based on the inhibition of silver nanoparticles oxidation. Microchem. J. 165, 106173. https://doi.org/10.1016/j.microc.2021.106173

Zhai, X., Xu, F., Li, Y., Jun, F., Li, S., Zhang, C., Wang, H., Cao, B., 2021. A highly selective and recyclable sensor for the electroanalysis of phosphothioate pesticides using silver-doped ZnO nanorods arrays. Anal. Chim. Acta 1152, 338285. https://doi.org/10.1016/j.aca.2021.338285

Zhang, J., Sun, Y., Li, X., Xu, J., 2020. Fabrication of $NiCo_2O_4$ nanobelt by a chemical co-precipitation method for non-enzymatic glucose electrochemical sensor application. J. Alloys Compd. 831, 154796. https://doi.org/10.1016/j.jallcom.2020.154796

Zhang, X., Rui, Y., Wang, Y., Xu, J., Wang, H., Zhang, Q., Müller-Buschbaum, P., 2018. SnO_2 nanorod arrays with tailored area density as efficient electron transport layers for perovskite solar cells. J. Power Sources 402, 460–467. https://doi.org/10.1016/j.jpowsour.2018.09.072

Zhang, Y., Wu, J., Zhao, S., Tang, X., He, Z., Huang, K., Yu, H., Zou, Z., Xiong, X., 2023. Self-assembled ZnO microspheres coated with carbon dot-doped CoNi LDH wrinkled films as electrochemical sensors for highly sensitive detection of hydrazine. Anal. Methods 15, 304–310. https://doi.org/10.1039/D2AY01698B

Zhao, S., Wang, L., Wang, T., Han, Q., Xu, S., 2016. A high-performance hydrazine electrochemical sensor based on gold nanoparticles/single-walled carbon nanohorns composite film. Appl. Surf. Sci. 369, 36–42. https://doi.org/10.1016/j.apsusc.2016.02.013

Zhao, Y., Tao, Y., Huang, Q., Huang, J., Kuang, J., Gu, R., Zeng, P., Li, H.-Y., Liang, H., Liu, H., 2022. Electrochemical biosensor employing Bi_2S_3 nanocrystals-modified electrode for bladder cancer biomarker detection. Chemosensors 10, 48. https://doi.org/10.3390/chemosensors10020048

Zhao, Y., Zuo, X., Lu, X., Li, Z., Gao, F., n.d. Hierarchical porous hollow N-doped Cu-based

MOF derivatives as highly sensitive electrochemical sensing platform for pesticides detection 362, 131749.

Zhao, Z., Sun, Y., Li, P., Sang, S., Zhang, W., Hu, J., Lian, K., 2014. A sensitive hydrazine electrochemical sensor based on zinc oxide nano-wires. J. Electrochem. Soc. 161, B157–B162. https://doi.org/10.1149/2.095406jes

Zheng, F., Zhang, M., Guo, M., 2013. Controllable preparation of WO_3 nanorod arrays by hydrothermal method. Thin Solid Films 534, 45–53. https://doi.org/10.1016/j.tsf.2013.01.102

Zhou, C., Feng, J., Tian, Y., Wu, Y., He, Q., Li, G., Liu, J., 2023. Non-enzymatic electrochemical sensors based on nanomaterials for detection of organophosphorus pesticide residues. Environ. Sci. Adv. 2, 933–956. https://doi.org/10.1039/D3VA00045A

Zhou, Q., Yang, L., Wang, G., Yang, Y., 2013. Acetylcholinesterase biosensor based on SnO_2 nanoparticles–carboxylic graphene–nafion modified electrode for detection of pesticides. Biosens. Bioelectron. 49, 25–31. https://doi.org/10.1016/j.bios.2013.04.037

Zhuang, Z., Chen, Y., Chen, K., Liu, Z., Guo, Z., Huang, X., 2023. In-situ synthesis of ZnO onto nanoporous gold microelectrode for the electrochemical sensing of arsenic(III) in near-neutral conditions. Sensors Actuators B Chem. 378, 133184. https://doi.org/10.1016/j.snb.2022.133184

Zokhtareh, R., Rahimnejad, M., Najafpour-Darzi, G., Karimi-Maleh, H., 2023. A novel sensing platform for electrochemical detection of metronidazole antibiotic based on green-synthesized magnetic Fe_3O_4 nanoparticles. Environ. Res. 216, 114643. https://doi.org/10.1016/j.envres.2022.114643

CHAPTER 2

Materials and Methodology

This chapter outlines the experimental procedures, including the chemical and bioinspired development of vertically aligned nanostructures (VANs) directly on fluorine-doped tin oxide (FTO) glass substrates, bio-based synthesis of nanostructures in powder form, the preparation of bio-extract, and the process for modification of glassy carbon electrode (GCE). This chapter also provides details on the reagents used, the equipment employed for the characterizations of nanostructures and target analytes, general theory, and the details of electrochemical characterizations applied in this study. The respective chapter mentions any changes or deviations from what is outlined herein.

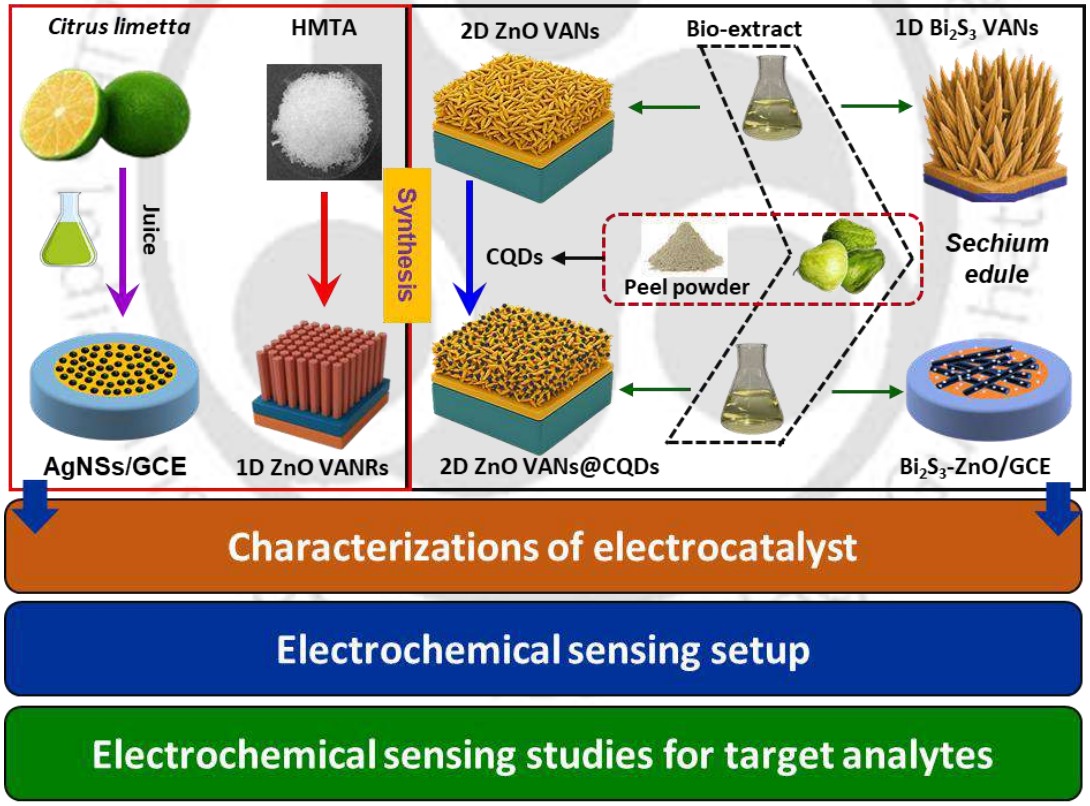

2.1 Reagents and chemicals

2.1.1 Analytical reagents

All chemicals, reagents, and materials were utilized as received without further purification unless otherwise stated and are listed in Table 2.1. The solutions were prepared using deionized (DI) water with a conductivity of 0.055 µS/cm at 25 °C (Millipore Elix-3, USA).

Table 2.1: List of reagents and chemicals used in this doctoral work.

Reagents/Chemicals	Chemical formula	Purity (%)	CAS/Catalogue no.	Make
Zinc acetate dihydrate	$Zn(CH_3COO)_2.2H_2O$	≥98.0	1.93692.0521	Merck, India
Diethanolamine	$NH(CH_2CH_2OH)_2$	≥99.0	1.94517.2521	
Ethanol	C_2H_6O	≥99.5	64-17-5	
Acetone	CH_3COCH_3	≥99.0	67-64-1	
Sodium hydroxide	NaOH	≥97.0	1310-73-2	
Hydrochloric acid	HCl	36.5-38.0	1-93001-2521	
Potassium chloride	KCl	≥98.5	1.93638.0521	
Phosphoric acid	H_3PO_4	≥88.0	7664-38-2	
Acetic acid	CH_3COOH	≥99.7	64-19-7	
Boric acid	H_3BO_3	≥99.8	10043-35-3	
Sodium nitrite	$NaNO_2$	≥98.0	1.93654.0521	
Mercury(II) chloride	$HgCl_2$	≥99.5	7487-94-7	
Sodium acetate anhydrous	CH_3COONa	≥99.0	1.93244.0251	
Sodium phosphate	Na_3PO_4	≥99.0	7558-79-4	
Sodium dihydrogen phosphate dihydrate	$NaH_2PO_4.2H_2O$	98-100.5	1.93624.0521	
Sodium hydrogen phosphate	Na_2HPO_4	≥99.0	1.93209.0521	
Hexaammineruthenium(II) chloride	$Ru(NH_3)_6Cl_2$	≥98.0	15305-72-3	
Cadmium chloride	$CdCl_2$	≥99.0	1.93715.0121	
Nickel chloride hexahydrate	$NiCl_2.6H_2O$	≥97.0	1.93655.0521	
Lead(II) nitrate	$Pb(NO_3)_2$	≥99.0	10099-74-8	
Hexamethylenetetramine	$C_6H_{12}N_4$	≥99.0%	1.94923.0521	
Bismuth(III) nitrate pentahydrate	$Bi(NO_3)_3 \cdot 5H_2O$	≥99.0	10035-06-0	

Thiourea	CH_4N_2S	≥99.0	1.94902.0521	
Silver nitrate	$AgNO_3$	≥99.0	1.93600.0121	
Sodium chloride	NaCl	≥99.0	1.93206.0521	
N,N-dimethylformamide	$HCON(CH_3)_2$	≥98.8	1.03034.0521	
Fluorine doped-tin oxide glass substrate (FTO, surface resistivity 7Ω/mm^2	-	-	1003319746	Sigma, India
p-Chloroaniline	C_6H_6ClN	≥99.0	106-47-8	
Carbendazim	$C_9H_9N_3O_2$	≥97.0	10605-21-7	
4-nitrophenol	$C_6H_5NO_3$	≥99.0	100-02-7	
Profenofos	$C_{11}H_{15}BrClO_3PS$	≥95.0	41198-08-7	
Chlorpyrifos	$C_9H_{11}Cl_3NO_3PS$	≥ 98.0	2921-88-2	
Chloramphenicol	$C_{11}H_{12}Cl_2N_2O_5$	≥ 98.0	56-75-7	
4-nitroaniline	$C_6H_6N_2O_2$	≥99.0	100-01-6	
Mancozeb	$C_8H_{12}MnN_4S_8Zn$	≥95.0	8018-01-7	
Malathion	$C_{10}H_{19}O_6PS_2$	≥99.9	121-75-5	
Thiram	$C_6H_{12}N_2S_4$	≥98.8	137-26-8	
Ziram	$C_6H_{12}N_2S_4Zn$	≥98.0	137-30-4	
Ciprofloxacin	$C_{17}H_{18}FN_3O_3$	≥98.0	85721-33-1	
Chloroquine phosphate	$C_{18}H_{26}ClN_3.2H_3PO_4$	≥98.0	50-63-5	
Phenylbutazone	$C_{19}H_{20}N_2O_2$	≥98.0	50-33-9	
Sulfamethoxazole	$C_{10}H_{11}N_3O_3S$	≥98.0	723-46-6	
Potassium ferricyanide	$K_3Fe(CN)_6$	≥98.0	13746-66-2	SRL, India
Chlorobenzene	C_6H_5Cl	≥99.5	108-90-7	
Tris HCl	$C_4H_{11}NO_3.HCl$	≥99.0	1185-53-1	
Aniline	C_6H_7N	≥99.5	62-53-3	
Chlorobenzene	C_6H_5Cl	≥99.5	108-90-7	
Cupric nitrate trihydrate	$Cu(NO_3)_2.3H_2O$	≥98.0	10031-43-3	
Albumin bovine	-	96.0-98.0	9048-46-8	
Polyvinylpyrrolidone K-30	$(C_6H_9NO)_x$ (PVP K-30)	-	9003-39-8	
Commercial AgNPs (diameter 60 nm, 0.02 mg/mL in aqueous media (2.6 x 10^{10} particles/mL))	Ag	≥99.9	7440-22-4	
Zinc oxide	ZnO	≥98.0	1314-13-2	Loba Chemie, India
Bisphenol a	$C_{15}H_{16}O_2$	≥98.0	80-05-7	

Norfloxacin	$C_{16}H_{18}FN_3O_3$	≥98.0	70458-96-7	CDH, India
Nafion®D-521 (dispersion in water and 1-propanol)	-	5% w/w	31175-20-9	Alfa Aesar, USA

2.1.2 Preparation of stock solutions

Stock solutions of aniline, p-Chloroaniline (p-CA), ciprofloxacin (CFX), phenylbutazone (PBZ), sulfamethoxazole (SMZ) were prepared in absolute ethanol. The stock solution of norfloxacin (NFX) and mancozeb (MCZ) was prepared in N,N-dimethylformamide and DI water, respectively.

2.1.3 Preparation of buffer solutions

2.1.3.1 Phosphate buffer solution

The phosphate buffer solution (PBS) of 0.1 M ionic strength was prepared by adding 0.1 M $NaH_2PO_4.2H_2O$ and 0.1 M Na_2HPO_4 in DI water and adjusting pH using 1 M NaOH/1 M HCl. The 0.1 M PBS was used as a supporting electrolyte for the electrochemical sensing of CFX (Chapter 3), aniline (Chapter 4), NFX (Chapter 6), and simultaneous PBZ and SMZ (Chapter 8).

2.1.3.2 Britton-Robinson (BR) buffer solution

The BR buffer of 0.04 M ionic strength was prepared by mixing 0.04 M of acetic acid, phosphoric acid, and boric acid each and adjusting the required pH with 2 M NaOH (Sarakhman et al., 2022). The 0.04 M BR buffer was used as a supporting electrolyte for the electrochemical sensing of p-CA (Chapter 5) and MCZ (Chapter 7).

2.1.4 Target analytes for electrocatalytic sensing

In this doctoral work, the selected target analytes are pesticides (MCZ), their intermediates (aniline and p-CA) and pharmaceuticals (CFX, NFX, PBZ, and SMZ). The chemical structures of the targeted analytes are depicted in Table 2.2.

Table 2.2: Chemical structures of selected analytes used in this doctoral work for electrochemical sensing.

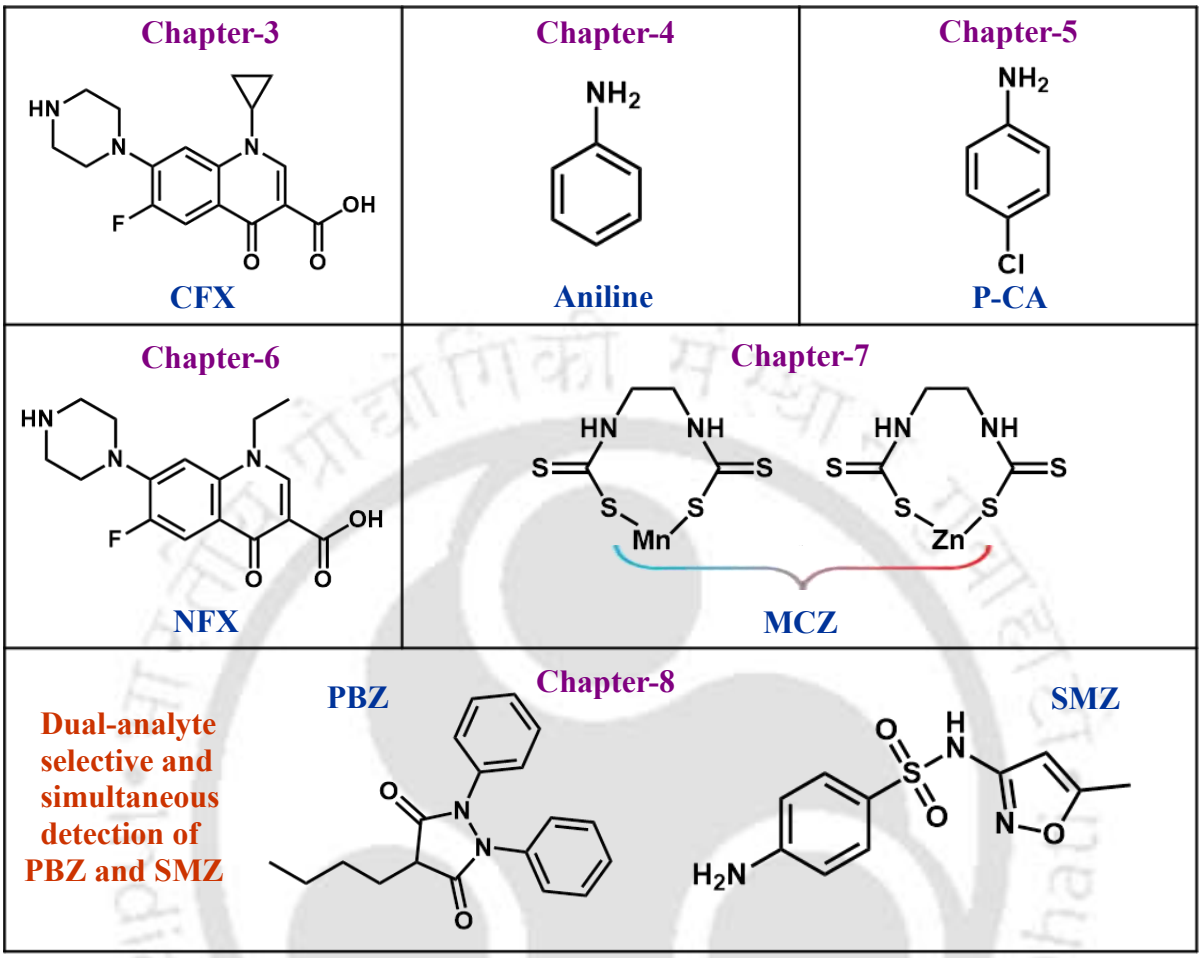

2.2 Bio-extract and bio-mass

2.2.1 Selection of *Sechium edule* and *Citrus limetta* fruit extract

The source of the bio-extract was selected considering factors like availability, reducing substance contents, economic importance, growth characteristics, etc. Diverse varieties of tropical plants are available in the northeastern part of India. They could be potential sources of reducing and capping agents that can be used for synthesizing nanostructures. Two groups of plants have been selected, including *Sechium edule* and *Citrus limetta*. *Sechium edule* fruits contain abundant amounts of reducing analytes (Ordonez et al., 2006), including ascorbic acid (AA, 0.294 mg/g on the dry basis) (Rao and Golder, 2016), amino acids (12.9 mg/g on the dry basis), flavonoids (19.3 mg/g on the dry basis) (Rao and Golder, 2016), and polyphenols (Flick et al., 1978). *Citrus limetta* fruits are rich sources of citric acid, polyphenolic compounds, flavonoids, etc.

The phytochemicals present in the bio-extract of *Sechium edule* and *Citrus limetta* fruit have been exploited for the growth and formation of stable nanostructures for electroanalytic sensing of target analytes.

2.2.2 Preparation of bio-extract of *Sechium edule* fruit

Fresh *Sechium edule*, locally also known as Chayote fruit (belongs to the Cucurbitaceae family, Fig. 2.1a) was purchased from the Campus market at IIT Guwahati, Assam, India. For bio-extract preparation, the obtained fruit was washed with DI water to remove any contaminants. After removing the seed and peel, the fruit was chopped into small pieces (~5 mm × 5 mm × 5 mm). The preparation of bio-extract was done by heating 125/150 g fruit pieces (Fig. 2.1b) in 500/200 mL DI water at 90±2°C for 12 h. The extract was then cooled to ambient temperature and mashed fruit in water filtered out using 0.45 µm membrane filter paper to obtain clear bio-extract (Fig. 2.1c). To reduce the impact of seasonal change in the chemical composition of *Sechium edule*, ZnO and Bi_2S_3 were synthesised during March-June 2022 and May-Aug 2023, respectively. A fixed ascorbic acid (AA) equivalent (AAE) of 3.62 (150 g fruit pieces 200 mL DI water) and 2.69 (125 g fruit pieces 500 mL DI water) mg/L was utilized for each set of ZnO and Bi_2S_3 nanostructures synthesis (Senguttuvan et al., 2014). The analytes present in the *Sechium edule* extract (Fig. 2.1c) were employed for the synthesis of ZnO and Bi_2S_3 nanostructures.

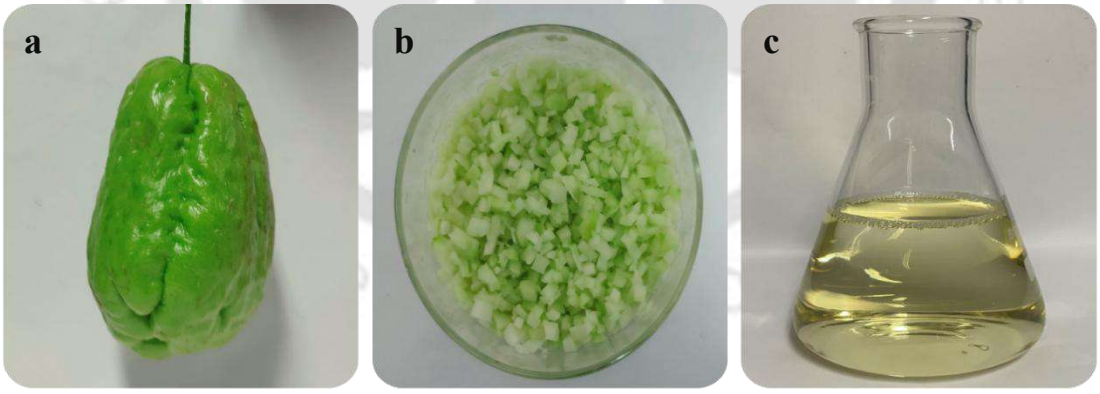

Figure 2.1: Pictorial view of (a) *Sechium edule* fruit, (b) fruit pieces, and (c) Clarified aqueous bio-extract of *Sechium edule* fruit.

2.2.3 Preparation of bio-extract of *Citrus limetta* fruit

Fresh *Citrus limetta* fruit was purchased from the local market of IIT Guwahati, India. To obtain the juice, the fruit was washed with DI water and sliced in half, followed by

squeezing. Subsequently, the freshly squeezed liquid was filtered using a 0.45 µm filter paper and stored at 4 °C for the formation of Ag nanostructures.

2.2.4 DPPH assay of *Sechium edule* bio-extract

For the 1,1-diphenyl-2-picrylhydrazyl (DPPH) assay, 0.2 mL of the bio-extract was added to 1.8 mL of a 50 µM DPPH solution, followed by incubation for 30 min. The absorbance was measured at 592 nm (λ_{max}) using a UV-Vis spectrophotometer. Additionally, AA at concentrations ranging from 10 to 50 mg L^{-1} was used in place of the bio-extract to generate a calibration curve. The absorbance values corresponding to each AA concentration were fitted linearly to derive a calibration equation. The AAE in the bio-extract was then determined using this linear equation, as shown in Fig. 2.2 (Senguttuvan et al., 2014).

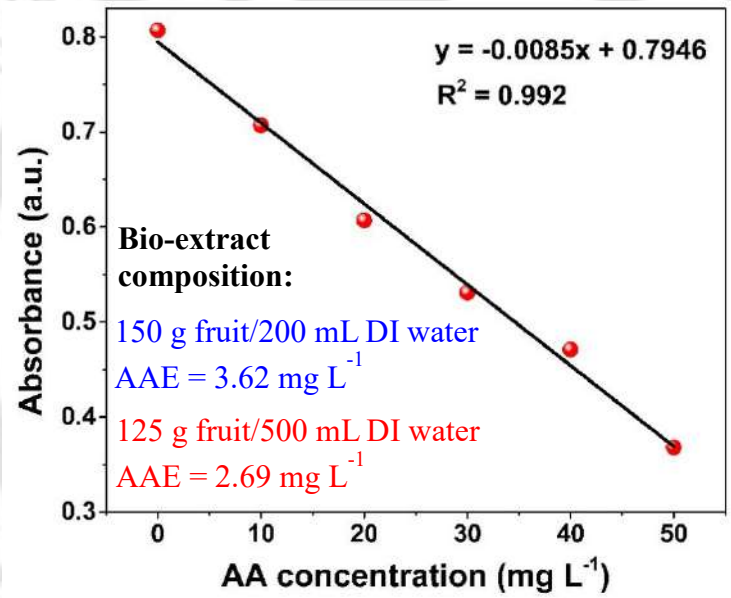

Figure 2.2: Determination of AAE in *Sechium edule* bio-extract prepared using 150/125 g of fruit pieces in 200/500 mL of DI, as measured by the DPPH assay.

2.3 Methodologies of electrocatalyst synthesis

2.3.1 Phyto-analytic synthesis of AgNSs

For the formation of phyto-analytic Ag nanostructures (AgNSs), fresh *Citrus limetta* was purchased from the local market of IIT Guwahati, India. To obtain the juice, the fruit was washed with DI water and sliced in half, followed by squeezing. Subsequently, the freshly squeezed liquid was filtered using a 0.45 µm filter paper and stored at 4 °C for further use. The formation of AgNSs was done in a bio-based protocol using *Citrus limetta* extract, as shown in Fig. 2.3. In brief, 0.5 g $AgNO_3$ and 3 g PVP K-30 were dissolved in 30 mL DI water by

stirring for 2 h at ambient temperature. Afterwards, 0.15 g NaCl and 30 mL of *Citrus limetta* extract were added to the above mixture, and then the solution was refluxed at 90 °C for 24 h. After the reaction, the solution was cooled to room temperature, and AgNSs were collected by centrifugation at 13500 rpm for 15 min. The collected AgNSs were washed with ethanol and DI water to remove the excess ions. Finally, the obtained pellets of AgNSs were dispersed in DI water (2.5-12.5 mg/mL) for further characterization and preparation of the working electrode.

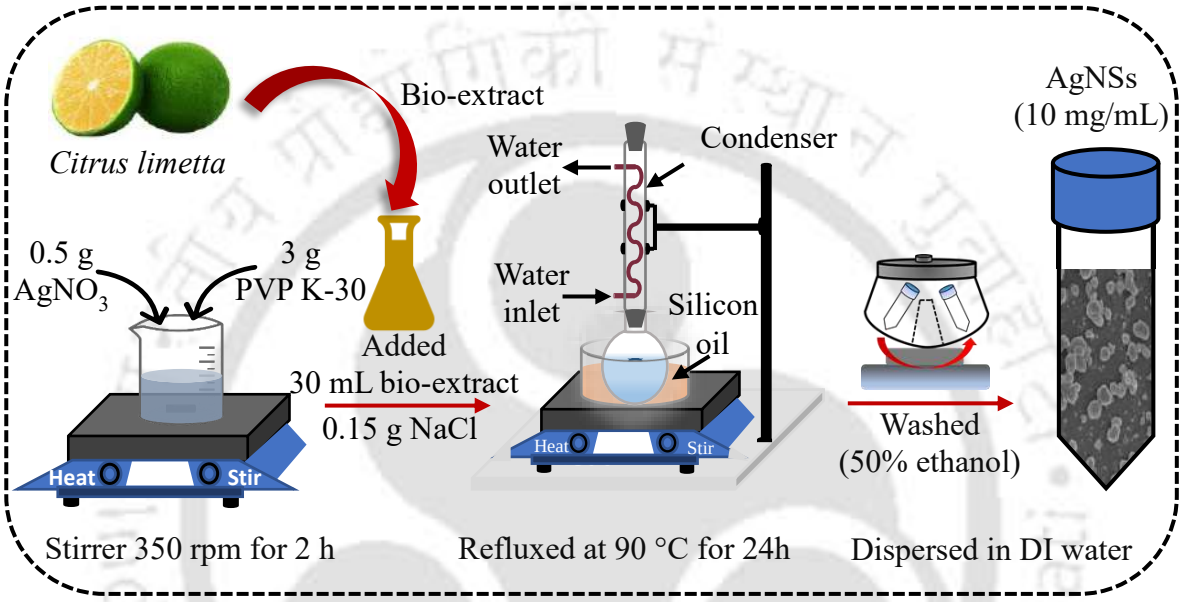

Figure 2.3: Graphical illustration of phyto-analytic formation of AgNSs using bio-extract of *Citrus limetta*.

2.3.1.1 Preparation of AgNSs/GCE

The glassy carbon electrode (GCE, 3 mm diameter) was meticulously cleaned by polishing with 0.3 µm alumina powder, followed by a rinse with DI water and drying at 25 °C. For immobilization of AgNSs onto the surface of GCE (AgNSs/GCE), 100 µL of AgNSs (2.5-12.5 mg/mL) was dispersed in 100 µL of 0.5% Nafion solution in isopropanol followed by ultrasonication for 1 h (Fig. 2.4). Subsequently, 5 µL of nanostructure solution was drop-casted onto the surface of GCE and then dried at 25 °C for further utilization in electrochemical characterizations.

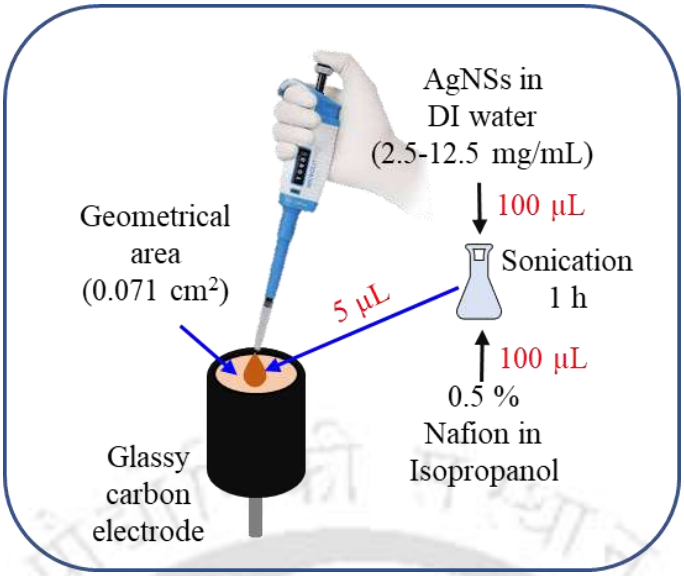

Figure 2.4: Preparation of AgNSs/GCE using Nafion as binder.

2.3.2 Synthesis of 1D surface VANRs of ZnO on the FTO

The development of ZnO vertically aligned nanorods (VANRs) on the surface of FTO (ZnO-VANRs/FTO) was done following an aqueous chemical growth method (Mali et al., 2013). The bare FTO was cleaned in an ultrasonication bath with acetone, ethanol, and DI water for 10 min each and dried overnight at room temperature. For the deposition of the seed layer, 0.05 M $Zn(CH_3COO)_2.2H_2O$ and 0.05 M $NH(CH_2CH_2OH)_2$ were dissolved in ethanol. After that, the cleaned FTO with an exposed area of 0.19 cm^2 was immersed in the seed solution for 10 s, and the substrate was left to air dry overnight at room temperature. The seeded FTO was annealed at 400°C for 10 min to form a uniform surface and improve the crystallinity with the structural integrity of ZnO-VANRs/FTO, leading to enhanced electrochemical sensor performance. The seeded FTO was subjected to highly dense uniform vertical-align growth of nanorods, removing the heterogeneous interface that occurs between the FTO and VANRs of ZnO. The nanostructures aligned in vertical configuration maximize surface area, facilitating increased analyte adsorption and improving sensor sensitivity. To grow VANRs of ZnO, the seeded substrate vertically hung in a 0.05 M $Zn(CH_3COO)_2.2H_2O$ and 0.05 M $C_6H_{12}N_4$ solution. The solution was subjected to reflux at 95°C for 5 h. Finally, ZnO-VANRs/FTO was washed with DI water followed by ethanol to get rid of zinc precursor residuals/excess ions and left to air dry overnight at 60°C. Fig. 2.5 demonstrates the synthesis protocol of 1D surface VANRs of ZnO onto the surface of FTO.

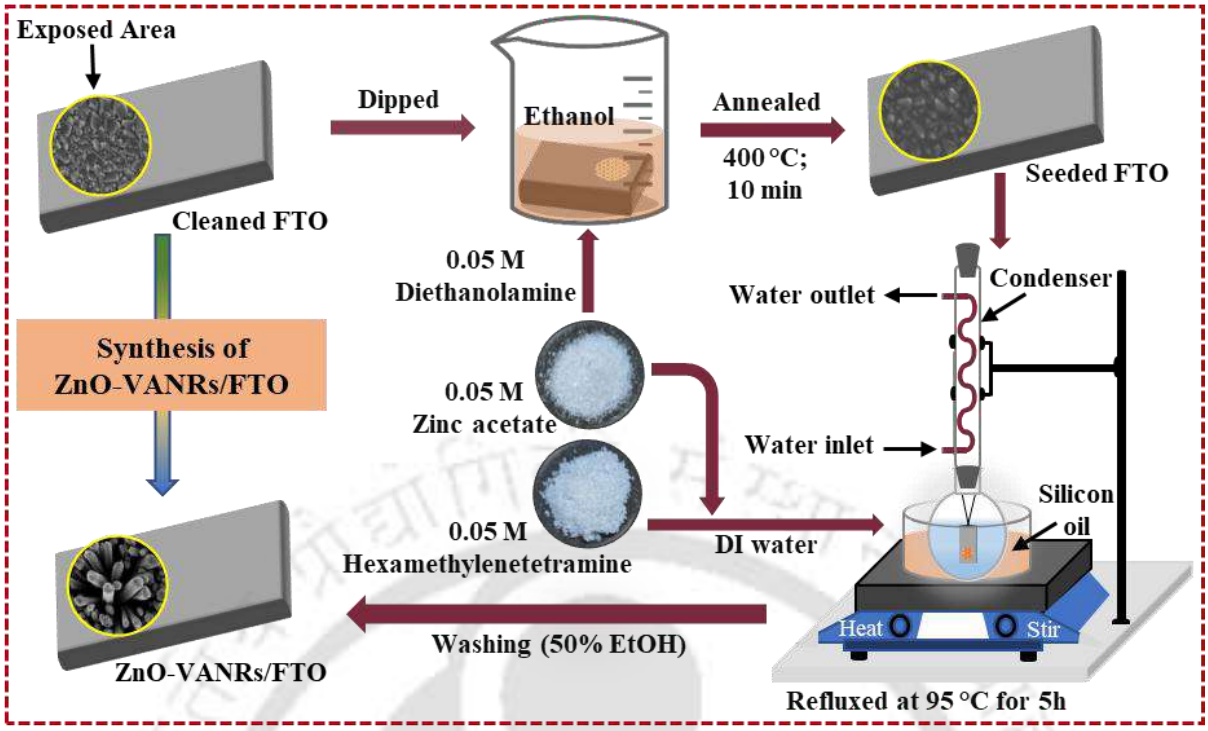

Figure 2.5: Schematic synthesis protocol of 1D surface VANRs of ZnO on the FTO (ZnO-VANRs/FTO).

2.3.3 Bio-based synthesis of 2D VANs of ZnO on the FTO

The synthesis of vertically aligned nanostructures (VANs) of ZnO onto the surface of the FTO glass substrate (ZnO-VANs(bio)/FTO) was done following a bioinspired protocol (Fig. 2.6). The FTO glass (3.5 cm × 0.6 cm) was consecutively cleaned in acetone, ethanol, and DI water for 15 min each in an ultrasonic bath and dried in N_2 environment. Briefly, 0.05 M zinc acetate dihydrate and 0.05 M diethanolamine were dissolved in absolute ethanol to prepare the seed solution. The clean FTO was dipped in the seed solution (after exposing 0.19 cm^2 area of the substrate) for 10 s and dried in the air overnight at ambient temperature. The seed layer deposited substrate was annealed for 10 min at 400°C to form a homogeneous surface and better crystallization of ZnO-VANs(bio)/FTO. The seed layer deposition was done to overcome the electron scattering (due to the heterogeneous interface) between VANs and FTO substrate and improve the nanostructure's density and vertical alignment. For the growth of VANs, 0.1 M zinc acetate dihydrate was dispersed in the 30 mL DI water, and the mixture was stirred for 10 min. Then, a volume of 30 mL bio-extract was added to the above solution, and adjusted pH (digital pH meter, L1164, Elico, Hyderabad, India) at different values of 3, 5, 7, 9, and 11 (ZnO-VANs(bio)/FTO@pH(3-11)) using 2 M NaOH and/or 2 M HCl. The seed layer deposited FTO was vertically hung in the solution for the effective growth of VANs. The

solution was refluxed for 5 h at 95°C. Finally, the ZnO modified FTO was washed with DI water, then with ethanol and DI water to remove excess ions and dried overnight at 60°C.

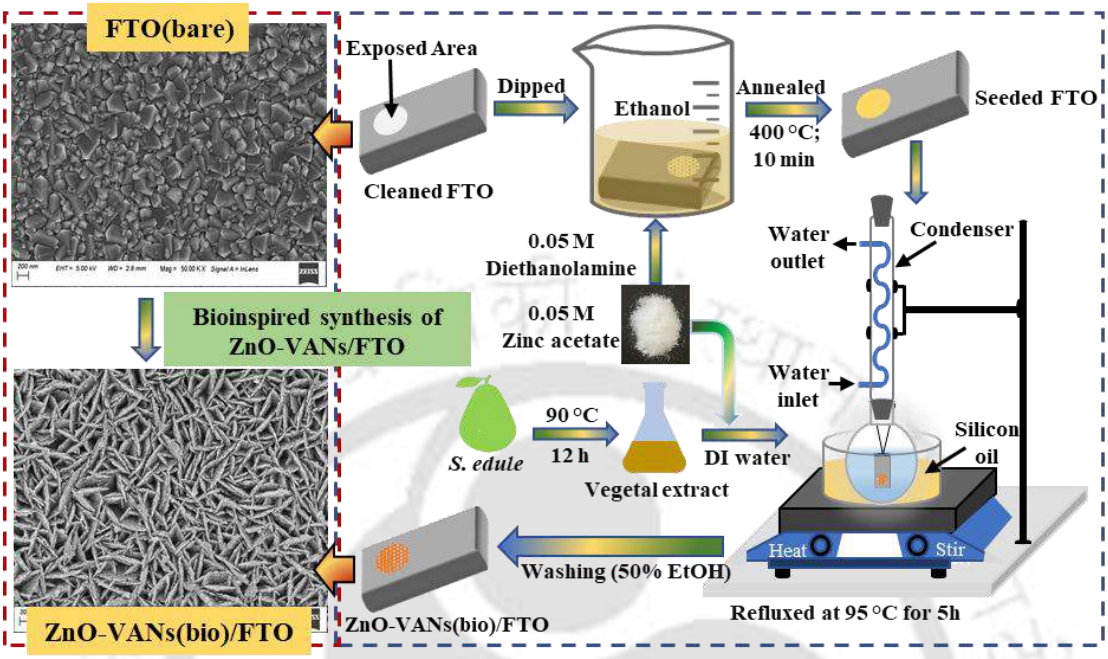

Figure 2.6: Schematic diagram of bioinspired synthesis of ZnO-VANs(bio) onto FTO substrate (ZnO-VANs(bio)/FTO).

2.3.4 Synthesis of CQDs modified 2D ZnOVANs on the FTO

The bioinspired ZnO VANs synthesized on the FTO (denoted as ZnOVANs(bio)/FTO) was carried out using the *Sechium edule* fruit extract (Fig. 2.7), following the previously reported protocol (section 2.3.2). In brief, bare FTO (3.5×0.6 cm^2) was ultrasonically cleaned in acetone, ethanol, and DI water for 15 min each, then dried overnight. To prepare a ZnO seed layer on FTO (ZnO(seed)/FTO), 0.05 M $Zn(CH_3COO)_2.2H_2O$ and 0.05 M $NH(CH_2CH_2OH)_2$ were dispersed in ethanol and stirred for 15 min. Subsequently, FTO (uncovered area 0.19 cm^2) was dipped in the solution for 10 s, then dried overnight, followed by annealing at 400 °C for 10 min, to improve crystallization and achieve a uniform surface. Furthermore, the seed layer could eliminate the problem associated with charge scattering to the heterogeneous interface between ZnO VANs and FTO glass. It also promotes a denser, uniform, and more rapid growth of nanostructures in a vertical configuration. To grow ZnO VANs, 0.1 M $Zn(CH_3COO)_2.2H_2O$ was introduced into 30 mL DI water and stirred for 10 min, followed by adding an equal volume of fruit extract, with a pH 7 of the mixture. The seeded FTO was positioned vertically in the solution for effective growth of VANs on FTO, and the test was performed at 95 °C for 5 h.

Finally, ZnOVANs(bio)/FTO was washed with 50% ethanol (v/v) to eliminate impurities and dried at 60 °C for 12 h. The control synthesis was carried out by replacing bio-extract with an equivalent volume of DI water under constant reaction conditions and denoted as ZnO-control (H_2O)/FTO.

After the *Sechium edule* bio-extract preparation, the leftover carbon-rich fruit peel was naturally dried and ground into a fine powder. 1 g of peel powder was dispersed in 60 mL DI water and stirred for 30 min to homogenize it. The solution is then transferred to a hydrothermal reactor and heated at 200 °C for 12 h. After cooling to room temperature, the obtained brownish-yellow liquid was centrifuged at 14000 rpm for 20 min, followed by vacuum filtration using a 0.2 µm Nylon filter. The yield of the resultant CQDs was 4.4 mg mL^{-1}.

To functionalize VANs with CQDs, ZnOVANs(bio)/FTO was immersed in CQDs dispersion for different times from 0.5 to 2.0 min, referred to as $CQDs_{(0.5\text{-}2.0)}$-ZnOVANs(bio)/FTO. Then, the modified $CQDs_{(0.5\text{-}2.0)}$-ZnOVANs(bio)/FTO were rinsed with DI water and dried overnight at 60°C.

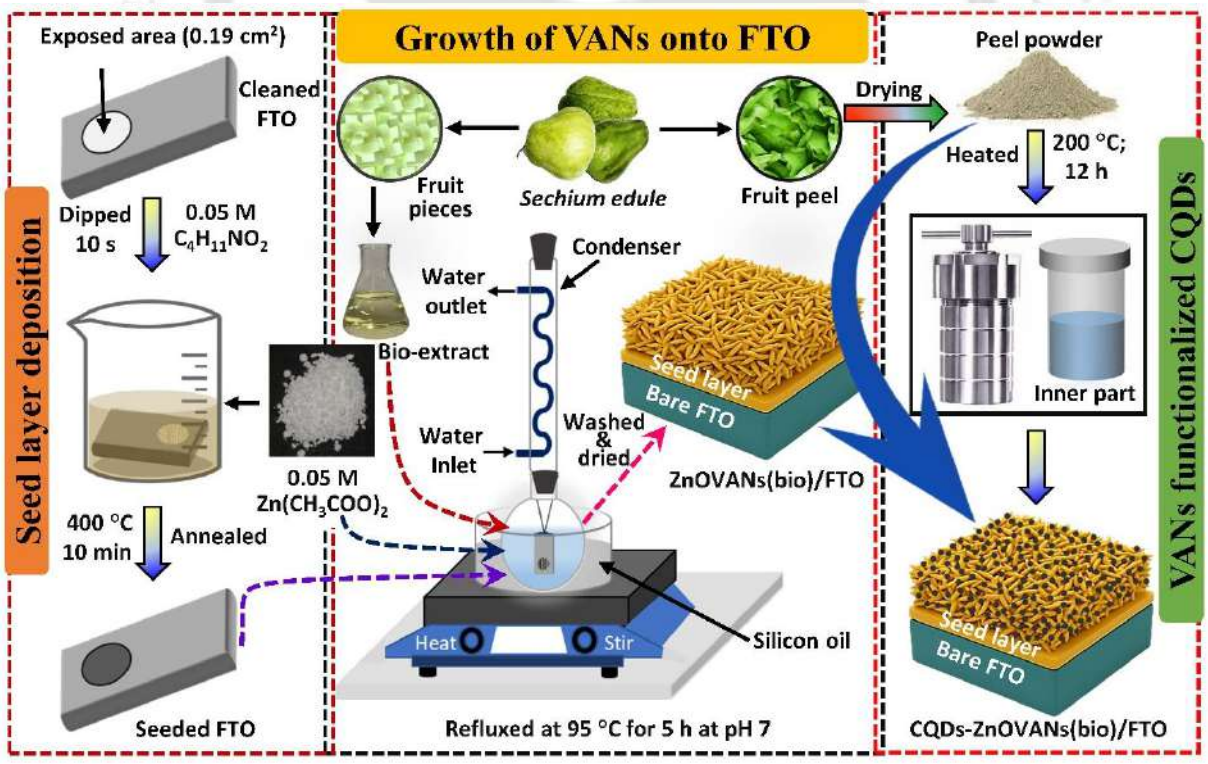

Figure 2.7: Schematic steps depicting 2D ZnO VANs synthesis onto FTO glass and its functionalization with CQDs.

2.3.5 Nature-inspired synthesis of VONs of Bi_2S_3

The growth of 1D surface vertically oriented nanorods (VONs) of Bi_2S_3 onto the FTO glass surface was performed by nature-inspired protocol using bio-extract of *Sechium edule* fruit, as depicted in Fig. 2.8. The FTO substrate (3.5×0.6 cm^2) was properly washed in acetone, ethanol, and finally in DI water followed by ultrasonication for 15 min. Then, it was dried in an N_2 environment. An amount of 0.92 g $Bi(NO_3)_3 \cdot 5H_2O$, 0.28 g CH_4N_2S, and 0.05 M (96.5 µL) $C_4H_{11}NO_2$ were dissolved in 20 mL ethanol and stirred for 2 h to prepare the seed solution. After that, FTO (uncovered area of 0.19 cm^2) was immersed in the solution for 10 s, followed by drying at room temperature, and then it was calcined at 400 °C for 10 min to achieve a uniform surface with high crystallinity of Bi_2S_3 nanostructures. Seed layer deposition aimed to remove a heterogeneous interface between the FTO glass surface and VONs (which could scatter charge carriers during the electrocatalytic reaction) to enhance the density and vertical orientation of Bi_2S_3 nanostructures. To develop VONs of Bi_2S_3, 2.3 g $Bi(NO_3)_3 \cdot 5H_2O$ was dispersed in 40 mL of DI water and sonicated for 20 min to achieve uniform suspension. After that, 0.71 g CH_4N_2S and 10 mL of bio-extract (1:5 v/v) were successively added to the above mixture, and pH was maintained at 2, 3, 4, and 5 (2.3Bi_2S_3-VONs(nat)/FTO@pH(2-5)) by using 1 M NaOH or/and HCl. For the growth of VONs, seeded FTO was positioned vertically within the solution and refluxed at 90 °C for 12 h. Finally, Bi_2S_3 functionalized FTO was rinsed with ethanol followed by DI water to remove precursors/excess ions residuals, and then it was dried at 50 °C for 12 h.

The formation of Bi_2S_3 VONs was also done by varying the precursor loading ($Bi(NO_3)_3 \cdot 5H_2O$) from 1.0 to 2.5 g at a reaction pH of 3 ((1-2.5)Bi_2S_3-VONs(nat)/FTO@pH3) keeping other experimental conditions same as specified previously. The control synthesis of Bi_2S_3 nanostructures was performed using 2.3 g of precursor loading at pH 3, replacing the bio-extract with an equal volume of DI water under the same experimental conditions. The control sample is denoted as 2.3Bi_2S_3-H_2O(control)/FTO@pH3.

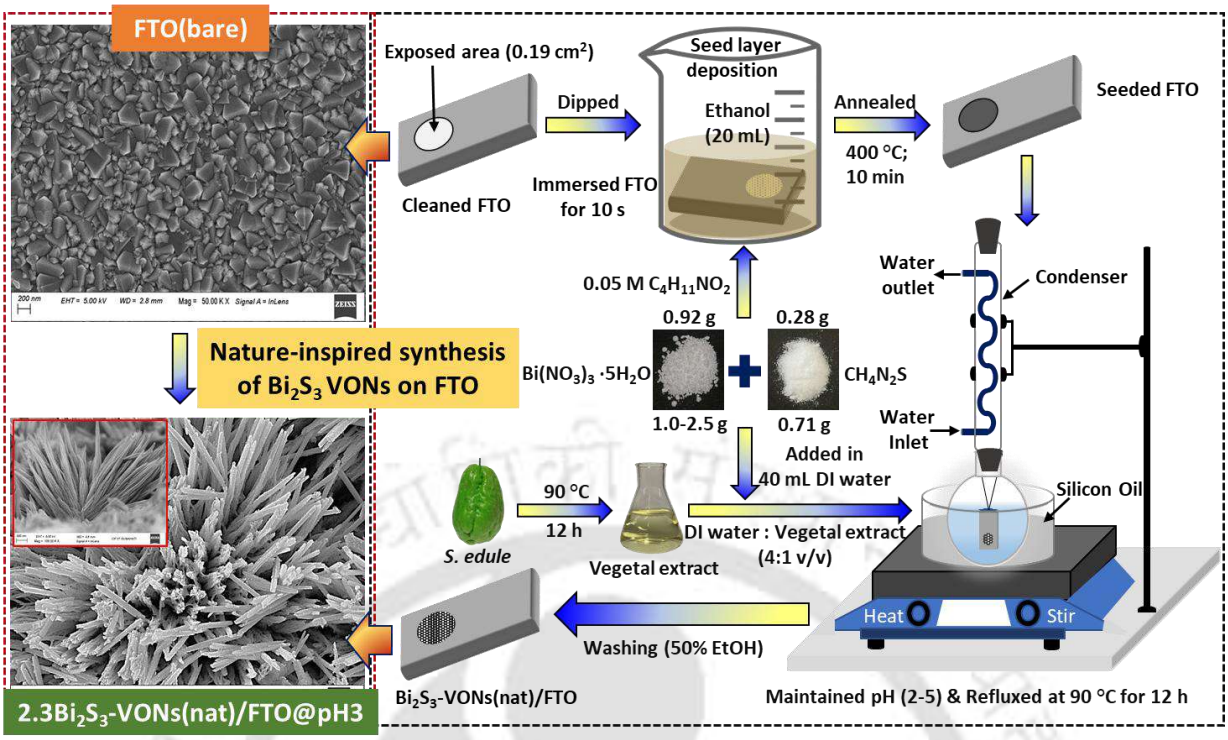

Figure 2.8: Schematic illustration of the nature-inspired synthesis protocol for the formation of Bi_2S_3 VONs on the FTO glass substrate.

2.3.6 Preparation of Bi_2S_3-ZnO(bio) nanocomposite

2.3.6.1 Synthesis of ZnO(bio) nanostructures

ZnO(bio) nanostructures were prepared using a previously reported protocol with some modifications, particularly for synthesizing nanostructures in powder form instead of growing them in a vertical configuration onto a working electrode (Bhan and Golder, 2023). To synthesize ZnO(bio), 0.05 M $Zn(CH_3COO)_2.2H_2O$ was dissolved in DI water by stirring at 350 rpm for 20 min. After that, bio extract was added (1:1 v/v) to the above mixture, and the reaction pH was maintained at 7 before refluxing at 95 °C for 5 h, followed by washing with 50% v/v ethanol and drying at 60 °C overnight. The control synthesis of ZnO(bio) nanostructures was performed with DI water instead of bio-extract with a constant reaction volume and denoted as ZnO(control).

2.3.6.2 Synthesis of Bi_2S_3(bio) nanostructures

Bi_2S_3(bio) nanostructures were synthesised using the previously reported method with some modifications, specifically to obtain the nanostructures in powder form instead of growing them in a vertical orientation (Bhan and Golder, 2025). For the preparation of Bi_2S_3 nanostructures, 2.3 g of $Bi(NO_3)_3{\cdot}5H_2O$ was dissolved in 40 mL of DI water and ultrasonicated

for 20 min. After that, 0.71 g of CH_4N_2S was added, followed by stirring for 20 min. Then, 10 mL of bio-extract (1:5 v/v) was introduced, and the pH of the solution was set to 3. The mixture was subjected to reflux at 90 °C for 12 h, followed by washing with 50% v/v ethanol and dried at 60 °C for 12 h. The control synthesis of Bi_2S_3(bio) was done by replacing bio-extract with the equivalent volume of DI water under identical conditions and denoted as Bi_2S_3(control).

2.3.6.3 Preparation of Bi_2S_3-ZnO(bio) nanocomposite

The Bi_2S_3-ZnO(bio) nanocomposites were prepared using a bio-based route, as shown in Fig. 2.9. In Brief, 2.3 g of $Bi(NO_3)_3 \cdot 5H_2O$ was dissolved in 40 mL DI water by ultrasonication for 20 min. Then, 0.71 g of CH_4N_2S was introduced to the above solution and stirred for 20 min. Subsequently, 10 mL of bio-extract (1:5 v/v) was added, and the solution pH was maintained at 3. Finally, 1 g of ZnO(bio) was introduced into the mixture and refluxed at 90 °C for 12 h, followed by washing with 50% v/v ethanol and drying at 60 °C for 12 h.

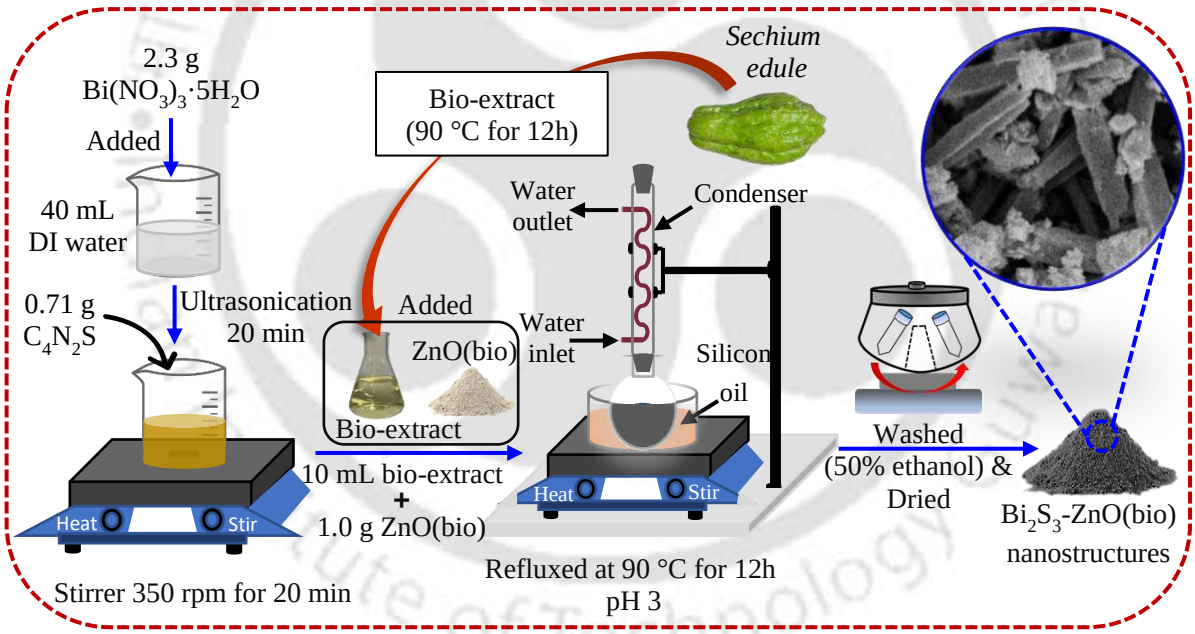

Figure 2.9: Schematic graphic of the bio-based synthesis of Bi_2S_3-ZnO(bio) nanostructures using bio-extract of *Sechium edule* and ZnO(bio) nanostructures.

2.3.6.4 Preparation of Bi_2S_3-ZnO(bio)/GCE

For the preparation of Bi_2S_3-ZnO(bio)/GCE, 10 mg of Bi_2S_3-ZnO(bio) nanocomposites was dispersed in 1 mL of Nafion/DI water (9:1 v/v) solution and ultrasonicated for 1 h to achieve a homogeneous dispersion (Fig. 2.10). Subsequently, GCE (diameter: 3 mm) was meticulously polished with alumina powder with 0.3 µm particle size and rinsed 3-4 times

using DI water, followed by drying at 25 °C. Then, 5 µL of the homogeneous Bi_2S_3-ZnO(bio) dispersion was drop-cast over the GCE surface and kept at 40 °C for 20 min for drying prior to electrochemical characterization.

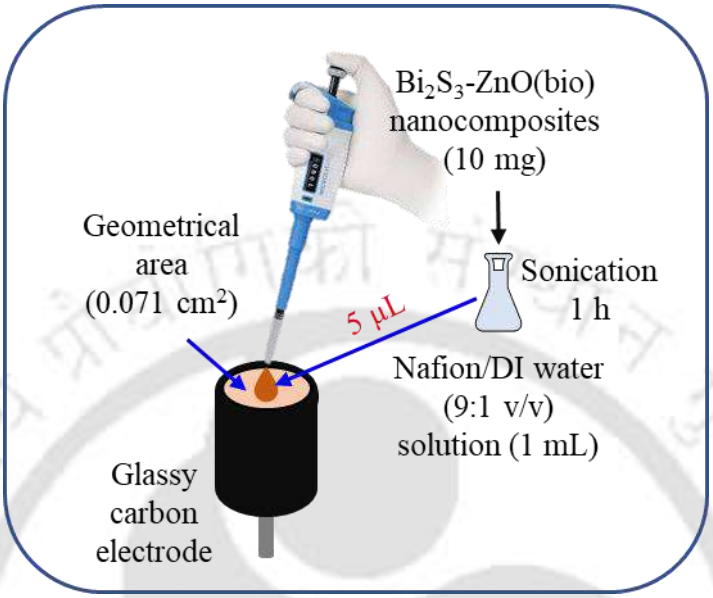

Figure 2.10: Preparation of Bi_2S_3-ZnO(bio)/GCE using Nafion as binder.

2.4 Characterization of electrocatalyst

2.4.1 Field emission scanning electron microscopy

Field emission scanning electron microscopy (FESEM, Sigma-300, Carl Zeiss, Jena, Germany) equipped with a Fe cathode electron gun and In-lens detector under system vacuum pressure of 1.2×10^{-5} mbar, was employed to investigate the surface morphology and topography of the synthesized electrocatalyst at the nanoscale level. FESEM analysis of VANs on FTO provides top-view and cross-sectional images, revealing detailed insights into their surface morphology and vertical alignment. The ZnO/Bi_2S_3-modified FTO and AgNSs drop-cast onto the aluminium foil-wrapped glass slide was mounted on a metal stub using conductive carbon tape for FESEM analysis. The powdered nanostructures were directly dispersed onto conductive carbon tape affixed to the metal stub for stable mounting during FESEM analysis.

2.4.2 Field emission transmission electron microscopy

Field emission transmission electron microscopy (FETEM, JEM-2100 F, JEOL, USA), equipped with a ZrO/W(100) Schottky electron gun and operated at a background pressure of 5.8×10^{-5} mbar, was employed to determine the morphology of the electrocatalyst, providing

high-resolution two-dimensional images. For the specimen preparation, VANs of ZnO/Bi_2S_3 were disintegrated on the surface of FTO via ultrasonication (ANTech, GT-1990QTS, frequency 33/40 kHz, ultrasonic power 200 W, China) for 1 h followed by drop caste onto the TEM grid and dried in hot air oven overnight. Furthermore, 1 mg of powder nanostructures was dispersed in 1 mL of an ethanol-water solution (1:1 v/v) and ultrasonication for 1 h, followed by drop casting onto a TEM grid and drying in an oven for 12 h. The TEM analysis provided details into the electrocatalyst, including morphology (from FETEM micrograph), fringe width (from HRTEM micrograph) and crystallinity (from SAED pattern), which confirmed the successful formation of nanomaterials.

2.4.3 Energy dispersive X-ray spectroscopy

The elemental composition and image mapping of the electrocatalyst was examined by Energy dispersive X-ray (EDX, Sigma, Carl Zeiss, Germany) operated with a Fe cathode electron gun and secondary electron (SE) detector at a background pressure of 4.6×10^{-5} mbar. In EDX, a focused beam of X-rays penetrates the sample and, interacting with it, induces the emission of characteristic X-rays, which are then detected by an energy-dispersive detector. The EDX specimen preparation follows the same procedure as the FESEM sample preparation. The EDX analysis provided detailed information on the electrocatalyst, such as elemental mapping and elemental composition (weight/atomic %) of the VANs and powder nanostructures.

2.4.4 X-ray diffraction

X-ray diffraction (XRD, D2 Advance, Bruker, Germany) analysis is an analytical technique employed to identify the crystalline phase, crystal size, dislocation density, d-spacing, and lattice strain. The XRD of the electrocatalyst was performed between 10° to 90° 2θ angles at a scanning speed of 10°/min using CuKα1 radiation (λ=0.154 nm) as an X-ray source in a diffractometer. The crystallite size (d, nm), lattice strain (ε), and dislocation density (δ, lines/nm^2) were determined using Eqs. 2.1-2.3 (Venieri et al., 2014).

$$d = \frac{k\lambda}{\beta\cos\theta_B} \tag{2.1}$$

$$\varepsilon = \frac{\beta}{4\mathrm{Tan}\theta_B} \tag{2.2}$$

$$\delta = \frac{1}{d^2} \tag{2.3}$$

Where β, θ_B, λ, and k are the full width at half maximum (FWHM), Bragg angle, the X-

ray wavelength (0.154 nm), and the shape factor (0.94), respectively. For XRD analysis, the nanomaterial modified FTO substrates were directly mounted on the sample holder to obtain the diffraction patterns, whereas for powdered nanostructures, 20 mg of the sample was placed on the holder for pattern recording.

2.4.5 Atomic force microscopy

Atomic force microscopy (AFM, Cypher S, Oxfordinstruments, Abingdon, UK) was used to examine the topography of the ZnO/Bi_2S_3 modified FTO surface with high-resolution surface imaging and quantitative surface roughness data at the resonance frequency of 209-286 kHz. For the AFM analysis, ZnO/Bi_2S_3 modified FTO was placed on the sample holder, and the AFM images were recorded. Gwaddian software is used to analyze AFM data, providing 2D and 3D images and calculating surface roughness parameters like root mean square (RMS) values, which are essential for understanding surface uniformity and texture.

2.4.6 X-ray photoelectron spectroscopy

X-ray photoelectron spectroscopy (XPS, PHI5000VersaProbe III) functioned with Cu-Kα X-ray beam (1486.6 eV) was operated at a background pressure of 9.8×10^{-6} mbar to examine the elemental composition and surface chemical state of the electrocatalyst. The peak correction was performed with reference to the C1 peak at 284.4 eV. The XPS sample preparation follows the same procedure as the FESEM/EDX specimen preparation. The basic principle of XPS analysis is detecting photoelectrons emitted from a material's surface when it is irradiated with X-rays. XPS analysis provides the binding energies of each element in nanomaterials by measuring the kinetic energy of ejected electrons, it allows the determination of elemental composition and chemical states of surface atoms. XPS offers surface chemical analysis by identifying elements and their oxidation states within a nanomaterial's surface.

2.4.7 Fourier transform infrared spectroscopy

Fourier transform infrared spectroscopy (FTIR, IRAffinity-1, Shimadzu, Japan) was employed to identify the functional groups present in VANs of ZnO/Bi_2S_3 on the surface of FTO before and after the electrochemical sensing reaction across a spectral range of 400-4000 cm^{-1} with a resolution of 4 cm^{-1}. This technique relies on the principle that molecules absorb specific frequencies of infrared radiation and transmit a certain amount of radiation depending on the types of functional groups present in the specimen. ZnO/Bi_2S_3 modified FTO was placed on the sample holder for the FTIR analysis, and the FTIR spectra were recorded.

2.4.8 Raman spectroscopy

Raman spectroscopy analysis (LabRam HR, Horiba Jobin Yvon, Germany) of ZnO/Bi_2S_3 modified FTO was carried out for a non-destructive investigation of a sample's chemical structure, phase, composition, and vibrations. The basic principle of this technique involves the inelastic scattering of a small portion of monochromatic laser light as it interacts with the specimen. This scattered light has a different energy than the incident light due to interactions with molecular vibrations. The resulting energy shift creates a Raman spectrum, which serves as a molecular fingerprint of the sample.

2.4.9 BET surface area analysis

The BET surface area and pore size analysis of AgNSs (Chapter 7) was determined using a BET surface area analyzer (Autosorb-IQ MP, Quantachrome, USA) by the N_2 adsorption-desorption isotherm. The sample (25 mg of AgNSs powder) was degassed at 200 °C for 4 h in an N_2 environment before the analysis. A heating rate of 10 °C min^{-1} with an N_2 flow rate of 20 mL min^{-1} was employed.

2.5 Electrochemical sensing setup

All the electrochemical analyses were done by a Potentiostat/Galvanostat (PGSTAT 302 N, Metrohm, Switzerland) featuring a three-electrode cell: counter electrode (platinum wire, 1 mm diameter), reference electrode (Ag/AgCl/3 M KCl), and working electrode (bare and modified FTO/GCE using various nanomaterials based on the application of sensor). In all the experiments, electrode spacing between the counter electrode to working electrode and reference electrode to working electrode were fixed at 20 mm and 10 mm (centre to centre), respectively. A reference electrode is placed at close proximity with the working electrode to maintain the applied value of the voltage to the actual voltage at the working electrode. Before starting the voltammetric test, N_2 was purged (1.2 L/min) for 5 min to eliminate the dissolved oxygen in the electrolyte media. All the experimental data were recorded with the help of NOVA 1.11 software on a desktop PC.

An electrochemical sensor typically consists of two fundamental components: a molecular (chemical) recognition system and a physicochemical transducer. The chemical recognition system is the utmost part of the sensor, responsible for selectively interacting with the target analyte. The physicochemical transducer converts the chemical response into a measurable signal that can be detected by modern electronic instrumentation. These two

combined parts form a working/sensing electrode. To enhance the performance of an electrochemical sensor, three key characteristics of the working electrode are particularly important, such as specific surface area, hydrophilicity, and electrical conductivity. A high specific surface area of the working electrode allows for the adsorption of a maximum number of recognition units. High electrical conductivity ensures efficient charge transport between the electrode/nanostructure surface and electrolyte solution, which is crucial for signal transduction. Hydrophilicity is also vital, as the target analyte solution is usually aqueous; a hydrophilic electrode surface promotes proper wetting, thereby improving sensor performance. In a three-electrode electrochemical sensing system, the reference electrode does not allow any current to flow through it, while the analytes undergo oxidation/reduction reactions at the working electrode, depending on the polarity of the applied voltage. This voltage determines the sensor's selectivity to the target analytes. The current generated by the electrochemical sensing reactions flows between the working electrode and the counter electrode, which completes the circuit. The counter electrode plays a crucial role by transferring electrons during redox events, thereby maintaining the electron balance within the electrochemical cell. All three electrodes are enclosed in the sensor housing, which is filled with 0.04 M BR/0.1 M PBS electrolyte. A schematic diagram of the electrochemical sensing setup is shown in Figure 2.11.

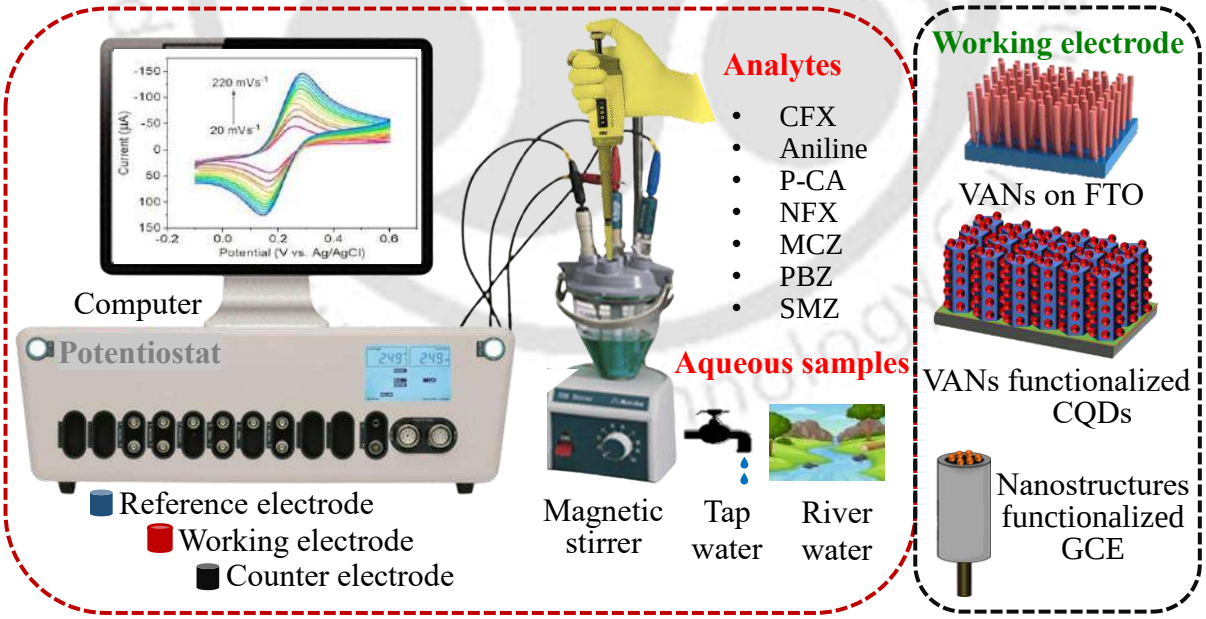

Figure 2.11: Experimental setup for the three-electrode electrochemical system used for electrochemical sensing of various analytes in environmental matrices displaying all the working electrodes for conducting the experiments.

2.6 Electrochemical sensing studies of target analytes

2.6.1 Electrochemical studies and CFX sensing

EIS analysis was used to obtain the kinetic resistance of bare GCE and AgNSs/GCE. CV was performed to determine the (i) active surface area of the functioning electrode (bare and AgNSs/GCE), (ii) effect of loading concentration of AgNSs, (iii) effect of pH during the course of CFX sensing, (iv) electro-kinetic parameters (formal potential, number of electrons participating in electrocatalytic reaction, and rate constant), and (v) surface coverage by adsorption of CFX. In addition, CV was conducted to compare the oxidation peak response of CFX using bare, commercial AgNSs, and AgNSs/GCE. SWV was performed to optimize the deposition parameters (deposition time and deposition potential) and to make a calibration curve (for the determination of limit of detection (LOD), limit of quantification (LOQ), and sensitivity). It was also conducted to determine the stability and reproducibility of the AgNSs/GCE for the detection of CFX. Furthermore, SWV was utilized to examine the practical applicability of the AgNSs/GCE in the tap and river water samples. Chronoamperometry was recorded to investigate the selectivity of the AgNSs/GCE in the presence of interferants, including norfloxacin, chloramphenicol, and chloroquine, at the oxidation potential of 1.116 V during the CFX sensing. It was also used to identify the oxidation product of CFX at the potential of 1.116 V vs. Ag/AgCl.

HPLC and LC-MS analyses were used to identify the major oxidation product of CFX using PBS electrolyte (0.1 M, pH 5) containing 250 µM CFX before and after performing chronoamperometry over AgNSs/GCE at 1.116 V for 1800 s. For HPLC and LC-MS analyses, the CFX solution, before and after the chronoamperometric test, was filtered through 0.2 µm filter paper. The obtained mass spectra were utilized to identify the CFX and its oxidation product based on their m/z values. HPLC was also employed to compare CFX concentration in tap and river water samples with the proposed sensor using reverse phase C-18 column as the solid phase and 80% acetonitrile as the mobile phase.

2.6.2 Electrochemical studies and aniline sensing

To determine the charge transfer resistance of bare and ZnO-VANRs/FTO electrodes, Electrochemical impedance spectrometry (EIS, PGSTAT 101, Metrohm, Switzerland) was done in 0.1 M KCl electrolyte using 1 mM $Ru(NH_3)_6Cl_2$ as an analyte probe between the frequency range of 10^{-2}-10^5 Hz at room temperature. The Nyquist parameters were obtained by

fitting and simulating the data of Nyquist plots in Randles equivalent circuit model using Nova 2.1.7.

Cyclic voltammetry (CV) was conducted in 0.1 M KCl electrolyte (25 °C) with 1 mM $Ru(NH_3)_6Cl_2$ as an analyte probe at several scan rates (15-500 mV/s) for the determination of effective electrocatalytic surface area using Randles-Sevcik equation. To examine the effect of pH during the course of aniline sensing, CV was recorded throughout the pH range of 2 to 7 in 0.1 M phosphate-buffered saline (PBS) electrolyte (aniline 60 µM) using ZnO-VANRs/FTO electrode at a scan rate of 0.05 V/s vs. Ag/AgCl and room temperature. CV was also performed to measure the electrokinetic parameters of aniline sensing at several scan rates (15-500 mV/s) from -0.25-0.8 V vs. Ag/AgCl over ZnO-VANRs/FTO electrode using 0.1 M PBS electrolyte at 45 °C.

Square wave voltammetry (SWV) was recorded from the potential range of -0.05 to 0.6 V vs. Ag/AgCl (step potential 0.002 V, pulse amplitude 0.020 V, frequency 25 Hz) in 0.1 M PBS electrolyte (pH 4) over the ZnO-VANRs/FTO electrode to realize the electrochemical behaviour of aniline detection. At a fixed aniline concentration of 60 µM, all the deposition parameters, such as deposition potential, deposition time, and deposition temperature were optimized. To determine the limit of detection (LOD) and limit of quantification (LOQ), the SWV test was recorded in 0.1 M PBS electrolyte (pH 4) at different concentrations of aniline (0-160 µM) following the optimized deposition parameters. The SWV test was also conducted to evaluate the steady response of the ZnO-VANRs/FTO electrode for aniline (60 µM) sensing from -0.05-0.6 V using 0.1 M PBS electrolyte media (pH 4) at the optimized deposition parameters, for consecutive 10 cycles.

The chronoamperometric test was conducted at different concentrations of aniline from 5 to 110 µM along with p-nitroaniline, chlorobenzene, chlorpyrifos, Cu^{2+}, Pb^{2+}, Ni^{2+}, Cd^{2+}, albumin bovine, *Escherichia coli*, and ciprofloxacin as interferants in 0.1 M PBS electrolyte (pH 4) at 45 °C. The cell current was measured at a redox potential of 0.289 V vs. Ag/AgCl at an interval of 20 s. Further, aniline (2-60 µM) was spiked in the environmental matrix (tap water and river water) diluted 10-fold with 0.1 M PBS buffer (pH 4) to investigate the effectiveness and selectivity of ZnO-VANRs/FTO electrode towards its sensing. The samples collected from tap and river water were subjected to filtration by 0.2 µm membrane filter paper to get rid of any suspended impurities. Subsequently, the filtered samples were thoroughly characterized to determine their conductivity, pH, total organic/inorganic carbon (TOC/TIC), total nitrogen (TN), total dissolved solids (TDS), and anions concentration investigated via Ion chromatography (Metrohm 792 Basic IC, Switzerland).

To identify the reaction products and their reaction pathways involved in aniline sensing, High-performance liquid chromatography (HPLC, 1260 Infinity II, USA) and Liquid chromatography-mass spectroscopy (LCMS, Thermo-3000, USA) analyses were conducted. Furthermore, the performance of aniline detection over the ZnO-VANRs/FTO electrode was also compared with the HPLC technique.

2.6.3 Electrochemical studies and p-CA detection

EIS analysis was performed to investigate the nature of electron transfer rate. It was conducted using FTO(bare), and ZnO-VANs(bio)/FTO@pH7 (ZnO VANs grown at pH 7 on FTO substrate) with 50 mL of 1 mM $K_3[Fe(CN)_6]$ as an electroactive species in 0.1 M KCl electrolyte solution at ambient temperature with the frequency varying from 10^{-2} to 10^5 Hz. The resistance of charge transfer of each of the WE (FTO(bare), ZnO-VANs(bio)/FTO@pH7) was determined using NOVA 1.11 software by fitting the data with the Randles equivalent circuit. The electroactive surface area (A_{eff}) of the WE was also calculated by the Randles-Sevcik equation using the 1 mM $Ru[(NH_3)_6]Cl_2$ as an electroactive species in 0.1 M KCl electrolyte solution (50 mL) at room temperature.

pH of the 0.04 M Britton-Robinson (BR) buffer electrolyte was optimized via CV tests at room temperature and a scan rate of 50 $mV.s^{-1}$. To study the electrokinetic parameters and redox pathway of p-CA sensing, a CV test was conducted using ZnO-VANs(bio)/FTO@pH7 electrode within the potential range of 0.7 to 1.4 V vs. Ag/AgCl, at different scan rates of 15-500 $mV.s^{-1}$, and temperature 45°C in 0.04 M BR buffer (pH 4).

Square wave anodic stripping voltammetry (SWASV) experiments were conducted from the potential 0.65-1.4 V vs. Ag/AgCl (with a pulse amplitude of 0.02 V and step potential of 0.002 V at a frequency of 25 Hz) using ZnO-VANs(bio)/FTO@pH7 as WE in 0.04 M BR buffer (pH 4). All the SWASV tests were conducted at a scan rate of 50 $mV.s^{-1}$. The deposition potential, time, and temperature were optimized at the fixed concentration of 40 µM p-CA. The electrolyte solution was stirred at 300 rpm to minimize the analytes diffusion resistance during the deposition and conditioning processes. To make a calibration curve, the concentration of the p-CA was changed from 2 to 200 µM in the 0.04 M BR buffer electrolyte media at pH 4. The stability and reproducibility of ZnO-VANs(bio)/FTO@pH7 electrode for p-CA sensing were determined using three fresh electrodes fabricated under identical conditions. SWASV tests were conducted in the potential window from 0.65 to 1.4 V vs. Ag/AgCl, and the response of peak current was measured for 15 repeated cycles during the course of p-CA (40 µM) sensing at temperature of 45°C.

The interference studies were performed by introducing chemically similar electroactive species, namely, chlorobenzene, carbendazim, profenofos, nitrite, 4-nitrophenol, bisphenol a, and mercury using ZnO-VANs(bio)/FTO@pH7 electrode for p-CA sensing by conducting the chronoamperometric test at 0.978 V vs. Ag/AgCl with an interval of 20 s and concentration of 30 µM of each interferants substance in the BR buffer (pH 4) at the optimized conditions. Intermittent addition of p-CA was done to investigate the changes in the peak current. In order to evaluate the effectiveness of ZnO-VANs(bio)/FTO@pH7 electrode for the sensing of p-CA found in environmental water samples, p-CA (2-80 µM) was spiked with the tap and river water samples. The collected samples were filtered through 0.2 µm filter paper to eliminate suspended contaminants. These samples were characterized for conductivity, pH, total dissolved solids (TDS), total organic carbon (TOC), total inorganic carbon (TIC), total nitrogen (TN), and anions content by ion chromatography (Metrohm, Basic IC 792, Switzerland) for detailed assays.

The LCMS and HPLC analyses were performed to investigate the reaction product during the course of p-CA sensing to determine the reaction pathways. HPLC was also used to compare the performance with the SWASV method for detecting p-CA at ZnO-VANs(bio)/FTO@pH7 electrode.

2.6.4 Electrochemical studies and NFX detection

To determine the charge transfer resistance of bare FTO, ZnOVANs(bio)/FTO, and $CQDs_{1.5}$-ZnOVANs(bio)/FTO electrodes, EIS analysis was done in 0.1 M KCl electrolyte using 1 mM $Ru(NH_3)_6Cl_2$ as an analyte probe between the frequency range of 10^{-2}-10^5 Hz at room temperature. The Nyquist parameters were obtained by fitting and simulating the data of Nyquist plots in the Randles equivalent circuit model.

CV was conducted in 0.1 M KCl electrolyte (25 °C) with 1 mM $Ru(NH_3)_6Cl_2$ as an analyte probe at various scan rates (5-500 mV/s) for the determination of effective electrocatalytic surface area using the Randles-Sevcik equation and comparison of anodic and cathodic peak currents. To examine the effect of pH during the NFX sensing, CV was recorded throughout the pH range of 2 to 9 in 0.1 M PBS electrolyte (NFX 60 µM) using $CQDs_{1.5}$-ZnOVANs(bio)/FTO at a scan rate of 50 mV/s vs. Ag/AgCl and 25 °C. CV was also performed to measure the electrokinetic parameters of NFX sensing at various scan rates (5-500 mV/s) over $CQDs_{1.5}$-ZnOVANs(bio)/FTO electrode using 0.1 M PBS electrolyte (pH 5) at 45 °C.

SWV was performed to (i) examine the effect of deposition potential, deposition time, and deposition temperature during NFX sensing in 0.1 M PBS electrolyte (pH 5), (ii) calibrate

NFX determination at various concentrations (0.25-300 µM) and calculate LOD, LOQ, and sensitivity in 0.1 M PBS electrolyte (pH 5, 45 °C), (iii) assess stability and reproducibility of developed electrode during NFX determination, and (iv) detect and quantify NFX in tap water and river water under identical conditions. All the SWV tests were performed using $CQDs_{1.5}$-ZnOVANs(bio)/FTO in a 0.1 M PBS (pH 5).

Chronoamperometry test was conducted to identify the redox products formed during NFX detection and to evaluate the selectivity of NFX sensing in the presence of common pharmaceuticals interferants, including, ciprofloxacin, phenylbutazone, and sulfamethoxazole. These experiments were performed using $CQDs_{1.5}$-ZnOVANs(bio)/FTO electrode in 0.1 M PBS electrolyte (pH 5, 45 °C) at 1.042 V vs. Ag/AgCl for 2000 s.

LC-MS analyses were used to identify the major oxidation product of NFX using 0.1 M PBS electrolyte (pH 5, 45 °C) containing 250 µM NFX before and after performing chronoamperometry over $CQDs_{1.5}$-ZnOVANs(bio)/FTO at 1.042 V for 2000 s. HPLC was performed for the comparative assay of NFX at $CQDs_{1.5}$-ZnOVANs(bio)/FTO in tap and river water samples.

2.6.5 Electrochemical studies and MCZ sensing

The electron-transfer resistance and electroactive surface area of the kinetic electrodes were determined by EIS (frequency range 10^{-2}-10^{5} Hz) and CV (scan speeds 5-500 mV/s) analyses using 1 mM $Ru(NH_3)_6Cl_2$ as a standard probe in 0.1 M KCl electrolyte at 25 °C.

CV was also utilized to (i) examine the effect of electrolyte (0.04 M BR buffer) pH (3-9) during MCZ sensing at 25 °C, (ii) capture anodic peak current profile of MCZ using FTO(bare) and $2.3Bi_2S_3$-VONs(nat)/FTO@pH3 at the optimized electrolyte pH and 25 °C, (iii) determine electro-kinetic parameters, such as the number of electrons involved in the redox reaction of MCZ, reaction rate constant, and the formal standard potential in 0.04 M BR buffer (pH 7, 45 °C), and (iv) investigate surface coverage of MCZ utilizing 0.04 M BR buffer (pH 7, 45 °C).

SWV was performed to (i) study the effect of deposition parameters (deposition potential (Dpote), deposition time (Dtime), and deposition temperature (Dtemp)) during MCZ sensing in 0.04 M BR buffer (pH 7), (ii) calibrate MCZ determination at various concentrations (0-200 µM) and calculate LOD, LOQ, and sensitivity in 0.04 M BR buffer (pH 7, 45 °C), (iii) assess stability and reproducibility of developed electrode during MCZ determination, and (iv) detect and quantify MCZ in tap water, river water, agricultural runoff, and wastewater under identical conditions.

Chronoamperometry test was performed to identify the redox products formed during MCZ sensing and to evaluate the selectivity of MCZ detection in the presence of common pesticide interferants, namely, chlorpyrifos, carbendazim, malathion, thiram, ziram, and profenofos. These experiments were performed using 2.3Bi_2S_3-VONs(nat)/FTO@pH3 electrode in 0.04 M BR buffer (pH 7, 45 °C) at 0.655 V vs. Ag/AgCl for 1800 s.

HPLC and LC-MS analyses were employed to detect the redox products of MCZ in 0.04 M BR buffer (pH 7, 45 °C) originated during sensing of 200 µM MCZ over the developed electrode at 0.655 V for 1800 s. HPLC was also utilized to compare the sensing performance of MCZ in tap water, river water, agricultural runoff, and wastewater with the fabricated electrode.

2.6.6 Electrochemical studies and simultaneous PBZ and SMZ sensing

EIS was performed to determine the charge transport resistance of the bare/GCE, ZnO(bio)/GCE, Bi_2S_3(bio)/GCE, and Bi_2S_3-ZnO(bio)/GCE in a 0.1 M KCl electrolyte using 1mM $Ru(NH_3)_6Cl_2$ as the standard probe at the amplitude of 0.01 V and potential of 0.4 V within the frequency range of 10^{-2} to 10^5 Hz.

CV was recorded to investigate the electrocatalytic surface area by varying scan rates from 5-500 mV/s and to compare the anodic/cathodic peak current using bare/GCE, ZnO(bio)/GCE, Bi_2S_3(bio)/GCE, and Bi_2S_3-ZnO(bio)/GCE in a 0.1 M KCl electrolyte with 1mM $Ru(NH_3)_6Cl_2$ as the standard probe (fixed scan rate of 50 mV/s). Furthermore, the following electrochemical characterizations were also performed using CV: (i) to investigate the effect of the supporting electrolyte (0.1 M PBS) pH (3-11) on the electrochemical sensing of PBZ and SMZ using the Bi_2S_3-ZnO(bio)/GCE and (ii) to investigate the electrokinetic parameters and surface coverage by the adsorption of PBZ and SMZ on the Bi_2S_3-ZnO(bio)/GCE in a 0.1 M PBS (pH 5, 25 °C) at various scan rates (5-500 mV/s).

SWV was conducted for the following electrochemical studies: (i) to optimize the deposition potential (D_P) and deposition time (D_T) for PBZ and SMZ sensing to enhance the sensing performance using Bi_2S_3-ZnO(bio)/GCE at a fixed concentration (40 µM) of PBZ/SMZ; (ii) to investigate the detection parameters for the individual and simultaneous sensing of PBZ and SMZ using Bi_2S_3-ZnO(bio)/GCE at a selected D_P of -0.4 V and a D_T of 60 s; and (iii) to examine Bi_2S_3-ZnO(bio)/GCE stability at the selected deposition parameters during the simultaneous sensing of PBZ and SMZ detection. Additionally, SWV of Bi_2S_3-ZnO(bio)/GCE in tap and river waters was also performed to assess its real-world applicability for the simultaneous electrochemical sensing of PBZ and SMZ. All the SWV tests were

conducted at a fixed frequency of 25.0 Hz, step potential of 0.002 V, amplitude of 0.02 V, and scan rate of 50 mV/s.

Chronoamperometry was conducted to analyze the oxidation product of PBZ and SMZ during the course of sensing using the Bi_2S_3-ZnO(bio)/GCE in a 0.1 M PBS (pH 5, 25 ℃) containing 120 µM of PBZ and SMZ at their respective redox potentials of 0.655 and 1.015 V for 2000 s. Additionally, chronoamperometry was conducted to study the selectivity of PBZ and SMZ sensing at the Bi_2S_3-ZnO(bio)/GCE in the existence of interfering substances at the redox potentials of 0.655 and 1.015 V, respectively. SMZ, ciprofloxacin, and norfloxacin were used as interfering substances during PBZ sensing, while PBZ, ciprofloxacin, and norfloxacin were employed during the course of SMZ detection.

LC-MS analysis of 120 µM of PBZ/SMZ in 0.1 M PBS (pH 5), both before and after the chronoamperometry test, was performed to analyze the oxidation products of PBZ and SMZ during the course of sensing.

References

Bhan, C., Golder, A.K., 2025. Nature-Inspired Vertically Oriented 1D Bi_2S_3 Surface Nanorods for Ultra-Selective Electrochemical Sensing of Mancozeb. Langmuir 41, 15331–15346. https://doi.org/10.1021/acs.langmuir.5c00915

Bhan, C., Kumar Golder, A., 2023. Bio-based hierarchical vertically aligned 2D ZnO nanostructures for ultra selective electrochemical sensing of p-Chloroaniline. Chem. Eng. J. 475, 146122. https://doi.org/10.1016/j.cej.2023.146122

Flick, G.J., Burnette, F.S., Aung, L.H., Ory, R.L., St. Angelo, A.J., 1978. Chemical composition and biochemical properties of mirlitons (*Sechium edule*) and purple, green, and white eggplants (*Solanum melongena*). J. Agric. Food Chem. 26, 1000–1005. https://doi.org/10.1021/jf60219a045

Mali, S.S., Kim, H., Patil, P.S., Hong, C.K., 2013. Chemically grown vertically aligned 1D ZnO nanorods with CdS coating for efficient quantum dot sensitized solar cells (QDSSC): a controlled synthesis route. Dalt. Trans. 42, 16961. https://doi.org/10.1039/c3dt51287h

Ordonez, A., Gomez, J., Vattuone, M., Lsla, M., 2006. Antioxidant activities of Sechium edule (Jacq.) Swartz extracts. Food Chem. 97, 452–458. https://doi.org/10.1016/j.foodchem.2005.05.024

Rao, C.V., Golder, A.K., 2016. Development of a bio-mediated technique of silver-doping on titania. Colloids Surfaces A Physicochem. Eng. Asp. 506, 557–565.

https://doi.org/10.1016/j.colsurfa.2016.07.031

Sarakhman, O., Benková, A., Švorc, Ľ., 2022. A modern and powerful electrochemical sensing platform for purines determination: Voltammetric determination of uric acid and caffeine in biological samples on miniaturized thick-film boron-doped diamond electrode. Microchem. J. 175, 107132. https://doi.org/10.1016/j.microc.2021.107132

Senguttuvan, J., Paulsamy, S., Karthika, K., 2014. Phytochemical analysis and evaluation of leaf and root parts of the medicinal herb, Hypochaeris radicata L. for in vitro antioxidant activities. Asian Pac. J. Trop. Biomed. 4, S359–S367. https://doi.org/10.12980/APJTB.4.2014C1030

Venieri, D., Fraggedaki, A., Kostadima, M., Chatzisymeon, E., Binas, V., Zachopoulos, A., Kiriakidis, G., Mantzavinos, D., 2014. Solar light and metal-doped TiO_2 to eliminate water-transmitted bacterial pathogens: Photocatalyst characterization and disinfection performance. Appl. Catal. B Environ. 154–155, 93–101. https://doi.org/10.1016/j.apcatb.2014.02.007

CHAPTER 3

Phyto-analytic Formation of Ag Nanostructures for Targeted Electrocatalytic Sensing of Ciprofloxacin

This chapter demonstrates the formation of phyto-analytic Ag nanostructures (*AgNSs) using plant bio-analytes present in the bio-extract of Citrus limetta. The phytochemicals in the bio-extract could leverage the formation of AgNSs. Subsequently, the AgNSs were immobilized onto the surface of a GCE using Nafion as a binder for electrochemical sensing of ciprofloxacin (CFX) via SWV technique. The real-world implication of the proposed electrochemical sensing platform was investigated in the environmental matrix by SWV and compared with the HPLC.*

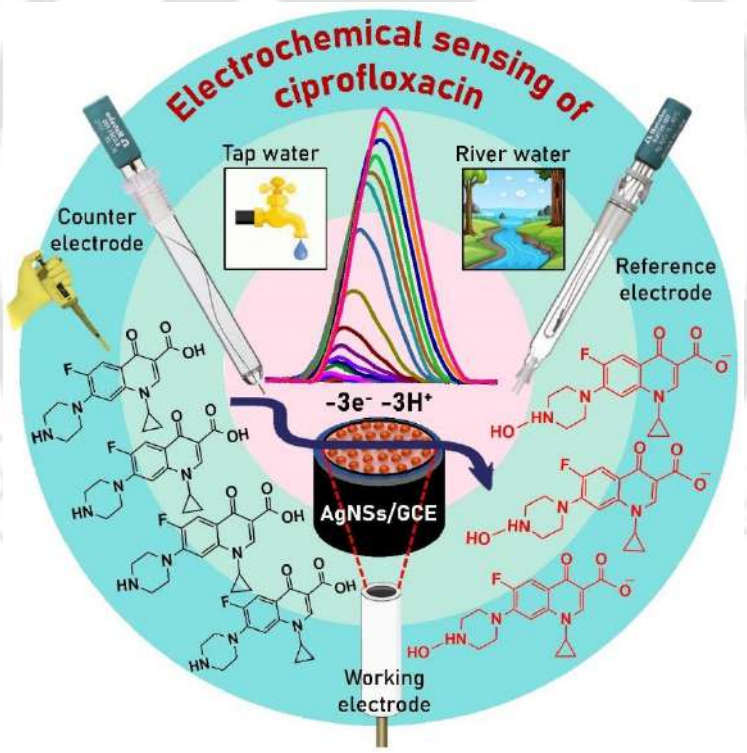

Chapter highlights

- Phyto-analytic development of Ag nanostructures using bio-extract of *Citrus limetta*
- AgNSs/GCE electro-catalysed ciprofloxacin sensing by square wave voltammetry
- Ciprofloxacin sensing involved three electrons and three protons transfer reaction
- Achieved detection limit of 0.199 µM and sensitivity of 0.354 µA. $\mu M^{-1}.cm^{-2}$
- AgNSs/GCE demonstrated ciprofloxacin ~100% recovery in tap and river water samples

3.1. Background and executive motivation

Advancements in electrocatalytic sensing have expressively boosted the sensing and quantifying of pharmaceutical compounds, such as ciprofloxacin (CFX), a fluoroquinolone antibiotic, is a prominent agent in the treatment of bacterial infections due to its broad-spectrum antimicrobial activity and effective penetration into tissues (Nejabatdoust et al., 2024). Despite its therapeutic benefits, the extensive use of CFX merging as a critical target due to its profound implications in clinical and environmental metrics raises concerns about its ecological and human health impacts. Ecotoxicological assessments indicate that CFX can adversely affect microbial communities, disrupt aquatic ecosystems, and contribute to the development of antibiotic-resistant bacteria. Moreover, the abuse of CFX can lead to allergies, nausea, diarrhea, vomiting, headache, etc., in human beings and chondrotoxic effects with tendon raptures in animals (Adane et al., 2023). The existence of CFX and other pharmaceutical residue in the environmental matrix is an emerging concern due to the development of antibiotic-resistant bacteria (Ravi and Golder, 2023a). Therefore, the detection and quantification of CFX in environmental and biological matrices are crucial for monitoring its prevalence and mitigating associated risks.

Traditional analytical techniques, such as high-performance liquid chromatography (HPLC) and mass spectroscopy are effective for sensing and quantifying pharmaceutical residue in environmental metrics (Cicek and Erdogan, 2024; Elgendy et al., 2023; He et al., 2020). Nevertheless, these analytical techniques involve complex procedures, high costs, lengthy sample preparation times, and require adept personnel. Therefore, developing an alternative phyto-analytic electrochemical sensing platform is a growing interest that offers enhanced selectivity and sensitivity with low cost for in-situ sensing and quantifying environmental pollutants.

Electrochemical sensing platforms have emerged as promising approaches for rapidly and efficiently detecting organic analytes, such as pesticides and pharmaceuticals (Monisha et al., 2023; Xu et al., 2024). They offer advantages, including economical pricing, easy functioning electrode modification, high sensitivity and selectivity with low detection limit for focus electroactive species. The electrochemical detection of pharmaceutical residue typically involves cyclic voltammetry (CV), chronoamperometry, differential pulse voltammetry (DPV), and square wave voltammetry (SWV). These techniques are employed to monitor the electrocatalytic response of target analytes upon interaction with the nanomaterial-modified

electrode. Among the aforementioned detection techniques, SWV provides higher sensitivity and selectivity for detecting low concentrations of the focus analytes (Malode et al., 2020).

Nanoparticles (NPs) such as AgNPs, AuNPs, $BiVO_4$, CuO, ZnO, MoS_2, etc., immobilized on the surface of the functioning (glassy carbon, Pt, Au, and graphite paste) electrode with the help of binders (Nafion, polyvinyl chloride, silicone, polystyrene, polyethylene glycol, and polytetrafluoroethylene) could enhance the performance of electrochemical sensor by several folds due to the high surface area-to-volume ratio, excellent electrical conductivity, and catalytic activity (Das et al., 2024; Liu et al., 2024; Magar et al., 2023; Malode et al., 2020; Wang et al., 2024; Xu et al., 2024). The Nafion binder helps to hold the nanostructures onto the surface of the functioning electrode, which enhances the stability and electric conductivity of the electrode by ensuring better contact between the nanocatalysts and the functioning electrode. Additionally, the binders allow the integration of various types of nanocatalysts that may not adhere well to the electrode surface and minimise the likelihood of catalyst detachment during the course of sensing (Ghanbari et al., 2024; Verma et al., 2024). Among the various synthesis methods of metal nanostructures, phyto-analytic formation routes minimize the use of environmentally intensive chemicals. However, bio-based routes are slower and produce particles with inconsistent sizes and structures. These limitations are significant obstacles to use a phyto-analytic approach to form tailor-made nanostructures (Dash et al., 2020). The phytochemicals present in the *Citrus limetta* extract, including citric acid, polyphenolic compounds, flavonoids, etc., could be exploited for the growth and formation of stable Ag nanostructures (AgNSs). Furthermore, utilizing natural extracts can reduce the production costs of nanostructures compared to synthetic chemicals used in traditional methods. Lastly, AgNSs synthesized by the phyto-analytic route could exhibit better biocompatibility and hydrophilicity, resulting in better conductivity than nanostructures synthesized by chemical-based methodologies (Ravi and Golder, 2023a). In a previous study, green synthesized AgNPs using bio-extract of *Camellia sinensis* combined with carbon black immobilized over glassy carbon electrode (GCE) employed for electrochemical sensing of CFX. The fabricated sensor displayed a detection limit of 0.48 µM (Meireles et al., 2024).

Simultaneously engineered nanostructures, including AgNSs, AuNPs, CdS, SnO_2, Bi_2S_3, CdS, etc., have garnered significant research interest due to their diverse catalytic applications in electrochemical sensing, wastewater treatment, CO_2 conversion, etc. (Bhan and Golder, 2023; Chowdhury et al., 2023, 2022; Gawal and Golder, 2024; Ravi and Golder, 2025, 2023b; Ravi and Kumar Golder, 2024). Among these, AgNSs have gained significant attention due to their unique physicochemical properties, including high surface area-to-volume ratio,

improved charge transfer characteristics, and high catalytic activity (Das et al., 2024). The immobilization of AgNSs onto the surface of functioning electrode has demonstrated substantial improvements in sensing performance, making them ideal candidates for the development of highly sensitive and selective electrochemical sensing platforms (Ehsani et al., 2021; Karimi et al., 2024). The enhanced performance of AgNSs-based electrocatalytic sensors is attributed to their ability to facilitate electron transfer, increase the effective surface area, and improve the catalytic oxidation of target analytes.

Chapter 3 proposes the formation of phyto-analytic AgNSs using plant bioactives present in the bio-extract of *Citrus limetta*. The phytochemicals in the bio-extract could leverage the formation of AgNSs. Subsequently, the AgNSs were immobilized onto the surface of a GCE using Nafion as a binder for electrochemical sensing of CFX via the SWV technique. The real-world implementation of the proposed electrochemical sensing platform was investigated in the environmental matrix (tap and river water) by SWV and compared with the HPLC. To our knowledge, the phyto-analytic formation of AgNSs using bio-extract of *Citrus limetta* for electrocatalytic sensing of CFX by SWV is reported for the time.

3.2. Result and discussions

3.2.1. Characterization of AgNSs

3.2.1.1 *Morphology and elemental analysis*

The FESEM and FETEM images of AgNSs are presented in Figs. 3.1a and 3.1b. The FESEM and FETEM analysis of dispersed AgNSs in DI water were performed after sonicated for 1 h, followed by drop-casting onto a glass slide for FESEM and a TEM grid for FETEM. The AgNSs particles were observed to be spherical with an average diameter of 43.5±3.9 nm, displaying a normal size distribution (inset of Fig. 3.1a). The small particles exhibit a high surface area with more active sites, enhancing their catalytic activity. Fig. 3.1c shows the elemental spectrum and mapping of AgNSs, revealing a uniform distribution of Ag with a weight % of about 100. The peak around 3.1 keV is due to the Au coating before the EDX analysis. The HRTEM image (Fig. 3.1d) displays fringes with d-spacing values of 0.233 nm and 0.201 nm, corresponding to Ag (111) and Ag (200) planes, respectively. Moreover, the SAED pattern of AgNSs confirms its polycrystalline nature (inset of Fig. 3.1d) (Das et al., 2024). These findings are consistent with the XRD results.

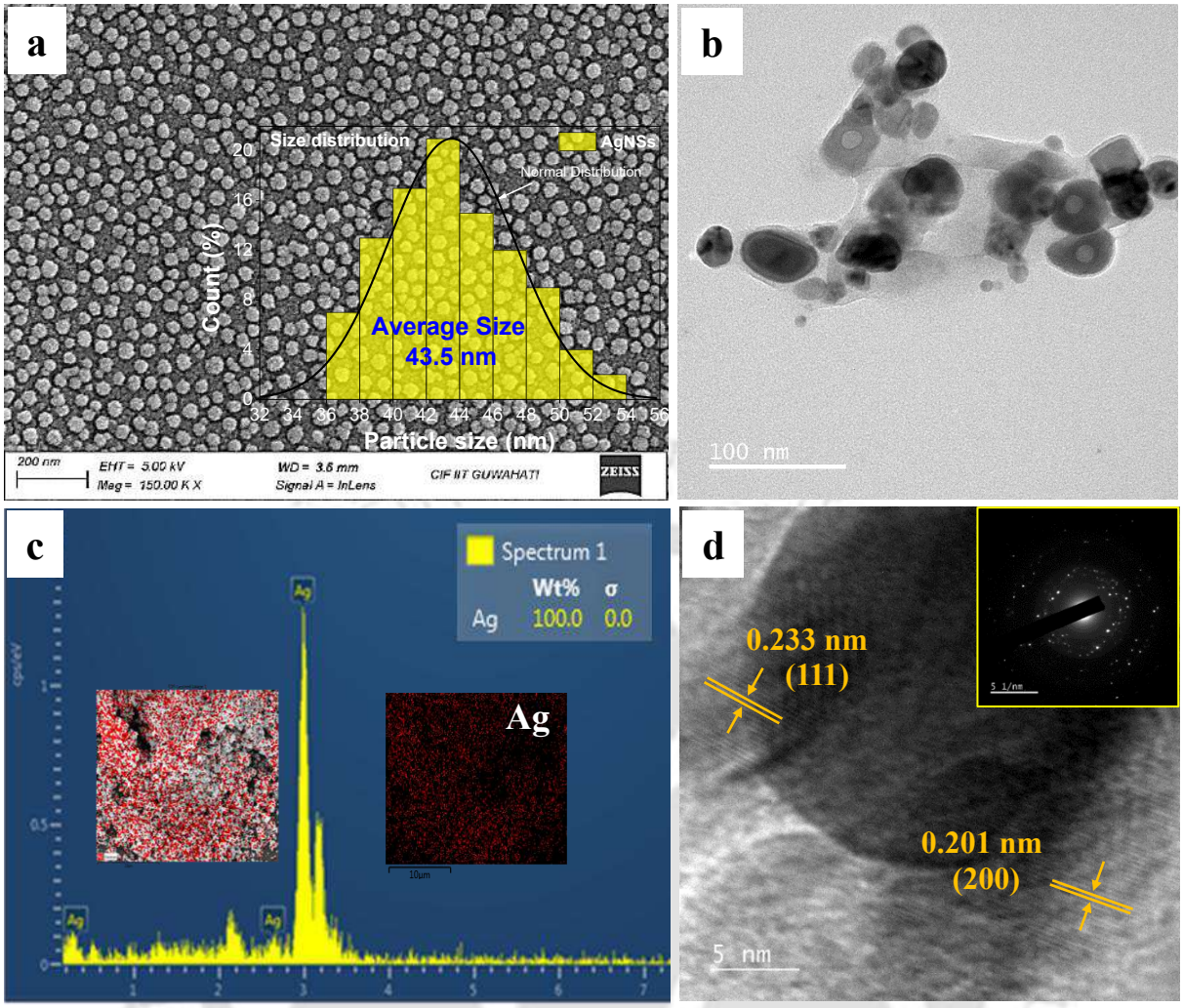

Figure 3.1: (a) FESEM image (inset: particle size distribution), (b) FETEM image, (c) EDX elemental spectrum (inset: elemental mapping), and (d) HRTEM image (inset: SAED pattern) of AgNSs.

3.2.1.2 *XRD analysis*

Fig. 3.2a presents the XRD pattern of AgNSs along with the corresponding JCPDS spectra. The results show sharp peaks at 2θ = 38.5°, 45.1°, 65.4°, 78.5°, and 81.8°, corresponding to the (111), (200), (220), (311), and (222) planes of Ag, respectively. The crystallite sizes for these planes were determined to be 31.8, 108.5, 114.7, 110.7, and 33.7 nm, respectively, with corresponding d-spacing values of 0.233, 0.201, 0.143, 0.122, and 0.118 nm. The average crystal size was calculated using the crystallite size and intensity fraction of each peak, resulting in an average crystallite size of 50.3 nm. This value is smaller than the observed particle size (43.5±3.9 nm) obtained from FESEM analysis (Fig. 3.1a), indicating that each AgNSs consists of multiple crystals, also supported by the SAED pattern (inset of Fig. 3.1d),

which confirms the polycrystalline nature of the AgNSs. The polycrystalline particles are reported to exhibit more surface and oxygen defects, enhancing the conductivity and catalytic activity (J. Li et al., 2017). The XRD spectra also indicate the high crystallinity of AgNSs, which is advantageous for better conductivity due to the uniform arrangement of elements, potentially enhancing its electrochemical activity (Mehtab et al., 2018).

3.2.1.3 *BET surface area analysis*

The BET parameters and N_2 adsorption-desorption curve are illustrated in Fig. 3.2b. The synthesized AgNSs exhibited a BET surface area of 1.26 m^2 g^{-1} with an average pore size of 5.92 nm and pore volume of 0.02 cc g^{-1}. It could provide enough active sites for the adsorption of target analytes during electrochemical sensing applications. Based on the N_2 adsorption-desorption curve, AgNSs follow a Type IV isotherm with a hysteresis loop, indicating that the Ag nanomaterial has a mesoporous structure, characterized by pores in the 2-50 nm range (Burhan et al., 2018). A similar BET profile of confined arc plasma-based AgNPs was also reported (Zhou et al., 2009), providing accessible pathways for enhanced diffusion and interaction within the analytes (Fato et al., 2019).

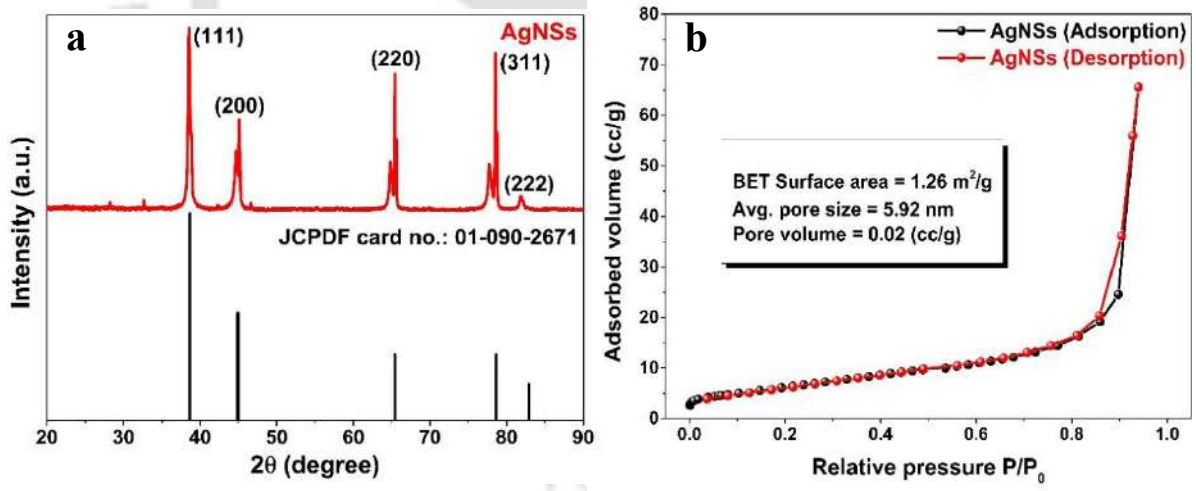

Figure 3.2: (a) XRD pattern of AgNSs along with the corresponding JCPDS pattern and (b) N_2 adsorption-desorption curve with BET parameters of AgNSs.

3.2.1.4 *XPS analysis*

Fig. 3.3a shows the XPS survey scan spectra of AgNSs, revealing peaks corresponding to Ag, C, and O. The high-resolution spectra of Ag (Fig. 3.3b) display two distinct peaks at 367.2 and 373.2 eV, corresponding to Ag (0) 3d5/2 and Ag (0) 3d3/2, respectively

(Ramaraghavulu et al., 2021). In Fig. 3.3c, the high-resolution spectra of C show peaks at 284.7 and 285.7 eV, attributed to sp^2/C=C and C–C/C–H bonds (Mohamedkhair et al., 2019). These carbon species mainly represent bio-analytes from the *Citrus limetta* extract adsorbed on the surface of AgNSs. Additionally, the presence of C in AgNSs could be attributed to the adsorption of gases from the surrounding atmosphere (not detected in EDX analysis) and the use of carbon tape during the analysis procedure (Das et al., 2024). The high-resolution spectra of O (Fig. 3.3d) indicate peaks at 532.1 and 533.2 eV, corresponding to lattice oxygen (O_L) and surface-adsorbed oxygen (O_A), respectively. These oxygen species originated from the existence of bio-analytes from the *Citrus limetta* extract present on the surface of AgNSs (Ravi and Golder, 2023b). It could provide a better interaction with CFX and improved conductivity, resulting in enhanced electrochemical sensing of CFX.

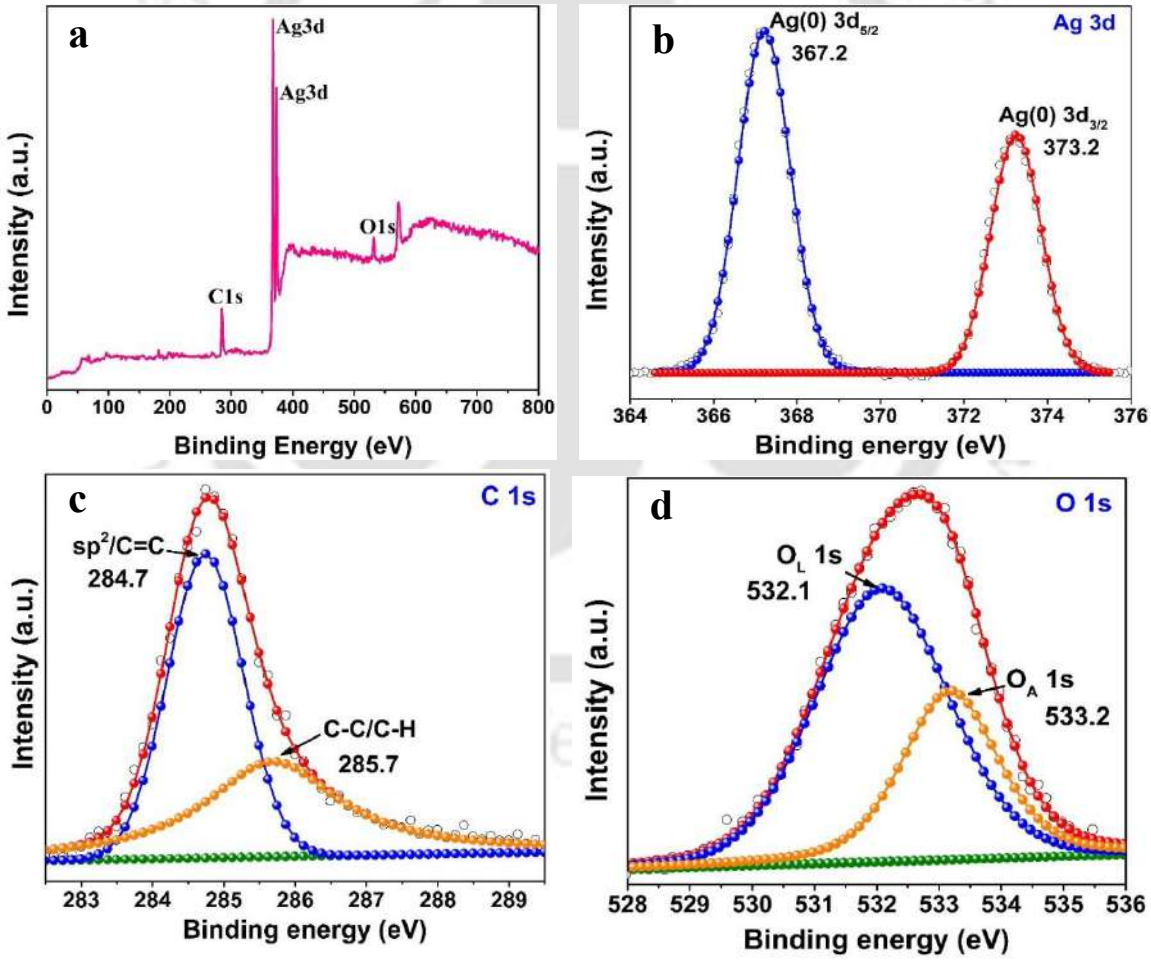

Figure 3.3: (a) XPS survey spectrum and high-resolution spectra of (b) Ag 3d, (c) C 1s, and (d) O 1s of AgNSs.

3.2.2. Electrochemical characterization of AgNSs/GCE

3.2.2.1 *EIS analysis*

To determine the charge transfer resistance of the functioning electrodes (bare and AgNSs immobilized GCE), EIS analysis was carried out in 0.1 M KCl (electrolyte) using 0.001 M $Ru(NH_3)_6Cl_2$ (redoxprobe) between the frequency window of 10^{-2}-10^5 Hz at 25 °C. KCl is used as a standard supporting electrolyte to maintain a stable ionic strength. However, 0.001 M $Ru(NH_3)_6Cl_2$ was used as a redoxprobe due to its favourable electrochemical characteristics, including high stability and well-defined redox behaviour (one-electron transfer process). Additionally, $Ru(NH_3)_6Cl_2$ is an outer sphere redoxprobe that typically participates in the outer sphere (outside the diffusion layer) electron transfer. It provides a straightforward mechanism for studying EIS due to their well-defined redox behaviour without the complexity of bonding interactions (Dash et al., 2021). Fig. 3.5a demonstrates the EIS profile of bare and AgNSs/GCE with the inset of the Randles impedance model, which provided electrode kinetic resistance (R_p), electrolyte resistance (R_s), and constant phase element (CPE) by fitting obtained data in the Nyquist plots (Kumar and Das, 2023). The R_p is directly proportional to the diameter of the semicircle in EIS spectra (Kumar and Das, 2024). The value of R_p was 3190 kΩ for bare GCE (large diameter semicircle), which decreases to 219 kΩ after the immobilization of AgNSs onto the surface of bare GCE, demonstrating higher conductivity of AgNSs/GCE (Moslah et al., 2021). The values of R_s were found to be 0.130 and 0.146 kΩ for the bare GCE and AgNSs/GCE, respectively. The variation in R_s could be attributed to the space between the electrodes varying slightly during the different sets of experiment. Additionally, the changes in the texture of the bare GCE after the modification with AgNSs could influence ions movement through the electrolyte, which could affect R_s. Moreover, compared to the R_p values, the variation in the R_s is negligible (Bhan and Golder, 2024). The difference in the CPE value is due to the conductivity variation of the functioning electrodes (Bhan and Kumar Golder, 2023). The obtained EIS parameters of bare GCE and AgNSs/GCE are presented in Table 3.1.

Table 3.1: EIS parameters of bare and AgNSs/GCE.

Functioning electrode	R_s (kΩ)	R_p (kΩ)	CPE (µMho)
Bare GCE	0.130	3190	14.2
AgNSs/GCE	0.146	219	11.8

3.2.2.2 *Surface area of bare and AgNSs/GCE*

The surface area of bare and AgNSs/GCE was obtained by recording cyclic voltammogram at different scan rates (5-500 mV/s) in 0.1 M KCl (electrolyte) using 0.001 M $Ru(NH_3)_6Cl_2$ (redoxprobe) at 25 °C (Figs. 3.5b and 3.5c). Randles-Sevcik equation (Eq. 3.1) was used to determine the surface area of the functioning electrode (Stanley et al., 2024).

$$I_{Pa} = (2.69 \times 10^5)n^{3/2}A_eD^{1/2}\upsilon^{1/2}C_0 \quad (3.1)$$

Where I_{pa}, C_0, υ, n, D, and A_e are the oxidation peak current (A), concentration of redoxprobe (mol/cm^3), scan rate (V/s), number of electron present in redox reaction (n = 1), diffusion coefficient (8.43×10^{-6} cm^2/s), and active surface area (cm^2), respectively (Wang et al., 2011). Fig. 3.5d exhibited the linearity of the I_{pa} vs. $\upsilon^{0.5}$ plot with a slope of 29.547 (R^2 = 0.997) and 76.825 µA. $V^{-1/2}.s^{1/2}$ (R^2 = 0.987) for bare and AgNSs/GCE, respectively. The A_e of bare and AgNSs/GCE were 0.038 and 0.098 cm^2 by equalizing the slopes of Fig. 3.5d with Eq. 3.1, respectively. After the immobilization of AgNSs over the surface of bare GCE A_e (61.22%) was increased, which facilitated maximum docking sites for CFX, enhancing the sensing performance of the fabricated sensor.

3.2.3. Optimization of loading concentration, pH, and calculation of electro-kinetic parameters

3.2.3.1 *Effect of AgNSs loading concentrations*

To investigate the effect of AgNSs loading concentrations (2.5, 5.0, 7.5, 10.0, and 12.5 mg/mL) at a GCE on the electrochemical sensing of CFX (70 µM), CV was recorded in a 0.1 M PBS electrolyte (pH 5) with a scan rate of 50 mV/s at 25 °C (Fig. 3.4a). The oxidation peak current increased with AgNSs loading concentrations from 2.5 to 10.0 mg/mL, which could be attributed to more adsorption sites for the CFX and improved electron transfer kinetics (Fig. 3.4b) (Ning et al., 2018). The decrease in oxidation peak current at AgNSs> 10.0 mg/mL could be of AgNSs agglomeration forming larger clusters that obstruct active sites and reduce active surface area. Additionally, at higher AgNSs loading concentrations, the resistance of the AgNSs/GCE increases, hindering efficient electron transfer, and the formation of a dense AgNSs layer may restrict the diffusion of CFX to the electrode surface (Muhammad et al., 2016).

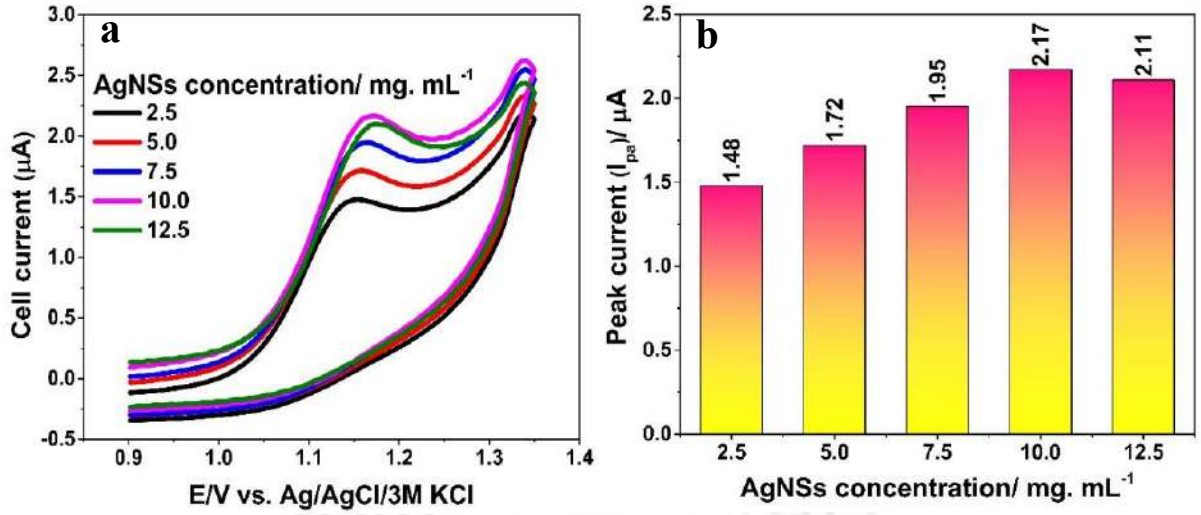

Figure 3.4: (a) CV at different AgNSs loading concentrations (2.5, 5.0, 7.5, 10.0, and 12.5 mg/mL) and (b) Oxidation peak current (I_{pa}) vs. AgNSs loading concentrations. Reaction conditions: 70 µM CFX in a 0.1 M PBS electrolyte (pH 5) with a scan rate of 50 mV/s at 25 °C.

3.2.3.2 *pH effect*

Fig. 3.5e illustrates the CV of electrocatalytic sensing of CFX (70 µM) using AgNSs/GCE in 0.1 M PBS electrolyte at different pH (3-9), scan rate of 50 mV/s, and 25 °C. The decrease in the oxidation peak potential (E_p) with increasing the pH of the electrolyte from 3 to 9 confirmed the presence of proton in the oxidation reaction of CFX (Fig. 3.5f) (Malode et al., 2020). The oxidation peak current was observed maximum at pH 5, indicating sensing and quantifying of CFX over AgNSs/GCE was favourable at pH 5 of 0.1 M PBS (Fig. 3.5g). The slope of the linear plot (E_p vs. pH, Fig. 3.5f) was -0.0494 V per unit pH (R^2 = 0.993), indicating equivalent number of electron and proton present in the oxidation event of CFX over the AgNSs/GCE (Manivannan et al., 2019). Fig. 3.5h shows the CV of CFX sensing using bare GCE, commercial AgNSs, and AgNSs/GCE in 0.1 M PBS (pH 5, 25 °C) at a CFX concentration of 70 µM and a scan rate of 50 mV/s. AgNSs/GCE exhibited a 34.1% increment in current density and a reduction in the peak potential from 1.219 to 1.159 V during CFX detection compared to bare GCE. Moreover, AgNSs/GCE showed a 15.4% increase in current density and a reduction in the peak potential from 1.228 to 1.159 V compared to commercial AgNSs. These results highlight the superior catalytic activity of bio-based AgNSs over commercial AgNSs.

3.2.3.3 *Calculation of electro-kinetic parameters*

The determination of electro-kinetic parameters associated with the oxidation event and adsorption of CFX onto AgNSs/GCE, CV was recorded at various scan rates (5-500 mV/s) in PBS electrolyte (0.1 M, pH 5, 25 °C) at CFX concentration of 70 µM (Fig. 3.5i). A linear plot was obtained between I_{pa} vs. $\upsilon^{0.5}$ with a slope of 48.883 µA. $V^{-1/2}.s^{1/2}$ (R^2 = 0.985), reveals that the oxidation event of CFX is a diffusion control (Fig. 3.5j) (Masood et al., 2024). The diffusion-controlled reaction is further confirmed by the slope of the linear plot of log I_{pa} vs. log υ (Fig. 3.6). A slope of 0.5 indicates that the reaction is diffusion-controlled, while a slope of 1 suggests that the reaction is adsorption-controlled (Garbellini et al., 2015). The slope value from the plot of log I_{pa} vs. log υ was found to be 0.575 (R^2 = 0.997), which is comparable to the theoretical slope value of 0.5, indicating that the electrochemical reaction of CFX is diffusion control. Therefore, the rate constant with the number of electrons for the diffusion control process and adsorption of CFX were determined by Eq. 3.2 (Laviron equation) and Eq. 3.3, respectively (Bhan and Kumar Golder, 2023; Elgrishi et al., 2018).

$$E_p = E^0 - \frac{2.303RT}{\alpha nF} \log \frac{RTk^0}{\alpha nF} + \frac{2.303RT}{\alpha nF} \log \upsilon \quad (3.2)$$

$$I_{pa} = \frac{n^2F^2}{4RT} A_e \upsilon \Gamma^* \quad (3.3)$$

Where E_p and E^0 are the oxidation and standard peak potential (V), respectively. k^0, υ, and n are the rate constant (s^{-1}), scan rate (V/s), and number of electrons present in the oxidation event, respectively. The constants R, F, α, and T are gas constant (8.314 $J.mol^{-1}K^{-1}$), Faraday's constant (96485 $C.mol^{-1}$), electron transfer coefficient, and temperature (K), respectively. Γ* is the CFX adsorption onto AgNSs/GCE ($mol.cm^{-2}$). By considering α = 0.5, the values of n and k were determined by equalizing the slope (0.035 V, R^2 = 0.998) and intercept (1.203 V) of Fig. 3.5k (E_p vs. log υ) with Eq. 3.2 when the value of E^0 know. The value of E^0 was obtained by extrapolating the plot E_p vs. υ in origin software at a scan rate equal to zero (υ = 0) (Bhan and Kumar Golder, 2023). The values of E^0, k^0, and n were determined to be 1.116 V, 0.216 s^{-1}, and 3.381, respectively. The value of n showed three elections participated in the redox reaction. The CFX adsorption (Γ*) onto the surface of the AgNSs/GCE was found by equating the slope (23.844 µA.V^{-1}.s, R^2 = 0.986) of Fig. 3.5l (I_{pa} vs. υ) with the Eq. 3.3. The obtained value of Γ* was 2.267 × 10^{-11} $mol.cm^{-2}$.

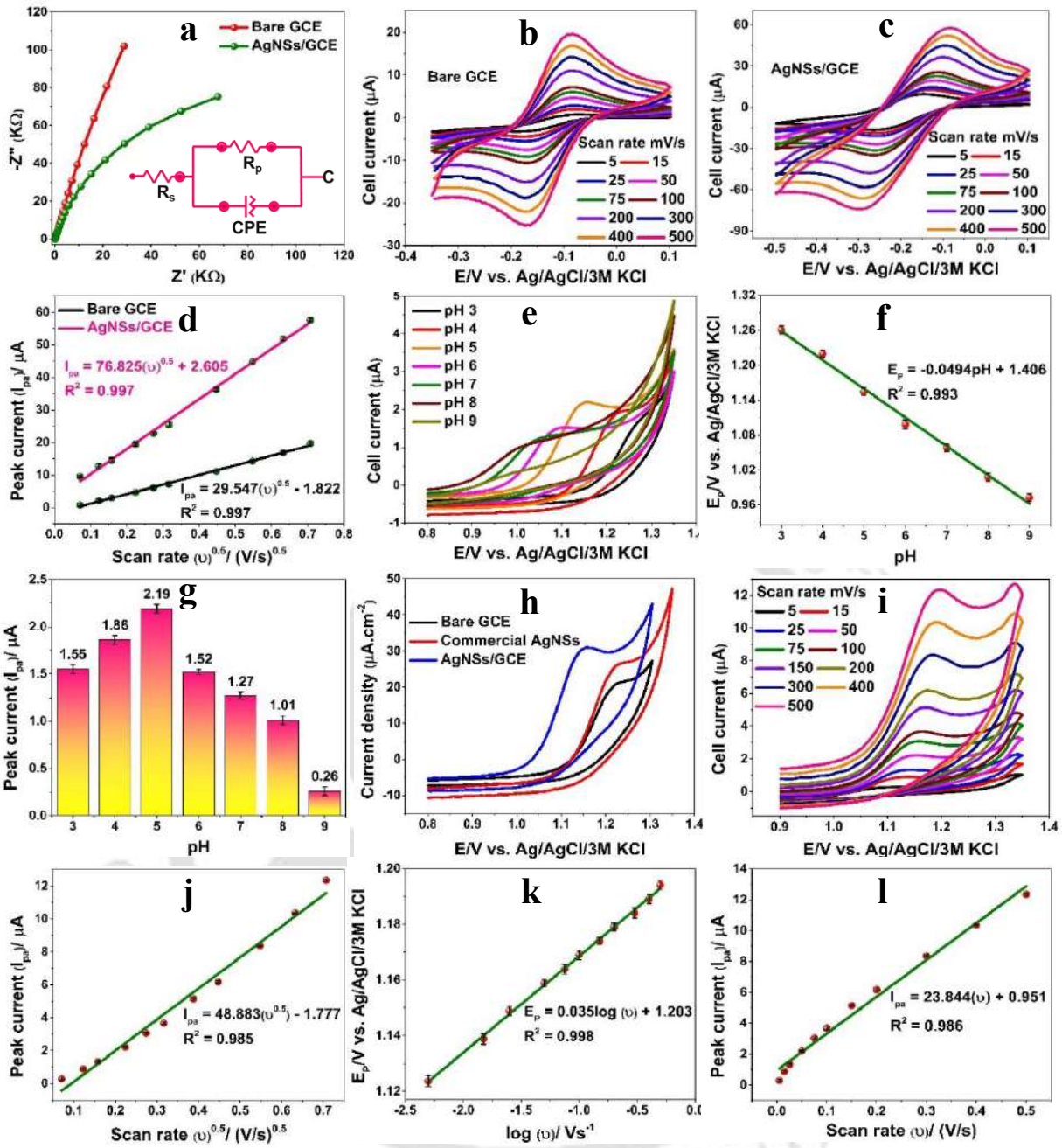

Figure 3.5: (a) EIS analysis of bare and AgNSs/GCE demonstrates working electrode resistance with inset of Randles impedance model, (b) and (c) CV of bare and AgNSs/GCE at different scan rates (5-500 mV/s), (d) Oxidation peak current (I_{pa}) vs. square root of scan rate ($\upsilon^{0.5}$) of bare and AgNSs/GCE, (e) CV of CFX at different pH (3-9) in 0.1 M PBS electrolyte using AgNSs/GCE, (f) Oxidation peak potential (E_p) vs. pH, (g) I_{pa} vs. pH, (h) CV of CFX sensing using bare GCE, commercial AgNSs, and AgNSs/GCE in 0.1 M PBS electrolyte (pH 5, 25 °C) at 50 mV/s scan rate, (i) CV of CFX at different scan rate (5-500 mV/s), (j) I_{pa} vs. $\upsilon^{0.5}$, (k) E_p vs. log υ, and (l) I_{pa} vs. υ.

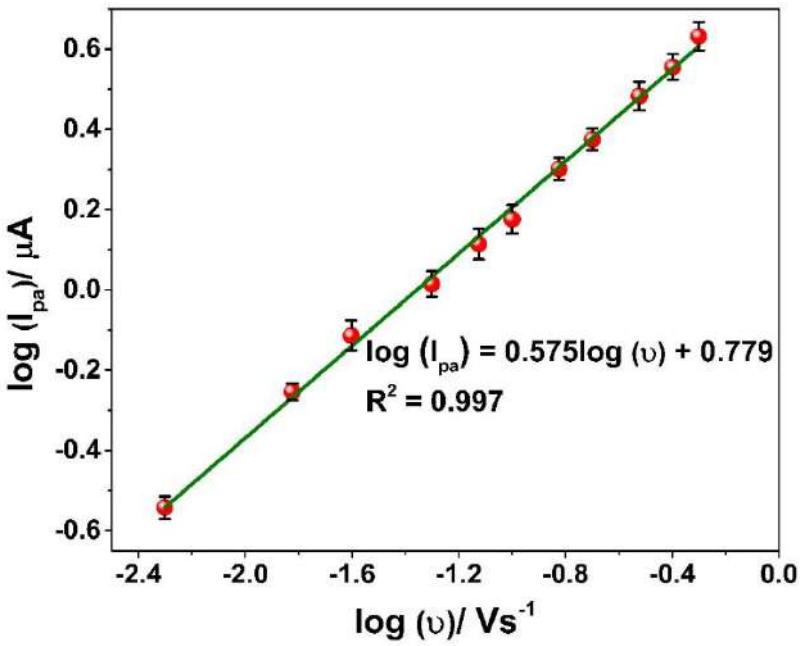

Figure 3.6: Linear plot of log I_{pa} vs. log υ corresponding to CV recorded at various scan rates (5-500 mV/s) in PBS electrolyte (0.1 M, pH 5, 25 °C) at CFX concentration of 70 µM.

3.2.4. Optimization of deposition parameters and CFX sensing at AgNSs/GCE

3.2.4.1 *Effect of deposition parameters*

SWV was conducted to determine the effect of deposition parameters, including deposition potential (DP vs. Ag/AgCl) and deposition time (DT), on the oxidation peak response of CFX sensing using AgNSs/GCE in PBS electrolyte (0.1 M, pH 5, 25 °C), at CFX concentration of 70 µM and scan rate of 50 mV/s. To comprehend the response of electrocatalytic sensing of CFX, DP was varied from -0.1 to -0.9 V at a fixed DT of 80 s (Fig. 3.7a), which could alter the sensitivity of the AgNSs/GCE. The oxidation peak response of CFX was increased progressively with a DT of -0.1 to -0.7 V attributed to the adsorption of CFX ions at the surface of AgNSs/GCE (Fig. 3.7b) (Das et al., 2024). After DP of -0.7 V (-0.7 to -0.9 V), the oxidation peak current of CFX decreased (Fig. 3.7b) due to the evolution of H_2 gas that could be generated as a side reaction during the electrochemical reaction under certain conditions such as high overpotentials (Gumpu et al., 2017). Therefore, DP of -0.7 V vs. Ag/AgCl was optimized for sensitive detection of CFX.

Figs. 3.7c and 3.7d demonstrate the impact of DT on the oxidation peak response of CFX over AgNSs/GCE at a fixed DP of -0.7 V. The oxidation peak response of CFX steadily increases with an increase in DT from 20 to 80 s as a result of the adsorption of CFX ions at the surface of AgNSs/GCE (Fig. 3.7d) (Bagheri et al., 2013). After 80 s of DT, the oxidation peak response of CFX ions marginally boosted, which could be attributed to CFX ions saturated

over the surface of AgNSs/GCE or a steady state reached between CFX ions over the surface of AgNSs/GCE and PBS electrolyte of a smaller amount of CFX ions present for the oxidation event because of fixed concentration of CFX ions in PBS electrolyte (0.1 M, pH 5, 25 °C) (Bhan and Kumar Golder, 2023). Hence, a DT of 80 s for CFX sensing was selected for ongoing investigations.

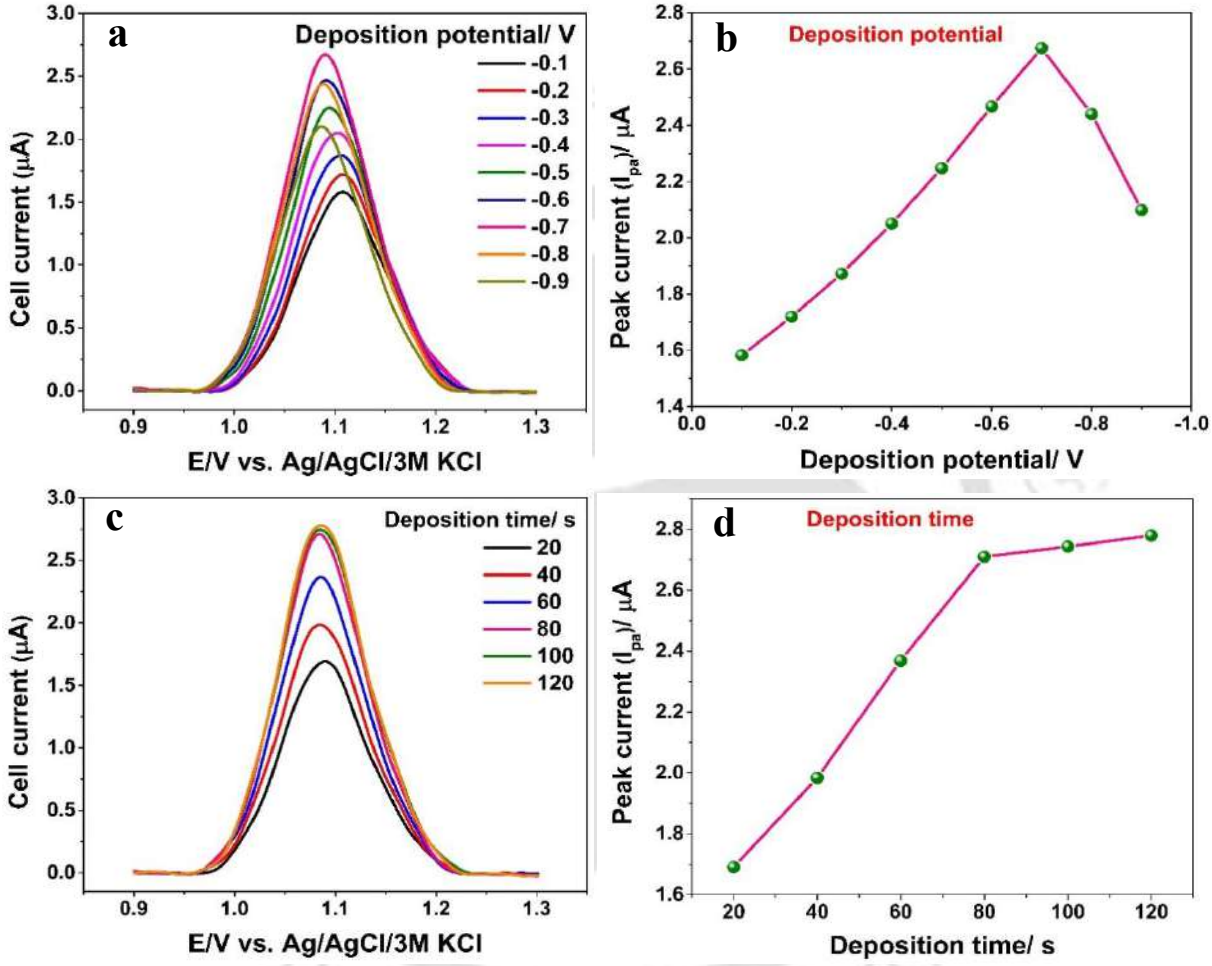

Figure 3.7: (a) SWV of CFX conducted at different DP from -0.1 to -0.9 V vs. Ag/AgCl, DT 80 s, and 25 °C, (b) DP vs. Oxidation peak current (I_{pa}), (c) SWV of CFX recorded at different DT from 20 to 120 s, DP -0.7 V, and 25 °C, (d) DT vs. I_{pa}. Reaction conditions: 70 µM CFX in 0.1 M PBS electrolyte at pH 5.

3.2.4.2 *CFX sensing over AgNSs/GCE*

Fig. 3.11a displays the SWV conducted over AgNSs/GCE using PBS electrolyte (0.1 M, pH 5, 25 °C) at optimized deposition parameters (DP -0.7 V and DT 80 s) and various CFX concentrations (0-250 µM). The plot of oxidation peak current (I_{pa}) vs. CFX concentration revealed two linear correlations between the concentration range of 0-100 and 100-250 µM

attributable to the profusion of accumulated CFX ions over AgNSs/GCE surface changed the oxidation event from diffusion (0-100 µM) to the surface (100-250 µM) control domain (Fig. 3.11b) (Bhan and Golder, 2024). The LOD and LOQ of the developed AgNSs/GCE for CFX sensing were determined by Eqs. 3.4 and 3.5, respectively (Bhan and Golder, 2024).

$$\text{LOD} = \frac{3S_d}{m} \tag{3.4}$$

$$\text{LOQ} = \frac{10S_d}{m} \tag{3.5}$$

Where m and S_d are the slopes of the plot I_{pa} vs. CFX concentration and standard deviation of blank measurement (0.0023), respectively. The I_{pa} vs. CFX concentration graph slopes were 0.0347 (R^2 = 0.991) and 0.0092 µA.µM^{-1} (R^2 = 0.996) between the concentration regime of 0-100 and 100-250 µM, respectively (Fig. 3.11b). The developed sensing platform revealed LOD of 0.199 µM (LOQ = 0.663 µM), and 0.750 µM (LOQ = 2.50 µM) within the concentration regime of 0-100 and 100-250 µM, respectively. The sensitivity of the AgNSs/GCE for CFX sensing is the ratio of the slope (0.0347 and 0.0092 µA.µM^{-1}) of I_{pa} vs. CFX concentration curve and active surface area (A_e = 0.098 cm^2) determined from Fig. 3.5c (Bhan and Kumar Golder, 2023). AgNSs/GCE demonstrates sensitivity of 0.354 and 0.094 µA. µM^{-1}.cm^{-2} within the CFX concentration regime of 0-100 and 100-250 µM, respectively.

3.2.4.3 *Electrocatalytic sensing mechanism and CFX reaction over AgNSs/GCE*

The modification of AgNSs over GCE provided a high surface area-to-volume ratio, unimpeded charge transport characteristics, and easy substrate penetration. Furthermore, AgNSs provide inherent catalytic properties that could further enhance the reaction rates, leading to rapid and efficient detection of CFX. To identify the oxidations product of CFX, chronoamperometry was conducted over AgNSs/GCE using PBS electrolyte (0.1 M, pH 5) containing 250 µM CFX at 1.116 V for 1800 s followed by the LC-MS and HPLC test of the same 0.1 M PBS electrolyte added 250 µM CFX used during the chronoamperometry. Figs. 3.8a and 3.8b show the HPLC analysis of 250 µM CFX in PBS electrolyte before and after the chronoamperometry analysis, which exhibited a CFX peak at the retention time of 3.935 and 3.921 min, respectively. The new peak at a retention time of 3.030 min was observed after the chronoamperometry of CFX, corresponding to the oxidation product of CFX (Fig. 3.8b), which was absent in before the chronoamperometry of CFX. Figs. 3.9a and 3.9b demonstrate mass spectra associated with LC-MS analysis of PBS electrolyte containing 250 µM CFX before and after the electrocatalytic reaction. Fig. 3.11c confirmed the oxidation of CFX (m/z = 332.13) produced CFX radical (m/z = 349.13) with the release of three electrons and three

protons, and the number of electrons involved in this reaction also matches with the number of electrons determined from the Laviron equation (Eq. 3.2). The oxidation of CFX during the electrochemical sensing over AgNSs/GCE was also confirmed by the obtained m/z value of 349.13 (CFX radical). Therefore, the sensing of CFX essentially involves the sensing of a CFX radical.

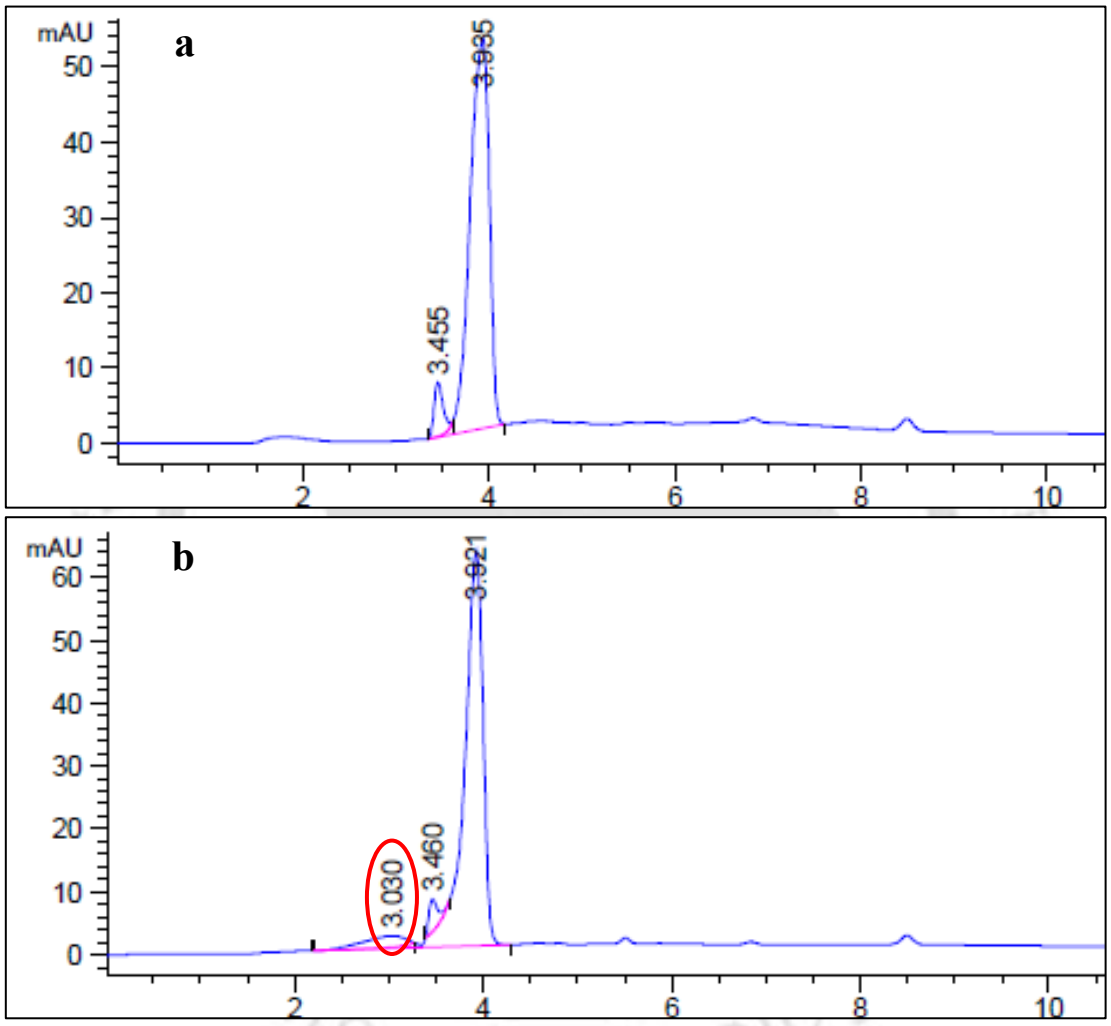

Figure 3.8: HPLC chromatograms (a) before and (b) after chronoamperometric test at 1.116 V vs. Ag/AgCl (1800 s) using AgNSs/GCE during the course of CFX sensing equipped with an ultra C18 column (UMISil C18(3), 250×4.6 mm, 5 µm particle size, thermoscientific). Acetonitrile (90%) and water (10%) were used as the mobile phase, and CFX was detected using a UV detector at a fixed wavelength of 256 nm.

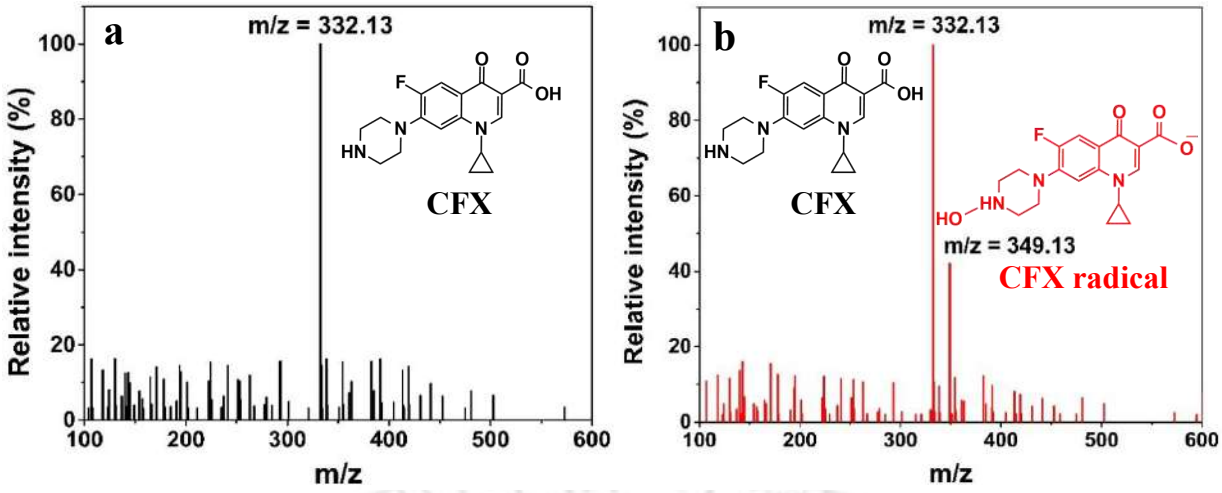

Figure 3.9: Mass spectra (a) before and (b) after chronoamperometric test at 1.116 V vs. Ag/AgCl (1800 s) using AgNSs/GCE during the course of CFX sensing.

3.2.4.4 *Stability of AgNSs/GCE during CFX detection*

To determine the stability and reproducibility of the AgNSs/GCE during the course of CFX sensing, SWV was conducted over the AgNSs/GCE using PBS electrolyte (0.1 M, pH 5, 25 °C) at selected deposition parameter (DP -0.7 V and DT 80 s), scan rate of 50 mV/s, and CFX concentration of 70 µM. For stability and reproducibility analysis, the same functioning electrode (AgNSs/GCE) was used in the same PBS electrolyte (0.1 M, pH 5, 25 °C) containing 70 µM CFX for sequential 15 cycles, and four different new electrodes (AgNSs/GCE) utilized in four different PBS electrolyte (0.1 M, pH 5, 25 °C) contain 70 µM CFX, respectively. Fig. 3.11d demonstrates the slight reduction in the oxidation peak current of CFX after each measurement, and only a 12.38 and 16.27% decrease in the oxidation peak response up to the 10^{th} and 15^{th} cycle, respectively. It implies that AgNSs/GCE resisted CFX oxidation peak current reduction compared to the prior studies (Dash et al., 2021). The decline in the oxidation peak current could be attributed to the accumulation of CFX ions over AgNSs/GCE, surface fouling, and loss of active sites during repeated use (Bhan and Kumar Golder, 2023). Fig. 3.10 shows the remarkable reproducibility of the AgNSs/GCE with a relative standard deviation (RSD) of 4.05%. The RSD of AgNSs/GCE for CFX sensing is within allowable ranges (Lotfi et al., 2021). Table 3.2 displays the performance of AgNSs/GCE for electrocatalytic detection of CFX and compares it with recently developed sensors. The proposed sensing platform significantly exceeded the performance of CFX detection compared to several previous studies.

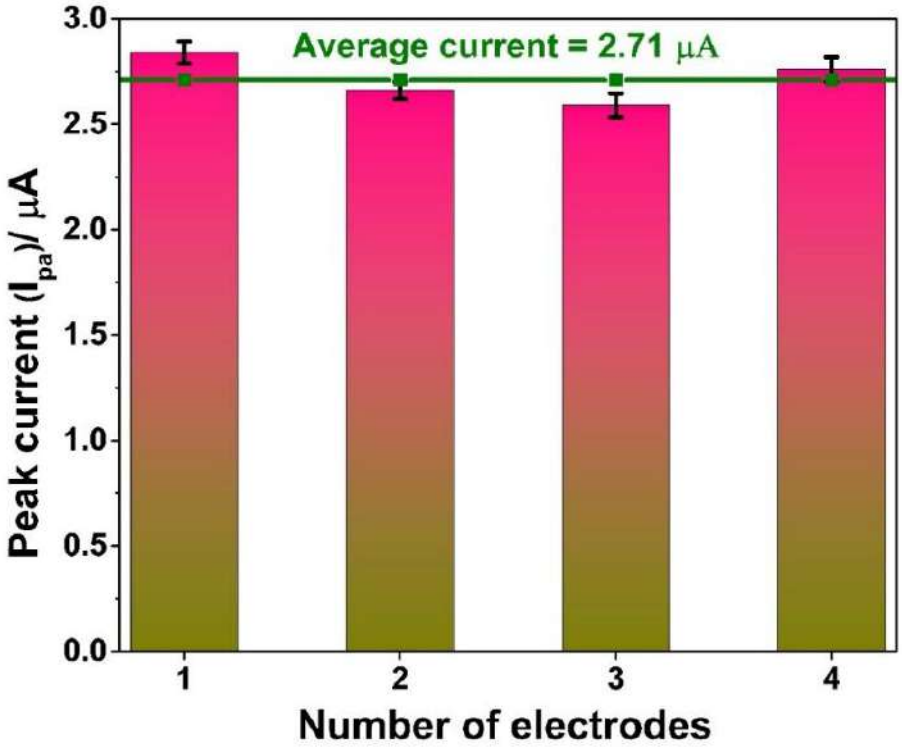

Figure 3.10: Reproducibility of AgNSs/GCE evaluated using four different fresh electrodes for CFX sensing at the same concentration of CFX (70 μM) by SWV in PBS electrolyte (0.1 M, pH 5, 25 °C) at DP of -0.7 V vs. Ag/AgCl and DT 80 s.

Table 3.2: Performance of AgNSs/GCE in electrochemical sensing of CFX and its comparison with the recently reported sensors.

Working electrodes	Technique	LOD (μM)	Sensitivity ($\mu A \mu M^{-1} cm^{-2}$)	Linear range (μM)	Sources
AgNSs/GCE	**SWV***	**0.199**	**0.354**	**0-100**	**Present work**
		0.750	**0.094**	**100-250**	
AgNPs-CB-Ch/GCE	SWV*	0.48	-	3.1-24.8	Meireles et al., 2024
CB/$ZnWO_4$/GCE	DPV⁂	0.02	1.71	0.02-120	Mariappan et al., 2023
PBE	DPV⁂	4.96	-	9.90-220	de Souza et al., 2022
GO/SPCE	DPV⁂	0.3	-	1-8	Pan et al., 2021
ZnS-Polyaniline	CV‡	0.5	-	50-0.75	Ali et al., 2023
MnO_2/ZnO/GCE	DPV⁂	0.21	-	0.5-120	Zhang et al., 2023
Lu-Cu@h-BN/GCE	SWV*	0.03	0.744	0.05-100	Nepfumbada et al., 2024

RGO-Ag/PLL/GCE	DPV⁂	0.54	-	1-80	Y. Li et al., 2017
Au/C_3N_4/GN/GCE	SWV*	0.42	-	0.6-120	Yuan et al., 2018
NC-3DPPY@Ag-Au	SWV*	0.017	11.64	0.5-50	Akhter et al., 2022

*Square wave voltammetry, ⁂Differential pulse voltammetry, ‡Cyclic voltammetry

3.2.5. Selectivity of CFX detection over AgNSs/GCE

Fig. 3.11e shows the effect of interferants, including norfloxacin, chloramphenicol, and chloroquine, during the CFX sensing investigated by conducting chronoamperometric using AgNSs/GCE in PBS electrolyte (0.1 M, pH 5, 25 °C) at the oxidation potential of 1.116 V vs. Ag/AgCl. The peak current was obtained by adding CFX (5-20 µM) followed by interferants (30 µM each) and then CFX (40-120 µM) in the intermission of 20 s, and after adding CFX, cell response reached stability rapidly. Furthermore, the variation in the current was detected after adding CFX (before and after the addition of interferants), and no notable change in the cell response was observed after adding the interferants mentioned above, as the different interferants exhibit different peak redox potentials. The developed AgNSs/GCE exhibited excellent selectivity for electrocatalytic sensing of CFX in the existence of interferants at the oxidation potential of 1.116 V (Kabir et al., 2019). Additionally, the existence of interferants could not alter the oxidation potential (1.116 V) of CFX detection. Therefore, AgNSs/GCE exhibited excellent selectivity for electrocatalytic sensing of CFX at the oxidation potential of 1.116 V vs. Ag/AgCl.

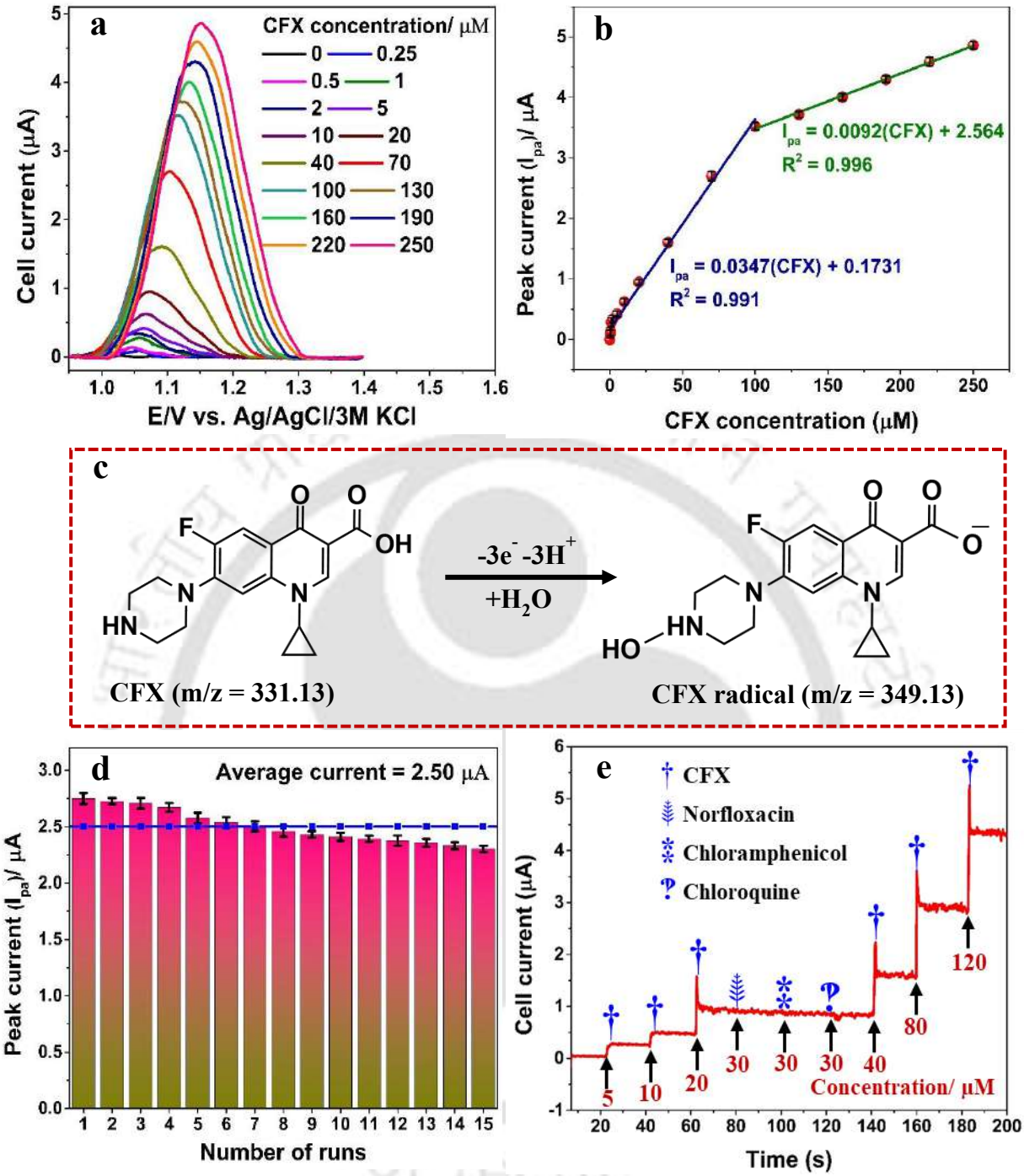

Figure 3.11: (a) Variation of peak current at different CFX concentrations (0-250 µM) during SWV onto AgNSs/GCE, (b) Calibration curve of CFX sensing (CFX concentration vs. I_{pa}), (c) Redox reaction during CFX sensing over AgNSs/GCE in accordance with the mass spectra (Fig. 3.9), (d) Stability of AgNSs/GCE, and (e) Selectivity of AgNSs/GCE in the existence of interferants, such as norfloxacin, chloramphenicol, and chloroquine.

3.2.6. CFX sensing in water samples

To examine the practical applicability of AgNSs/GCE for CFX detection and determination in tap and river water samples, SWV was recorded using 50 mL of 0.1 M PBS electrolyte (pH 5) and water samples with a certain amount of spiked CFX (0-120 µM) at selected deposition parameters (DP -0.7 V and DT 80 s) and 25 °C. The water samples were obtained from the Brahmaputra River and the residential water supply of IIT Guwahati, India. These water samples were passed through 0.2 µm filter paper to eliminate any suspended impurities and prevent the surface fouling of the AgNSs/GCE. The sensing performance of AgNSs/GCE was tested by determining spiked CFX concentration in water samples using the obtained calibration curve (Fig. 3.11b) and compared with HPLC. The performance of the developed AgNSs/GCE for electrocatalytic sensing of CFX and its comparison with HPLC is summarized in Table 3.3. The CFX recovery was ~100% observed in tap and river water samples. The CFX concentration deviations from HPLC in the tap water and river water samples were 5.1% (with a maximum RSD of 4.5%) and 7.6% (with a maximum RSD of 5.6%), respectively. Therefore, the obtained parameters (recovery, deviation, and RSD) indicated the fabricated AgNSs/GCE have the potential for in-field sensing and quantifying CFX in the environmental matrix.

Table 3.3: Performance of AgNSs/GCE for CFX determination in tap and river water and its comparison with HPLC.

Sample	**CFX spiked (µM)**	**Performance of AgNSs/GCE**			**CFX determination using HPLC (µM)**	**Deviation (%)**
		CFX determination (µM)	Recovery (%)	RSD (%)		
Tap water	0	ND	-	-	0.27	-
	10	10.39	103.9	4.5	9.86	5.1
	30	29.85	99.5	3.7	30.65	-2.7
	60	59.83	99.7	3.4	60.83	-1.7
	120	120.53	100.4	4.1	119.75	0.6
River water	0	ND	-	-	0.38	-
	10	10.57	105.7	5.6	9.77	7.6
	30	29.95	99.8	3.9	30.86	-3.0

	60	60.12	100.2	4.3	58.01	3.5
	120	120.59	100.5	4.7	121.96	-1.1

3.3. Major findings

We have developed phyto-analytic AgNSs using bio-extract of *Citrus limetta* for highly selective voltammetric sensing of CFX. The morphological and elemental analysis of AgNSs confirmed the spherical-shaped nanostructures of 43.5±3.9 nm particle size and uniform distribution of Ag. Immobilization of AgNSs over GCE decreased the electrode kinetic resistance by 93.13% and increased the active surface by 61.22%. The AgNSs/GCE showed a 34.1% increment in current density and a reduction in the oxidation peak potential from 1.219 to 1.159 V of CFX than bare GCE under similar reaction conditions. The oxidation of CFX followed a diffusion control pathway involving three electrons and three protons with k^0 of 0.216 s^{-1} and E^0 of 1.116 V. The adsorption of CFX over AgNSs/GCE was 2.267×10^{-11} mol.cm^{-2}. AgNSs/GCE exhibited LOD of 0.199 µM (LOQ of 0.663 µM and sensitivity of 0.354 µA. $\mu M^{-1}.cm^{-2}$) and 0.750 µM (LOQ of 2.50 µM and sensitivity of 0.094 µA. $\mu M^{-1}.cm^{-2}$) within the concentration range of 0-100 and 100-250 µM, respectively. AgNSs/GCE exhibited superior selectivity towards CFX detection in the existence of interferants, including norfloxacin, chloramphenicol, and chloroquine, and only 16.27% decreases in the oxidation peak current was observed up to the 15th cycle. The deviation of CFX concentration from HPLC in tap and river water was observed to be 5.1 and 7.6%, respectively, with about 100 % recovery in both samples. Therefore, the fabricated sensing platform with superior sensing performance has the potential for in-field sensing and quantifying pharmaceutical residuals. A quick delamination of catalysts (16.27% decrease in peak current) embedded at the electrode surface is a major setback, and it could limit the life and reproducibility of the sensor's response. In fact, the growth of the catalyst directly on the support electrode surface could eliminate the entire process involved of its surface-coating. It in turns could increase the stability of the sensors by minimizing the potential problem of catalyst delamination.

References

Adane, W.D., Chandravanshi, B.S., Tessema, M., 2023. A simple, ultrasensitive and cost-effective electrochemical sensor for the determination of ciprofloxacin in various types of samples. Sens. Bio-Sensing Res. 39. https://doi.org/10.1016/j.sbsr.2022.100547

Akhter, S., Shalauddin, M., Basirun, W.J., Lee, V.S., Ahmed, S.R., Rajabzadeh, A.R.,

Srinivasan, S., 2022. A highly selective bifunctional nanosensor based on nanocellulose and 3D polypyrrole decorated with silver-gold bimetallic alloy to simultaneously detect methotrexate and ciprofloxacin. Sensors Actuators B Chem. 373, 132743. https://doi.org/10.1016/j.snb.2022.132743

Ali, S.K., Alamier, W.M., Hasan, N., Ahmed, S., Ansari, A., Imran, M., 2023. Synergistic nanomaterials: zinc sulfide-polyaniline for ciprofloxacin electrochemical sensing. Appl. Phys. A 129, 859. https://doi.org/10.1007/s00339-023-07124-9

Bagheri, H., Afkhami, A., Khoshsafar, H., Rezaei, M., Shirzadmehr, A., 2013. Simultaneous electrochemical determination of heavy metals using a triphenylphosphine/MWCNTs composite carbon ionic liquid electrode. Sensors Actuators B Chem. 186, 451–460. https://doi.org/10.1016/j.snb.2013.06.051

Bhan, C., Golder, A.K., 2024. ZnO Nanorods Aligned in a Vertical Configuration for Targeted Electrochemical Detection of Aniline. ACS Appl. Bio Mater. 7, 7413–7428. https://doi.org/10.1021/acsabm.4c01050

Bhan, C., Golder, A.K., 2023. Utilizing bioinspired AgNPs as an antibacterial agent to enhance ceramic membrane performance. J. Environ. Chem. Eng. 11, 110283. https://doi.org/10.1016/j.jece.2023.110283

Bhan, C., Kumar Golder, A., 2023. Bio-based hierarchical vertically aligned 2D ZnO nanostructures for ultra selective electrochemical sensing of p-Chloroaniline. Chem. Eng. J. 475, 146122. https://doi.org/10.1016/j.cej.2023.146122

Burhan, M., Shahzad, M.W., Ng, K.C., 2018. Energy distribution function based universal adsorption isotherm model for all types of isotherm. Int. J. Low-Carbon Technol. 13, 292–297. https://doi.org/10.1093/ijlct/cty031

Chowdhury, A., Bhan, C., Peela, N.R., Golder, A.K., 2022. A tunable bioinspired process of SnO_2 NPs synthesis for electrochemical CO_2-into-formate conversion. J. CO_2 Util. 66, 102263. https://doi.org/10.1016/j.jcou.2022.102263

Chowdhury, A., Bhan, C., Rao Peela, N., Kumar Golder, A., 2023. A simple template-free bioinspired route of 1D Bi_2S_3 nanorods synthesis for electrochemical CO_2 reduction to formate. J. Ind. Eng. Chem. 127, 138–148. https://doi.org/10.1016/j.jiec.2023.06.055

Cicek, C., Erdogan, Z.O., 2024. Detection of ciprofloxacin in ear drop using UV spectrophotometric method based on gold nanoparticles as a sensing probe. J. Nanoparticle Res. 26, 121. https://doi.org/10.1007/s11051-024-06027-x

Das, D., Bhan, C., Mukherjee, C., Golder, A.K., 2024. Improved selectivity of electrochemical aniline sensing using one-dimensional silver nanorods with high aspect ratio synthesized

by ascorbic acid assisted method. Anal. Chim. Acta 1310, 342697. https://doi.org/10.1016/j.aca.2024.342697

Dash, S.R., Bag, S.S., Golder, A.K., 2021. Bio-inspired PtNPs/Graphene nanocomposite based electrocatalytic sensing of metabolites of dipyrone. Anal. Chim. Acta 1167, 338562. https://doi.org/10.1016/j.aca.2021.338562

Dash, S.R., Bag, S.S., Golder, A.K., 2020. Synthesis of highly structured spherical Ag@Pt core-shell NPs using bio-analytes for electrocatalytic Pb(II) sensing. Sensors Actuators B Chem. 314, 128062. https://doi.org/10.1016/j.snb.2020.128062

de Souza, C.C., Alves, G.F., Lisboa, T.P., Matos, M.A.C., Matos, R.C., 2022. Low-cost paper-based electrochemical sensor for the detection of ciprofloxacin in honey and milk samples. J. Food Compos. Anal. 112, 104700. https://doi.org/10.1016/j.jfca.2022.104700

Ehsani, M., Soleymani, J., Mohammadalizadeh, P., Hasanzadeh, M., Jouyban, A., Khoubnasabjafari, M., Vaez-Gharamaleki, Y., 2021. Low potential detection of doxorubicin using a sensitive electrochemical sensor based on glassy carbon electrode modified with silver nanoparticles-supported poly(chitosan): A new platform in pharmaceutical analysis. Microchem. J. 165, 106101. https://doi.org/10.1016/j.microc.2021.106101

Elgendy, K., Zaky, M., Alaa Eldin, T., Fadel, S., 2023. Rapid HPLC determination of ciprofloxacin, ofloxacin, and marbofloxacin alone or in a mixture. Results Chem. 5, 100749. https://doi.org/10.1016/j.rechem.2022.100749

Elgrishi, N., Rountree, K.J., McCarthy, B.D., Rountree, E.S., Eisenhart, T.T., Dempsey, J.L., 2018. A Practical Beginner's Guide to Cyclic Voltammetry. J. Chem. Educ. 95, 197–206. https://doi.org/10.1021/acs.jchemed.7b00361

Fato, T.P., Li, D.-W., Zhao, L.-J., Qiu, K., Long, Y.-T., 2019. Simultaneous Removal of Multiple Heavy Metal Ions from River Water Using Ultrafine Mesoporous Magnetite Nanoparticles. ACS Omega 4, 7543–7549. https://doi.org/10.1021/acsomega.9b00731

Garbellini, G.S., Rocha-Filho, R.C., Fatibello-Filho, O., 2015. Voltammetric determination of ciprofloxacin in urine samples and its interaction with dsDNA on a cathodically pretreated boron-doped diamond electrode. Anal. Methods 7, 3411–3418. https://doi.org/10.1039/C5AY00625B

Gawal, P.M., Golder, A.K., 2024. Plant-Based Phytochemicals for Synthesis of Z-Scheme In_2O_3/CdS Heterostructures: DFT Analysis and Photocatalytic CO_2 Reduction to HCOOH and CO. Langmuir 40, 13538–13549. https://doi.org/10.1021/acs.langmuir.4c01015

Ghanbari, M.H., Norouzi, Z., Biesalski, M., Etzold, B.J.M., 2024. Superior performance of N-

doped carbon Nanoonions/Nafion based microfluidic electrochemical Cd^{2+} sensor when compared to Screen-Printed Carbon-Based electrode devices. Microchem. J. 201, 110506. https://doi.org/10.1016/j.microc.2024.110506

Gumpu, M.B., Veerapandian, M., Krishnan, U.M., Rayappan, J.B.B., 2017. Simultaneous electrochemical detection of Cd(II), Pb(II), As(III) and Hg(II) ions using ruthenium(II)-textured graphene oxide nanocomposite. Talanta 162, 574–582. https://doi.org/10.1016/j.talanta.2016.10.076

He, J., Li, N., Zhang, D., Zheng, G., Zhang, H., Yu, K., Jiang, J., 2020. Real-time monitoring of ciprofloxacin degradation in an electro-Fenton-like system using electrochemical-mass spectrometry. Environ. Sci. Water Res. Technol. 6, 181–188. https://doi.org/10.1039/C9EW00868C

Kabir, H., Ma, P.Y., Renn, N., Nicholas, N.W., Cheng, I.F., 2019. Electrochemical determination of free chlorine on pseudo-graphite electrode. Talanta 205, 120101. https://doi.org/10.1016/j.talanta.2019.06.101

Karimi, F., Altuner, E.E., Aygun, A., Bayat, R., Rajendran, S., Sen, F., 2024. Synthesis of Silver Nanoparticles by Biogenic Methods: Characterization and Development of a Sensor Sensible to Pharmaceutical Medicine Paracetamol. Top. Catal. 67, 585–593. https://doi.org/10.1007/s11244-023-01887-4

Kumar, A., Das, C., 2024. Corrosion inhibition of mild steel by Praecitrullus fistulosus (tinda fruit and peel) extracts. Sci. Total Environ. 929, 172569. https://doi.org/10.1016/j.scitotenv.2024.172569

Kumar, A., Das, C., 2023. A novel eco-friendly inhibitor of chayote fruit extract for mild steel corrosion in 1 M HCl: Electrochemical, weight loss studies, and the effect of temperature. Sustain. Chem. Pharm. 36, 101261. https://doi.org/10.1016/j.scp.2023.101261

Li, J., Cameron, A.R., Li, H., Glazier, S., Xiong, D., Chatzidakis, M., Allen, J., Botton, G.A., Dahn, J.R., 2017. Comparison of Single Crystal and Polycrystalline $LiNi_{0.5}Mn_{0.3}Co_{0.2}O_2$ Positive Electrode Materials for High Voltage Li-Ion Cells. J. Electrochem. Soc. 164, A1534–A1544. https://doi.org/10.1149/2.0991707jes

Li, Y., Wang, H., Yan, B., Zhang, H., 2017. An electrochemical sensor for the determination of bisphenol A using glassy carbon electrode modified with reduced graphene oxide-silver/poly-l-lysine nanocomposites. J. Electroanal. Chem. 805, 39–46. https://doi.org/10.1016/j.jelechem.2017.10.022

Liu, Y., Yan, X., Xing, Y., Zhao, P., Zhu, Y., Li, L., Liu, N., Zhang, Z., 2024. Dispersed Au Nanoparticles Anchored on Covalent Organic Frameworks/Carbon Nanotubes via Self-

Reduction for Electrochemical Sensing of Acetaminophen. ACS Appl. Nano Mater. 7, 4980–4988. https://doi.org/10.1021/acsanm.3c05742

Lotfi, S., Veisi, H., Karmakar, B., 2021. A convenient strategy for the electrochemical evaluation of acetaminophen and caffeine in combined drugs and biological samples over TiO_2@polymethyldopa/Pd nanocomposite functionalized glassy carbon electrodes. Measurement 186, 110156. https://doi.org/10.1016/j.measurement.2021.110156

Magar, H.S., Hassan, R.Y.A., Abbas, M.N., 2023. Non-enzymatic disposable electrochemical sensors based on CuO/Co_3O_4@MWCNTs nanocomposite modified screen-printed electrode for the direct determination of urea. Sci. Rep. 13, 2034. https://doi.org/10.1038/s41598-023-28930-4

Malode, S.J., Keerthi, P.K., Shetti, N.P., Kulkarni, R.M., 2020. Electroanalysis of Carbendazim using MWCNT/Ca-ZnO Modified Electrode. Electroanalysis 32, 1590–1599. https://doi.org/10.1002/elan.201900776

Manivannan, K., Sivakumar, M., Cheng, C.-C., Lu, C.-H., Chen, J.-K., 2019. An effective electrochemical detection of chlorogenic acid in real samples: Flower-like ZnO surface covered on PEDOT:PSS composites modified glassy carbon electrode. Sensors Actuators B Chem. 301, 127002. https://doi.org/10.1016/j.snb.2019.127002

Mariappan, K., Alagarsamy, S., Chen, S.-M., Sakthinathan, S., 2023. Fabrication of $ZnWO_4$/Carbon Black Nanocomposites Modified Glassy Carbon Electrode for Enhanced Electrochemical Determination of Ciprofloxacin in Environmental Water Samples. Materials (Basel). 16, 741. https://doi.org/10.3390/ma16020741

Masood, Z., Muhammad, H., Tahiri, I.A., 2024. Comparison of Different Electrochemical Methodologies for Electrode Reactions: A Case Study of Paracetamol. Electrochem 5, 57–69. https://doi.org/10.3390/electrochem5010004

Mehtab, S., Zaidi, M.G.H., Irshad Siddiqi, T., 2018. Designing Fructose Stabilized Silver Nanoparticles for Mercury(II) Detection and Potential Antibacterial Agents. Mater. Sci. Res. India 15, 241–249. https://doi.org/10.13005/msri/150305

Meireles, L.M., Silva, R.M., da Silva, R.C., Okumura, L.L., Moreira, R.P.L., Silva, T.A., 2024. Low-cost electrochemical sensor for ciprofloxacin antibiotic based on green-synthesized silver nanoparticles and carbon black. J. Solid State Electrochem. https://doi.org/10.1007/s10008-024-06033-y

Mohamedkhair, A.K., Drmosh, Q.A., Yamani, Z.H., 2019. Silver Nanoparticle-Decorated Tin Oxide Thin Films: Synthesis, Characterization, and Hydrogen Gas Sensing. Front. Mater. 6. https://doi.org/10.3389/fmats.2019.00188

Monisha, Kant, T., Tikeshwari, Shrivas, K., Kumar, A., Dewangan, K., 2023. Graphene-silver nano-ink for inkjet printing of paper electrode for electrochemical sensing of 4-nitrophenol. Mater. Chem. Phys. 307, 128161. https://doi.org/10.1016/j.matchemphys.2023.128161

Moslah, M., Fredj, Z., Dridi, C., 2021. Development of a new highly sensitive serotonin sensor based on green synthesized silver nanoparticle decorated reduced graphene oxide. Anal. Methods 13, 5187–5194. https://doi.org/10.1039/D1AY01532J

Muhammad, A., Yusof, N., Hajian, R., Abdullah, J., 2016. Construction of an Electrochemical Sensor Based on Carbon Nanotubes/Gold Nanoparticles for Trace Determination of Amoxicillin in Bovine Milk. Sensors 16, 56. https://doi.org/10.3390/s16010056

Nejabatdoust, A., Mirmiran, S.D., Salehzadeh, A., Masouleh, F.R., 2024. Effective Release of Ciprofloxacin and Rifampicin Antibiotics from Alginate-Chitosan Complex and Its Application Against Clinical Strains of Staphylococcus aureus. Bionanoscience 14, 532–546. https://doi.org/10.1007/s12668-023-01262-3

Nepfumbada, C., Mamba, B.B., Bartlett, B.M., Fernández-Sánchez, J.F., Feleni, U., 2024. Lutetium Copper@Hexagonal Boron Nitride Nanocomposite Electrode System for Sensing and Signalling Ciprofloxacin. ChemElectroChem 11. https://doi.org/10.1002/celc.202400168

Ning, J., Luo, X., Wang, M., Li, J., Liu, D., Rong, H., Chen, D., Wang, J., 2018. Ultrasensitive Electrochemical Sensor Based on Polyelectrolyte Composite Film Decorated Glassy Carbon Electrode for Detection of Nitrite in Curing Food at Sub-Micromolar Level. Molecules 23, 2580. https://doi.org/10.3390/molecules23102580

Pan, M., Guo, P., Liu, H., Lu, J., Xie, Q., 2021. Graphene oxide modified screen-printed electrode for highly sensitive and selective electrochemical detection of ciprofloxacin residues in milk. J. Anal. Sci. Technol. 12, 55. https://doi.org/10.1186/s40543-021-00309-y

Ramaraghavulu, R., Rao, V.K., Devarayapalli, K.C., Yoo, K., Nagajyothi, P.C., Shim, J., 2021. Green synthesized AgNPs decorated on Ketjen black for enhanced catalytic dye degradation. Res. Chem. Intermed. 47, 637–648. https://doi.org/10.1007/s11164-020-04290-w

Ravi, R., Golder, A.K., 2025. Photocatalytic and biological degradation processes to mineralize pharmaceutically active compounds and catalyst recovery: A review. Coord. Chem. Rev. 523, 216267. https://doi.org/10.1016/j.ccr.2024.216267

Ravi, R., Golder, A.K., 2023a. A tuneable bioinspired process of Pt-doping in TiO_2 for

improved photoelectrochemical and photocatalytic functionalities. Colloids Surfaces A Physicochem. Eng. Asp. 663, 131034. https://doi.org/10.1016/j.colsurfa.2023.131034

Ravi, R., Golder, A.K., 2023b. Bio-based Au Doping with Dominant Oxygen Vacancies and Ti^{3+} Defects on Photocatalytic Functionalities of TiO_2. Ind. Eng. Chem. Res. 62, 20702–20715. https://doi.org/10.1021/acs.iecr.3c02850

Ravi, R., Kumar Golder, A., 2024. Efficient recovery of TiO_2 and Pt-doped TiO_2 photocatalysts in wastewater treatment using a pilot-scale cross-flow ultrafiltration membrane system. Sep. Purif. Technol. 339, 126710. https://doi.org/10.1016/j.seppur.2024.126710

Stanley, M.M., Sriram, B., Wang, S.-F., Sherlin, A., Kogularasu, S., Lee, Y.-Y., George, M., 2024. Rational confinement of ternary layered double hydroxide within three-dimensional graphene aerogel: An electrochemical tool for propyl gallate sensing. Chem. Eng. J. 485, 149682. https://doi.org/10.1016/j.cej.2024.149682

Verma, S., Sen, A., Dutta, N., Sengupta, P., Chakraborty, P., Dutta, G., 2024. Highly Specific Non-Enzymatic Electrochemical Sensor for the Detection of Uric Acid Using Carboxylated Multiwalled Carbon Nanotubes Intertwined with GdS-Gd_2O_3 Nanoplates in Human Urine and Serum. Langmuir 40, 21427–21441. https://doi.org/10.1021/acs.langmuir.4c02233

Wang, M., Wang, Q., Wang, X., Wang, S., 2024. Nitrogen doped biomass derived carbon and $BiVO_4$ composite for simultaneous detection of furazolidone and chloramphenicol. Microchem. J. 197, 109810. https://doi.org/10.1016/j.microc.2023.109810

Wang, Y., Limon-Petersen, J.G., Compton, R.G., 2011. Measurement of the diffusion coefficients of $[Ru(NH_3)_6]^{3+}$ and $[Ru(NH_3)_6]^{2+}$ in aqueous solution using microelectrode double potential step chronoamperometry. J. Electroanal. Chem. 652, 13–17. https://doi.org/10.1016/j.jelechem.2010.12.011

Xu, J.-T., Hu, H.-T., Chen, Z., Feng, X.-Z., Han, G.-C., Kraatz, H.-B., 2024. One-step construction of MWCNTs@MoS_2@Chitosan film for ciprofloxacin sensing and its oxidation mechanism. Microchem. J. 205, 111184. https://doi.org/10.1016/j.microc.2024.111184

Yuan, Y., Zhang, F., Wang, H., Gao, L., Wang, Z., 2018. A Sensor Based on Au Nanoparticles/Carbon Nitride/Graphene Composites for the Detection of Chloramphenicol and Ciprofloxacin. ECS J. Solid State Sci. Technol. 7, M201–M208. https://doi.org/10.1149/2.0111812jss

Zhang, S., Yu, S., Wang, X., Zhang, Y., Yue, Z., Li, C., Ma, Y., 2023. An electrochemical sensor based on MnO_2/ZnO composites for the detection of ciprofloxacin in honey.

Microchem. J. 194, 109355. https://doi.org/10.1016/j.microc.2023.109355

Zhou, M., Wei, Z., Qiao, H., Zhu, L., Yang, H., Xia, T., 2009. Particle Size and Pore Structure Characterization of Silver Nanoparticles Prepared by Confined Arc Plasma. J. Nanomater. 2009, 5–9. https://doi.org/10.1155/2009/968058

CHAPTER 4

ZnO Nanorods Aligned in a Vertical Configuration for Targeted Electrochemical Detection of Aniline

This chapter presents synthesis of 1D surface vertically aligned nanorods (VANRs) of ZnO on FTO by chemical growth method for electrochemical sensing of aniline using SWV technique. The high surface area and enhanced charge transport characteristics of VANRs could significantly improve the sensitivity and selectivity of the sensor. Furthermore, this reusable electrode has the potential to prevent the rapid delamination of nanostructures from the electrode surface. The fabricated electrode demonstrated remarkable stability and selectivity even in the coexistence of interferants. To demonstrate the practical applicability of the fabricated electrode, aniline was detected and determined in tap and river water samples and compared with the HPLC, showcasing promising potential of ZnO-VANRs/FTO electrodes in real-world environmental monitoring.

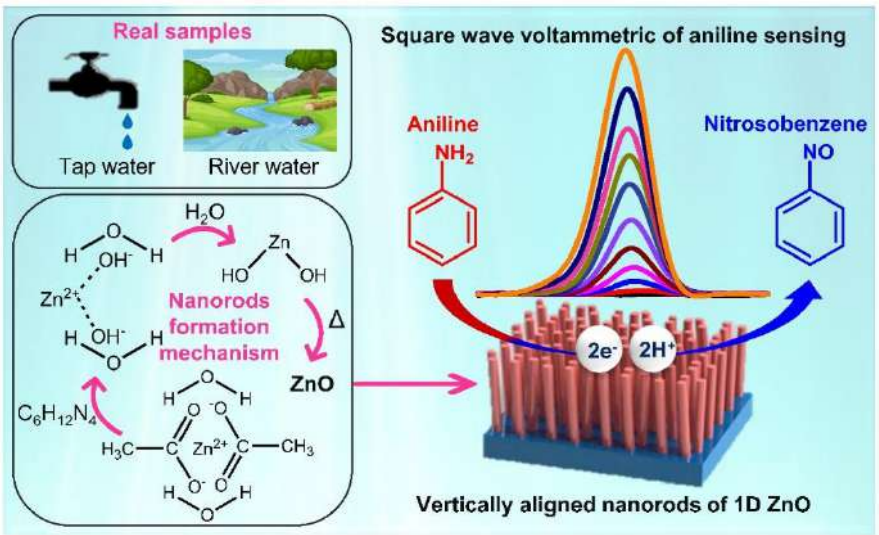

Chapter highlights

- ZnO-VANs/FTO catalyzed electrochemical aniline sensing by square wave voltammetry
- Aniline sensing through two-electron and two-proton transfer reaction mechanism
- Detection limit of 0.193 µM and excellent sensitivity of 0.198 µA. $\mu M^{-1}.cm^{-2}$
- Unprecedently selective aniline sensing in presence of interferants along with anions
- ZnO-VANs/FTO catalyzed electrochemical detection of aniline from tap and river water

4.1. Background and executive motivation

Aniline and its derivatives are extensively utilized in the production of pesticides (i.e. propachlor, butachlor, alachlor, metolachlor, and acetochlor), pharmaceuticals, dyes, and paints (Mohammed et al., 2020). The release of aniline into the environment could cause detrimental effects on human health, including methemoglobinemia, red blood cell destruction, liver disease, and anaemia (Messmer et al., 2015). The accumulation of pesticides in the environment has shown an increasing trend over the years due to their widespread use in modern agricultural practices (Carvalho, 2017). The persistence of pesticides in the environment poses a potential threat to the environmental ecosystem. In fact, pesticides containing aniline or substituted aniline moieties eventually release anilines when subjected to biodegradation (Lyons et al., 1985). In-situ detection and determination of such compounds is extremely important to assess the severity of contamination at the point of their origin. Many a times as a preventive measure, stringent laws and regulations are imposed to control pesticide pollution.

In particular, the presence of aniline in the environmental matrix can be detected by liquid (Chen et al., 2010) and gas (Okumura et al., 1996) chromatographies, and fluorescence (Gao et al., 2022), surface-enhanced Raman (Li et al., 2010) and mass (Chiang, 2008) spectroscopies. Specialized instrumentation preferring a fixed-point installation and the requirement of skilled personnel are integral parts of such techniques. It triggers high detection cost, making them less or non-accessible in most of the geographical locations. Therefore, the development of an efficient and portable technique for real-time field monitoring of the target analytes at the source of their origin is essential.

On the other hand, electrochemical sensors are usually portable in nature and show great promises for the detection and determination of pesticides (Dash et al., 2022), heavy metal ions (Liang et al., 2023), pharmaceuticals (Mohan et al., 2023; Zhou et al., 2023), antioxidants (Yan and Su, 2016), etc. They offer several advantages, such as easy sample preparation, low cost, high sensitivity, selectivity, and low detection limit. Furthermore, modifying the base electrode surface with nanostructured-based catalysts such as ZnO (Zhuang et al., 2023), Co_3O_4 (Liu et al., 2022), SnO_2 (Karuppusamy et al., 2023), CuO (Singh et al., 2017), Bi_2S_3 (Zhao et al., 2022), AuNPs (P. Wang et al., 2014), PtNPs (Ding and Su, 2015), and AgNPs (Ettadili et al., 2023) could significantly enhance the sensor's performance by promoting catalytic reaction during sensing. At the same time, nanostructures have attracted considerable research interest for a wide range of catalytic applications, including CO_2 reduction, wastewater treatment, water

splitting, corrosion inhibitors, etc. (Gawal and Golder, 2024; Kumar and Das, 2024; Ravi and Kumar Golder, 2024). Particularly, ZnO nanomaterials are recognized for their broad bandgap of 3.37 eV and high excitation binding energy of 60 meV exhibiting strong electro- and photo-catalytic functionalities (Bhan and Kumar Golder, 2023). In addition, ZnO nanostructures are merited by their high surface area, superior electrical characteristics, excellent crystallinity, and environmental stability. However, it suffers from potential agglomeration and large-scale productivity(Ahmad et al., 2017b). ZnO nanostructures aligned in vertical configuration could be prepared rapidly using chemical bath deposition, hydrothermal, and electrochemical deposition methods (Ahmad et al., 2017a; Sadhasivam et al., 2023; Son et al., 2016). The development of ZnO nanostructures has demonstrated various catalytic applications, including electrochemical sensing, photocatalysis, and sensitized solar cells (Bhan and Kumar Golder, 2023; Hussain et al., 2016; Mali et al., 2013). However, the response of the sensor could easily be a setback as the embedded nanostructures from the base electrode surface are delaminated, and the life of the electrochemical sensor is also shortened.

In a conventional approach, nano-catalysts are coated on the support electrode using a binder. The binder could block catalytic active sites forming a dense and inhomogeneous film of immobilized nanostructures via drop casting/spin coating. It could also increase the cost of electrode fabrication. The recent studies report that vertically aligned nanorods (VANRs) of ZnO (binder-free) grown on fluorine-doped tin oxide coated glass substrate (FTO), namely CuO-ZnO/FTO (Ahmad et al., 2017a), Cu-ZnO/FTO (Arsalan et al., 2022), Au-ZnO/FTO (Awais et al., 2021), and ZnO/FTO (Khan et al., 2019) showed good sensing performance than binder-based sensors, including ZnO-Cu_xO/GCE (Jain et al., 2022a), ZnO/GCE (Ameen et al., 2015), and Ag-ZnO/GCE (Hussain et al., 2016). Additionally, ZnO/FTO showed a marginally low limit of detection compared to binder-based and binder-free sensors (Fig. 4.1). Other recently reported binder-based electrochemical sensors such as IL-f-ZnONPs@MWCNTs@GCE,IL@$CoFe_2O_4$NPs@MWCNTs@GCE, TiO_2/MWCNTs/IL/GCE, RGO-Fe_3O_4/GCE, and AgNRs/GCE have been employed for sensing of sulfamethoxazole, fenitrothion, terbutaline, aflatoxin B1, and aniline, respectively (Chokkareddy et al., 2023, 2022; Chokkareddy and Redhi, 2022; Das et al., 2024; Kilele et al., 2021). Binder-based (AgNRs/GCE) electrochemical sensor exhibited a detection limit of 0.032 µM, sensitivity of 1.484 µA. $\mu M^{-1}.cm^{-2}$, decrease in peak current up to the 10^{th} cycle of 26 %, and a maximum deviation of 7.33 % in river water for sensing of aniline (Das et al., 2024). In comparison, the binder-free (ZnO-VANs(bio)/FTO@pH3) electrochemical sensor demonstrates a detection limit of 0.021 µM, sensitivity of 0.194 µA. $\mu M^{-1}.cm^{-2}$, decrease in peak current up to the 15^{th}

cycle of 8.5 %, and a maximum deviation of 4.4 % in river water for detection of p-Chloroaniline (Bhan and Kumar Golder, 2023). In addition, electrochemical sensors provided superior detection limit compared to the fluorescence and colorimetric sensors for detecting aniline (Huang et al., 2022; Li et al., 2021, 2017). Furthermore, recent studies have highlighted innovative applications of ZnO nanostructures incorporated onto the surface of FTO across various fields, including electrochemical sensing, antimicrobial activity, and supercapacitor applications (Ahmad et al., 2024; Bhan and Kumar Golder, 2023; Chauhan et al., 2024; Kara et al., 2024).

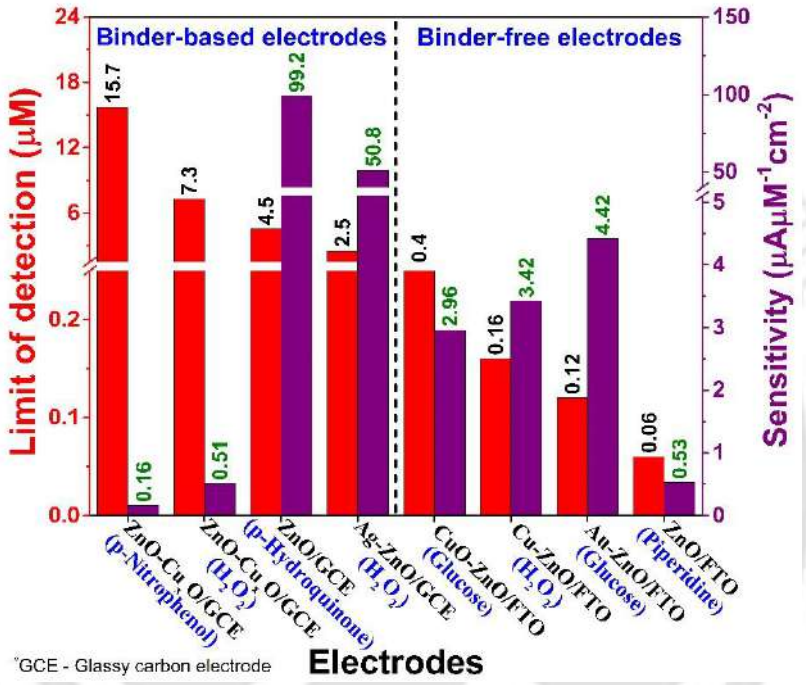

Figure 4.1: Sensing performance of ZnO-based electrodes for electrochemical sensing. The analytes used in sensing studies are in brackets of the x-axis labelling.

FTO are merited with high-temperature resistance, fast charge transfer rate, low surface resistivity, and larger weather stability (Cirocka et al., 2021). VANRs of metal oxides grown on the surface of FTO (Ahmad et al., 2017a; Al-She'irey et al., 2022) could offer high surface area, providing more docking sites for interaction with the targeted analyte, unimpeded charge transfer characteristics allowing efficient movement of electrons/ions between the electrode surface and the electrolyte, maximum surface roughness giving more binding sites, high chemical stability, and large aspect ratio. It also could eliminate the potent problem of quick catalyst delamination from the electrode surface. Moreover, VANRs could overcome the interference caused by a binder in the case of catalyst surface embedment. VANRs ensure a seamless interface between catalysts and electrode, and facilitate faster electron transfer.

This chapter documents the synthesis of 1D surface VANRs of ZnO on the FTO by a chemical growth method for electrochemical sensing of aniline using the SWV technique. This approach not only highlights the effectiveness of the developed sensing platform but also marks a significant advancement in the field, as this is the first report detailing with the utilization of 1D surface VANRs of ZnO for sensitive electrochemical detection and quantification of aniline. The high surface area and enhanced charge transport characteristics of the VANRs could significantly improve the sensitivity and selectivity of the sensor. Moreover, this reusable electrode has the potential to prevent the rapid delamination of nanostructures from the electrode surface. The fabricated electrode demonstrated remarkable stability, repeatability, and selectivity even in the coexistence of interferants. To demonstrate the practical applicability of the fabricated electrode, aniline was detected and determined in tap and river water samples and compared with the HPLC, showcasing the promising potential of ZnO-VANRs/FTO electrodes in real-world environmental monitoring.

4.2. Results and discussion

4.2.1. Characterizations of ZnO-VANRs/FTO

4.2.1.1 *FESEM analysis*

Figs. 4.4a-4.4d illustrates the FESEM micrographs (top-view) of (a) bare FTO, (b) seed layer of ZnO on bare FTO (ZnO-seed/FTO), (c) synthesized VANRs of ZnO on seeded FTO (ZnO-VANRs/FTO), and (d) cross-sectional image of ZnO-VANRs/FTO. Fig. 4.4a demonstrates the bare FTO has an uneven surface. After deposition of the seed layer, the surface of bare FTO became smoother (Fig. 4.4b). The surface roughness of ZnO-seed/FTO was decreased 2-fold than bare FTO (Figs. 4.5a and 4.5b). Fig. 4.4c shows the uniform distribution of hexagonal-shaped ZnO nanorods with high density (1.52×10^{13} number density/m^2). The average distance across the corners and flats of hexagonal rods of ZnO was 0.32±0.05 and 0.19±0.02 µm, respectively (Fig. 4.2). The surface roughness of ZnO-VANRs/FTO was higher by about 2.4 and 4.7 folds compared to bare FTO and ZnO-seed/FTO, respectively (Figs. 4.5a, 4.5b, and 4.5c). The cross-sectional image of ZnO-VANRs/FTO confirms the vertical alignment of ZnO nanorods with an average height of 1.57±0.03 µm (Al-She'irey et al., 2022; Mali et al., 2013) (Fig. 4.4d). Nanostructures aligned in vertical configuration merited with high surface area-to-volume ratio provides more active sites for targeted analytes and facilitating improved charge transfer, which enhances the sensitivity of

the sensor. The reproducibility of developed ZnO-VANRs/FTO revealed no notable variations in a shape corresponding to three batches of ZnO VANRs (Fig. 4.3).

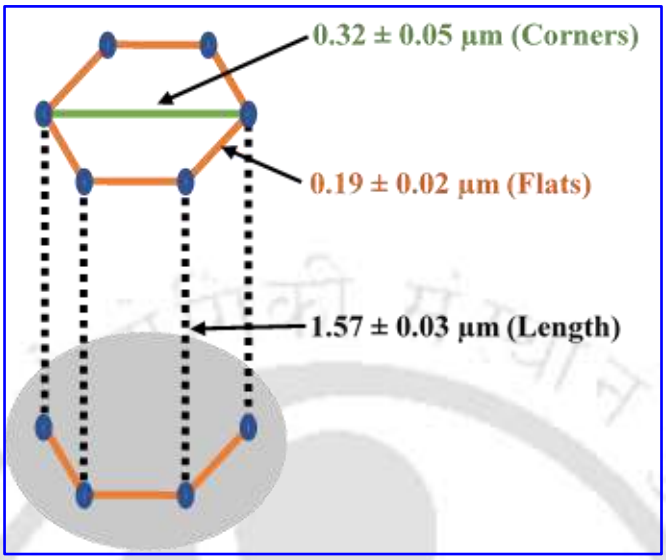

Figure 4.2: Pictorial view of 1D surface VANRs of ZnO (ZnO-VANRs/FTO).

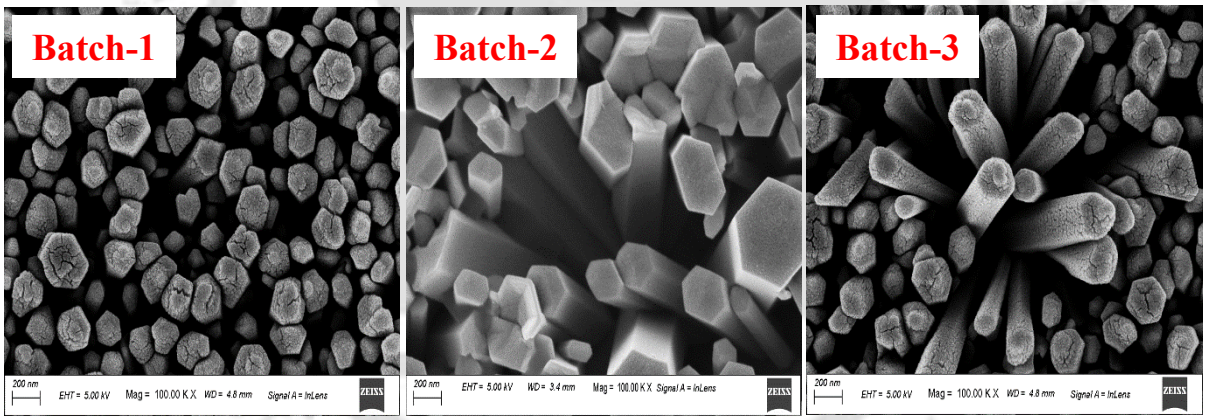

Figure 4.3: Reproducibility of developed ZnO-VANRs/FTO in three different batches synthesized under identical conditions.

4.2.1.2 *FETEM analysis*

Figs. 4.4e-4.4g demonstrates the FETEM micrographs of ZnO-VANRs/FTO. The VANRs of ZnO were disintegrated from the surface of the FTO using an ultrasonicator (ANTech, power 200 W, GT-1990QTS, China) for 1 h. After that, disintegrated nanorods were drop cast onto the TEM grid (CF300-CU, CAS No: 71150) for determination of its morphology (Fig. 4.4e), HRTEM (Fig. 4.4f), and SAED (Fig. 4.4g) patterns. Fig. 4.4e confirms the rod-shaped ZnO formation with a length of 1.47 µm. Fig. 4.4f illustrates the d-spacing values of

2.43 Å corresponding to 101 phases of ZnO nanorods, which is in accordance with XRD analysis (Mudusu et al., 2016). The SAED pattern of ZnO-VANRs/FTO shows the polycrystalline nature of ZnO nanorods (Fig. 4.4g).

4.2.1.3 *EDX analysis*

Figs. 4.4h and 4.4i depict the elemental weight percentage (wt%) and image mapping of ZnO-VANRs/FTO. The wt% of Zn and O were 82.6 and 17.4 %, respectively (Fig. 4.4h). EDX image mapping demonstrates a uniform distribution of Zn and O in the ZnO-VANRs/FTO (Fig. 4.4i). In Fig. 4.4h, there are three unknown peaks around Zn and O, representing C (~0.29 keV, from $Zn(CH_3COO)_2.2H_2O$ used during the synthesis) and Au (~1.65 and 2.14 keV, from Au coating during sample analysis).

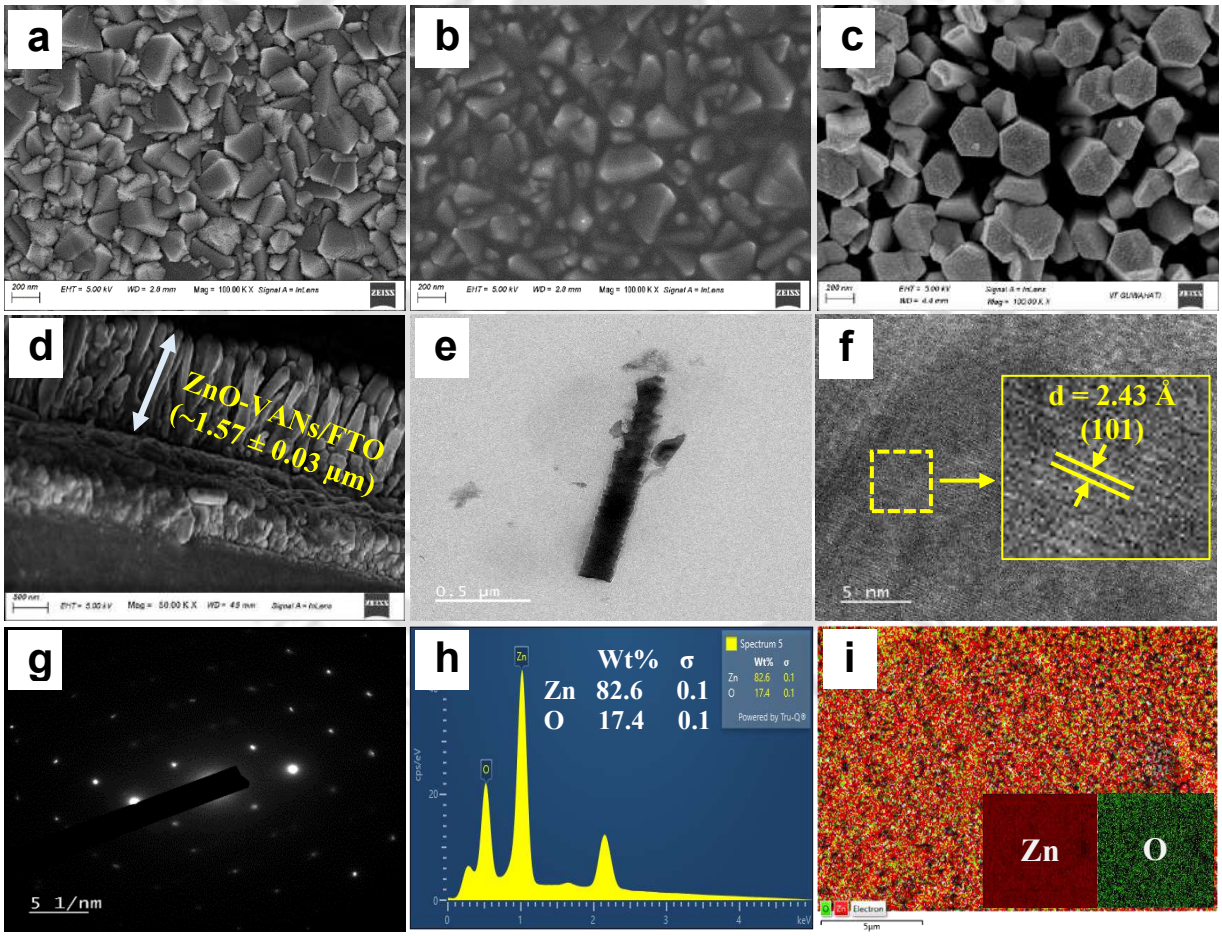

Figure 4.4: FESEM images (top view) of (a) bare FTO, (b) ZnO-seed/FTO, (c) ZnO-VANRs/FTO, (d) Cross-sectional view of ZnO-VANRs/FTO, (e) FETEM image, (f) HRTEM micrograph, (g) SAED pattern (ZnO nanorods were disintegrated from the FTO by sonication

for 1 h), (h) EDX elemental spectrum, and (i) EDX elemental image mappings of ZnO-VANRs/FTO.

4.2.1.4 *AFM analysis*

Fig. 4.5a-4.5c displays the AFM analysis (for determination of surface roughness) of bare FTO, ZnO-seed/FTO, and ZnO-VANRs/FTO. In a scan area of 5 × 5 μm^2, the root-mean-square (RMS) value of bare FTO (Fig. 4.5a), ZnO-seed/FTO (Fig. 4.5b), and ZnO-VANRs/FTO (Fig. 4.5c) were 31.43, 15.79, and 74.44 nm, respectively. The decrease in the surface roughness of bare FTO after seed layer deposition followed by annealing due to the retrenchment of agglomerates during cooling after annealing, resulting smallest distance between the top and base of agglomerates of nanostructures (Shukla et al., 2019). However, the surface roughness of the synthesized ZnO-VANRs/FTO is about 2.4 and 4.7 folds higher than that of bare FTO and ZnO-seed/FTO, respectively. Additionally, higher surface roughness provides more nucleation sites for the targeted analytes, which increases the interaction of nanorods with the electroactive species. These nucleation sites could improve charge transfer kinetics and promote better adsorption of analyte molecules, boosting the sensitivity of the sensor (Bhan and Kumar Golder, 2023).

4.2.1.5 *XRD analysis*

Fig. 4.5d represents the XRD patterns of commercial ZnO, bare FTO, ZnO-seed/FTO, and ZnO-VANRs/FTO. The peaks correspondence to bare FTO is represented by a red star (JCPDS, file No. 00-001-0657 and 01-083-7977), while the blue star symbol corresponds to the formation of ZnO in ZnO-VANRs/FTO (JCPDS, file No. 01-077-9355 and 01-075-9187). A peak shifting at 2θ = 52.07° indicates a change in the lattice structure and crystal size of FTO after incorporating ZnO. The lattice strain, crystallite size (Eq. 4.1, Scherrer equation), and dislocation density were determined by Eqs. 4.1-4.3 (Ravi and Golder, 2023a, 2023b).

$$d = \frac{k\lambda}{\beta \cos\theta_B} \tag{4.1}$$

$$\varepsilon = \frac{\beta}{4 \mathrm{Tan}\theta_B} \tag{4.2}$$

$$\delta = \frac{1}{d^2} \tag{4.3}$$

Where d, ε, β, θ_B, and δ represent the crystal size (nm), lattice strain, half-width at full maxima (FWHM), Bragg angle, and dislocation density (lines/nm^2), respectively. The constant parameters of the XRD diffractometer, k and λ have a value of 0.94 and 0.154 nm, respectively.

All the calculated parameters are presented in Table 4.1. The highest intensity peaks were used to calculate the crystal size of FTO and ZnO using the Scherrer equation (Chekin et al., 2013). A slight decrease in the crystal size was observed after the formation of ZnO VANRs than bare FTO, decreased d-spacing value and increased lattice strain and dislocation density indicate increased defects in ZnO-VANRs/FTO. These defects might include oxygen vacancies or Sn atoms with an atomic size of 225 pm replaced by a smaller atomic size of Zn atom (atomic size 139 pm). The XRD nature of the ZnO phase in ZnO-VANRs/FTO is well comparable with commercial ZnO (Fig. 4.5d and Table 4.1). However, the overlapping of FTO and ZnO peaks resulted in a slight shifting of the peak at 2θ = 52.07°.

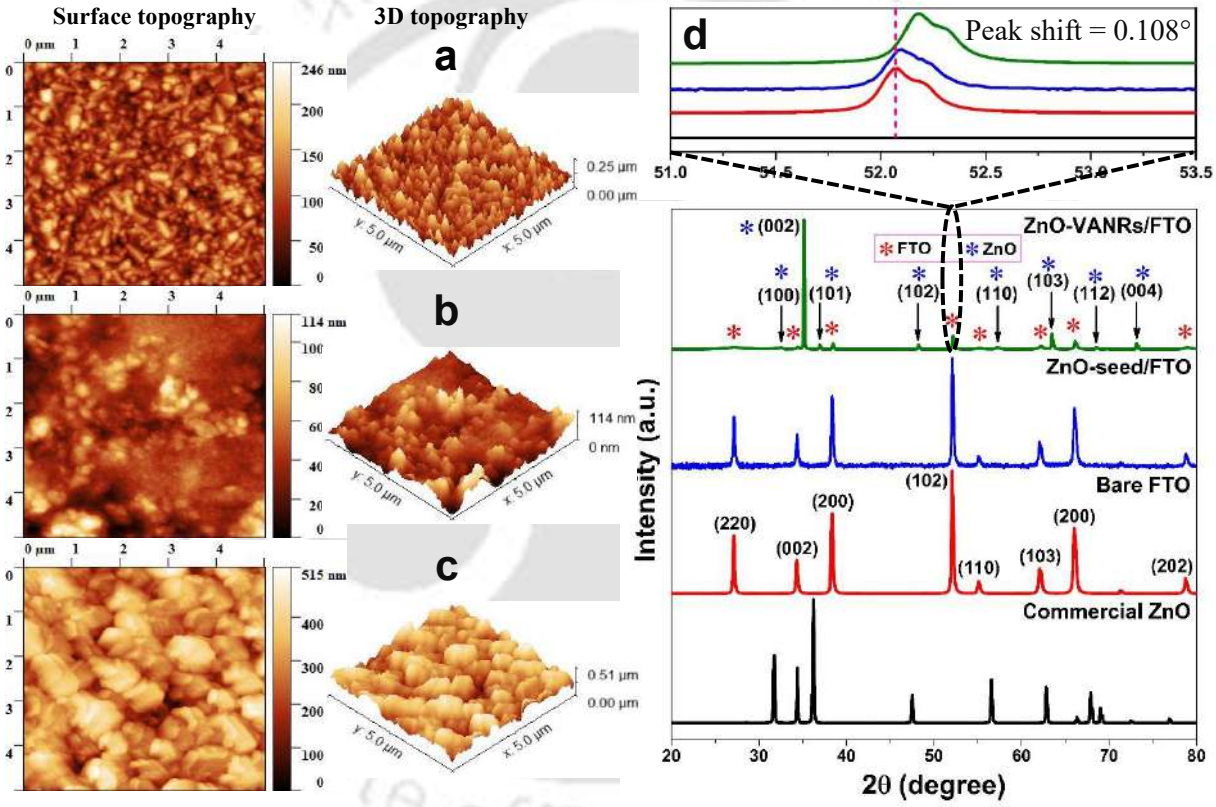

Figure 4.5: AFM micrographs of (a) bare FTO, (b) ZnO-seed/FTO, (c) ZnO-VANRs/FTO in a 5×5 μm^2 scan area, and (d) XRD patterns of commercial ZnO, bare FTO, ZnO-seed/FTO, and ZnO-VANRs/FTO.

Table 4.1: XRD diffraction parameters of commercial ZnO, bare FTO, ZnO-seed/FTO, and ZnO-VANRs/FTO.

Sample code	Peak position, 2θ (Å)	Crystal size (nm)	d-spacing (Å)	Lattice strain (ε)	Dislocation density (Lines/nm^2)
Commercial ZnO	36.25	76.99	2.742	1.51×10^{-3}	1.69×10^{-4}
Bare FTO	52.07	57.57	1.754	1.43×10^{-3}	3.02×10^{-4}
ZnO-seed/FTO	52.17	53.46	1.752	1.54×10^{-3}	3.50×10^{-4}
ZnO-VANRs/FTO	52.17	55.86	1.752	1.47×10^{-3}	3.21×10^{-4}
	36.96	80.34	2.430	1.40×10^{-3}	1.55×10^{-4}

4.2.1.6 *XPS analysis*

Fig. 4.6 demonstrates the surface composition and chemical state of bare FTO and ZnO-VANRs/FTO. Furthermore, it also provides information about the binding energies of the core-level electrons, which can be used to determine the oxidation state of the elements and detect any chemical changes induced during the synthesis of VANRs of ZnO. The survey spectrum of ZnO-VANRs/FTO reveals the presence of Zn (1021.53, 1044.53 eV), O (530.01 eV), Sn (497.52 eV), and C (284.76 eV), as shown in Fig. 4.6a. The presence of C could be due to the ubiquitous existence of atmospheric gases (not detected in EDX, Fig. 4.4h) on the surface of the ZnO-VANRs/FTO and the reaction salts. The high-resolution spectrum in the Zn 2p region of ZnO-VANRs/FTO showed two major peaks at a binding energy of 1021.53 and 1044.53 eV corresponding to the spin-orbital of Zn $2p_{3/2}$ and $2p_{1/2}$, respectively (Fig. 4.6b). These values are consistent and indicate the presence of Zn in the Zn^{2+} chemical state of ZnO-VANRs/FTO (Mali et al., 2013). The high-resolution spectra in the O 1s region exhibited peaks at a binding energy of 530.47 and 530.14 eV corresponding to the bare FTO (Fig. 4.6c) and ZnO-VANRs/FTO (Fig. 4.6d), respectively. The O 1s spectrum of bare FTO revealed two peaks at 530.42 and 531.52 eV (Fig. 4.6c), demonstrating the lattice oxygen (O_{lat}) and surface adsorbed oxygen (O_{ads}), respectively. Fig. 4.6d exhibited two identical peaks at 530.14 eV (O_{lat}) and 531.64 eV (O_{ads}) corresponding to ZnO-VANRs/FTO. Aniline ions exhibit an inherent affinity towards the oxygen functionalities that are prevalent on the surface of the ZnO-VANRs/FTO electrode. Therefore, an improved sensitivity is previsedd due to augmentation in aniline ions adsorption, and the explanation provided earlier is also applicable here (section 3.1.4) (Wiench et al., 2018).

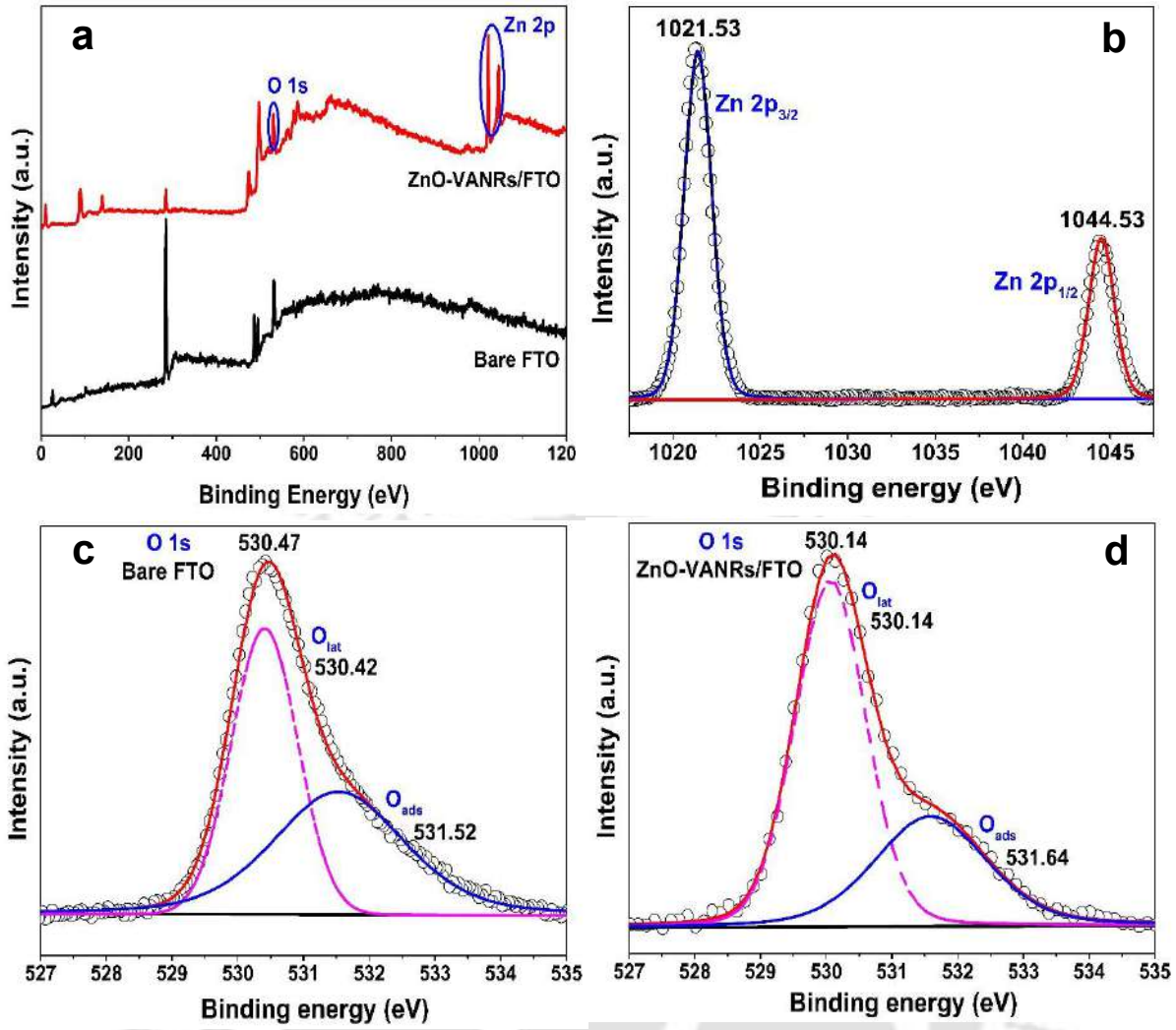

Figure 4.6: (a) XPS survey spectra of bare FTO and ZnO-VANRs/FTO, (b) High-resolution spectra in Zn 2p region of ZnO-VANRs/FTO, (c), and (d) High-resolution spectra in O 1s region of bare FTO, and ZnO-VANRs/FTO, respectively.

4.2.2. Growth mechanism of VANRs of ZnO

Fig. 4.7 demonstrates the possible pathway for the growth mechanism of VANRs of ZnO on the FTO. In ZnO nanomaterial, anisotropic development is promoted thru the inherent internal dipole moment across the prime axis of the crystal lattice. Moreover, partial polar and anisotropic characteristics of ZnO nanomaterials facilitate the formation of nanoparticles in (0001) direction (highest favourable polar face) owing to the positive (Zn lattice) and negative (O lattice) charge at the opposite end of a polar face (0001). Complex (I) is formed with the introduction of $Zn(CH_3COO)_2.2H_2O$ to ethanol (for seed layer) or H_2O (for growth of nanorods). For the deposition of the ZnO seed layer, complex (I) reacted with $NH(CH_2CH_2OH)_2$ (DEA) to form a complex (II), which dissociates into $Zn(OH)_2$ and DEA by

hydrolysis. Lastly, a uniform ZnO seed layer was formed on FTO through annealing, facilitating the conversion of $Zn(OH)_2$ to ZnO nanostructures. For the development of VANRs, $C_6H_{12}N_4$ (HMTA) and $Zn(CH_3COO)_2.2H_2O$ are dissolved in the aqueous solution, providing OH^- and Zn^{2+} ions to the seeded FTO, respectively. Moreover, HMTA readily hydrolyzes in water to produce NH_3 and HCHO. Subsequently, NH_3 reacts with water, leading to the generation of OH^- ions and NH_4^+ (Son et al., 2016). The complex (I) reacted with OH^- to form a complex (II), which dissociates into $Zn(OH)_2$ through hydrolysis. Finally, VANRs of ZnO developed on FTO by drying, facilitating the transformation of $Zn(OH)_2$ into ZnO nanorods. In addition, HMTA used in an aqueous chemical growth of VANRs is overlaid on the non-polar faces such as $(0\bar{1}10)$, $(1\bar{1}00)$, $(10\bar{1}0)$, $(\bar{1}100)$, $(1\bar{1}00)$, and $(01\bar{1}0)$ which hindered the lateral growth of nanostructures along these directions. Therefore, the development of nanostructures occurs in the (0001) direction (zero growth along the $(000\bar{1})$ direction is observed due to the surface of FTO), resulting 1D surface ZnO nanorods aligned in a vertical configuration (Abdelmohsen et al., 2017; Rajamanickam et al., 2020). Moreover, to emphasize the sensitivity of the ZnO-VANRs/FTO electrode for sensing of aniline, the interpretation is provided in sections 3.1.1 and 3.1.4.

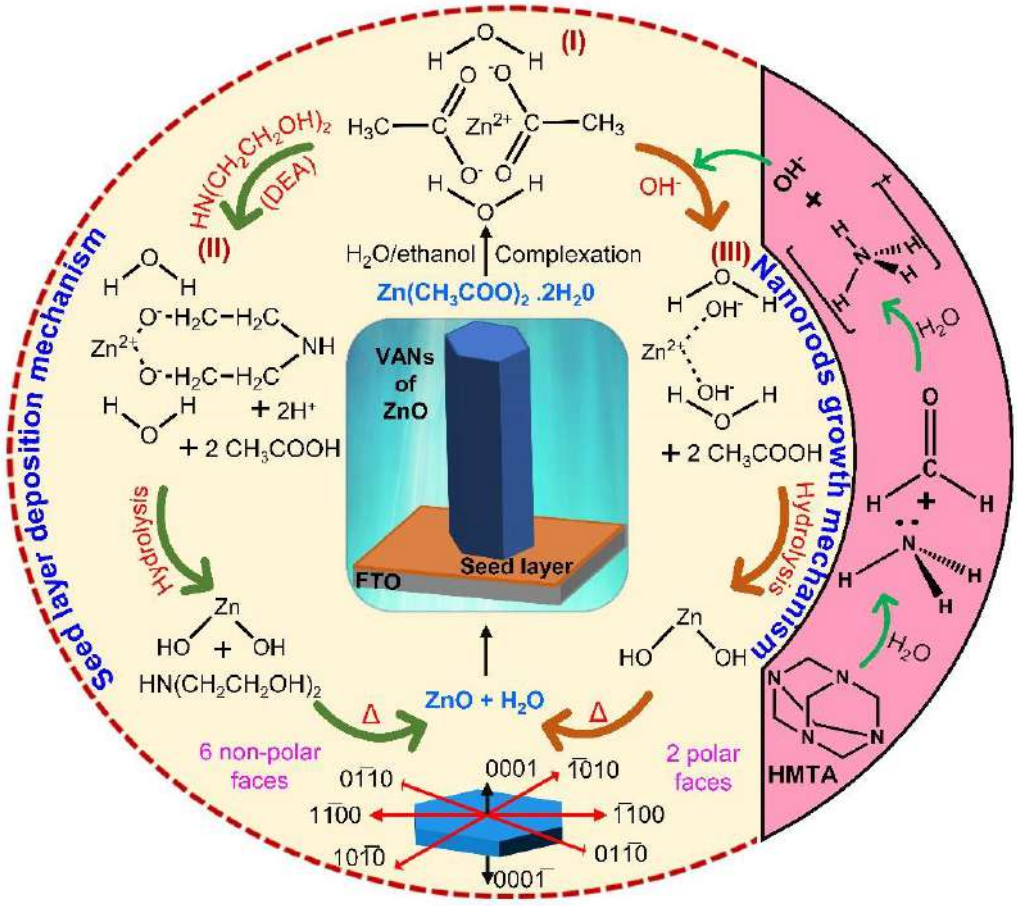

Figure 4.7: Growth mechanism of 1D surface VANRs of ZnO on FTO surface.

4.2.3. Electrochemical characteristics of ZnO-VANRs/FTO electrode

4.2.3.1 *EIS of ZnO-VANRs/FTO*

The EIS spectra of bare FTO and ZnO-VANRs/FTO were recorded using 1 mM $Ru(NH_3)_6Cl_2$ as an electroactive probe in 0.1 M KCl electrolyte media in the frequency range of 10^{-2}-10^5 Hz (Fig. 4.8a). The charge transfer resistance (R_p), electrolyte resistance (R_s), and constant phase element (CPE), including Y_0 and n, were found from the Randles equivalent circuit (inset of Fig. 4.8a) using Nova 2.1.7 by fitting and simulating the data of Nyquist plots, as shown in Table 4.2. The other inset of Fig. 4.8a provides a magnified vie of the Nyquist plot about 0 kΩ. In this plot, the first point represents the value of R_s corresponding to the impedance on the x-axis at a higher frequency of 10^5 Hz (McCarter et al., 2015). The shape of the Nyquist plot is indicative of the physical processes occurring on the conductive interfaces (Aguedo et al., 2020). Moreover, in Nyquist plots, the semicircle's diameter represents R_p across the capacitance double layer at lower frequency values. The bare FTO had a large diameter truncated semicircle compared to ZnO-VANRs/FTO, which demonstrated a high charge transfer resistance (Kumar and Das, 2023). The value of R_p for bare FTO and ZnO-VANRs/FTO was 958 (R_s 0.081 kΩ) and 126 kΩ (R_s 0.072 kΩ), respectively. The significant decrease in R_p (7.6 folds) of ZnO-VANRs/FTO electrode was observed compared to bare FTO and enhanced interaction of ZnO nanorods towards analyte probe on the electrode-electrolyte interface, resulting faster electron transfer kinetics and high conductivity of ZnO-VANRs/FTO (Gogoi et al., 2020). Moreover, the variation in CPE parameters could be due to the variation in conductivity and effective surface area of the electrodes, as shown in Table 4.2 (Dash et al., 2020).

Table 4.2: Fitting parameters of Nyquist's plots for bare FTO and ZnO-VANRs/FTO electrode.

Working electrode	R_s (kΩ)	R_p (kΩ)	CPE parameters	
			Y_0 (µMho)	n
Bare FTO	0.081	958	22.2	0.86
ZnO-VANRs/FTO	0.072	126	10.6	0.75

4.2.3.2 *Electrocatalytic surface area of ZnO-VANRs/FTO*

Figs. 4.8b and 4.8c illustrate the cyclic voltammograms (CVs) of bare FTO and ZnO-VANRs/FTO using 1 mM $Ru(NH_3)_6Cl_2$ as an analyte probe in 0.1 M KCl electrolyte at various

scan rates (15-500 mV/s) and ambient temperature. The electrocatalytic surface area of bare FTO and ZnO-VANRs/FTO was calculated using the Randles-Sevcik equation (Eq. 4.4) (Stanley et al., 2024).

$$I_{Pa} = (2.69 \times 10^5)n^{3/2}A_eD^{1/2}\upsilon^{1/2}C_0 \quad (4.4)$$

Where I_{pa} is the anodic peak response in A, υ is the scan rate in V/s, n is the number of electrons involved in the electrocatalytic reaction, D is the diffusion coefficient of electroactive probe in cm^2/s, A_e is the effective electrocatalytic surface area in cm^2, and C_0 is the bulk concentration of electroactive probe in mol/cm^3. The slope of linear plots (Ipa vs. $\upsilon^{0.5}$) of bare FTO and ZnO-VANRs/FTO were 119.91 (R^2 = 0.998) and 300.33 µA. $V^{-1/2}.s^{1/2}$ (R^2 = 0.980), respectively (Fig. 4.8d). By considering n=1 with D = 8.43×10^{-6} cm^2/s for analyte probe, the A_e of bare FTO and ZnO-VANRs/FTO was 0.154 and 0.384 cm^2, respectively (Wang et al., 2011). The A_e of bare FTO was nearly equal to the base electrode's geometrical surface area (0.19 cm^2). Hence, for electrocatalytic sensing of aniline, the fabricated ZnO-VANRs/FTO electrode could provide a 2.5-fold higher surface area than bare FTO, which is well supported by AFM analysis.

4.2.4. Optimization of aniline sensing parameters

4.2.4.1 *Effect of pH*

To investigate the pH effect, CVs were performed in the various pH of 2-7 for electrochemical detection of aniline (60 µM) in 0.1 M PBS electrolyte at a scan rate of 0.05 V/s by ZnO-VANRs/FTO electrode (Fig. 4.8e). When pH increases from 2 to 6, the anodic peak potential (E_p) was switched to the less positive side (Fig. 4.8f, pH vs. E_p), which indicates involvement of proton in the aniline sensing reaction (Malode et al., 2020). The anodic peak response was observed maximum at pH 4 (Fig. 4.8f, pH vs. I_{pa}) in 0.1 M PBS electrolyte, which implies the electrochemical detection of aniline is suitable in the acidic medium. Therefore, pH 4 was used in all of the experimentation. The linear relationship from the plot E_p vs. pH was found to be E_p = -0.0463pH + 0.524 (R^2 = 0.984). The slope and intercept of the linear plot E_p vs. pH were -0.0463 V per unit pH and 0.524 V, respectively. Therefore, the Nernstian equation (Eq. 4.5) was used to calculate the ratio of electron and proton involved during the electrochemical sensing reaction (Manivannan et al., 2019).

$$\frac{dE_p}{dpH} = -2.303\frac{mRT}{nF} \quad (4.5)$$

Where E_p, m, R, n, T, and F are the anodic peak potential (V), number of protons involved in the electrocatalytic reaction, gas constant (8.314 J/mol.K), number of electrons involved in

the electrocatalytic reaction, temperature (K), and Faraday's constant (96485 C/mol), respectively. The ratio of electron and proton (n/m) was found to be 1.27 (~1) by equating the linear relationship E_p vs. pH and Eq. 4.5. It implies that an equal number of electrons and protons involved during aniline sensing (Dash et al., 2022). The CVs of aniline sensing using bare FTO and ZnO-VANRs/FTO electrode in 0.1 M PBS electrolyte (pH 4, 25 °C) at fixed aniline concentration of 60 µM and a scan rate of 0.05 V/s, is shown in Fig. 4.9a. ZnO-VANRs/FTO electrode exhibited 62.8 % increase in anodic peak current of aniline sensing compared to bare FTO (Fig. 4.9b).

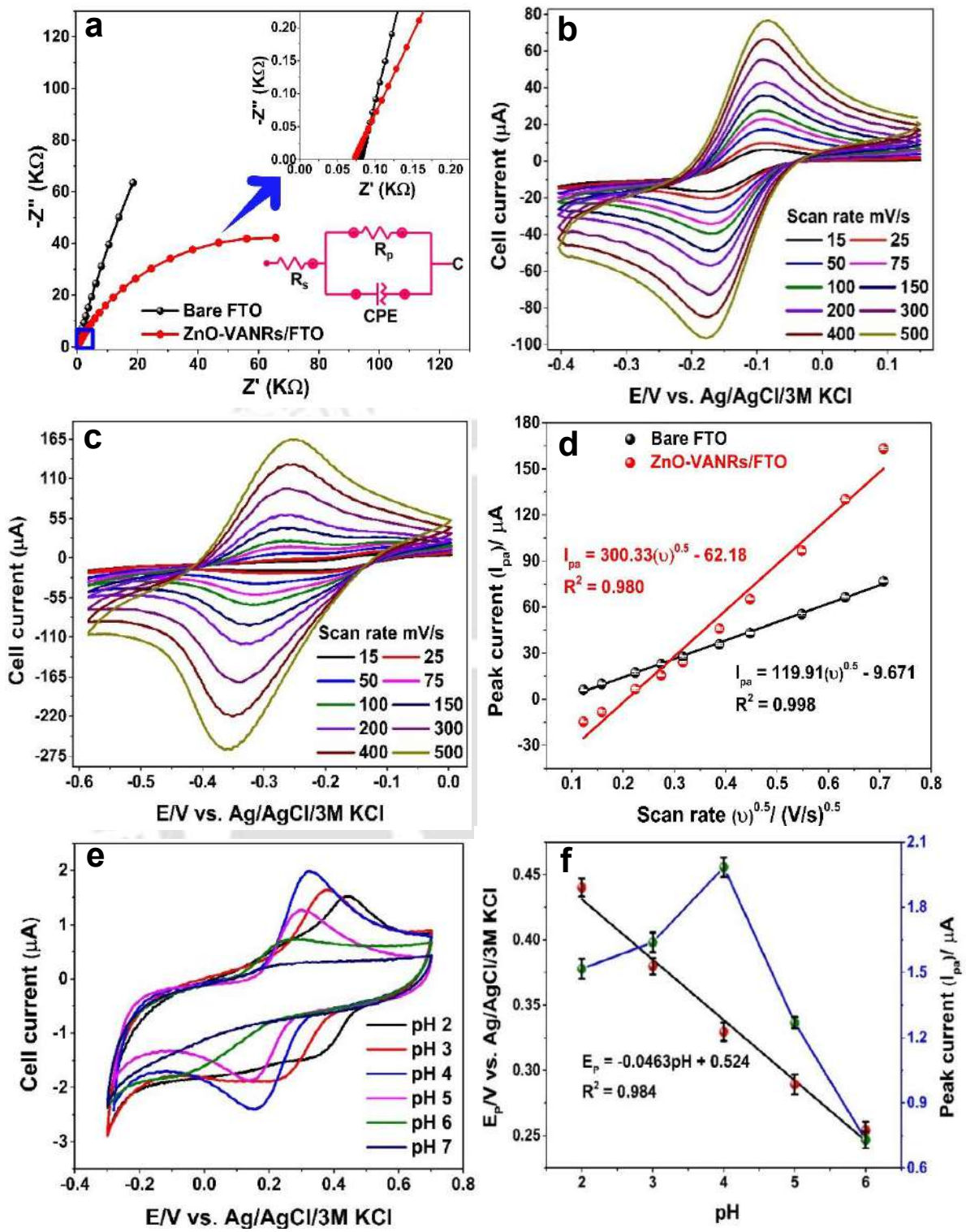

Figure 4.8: (a) Nyquist plots of bare FTO and ZnO-VANRs/FTO with a magnified plot (inset) at about 0 KΩ and Randles equivalent circuit (inset) demonstrating base electrode resistance (Reaction conditions: 1mM $Ru(NH_3)_6Cl_2$ as an electroactive probe in 0.1 M KCl electrolyte media at room temperature and frequency range of 10^{-2}-10^5 Hz), (b) CVs of bare FTO, (c) CVs of ZnO-VANRs/FTO, (d) Anodic peak current (I_{pa}) vs. $\upsilon^{0.5}$ graph of bare FTO and ZnO-VANRs/FTO (Reaction conditions: 1 mM $Ru(NH_3)_6Cl_2$ as an electroactive probe in 0.1 M KCl

electrolyte media at room temperature and scan rates of 15-500 mV/s), (e) CVs of aniline (60 µM) recorded at pH 2 to 7 using ZnO-VANRs/FTO, and (f) pH vs. Anodic peak potential (E_P) and Peak current (I_{pa}) in 0.1 M PBS electrolyte at room temperature and 0.05 V/s scan rate.

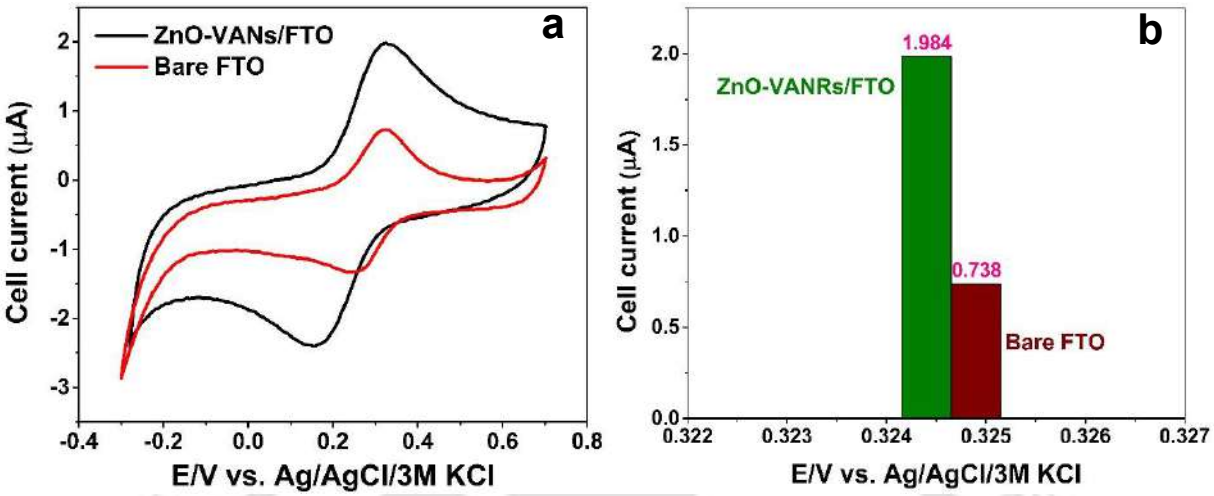

Figure 4.9: (a) CVs of aniline (60 µM) sensing using bare FTO and ZnO-VANRs/FTO electrodes in 0.1 M PBS electrolyte (pH 4) at 0.05 V/s scan rate (25 °C) and (b) Comparison of the anodic peak currents obtained at bare FTO and ZnO-VANRs/FTO electrodes.

4.2.4.2 *Optimization of aniline deposition parameters*

The effect of deposition potential, deposition time, and deposition temperature on the anodic peak response of aniline (60 µM) was investigated by SWV from -0.05-0.6 V using 0.1 M PBS electrolyte (pH 4) over ZnO-VANRs/FTO electrode to understand the electrochemical deposition behaviour for aniline sensing. The deposition potential could substantially impact the sensitivity of the ZnO-VANRs/FTO for sensing of aniline, and it was changed from 0 to -0.9 V in 0.1 M PBS electrolyte (pH 4) at ambient temperature (Fig. 4.10a). It was found that the anodic peak response of aniline was gradually increased from deposition potential 0 to -0.6 V due to the accumulation of aniline ions at the surface of the ZnO-VANRs/FTO electrode (Fig. 4.10b). The reduction in the anodic peak response of aniline ions was observed from deposition potential -0.6 to -0.9 V, which could be due to the evaluation of H_2 gas (Gumpu et al., 2017). The slight switch in the anodic peak potential towards a more positive potential might be ascribed to the over-potential deposition of aniline ions, which created a strong interaction of adsorbate (aniline ions) to the FTO and made it strenuous for the aniline ions to detach from the substrate (Dash et al., 2020). The over-potential deposition indicates that the anodic potential shifted toward a more positive value than the standard potential calculated

from the Laviron equation. Hence, the deposition potential of -0.6 V was selected for the electrochemical detection of aniline.

Fig. 4.10c demonstrates the effect of time of aniline deposition onto the ZnO-VANRs/FTO electrode surface. The deposition time could substantially affect the anodic current of the ZnO-VANRs/FTO for aniline detection, and it was varied from 30 to 150 s in 0.1 M PBS electrolyte (pH 4) at room temperature (Fig. 4.10c). The obtained result confirmed that the peak response was increased gradually from a deposition time of 30 to 90 s as aniline ions were accumulated at ZnO-VANRs/FTO electrode surface (Bagheri et al., 2013), as illustrated in Fig. 4.10d. After 90 s of deposition time, the peak current of aniline ions slightly increased, which could be ascribed to either saturation of aniline ions at the ZnO-VANRs/FTO electrode surface or equilibrium established between aniline ions at the electrode surface and in the electrolyte or fewer aniline ions available for the redox reaction owing to a fixed concentration (60 µM) of aniline ions in the electrolyte solution (Dash et al., 2020). Therefore, the deposition time of 90 s was chosen for further experiments.

Fig. 4.10e illustrates the effect of deposition temperature on the ZnO-VANRs/FTO in 0.1 M PBS electrolyte media at pH 4 during the course of aniline (60 µM) sensing. A significant increase in peak response with an increase in temperature from 15-45 °C was observed owing to the accumulation of aniline ions at the ZnO-VANRs/FTO (Fig. 4.10e). Furthermore, high temperature promotes the rapid diffusion of aniline ions from the supporting electrolyte media to the surface of the ZnO-VANRs/FTO. Fig. 4.10f demonstrated the insignificant change in response current with further increase in the aniline deposition temperature (>45 °C) could be due to equilibrium between aniline ions at ZnO-VANRs/FTO surface and electrolyte media (0.1 M PBS pH 4) and/or surface saturation of aniline ions. Additionally, the maximum temperature for field applications is typically about 45 °C. Therefore, the deposition temperature of 45 °C was selected for further experiments. The selection of deposition parameters for organic analytes has also been reported previously (Dash et al., 2022).

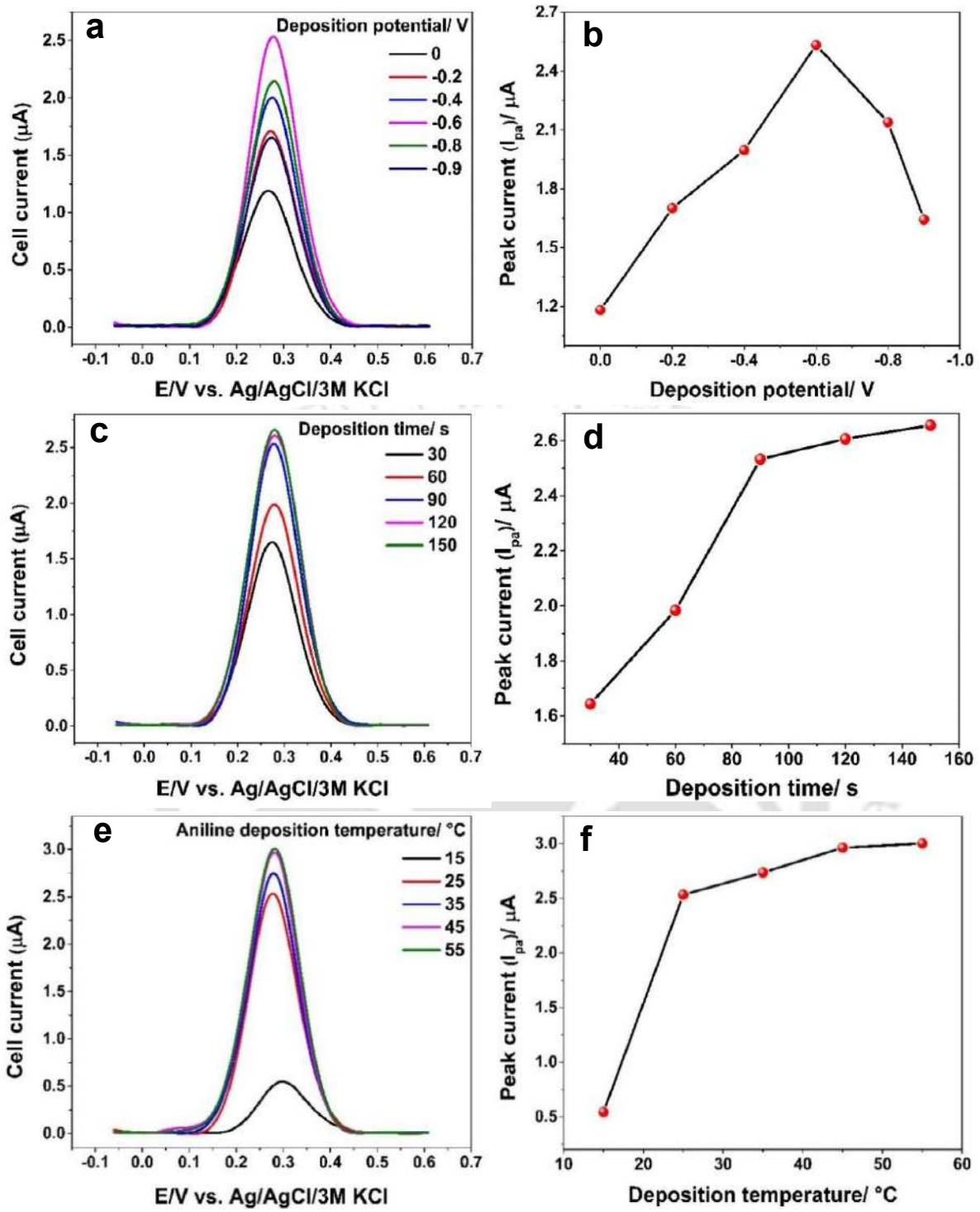

Figure 4.10: (a) SWV of aniline recorded at different deposition potentials from 0 to -0.9 V vs. Ag/AgCl, deposition time 90 s, and 25 °C, (b) Deposition potential vs. Anodic peak current (I_{pa}), (c) SWV of aniline recorded at different deposition times from 30 to 150 s, deposition potential -0.6 V, and 25 °C, (d) Deposition time vs. I_{pa}, (e) SWV of aniline recorded at different deposition temperatures from 15 to 55 °C, deposition potential -0.6 V, and deposition time 90 s, and (f) Deposition temperature vs. I_{pa}. Reaction conditions: 60 µM aniline in 0.1 M PBS electrolyte at pH 4.

4.2.5. Electrocatalytic aniline sensing at ZnO-VANRs/FTO

4.2.5.1 *Determination of electrokinetic parameters and adsorption of aniline*

To evaluate the electrokinetic parameters and adsorption of aniline sensing, CVs were recorded at different scan rates (15-500 mV/s) from -0.28 to 0.8 V on the ZnO-VANRs/FTO electrode using 0.1 M PBS electrolyte at 45 °C (Fig. 4.12a). A linear plot was found between the anodic peak response (I_{pa}) and the square root of scan rate ($\upsilon^{0.5}$) with a slope of 49.925 $\mu A.V^{-0.5}.s^{0.5}$ ($R^2 = 0.983$), which demonstrates the electrochemical reaction is diffusion control (Fig. 4.12b) (Dash et al., 2021). Therefore, the Laviron equation (Eq. 4.6) was employed to determine the electrokinetic parameters of aniline sensing for the diffusion-controlled process (Bhan and Kumar Golder, 2023).

$$E_p = E^0 - \frac{2.303RT}{\alpha nF} \log \frac{RTk^0}{\alpha nF} + \frac{2.303RT}{\alpha nF} \log \upsilon \quad (4.6)$$

Where E_p is the anodic peak potential in (V), E^0 is the standard formal potential (V), α is the electron transfer coefficient, n is the number of electrons involved in the electrocatalytic reaction, k^0 is the heterogeneous rate constant in s^{-1}, and υ is the scan rate in V/s. E^0 was calculated from the extrapolation of the graph between E_p vs. υ at scan rate zero (υ = 0). The value of E^0 was found to be 0.289 V from the graph E_p vs. υ by extrapolating at scan rate 0 (υ = 0). From linear graph E_p vs. log υ, the slope and intercept were obtained as 0.053 V and 0.362 V ($R^2 = 0.982$), respectively (Fig. 4.12c). By assuming α = 0.5 (for anodic peak), the value of electrokinetic parameters n and k were found from the slope and intercept of graph E_p vs. log υ, when the value of E^0 know. The values of n and k^0 were 2.38 and 1.82 s^{-1}, respectively. The value of n implies that the two electrons participate in an electrocatalytic reaction. To study the adsorption of aniline on the ZnO-VANRs/FTO electrode surface, Eq. 4.7 was employed (Elgrishi et al., 2018).

$$I_{pa} = \frac{n^2F^2}{4RT} A_{eff}\, \upsilon\, \Gamma^* \quad (4.7)$$

Where Γ* is the surface coverage by the adsorption of aniline ($mol.cm^{-2}$). A linear plot was found between the I_{pa} vs. υ (Fig. 4.12d) with a slope of 61.256 $\mu A.V^{-1}.s$ ($R^2 = 0.996$), which slope equates with the Eq. 4.7 to estimate the adsorption of aniline (3.25×10^{-11} $mol.cm^{-2}$).

4.2.5.2 *Electrocatalytic aniline sensing over ZnO-VANRs/FTO electrode*

Figs. 4.12e and 4.12f depict the SWV and the corresponding calibration curve of aniline sensing over the ZnO-VANRs/FTO electrode in 0.1 M PBS electrolyte (pH 4) at selected deposition parameters (deposition potential -0.6 V vs. Ag/AgCl, deposition time 90 s, and deposition temperature 45°C). The plot of aniline concentration vs. anodic peak current (I_{pa})

exhibited the two linear relationships between the concentration range of 0-20 and 20-160 µM (Fig. 4.12f). The two linear domains of aniline concentration were observed due to the abundance of accumulated aniline ions over the ZnO-VANRs/FTO electrode proximity at a high concentration switched the electrocatalytic reaction from diffusion-controlled domain to surface-controlled domain (Dash et al., 2018). LOD and LOQ of the aniline sensing over the ZnO-VANRs/FTO electrode were calculated by Eqs. 4.8 and 4.9, respectively (Dash et al., 2022).

$$\mathrm{LOD} = \frac{3S_d}{m} \tag{4.8}$$

$$\mathrm{LOQ} = \frac{10S_d}{m} \tag{4.9}$$

Where m is the slope of the calibration curve in µA. μM^{-1} and S_d is the standard deviation of the blank run (0.0049). From Fig. 4.12f, the slope of linear plots was 0.076 µA. μM^{-1} (R^2 = 0.977) and 0.025 µA. μM^{-1} (R^2 = 0.981) between the concentration range of 0-20 µM and 20-160 µM, respectively. LOD of the ZnO-VANRs/FTO electrode was 0.193 µM (LOQ 0.645 µM) and 0.588 µM (LOQ 1.96 µM) between the linear working range of 0-20 and 20-160 µM, respectively. The sensitivity of the ZnO-VANRs/FTO electrode, having A_e of 0.384 cm^2 (Fig. 4.8c), was found from the slopes (0.076 and 0.025 µA. μM^{-1}) of the calibration curve, as obtained from the Fig. 4.12f. It was 0.198 and 0.065 µA. $\mu M^{-1}.cm^{-2}$ between the concentration range of 0-20 and 20-160 µM, respectively. In addition, SWV and the corresponding calibration curve of aniline sensing over the bare FTO in 0.1 M PBS electrolyte (pH 4) at selected deposition parameters are shown in Figs. 4.11a and 4.11b. The slope of linear plots was 0.019 µA. μM^{-1} (R^2 = 0.991) between the concentration range of 0-160 µM (Fig. 4.11b). Bare FTO displayed LOD of 0.774 µM, LOQ of 2.58 µM, and sensitivity of 0.123 µA. $\mu M^{-1}.cm^{-2}$ (having A_e of 0.154 cm^2, Fig. 4.8b) within the linear aniline concentration range of 0-160 µM. The LOD of ZnO-VANRs/FTO for aniline sensing is about 4-fold lower than bare FTO.

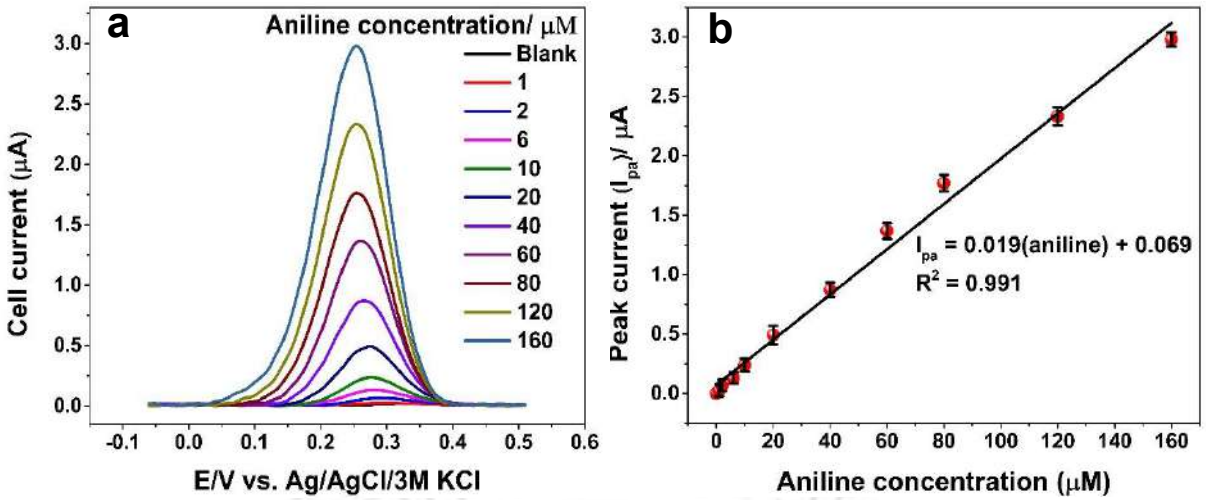

Figure 4.11: (a) SWV of bare FTO at a varying concentration of aniline from 0 to 160 µM and (b) Aniline concentration vs. peak current (I_{pa}). Reaction conditions: Deposition potential -0.6 V vs. Ag/AgCl, deposition time 90 s, and deposition temperature 45 °C in 0.1 M PBS electrolyte media (50 mL) at pH 4.

4.2.5.3 *Aniline reaction at ZnO-VANRs/FTO electrode and detection mechanism*

To identify the reaction products during electrochemical sensing of aniline, HPLC and LC-MS analysis were conducted before and after the chronoamperometry analysis at 0.289 V (1200 s) over ZnO-VANRs/FTO in 0.1 M PBS (pH 4) supporting electrolyte at a fixed concentration of aniline (160 µM). HPLC analysis identifies a sharp peak corresponding to aniline at a retention time of 4.568 min prior to the redox reaction (Fig. 4.13a). After the chronoamperometry test, the peak at a retention time of 4.568 min disappeared, and the new peak at a retention time of 5.034 min was identified (Fig. 4.13b). Further, mass spectra were obtained before (Fig. 4.14a) and after the (Fig. 4.14b) chronoamperometry analysis at a retention time of 9.30 and 9.57 min, respectively. Aniline (m/z = 93.06) is converted to a nitrosobenzene (m/z = 107.06) with the transfer of two electrons and two protons (Fig. 4.12g). Mass spectra obtained before and after the redox reaction showed the traces of aniline (m/z = 93.06, Fig. 4.14a) and nitrosobenzene molecules (m/z = 107.06, Fig. 4.14b).

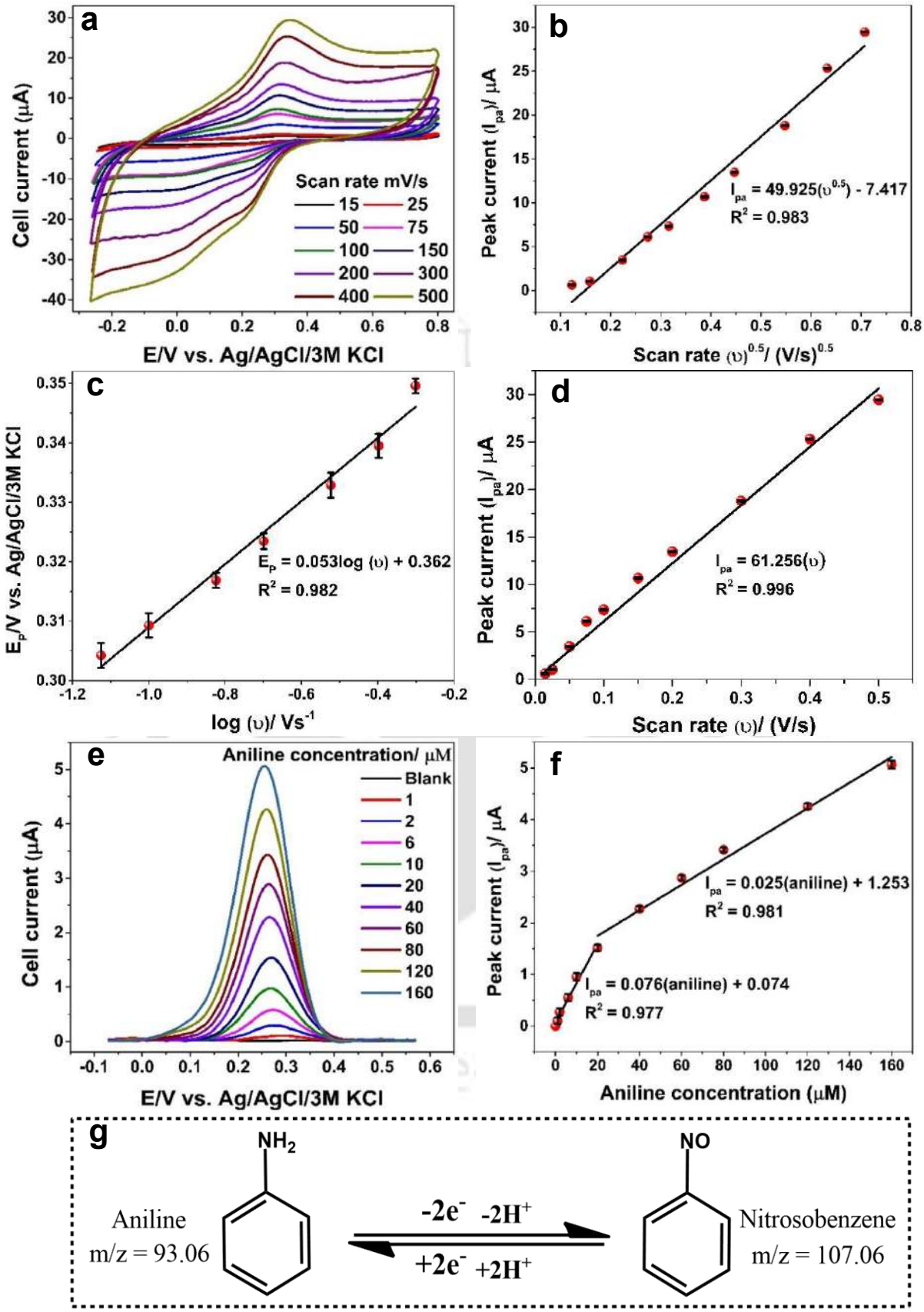

Figure 4.12: (a) CVs of ZnO-VANRs/FTO at different scan rates (15-500 mV/s), (b) $\upsilon^{0.5}$ vs. I_{pa}, (c) log υ vs. E_P, (d) υ vs. I_{pa} (Reaction conditions: 60 μM aniline in supporting electrolyte

media (0.1 M PBS pH 4) at 45°C), (e) SWV of ZnO-VANRs/FTO electrode at different aniline concentrations from 0 to 160 µM, (f) Aniline concentration vs. I_{pa} (Reaction conditions: Deposition potential -0.6 V vs. Ag/AgCl, deposition time 90 s, and deposition temperature 45 °C in 0.1 M PBS electrolyte media (50 mL) at pH 4), and (g) Reaction pathway of aniline sensing in 0.1 M PBS electrolyte (pH 4) at 0.289 V (1200 s) using ZnO-VANRs/FTO corresponding to mass spectrum (Fig. 4.14).

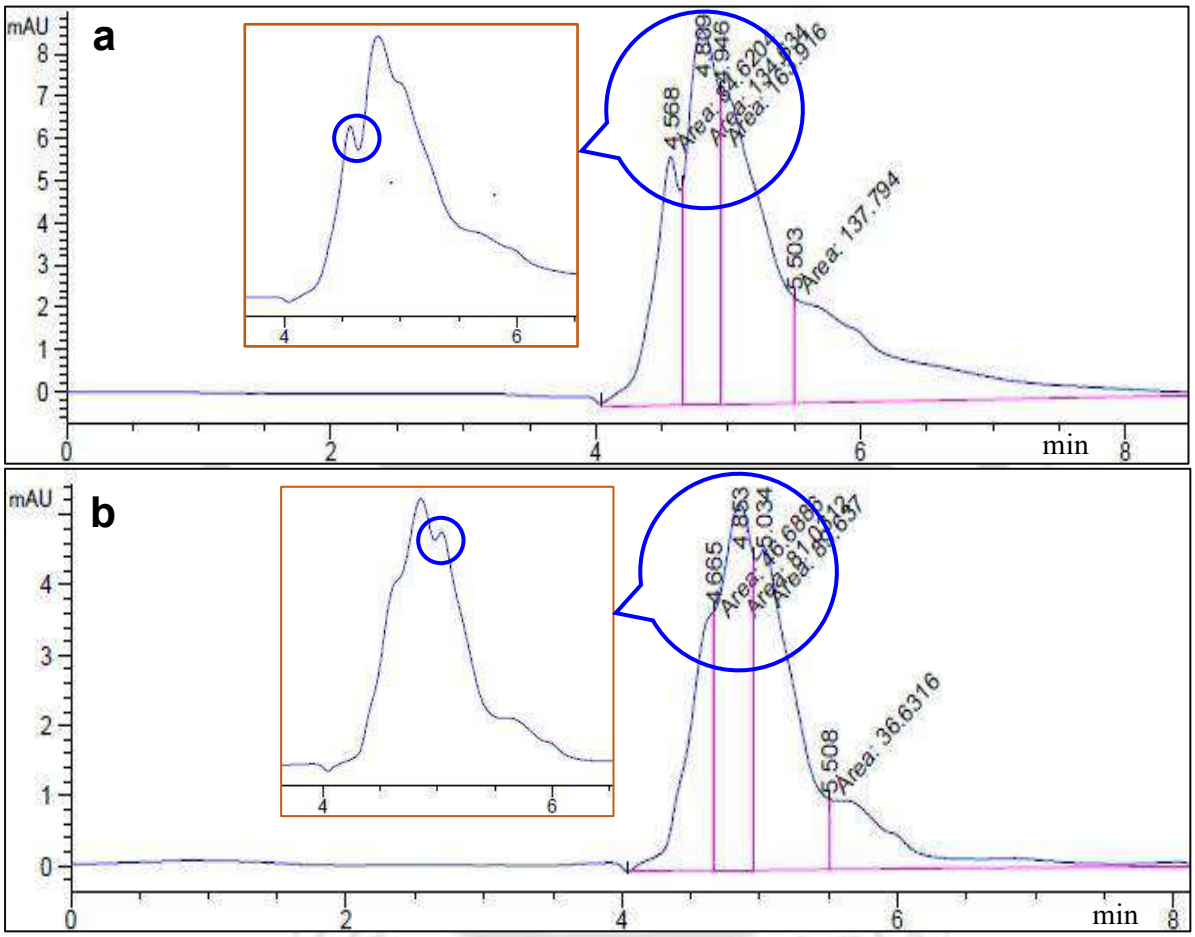

Figure 4.13: HPLC chromatograms analyte solution (a) before (retention time 4.568 min) and (b) after (retention time 5.034 min) chronoamperometry test at 0.289 V vs. Ag/AgCl (1200 s) using ZnO-VANRs/FTO electrode. HPLC is equipped with an ultra C18 column (UMISil C18(3), 250 × 4.6 mm, 5 µm particle size, thermoscientific). Acetonitrile (90%) and water (10%) were used as the mobile phase, and aniline was detected using a UV detector at a fixed wavelength of 281 nm.

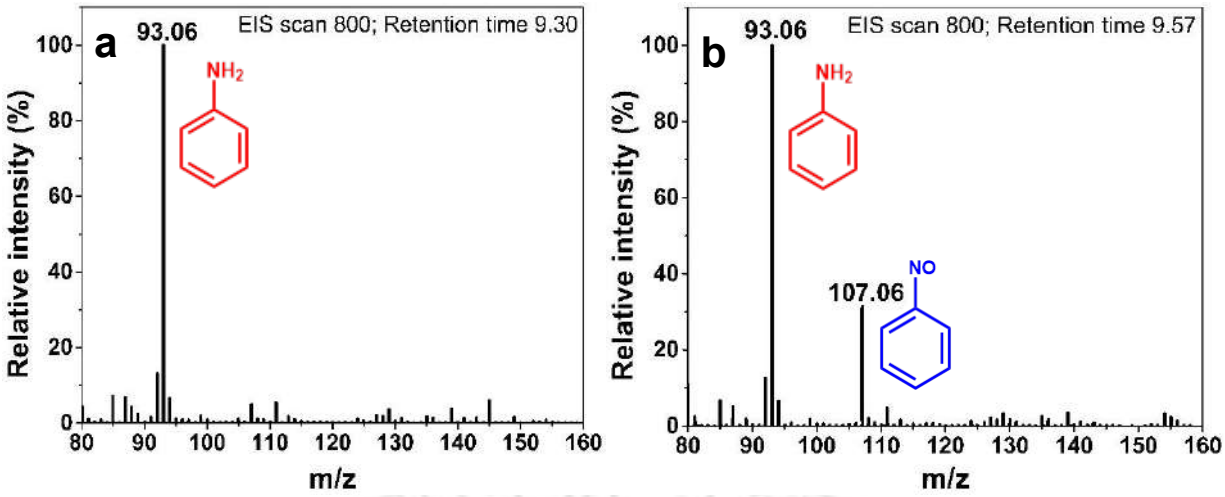

Figure 4.14: Mass spectra of analyte solution (a) before and (b) after chronoamperometric test at 0.289 V vs. Ag/AgCl (1200 s) using ZnO-VANRs/FTO electrode.

4.2.5.4 *Repeatability and reproducibility of ZnO-VANRs/FTO electrode for aniline sensing*

The steady response of aniline sensing was examined using the same ZnO-VANRs/FTO electrode in the same aniline solution of concentration 60 µM by SWV in 0.1 M PBS electrolyte media (pH 4) from -0.05 to 0.6 V vs. Ag/AgCl following the selected deposition parameters (deposition potential -0.6 V vs. Ag/AgCl, deposition time 90 s, and deposition temperature 45°C), for consequent 10 cycles (Fig. 4.18a). No significant decay in the peak response was detected throughout the first four cycles. After that, a continuous decline in the peak response with each aniline sensing cycle was noted. The reduction in the anodic peak response was 2.63, 9.44, and 11.97 % from the 1^{st}-6^{th}, 6^{th}-10^{th}, and 1^{st}-10^{th} cycle, respectively. The decrease in the anodic peak current was 23.24, 28.52, 31.34, 33.09, and 34.51 % up to the 20, 30, 40, 50, and 60^{th} run of aniline sensing, respectively (Fig. 4.15a). The decline in the peak current could be attributed to the accumulation of aniline ions over the ZnO-VANRs/FTO electrode surface (Dash et al., 2021). The present study demonstrates a decrease in anodic peak current (11.97 %) up to the 10^{th} cycle is less than that of recently reported sensors, such as AgNRs/GCE (26 % up to the 10^{th} cycle) and PtNPs/graphene/GCE (20 % up to the 10^{th} cycle) for electrochemical sensing of aniline and dipyrone, respectively (Das et al., 2024; Dash et al., 2021). The reproducibility of aniline sensing was evaluated using three different fresh ZnO-VANRs/FTO electrodes in three different 0.1 M PBS electrolytes (pH 4) at the same concentration of aniline (60 µM) by SWV at selected deposition parameters (Fig. 4.15b). The reproducibility studies revealed no significant differences in peak current, with only a relative standard deviation (RSD) of 2.34 %, eliminating the calibration and blank run steps for every fresh electrode

during in-field applications. Therefore, the ZnO-VANRs/FTO electrode exhibited excellent reproducibility during aniline sensing within acceptable limits of RSD (2.34 %) (Lotfi et al., 2021). Further, the long-term stability of the ZnO-VANRs/FTO electrode was studied over a long time (0-90 days) of its fabrication by SWV in 0.1 M PBS electrolyte (pH 4) at 60 µM aniline concentration and selected deposition parameters (Fig. 4.15c). ZnO-VANRs/FTO electrode exhibited only a 5.24 % reduction in anodic peak current after 90 days of storage at room temperature compared to freshly prepared electrode under identical experimental conditions.

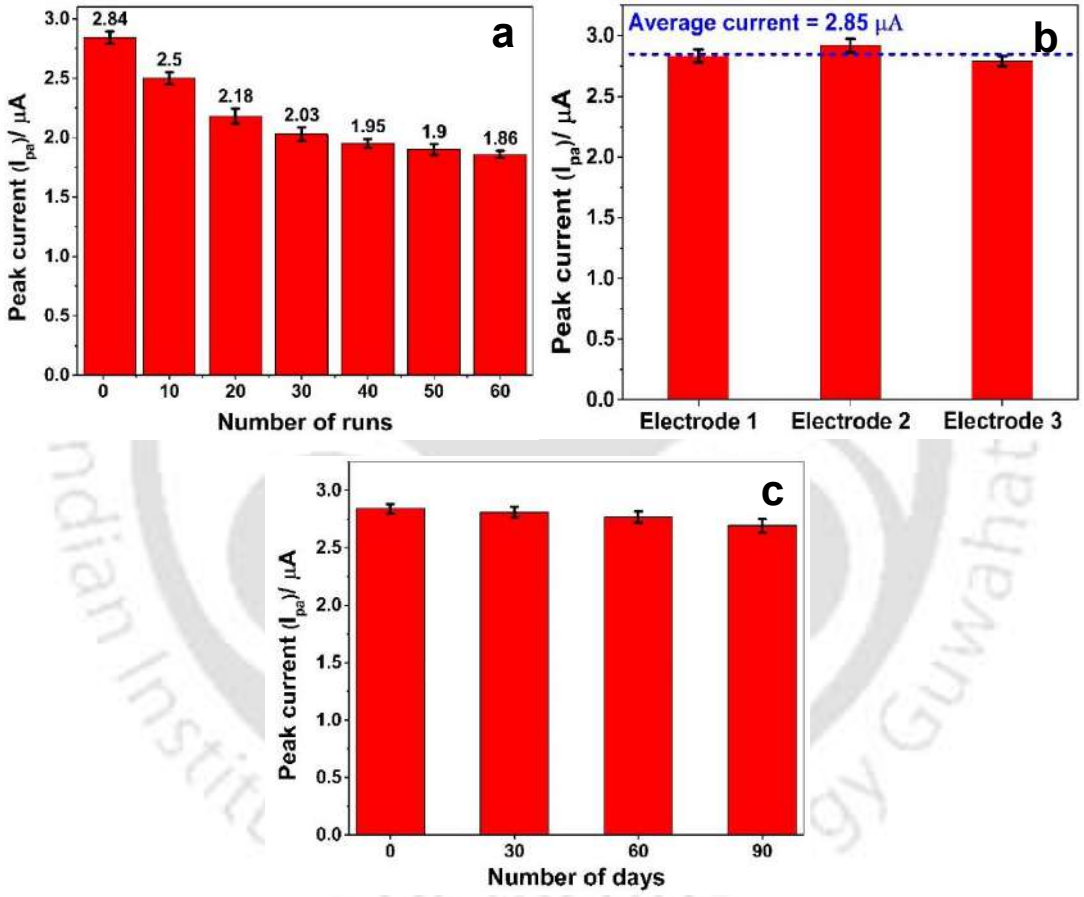

Figure 4.15: (a) Repeatability of the same ZnO-VANRs/FTO electrode tested up to the 60th cycle in 60 µM aniline by SWV from -0.05 to 0.6 V vs. Ag/AgCl (Reaction condition: Deposition potential -0.6 V vs. Ag/AgCl, deposition time 90 s, and deposition temperature 45 °C in 0.1 M PBS electrolyte media (50 mL) at pH 4), (b) Reproducibility of aniline sensing using three different fresh ZnO-VANRs/FTO electrodes at the same concentration of aniline (60 µM) by SWV from -0.05 to 0.6 V vs. Ag/AgCl, and (c) Peak current after 90 days of storage at room temperature. Reaction condition: Deposition potential -0.6 V vs. Ag/AgCl, deposition time 90 s, and deposition temperature 45 °C in 0.1 M PBS electrolyte media (50 mL) at pH 4.

The FESEM micrograph (Fig. 4.18b) of the used ZnO-VANRs/FTO electrode (10^{th} cycle, Fig. 4.18a) demonstrates well-distributed 1D surface VANRs of ZnO on the FTO. An inconsequential change in the morphology of ZnO-VANRs/FTO was observed after the 10^{th} cycle of aniline sensing.

The XRD analyses of the ZnO-VANRs/FTO electrode (10^{th} cycle, Fig. 4.18a) was done to investigate its structural characteristics, as shown in Fig. 4.18c. It indicates that the ZnO-VANRs/FTO electrode didn't undergo notable crystalline transformation after the electrochemical reaction.

The XPS analysis of used ZnO-VANRs/FTO (10^{th} cycle, Fig. 4.18a) of aniline sensing was done to determine its chemical state and compositional attributes. The high-resolution spectrum in the Zn 2p region of ZnO-VANRs/FTO after the stability analysis showed two predominant peaks at a binding energy of 1021.82 and 1044.95 eV corresponding to the spin-orbital of Zn $2p_{3/2}$ and $2p_{1/2}$, respectively (Fig. 4.18d). The intensities of the peaks were determined to be almost identical before (Fig. 4.6b) and after (Fig. 4.18d) the electrocatalytic reaction. The high-resolution spectra in the O 1s region of ZnO-VANRs/FTO exhibited a peak at a binding energy of 531.69 eV (Fig. 4.18e). Moreover, two identical peaks were observed at 531.69 (O_{lat}) and 535.19 eV (O_{ads}) in the O 1s spectrum of ZnO-VANRs/FTO. It shows that insignificant changes were observed in the compositional attributes of ZnO-VANRs/FTO electrode for detection and determination of aniline.

The Raman spectra of bare FTO, ZnO-VANRs/FTO, and ZnO-VANRs/FTO post-reaction (10^{th} cycle of aniline measurement, Fig. 4.18a) are displayed in Fig. 4.16. Two peaks corresponding to Raman vibrations of bare FTO at 578 and 1100 cm^{-1} were observed (N. Wang et al., 2014). Moreover, the Raman spectra of ZnO-VANRs/FTO and ZnO-VANRs/FTO post-reaction contain a sharp peak at 436 cm^{-1} and a shoulder peak at 336 cm^{-1}, corresponding to ZnO nanostructures (Pandey et al., 2017). In previous studies, it has been reported that the peaks at 1352 and 1581 cm^{-1} indicate the polymeric form of aniline (polyaniline) (Aranthady et al., 2022). However, neither a new peak nor a major peak shift was observed after the 10^{th} cycle of aniline sensing, indicating retention of the basic crystal structure of ZnO-VANRs/FTO and the absence of polyaniline at the surface of the working electrode, confirming its stability.

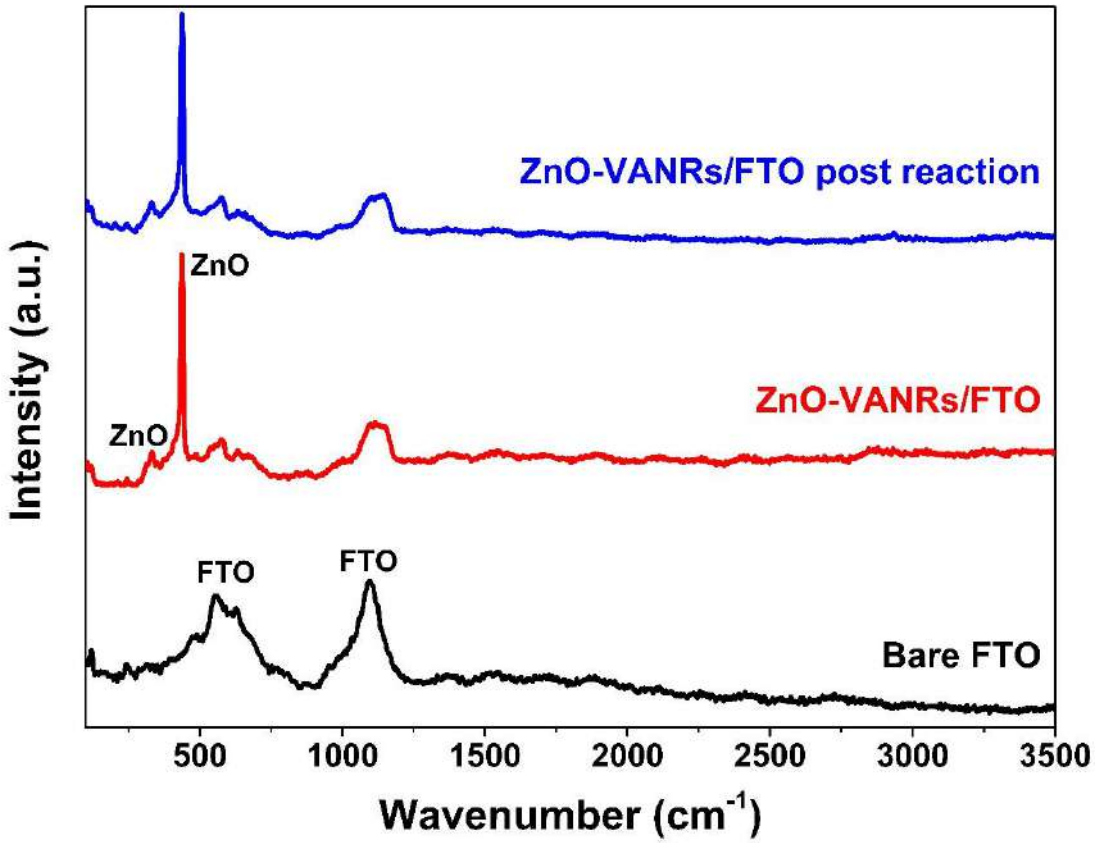

Figure 4.16: RAMAN analysis of bare FTO, ZnO-VANRs/FTO and ZnO-VANRs/FTO post-reaction (after the 10th cycle of aniline sensing).

The FTIR studies of bare FTO, ZnO-VANRs/FTO, and ZnO-VANRs/FTO post-reaction (10th cycle of measurement, Fig. 4.18a) are demonstrated in Fig. 4.17. The peaks observed in bare FTO at 585 and 753 cm^{-1} correspond to the Sn-O and Sn-O-Sn groups of FTO, respectively (Banerjee et al., 2003). In the FTIR spectrum of ZnO-VANRs/FTO, additional peaks at 515 and 1064 cm^{-1} represent ZnO nanostructures. Further, peaks at 1160, 1456, 1730, and 2960 cm^{-1} correspond to C-O, C=C, C=O, and -OH groups of traces of surface-adsorbed organic compounds from the reaction salt, respectively (Dulta et al., 2022). In addition to these peaks, a sharp rise in peak intensity at 2925 cm^{-1} and a trace peak at 630 cm^{-1} were observed in ZnO-VANRs/FTO post-reaction (10th cycle), corresponding to N-H and C-H/C-C groups of aniline, respectively (Khasanah et al., 2017; Saravanan et al., 2004). However, no new peak corresponding to polyaniline (~2300-2400 cm^{-1}) was observed.

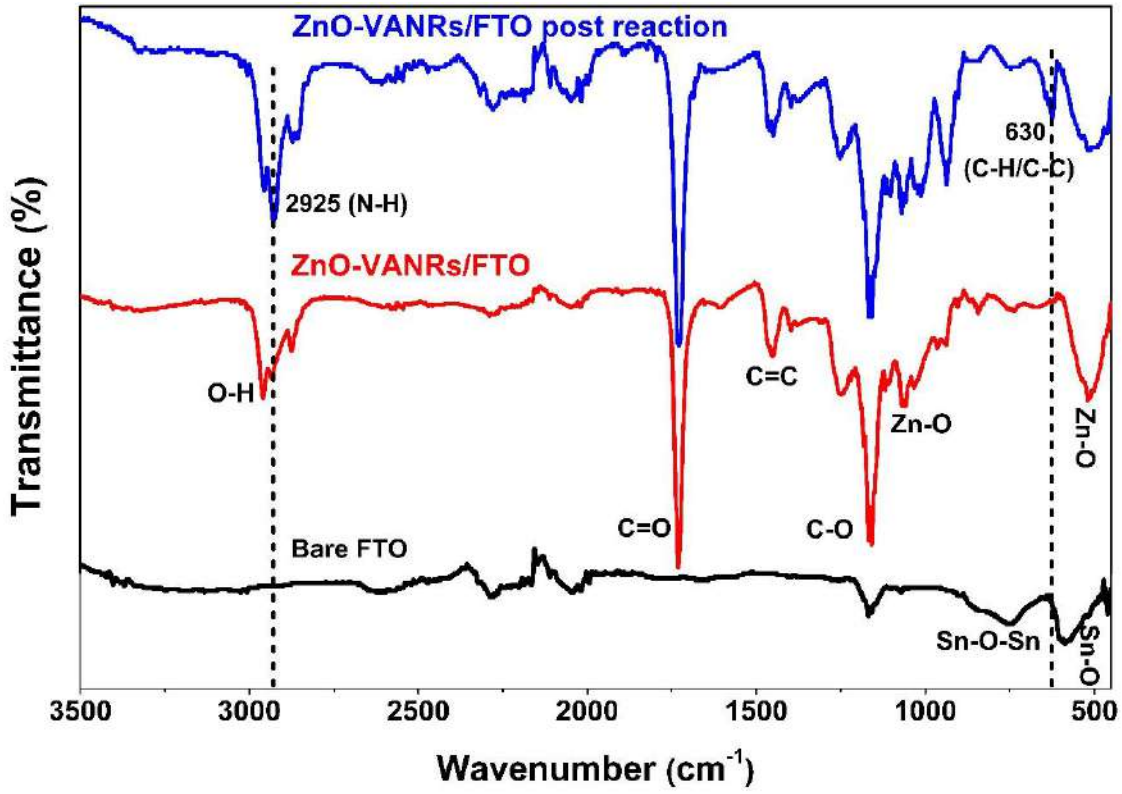

Figure 4.17: FTIR analysis of bare FTO, ZnO-VANRs/FTO and ZnO-VANRs/FTO post-reaction (after the 10th run of aniline measurement).

The comparison of electrochemical sensing of aniline with various methods (electrochemical and non-electrochemical) based on the detection limit is shown in Table 4.3. Electrochemical sensors provided good sensing performance compared to the fluorescence and colorimetric sensors for detecting aniline. In addition, the present work exhibited a clear superiority compared to several recently reported electrochemical, fluorescence, and colorimetric sensors of aniline (Table 4.3). The electrochemical activity of the ZnO-VANRs/FTO electrode was compared with the recently published ZnO nanocomposite-based electrodes. The present work demonstrated a definite superiority compared to several prior works (Table 4.4).

Table 4.3: Comparison of electrochemical sensing of aniline with non-electrochemical studies based on the limit of detection.

Sl. No	Material used	Methods	Detection limit (μM)	References
1.	Zn-Eu	Fluorescence	7.5	Li et al., 2017
	Zn-Tb		5.2	
2.	Polymers P1-P6	Fluorescence	5	Lin et al., 2022
3.	HOF-20	Fluorescence	2.24	Wang et al., 2020
4.	GQDs	Fluorescence	0.234	Aly et al., 2024
5.	FJU-10	Fluorescence	0.58	Liu et al., 2019
	dye@FJU-10		0.62	
6.	Charge-transfer complex	Colorimetric	9.86	Huang et al., 2022
7.	CA-MnO_2@Co-N/C	Colorimetric	0.185	Xing et al., 2024
8.	AgNRs/GCE	Electrochemical (SWV)	0.032	Das et al., 2024
9.	BND	Electrochemical (DPV)	0.29	Li et al., 2021
10.	NP-Au	Electrochemical (Amperometry)	0.5	Lee et al., 2017
11.	NPG/GCE	Electrochemical (CV)	0.5	Wan et al., 2023
12.	**ZnO-VANRs/FTO**	**Electrochemical (SWV)**	**0.193**	**Present study**

Table 4.4: Comparison of electrocatalytic activity of ZnO-VANRs/FTO electrode with the recently published ZnO nanocomposite-based sensors for various analytes.

Working electrodes	Technique	LOD (μM)	Sensitivity ($\mu A \mu M^{-1} cm^{-2}$)	Analytes	References
ZnO-VANRs/FTO	**SWV***	**0.193**	**0.198**	**Aniline**	**Present work**
		0.588	**0.065**		
Bio-Ag/ZnO NCs	DPV⁂	0.27	0.303	Carbaryl	Le Nhat Trang et al., 2023
ZnO@CoNi/LDH-NCDs	CA	0.2	13.040	Hydrazine	Zhang et al., 2023
ZnO NGs@CC	DPV⁂	0.09	0.279	Hydroxychloroquine	Kokulnathan et al., 2023
GA_2–ZnO/BDDE	DPV⁂	0.075	-	Metoprolol	Koçak et al., 2023
ZnO/Co_3O_4/rGO/GCE	CA	0.043	1.55	Glucose	Hussein et al., 2023

ZnO/NPG microelectrode	SWASV	0.004	102.343	Arsenic(III)	Zhuang et al., 2023
Gd@ZnO-MWCNTs/GCE	DPV⁂	0.2	-	Bisphenol derivative	Agrahari et al., 2023
Hexagonal ChAc-ZnO NS/Au	LSV	0.4	2.66	Hydrazine	Kaur et al., 2022
Sb-ZnO/N-rGO/GCE	CA	0.13	0.294	Nitrite	Cheng et al., 2022
	LSV⁴	0.43	0.398		
ZnO-Cu_xO/GCE	CV	7.3	0.504	H_2O_2	Jain et al., 2022b
	CV	15.7	0.158	p-Nitrophenol	
ZMO/ZnO/GCE	DPV⁂	0.019	0.760	Chlorpromazine	Balamurugan et al., 2022
ZnO@ZIF-8/ITO	CA†	3	0.0047	H_2O_2	Mei et al., 2022

*Square wave anodic stripping voltammetry, ?Square wave voltammetry, †Chronoamperometry, ⁴Linear sweep voltammetry, ‡Cyclic voltammetry, ⁂Differential pulse voltammetry

4.2.6. Selectivity of aniline sensing over ZnO-VANRs/FTO electrode

The chronoamperometric response of ZnO-VANRs/FTO electrode was recorded at different concentrations of aniline from 5 to 110 µM along with the coexistence of p-nitroaniline, chlorobenzene, and chlorpyrifos in 0.1 M PBS electrolyte media (pH 4) at 45 °C (Fig. 4.18f). The concentration of aniline calculated from the calibration curve (Fig. 4.12f) were 3.82, 10.4, 17.2, 56.6, 88.1, and 112.4 µM, corresponding to the actual spiked aniline concentrations 5, 10, 20, 60, 90, and 110 µM, respectively. Additionally, the selectivity of the ZnO-VANRs/FTO electrode was also investigated by adding different concentrations of aniline (5-110 µM) in the presence of potential interferences, including Cu^{2+}, Pb^{2+}, Ni^{2+}, Cd^{2+}, albumin bovine, *Escherichia coli*, and ciprofloxacin in 0.1 M PBS electrolyte media (pH 4) at 45 °C, as shown in Fig. 4.19. The cell current was measured at redox potential and interval of 0.289 V vs. Ag/AgCl and 20 s, respectively (Figs. 4.18f and 4.19). Moreover, the current response changes after adding aniline and remains unchanged after adding interferants. The fabricated ZnO-VANRs/FTO electrode was unprecedently selective towards aniline detection even in the coexistence of interferants. Furthermore, the presence of interferants could not change the potential (0.289 V vs. Ag/AgCl) and sensitivity of the ZnO-VANRs/FTO electrode during the course of aniline sensing.

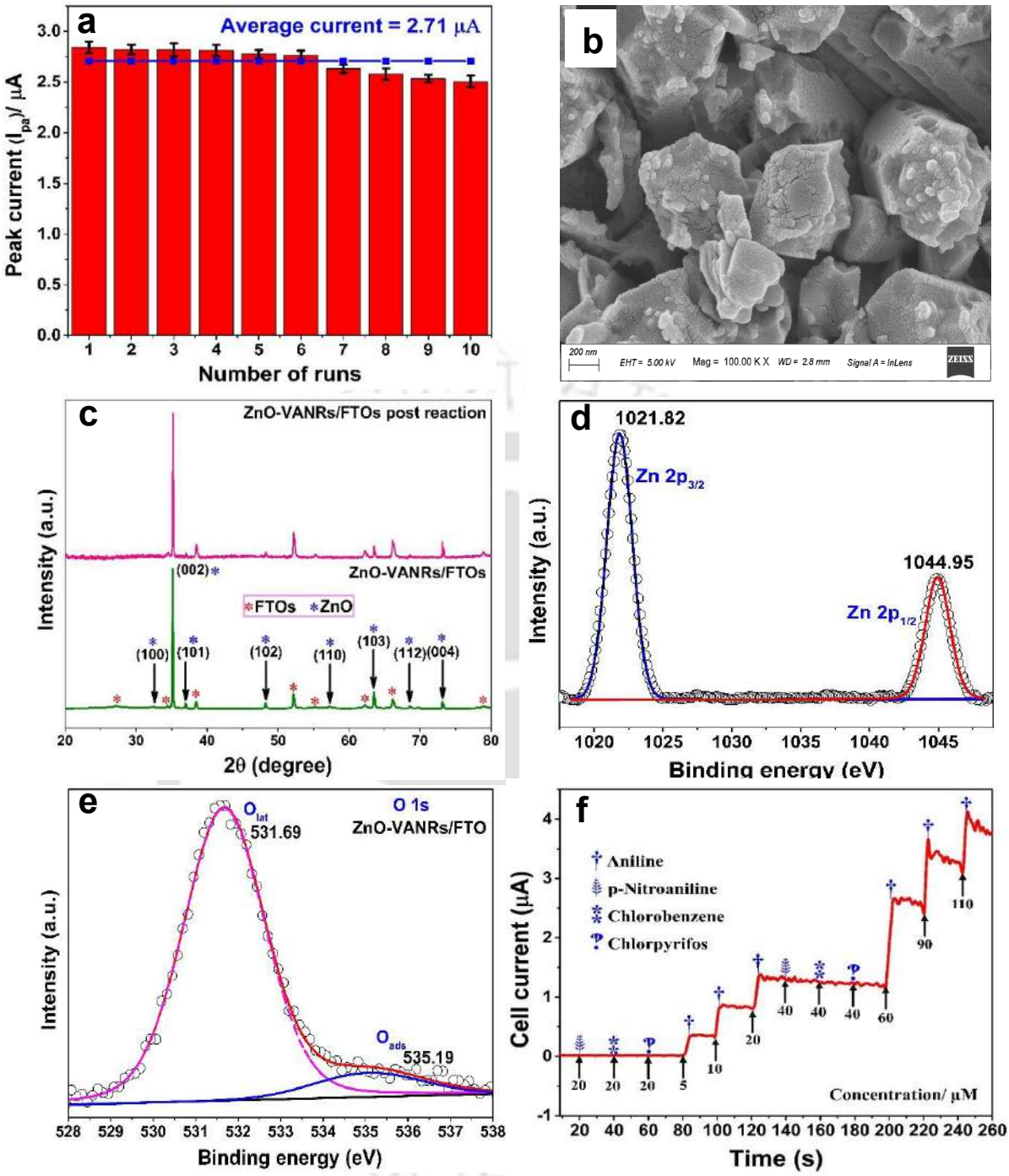

Figure 4.18: (a) Repeatability of the same ZnO-VANRs/FTO electrode tested in 60 µM aniline by SWV from -0.05 to 0.6 V vs. Ag/AgCl (Reaction condition: Deposition potential -0.6 V vs. Ag/AgCl, deposition time 90 s, and deposition temperature 45 °C in 0.1 M PBS electrolyte media (50 mL) at pH 4), (b) FESEM image, (c) XRD pattern, and (d and e) XPS spectra of post-reaction ZnO-VANRs/FTO electrode (after 10th cycles of aniline sensing), and (f) Chronoamperometric profile with step-wise addition of aniline (5-110 µM) along with interferants addition, namely p-nitroaniline, chlorobenzene, and chlorpyrifos at ZnO-

VANRs/FTO (Reaction condition: E_{anode} = 0.289V vs. Ag/AgCl, reaction time 260 s, and temperature 45 °C in 0.1 M PBS electrolyte media at pH 4).

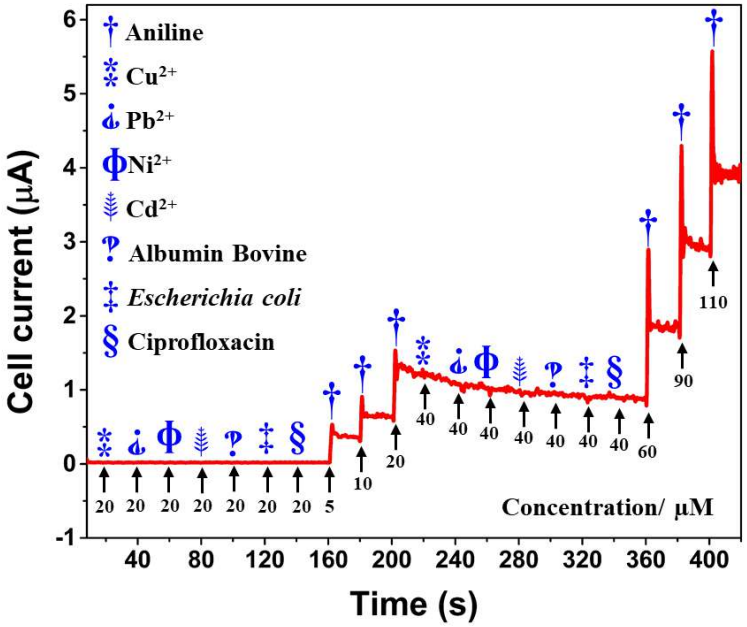

Figure 4.19: The selectivity of the ZnO-VANRs/FTO electrode was investigated via performing chronoamperometric test by adding (time interval 20 s) different concentrations of aniline (5-110 µM) in the presence of potential interferences, including Cu^{2+}, Pb^{2+}, Ni^{2+}, Cd^{2+}, albumin bovine, *Escherichia coli*, and ciprofloxacin in 0.1 M PBS electrolyte media (pH 4) at 45 °C and redox potential of 0.289V vs. Ag/AgCl.

4.2.7. Aniline detection in environmental matrices

Water samples were obtained from the domestic water supply at IIT Guwahati, India and Brahmaputra River (26°10′54.64″N, 91°41′47.96″E). The water samples were subjected to filtration with 0.2 µm membrane filter paper to eliminate any suspended contaminants and to reduce surface fouling of the ZnO-VANRs/FTO electrode, which could affect the LOD and sensitivity of the sensor. The filtered water samples were subjected to characteristic assays (Tables 4.5 and 4.6). Additionally, both samples contained various background anions, including sulphate, fluoride, nitrate, and chloride, as shown in Figs. 4.20a and 4.20b.

After the water samples were filtered and diluted 10-fold with 0.1 M PBS buffer (pH 4), they were spiked with aniline in concentrations ranging from 2 to 60 µM. The performance of the ZnO-VANRs/FTO was then evaluated by measuring the concentration of aniline in both samples (Fig. 4.12f). The performance of the ZnO-VANRs/FTO electrode is summarized in

Table 4.7. Remarkably, the aniline recovery was nearly 100% both in tap and river water, even in the existence of various background anions and organic traces, as indicated in Tables 4.5 and 4.6. This demonstrates the effectiveness of the ZnO-VANRs/FTO electrode in accurately detecting aniline in complex environmental matrices. A comparison was made with HPLC to validate the aniline concentration determined by the ZnO-VANRs/FTO electrode. The concentration variation of aniline between the two methods was found to be within acceptable limits, with a maximum deviation of 9.1% in tap water and 9.8% in river water.

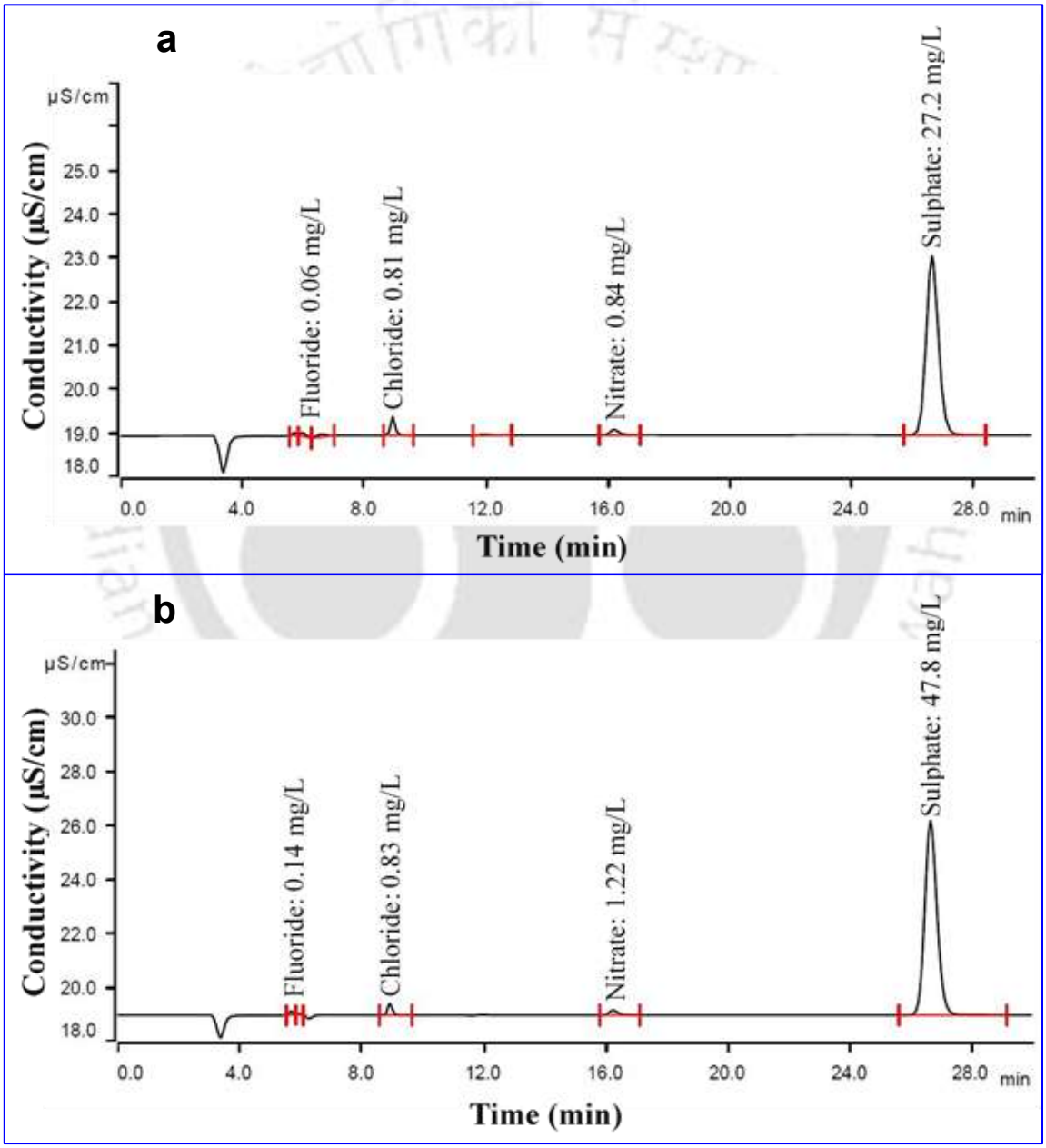

Figure 4.20: Anions concentration in (a) tap water and (b) river water.

Table 4.5: Anions concentration in tap and river water.

Ions	Anions concentration in tap water (mg/L)	Anions concentration in river water (mg/L)
Fluoride	0.06	0.14
Chloride	0.81	0.83
Nitrate	0.84	1.22
Sulphate	27.2	47.8

Table 4.6: Tap and river water characterizations.

Parameters	Tap water	River water
pH	6.35	6.74
Conductivity (µS)	279	255
TDS (mg/L)	52	50
TOC (mg/L)	0	3.83
TIC (mg/L)	8.29	1.91
TN (mg/L)	0.84	1.93

Table 4.7: Performance of ZnO-VANRs/FTO for aniline detection in environmental matrices and its comparison with HPLC.

Sample	Aniline spiked (µM)	Performance of ZnO-VANRs/FTO			Aniline determination using HPLC (µM)	Deviation (%)
		Aniline determination (µM)	Recovery (%)	RSD (%)		
Tap water	0	ND	-	-	0.4	-
	2	2.06	103.1	2.2	2.25	-9.1
	10	10.44	104.4	2.0	10.37	0.6
	30	30.79	102.6	0.6	29.78	3.3
	60	59.87	99.8	0.5	60.17	-0.5
River water	0	ND	-	-	0.42	-
	2	2.16	108.1	2.8	2.14	1.1
	10	10.37	103.7	2.3	9.36	9.8
	30	29.05	96.8	0.6	28.85	0.7
	60	60.69	101.2	1.1	58.99	2.8

4.3. Major findings

The 1D surface VANRs of ZnO fabricated on the FTO using a chemical method is an excellent platform for electrocatalytic sensing of aniline in tap and river water. ZnO-VANRs were grown up to 1.57± 0.03 µm in length with excellent crystalline nature and surface roughness of 2.4 and 4.7 folds higher than bare FTO and ZnO-seed/FTO. ZnO-VANRs formation resulted in 2.5 times more effective surface area and 86.85 % less charge transfer resistance compared to bare FTO. The fabricated ZnO-VANRs/FTO electrode exhibited well-defied redox peaks with an outstanding enhancement of peak current compared to bare FTO under identical conditions. The high temperature was favourable for aniline deposition as it could increase the current response by 81.52 % with the rise in temperature from 15 to 45 °C. ZnO-VANRs/FTO electrode could detect aniline as low as 0.193 µM with a sensitivity of 0.198 µA. $\mu M^{-1}.cm^{-2}$ in the working range of 0-20 µM, demonstrating an outstanding LOD compared to previously reported electrochemical, fluorescence, and colorimetric sensors for aniline sensing. The reversible redox reaction of aniline involving two electrons proceeded via a diffusion control process with a formal standard potential (E^0) of 0.289 V and a heterogeneous reaction rate constant (k^0) of 1.82 s^{-1}. ZnO-VANRs/FTO electrode exhibited a marginal decay (2.63 % up to the 6^{th} cycle) in aniline sensing with the reuse of the same sensing platform. However, p-nitroaniline, chlorobenzene, chlorpyrifos, Cu^{2+}, Pb^{2+}, Ni^{2+}, Cd^{2+}, albumin bovine, *Escherichia coli*, and ciprofloxacin could not alter the sensitivity and performance of aniline sensing at the ZnO-VANRs/FTO electrode. The determination of aniline spiked in tap water and river water using ZnO-VANRs/FTO electrode was comparable to HPLC. Therefore, the proposed sensor holds prospective applications due to its binder-free, easy, and reusable, offering low detection limit, high stability, repeatability, and selectivity for sensing aniline in the environmental matrix. Moreover, the integration of these ZnO VANRs with biosensing technologies can facilitate real-time sensing and quantification of aniline levels in biological samples, contributing to enhanced safety protocols in clinical and environmental fields. This capability could lead to the development of portable, efficient devices for on-site testing, making it easier to assess the presence of harmful substances in biological samples. However, the reported approaches for the formation of ZnO VANRs involve chemical-based methodologies. In contrast, bio-based synthesis of ZnO VANRs onto FTO substrate is fundamentally a challenging task.

References

Abdelmohsen, A.H., Rouby, W.M.A. El, Ismail, N., Farghali, A.A., 2017. Morphology Transition Engineering of ZnO Nanorods to Nanoplatelets Grafted Mo_8O_{23}-MoO_2 by Polyoxometalates: Mechanism and Possible Applicability to other Oxides. Sci. Rep. 7, 5946. https://doi.org/10.1038/s41598-017-05750-x

Agrahari, S., Singh, A.K., Gautam, R.K., Tiwari, I., 2023. Fabrication of gadolinium decorated spherical zinc oxide attached on carbon nanotubes (Gd@ZnO-MWCNTs) for electrochemical detection of a bisphenol derivative BPSIP in real sample matrices. J. Appl. Electrochem. 53. https://doi.org/10.1007/s10800-022-01768-w

Aguedo, J., Lorencova, L., Barath, M., Farkas, P., Tkac, J., 2020. Electrochemical Impedance Spectroscopy on 2D Nanomaterial MXene Modified Interfaces: Application as a Characterization and Transducing Tool. Chemosensors 8, 127. https://doi.org/10.3390/chemosensors8040127

Ahmad, R., Bhat, K.S., Nagal, V., Nakate, U.T., Ahmad, A., Alshammari, M.B., Alam, S., Lee, B.-I., 2024. Surface-engineered vertically-aligned ZnO nanorod for sensitive non-enzymatic electrochemical monitoring of cholesterol. Heliyon 10, e37847. https://doi.org/10.1016/j.heliyon.2024.e37847

Ahmad, R., Tripathy, N., Ahn, M.-S., Bhat, K.S., Mahmoudi, T., Wang, Y., Yoo, J.-Y., Kwon, D.-W., Yang, H.-Y., Hahn, Y.-B., 2017a. Highly Efficient Non-Enzymatic Glucose Sensor Based on CuO Modified Vertically-Grown ZnO Nanorods on Electrode. Sci. Rep. 7, 5715. https://doi.org/10.1038/s41598-017-06064-8

Ahmad, R., Tripathy, N., Ahn, M.-S., Hahn, Y.-B., 2017b. Development of highly-stable binder-free chemical sensor electrodes for p-nitroaniline detection. J. Colloid Interface Sci. 494, 300–306. https://doi.org/10.1016/j.jcis.2017.01.099

Al-She'irey, A.Y., Balouch, A., Mawarnis, E.R., Roza, L., Rahman, M.Y.A., Abdullah, Mahar, A.M., 2022. Effect of ZnO seed layer annealing temperature on the growth of ZnO nanorods and its catalytic application. Opt. Mater. (Amst). 131, 112652. https://doi.org/10.1016/j.optmat.2022.112652

Aly, A., Ghali, M., Osman, A., El Nimr, M.K., 2024. Non-synthetic luminescent graphene quantum dots in coconut water for aniline sensing applications. Mater. Res. Bull. 171, 112603. https://doi.org/10.1016/j.materresbull.2023.112603

Ameen, S., Shaheer Akhtar, M., Shik Shin, H., 2015. Highly dense ZnO nanowhiskers for the low level detection of p-hydroquinone. Mater. Lett. 155, 82–86.

https://doi.org/10.1016/j.matlet.2015.04.111

Aranthady, C., Shanbhag, G. V., Sundaram, N.G., 2022. Polyaniline/(Ta_2O_5–SnO_2) hybrid nanocomposite for efficient room temperature CO gas sensing. RSC Adv. 12, 15759–15766. https://doi.org/10.1039/D2RA00602B

Arsalan, M., Saddique, I., Baoji, M., Awais, A., Khan, I., Shamseldin, M.A., Mehrez, S., 2022. Novel Synthesis of Sensitive Cu-ZnO Nanorod–Based Sensor for Hydrogen Peroxide Sensing. Front. Chem. 10, 932985. https://doi.org/10.3389/fchem.2022.932985

Awais, A., Arsalan, M., Qiao, X., Yahui, W., Sheng, Q., Yue, T., He, Y., 2021. Facial synthesis of highly efficient non-enzymatic glucose sensor based on vertically aligned Au-ZnO NRs. J. Electroanal. Chem. 895, 115424. https://doi.org/10.1016/j.jelechem.2021.115424

Bagheri, H., Afkhami, A., Khoshsafar, H., Rezaei, M., Shirzadmehr, A., 2013. Simultaneous electrochemical determination of heavy metals using a triphenylphosphine/MWCNTs composite carbon ionic liquid electrode. Sensors Actuators B Chem. 186, 451–460. https://doi.org/10.1016/j.snb.2013.06.051

Balamurugan, K., Karthik, R., Chen, S.M., Sukanya, R., Thasma Subramanian, B., Biju, V.M.N., Shim, J.J., Breslin, C.B., 2022. Heterostructures of mixed metal oxides ($ZnMnO_3$/ZnO) synthesized by a wet-chemical approach and their application for the electrochemical detection of the drug chlorpromazine. Compos. Part B Eng. 236, 109822. https://doi.org/10.1016/j.compositesb.2022.109822

Banerjee, A.N., Kundoo, S., Saha, P., Chattopadhyay, K.K., 2003. Synthesis and Characterization of Nano-Crystalline Fluorine-Doped Tin Oxide Thin Films by Sol-Gel Method. J. Sol-Gel Sci. Technol. 28, 105–110. https://doi.org/10.1023/A:1025697322395

Bhan, C., Kumar Golder, A., 2023. Bio-based hierarchical vertically aligned 2D ZnO nanostructures for ultra selective electrochemical sensing of p-Chloroaniline. Chem. Eng. J. 475, 146122. https://doi.org/10.1016/j.cej.2023.146122

Carvalho, F.P., 2017. Pesticides, environment, and food safety. Food Energy Secur. 6, 48–60. https://doi.org/10.1002/fes3.108

Chauhan, P.S., Parekh, M., Sahoo, S., Kumar, S., Mahapatra, A. Das, Sharma, P., Panwar, V., Rao, A.M., Misra, A., 2024. Influence of electrolyte on the photo-charging capability of a ZnO–FTO supercapacitor. J. Mater. Chem. A 12, 22725–22736. https://doi.org/10.1039/D4TA04702H

Chekin, F., Bagheri, S., Abd Hamid, S.B., 2013. Synthesis of Pt doped TiO_2 nanoparticles: Characterization and application for electrocatalytic oxidation of l-methionine. Sensors Actuators B Chem. 177, 898–903. https://doi.org/10.1016/j.snb.2012.12.002

Chen, S., Liang, H., Han, D., 2010. Determination of aniline derivatives in water samples by high performance liquid chromatography coupled with on-line flow injection preconcentration. Anal. Lett. 43, 2349–2355. https://doi.org/10.1080/00032711003717398

Cheng, Z., Song, H., Zhang, X., Cheng, X., Xu, Y., Zhao, H., Gao, S., Huo, L., 2022. Enhanced non-enzyme nitrite electrochemical sensing property based on stir bar-shaped ZnO nanorods decorated with nitrogen-doped reduced graphene oxide. Sensors Actuators B Chem. 355, 131313. https://doi.org/10.1016/j.snb.2021.131313

Chiang, J., 2008. Simultaneous derivatization and extraction of anilines in waste water with dispersive liquid–liquid microextraction followed by gas chromatography–mass spectrometric detection. Talanta 75, 70–75. https://doi.org/10.1016/j.talanta.2007.10.036

Chokkareddy, R., Kanchi, S., Redhi, G.G., 2022. A novel IL-f-ZnONPs@MWCNTs nanocomposite fabricated glassy carbon electrode for the determination of sulfamethoxazole. J. Mol. Liq. 359, 119232. https://doi.org/10.1016/j.molliq.2022.119232

Chokkareddy, R., Kilele, J.C., Redhi, G.G., 2023. A novel electron transfer kinetic for terbutaline detection using TiO_2-MWCNTs-IL modified GCE. Mater. Chem. Phys. 307, 128104. https://doi.org/10.1016/j.matchemphys.2023.128104

Chokkareddy, R., Redhi, G.G., 2022. Fe_3O_4 Nanorods-RGO-ionic Liquid Nanocomposite Based Electrochemical Sensor for Aflatoxin B1 in Ground Paprika. Electroanalysis 34, 501–511. https://doi.org/10.1002/elan.202100377

Cirocka, A., Zarzeczańska, D., Wcisło, A., 2021. Good choice of electrode material as the key to creating electrochemical sensors-characteristics of carbon materials and transparent conductive oxides (TCO). Materials (Basel). 14, 4743. https://doi.org/10.3390/ma14164743

Das, D., Bhan, C., Mukherjee, C., Golder, A.K., 2024. Improved selectivity of electrochemical aniline sensing using one-dimensional silver nanorods with high aspect ratio synthesized by ascorbic acid assisted method. Anal. Chim. Acta 1310, 342697. https://doi.org/10.1016/j.aca.2024.342697

Dash, S.R., Bag, S.S., Golder, A.K., 2022. Carbon Dots Derived from Waste Psidium Guajava Leaves for Electrocatalytic Sensing of Chlorpyrifos. Electroanalysis 34, 1141–1149. https://doi.org/10.1002/elan.202100344

Dash, S.R., Bag, S.S., Golder, A.K., 2021. Bio-inspired PtNPs/Graphene nanocomposite based electrocatalytic sensing of metabolites of dipyrone. Anal. Chim. Acta 1167, 338562.

https://doi.org/10.1016/j.aca.2021.338562

Dash, S.R., Bag, S.S., Golder, A.K., 2020. Synthesis of highly structured spherical Ag@Pt core-shell NPs using bio-analytes for electrocatalytic Pb(II) sensing. Sensors Actuators B Chem. 314, 128062. https://doi.org/10.1016/j.snb.2020.128062

Dash, S.R., Bag, S.S., Golder, A.K., 2018. Synergized AgNPs formation using microwave in a bio-mediated route: Studies on particle aggregation and electrocatalytic sensing of ascorbic acid from biological entities. J. Electroanal. Chem. 827, 181–192. https://doi.org/10.1016/j.jelechem.2018.09.023

Ding, L., Su, B., 2015. A non-enzymatic hydrogen peroxide sensor based on platinum nanoparticle–polyaniline nanocomposites hosted in mesoporous silica film. J. Electroanal. Chem. 736, 83–87. https://doi.org/10.1016/j.jelechem.2014.11.001

Dulta, K., Koşarsoy Ağçeli, G., Chauhan, P., Jasrotia, R., Chauhan, P.K., 2022. Ecofriendly Synthesis of Zinc Oxide Nanoparticles by Carica papaya Leaf Extract and Their Applications. J. Clust. Sci. 33, 603–617. https://doi.org/10.1007/s10876-020-01962-w

Elgrishi, N., Rountree, K.J., McCarthy, B.D., Rountree, E.S., Eisenhart, T.T., Dempsey, J.L., 2018. A Practical Beginner's Guide to Cyclic Voltammetry. J. Chem. Educ. 95, 197–206. https://doi.org/10.1021/acs.jchemed.7b00361

Ettadili, F.E., Aghris, S., Laghrib, F., Farahi, A., Bakasse, M., Lahrich, S., El Mhammedi, M.A., 2023. Electrochemical detection of ornidazole in commercial milk and water samples using an electrode based on green synthesis of silver nanoparticles using cellulose separated from Phoenix dactylifera seed. Int. J. Biol. Macromol. 242, 124995. https://doi.org/10.1016/j.ijbiomac.2023.124995

Gao, X., Huang, R., Fang, W., Huang, W., Yin, Z., Liu, Y., Huang, X., Ding, L., Peng, H., Fang, Y., 2022. A portable fluorescence sensor with improved performance for aniline monitoring. Adv. Mater. Interfaces 9, 2201275. https://doi.org/10.1002/admi.202201275

Gawal, P.M., Golder, A.K., 2024. Plant-Based Phytochemicals for Synthesis of Z-Scheme In_2O_3/CdS Heterostructures: DFT Analysis and Photocatalytic CO_2 Reduction to HCOOH and CO. Langmuir 40, 13538–13549. https://doi.org/10.1021/acs.langmuir.4c01015

Gogoi, D., Koyani, R., Golder, A.K., Peela, N.R., 2020. Enhanced photocatalytic hydrogen evolution using green carbon quantum dots modified 1-D CdS nanowires under visible light irradiation. Sol. Energy 208, 966–977. https://doi.org/10.1016/j.solener.2020.08.061

Gumpu, M.B., Veerapandian, M., Krishnan, U.M., Rayappan, J.B.B., 2017. Simultaneous electrochemical detection of Cd(II), Pb(II), As(III) and Hg(II) ions using ruthenium(II)-textured graphene oxide nanocomposite. Talanta 162, 574–582.

https://doi.org/10.1016/j.talanta.2016.10.076

Huang, S.Z., Tang, Q., Wei, K.N., Yang, R.P., Tao, Z., Huang, Y., Xiao, X., 2022. A colorimetric supramolecular sensor array based on charge-transfer complexes for multiplex aniline and phenolic pollutants detection. Anal. Chim. Acta 1233, 340504. https://doi.org/10.1016/j.aca.2022.340504

Hussain, M., Sun, H., Karim, S., Nisar, A., Khan, M., ul Haq, A., Iqbal, M., Ahmad, M., 2016. Noble metal nanoparticle-functionalized ZnO nanoflowers for photocatalytic degradation of RhB dye and electrochemical sensing of hydrogen peroxide. J. Nanoparticle Res. 18, 95. https://doi.org/10.1007/s11051-016-3397-y

Hussein, B.A., Tsegaye, A.A., Shifera, G., M. Taddesse, A., 2023. A sensitive non-enzymatic electrochemical glucose sensor based on a ZnO/Co_3O_4/reduced graphene oxide nanocomposite. Sensors & Diagnostics 2, 347–360. https://doi.org/10.1039/D2SD00183G

Jain, S., Chakraborty, A., Sharma, B., Sarma, T.K., 2022a. Cu^{2+} ion doping-induced self-assembled ZnO-Cu_xO nanostructures for electrochemical sensing of hydrogen peroxide and p-Nitrophenol. ACS Appl. Nano Mater. 5, 11973–11983. https://doi.org/10.1021/acsanm.2c03073

Jain, S., Chakraborty, A., Sharma, B., Sarma, T.K., 2022b. Cu^{2+} Ion Doping-Induced Self-Assembled ZnO-Cu_xO Nanostructures for Electrochemical Sensing of Hydrogen Peroxide and p-Nitrophenol. ACS Appl. Nano Mater. 5, 11973–11983. https://doi.org/10.1021/acsanm.2c03073

Kara, I., Hafedh, A.I.R., Alhusseinawi, N.K.H., Kayış, A.F., Yalçınkaya, Ö., Acar, B.C., Yuksekdag, Z., Ozen, Y., Gençyılmaz, O., Ozkan, E.C., Oner, H., 2024. Analyzing antimicrobial activity of ZnO/FTO, Sn–Cu-doped ZnO/FTO thin films: Production and characterizations. Microsc. Res. Tech. 1–14. https://doi.org/10.1002/jemt.24638

Karuppusamy, N., Jeyaraman, A., Chen, S.-M., Manavalan, S., Mi Jung, S., 2023. Electronic structure modulation on SnO_2 and hexagonal boron nitride with sulfur atom for effective electrochemical sensing of Bendiocarb. Chem. Eng. J. 475, 145834. https://doi.org/10.1016/j.cej.2023.145834

Kaur, A., Chakraborty, U., Chauhan, M., Sharma, R., Kaur, G., Chaudhary, G.R., 2022. Choline acetate modified ZnO nanostructure as efficient electrochemical sensor for hydrazine detection. Electrochim. Acta 419, 140384. https://doi.org/10.1016/j.electacta.2022.140384

Khan, R., Periyayya, U., Kim, G.C., Lee, I.-H., 2019. Fabrication of ultra-sensitive piperidine

chemical sensor with a direct grown well-aligned ZnO nanorods on FTO substrate as a working electrode. Solid State Sci. 97, 105986. https://doi.org/10.1016/j.solidstatesciences.2019.105986

Khasanah, M., Darmokoesoemo, H., Sari, N.M., Kadmi, Y., Elmsellem, H., Kusuma, H.S., 2017. RETRACTED: Development of electrode carbon paste modified by molecularly imprinted polymer as sensor for analysis of creatinine by potentiometric. Results Phys. 7, 1808–1817. https://doi.org/10.1016/j.rinp.2017.05.012

Kilele, J.C., Chokkareddy, R., Redhi, G.G., 2021. Ultra-sensitive electrochemical sensor for fenitrothion pesticide residues in fruit samples using IL@$CoFe_2O_4$NPs@MWCNTs nanocomposite. Microchem. J. 164, 106012. https://doi.org/10.1016/j.microc.2021.106012

Koçak, B., İpek, Y., Keçeci, A., 2023. A novel electrochemical sensor for metoprolol analysis based on glutardialdehyde–zinc oxide modified boron doped diamond electrode. Diam. Relat. Mater. 131. https://doi.org/10.1016/j.diamond.2022.109558

Kokulnathan, T., Wang, T.-J., Murugesan, T., Anthuvan, A.J., Kumar, R.R., Ahmed, F., Arshi, N., 2023. Structural growth of zinc oxide nanograins on carbon cloth as flexible electrochemical platform for hydroxychloroquine detection. Chemosphere 312, 137186. https://doi.org/10.1016/j.chemosphere.2022.137186

Kumar, A., Das, C., 2024. Corrosion inhibition of mild steel by Praecitrullus fistulosus (tinda fruit and peel) extracts. Sci. Total Environ. 929, 172569. https://doi.org/10.1016/j.scitotenv.2024.172569

Kumar, A., Das, C., 2023. A novel eco-friendly inhibitor of chayote fruit extract for mild steel corrosion in 1 M HCl: Electrochemical, weight loss studies, and the effect of temperature. Sustain. Chem. Pharm. 36, 101261. https://doi.org/10.1016/j.scp.2023.101261

Le Nhat Trang, N., Thi Nguyet Nga, D., Tufa, L.T., Tran, V.T., Hung, T.-T., Ngoc Phan, V., Pham, T.N., Hoang, V.-T., Le, A.-T., 2023. Unveiling the effect of crystallinity and particle size of biogenic Ag/ZnO nanocomposites on the electrochemical sensing performance of carbaryl detection in agricultural products. RSC Adv. 13, 8753–8764. https://doi.org/10.1039/D3RA00399J

Lee, K.-U., Tran, T.H., Kim, S.H., Shin, H.-J., 2017. Fabrication of nanoporous gold thin films on glass substrates for amperometric sensing of aniline. J. Alloys Compd. 713, 132–137. https://doi.org/10.1016/j.jallcom.2017.04.173

Li, D., Li, D.-W., Fossey, J.S., Long, Y.-T., 2010. Portable surface-enhanced raman scattering sensor for rapid detection of aniline and phenol derivatives by on-site electrostatic

preconcentration. Anal. Chem. 82, 9299–9305. https://doi.org/10.1021/ac101812x

Li, J., Wang, Q., Liu, Y., Jiang, Z., Liu, J., Li, H., Yuan, X., 2021. Boron/nitrogen co-doped diamond electrode for highly efficient electrochemistry detection of aniline. Funct. Diam. 1, 135–142. https://doi.org/10.1080/26941112.2021.1939170

Li, L., Zou, J.-Y., You, S.-Y., Cui, H.-M., Zeng, G.-P., Cui, J.-Z., 2017. Tuning the luminescence of two 3d–4f metal–organic frameworks for the fast response and highly selective detection of aniline. Dalt. Trans. 46, 16432–16438. https://doi.org/10.1039/C7DT03545D

Liang, Q., Xiao, W., Zhang, C., Zhu, D., Wang, S.-L., Tian, S.-Y., Long, T., Yue, E.-L., Wang, J.-J., Hou, X.-Y., 2023. MOFs-based Fe@YAU-101/GCE electrochemical sensor platform for highly selective detecting trace multiplex heavy metal ions. Talanta 259, 124491. https://doi.org/10.1016/j.talanta.2023.124491

Lin, C.-J., Lin, Y.-H., Chiang, T.-C., Yu, C.-Y., 2022. Synthesis of the polymers containing norbornene and tetraphenylethene by ring-opening metathesis polymerization and their structural characterization, aggregation-induced emission and aniline detection. Polymer (Guildf). 260, 125374. https://doi.org/10.1016/j.polymer.2022.125374

Liu, L., Yao, Z., Ye, Y., Liu, C., Lin, Q., Chen, S., Xiang, S., Zhang, Z., 2019. Enhancement of Intrinsic Proton Conductivity and Aniline Sensitivity by Introducing Dye Molecules into the MOF Channel. ACS Appl. Mater. Interfaces 11, 16490–16495. https://doi.org/10.1021/acsami.8b22327

Liu, Z., Xia, X., Guan, H.-K., Liu, Q., Zhao, S.-S., Cheng, X.-L., Xu, Q.-Q., Li, S.-S., 2022. Hypersensitized electrochemical detection of Hg(II) based on tunable sulfur-doped porous Co_3O_4 nanosheets: Promotion Co^{2+}/Co^{3+} valence change cycle and adsorption via introducing S. Chem. Eng. J. 435, 134950. https://doi.org/10.1016/j.cej.2022.134950

Lotfi, S., Veisi, H., Karmakar, B., 2021. A convenient strategy for the electrochemical evaluation of acetaminophen and caffeine in combined drugs and biological samples over TiO_2@polymethyldopa/Pd nanocomposite functionalized glassy carbon electrodes. Measurement 186, 110156. https://doi.org/10.1016/j.measurement.2021.110156

Lyons, C.D., Katz, S.E., Bartha, R., 1985. Persistence and mutagenic potential of herbicide-derived aniline residues in pond water. Bull. Environ. Contam. Toxicol. 35, 696–703. https://doi.org/10.1007/BF01636575

Mali, S.S., Kim, H., Patil, P.S., Hong, C.K., 2013. Chemically grown vertically aligned 1D ZnO nanorods with CdS coating for efficient quantum dot sensitized solar cells (QDSSC): a controlled synthesis route. Dalt. Trans. 42, 16961. https://doi.org/10.1039/c3dt51287h

Malode, S.J., Keerthi, P.K., Shetti, N.P., Kulkarni, R.M., 2020. Electroanalysis of Carbendazim using MWCNT/Ca-ZnO Modified Electrode. Electroanalysis 32, 1590–1599. https://doi.org/10.1002/elan.201900776

Manivannan, K., Sivakumar, M., Cheng, C.-C., Lu, C.-H., Chen, J.-K., 2019. An effective electrochemical detection of chlorogenic acid in real samples: Flower-like ZnO surface covered on PEDOT:PSS composites modified glassy carbon electrode. Sensors Actuators B Chem. 301, 127002. https://doi.org/10.1016/j.snb.2019.127002

McCarter, W.J., Taha, H.M., Suryanto, B., Starrs, G., 2015. Two-point concrete resistivity measurements: interfacial phenomena at the electrode–concrete contact zone. Meas. Sci. Technol. 26, 085007. https://doi.org/10.1088/0957-0233/26/8/085007

Mei, H., Xie, J., Li, Z., Lou, C., Lei, G., Liu, X., Zhang, J., 2022. Rational design of ZnO@ZIF-8 nanoarrays for improved electrochemical detection of H_2O_2. CrystEngComm 24, 1645–1654. https://doi.org/10.1039/D1CE01704G

Messmer, A.S., Nickel, C.H., Bareiss, D., 2015. p-Chloroaniline poisoning causing methemoglobinemia: A case report and review of the literature. Case Rep. Emerg. Med. 2015, 1–4. https://doi.org/10.1155/2015/208732

Mohammed, M., Mekala, L.P., Chintalapati, S., Chintalapati, V.R., 2020. New insights into aniline toxicity: Aniline exposure triggers envelope stress and extracellular polymeric substance formation in Rubrivivax benzoatilyticus JA2. J. Hazard. Mater. 385, 121571. https://doi.org/10.1016/j.jhazmat.2019.121571

Mohan, B., Kumari, R., Virender, Singh, G., Singh, K., Pombeiro, A.J.L., Yang, X., Ren, P., 2023. Covalent organic frameworks (COFs) and metal–organic frameworks (MOFs) as electrochemical sensors for the efficient detection of pharmaceutical residues. Environ. Int. 175, 107928. https://doi.org/10.1016/j.envint.2023.107928

Mudusu, D., Nandanapalli, K.R., Dugasani, S.R., Park, S.H., Tu, C.W., 2016. Zinc Oxide Nanorods Shielded with an Ultrathin Nickel Layer: Tailoring of Physical Properties. Sci. Rep. 6, 28561. https://doi.org/10.1038/srep28561

Okumura, T., Imamura, K., Nishikawa, Y., 1996. Determination of anilines in river water, sediment, and fish samples by gas chromatography-mass spectrometry. J. Chromatogr. Sci. 34, 190–198. https://doi.org/10.1093/chromsci/34.4.190

Pandey, P., Parra, M.R., Haque, F.Z., Kurchania, R., 2017. Effects of annealing temperature optimization on the efficiency of ZnO nanoparticles photoanode based dye sensitized solar cells. J. Mater. Sci. Mater. Electron. 28, 1537–1545. https://doi.org/10.1007/s10854-016-5693-9

Rajamanickam, S., Mohammad, S.M., Hassan, Z., 2020. Effect of zinc acetate dihydrate concentration on morphology of ZnO seed layer and ZnO nanorods grown by hydrothermal method. Colloid Interface Sci. Commun. 38, 100312. https://doi.org/10.1016/j.colcom.2020.100312

Ravi, R., Golder, A.K., 2023a. A tuneable bioinspired process of Pt-doping in TiO_2 for improved photoelectrochemical and photocatalytic functionalities. Colloids Surfaces A Physicochem. Eng. Asp. 663, 131034. https://doi.org/10.1016/j.colsurfa.2023.131034

Ravi, R., Golder, A.K., 2023b. Bio-based Au Doping with Dominant Oxygen Vacancies and Ti^{3+} Defects on Photocatalytic Functionalities of TiO_2. Ind. Eng. Chem. Res. 62, 20702–20715. https://doi.org/10.1021/acs.iecr.3c02850

Ravi, R., Kumar Golder, A., 2024. Efficient recovery of TiO_2 and Pt-doped TiO_2 photocatalysts in wastewater treatment using a pilot-scale cross-flow ultrafiltration membrane system. Sep. Purif. Technol. 339, 126710. https://doi.org/10.1016/j.seppur.2024.126710

Sadhasivam, S., Sadhasivam, T., Oh, T.H., 2023. Electrochemically synthesized Cd doped ZnO nanorods and integrated atomic Cd-S bridged Cd:ZnO/CdS heterostructure photoanode for enhanced visible light responsive water oxidation applications. J. Electroanal. Chem. 934, 117289. https://doi.org/10.1016/j.jelechem.2023.117289

Saravanan, S., Mathai, C.J., Venkatachalam, S., Anantharaman, M.R., 2004. Low k thin films based on rf plasma-polymerized aniline. New J. Phys. 6, 64–64. https://doi.org/10.1088/1367-2630/6/1/064

Shukla, G., Kumar, C., Angappane, S., 2019. Structural properties and wettability of TiO_2 nanorods. Phys. status solidi 256. https://doi.org/10.1002/pssb.201900032

Singh, S., Kumar, N., Kumar, M., Jyoti, Agarwal, A., Mizaikoff, B., 2017. Electrochemical sensing and remediation of 4-Nitrophenol using bio-synthesized copper oxide nanoparticles. Chem. Eng. J. 313, 283–292. https://doi.org/10.1016/j.cej.2016.12.049

Son, N.T., Noh, J.-S., Park, S., 2016. Role of ZnO thin film in the vertically aligned growth of ZnO nanorods by chemical bath deposition. Appl. Surf. Sci. 379, 440–445. https://doi.org/10.1016/j.apsusc.2016.04.107

Stanley, M.M., Sriram, B., Wang, S.-F., Sherlin, A., Kogularasu, S., Lee, Y.-Y., George, M., 2024. Rational confinement of ternary layered double hydroxide within three-dimensional graphene aerogel: An electrochemical tool for propyl gallate sensing. Chem. Eng. J. 485, 149682. https://doi.org/10.1016/j.cej.2024.149682

Wan, Q., Li, J., Liu, Z., Han, L., Huang, S., Wang, Z., 2023. Fabrication of Nanoporous Gold via an Improved Solid-Phase Method for Non-Enzymatic Detection of Aniline. Metals

(Basel). 13, 754. https://doi.org/10.3390/met13040754

Wang, B., He, R., Xie, L.-H., Lin, Z.-J., Zhang, X., Wang, J., Huang, H., Zhang, Z., Schanze, K.S., Zhang, J., Xiang, S., Chen, B., 2020. Microporous Hydrogen-Bonded Organic Framework for Highly Efficient Turn-Up Fluorescent Sensing of Aniline. J. Am. Chem. Soc. 142, 12478–12485. https://doi.org/10.1021/jacs.0c05277

Wang, N., Zhu, J., Zheng, X., Xiong, F., Huang, B., Shi, J., Li, C., 2014. A facile two-step method for fabrication of plate-like WO_3 photoanode under mild conditions. Faraday Discuss. 176, 185–197. https://doi.org/10.1039/C4FD00139G

Wang, P., Du, M., Zhang, M., Zhu, H., Bao, S., Zou, M., Yang, T., 2014. Facile fabrication of AuNPs/PANI/HNTs nanostructures for high-performance electrochemical sensors towards hydrogen peroxide. Chem. Eng. J. 248, 307–314. https://doi.org/10.1016/j.cej.2014.03.044

Wang, Y., Limon-Petersen, J.G., Compton, R.G., 2011. Measurement of the diffusion coefficients of $[Ru(NH_3)_6]^{3+}$ and $[Ru(NH_3)_6]^{2+}$ in aqueous solution using microelectrode double potential step chronoamperometry. J. Electroanal. Chem. 652, 13–17. https://doi.org/10.1016/j.jelechem.2010.12.011

Wiench, P., González, Z., Menéndez, R., Grzyb, B., Gryglewicz, G., 2018. Beneficial impact of oxygen on the electrochemical performance of dopamine sensors based on N-doped reduced graphene oxides. Sensors Actuators B Chem. 257, 143–153. https://doi.org/10.1016/j.snb.2017.10.106

Xing, N., Lyu, Y., Zhao, W., Lan, Z., Zuo, M., Li, J., 2024. Micromotor-assisted bifunctional platform for efficient detection and removal of aniline. Environ. Sci. Nano. https://doi.org/10.1039/D4EN00097H

Yan, F., Su, B., 2016. Tailoring Molecular Permeability of Nanochannel-Micelle Membranes for Electrochemical Analysis of Antioxidants in Fruit Juices without Sample Treatment. Anal. Chem. 88, 11001–11006. https://doi.org/10.1021/acs.analchem.6b02823

Zhang, Y., Wu, J., Zhao, S., Tang, X., He, Z., Huang, K., Yu, H., Zou, Z., Xiong, X., 2023. Self-assembled ZnO microspheres coated with carbon dot-doped CoNi LDH wrinkled films as electrochemical sensors for highly sensitive detection of hydrazine. Anal. Methods 15, 304–310. https://doi.org/10.1039/D2AY01698B

Zhao, Y., Tao, Y., Huang, Q., Huang, J., Kuang, J., Gu, R., Zeng, P., Li, H.-Y., Liang, H., Liu, H., 2022. Electrochemical biosensor employing Bi_2S_3 nanocrystals-modified electrode for bladder cancer biomarker detection. Chemosensors 10, 48. https://doi.org/10.3390/chemosensors10020048

Zhou, L., Yang, R., Li, X., Dong, N., Zhu, B., Wang, J., Lin, X., Su, B., 2023. COF-Coated Microelectrode for Space-Confined Electrochemical Sensing of Dopamine in Parkinson's Disease Model Mouse Brain. J. Am. Chem. Soc. 145, 23727–23738. https://doi.org/10.1021/jacs.3c08256

Zhuang, Z., Chen, Y., Chen, K., Liu, Z., Guo, Z., Huang, X., 2023. In-situ synthesis of ZnO onto nanoporous gold microelectrode for the electrochemical sensing of arsenic(III) in near-neutral conditions. Sensors Actuators B Chem. 378, 133184. https://doi.org/10.1016/j.snb.2022.133184

CHAPTER 5

Bio-based Hierarchical Vertically Aligned 2D ZnO Nanostructures for Ultra Selective Electrochemical Sensing of p-Chloroaniline

In this chapter, we have synthesized hierarchical 2D vertically aligned nanostructures (VANs) of ZnO onto the surface of FTO glass via a bioinspired route using the bio-extract of Sechium edule fruit for targeted electrocatalytic sensing of p-Chloroaniline (p-CA). This reusable sensor could eliminate the quick delamination of catalysts from the electrode surface. Furthermore, the practical applications of the fabricated sensor were tested to detect and determine p-CA in the environmental matrix.

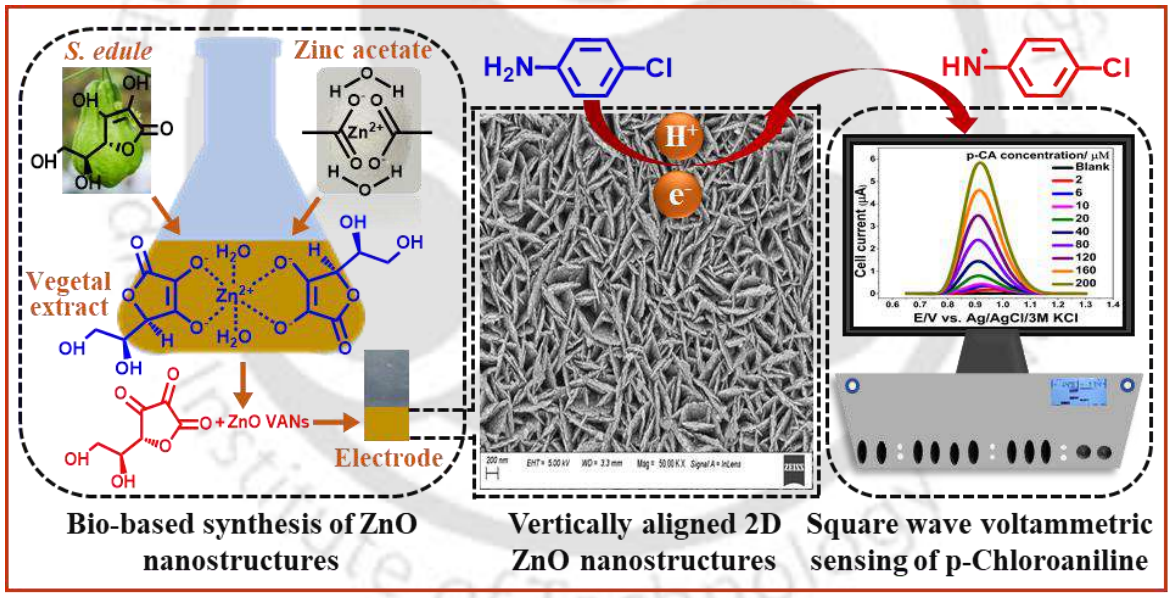

Chapter highlights

- Bio-based formation of vertically aligned nanostructures of 2D ZnO onto FTO
- VANs/ZnO(bio) catalyzed p-Chloroaniline sensing by square wave voltammetry
- p-Chloroaniline is sensed thru single proton and single electron transfer reaction
- Excellent detection limit of 0.021 µM and sensitivity of 0.194 µA. $\mu M^{-1}.cm^{-2}$
- Selective p-Chloroaniline sensing free of common cations/anions interference

5.1. Background and executive motivation

The pollutants of emerging nature are major concerns of the environmental scientist as their long-term health and environmental consequences are unknown to a large extent. p-Chloroaniline (p-CA), a derivative of aniline is extensively used as a precursor for a variety of commercial products, i.e. pesticides (anilofos, chlorphthalim, and monolinuron), herbicides (monuron), insecticides (diflubenzuron), pharmaceuticals, pigments, painting, polymer, rubber, and explosive (Mohamadighader et al., 2020). The release of p-CA in the environment could lead to a diverse impact on human health, and it can potentially cause methemoglobinemia (Messmer et al., 2015). The existence of p-CA in the environment can be monitored by high-performance liquid chromatography (Havlíková et al., 2007), gas chromatography (Gavlick and Davis, 1994), liquid chromatography-tandem mass spectrometry (Gonçalves et al., 2016), and mass spectrometry (Arratia et al., 2019). All these methods involve laboratory installation and trained workmanship triggering high analytical cost. A low-cost, ultra-sensitive, and environmentally benign method is highly imperative for in-situ p-CA detection and determination.

Electrochemical sensors are reported to be effective for the determination of trace analytes such as agriculture pesticides (Ezhil Vilian et al., 2022) and their intermediates (Castro et al., 2020; Khan et al., 2022), pharmaceuticals (Imran et al., 2023), heavy metal ions (Dash et al., 2020), nitrite (Salagare et al., 2021), etc. They are merited with low-cost, easy sample preparation, low detection limit, and high sensitivity and selectivity towards the target analyte. Moreover, the modification of the electrode surface by using metal, metal oxide, and metal sulphide nanocatalysts such as AgNPs (Mohammad et al., 2022), AuNPs (Wu et al., 2022), ZnO (Ahmad et al., 2017; Chakraborty et al., 2023), Co_3O_4 (Liu et al., 2022), Bi_2S_3 (Ganesamurthi et al., 2022), CdS (Lotfi et al., 2022), etc. could further improve the performance of the electrochemical sensors by increasing specific reaction sites, chemical stability, and surface roughness. However, a quick delamination of catalysts embedded at the electrode surface is a major setback, and it could limit the life and reproducibility of the sensing response. In fact, the growth of catalyst directly on the support electrode surface could eliminate the entire process involved for its surface-coating. It in turns could increase the stability of the sensors by minimizing the potential problem of catalyst delamination.

In the recent studies, it has been reported that the formation of vertically aligned nanostructures (VANs) of metals (Wu et al., 2015), metal oxides (Wang et al., 2010), and metal sulfides (Tang et al., 2016) onto the surface of fluorine-doped tin oxide (FTO)/Indium tin oxide

(ITO) glass substrates could enhance the performance of the electrochemical sensors by providing improved charge transport properties, high surface area, chemical stability, and surface roughness. High surface roughness increases the maximum nucleation site. High surface area allows the transfer of a large number of ions inside or/and outside of the electrode surface area, which maximizes the docking site for the target analytes per unit electrode area. However, the reported approaches for the formation of VANs involve chemical-based methodologies.

At the same time, engineered metal oxides nanomaterials such as ZnO (Manimozhi et al., 2022; Oh et al., 2021; Sharwani et al., 2022), CuO (Pino et al., 2016), Bi_2O_3 (Kokulnathan et al., 2021), SnO_2 (Supraja et al., 2019), and NiO (Bakhsh et al., 2021) have attracted immense research attractions for various catalytic applications, namely electrochemical sensing, CO_2 reduction, degradation, antimicrobial activity, water splitting, dye removal, lithium-ion batteries, etc. (Ravi and Pandey, 2019; Ravi and Golder, 2023a). Among them in particular, ZnO-based nanomaterials are merited with high excitation energy (60 meV) and wide bandgap (3.37 eV) for its strong photo- and electro-catalytic functionalities (Ahmad et al., 2017). ZnO nanoparticles are easy to synthesize and exhibit high crystallinity, biocompatibility, and excellent electrical properties (Hahn, 2011). In fact, the growth of VANs of ZnO (chemical-based) showed excellent sensing performance for biological and chemical analytes (Ahmad et al., 2012b, 2012a). Bio-based synthesis of VANs of metal oxide onto the surface of FTO substrate is fundamentally a challenging task. In this work, we report a greener route for the synthesis of VANs of ZnO.

The source of the bio-extract was selected considering factors like availability, reducing substance contents, economic importance, growth characteristics, etc. Diverse varieties of tropical plants are available in the northeastern part of India. They could be potential sources of reducing and capping agents that can be used for synthesizing metal nanostructures. Chowdhury et al. (2023) synthesized 1D Bi_2S_3 nanorods via a bioinspired method using *Sechium edule* fruit extract for electrochemical CO_2 conversion to formate with a faradaic efficiency of 92.3 % (Chowdhury et al., 2023). ZnO nanoparticles were synthesized via a green method using an aqueous extract of *Citrus sinensis* (orange) peel for electrochemical sensing of formaldehyde with a detection limit of 18 µM (Wicaksono et al., 2022). *Sechium edule* fruits contain abundant amounts of reducing analytes (Ordonez et al., 2006), including ascorbic acid (AA) (0.294 mg/g on the dry basis) (Rao and Golder, 2016), amino acids (12.9 mg/g on the dry basis), flavonoids (19.3 mg/g on the dry basis) (Rao and Golder, 2016), and polyphenols (Flick

et al., 1978). The phytochemicals present in the bio-extract of *Sechium edule* have been exploited for the growth and formation of stable VANs of ZnO on the FTO substrate.

In this chapter, we have reported hierarchical 2D VANs of ZnO onto the surface of FTO glass via a bioinspired route using the bio-extract of *Sechium edule* fruit for targeted electrocatalytic sensing of p-CA. This reusable sensor could eliminate the quick delamination of catalysts from the electrode surface. Furthermore, the practical applications of the fabricated sensor were examined to detect and determine p-CA in the environmental matrix. The bio-based development of vertically aligned 2D ZnO nanostructures for electrocatalytic sensing of p-CA is reported for the time.

5.2. Result and discussions

5.2.1. Characteristic results of ZnO-VANs(bio)/FTO

5.2.1.1 *FESEM analysis*

Fig. 5.1 depicts the FESEM images (top-view) of (a) FTO(bare), (b) after seed layer deposition on FTO (ZnO@seed/FTO), (c, d, e, f, and g) bioinspired synthesized ZnO nanostructures on seeded FTO at pH 3, 5, 7, 9, and 11 (ZnO-VANs(bio)/FTO@pH3, ZnO-VANs(bio)/FTO@pH5, ZnO-VANs(bio)/FTO@pH7, ZnO-VANs(bio)/FTO@pH9, and ZnO-VANs(bio)/FTO@pH11), respectively, (h) control (same volume DI water used instead of bio-extract) synthesis of ZnO nanostructures on seeded FTO at pH 7 (ZnO-H_2O(control)/FTO@pH7), and (i) cross-sectional view of ZnO-VANs(bio)/FTO@pH7. Fig. 5.1a shows that the surface of FTO(bare) is uneven. The surface of FTO(bare) became smooth with the development of seed layer (Fig. 5.1b), and the roughness was decreased by about 2-folds in comparison to the bare FTO (Figs. 5.4a and 5.4b).

pH is a crucial parameter for the growth of ZnO-VANs(bio) on FTO. However, hardly any ZnO VANs were grown at pH 3 (Fig. 5.1c). With increasing pH values from 3 to 5, the growth of ZnO was noted with inter-connected spherical nanostructures (Fig. 5.1d). At pH 7, ZnO-VANs(bio) with good surface roughness was observed (Fig. 5.1e), which about 2.2 folds higher than of ZnO@seed/FTO (Figs. 5.4b and 5.4c). At a larger pH value (9-11), narrow ZnO nanostructures were formed instead of growth of vertical structures of ZnO on FTO (Figs. 5.1f and 5.1g). An optimal pH for the growth of ZnO-VANs(bio) is found to be pH 7 (Fig. 5.1e). A control experiment was performed using H_2O at pH 7 in place of bio-extract (Fig. 5.1h). The formation of loosely packed ZnO particles was noted. The FTO and seed layer thicknesses are determined to be 295 nm and 240 nm, respectively (Fig. 5.1i). The length and thickness of

ZnO-VANs(bio)/FTO@pH7 are determined to be 820 nm (Fig. 5.1i) and 27.11 nm (Fig. 5.1e), respectively. The reproducibility of ZnO-VANs(bio)/FTO@pH7 exhibited no noteworthy changes in morphology across the three batches of nanostructures (Fig. 5.2). The pH impact on the morphological characteristics of ZnO nanostructure has also been reported earlier during synthesis of ZnO nanorods (Lee et al., 2008; Rafaie et al., 2014), and ZnO nanoflowers (Wahab et al., 2009).

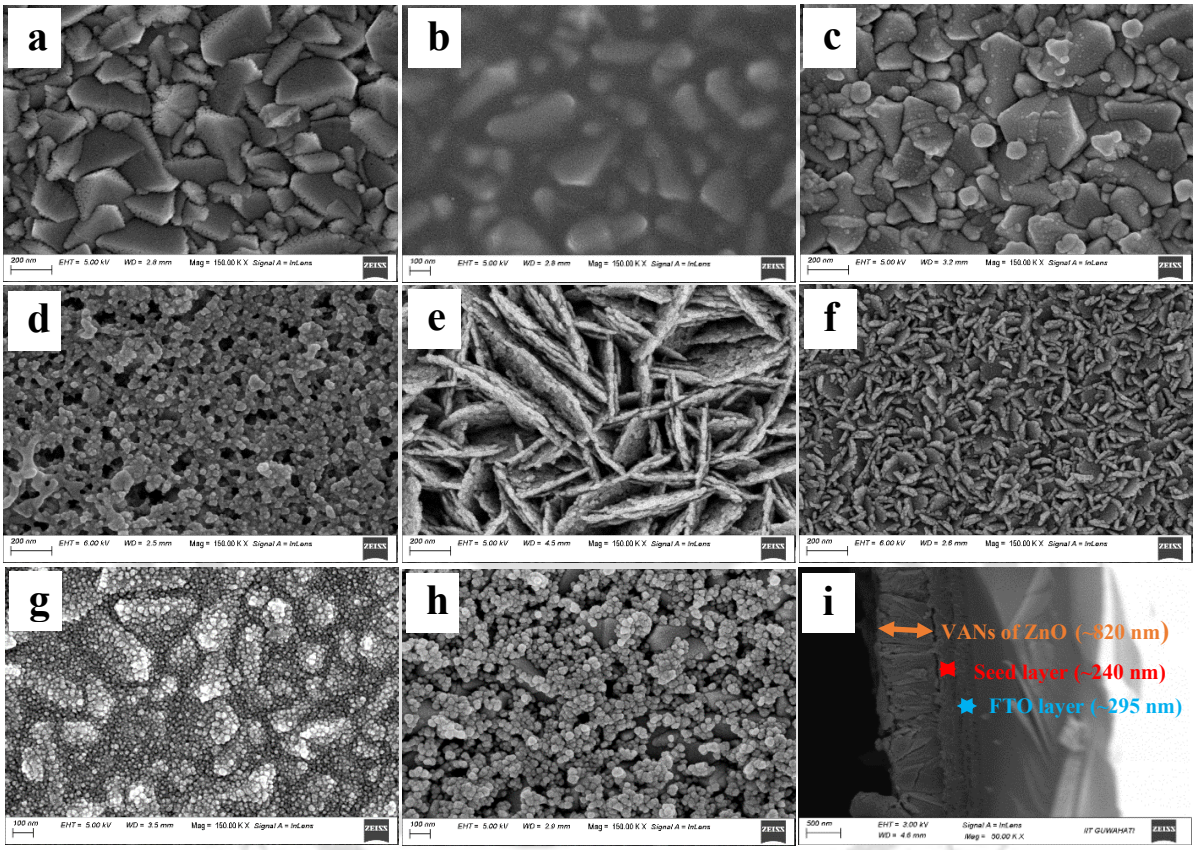

Figure 5.1: FESEM images (top view) of (a) FTO(bare), (b) ZnO@seed/FTO, (c) ZnO-VANs(bio)/FTO@pH3, (d) ZnO-VANs(bio)/FTO@pH5, (e) ZnO-VANs(bio)/FTO@pH7, (f) ZnO-VANs(bio)/FTO@pH9, (g) ZnO-VANs(bio)/FTO@pH11, (h) ZnO-H_2O(control)/FTO@pH7, and (i) cross-sectional view of ZnO-VANs(bio)/FTO@pH7.

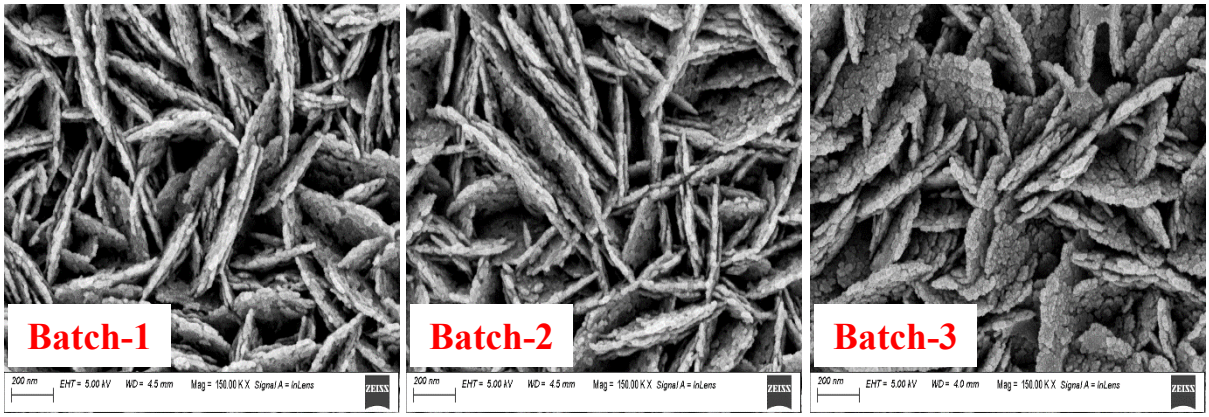

Figure 5.2: Reproducibility of ZnO-VANs(bio)/FTO@pH7 formation in three different batches under identical synthesis conditions.

5.2.1.2 *XRD analysis*

X-ray diffraction analysis of ZnO(commercial), FTO(bare), ZnO@seed/FTO, ZnO-VANs(bio)/FTO@pH(3-11), and ZnO-H_2O(control)/FTO@pH7 are illustrated in Fig. 5.3. The peak positions at $2\theta = 27.14$ (220), 34.33 (002), 38.32 (200), 52.09 (102), 55.10 (110), 62.08 (103), 66.04 (200), and 78.74° (202) are representing the phases of FTO(bare) (JCPDS, file No. 01-083-7977 and 00-001-0657). While the XRD spectrum of ZnO-VANs(bio)/FTO@pH7 showed peaks at $2\theta = 32.45$ (100), 36.91 (101), 48.18 (102), 57.21 (110), 63.44 (103), 68.52 (112), and 69.67° (201), which confirmed the presence of ZnO (JCPDS, file No. 01-075-9187 and 01-077-9355).

The obtained XRD patterns and parameters were further used to study the variations in the lattice strain, dislocation density, and crystallite size of FTO(bare) and ZnO modified FTOs (Table 5.2). The crystalline nature of ZnO(commercial), ZnO-VANs(bio)/FTO@pH7, and ZnO-H_2O(control)/FTO@pH7 was evaluated (Table 5.1). The crystallite size, lattice strain and dislocation density were calculated using Eqs. 5.1-5.3 (Venieri et al., 2014).

$$d = \frac{k\lambda}{\beta \cos\theta_B} \quad (5.1)$$

$$\varepsilon = \frac{\beta}{4\mathrm{Tan}\theta_B} \quad (5.2)$$

$$\delta = \frac{1}{d^2} \quad (5.3)$$

Where d, ε, θ_B, β, δ, k, and λ is the crystallite size (nm), lattice strain, Bragg angle, FWHM of diffraction peak, dislocation density (lines/nm^2), 0.94 nm, and 0.154 nm, respectively.

Scherrer relation (Eq. 5.1) were used to determine the crystallite size (d) of ZnO(commercial), FTO(bare), and all the fabricated ZnO modified FTOs. The crystallite size of ZnO(commercial), ZnO-VANs(bio)/FTO@pH7, and ZnO-H_2O(control)/FTO@pH7 calculated corresponding to the $2\theta = 36.91$ (101), as shown in Table 5.1. The crystallite size of FTO(bare) and all the fabricated ZnO modified FTOs determined corresponding to the $2\theta = 52.09$ (102), as illustrated in Table 5.2 (Chekin et al., 2013). After the growth of ZnO-VANs(bio) over FTO, the crystallite size of the FTO(bare) was reduced (Table 5.2). However, the crystallite size of ZnO-VANs(bio)@pH7 was found to be similar as ZnO(commercial), as shown in Table 5.1. Hence, the bioinspired method is effective in forming smaller crystallites, which in turn could provide more active sites.

Additionally, the variations in the d-spacing value after the fabrication of ZnO-VANs(bio) over FTO with different pH are attributed to the reorganization of the lattice's position. All the obtained parameters are tabulated in Table 5.2. Further, the lattice strain and dislocation density were increased after the fabrication of ZnO-VANs(bio) over FTO due to vacancies in FTO. The increased lattice strain and dislocation density could give a higher compressive strain. A slight peak shifting at $2\theta = 52.09°$, corresponding to bare FTO, was observed in all ZnO modified FTOs. This might be due to the creation of oxygen vacancies or replacement of the Sn atom (atomic size 225 pm) by the Zn atom (atomic size 139 pm), which is supported by decreases in the crystal size and increases in the lattice strain and dislocation density after the growth of ZnO nanostructures onto the FTO glass surface (Sen et al., 2021; Yang et al., 2022). Additionally, bio-extracts are reported as a potential source for creating oxygen vacancies in metal oxides (Wang et al., 2021). After ZnO modification, no significant change was observed in the peaks corresponding to FTO phases, which confirmed the stability of FTO (Fig. 5.3). Additionally, most of the parameters of the ZnO phase of ZnO-VANs(bio)/FTO@pH7 are similar to commercial ZnO.

Table 5.1: XRD diffraction features of ZnO(commercial), ZnO-VANs(bio)/FTO@pH7, and ZnO-H_2O(control)/FTO@pH7.

Sample code	Crystallite size (nm)	d-spacing (nm)	Lattice strain (ε)	Dislocation densities (Lines/nm^2)
ZnO(commercial)	76.25	0.24772	1.53×10^{-3}	1.72×10^{-4}
ZnO-VANs(bio)/FTO@pH7	78.73	0.24331	1.45×10^{-3}	1.61×10^{-4}
ZnO-H_2O(control)/FTO@pH7	50.70	0.24324	1.02×10^{-3}	7.89×10^{-5}

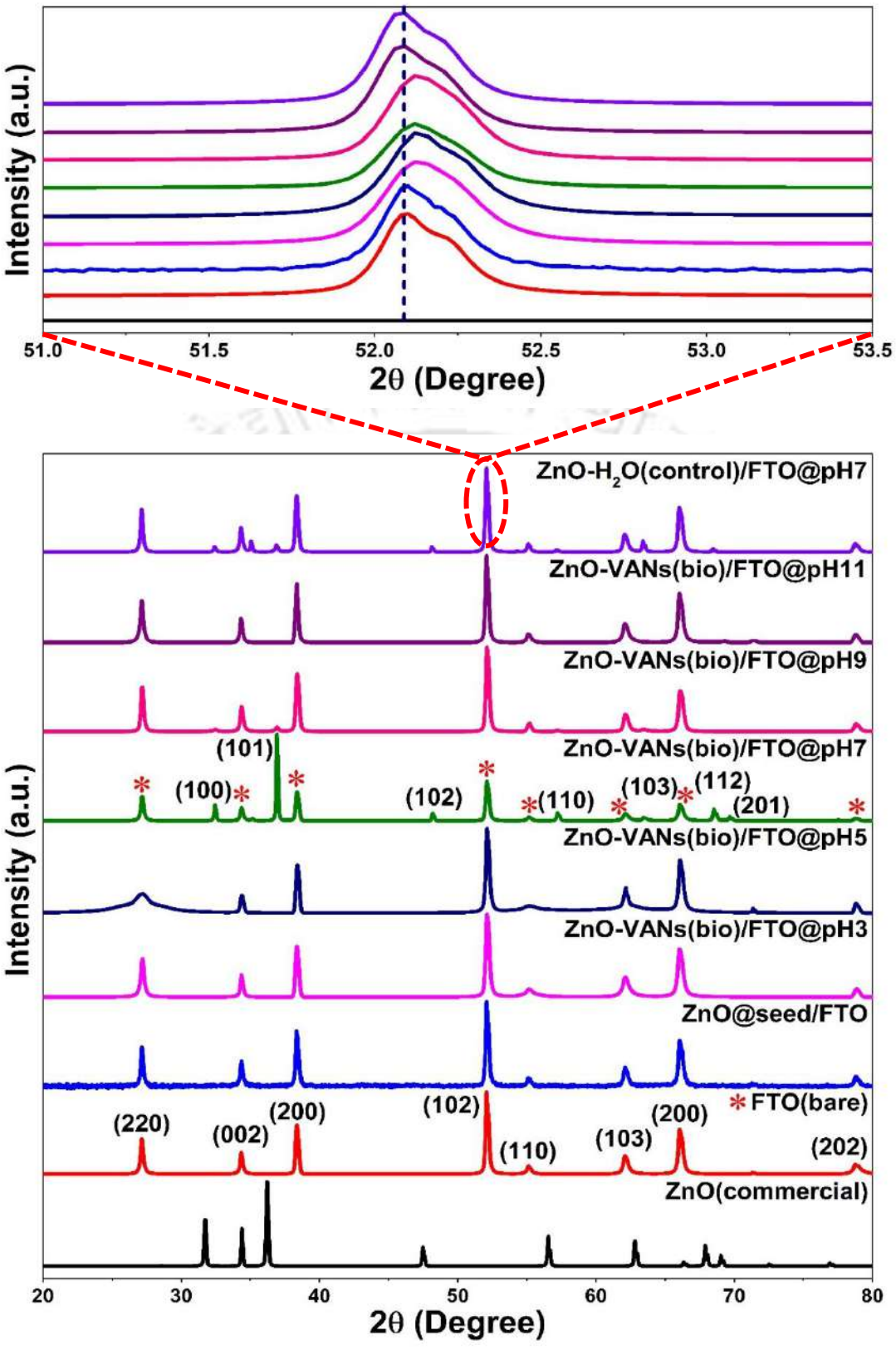

Figure 5.3: XRD patterns of ZnO(commercial), FTO(bare), ZnO@seed/FTO, ZnO-VANs(bio)/FTO@pH3, ZnO-VANs(bio)/FTO@pH5, ZnO-VANs(bio)/FTO@pH7, ZnO-VANs(bio)/FTO@pH9, ZnO-VANs(bio)/FTO@pH11, and ZnO-H_2O(control)/FTO@pH7.

Table 5.2: XRD diffraction characteristic parameters of bare FTO(bare), ZnO@seed/FTO, ZnO-VANs(bio)/FTO@pH3, ZnO-VANs(bio)/FTO@pH5, ZnO-VANs(bio)/FTO@pH7, ZnO-VANs(bio)/FTO@pH9, ZnO-VANs(bio)/FTO@pH11, and ZnO-H_2O(control)/FTO@pH7.

Sample	Crystallite size (nm)	d-spacing (nm)	Lattice strain (ε)	Dislocation densities (Lines/nm^2)
FTO(bare)	54.87	0.17544	1.50×10^{-3}	3.32×10^{-4}
ZnO@seed/FTO	53.57	0.17543	1.54×10^{-3}	3.48×10^{-4}
ZnO-VANs(bio)/FTO@pH3	41.18	0.17537	2.00×10^{-3}	5.90×10^{-4}
ZnO-VANs(bio)/FTO@pH5	46.86	0.17533	1.76×10^{-3}	4.55×10^{-4}
ZnO-VANs(bio)/FTO@pH7	46.41	0.17538	1.78×10^{-3}	4.64×10^{-4}
ZnO-VANs(bio)/FTO@pH9	46.20	0.17536	1.78×10^{-3}	4.68×10^{-4}
ZnO-VANs(bio)/FTO@pH11	52.29	0.17549	1.58×10^{-3}	3.66×10^{-4}
ZnO-H_2O(control)/FTO@pH7	54.07	0.17549	1.53×10^{-3}	3.42×10^{-4}

5.2.1.3 *AFM analysis*

The surface roughness of FTO(bare) (Fig. 5.4a), ZnO/FTO@seed (Fig. 5.4b), ZnO-VANs(bio)/FTO@pH7 (Fig. 5.4c), and ZnO-H_2O(control)/FTO@pH7 (Fig. 5.4d) were determined using AFM analysis. The root-mean-square (RMS) value of FTO(bare), ZnO@seed/FTO, ZnO-VANs(bio)/FTO@pH7, and ZnO-H_2O(control)/FTO@pH7 were 32.11, 17.13, 37.30, and 19.68 nm, respectively in 5 × 5 μm^2 scan area. However, the bioinspired synthesized ZnO-VANs(bio) on FTO at pH 7 show a higher surface roughness with RMS value of 37.30 nm, which is almost 1.2, 2.2, and 1.9 folds higher than the FTO(bare), ZnO@seed/FTO, and ZnO-H_2O(control)/FTO@pH7, respectively. Hence, ZnO-VANs(bio)/FTO@pH 7 would offer a higher surface area for electrochemical sensing of p-CA (Ahmad et al., 2017).

5.2.1.4 *FETEM analysis of ZnO-VANs(bio) by disintegrated from FTO*

FETEM micrographs are illustrated in Figs. 5.4e to 5.4g. The ZnO layer was disintegrated from ZnO-VANs(bio)/FTO@pH7 via sonication (ANTech, GT-1990QTS, frequency 33/40 kHz, ultrasonic power 200 W, China) for 45 min and FETEM analysis was performed to determine its shape (Fig. 5.4e), HRTEM pattern (Fig. 5.4f), and SAED pattern

(Fig. 5.4g). Fig. 5.4e shows a bean-shaped ZnO nanostructure with ~875 nm height (horizontally aligned in Fig. 5.4e). The d-spacing values of 0.243 and 0.276 nm belong to 101, and 100 phases of ZnO, respectively (Fig. 5.4f). The multiple phases and electron diffraction rings (Fig. 5.4g) confirmed the presence of polycrystalline ZnO, which is well supported by XRD results.

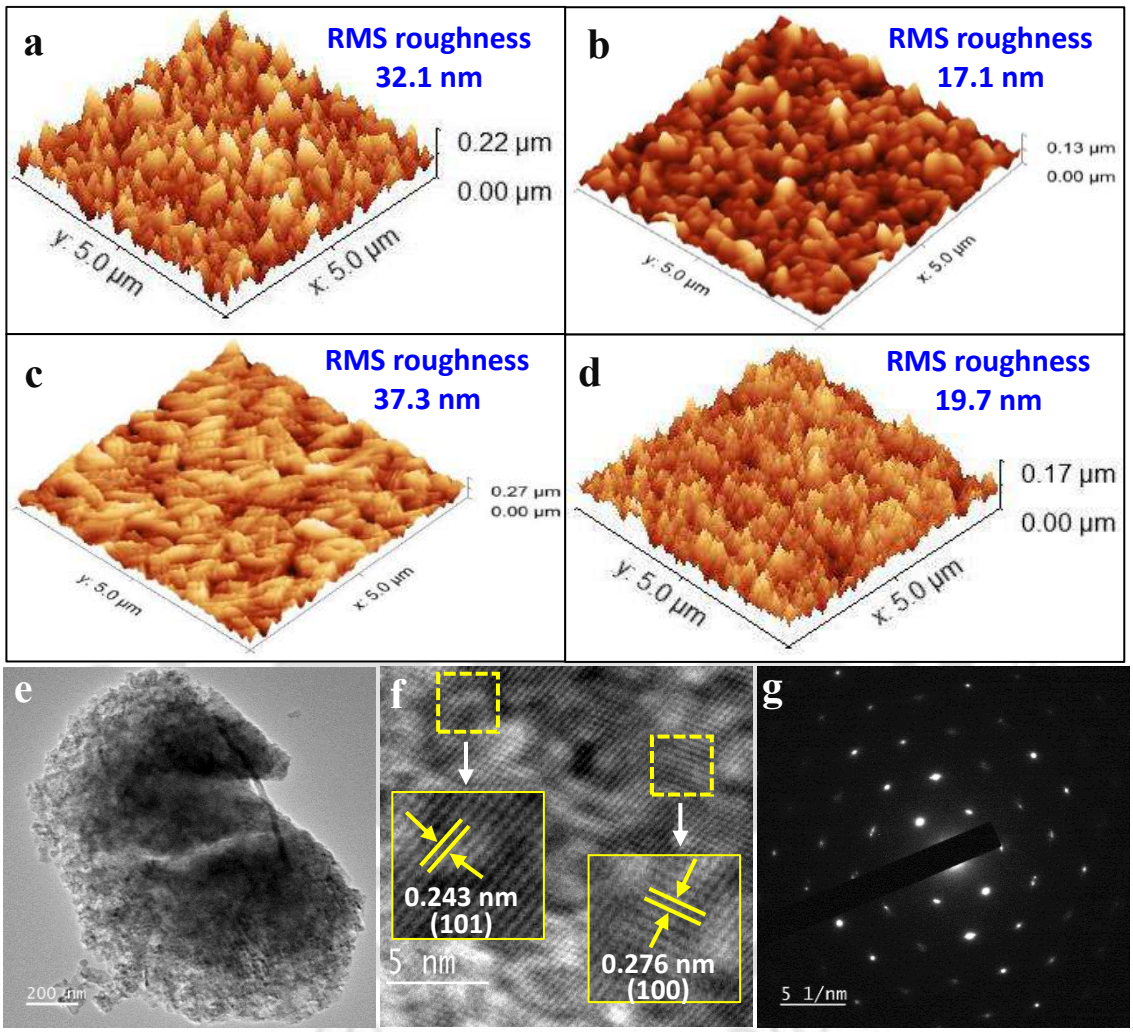

Figure 5.4: AFM images of (a) FTO(bare), (b) ZnO@seed/FTO, (c) ZnO-VANs(bio)/FTO@pH7, and (d) ZnO-H_2O(control)/FTO@pH7 with scan area of 5 µm × 5 µm. (e) FETEM image, (f) HRTEM image, and (g) SAED pattern of ZnO (ZnO layer was disintegrated from ZnO-VANs(bio)/FTO@pH7 via sonication for 45 min).

5.2.1.5 *EDX analysis of ZnO-VANs(bio)*

The elemental analysis of ZnO-VANs(bio)/FTO@pH7 was done using EDX. The atomic percentage of Zn, O, and Sn were 76.3, 21.3, and 2.4 (Fig. 5.5b), respectively. The EDX spectra

(Fig. 5.5a) demonstrate that VANs are made of Zn and O only. It implies that ZnO-VANs(bio) were formed without any impurity.

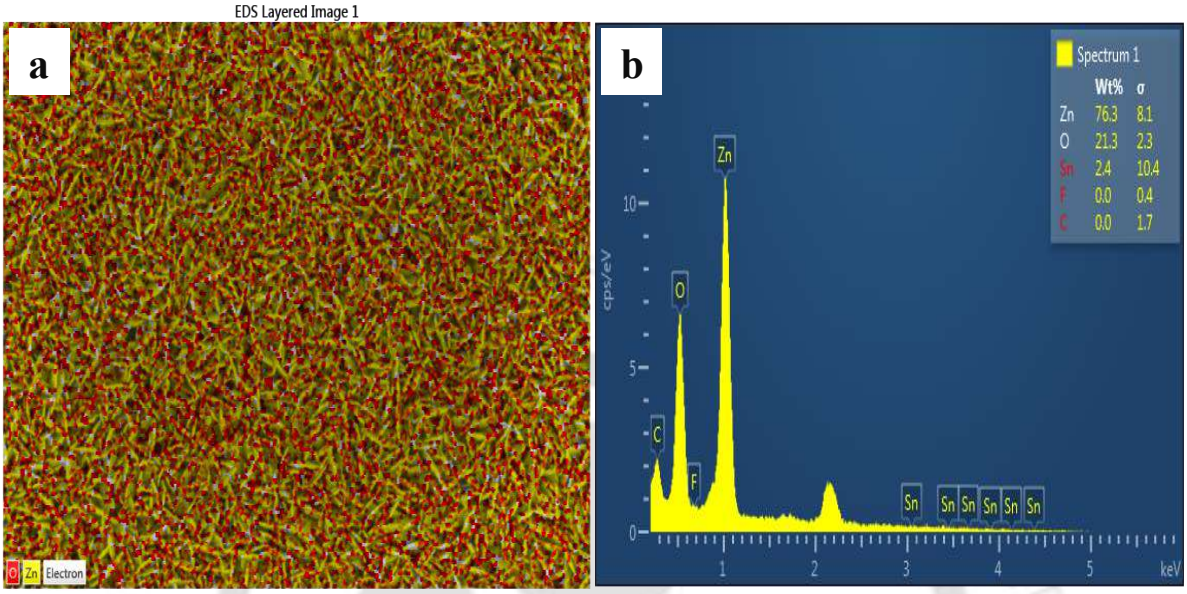

Figure 5.5: (a) EDX elemental image mapping and (b) Elemental spectrum of ZnO-VANs(bio)/FTO@pH7.

5.2.1.6 *XPS analysis*

The composition of the FTO(bare) and ZnO-VANs(bio)/FTO@pH7 surface was studied by XPS analysis (Fig. 5.6). The XPS survey spectrum of FTO(bare) indicates the presence of Sn and O with C, and the survey spectrum of ZnO-VANs(bio)/FTO@pH7 reveals the presence of Zn, Sn, and O with C (Fig 5.6a). The existence of C could be due to the adsorption of atmospheric gases (undetectable in EDX analysis, Fig. 5.5) on the surface of bare/modified FTOs and the initial precursor, like diethanolamine (seed layer), and zinc acetate. The Zn 2p spectra of ZnO-VANs(bio)/FTO@pH7 (Fig. 5.6b) exhibited two predominant peaks at 1021.82 and 1044.9 eV which are ascribed to the spin-orbital splitting of Zn $2p_{3/2}$ and $2p_{1/2}$, respectively, a feature of Zn^{2+} of ZnO (Mali et al., 2013). The peaks at 530.43 and 530.56 eV correspond to the O1s region, ascribing to FTO(bare) (Fig. 5.6c) and ZnO-VANs(bio)/FTO@pH7 (Fig. 5.6d), respectively. The FTO(bare) high-resolution O 1s spectrum (Fig. 5.6c) has two peaks at 530.39 and 531.5 eV, which ascribe to the lattice (O_L) and surface adsorbed oxygen (O_{ads}), respectively. As indicated in Fig. 5.6d, two identical peaks were detected at 530.45 (O_L) and 531.76 eV (O_{ads}), and an additional peak was observed at 533.38 eV, which might be of the adsorbed bio-analytes during the growth of ZnO-VANs(bio) onto the FTO substrate. Hence,

an increase in the O_{ads} in ZnO-VANs(bio)/FTO@pH7 improved its sensitivity by enhancing the surface adsorption of p-CA molecules (Wiench et al., 2018).

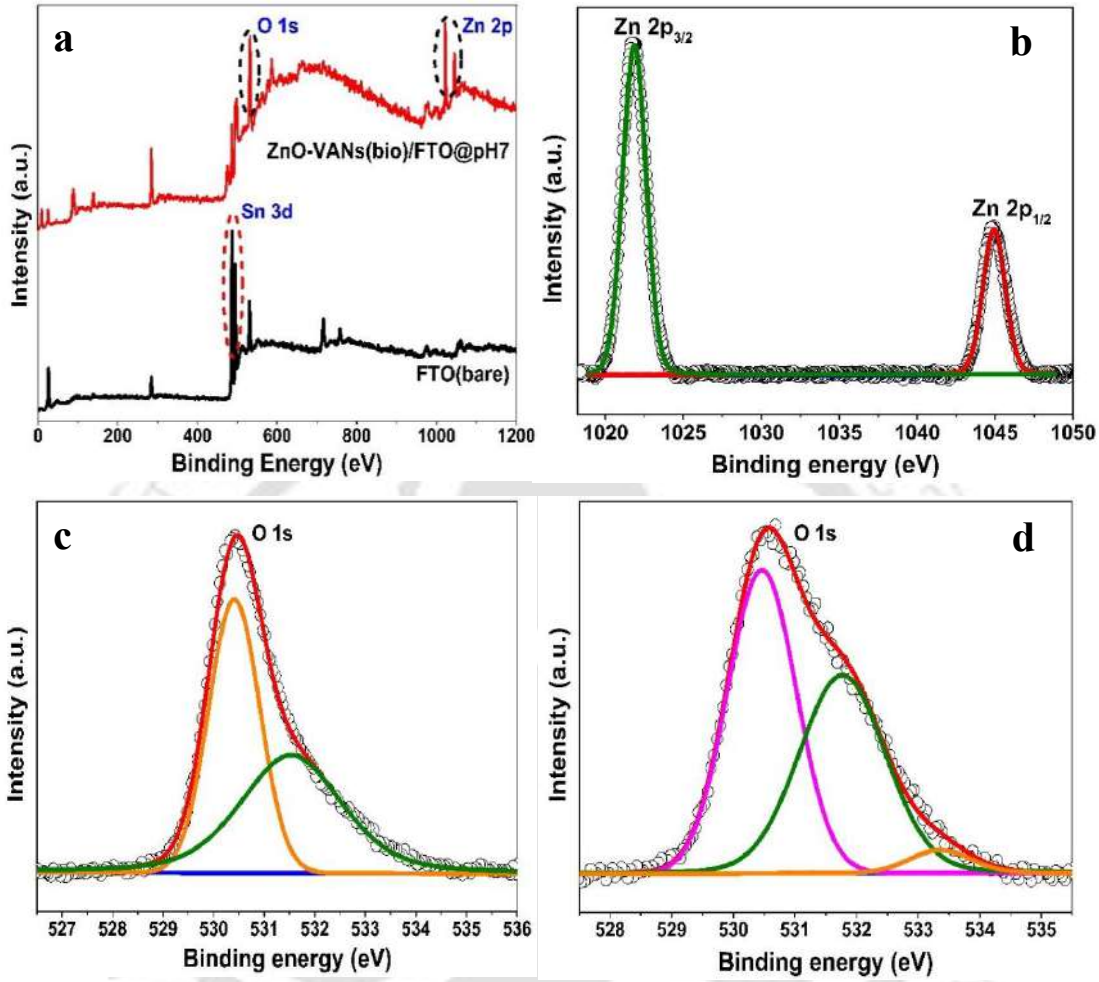

Figure 5.6: (a) XPS survey spectrum of FTO(bare) and ZnO-VANs(bio)/FTO@pH7, (b) Zn 2p core level spectrum of ZnO-VANs(bio)/FTO@pH7, (c) O 1s spectrum of FTO(bare), and (d) O 1s spectrum of ZnO-VANs(bio)/FTO@pH7.

5.2.2. Growth mechanism of ZnO nanostructures

Figs. 5.7a and 5.7b depict the proposed mechanism for the growth of 2D ZnO nanostructures using *Sechium edule* extract. AA is the major analyte present in the *Sechium edule* extract (Chowdhury et al., 2021). In ZnO nanostructures, the anisotropic growth is facilitated by the corresponding internal dipole moment along the crystal lattice's primary axis. Furthermore, anisotropic and partial polar properties of the ZnO crystal structure ease nanostructures growth in a specific direction (Ejsmont and Goscianska, 2023). The basal plane (0001) is a crystallite's most polar surface, whereas anisotropic growth of nanostructure takes

place along the c-axis in the $(10\bar{1}0)$ and $(01\bar{1}0)$ directions (Pradhan and Leung, 2008). It is due to the Zn lattice having a moderately positive charge point at one end and the oxygen lattice having a negative charge point at another end of the basal polar plane (0001) (Ejsmont and Goscianska, 2023). The adsorption of the capping agent (oxidized form of AA, dehydroascorbic acid) onto the direction (0001) of the growing nanostructure, could hinder its growth in this direction and lead to a preferential growth in the $(10\bar{1}0)$ and $(01\bar{1}0)$ directions (Fig. 5.7c). Moreover, the formation of the nanostructures in the lateral direction seems to block when one nanostructure meets with other, but their height grows with reaction time without significant changes in its thickness (Pradhan and Leung, 2008). As a result, 2D vertically aligned ZnO nanostructures were formed in a hierarchical fashion. AA dissociates to reactive species (complex (I)), and $Zn(CH_3COO)_2.2H_2O$ dissociates into complex (II) after it is being introduced to an aqueous solution. After that, AA reacts to complex (II), and complex (III) is formed and oxidized to dehydroascorbic acid via the transfer of an electron from AA to Zn^{2+} ions, and Zn^0 is formed at 95 °C. After that, highly active Zn^0 interact with O_2 (in the air), and 2D ZnO nanostructures are formed (Fig. 5.7b) (Chowdhury et al., 2022).

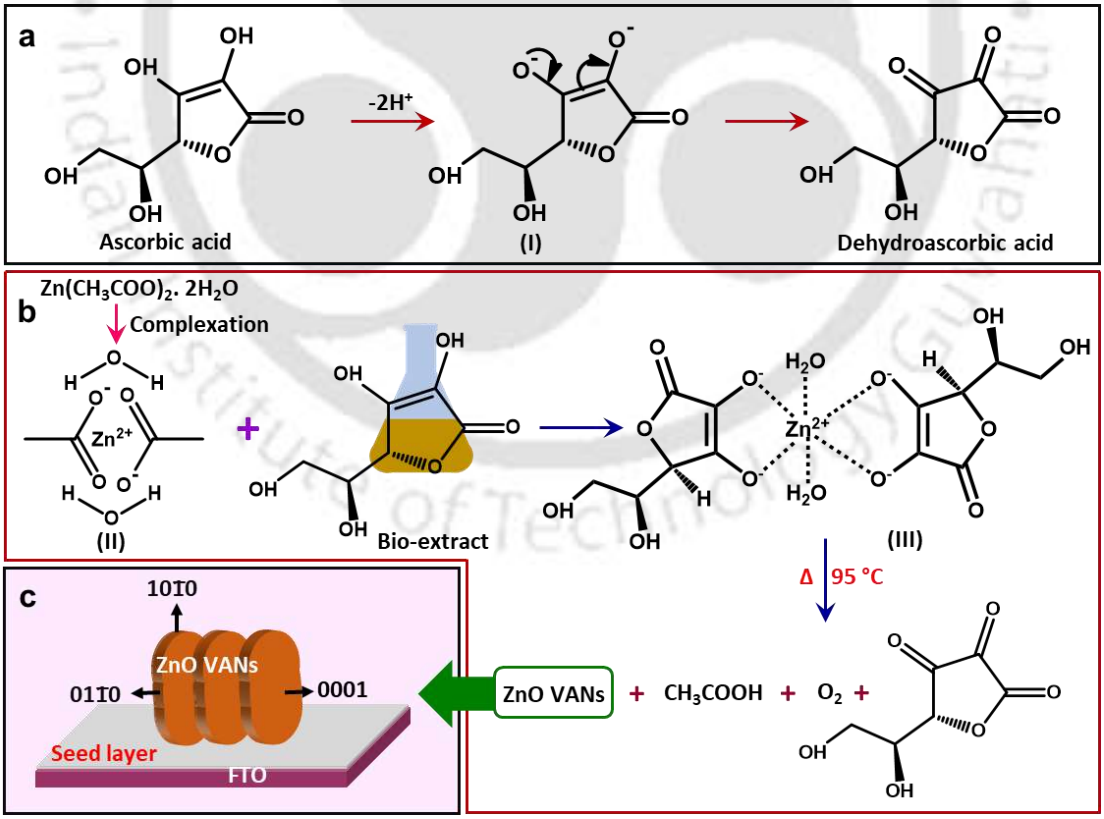

Figure 5.7: (a) Oxidation of AA, (b) pathway of 2D ZnO VANs formation considering AA as the primary analyte present in *Sechium edule* bio-extract, and (c) schematic diagram of 2D ZnO VANs formation on FTO.

5.2.3. Electrochemical characterizations of ZnO-VANs(bio)/FTO@pH7 electrode

5.2.3.1 *EIS analysis*

The EIS spectrum of FTO(bare) and ZnO-VANs(bio)/FTO@pH7 were recorded using 1 mM $K_3[Fe(CN)_6]$ in 0.1 M KCl electrolyte solution between a certain frequency range of 10^{-2} to 10^5 Hz (Fig. 5.8a). In EIS plot, the arc radius shows the electrode surface charge transport resistance. The arc radius of ZnO-VANs(bio)/FTO@pH7 was reduced compared to FTO(bare), demonstrating the faster charge transfer kinetics (Dash et al., 2020). The data were fitted to the corresponding circuit model (insert of Fig. 5.8a), and all the fitting parameters were reported in Table 5.3. The coated layer is imperfect due to the pores present in the surface, and a pore can be considered as a non-coated portion of the substrate. When the pore size is very small, the electrolyte exchange is hampered between the pore and bulk. Therefore, the concentration of ions could differ between the bulk and pores. Hence, the bulk electrolyte resistance (R_s) is different from the electrolyte resistance (R) in FTO(bare), as shown in Table 5.3. The absence of electrolyte resistance (R) indicates the perfect surface of the ZnO-VANs(bio)/FTO@pH7 electrode, and the lack of capacitance (C) is due to the fabrication of the seed layer onto FTO. The seed layer reduces the heterogeneous interface between the vertically aligned nanostructure and FTO substrate, overcoming electron scattering (Lai et al., 2010). The charge transfer resistance (R_p) values for FTO(bare) and ZnO-VANs(bio)/FTO@pH7 were found to be 7.78 and 3.02 MΩ, respectively, which implies a facilitated charge transfer resistance of ZnO-VANs(bio)/FTO@pH7 compared to FTO(bare) due to higher electrical conductivity of ZnO-VANs(bio)/FTO@pH7 (Gogoi et al., 2020). It can be observed that the bulk electrolyte resistance (R_s) remains equitably constant, and the variation in constant phase element (CPE) could be due to the conductivity of the electrode surface (Table 5.3).

5.2.3.2 *Effective surface area of FTO(bare) and ZnO-VANs(bio)/FTO@pH7*

The cyclic voltammograms (CVs) of FTO(bare) and ZnO-VANs(bio)/FTO@pH7 at several scan rates (5-500 mV/s) are illustrated in Figs. 5.8b and 5.8c. The electroactive surface area of the FTO(bare) and ZnO-VANs(bio)/FTO@pH7 was determined by the Randles-Sevcik equation (Eq. 5.4) (Malode et al., 2020). We employed 1 mM $[Ru(NH_3)_6]Cl_2$ and 0.1 M KCl as a redox probe and supporting electrolyte, respectively, at ambient temperature.

$$I_{Pa} = (2.69 \times 10^5)\, n^{3/2}\, A_{eff}\, D^{1/2}\, \upsilon^{1/2}\, C_0 \qquad (5.4)$$

Where I_{Pa}, n, A_{eff}, υ, D, and C_0 indicate anodic peak current (A), number of electron transfers in the redox event, effective surface area (cm^2), scan rate (V/s), diffusion coefficient (cm^2/s), and bulk concentration of analyte (mol/cm^3), respectively. From the linear plot of I_{Pa} vs. $\upsilon^{1/2}$ (Fig. 5.8d), the slope of the FTO(bare) and ZnO-VANs(bio)/FTO@pH7 was found to be 95.02 ($R^2 = 0.999$) and 112.102 $\mu A.V^{-1/2}.s^{1/2}$ ($R^2 = 0.999$), respectively. By considering n = 1, and D = 8.43×10^{-6} cm^2/s for 1 mM $[Ru(NH_3)_6]Cl_2$ in 0.1 M KCl (Wang et al., 2011) and equating the slopes with the Randles-Sevcik equation, the effective surface area of FTO(bare) and ZnO-VANs(bio)/FTO@pH7 was found to be 0.122 and 0.144 cm^2, respectively (Gopi et al., 2022). The current response of FTO(bare) and ZnO-VANs(bio)/FTO@pH7 was invariant at lower scan rates up to 50 mV/s as the outer sphere redox probe, ($[Ru(NH_3)_6]Cl_2$) was used. The roughness created by the nanostructures is much lower than the diffusion layer thickness at lower scan rates (<50 mV/s) (Dash et al., 2021). Therefore, bioinspired synthesized ZnO-VANs(bio) on FTO at pH 7 provided a higher surface area for electrochemical sensing of p-CA, which is almost 1.2 times higher than the bare FTO.

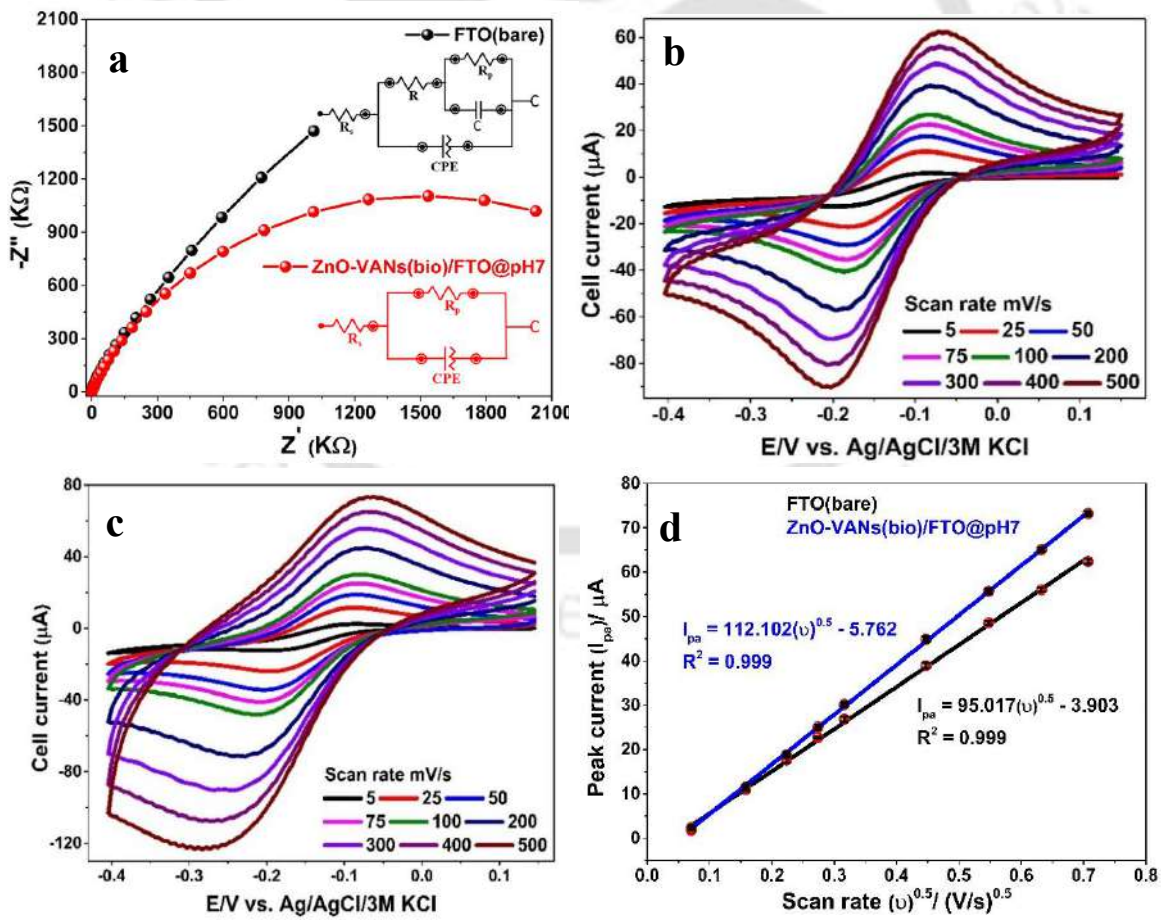

Figure 5.8: (a) Nyquist plots for EIS measurements using FTO(bare) and ZnO-VANs(bio)/FTO@pH7 electrodes with equivalent circuit diagram of FTO(bare) and ZnO-

VANs(bio)/FTO@pH7 (inset), showing resistance of the working electrode (Reaction conditions: 1 mM $K_3[Fe(CN)_6]$, in 50 mL of 0.1 M KCl electrolyte at room temperature), (b) Cyclic voltammograms of FTO(bare), (c) Cyclic voltammograms of ZnO-VANs(bio)/FTO@pH7, and (d) Anodic peak current (I_{pa}) vs. $\upsilon^{0.5}$ graph of FTO(bare) and ZnO-VANs(bio)/FTO@pH7 (Reaction conditions: 1 mM $[Ru(NH_3)_6]Cl_2$, in 50 mL of 0.1 M KCl electrolyte solution at different scan rates (5-500 mV/s) and room temperature).

Table 5.3: Nyquist plots fitting parameters for FTO(bare) and ZnO-VANs(bio)/FTO@pH7.

Electrode	R_s (Ω)	R_p (MΩ)	R (Ω)	C (µF)	CPE (µMho)
FTO(bare)	55.4	7.78	48.8	1.38	2.65
ZnO-VANs(bio)/FTO@pH7	66.2	3.02	-	-	1.58

5.2.4. Optimization of electrochemical p-CA sensing parameters

5.2.4.1 *Effect of pH*

To study the effect of the pH (Fig. 5.9a), CV was performed within the pH range from pH 2 to 8 for electrocatalytic sensing of p-CA (40 µM) in 0.04 M BR buffer at a fixed scan rate of 50 mV/s vs. Ag/AgCl using ZnO-VANs(bio)/FTO@pH7. The anodic peak potential (E_p) of p-CA was shifted towards the less positive and more positive sides when the pH increased from 2 to 4 and 4 to 8, respectively, which implies that the sensing reaction involves proton (Malode et al., 2020). At pH 4 (0.04 M BR buffer), the anodic peak potential and current were found to be minimum (less positive) and maximum, respectively. It indicates that the electrocatalytic sensing of p-CA is favourable in the acidic medium (pH 4). Hence, pH 4 was selected throughout the experiment. From the liner plot of E_p (peak potential) vs. pH (Fig. 5.9b), the slope was found to be 0.0453 V per unit pH ($R^2 = 0.985$), which indicates the reaction involves an equal number of proton and electron (Manivannan et al., 2019).

5.2.4.2 *Effect of electrolytes*

The effect of electrolytes at pH 4 for electrochemical sensing of p-CA (40 µM) over ZnO-VANs(bio)/FTO@pH7 electrode was investigated using the CV test at a fixed scan rate of 50 mV/s vs. Ag/AgCl and room temperature (Fig. 5.10). No sharp peak was found in 0.1 M phosphate buffer solution (PBS, pH 4) and 0.1 M Tris-HCl (pH 4) buffer during sensing of p-CA over ZnO-VANs(bio)/FTO@pH7. The increase in anodic peak current (39.53%) was observed in 0.04 M BR (pH 4) buffer than in 0.1 M acetate (pH 4) buffer. Additionally, the

anodic peak potential is less in 0.04 M BR (pH 4) buffer than in 0.1 M acetate (pH 4) buffer. BR buffer contains a mixture of weak acids (0.04 M each of acetic acid, phosphoric acid, and boric acid) and their corresponding conjugate bases. This combination could tweak ionic mobility and conductivity for selective p-CA sensing with a high peak current.

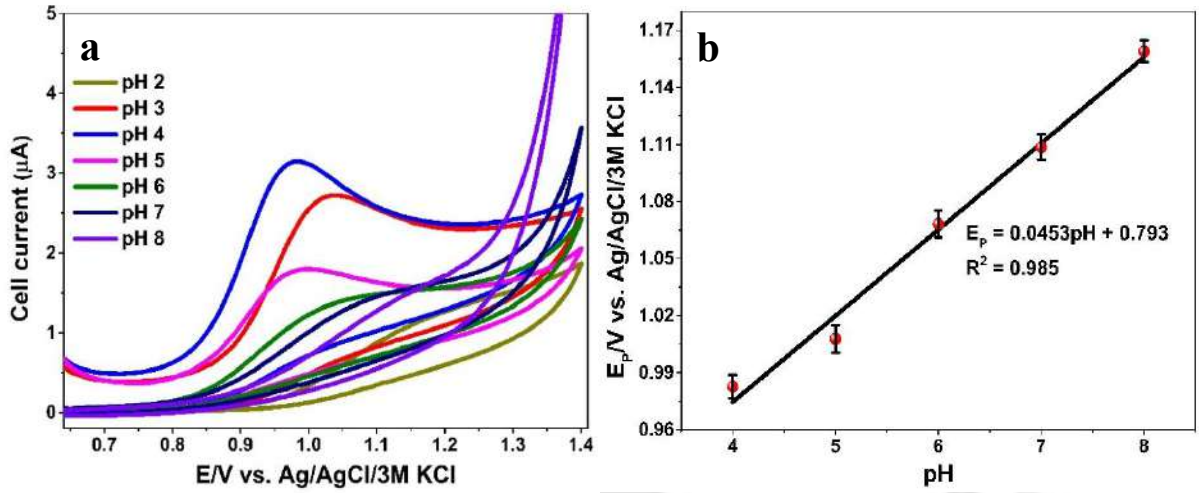

Figure 5.9: (a) Cyclic voltammograms at different pH (2-8) using ZnO-VANs(bio)/FTO@pH7 electrodes and (b) E_P vs. pH. Reaction conditions: 40 μM p-CA in 0.04 M BR buffer at room temperature. Cyclic voltammetry parameters: Scan rate 50 mV/s.

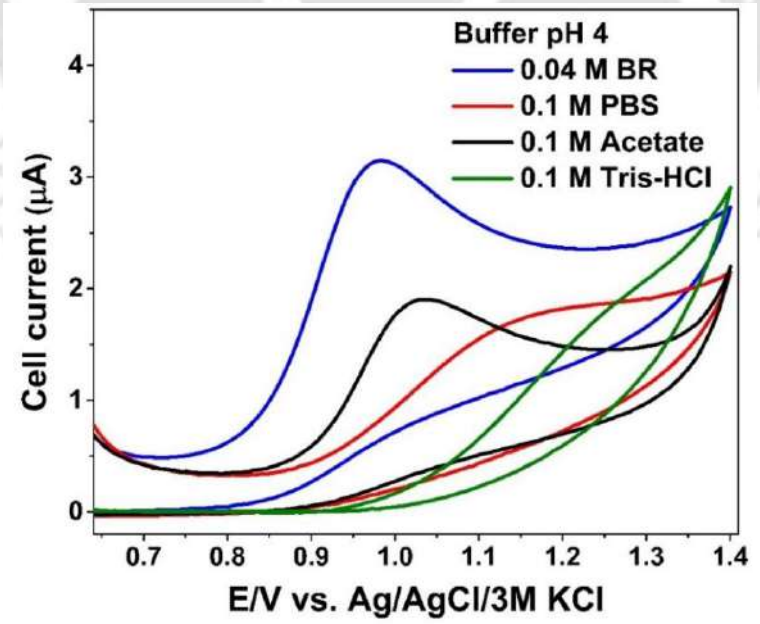

Figure 5.10: Cyclic voltammograms using different electrolytes, namely, 0.04 M BR (pH 4), 0.1 M PBS (pH 4), 0.1 M acetate (pH 4), and 0.1 M Tris-HCl (pH 4) buffer using ZnO-VANs(bio)/FTO@pH7 electrodes. Reaction conditions: 40 μM p-CA in electrolytes at room temperature. Cyclic voltammetry rate 50 mV/s.

5.2.4.3 *Sensing of p-CA deposition potential*

SWASV was performed at a scan rate of 50 mV/s (with a pulse amplitude of 0.02 V, step potential of 0.002 V, and a frequency of 25 Hz) from 0.65 to 1.3 V vs. Ag/AgCl using 0.04 M BR buffer (pH 4) at the ZnO-VANs(bio)/FTO@pH7 electrode to determine the deposition potential and to understand the electrocatalytic behaviour of p-CA sensing (Fig. 5.11a). Deposition potential could affect the electrocatalytic sensitivity for the detection of p-CA. At room temperature, it was varied from 0 to -0.9 V vs. Ag/AgCl in 0.04 M BR buffer at pH 4. The anodic peak current (I_{pa}) of p-CA was increased gradually from potential 0 to -0.6 V vs. Ag/AgCl due to p-CA ions accumulated at the ZnO-VANs(bio)/FTO@pH7 electrode surface (Fig. 5.11b). The decrease in p-CA deposition at potential -0.6 to -0.9 V vs. Ag/AgCl could be of H_2 gas evaluation (Gumpu et al., 2017). So, a reduction in anodic peak current was observed from -0.6 to -0.9 V vs. Ag/AgCl (Fig. 5.11b). The shift in the peak potential to a more positive could be attributed to the overpotential deposition (deposition potential more positive than the standard potential, as determined from Eq. 5.5) of p-CA ions. It implies a strong contact of analytes to the substrate, which can be difficult for the p-CA ions to remove from the substrate. Hence, the deposition potential -0.6 V vs. Ag/AgCl was selected for the electrocatalytic sensing of p-CA (Dash et al., 2020).

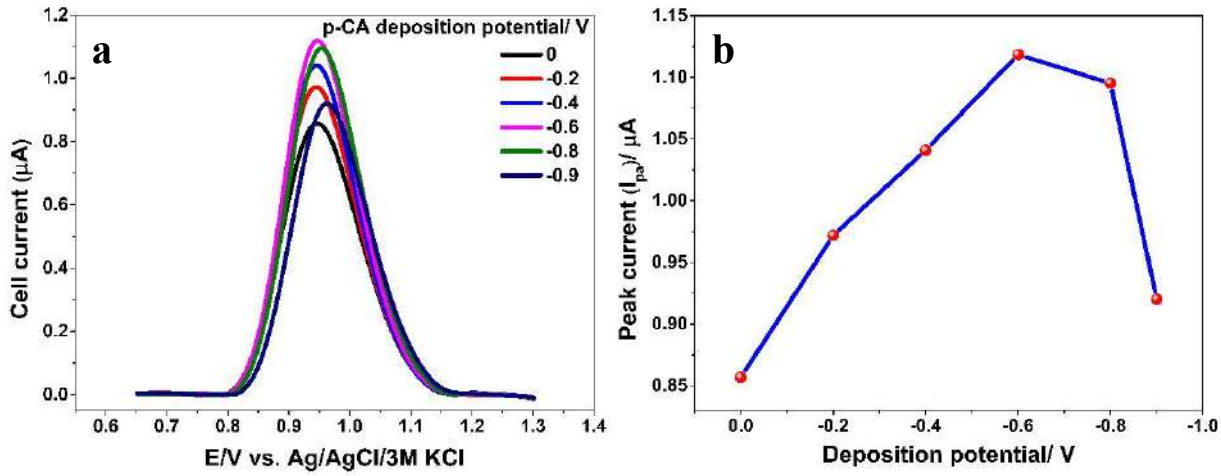

Figure 5.11: (a) SWASV of p-CA at varying deposition potential from 0 to -0.9 V vs. Ag/AgCl and (b) Deposition potential vs. Peak current. Reaction conditions: Deposition time 120 s and 40 μM p-CA in 50 mL 0.04 M BR buffer (pH 4) at room temperature.

5.2.4.4 *Determination of p-CA deposition time*

The effect of time of p-CA deposition over ZnO-VANs(bio)/FTO@pH7 electrode surface was investigated using the SWASV test at a scan rate of 50 mV/s (0.65 to 1.3 V vs.

Ag/AgCl) and room temperature (Fig. 5.12a). The change in the peak response with an increase in the deposition time is illustrated in Fig. 5.12b. The obtained trend confirmed the gradual increase in the peak response with an increase in the deposition time up to 120 s due to p-CA ions accumulated at the surface of the ZnO-VANs(bio)/FTO@pH7 electrode (Bagheri et al., 2013). The peak current didn't significantly increased with further increase in the deposition time (>120 s), which might be attributed to either saturation of the electrode surface or establishment of equilibrium between p-CA ions at the surface of the electrode and in the solution (Dash et al., 2020). Therefore, the deposition time was optimized at 120 s.

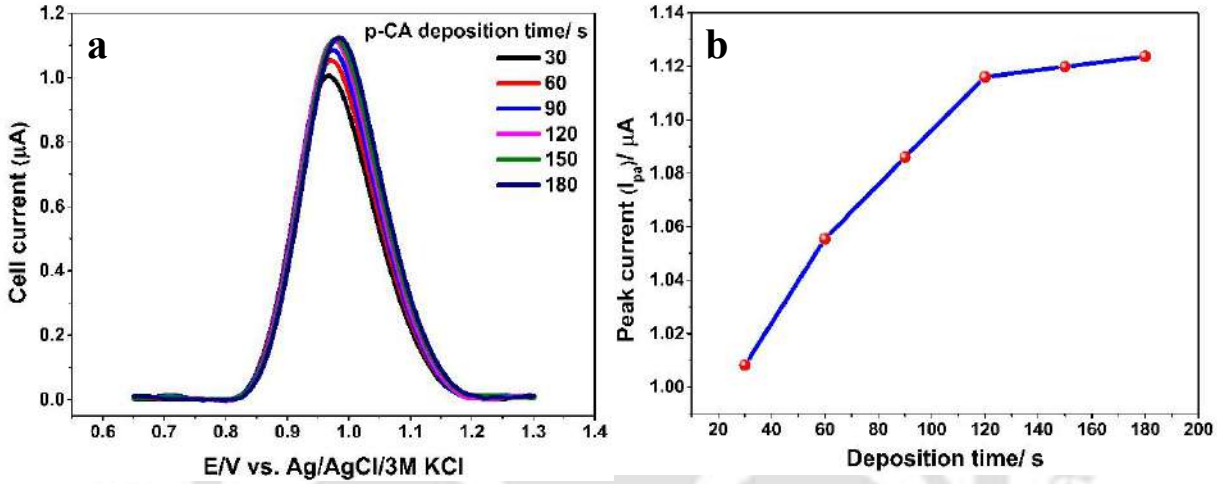

Figure 5.12: (a) SWASV of p-CA at varying deposition time from 30 to 180 s and (b) Deposition time vs. Peak current. Reaction conditions: Deposition potential -0.6 V vs. Ag/AgCl and 40 µM p-CA in 50 mL 0.04 M BR buffer (pH 4) at room temperature.

5.2.4.5 *Determination of p-CA deposition temperature for p-CA sensing*

Fig. 5.13a demonstrates the change in peak current at different electrolyte temperatures (15-65 °C) at a scan rate of 50 mV/s from 0.65 to 1.3V vs. Ag/AgCl using 0.04 M BR buffer at pH 4. The rise in peak current with increasing temperature from 15-55 °C due to the deposition of p-CA over the ZnO-VANs(bio)/FTO@pH7 electrode surface. Additionally, high temperature provides a high diffusion rate of p-CA ions from the electrolyte to the working electrode surface. The desorption of p-CA molecules and instituting exothermic equilibrium result in a decrease in the p-CA deposition with a further increase in the temperature (65 °C), as shown in Fig 5.13b. The increase in peak current (53.12 %) was observed from temperature 25 to 45 °C. By focusing on field application, where the maximum temperature is usually around 45 °C, which was selected for further experiments.

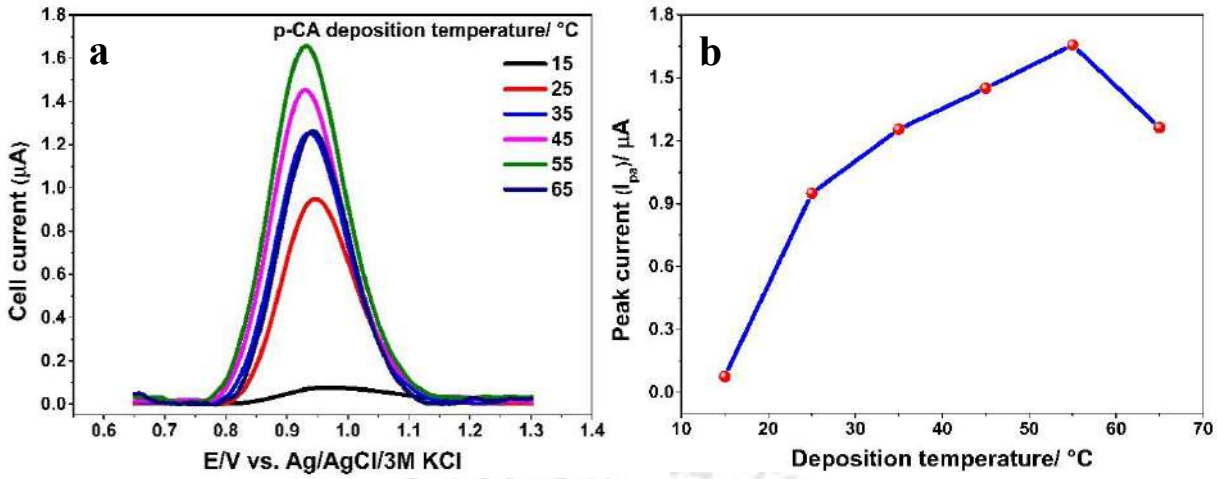

Figure 5.13: (a) SWASV of p-CA at varying deposition temperatures from 15 to 65°C and (b) Deposition temperature vs. Peak current. Reaction conditions: Deposition potential -0.6 V vs. Ag/AgCl, Deposition time 120 s and 40 µM p-CA in 50 mL 0.04 M BR buffer at pH 4.

5.2.5. Electrochemical p-CA sensing at ZnO-VANs(bio)/FTO@pH7 electrode

5.2.5.1 *Determination of electrokinetic parameters of p-CA sensing*

Cyclic voltammetry was conducted to understand the electrokinetic behaviour and determine the parameters of p-CA sensing. It was performed at various scan rates (15-500 mV/s) from 0.7-1.4 V vs. Ag/AgCl over ZnO-VANs(bio)/FTO@pH7 electrode using 0.04 M BR buffer (pH 4) at 45 °C (Fig. 5.14a). The plot between peak current (I_{pa}) vs. square root of scan rate ($\upsilon^{1/2}$) was obtained to be linear (Fig. 5.14b), which indicates the reaction is diffusion control (Dash et al., 2021). Thus, the Laviron equation (Eq. 5.5) of the diffusion-control process for the anodic peak was used to calculate the kinetic parameters (Li et al., 2019).

$$E_p = E_0 - \frac{2.303RT}{\alpha nF} \log \frac{RTk}{\alpha nF} + \frac{2.303RT}{\alpha nF} \log \upsilon \qquad (5.5)$$

Where E_p, E_0, k, n, α, R, F, T, and υ is the anodic peak potential (V), formal standard potential (V), standard heterogeneous rate constant (s^{-1}), number of electron transfer, anodic charge transfer coefficient, universal gas constant (8.314 J/mol.K), Faraday's constant (96,485 C/mol), temperature (K), and scan rate (V/s), respectively. By considering α = 0.5, the value of n and k was determined from the slope and intercept of the linear plot between the peak potential (E_p) vs. log υ (Fig. 5.14c), with a known E_0. The value of E_0 was determined from the plot between E_p vs. υ by extrapolating (υ = 0). From the plot E_p vs. log υ, the slope and intercept values were found to be 0.097 V and 1.124 V, respectively. The value of E_0 was 0.978 V from the plot E_p vs. υ by extrapolating (υ = 0). The values of n and k were determined to be 1.3 and 0.737 s^{-1}. The value of n indicates that the reaction involved one electron.

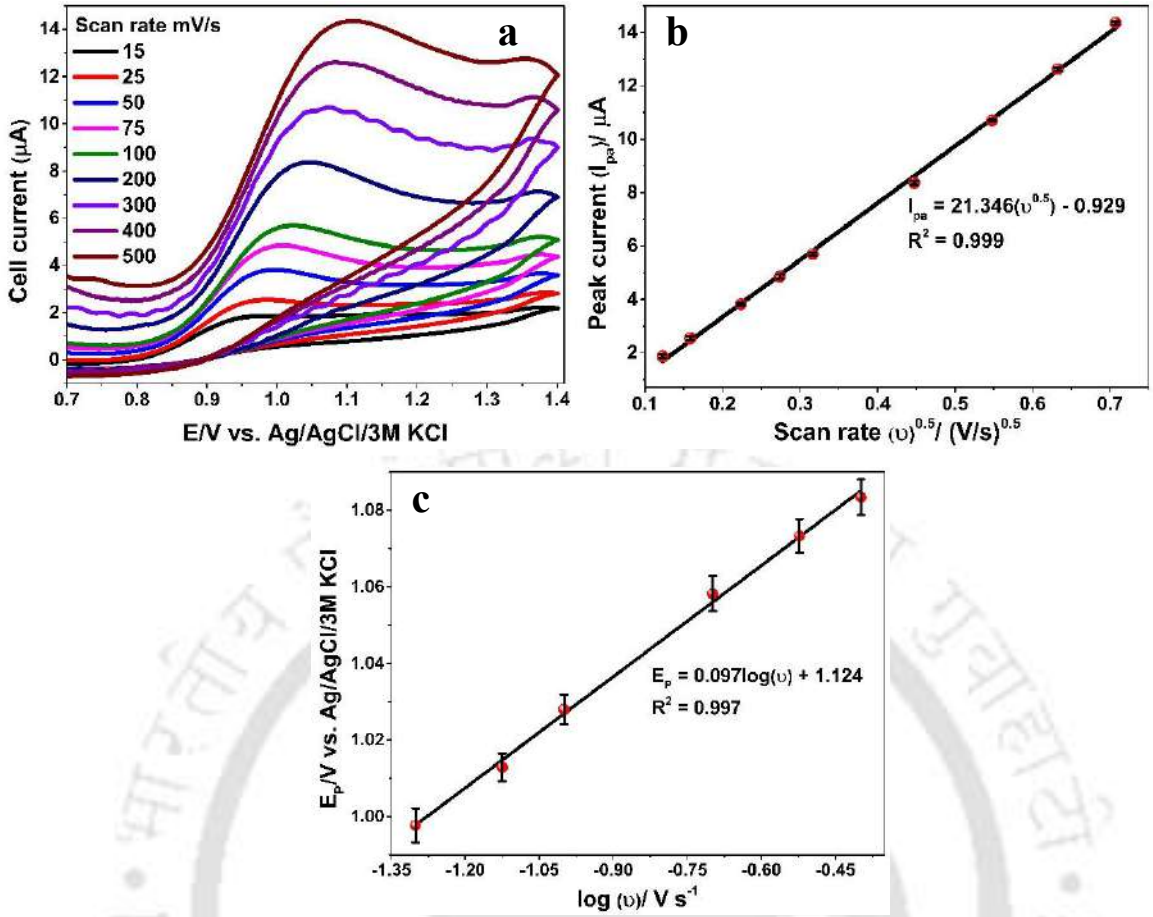

Figure 5.14: (a) Cyclic voltammograms at various scan rates from 15 to 500 mV/s, (b) Square root of scan rate ($\upsilon^{0.5}$) vs. I_{pa}, and (c) log(υ) vs. peak potential (E_P). Reaction conditions: 40 µM p-CA in 0.04 M BR buffer (pH 4) supporting electrolyte at a temperature of 45°C.

5.2.5.2 *Electrochemical p-CA sensing at ZnO-VANs(bio)/FTO@pH7 electrode*

Figs. 5.15a and 5.15b illustrate the SWASV and the associated calibration curves of p-CA detection at ZnO-VANs(bio)/FTO@pH7 electrode using 0.04 M BR buffer (pH 4) at a scan rate of 50 mV/s. The plot between the peak current (I_{pa}) and p-CA concentration exhibited a linear relationship between 2 to 200 µM p-CA (Fig. 5.15b). The slope (m) of the linear plot was determined to be 0.028 µA. μM^{-1} with a good correlation coefficient (R^2 = 0.998). The limit of detection (LOD) and limit of quantification (LOQ) of p-CA sensing were determined by Eqs. 5.6 and 5.7, respectively (Dash et al., 2022).

$$\text{LOD} = \frac{3S_b}{m} \tag{5.6}$$

$$\text{LOQ} = \frac{10S_b}{m} \tag{5.7}$$

Where m and S_b are the slope of the calibration curve and standard deviation of the blank run (0.0002), respectively. LOD and LOQ were calculated to be 0.021 and 0.071 µM,

respectively. It was about two folds lower with ZnO-VANs(bio)/FTO@pH7 electrode compared to FTO(bare) (Figs. 5.15c and 5.15d). The sensitivity of the ZnO-VANs(bio)/FTO@pH7, having A_{eff} of 0.144 cm^2 was obtained from the slope of the calibration curve (Fig. 5.15b). It was 0.194 µA. $\mu M^{-1}.cm^{-2}$ for the concentration between 2-200 µM p-CA.

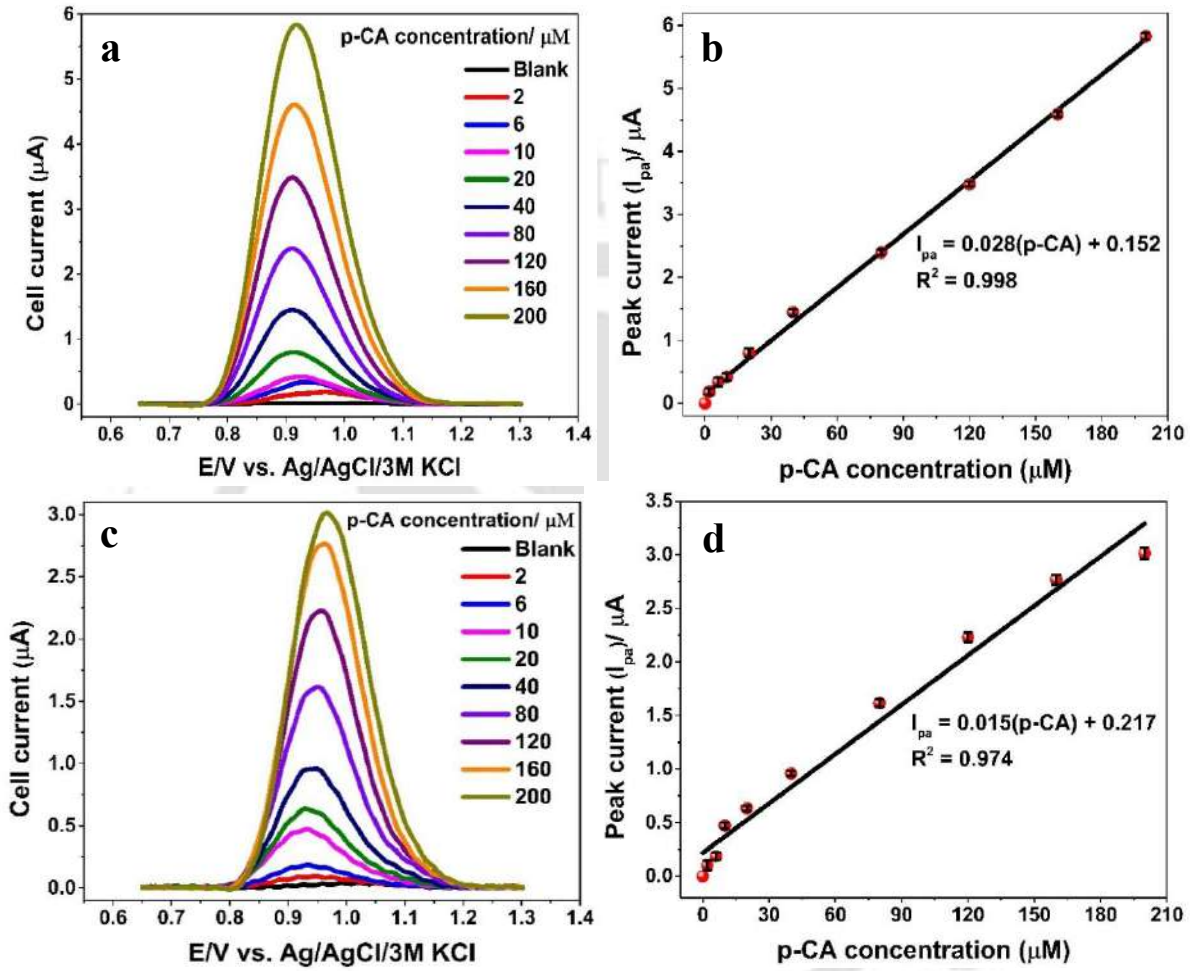

Figure 5.15: (a) SWASV of ZnO-VANs(bio)/FTO@pH7 at a varying concentration of p-CA from 0 to 200 µM, (b) p-CA concentration vs. Peak current (I_{pa}), (c) SWASV of FTO(bare) at a varying concentration of p-CA from 0 to 200 µM and (b) p-CA concentration vs. I_{pa}. Reaction conditions: Deposition potential -0.6 V vs. Ag/AgCl, deposition time 120 s, and deposition temperature 45 °C in 50 mL 0.04 M BR buffer at pH 4.

5.2.5.3 *p-CA reaction at ZnO-VANs(bio)/FTO@pH7 and sensing mechanism*

To recognize the reaction product, p-CA concentration of 200 µM in BR buffer (pH 4) was subjected to LC-MS and HPLC analyses before and after the chronoamperometric test at 0.978 V (3600 s) using ZnO-VANs(bio)/FTO@pH7. In HPLC analysis, a sharp peak (retention

time: 4.75 min) corresponding to p-CA was identified (Figs. 5.16a and 5.16b). Additionally, a new peak (retention time: 9.07 min) was observed after the chronoamperometric test, which is the oxidised product of p-CA (Fig. 5.16b). Further, LC-MS analysis was performed, and mass spectra were acquired before (retention time: 8.44 min), and after (retention time: 8.63 min) the electrochemical reaction (Figs. 5.17a and 5.17b). After the chronoamperometric test at 0.978 V vs. Ag/AgCl using ZnO-VANs(bio)/FTO@pH7 electrode, p-CA (m/z = 127.02) is converted to p-CA radical (m/z = 126.01) with the release of one proton and one electron (Mohamadighader et al., 2020). Mass spectra recorded before and after the chronoamperometric test confirmed the remnant p-CA molecule (m/z = 127.02, Fig. 5.17a) and p-CA radical (m/z = 126.01, Fig. 5.17b). The first oxidation peak is associated with p-CA at 0.978 V vs. Ag/AgCl corresponding to a reaction mechanism involving the transfer of one proton and one electron (Fig. 5.18). The decrease in m/z value from 127.02 to 126.01 further supports the oxidation of p-CA during the course of sensing. It is in line with the electrokinetic parameters determined for the irreversible diffusion-control process of p-CA sensing at 0.978 V vs. Ag/AgCl (Fig. 5.14c). Hence, the detection of p-CA fundamentally follows the detection of p-CA radical under environmental conditions.

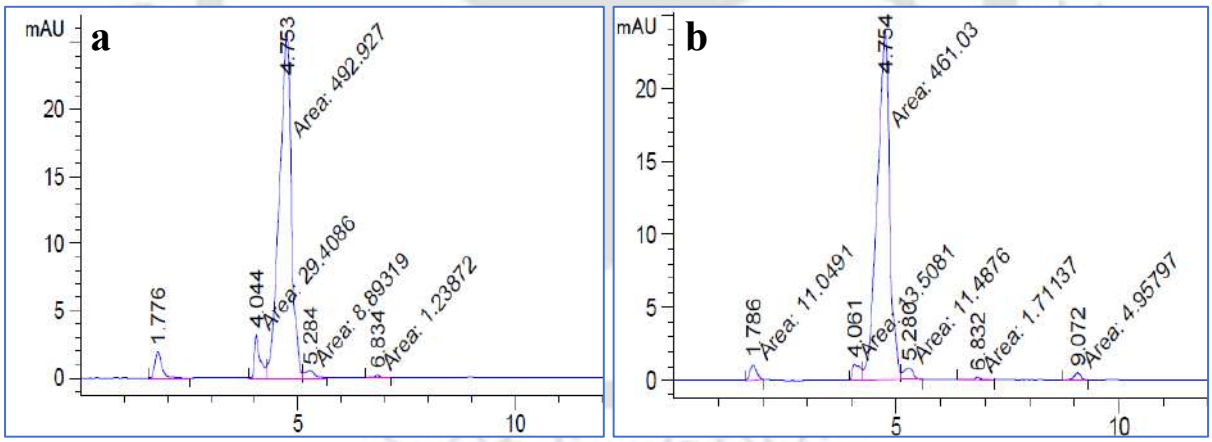

Figure 5.16: HPLC chromatograms (a) before and (b) after chronoamperometric test at 0.978 V (3600 s) using ZnO-VANs(bio)/FTO@pH7 during the course of p-CA sensing equipped with an ultra C18 column (UMISil C18(3), 250 × 4.6 mm, 5 µm particle size, thermoscientific). Acetonitrile (90%) and water (10%) were used as the mobile phase, and p-CA was detected using a UV detector at a fixed wavelength of 290 nm.

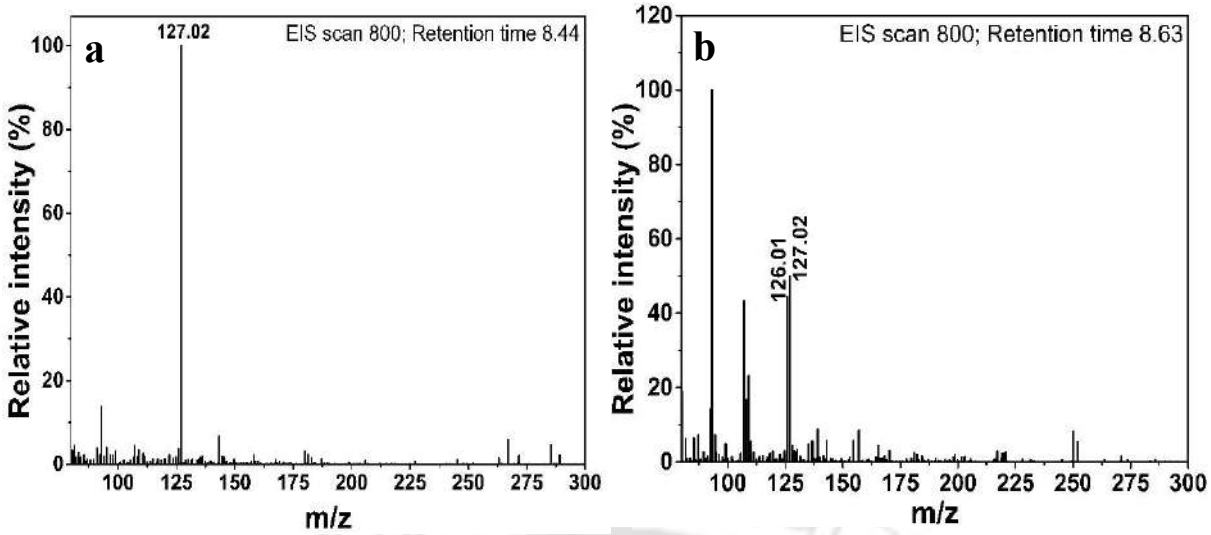

Figure 5.17: Mass spectrum (a) before and (b) after chronoamperometric test at 0.978 V (3600 s) using ZnO-VANs(bio)/FTO@pH7 during the course of p-CA sensing.

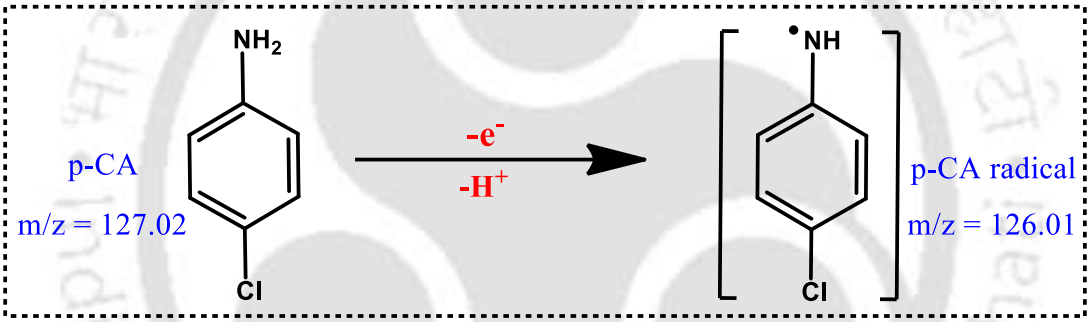

Figure 5.18: Proposed mechanism of redox pathway of p-CA sensing in BR buffer (pH 4) at 0.978 V (3600 s) using ZnO-VANs(bio)/FTO@pH7 corresponding to Fig. 5.17.

5.2.5.4 *Stability of ZnO-VANs(bio)/FTO@pH7 electrode during p-CA sensing*

The steady response of ZnO-VANs(bio)/FTO@pH7 electrode of p-CA sensing was evaluated, at a scan rate of 50 mV/s from 0.65 to 1.3 V vs. Ag/AgCl using 0.04 M BR buffer (pH 4) following deposition at -0.6 V vs. Ag/AgCl for 120 s, for subsequent 15 cycles. Fig. 5.19 shows the change in peak current with each p- CA detection cycle. Insignificant but a slight incessant decrease in the peak response was noted up to the 9th cycle. Although, only 4.7% decrease in the peak response (from the 1st cycle) was observed in the 9th cycle, which further decreased by 8.5% (from the 1st cycle) during the 15th cycle. The decrease in the peak response could be due to the accumulation of the oxidation product of p-CA on the ZnO-VANs(bio)/FTO@pH7 electrode.

The FESEM image (Fig. 5.20a) of the ZnO-VANs(bio)/FTO@pH7 electrode after the 15th cycle (Fig. 5.19) of p-CA sensing shows well-distributed 2D ZnO nanostructures onto the FTO substrate. A minor morphological change was noted (Fig. 5.20a) during the course of p-CA sensing (Dash et al., 2021).

The XRD analyses of ZnO-VANs(bio)/FTO@pH7 post-reaction (after 15th cycles of p-CA sensing) were done to analyse its structural attributes (Fig. 5.20b). It demonstrates that there is no notable change in ZnO-VANs(bio)/FTO@pH7 lattice structure after reaction in comparison to before the reaction (Fig. 5.3).

The XPS analysis of ZnO-VANs(bio)/FTO@pH7 after the 15th cycle of p-CA sensing was studied to investigate its compositional characteristics. The Zn 2p spectra of ZnO-VANs(bio)/FTO@pH7 (post reaction) exhibit two predominant peaks at 1022.09 and 1045.24 eV, and the peak intensities were found to be almost identical before (Fig. 5.6b) and after (Fig. 5.20c) the reaction. Furthermore, two characteristic peaks at 530.60 (O_L) and 531.78 eV (O_{ads}) were found in the high-resolution O 1s spectrum of ZnO-VANs(bio)/FTO@pH7 (Fig. 5.20d). In comparison to Fig. 5.6d, an additional peak in Fig. 5.20d was not observed, which could be due to the desorption of the C-O group from the bio-extract during the course of p-CA sensing (Ravi and Golder, 2023b). The electrocatalytic activity of the ZnO-VANs(bio)@pH7 sensor was compared with the recently reported ZnO nanostructure-based sensors. The current study demonstrated a clear superiority over several previous studies (Table 5.4).

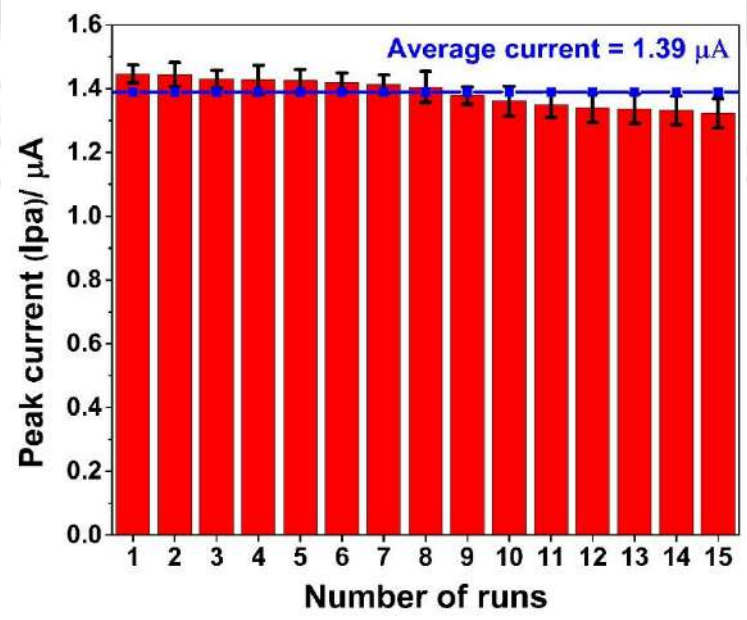

Figure 5.19: Repeatability of p-CA sensing. Reaction conditions: Deposition time 120 s, deposition potential -0.6 V vs. Ag/AgCl, and deposition temperature 45 °C in 50 mL 0.04 M BR buffer supporting electrolyte at pH 4.

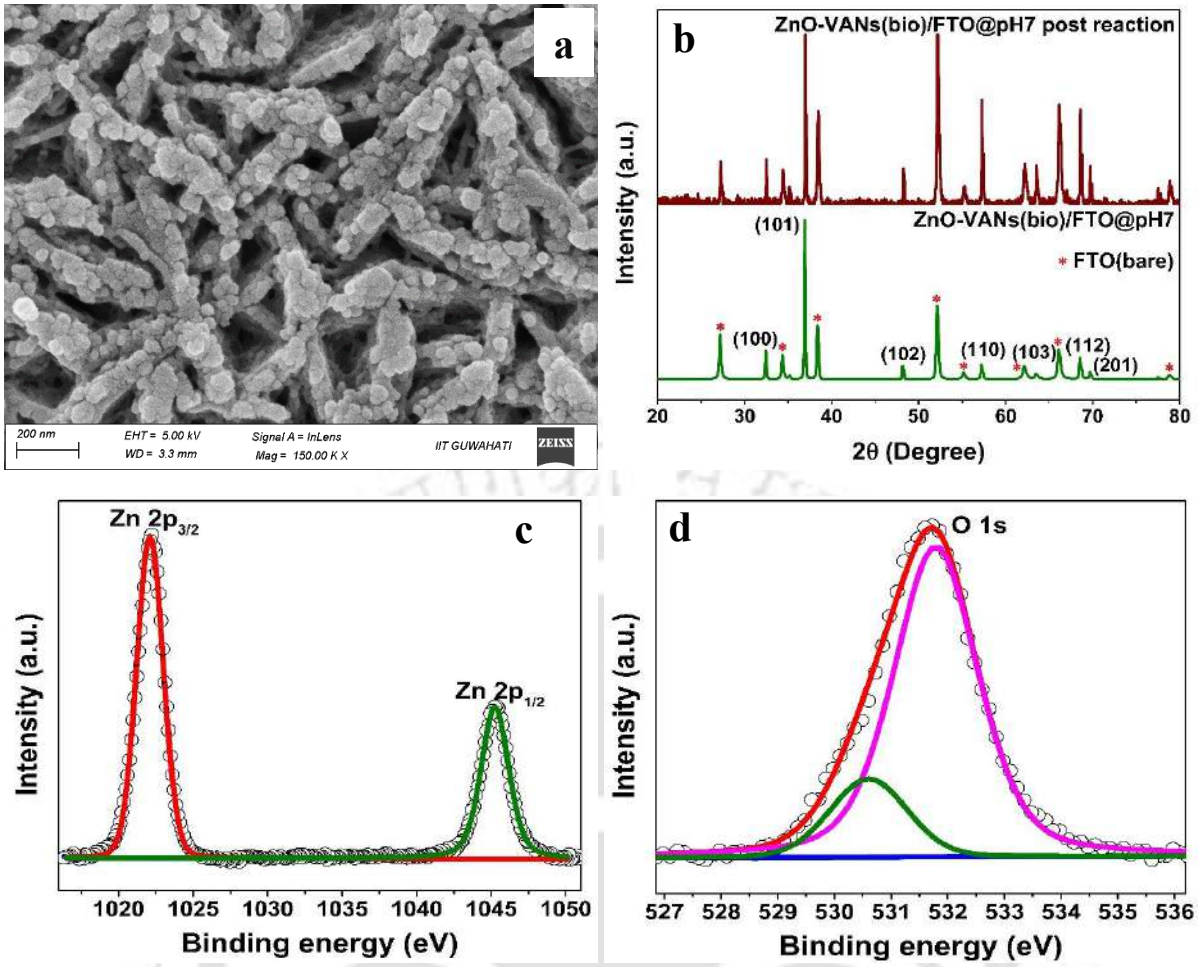

Figure 5.20: (a) FESEM image, (b) XRD pattern, and (c and d) XPS spectra of post-reaction ZnO-VANs(bio)/FTO@pH7 electrode (after 15th cycles of p-CA sensing).

Table 5.4. Comparison of electrocatalytic activity of the ZnO-VANs(bio)@pH7 electrode with the recently published ZnO nanoparticles-based sensors.

Working electrodes	Technique	LOD (μM)	Sensitivity ($\mu A \mu M^{-1} cm^{-2}$)	Analytes	References
ZnO-VANs(bio)/FTO@pH7	**SWASV***	**0.022**	**0.194**	**p-CA**	**Present work**
ZnO/NPG microelectrode	SWASV	0.004	102.343	Arsenic(III)	Zhuang et al., 2023
Pd/ZnO/APC/GCE	SWV[ᵠ]	0.01	-	Carbaryl	Jemai et al., 2022
ZnO@ZIF-8/ITO	CA[†]	3	0.0047	H_2O_2	Mei et al., 2022
MoS_2-ZnO/GCE	CA	0.025	0.639	Glucose	Ali et al., 2022
ZnO/Co_3O_4/rGO/GCE	CA	0.043	1.55	Glucose	Hussein et al., 2023

Sb-ZnO/N-rGO/GCE	CA	0.13	0.294	Nitrite	Cheng et al., 2022
	LSV[ɬ]	0.43	0.398		
ZnO/CNO/GCE	CV[ǂ]	-	0.607	Glucose	Sharma et al., 2022
ZnO@CoNi/LDH-NCDs	CA	0.2	13.040	Hydrazine	Zhang et al., 2023
ZnO-Cu_xO/GCE	CV	7.3	0.504	H_2O_2	Jain et al., 2022
	CV	15.7	0.158	p-Nitrophenol	
ZMO/ZnO/GCE	DPV[⁂]	0.019	0.760	Chlorpromazine	Balamurugan et al., 2022
Hexagonal ChAc-ZnO NS/Au	LSV	0.4	2.66	Hydrazine	Kaur et al., 2022

[*]Square wave anodic stripping voltammetry, [ʔ]Square wave voltammetry, [†]Chronoamperometry, [ɬ]Linear sweep voltammetry, [ǂ]Cyclic voltammetry, [⁂]Differential pulse voltammetry

5.2.5.5 *Reusability, reproducibility, and long-term usability of ZnO-VANs(bio)/FTO@pH7*

The reusability of the p-CA sensing was studied using the same electrode (ZnO-VANs(bio)/FTO@pH7) in 5 different p-CA solutions of the same concentration of p-CA (40 µM) by SWASV in 0.04 M BR buffer (pH 4) at optimized deposition conditions. The relative standard deviation of peak current during p-CA sensing was determined to be only 3.52 % (Fig. 5.21a). The reproducibility of the ZnO-VANs(bio)/FTO@pH7 was tested using 3 different fresh electrodes in 3 different p-CA solutions of the same concentration of p-CA (40 µM). ZnO-VANs(bio)/FTO@pH7 electrode displayed excellent reproducibility with a relative standard deviation of 1.8 % (Fig. 5.21b). The relative standard deviations are within the acceptable limits for p-CA sensing using ZnO-VANs(bio)/FTO@pH7 (Dash et al., 2018). Further, the reproducibility of the ZnO-VANs(bio)/FTO@pH7 electrode was examined over a long time (90 days, storage at room temperature) of its fabrication using SWASV in 0.04 M BR buffer (pH 4) at p-CA concentration of 40 µM and optimized deposition parameters. The reduction in the response current of 5.5 % was observed after 90 days of storage at room temperature of the ZnO-VANs(bio)/FTO@pH7 electrode compared to freshly prepared ZnO-VANs(bio)/FTO@pH7 electrode under identical experimental conditions (Fig. 5.21c).

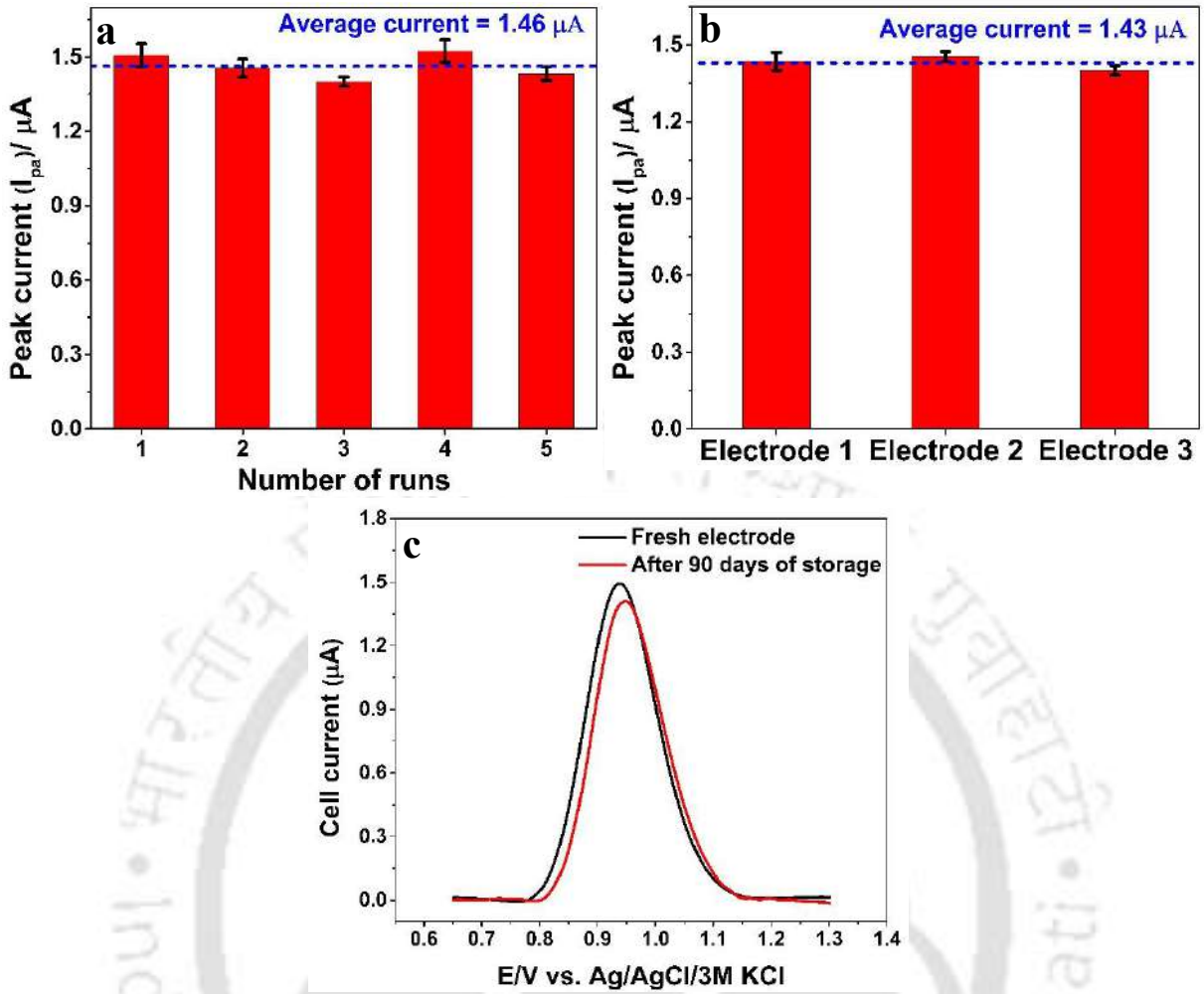

Figure 5.21: Peak current variation during p-CA (40 µM) sensing using ZnO-VANs(bio)/FTO@pH7 electrode: (a) Reusability of p-CA sensing using the same electrode in 5 different p-CA solutions of same p-CA concentration (40 µM), (b) Reproductivity of p-CA sensing using 3 different fresh electrodes in 3 different p-CA solutions of same p-CA concentration (40 µM), and (c) Peak current after 90 days of storage at room temperature. Reaction conditions: Deposition time 120 s, deposition potential -0.6 V vs. Ag/AgCl, and deposition temperature 45 °C in 50 mL 0.04 M BR buffer supporting electrolyte at pH 4.

5.2.6. Selectivity of p-CA sensing at ZnO-VANs(bio)/FTO@pH7 electrode

The chronoamperometric test using ZnO-VANs(bio)/FTO@pH7 electrode was conducted at various concentrations of p-CA ranging from a 5 to 90 µM along with the addition of interferants, namely, chlorobenzene (30 µM), carbendazim (30 µM), profenofos (30 µM), nitrite (30 µM), 4-nitrophenol (30 µM), bisphenol a (30 µM), and mercury (30 µM). The response of current was determined at 0.978 V vs. Ag/AgCl at an interval of 20 s, and the cell current stabilized very quickly after the addition of p-CA. The addition of p-CA caused changes

in the current response before and after the addition of interfering agents. In comparison to the actual spiked concentration of 5, 10, 30, 60, and 90 µM, the concentration of p-CA as measured using the calibration curve (Fig. 5.15b) is 4.84, 12.19, 29.36, 57.11, and 89.29 µM, respectively. It is evident that the response current remained unchanged by adding interferants (Fig. 5.22). The fabricated ZnO-VANs(bio)/FTO@pH7 nanostructures exhibited strong selectivity towards p-CA sensing even in the presence of chlorobenzene, carbendazim, profenofos, nitrite, 4-nitrophenol, bisphenol a, and mercury.

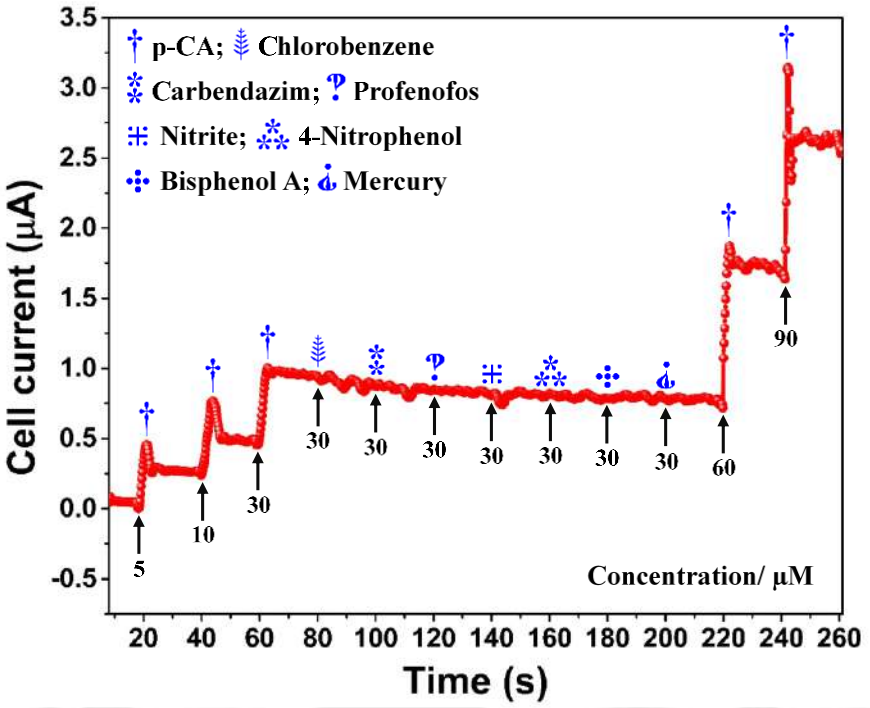

Figure 5.22: Chronoamperometric profile with step-wise addition of p-CA (5-90 µM) along with interferants addition of chlorobenzene (30 µM), carbendazim (30 µM), profenofos (30 µM), nitrite (30 µM), 4-nitrophenol (30 µM), bisphenol a (30 µM), and mercury (30 µM) at ZnO-VANs(bio)/FTO@pH7. Experimental conditions: E_{anode} = 0.978V vs. Ag/AgCl, reaction time 260 s, and temperature 45 °C in 50 mL 0.04 M BR buffer at pH 4.

5.2.7. p-CA determination in environmental water samples

Water samples were collected from the Brahmaputra river (26° 10′ 54.64″ N, 91° 41′ 47.96″ E) and residential water supply located at IIT Guwahati, India. The obtained water samples were filtered using 0.2 µm filter paper in order to remove suspended contaminants, if any, to minimize surface fouling of ZnO-VANs(bio)/FTO@pH7 electrode that could affect the sensor sensitivity. A thorough characteristic assays of these samples were performed, and the

resulted are summarized in Tables 5.5 and 5.6. Both samples included several background anions, namely fluoride, chloride, nitrate, phosphate, and sulphate. The ion chromatographs are shown in Figs. 5.23 and 5.24. Both river water and tap water samples could mimic a real p-CA sample as it contains a variable quantity of TDS, TOC, TIC, and TN.

The samples were then spiked with p-CA of 2-80 µM. The performance of ZnO-VANs(bio)/FTO@pH7 was then tested by determining the concentration of p-CA. These samples were then subjected to SWASV for the determination of p-CA concentration using the same calibration curve (Fig. 5.15b). The senor performance is listed in Table 5.7. The recovery of p-CA was almost 100 % noted in both water samples, even in the presence of several background organic traces and anions (Tables 5.5 and 5.6). The concentration variation of p-CA sensing at the ZnO-VANs(bio)/FTO@pH7 was also determined in comparison to HPLC. The maximum deviation of p-CA concentration was 4.6 % and 4.4 % in the tap and river water, respectively.

Table 5.5: Anions concentration in tap and river water.

Ions	Anions concentration in tap water (mg/L)	Anions concentration in river water (mg/L)
Fluoride	0.06	0.13
Chloride	0.69	0.76
Nitrate	0.81	1.16
Phosphate	0.44	-
Sulphate	26.9	44.91

Table 5.6: Tap and river water characterizations.

Parameters	Tap water	River water
pH	6.43	6.13
Conductivity (µS)	122.5	117.7
TDS (mg/L)	54	51
TOC (mg/L)	0	3.57
TIC (mg/L)	8.18	1.81
TN (mg/L)	0.81	1.79

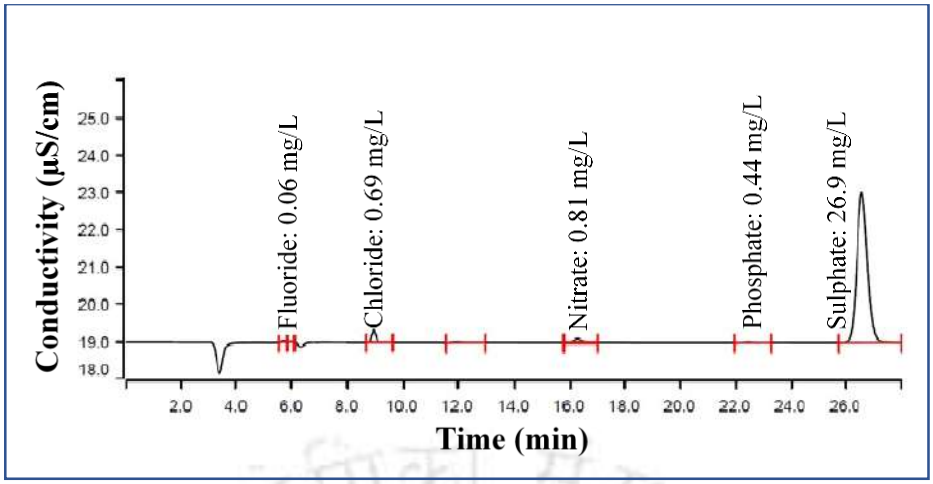

Figure 5.23: Anions concentration in tap water.

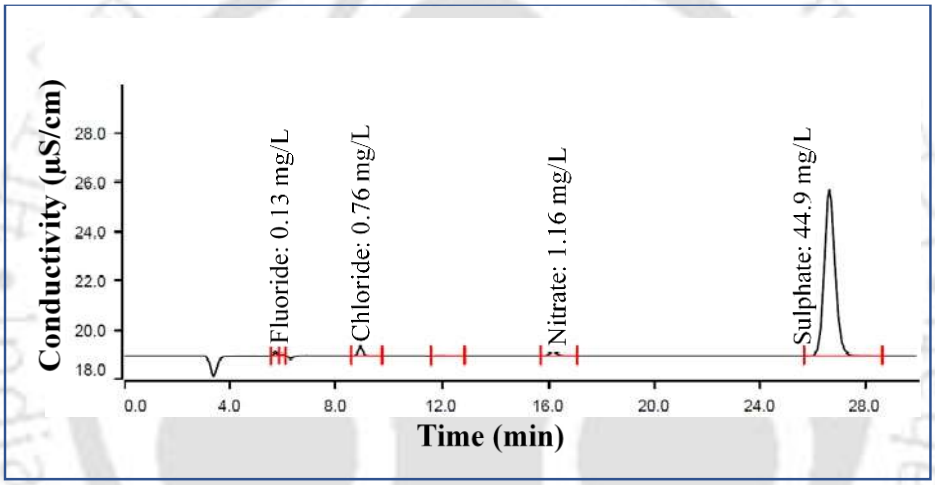

Figure 5.24: Anions concentration in river water.

Table 5.7: Performance of ZnO-VANs(bio)/FTO@pH7 electrode for p-CA determination from environmental water samples and its comparison with HPLC.

Sample	p-CA spiked (µM)	Performance of ZnO-VANs(bio)/FTO@pH7			p-CA determination using HPLC (µM)	Deviation (%)
		p-CA determination (µM)	Recovery (%)	RSD (%)		
Tap water	2	2.01	100.5	0.9	1.97	1.9
	10	10.35	103.5	1.0	10.8	- 4.6
	40	39.97	99.9	0.8	39.3	1.6
	80	79.31	99.1	0.4	79.4	-0.1

River water	2	2.05	102.5	1.5	2.1	- 2.4
	10	10.15	101.5	2.2	10.6	- 4.4
	40	39.96	99.9	1.1	39.6	0.9
	80	79.81	99.8	0.7	79.1	0.9

5.3. Major findings

We have successfully developed a bioinspired approach for the synthesis of hierarchical 2D ZnO-VANs(bio) on FTO glass substrate using the bio-extract of *Sechium edule* fruit. The synthesis process was strongly pH dependent, which in turn affects the shape, size, mechanism of formation, and VANs self-stabilization. ZnO-VANs(bio)/FTO@pH7 exhibited good crystallinity along with a uniform growth of ZnO with an average length of ~ 820 nm and thickness of ~ 27.11 nm. The synthesized ZnO-VANs(bio)/FTO@pH7 electrode showed 2.2, 1.9, and 1.2 folds higher surface roughness than ZnO@seed/FTO, ZnO-H_2O(control)/FTO@pH7, and FTO(bare), respectively. ZnO-VANs(bio)/FTO@pH7 electrode showed a 61.18 % decrease in electron transfer resistance with an increase in effective surface area (1.2 folds) in comparison to FTO(bare). The deposition potential, time, and temperature of p-CA sensing by ZnO-VANs(bio)/FTO@pH7 electrode were optimized as -0.6 V vs. Ag/AgCl, 120 s, and 45°C (peak current response increased by 53.12 % at 25 °C) using SWASV. The LOD and LOQ of the ZnO-VANs(bio)/FTO@pH7 sensor were obtained as 0.021 and 0.071 µM (2-folds lower than FTO(bare)), respectively, with a high sensitivity of 0.194 µA. $\mu M^{-1}.cm^{-2}$ for p-CA sensing in BR buffer at pH 4. The sensing of p-CA took place through a single proton and single electron transfer reaction forming a p-CA radical. Only a 4.7% decrease in response current of p-CA sensing was noted up to the 9^{th} cycle, even in the presence of common interferants in the environmental matrix. ZnO-VANs(bio)/FTO@pH7 was unprecedently selective towards p-CA sensing, and the coexistence of chlorobenzene, carbendazim, profenofos, nitrite, 4-nitrophenol, bisphenol a, and mercury could not alter its sensitivity and redox potential (0.978 V vs. Ag/AgCl) of p-CA. Therefore, the fabricated sensor holds prospective applications owing to a binder-free, ease, and bio-based catalysts synthesis approach with high stability and sensitivity, and low detection limit for sensing of agriculture pesticides and their intermediates. Furthermore, VANs modified with carbon quantum dots derived from the remnant carbon-rich biomass could significantly enhance the performance of the electrochemical sensor.

References

Ahmad, R., Tripathy, N., Ahn, M.-S., Hahn, Y.-B., 2017. Development of highly-stable binder-free chemical sensor electrodes for p-nitroaniline detection. J. Colloid Interface Sci. 494, 300–306. https://doi.org/10.1016/j.jcis.2017.01.099

Ahmad, R., Tripathy, N., Hahn, Y.-B., 2012a. Wide linear-range detecting high sensitivity cholesterol biosensors based on aspect-ratio controlled ZnO nanorods grown on silver electrodes. Sensors Actuators B Chem. 169, 382–386. https://doi.org/10.1016/j.snb.2012.05.027

Ahmad, R., Tripathy, N., Kim, J.H., Hahn, Y.-B., 2012b. Highly selective wide linear-range detecting glucose biosensors based on aspect-ratio controlled ZnO nanorods directly grown on electrodes. Sensors Actuators B Chem. 174, 195–201. https://doi.org/10.1016/j.snb.2012.08.011

Ali, F., Zafar, A., Nisar, A., Liu, Y., Karim, S., Faiz, F., Zafar, Z., Sun, H., Hussain, S., Faiz, Y., Ali, T., Javed, S., Yu, Y., Ahmad, M., 2022. Development of MoS_2-ZnO heterostructures: An efficient bifunctional catalyst for the detection of glucose and degradation of toxic organic dyes. New J. Chem. 47, 681–690. https://doi.org/10.1039/d2nj04758f

Arratia, M.M., Rebollo, M. de L.L., Flores, F.J.P., Contreras, R.G., Soriano, J.L.M., Presas, A.M.F., 2019. Detection of para-Chloroaniline resulting from the interaction between sodium hypochlorite and chlorhexidine analyzed by mass spectrometry. Am. J. Anal. Chem. 10, 629–640. https://doi.org/10.4236/ajac.2019.1012044

Bagheri, H., Afkhami, A., Khoshsafar, H., Rezaei, M., Shirzadmehr, A., 2013. Simultaneous electrochemical determination of heavy metals using a triphenylphosphine/MWCNTs composite carbon ionic liquid electrode. Sensors Actuators B Chem. 186, 451–460. https://doi.org/10.1016/j.snb.2013.06.051

Bakhsh, H., Buledi, J.A., Ghumro, T., Khand, N.H., Ameen, S., Solangi, A.R., Sherazi, S.T.H., Shah, Z.-H. ul H., 2021. Sodium dodecyl sulfate stabilized NiO nanoseeds: A potential procedure for ultra-sensitive determination of bentazone in vegetables. J. Mater. Sci. Mater. Electron. 32, 15917–15929. https://doi.org/10.1007/s10854-021-06143-7

Balamurugan, K., Karthik, R., Chen, S.M., Sukanya, R., Thasma Subramanian, B., Biju, V.M.N., Shim, J.J., Breslin, C.B., 2022. Heterostructures of mixed metal oxides ($ZnMnO_3$/ZnO) synthesized by a wet-chemical approach and their application for the electrochemical detection of the drug chlorpromazine. Compos. Part B Eng. 236, 109822.

https://doi.org/10.1016/j.compositesb.2022.109822

Castro, S.V.F., Silva, C. V., Stefano, J.S., Richter, E.M., Munoz, R.A.A., 2020. Voltammetric determination of traces of 4-Chloroaniline in antiseptic samples on a cathodically-treated boron-doped diamond electrode. J. Electroanal. Chem. 877, 2–8. https://doi.org/10.1016/j.jelechem.2020.114500

Chakraborty, U., Kaur, G., Rubahn, H., Kaushik, A., Ram Chaudhary, G., Kumar Mishra, Y., 2023. Advanced metal oxides nanostructures to recognize and eradicate water pollutants. Prog. Mater. Sci. 101169. https://doi.org/10.1016/j.pmatsci.2023.101169

Chekin, F., Bagheri, S., Abd Hamid, S.B., 2013. Synthesis of Pt doped TiO_2 nanoparticles: Characterization and application for electrocatalytic oxidation of l-methionine. Sensors Actuators B Chem. 177, 898–903. https://doi.org/10.1016/j.snb.2012.12.002

Cheng, Z., Song, H., Zhang, X., Cheng, X., Xu, Y., Zhao, H., Gao, S., Huo, L., 2022. Enhanced non-enzyme nitrite electrochemical sensing property based on stir bar-shaped ZnO nanorods decorated with nitrogen-doped reduced graphene oxide. Sensors Actuators B Chem. 355, 131313. https://doi.org/10.1016/j.snb.2021.131313

Chowdhury, A., Bhan, C., Peela, N.R., Golder, A.K., 2022. A tunable bioinspired process of SnO_2 NPs synthesis for electrochemical CO_2-into-formate conversion. J. CO_2 Util. 66, 102263. https://doi.org/10.1016/j.jcou.2022.102263

Chowdhury, A., Bhan, C., Rao Peela, N., Kumar Golder, A., 2023. A simple template-free bioinspired route of 1D Bi_2S_3 nanorods synthesis for electrochemical CO_2 reduction to formate. J. Ind. Eng. Chem. 127, 138–148. https://doi.org/10.1016/j.jiec.2023.06.055

Chowdhury, A., Peela, N.R., Golder, A.K., 2021. Synthesis of Cu_2O NPs using bioanalytes present in *Sechium edule*: Mechanistic insights and application in electrocatalytic CO_2 reduction to formate. J. CO_2 Util. 51, 101622. https://doi.org/10.1016/j.jcou.2021.101622

Dash, S.R., Bag, S.S., Golder, A.K., 2022. Carbon Dots Derived from Waste Psidium Guajava Leaves for Electrocatalytic Sensing of Chlorpyrifos. Electroanalysis 34, 1141–1149. https://doi.org/10.1002/elan.202100344

Dash, S.R., Bag, S.S., Golder, A.K., 2021. Bio-inspired PtNPs/Graphene nanocomposite based electrocatalytic sensing of metabolites of dipyrone. Anal. Chim. Acta 1167, 338562. https://doi.org/10.1016/j.aca.2021.338562

Dash, S.R., Bag, S.S., Golder, A.K., 2020. Synthesis of highly structured spherical Ag@Pt core-shell NPs using bio-analytes for electrocatalytic Pb(II) sensing. Sensors Actuators B Chem. 314, 128062. https://doi.org/10.1016/j.snb.2020.128062

Dash, S.R., Bag, S.S., Golder, A.K., 2018. Synergized AgNPs formation using microwave in

a bio-mediated route: Studies on particle aggregation and electrocatalytic sensing of ascorbic acid from biological entities. J. Electroanal. Chem. 827, 181–192. https://doi.org/10.1016/j.jelechem.2018.09.023

Ejsmont, A., Goscianska, J., 2023. Hydrothermal synthesis of ZnO superstructures with controlled morphology via temperature and pH optimization. Materials (Basel). 16, 1641. https://doi.org/10.3390/ma16041641

Ezhil Vilian, A.T., Hwang, S.-K., Lee, M.J., Huh, Y.S., Han, Y.-K., 2022. Manganese-doped zinc sulfide microspheres for improved electrocatalytic sensing ability toward carbendazim in food samples. Microchem. J. 175, 107204. https://doi.org/10.1016/j.microc.2022.107204

Flick, G.J., Burnette, F.S., Aung, L.H., Ory, R.L., St. Angelo, A.J., 1978. Chemical composition and biochemical properties of mirlitons (*Sechium edule*) and purple, green, and white eggplants (*Solanum melongena*). J. Agric. Food Chem. 26, 1000–1005. https://doi.org/10.1021/jf60219a045

Ganesamurthi, J., Shanmugam, R., Chen, S.M., Veerakumar, P., 2022. Bismuth sulfide/zinc-doped graphitic carbon nitride nanocomposite for electrochemical detection of hazardous nitric oxide. J. Electroanal. Chem. 910, 116174. https://doi.org/10.1016/j.jelechem.2022.116174

Gavlick, W.K., Davis, P.K., 1994. Gas chromatographic determination of p-Chloroaniline in a chlorhexidine digluconate-containing alcohol foam surgical scrub product. J. AOAC Int. 77, 583–586. https://doi.org/10.1093/jaoac/77.3.583

Gogoi, D., Koyani, R., Golder, A.K., Peela, N.R., 2020. Enhanced photocatalytic hydrogen evolution using green carbon quantum dots modified 1-D CdS nanowires under visible light irradiation. Sol. Energy 208, 966–977. https://doi.org/10.1016/j.solener.2020.08.061

Gonçalves, A.R., do Nascimento, H.L., Duarte, G.H.B., Simas, R.C., de Jesus Soares, A., Eberlin, M.N., Marques, L.A., 2016. Liquid chromatography-tandem mass spectrometry determination of p-Chloroaniline in gel and aqueous chlorhexidine products used in dentistry. Chromatographia 79, 841–849. https://doi.org/10.1007/s10337-016-3100-6

Gopi, P.K., Ngo, D.B., Chen, S.-M., Ravikumar, C.H., Surareungchai, W., 2022. High-performance electrochemical sensing of hazardous pesticide Paraoxon using $BiVO_4$ nano dendrites equipped catalytic strips. Chemosphere 288, 132511. https://doi.org/10.1016/j.chemosphere.2021.132511

Gumpu, M.B., Veerapandian, M., Krishnan, U.M., Rayappan, J.B.B., 2017. Simultaneous electrochemical detection of Cd(II), Pb(II), As(III) and Hg(II) ions using ruthenium(II)-

textured graphene oxide nanocomposite. Talanta 162, 574–582. https://doi.org/10.1016/j.talanta.2016.10.076

Hahn, Y.-B., 2011. Zinc oxide nanostructures and their applications. Korean J. Chem. Eng. 28, 1797–1813. https://doi.org/10.1007/s11814-011-0213-3

Havlíková, L., Matysová, L., Nováková, L., Hájková, R., Solich, P., 2007. HPLC determination of chlorhexidine gluconate and p-Chloroaniline in topical ointment. J. Pharm. Biomed. Anal. 43, 1169–1173. https://doi.org/10.1016/j.jpba.2006.09.037

Hussein, B.A., Tsegaye, A.A., Shifera, G., M. Taddesse, A., 2023. A sensitive non-enzymatic electrochemical glucose sensor based on a ZnO/Co_3O_4/reduced graphene oxide nanocomposite. Sensors & Diagnostics 2, 347–360. https://doi.org/10.1039/D2SD00183G

Imran, M., Ahmed, S., Al-Harthi, E.A., Khan, M.E., Alam, M.M., Haouala, F., Chaudhary, A.A., Asghar, A., 2023. Electrochemical detection of nitrazepam using leaf-like graphitic carbon nitride nanosheets. Phys. Scr. 98, 075003. https://doi.org/10.1088/1402-4896/acd7b0

Jain, S., Chakraborty, A., Sharma, B., Sarma, T.K., 2022. Cu^{2+} Ion Doping-Induced Self-Assembled ZnO-Cu_xO Nanostructures for Electrochemical Sensing of Hydrogen Peroxide and p -Nitrophenol. ACS Appl. Nano Mater. 5, 11973–11983. https://doi.org/10.1021/acsanm.2c03073

Jemai, R., Djebbi, M.A., Hussain, N., Yang, B., Hirtz, M., Trouillet, V., Ben Rhaiem, H., Ben Haj Amara, A., 2022. Activated porous carbon supported Pd and ZnO nanocatalysts for trace sensing of carbaryl pesticide in water and food products. New J. Chem. 46, 13880–13895. https://doi.org/10.1039/d2nj01844f

Kaur, A., Chakraborty, U., Chauhan, M., Sharma, R., Kaur, G., Chaudhary, G.R., 2022. Choline acetate modified ZnO nanostructure as efficient electrochemical sensor for hydrazine detection. Electrochim. Acta 419, 140384. https://doi.org/10.1016/j.electacta.2022.140384

Khan, M.E., Mohammad, A., Ali, W., Khan, A.U., Hazmi, W., Zakri, W., Yoon, T., 2022. Excellent visible-light photocatalytic activity towards the degradation of tetracycline antibiotic and electrochemical sensing of hydrazine by SnO_2–CdS nanostructures. J. Clean. Prod. 349, 131249. https://doi.org/10.1016/j.jclepro.2022.131249

Kokulnathan, T., Vishnuraj, R., Wang, T.-J.J., Kumar, E.A., Pullithadathil, B., 2021. Heterostructured bismuth oxide/hexagonal-boron nitride nanocomposite: A disposable electrochemical sensor for detection of flutamide. Ecotoxicol. Environ. Saf. 207, 111276.

https://doi.org/10.1016/j.ecoenv.2020.111276

Lai, M.-H., Tubtimtae, A., Lee, M.-W., Wang, G.-J., 2010. ZnO-nanorod dye-sensitized solar cells: New structure without a transparent conducting oxide layer. Int. J. Photoenergy 2010, 1–5. https://doi.org/10.1155/2010/497095

Lee, Y.J., Sounart, T.L., Liu, J., Spoerke, E.D., McKenzie, B.B., Hsu, J.W.P., Voigt, J.A., 2008. Tunable arrays of ZnO nanorods and nanoneedles via seed layer and solution chemistry. Cryst. Growth Des. 8, 2036–2040. https://doi.org/10.1021/cg800052p

Li, K., Li, Y., Wang, L., Yang, L., Ye, B., 2019. Study the voltammetric behavior of 10-Hydroxycamptothecin and its sensitive determination at electrochemically reduced graphene oxide modified glassy carbon electrode. Arab. J. Chem. 12, 2732–2739. https://doi.org/10.1016/j.arabjc.2015.05.014

Liu, Z., Xia, X., Guan, H.-K., Liu, Q., Zhao, S.-S., Cheng, X.-L., Xu, Q.-Q., Li, S.-S., 2022. Hypersensitized electrochemical detection of Hg(II) based on tunable sulfur-doped porous Co_3O_4 nanosheets: Promotion Co^{2+}/Co^{3+} valence change cycle and adsorption via introducing S. Chem. Eng. J. 435, 134950. https://doi.org/10.1016/j.cej.2022.134950

Lotfi, Z., Gholivand, M.B., Shamsipur, M., mirzaei, M., 2022. An electrochemical sensor based on Ag nanoparticles decorated on cadmium sulfide nanowires/reduced graphene oxide for the determination of acyclovir. J. Alloys Compd. 903, 163912. https://doi.org/10.1016/j.jallcom.2022.163912

Mali, S.S., Kim, H., Patil, P.S., Hong, C.K., 2013. Chemically grown vertically aligned 1D ZnO nanorods with CdS coating for efficient quantum dot sensitized solar cells (QDSSC): a controlled synthesis route. Dalt. Trans. 42, 16961. https://doi.org/10.1039/c3dt51287h

Malode, S.J., Keerthi, P.K., Shetti, N.P., Kulkarni, R.M., 2020. Electroanalysis of Carbendazim using MWCNT/Ca-ZnO Modified Electrode. Electroanalysis 32, 1590–1599. https://doi.org/10.1002/elan.201900776

Manimozhi, R., Rajkumar, K., Sabarish, K., Talwar, M.N., Prakash, A.P.G., 2022. Solution combustion synthesized ZnO/$Na_2Ti_6O_{13}$ composite for degradation of 4-Nitrophenol under solar irradiation. Carbon Lett. 32, 1355–1363. https://doi.org/10.1007/s42823-022-00357-3

Manivannan, K., Sivakumar, M., Cheng, C.-C., Lu, C.-H., Chen, J.-K., 2019. An effective electrochemical detection of chlorogenic acid in real samples: Flower-like ZnO surface covered on PEDOT:PSS composites modified glassy carbon electrode. Sensors Actuators B Chem. 301, 127002. https://doi.org/10.1016/j.snb.2019.127002

Mei, H., Xie, J., Li, Z., Lou, C., Lei, G., Liu, X., Zhang, J., 2022. Rational design of ZnO@ZIF-

8 nanoarrays for improved electrochemical detection of H_2O_2. CrystEngComm 24, 1645–1654. https://doi.org/10.1039/D1CE01704G

Messmer, A.S., Nickel, C.H., Bareiss, D., 2015. p-Chloroaniline poisoning causing methemoglobinemia: A case report and review of the literature. Case Rep. Emerg. Med. 2015, 1–4. https://doi.org/10.1155/2015/208732

Mohamadighader, N., Saraei, M., Nematollahi, D., Goljani, H., 2020. Electrochemical study of 4-chloroaniline in a water/acetonitrile mixture. A new method for the synthesis of 4-chloro-2-(phenylsulfonyl)aniline and: N -(4-chlorophenyl)benzenesulfonamide. RSC Adv. 10, 31563–31569. https://doi.org/10.1039/d0ra05680d

Mohammad, A., Karim, M.R., Khan, M.E., AlSukaibi, A.K.D., Yoon, T., 2022. Eco-benign fabrication of silver nanoparticle-modified zeolitic imidazolate framework and construction of a non-enzymatic electrochemical sensor. Mater. Today Sustain. 19, 100182. https://doi.org/10.1016/j.mtsust.2022.100182

Oh, Y.J., Shin, M.C., Kim, J.H., Yang, S.J., 2021. Facile preparation of ZnO quantum dots@porous carbon composites through direct carbonization of metal–organic complex for high-performance lithium ion batteries. Carbon Lett. 31, 323–329. https://doi.org/10.1007/s42823-020-00175-5

Ordonez, A., Gomez, J., Vattuone, M., Lsla, M., 2006. Antioxidant activities of *Sechium edule* (Jacq.) Swartz extracts. Food Chem. 97, 452–458. https://doi.org/10.1016/j.foodchem.2005.05.024

Pino, F., Mayorga-Martinez, C.C., Merkoçi, A., 2016. High-performance sensor based on copper oxide nanoparticles for dual detection of phenolic compounds and a pesticide. Electrochem. commun. 71, 33–37. https://doi.org/10.1016/j.elecom.2016.08.001

Pradhan, D., Leung, K.T., 2008. Vertical growth of two-dimensional zinc oxide nanostructures on ITO-coated glass: Effects of deposition temperature and deposition time. J. Phys. Chem. C 112, 1357–1364. https://doi.org/10.1021/jp076890n

Rafaie, H.A., Samat, N.A., Nor, R.M., 2014. Effect of pH on the growth of zinc oxide nanorods using Citrus aurantifolia extracts. Mater. Lett. 137, 297–299. https://doi.org/10.1016/j.matlet.2014.09.033

Rao, C.V., Golder, A.K., 2016. Development of a bio-mediated technique of silver-doping on titania. Colloids Surfaces A Physicochem. Eng. Asp. 506, 557–565. https://doi.org/10.1016/j.colsurfa.2016.07.031

Ravi, Pandey, L.M., 2019. Enhanced adsorption capacity of designed bentonite and alginate beads for the effective removal of methylene blue. Appl. Clay Sci. 169, 102–111.

https://doi.org/10.1016/j.clay.2018.12.019

Ravi, R., Golder, A.K., 2023a. Pharmaceutically Active Compounds' (PhACs) Threat: An Environmental Prospective, in: Sustainable Environment. Springer Nature Singapore, Singapore, pp. 51–66. https://doi.org/10.1007/978-981-19-8464-8_3

Ravi, R., Golder, A.K., 2023b. A tuneable bioinspired process of Pt-doping in TiO_2 for improved photoelectrochemical and photocatalytic functionalities. Colloids Surfaces A Physicochem. Eng. Asp. 663, 131034. https://doi.org/10.1016/j.colsurfa.2023.131034

Salagare, S., Adarakatti, P.S., Yarradoddappa, V., 2021. Facile synthesis of silver nanoparticle-decorated zinc oxide nanocomposite-based pencil graphite electrode for selective electrochemical determination of nitrite. Carbon Lett. 31, 1273–1286. https://doi.org/10.1007/s42823-021-00251-4

Sen, S.K., Jalil, M.A., Hossain, M., Manir, M.S., Hoque, K., Islam, M.A., Hossain, M.N., 2021. Silver incorporated α-MoO_3 nanoplates to nanorods: Exploring the effects of doping on structural, morphological and optical properties. Mater. Today Commun. 27, 102404. https://doi.org/10.1016/j.mtcomm.2021.102404

Sharma, A., Agrawal, A., Pandey, G., Kumar, S., Awasthi, K., Awasthi, A., 2022. Carbon nano-onion-decorated ZnO composite-based enzyme-less electrochemical biosensing approach for glucose. ACS Omega 7, 37748–37756. https://doi.org/10.1021/acsomega.2c04730

Sharwani, A.A., Narayanan, K.B., Khan, M.E., Han, S.S., 2022. Photocatalytic degradation activity of goji berry extract synthesized silver-loaded mesoporous zinc oxide (Ag@ZnO) nanocomposites under simulated solar light irradiation. Sci. Rep. 12, 1–18. https://doi.org/10.1038/s41598-022-14117-w

Supraja, P., Tripathy, S., Krishna Vanjari, S.R., Singh, V., Singh, S.G., 2019. Electrospun tin (IV) oxide nanofiber based electrochemical sensor for ultra-sensitive and selective detection of atrazine in water at trace levels. Biosens. Bioelectron. 141, 111441. https://doi.org/10.1016/j.bios.2019.111441

Tang, C., Zhang, Y., Su, J., Wang, C., Sun, R., Zhang, J., Li, G., 2016. Synthesis and photocatalytic properties of vertically aligned Bi_2S_3 platelets. Solid State Sci. 51, 24–29. https://doi.org/10.1016/j.solidstatesciences.2015.11.004

Venieri, D., Fraggedaki, A., Kostadima, M., Chatzisymeon, E., Binas, V., Zachopoulos, A., Kiriakidis, G., Mantzavinos, D., 2014. Solar light and metal-doped TiO_2 to eliminate water-transmitted bacterial pathogens: Photocatalyst characterization and disinfection performance. Appl. Catal. B Environ. 154–155, 93–101.

https://doi.org/10.1016/j.apcatb.2014.02.007

Wahab, R., Ansari, S.G., Kim, Y.S., Song, M., Shin, H.-S., 2009. The role of pH variation on the growth of zinc oxide nanostructures. Appl. Surf. Sci. 255, 4891–4896. https://doi.org/10.1016/j.apsusc.2008.12.037

Wang, L., Li, X., Xiong, S., Lin, H., Xu, Y., Jiao, Y., Chen, J., 2021. Plant polyphenols induced the synthesis of rich oxygen vacancies Co_3O_4/Co@N-doped carbon hollow nanomaterials for electrochemical energy storage and conversion. J. Colloid Interface Sci. 600, 58–71. https://doi.org/10.1016/j.jcis.2021.05.011

Wang, L., Liu, G., Zou, L., Xue, D., 2010. Phase evolution from rod-like ZnO to plate-like zinc hydroxysulfate during electrochemical deposition. J. Alloys Compd. 493, 471–475. https://doi.org/10.1016/j.jallcom.2009.12.129

Wang, Y., Limon-Petersen, J.G., Compton, R.G., 2011. Measurement of the diffusion coefficients of $[Ru(NH_3)_6]^{3+}$ and $[Ru(NH_3)_6]^{2+}$ in aqueous solution using microelectrode double potential step chronoamperometry. J. Electroanal. Chem. 652, 13–17. https://doi.org/10.1016/j.jelechem.2010.12.011

Wicaksono, W.P., Fadilla, N.I., Zamar, A.A., Fadillah, G., Anugrahwati, M., Anas, A.K., Kadja, G.T.M., 2022. Formaldehyde electrochemical sensor using graphite paste-modified green synthesized zinc oxide nanoparticles. Inorg. Chem. Commun. 143, 109729. https://doi.org/10.1016/j.inoche.2022.109729

Wiench, P., González, Z., Menéndez, R., Grzyb, B., Gryglewicz, G., 2018. Beneficial impact of oxygen on the electrochemical performance of dopamine sensors based on N-doped reduced graphene oxides. Sensors Actuators B Chem. 257, 143–153. https://doi.org/10.1016/j.snb.2017.10.106

Wu, B., Yeasmin, S., Liu, Y., Cheng, L.J., 2022. Sensitive and selective electrochemical sensor for serotonin detection based on ferrocene-gold nanoparticles decorated multiwall carbon nanotubes. Sensors Actuators B Chem. 354, 131216. https://doi.org/10.1016/j.snb.2021.131216

Wu, Q., Diao, P., Sun, J., Jin, T., Xu, D., Xiang, M., 2015. Electrodeposition of vertically aligned silver nanoplate arrays on indium tin oxide substrates. J. Phys. Chem. C 119, 20709–20720. https://doi.org/10.1021/acs.jpcc.5b05109

Yang, X., Wang, Y., Tong, X., Yang, N., 2022. Strain engineering in electrocatalysts: Fundamentals, progress, and perspectives. Adv. Energy Mater. 12, 2102261. https://doi.org/10.1002/aenm.202102261

Zhang, Y., Wu, J., Zhao, S., Tang, X., He, Z., Huang, K., Yu, H., Zou, Z., Xiong, X., 2023.

Self-assembled ZnO microspheres coated with carbon dot-doped CoNi LDH wrinkled films as electrochemical sensors for highly sensitive detection of hydrazine. Anal. Methods 15, 304–310. https://doi.org/10.1039/D2AY01698B

Zhuang, Z., Chen, Y., Chen, K., Liu, Z., Guo, Z., Huang, X., 2023. In-situ synthesis of ZnO onto nanoporous gold microelectrode for the electrochemical sensing of arsenic(III) in near-neutral conditions. Sensors Actuators B Chem. 378, 133184. https://doi.org/10.1016/j.snb.2022.133184

CHAPTER 6

Bioinspired Vertically Aligned 2D ZnO Surface Nanostructures Functionalized with Carbon Quantum Dots for Electrocatalytic Monitoring of Norfloxacin

This chapter presents the bioinspired synthesis of 2D surface ZnO vertically aligned nanostructures (VANs) on FTO glass using the bio-extract of Sechium edule fruit. Subsequently, the remnant carbon-rich fruit peel was used for the preparation of carbon quantum dots (CQDs). Finally, ZnO VANs were functionalized with CQDs to develop an electrochemical platform for monitoring of norfloxacin (NFX) using SWV technique. The practical application of the developed platform was tested by sensing NFX in an environmental matrix and compared with HPLC.

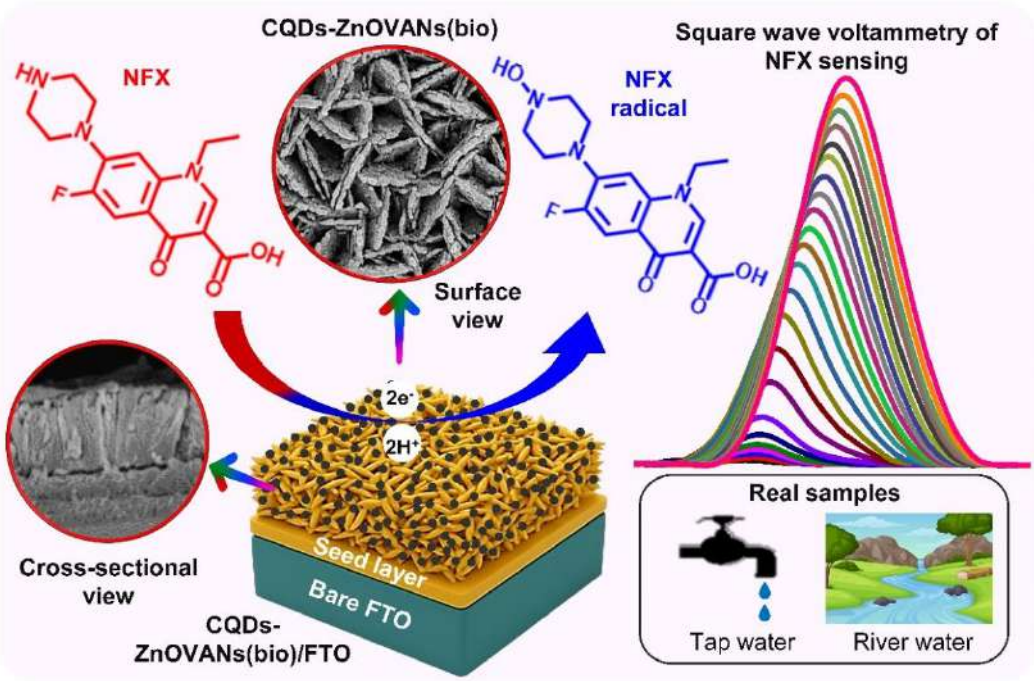

Chapter highlights

- Bioinspired CQDs modified 2D ZnO nanostructures (CQDs-ZnOVANs(bio)/FTO)
- CQDs-ZnOVANs(bio)/FTO catalysed norfloxacin sensing by square wave voltammetry
- Sensing involves two-electron and two-proton transfer in a diffusion-controlled process
- Norfloxacin detection limit of 0.0066 µM and sensitivity of 0.1903 µA. $\mu M^{-1}.cm^{-2}$
- Norfloxacin sensing highly selective against common antibiotics and ionic interferents

6.1. Background and executive motivation

Norfloxacin (NFX), a fluoroquinolone drug, is known for their broad-spectrum activity and high clinical effectiveness (Liu et al., 2019). NFX is effective against a broad spectrum of bacteria, such as Gram-positive and -negative, making it a versatile medicine in treating urinary and respiratory tract infections (Liu et al., 2018). However, NFX was detected in several environmental matrices, including municipal and hospital waters and surface and ground waters, at concentrations ranging from nano to micro levels (Muungani and van Zyl, 2023). However, the presence of NFX in environmental matrices results in the development of antibiotic-resistant bacteria and disrupts hormonal systems in aquatic species. Additionally, the abuse of NFX can severely impact the kidneys and reproductive system, and may cause allergic reactions, vomiting, headache, and other adverse effects (Fu et al., 2023; Vu et al., 2023). The growing presence of NFX and other antibiotic residues in the environment has become a global concern due to their potential risks to human and ecological systems. Therefore, advanced sensing methodologies are highly warranted for monitoring trace levels of antibiotic residues with superior sensitivity and selectivity.

Analytic monitoring techniques, including chromatography and spectrometry, are effective for trace-level detection and quantification of antibiotic residues in the environmental matrix (Cicek and Erdogan, 2024; Espinosa-Mansilla et al., 2005; Wang et al., 2020). However, these analytical methods are bulky, costly, require adept personnel, and are not suited for real-time, on-site monitoring, considering the growing pollution concerns caused by pharmaceutically active compounds. Therefore, the development of an alternate cost-effective, highly sensitive, and portable electrocatalytic platform for monitoring and quantification of NFX in environmental matrices is urgently needed.

Electrochemical sensors have the potential to detect antibiotic residues at a low concentration, offering a promising alternative to conventional analytical techniques (Lv et al., 2025). The performance of electrochemical sensors can be enhanced by using functionalizing nanoparticles (NPs) such as MoS_2, ZnO, $BiVO_4$, SnO_2, Bi_2S_3, AgNPs, etc., onto the working electrode, facilitating electrocatalytic reactions at the interface of the catalyst surface and target analytes (Malode et al., 2020; Meireles et al., 2024; Wang et al., 2024; Xu et al., 2024). However, the embedded catalysts using a binder (Nafion, polypyrrole, polyurethane, etc.) are delaminated quickly during the course of sensing. It could deter repeatability and reproducibility (Verma et al., 2024). Moreover, the binder could potentially interfere with the electrochemical sensor, which could affect its sensing performance. In recent studies, surface-embedded catalysts based electrochemical platform exhibited 26 and 20% reduction in peak

response up to 10 reuse cycles for monitoring aniline and dipyrone, respectively (Das et al., 2024; Dash et al., 2021). Therefore, the direct growth of nanostructures formed vertically onto the base electrode's surface could resolve the catalyst delamination problem and avoid the usage of binding agents, the surface modification process, and the footprint of waste generation.

The current researches exhibit that vertically aligned nanostructures (VANs) of ZnO, WO_3, SnO_2, MoS_2, and Bi_2S_3 grown on the working electrode's surface could significantly enhance the performance of electrochemical sensors by several folds (Ahmad et al., 2024; Bikesh et al., 2024; Mao et al., 2022). They are merited with high specific surface area and roughness, unimpeded electron transport characteristics, large aspect ratio, high chemical stability, and easy substrate penetration morphologies (Ahmad and Lee, 2024; Awais et al., 2021; Zhang et al., 2024). High surface area could provide unimpeded electron transport characteristics, allowing effective charge transport between the electrode/electrolyte solution. VAN based (binder-free) sensors have promising prospects for detecting environmental pollutants (Arsalan et al., 2022). These sensors are highly sensitive, selective and can detect trace amounts of target analytes in real time with minimal interference from other environmental factors. In our previous research, we developed a binder-free electrocatalytic platform for aniline monitoring, which exhibited only an 11.97% decrement in peak response up to 10 reuse cycles (Bhan and Golder, 2024). However, the existing methods for fabricating VANs involve chemical-based techniques. Thus, there is a need to develop an eco-friendly, rapid detection and reusable electrocatalytic platform with high sensitivity for monitoring antibiotic residues in the environmental matrix.

On the other hand, metal oxide nanostructures, including Bi_2O_3, SnO_2, Fe_2O_3, ZnO, CeO_2, MnO_2, and Co_3O_4, have gained increasing interest in recent years for various applications such as electrocatalytic monitoring of noxious waste, electrocatalytic reduction of CO_2 by photo and electrochemical methods, wastewater treatment, corrosion mitigation, etc. (Chowdhury et al., 2022; Kumar and Das, 2025; Pino et al., 2016). Among these, ZnO has attracted notable research attention due to their higher excitation energy of 60 meV, bandgap of 3.37 eV, exceptional physicochemical characteristics, highly crystalline, ease of fabrication, biocompatibility, and high surface area for various nanocatalytic applications (Bhan and Golder, 2024). Furthermore, the synthesis of ZnO VANs demonstrates a high surface area and improved charge transport, which are crucial factors in fabricating efficient electrocatalytic monitoring platforms (Ahmad et al., 2017). Additionally, functionalizing VANs with carbon quantum dots (CQDs) could significantly boost the performance of the electrochemical monitoring platform.

CQDs (<10 nm) exhibit high thermal stability, low toxicity, and a wide range of catalytic applications (Gawal et al., 2025). Furthermore, due to the excellent charge transport characteristics, CQDs are highly promising candidates for the functionalization of nanostructures to enhance the electrochemical sensor's performance. Previous studies have demonstrated that CQDs modified CuO and Fe_3O_4 nanocomposites were employed for the electrocatalytic monitoring of dopamine and uric acid, with an enhancement of 81.1 and 71.7% increment in peak current compared to only CuO and Fe_3O_4 NPs, respectively (Abbas et al., 2019; Elugoke et al., 2022). Carbon-rich sources, namely polyethylene glycol, thiourea, urea, and citric acid, are commonly employed for synthesising CQDs (Jung et al., 2022). However, biomass resources such as fruit peels, leaves, roots, flowers, or food wastes present a promising eco-friendly and cost-effective alternative as carbon sources in the preparation of CQDs (Gawal and Golder, 2024).

The selection of bio-extract and biomass for the syntheses of VANs and CQDs is mainly based on the availability of reducing analytes, growth profile, and economic significance. In our previous study, we developed an electrochemical platform based on bioinspired VANs of Bi_2S_3 onto the base electrode, synthesized using *Sechium edule* fruit extract for the monitoring of mancozeb with a detection limit of 0.0085 µM (Bhan and Golder, 2025). The fruit contains major reducing agents, namely ascorbic acid (AA), amino acids, and flavonoids of 0.294, 12.9, and 19.3 mg/g on the dry basis, respectively (Bhan and Golder, 2025; Ordonez et al., 2006). The reducing agents found in the *Sechium edule* fruit extract were utilized to grow and develop stable VANs onto the base electrode's surface.

In Chapter 6, the effects of morphological attributes of ZnO VANs on electrochemical sensing have been investigated. 2D surface ZnO VANs were gown on fluorine-doped tin oxide (FTO) substrate using the bio-extract of *Sechium edule* fruit. Subsequently, the remnant carbon-rich fruit peel was used for the preparation of CQDs. Finally, ZnO VANs were functionalized with CQDs to develop an electrochemical platform for monitoring of NFX using the square wave voltammetry (SWV). This reusable bioinspired electrochemical monitoring platform could resolve the problem related to the nanocatalyst delamination and ensure stable sensitivity and selectivity by optimizing nanostructure synthesis and sensing parameters. The practical application of the developed platform was tested by sensing NFX in an environmental matrix and compared with HPLC. To our knowledge, the bioinspired development of ZnO VANs functionalized with CQDs for selective electrocatalytic monitoring and quantification of NFX presents a novel approach.

6.2. Result and discussions

6.2.1. Characterization of electrocatalysts

6.2.1.1 *FESEM analysis*

Fig. 6.2 exhibits the FESEM micrographs of top surface of (a) bare/FTO, (b) ZnO(seed)/FTO, (c) ZnOVANs(bio)/FTO, (d) $CQDs_{1.5}$-ZnOVANs(bio)/FTO, (e) ZnO-control(H_2O)/FTO, and (f) side image of $CQDs_{1.5}$-ZnOVANs(bio)/FTO. Fig. 6.2a demonstrates that the surface of bare/FTO is rough. The surface became smooth with the deposition of the seed layer, as shown in Fig. 6.2b. It could help to minimize charge scattering owing to the heterogeneous interface between VANs and the FTO surface, but also promote more uniform and denser growth of VANs. Fig. 6.2c reveals that the bioinspired ZnO nanostructures grow vertically onto the FTO surface at pH 7 with a thickness of 27.33 nm. Fig. 6.2d shows ZnOVANs(bio)/FTO surface modified with CQDs for an immersion time of 1.5 min, having a thickness of 46.28 nm. No notable changes in the morphology of $CQDs_{1.5}$-ZnOVANs(bio)/FTO were observed compared to ZnOVANs(bio)/FTO, because of the smaller size attribute of CQDs. ZnOVANs(bio)/FTO surface modified with CQDs at various immersion times from 0.5, 1.0, and 2.0 min (denoted as $CQDs_{0.5}$-ZnOVANs(bio)/FTO, $CQDs_{1.0}$-ZnOVANs(bio)/FTO, and $CQDs_{2.0}$-ZnOVANs(bio)/FTO), as shown in Fig. 6.1. The control synthesis (ZnO-control(H_2O)/FTO) of ZnOVANs(bio)/FTO exhibited loosely packed nanostructures of ZnO (Fig. 6.2e). Fig. 6.2f demonstrates the side image of $CQDs_{1.5}$-ZnOVANs(bio)/FTO with an average length of 965.3 nm. The effect of synthesis pH on the morphology of ZnO nanostructures has been documented previously (Bhan and Kumar Golder, 2023; Rafaie et al., 2014; Wahab et al., 2009).

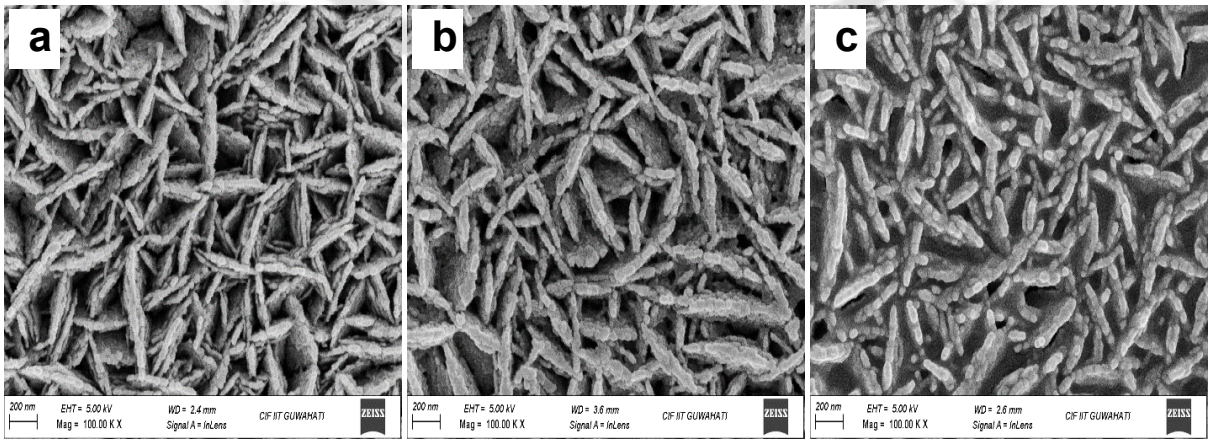

Figure 6.1: FESEM images of (a) $CQDs_{0.5}$-ZnOVANs(bio)/FTO, (b) $CQDs_{1.0}$-ZnOVANs(bio)/FTO, and (c) $CQDs_{2.0}$-ZnOVANs(bio)/FTO.

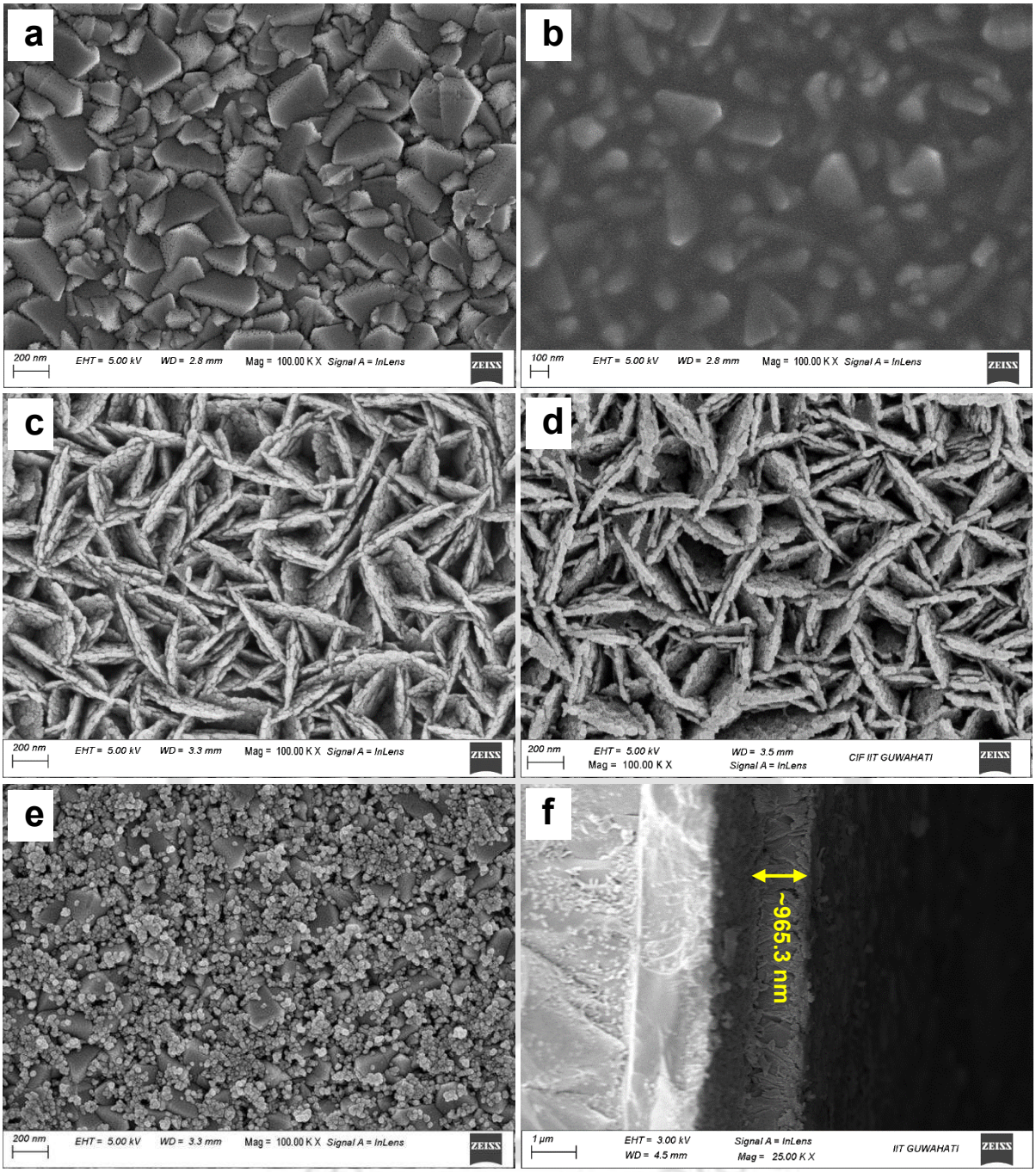

Figure 6.2: FESEM top surface image of (a) bare/FTO, (b) ZnO(seed)/FTO, (c) ZnOVANs(bio)/FTO, (d) $CQDs_{1.5}$-ZnOVANs(bio)/FTO, (e) ZnO-control(H_2O)/FTO, and (f) Side image of $CQDs_{1.5}$-ZnOVANs(bio)/FTO.

6.2.1.2 *XRD analysis*

Fig. 6.3 presents the XRD patterns of bare/FTO, ZnO(seed)/FTO, ZnOVANs(bio)/FTO, $CQDs_{0.5}$-ZnOVANs(bio)/FTO, $CQDs_{1.0}$-ZnOVANs(bio)/FTO, $CQDs_{1.5}$-ZnOVANs(bio)/FTO, $CQDs_{2.0}$-ZnOVANs(bio)/FTO, and ZnO-control(H_2O)/FTO. The peaks corresponding to bare/FTO is marked by a black stars at 2θ = 34.46°(002), 38.57°(200),

52.17°(102), 55.25°(110), 62.23°(103), 66.20°(200), and 78.89°(202) (JCPDS Card No. of 00-001-0657). The peaks obtained at 2θ = 32.49°(100), 36.94°(101), 48.23°(102), 57.22°(110), 63.48°(103), 68.54°(112) and 69.69°(201), confirm the formation of ZnO in ZnOVANs(bio)/FTO (JCPDS Card No. 01-075-9187). In ZnO(seed)/FTO, additional peaks were observed compared to bare/FTO, ascribed to the formation of a ZnO layer on bare/FTO. Eqs. 6.1-6.3 were employed to calculate dislocation density (δ, lines/nm^2), crystal size (d, nm) and lattice strain (ε) (Ravi and Golder, 2025, 2023a).

$$d = \frac{k\lambda}{\beta \cos\theta_B} \quad (6.1)$$

$$\varepsilon = \frac{\beta}{4\mathrm{Tan}\theta_B} \quad (6.2)$$

$$\delta = \frac{1}{d^2} \quad (6.3)$$

Where θ_B, β, k, and λ represent the Bragg angle, full width at half maximum (FWHM), shape factor (0.94) and X-ray wavelength (0.154 nm), respectively. The values of d, δ, and ε of all specimens such as bare/FTO, ZnO(seed)/FTO, ZnOVANs(bio)/FTO, CQDs$_{(0.5\text{-}2.0)}$-ZnOVANs(bio)/FTO, and ZnO-control(H_2O)/FTO were determined at 2θ = 52.17°(102) (Table 6.1). CQDs$_{1.5}$-ZnOVANs(bio)/FTO showed a decrement in the value of d and an increment in the value of δ and ε over other fabricated catalysts (Bhan and Golder, 2024). It implies an enhancement in active sites and defects formation. Therefore, CQDs$_{1.5}$-ZnOVANs(bio)/FTO offers more adsorption sites for the target analytes and improved charge transport characteristics (Bhan and Golder, 2023).

Table 6.1: XRD crystallographic attributes of bare/FTO, ZnO(seed)/FTO, ZnOVANs(bio)/FTO, CQDs$_{(0.5\text{-}2.0)}$-ZnOVANs(bio)/FTO, and ZnO-control(H_2O)/FTO.

Sample code	Crystal size (nm)	d-spacing (Å)	Lattice strain (ε)	Dislocation density (Lines/nm^2)
Bare/FTO	57.88	1.752	1.42×10^{-3}	2.98×10^{-4}
ZnO(seed)/FTO	51.81	1.756	1.59×10^{-3}	3.72×10^{-4}
ZnOVANs(bio)/FTO	53.05	1.753	1.55×10^{-3}	3.55×10^{-4}
CQDs$_{0.5}$-ZnOVANs(bio)/FTO	53.53	1.755	1.54×10^{-3}	3.49×10^{-4}
CQDs$_{1.0}$-ZnOVANs(bio)/FTO	53.18	1.753	1.55×10^{-3}	3.54×10^{-4}
CQDs$_{1.5}$-ZnOVANs(bio)/FTO	51.73	1.755	1.59×10^{-3}	3.74×10^{-4}
CQDs$_{2.0}$-ZnOVANs(bio)/FTO	55.50	1.755	1.49×10^{-3}	3.25×10^{-4}
ZnO-control(H_2O)/FTO	53.31	1.752	1.55×10^{-3}	3.52×10^{-4}

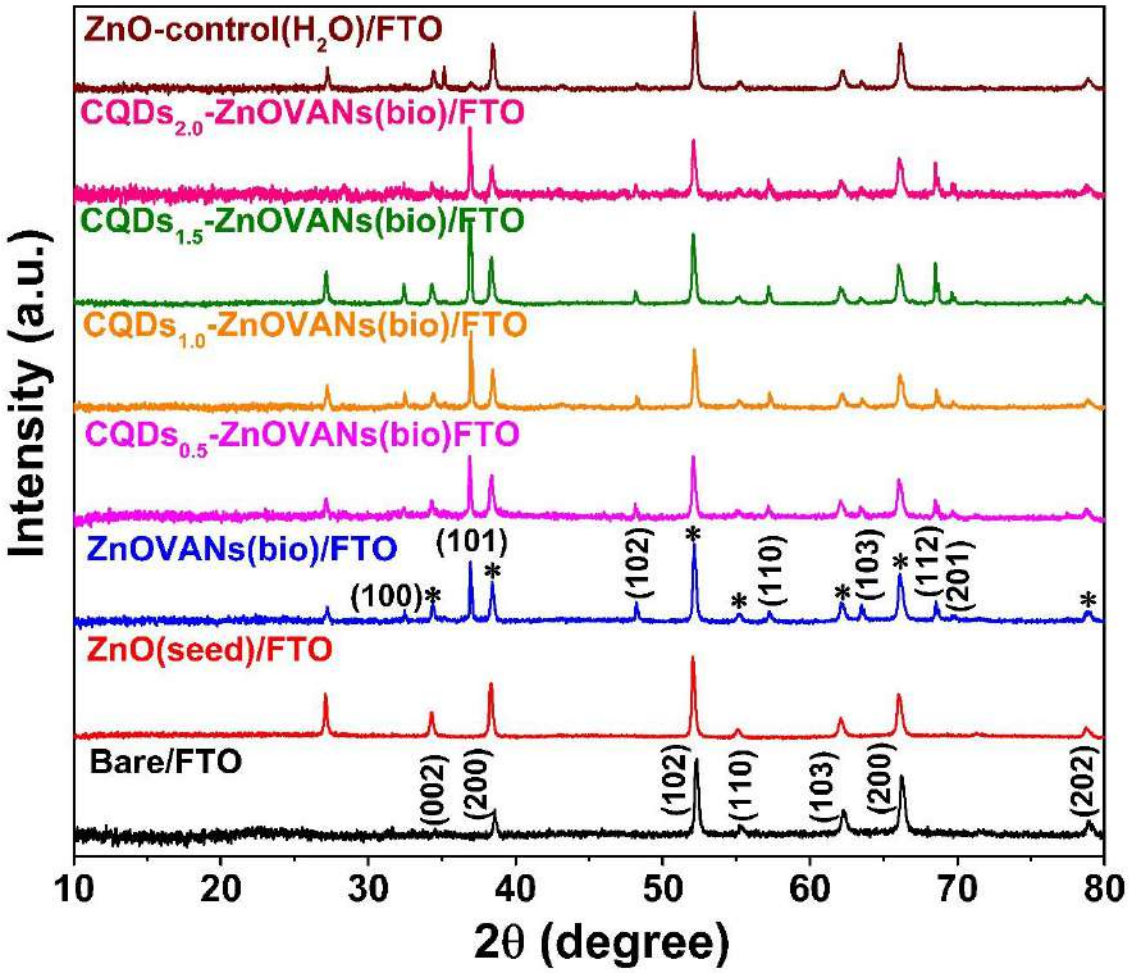

Figure 6.3: XRD patterns of bare/FTO, ZnO(seed)/FTO, ZnOVANs(bio)/FTO, $CQDs_{0.5}$-ZnOVANs(bio)/FTO, $CQDs_{1.0}$-ZnOVANs(bio)/FTO, $CQDs_{1.5}$-ZnOVANs(bio)/FTO, $CQDs_{2.0}$-ZnOVANs(bio)/FTO, and ZnO-control(H_2O)/FTO.

6.2.1.3 *FETEM analysis*

The FETEM images are shown in Fig. 6.4. ZnO and CQDs-ZnO layers were detached from the surface of ZnOVANs(bio)/FTO and $CQDs_{1.5}$-ZnOVANs(bio)/FTO by ultrasonication for 1 h, followed by drop-casting onto a TEM grid. In the case of CQDs, the solution was ultrasonicated for 1 h, then drop-cast onto the TEM grid. The FETEM, HRTEM, and SAED patterns of ZnOVANs(bio)/FTO, CQDs, and $CQDs_{1.5}$-ZnOVANs(bio)/FTO are shown in Figs. 6.4a-6.4c, 6.4d-6.4f, and 6.4g-6.4i, respectively. Figs. 6.4a and 6.4c exhibit sheet-shaped nanostructures of ZnO. The nanostructures were crumbled during ultrasonication, which is evident from Figs. 6.4a and 6.4c. The average size of CQDs was found to be 4.7 nm (Fig. 6.4b). The d-spacing values were determined to be 0.174 and 0.175 nm corresponding to the (102) planes of ZnOVANs(bio)/FTO (Fig. 6.4d) and $CQDs_{1.5}$-ZnOVANs(bio)/FTO (Fig. 6.4f),

respectively (Bhan and Kumar Golder, 2023). The d-spacing value for CQDs was 0.321 (Fig. 6.4e) (Gawal and Golder, 2024). Figs. 6.4g and 6.4h confirm the polycrystalline nature of ZnOVANs(bio)/FTO and $CQDs_{1.5}$-ZnOVANs(bio)/FTO, well aligned with XRD analysis (Bhan and Kumar Golder, 2023). Furthermore, Fig. 6.4i indicates the amorphous nature of CQDs (Patra et al., 2024).

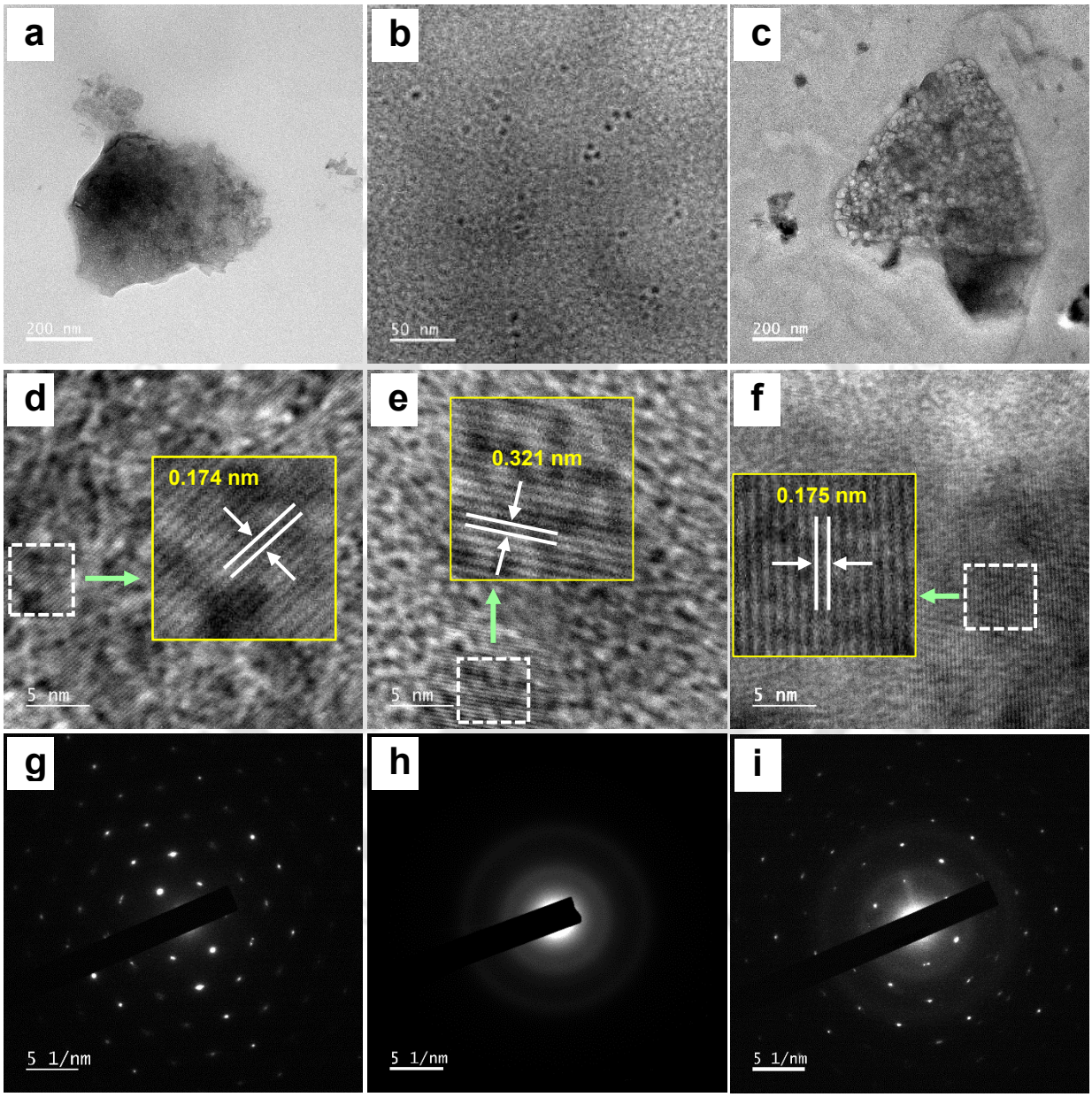

Figure 6.4: (a-c) FETEM micrographs, (d-f) HRTEM micrographs, and (g-i) SAED patterns of ZnOVANs(bio)/FTO, CQDs, and $CQDs_{1.5}$-ZnOVANs(bio)/FTO, respectively.

6.2.1.4 *EDX analysis*

Fig. 6.5 demonstrates the elemental analysis and image mapping (inset) of $CQDs_{1.5}$-ZnOVANs(bio)/FTO. It reveals a uniform distribution of Zn, O, and C with a relative abundance of 53.11, 26.07, and 20.83 % (w/w), respectively. The corresponding atomic percentage of Zn, O, and C were 19.46, 39.02, and 41.53% (inset of Fig. 6.5).

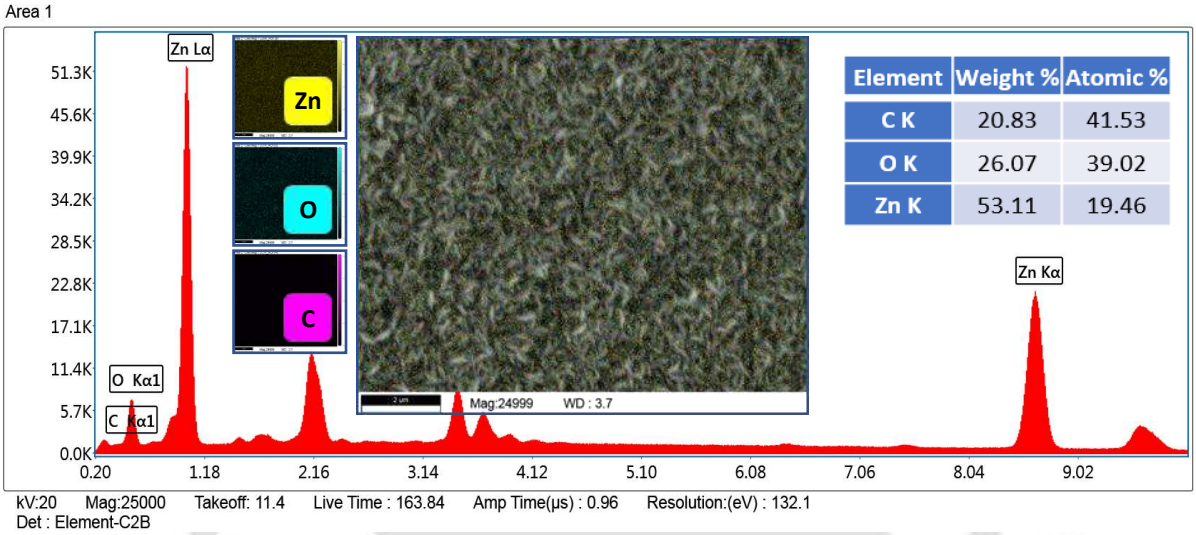

Figure 6.5: Elemental analysis and image mapping (inset) of $CQDs_{1.5}$-ZnOVANs(bio)/FTO.

6.2.1.5 *XPS analysis*

The surface composition of $CQDs_{1.5}$-ZnOVANs(bio)/FTO was investigated using an XPS analysis. Fig. 6.6a exhibits the survey spectrum of $CQDs_{1.5}$-ZnOVANs(bio)/FTO. The high-resolution Zn 2p profile of $CQDs_{1.5}$-ZnOVANs(bio)/FTO presents two distinct peaks at binding energies of 1021.43 and 1044.49 eV (Fig. 6.6b), corresponding to the Zn $2p_{3/2}$ and $2p_{1/2}$ spin-orbits, which is indicative of Zn^{2+} in the ZnO lattice. It offers the catalytic sites (Dan et al., 2023). The prominent peaks at 530.55 and 284.82 eV are associated with O 1s and C 1s regions (Figs. 6.6c and 6.6d). Two distinct peaks in the O 1s profile of $CQDs_{1.5}$-ZnOVANs(bio)/FTO were observed at 530.42 and 531.45 eV, attributed to the lattice and surface-adsorbed oxygen, respectively (Fig. 6.6c). It indicates the presence of surface-bound carboxyl and carbonyl groups, which could enhance charge transport properties (Bhan and Golder, 2024). An additional peak in the O 1s spectrum at 532.44 was observed due to the adsorption of reducing analytes from the bio-extract on the surface of $CQDs_{1.5}$-ZnOVANs(bio)/FTO (Ravi and Golder, 2023b). In the C 1s spectra (Fig. 6.6d), three major peaks at 284.78, 285.46, and 288.35 eV were detected corresponding to C-C/C=C, C-O, and C=O/O-C=O bonds, respectively. It signifies the graphitic nature and oxygenated functional

groups (hydroxyl, ether, carboxylic, and carbonyl groups) of CQDs (Gawal et al., 2025). Therefore, an increase in catalytic sites, charge transport, and analyte interaction could enhance the performance of the electrochemical sensor (Bhan and Kumar Golder, 2023).

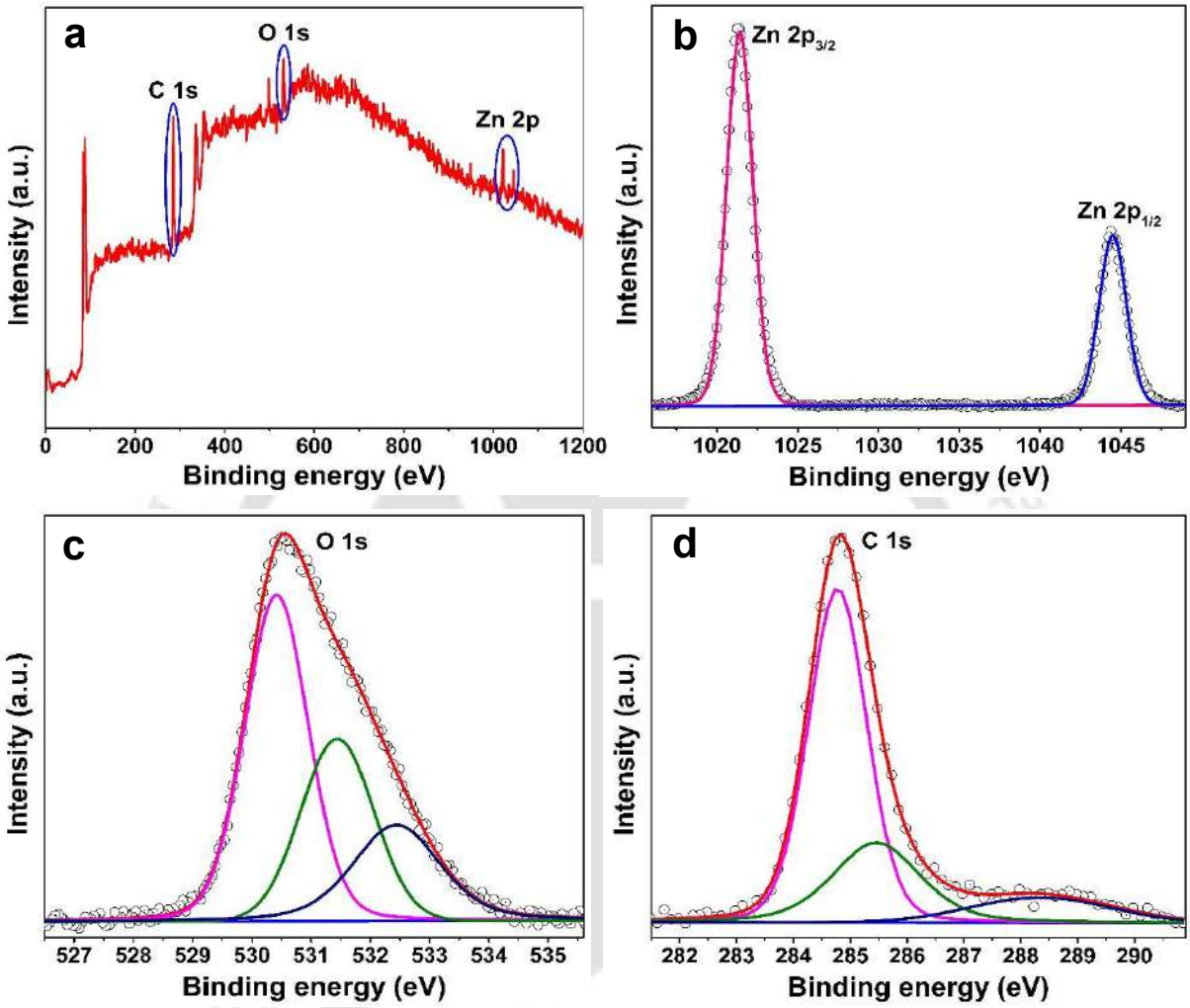

Figure 6.6: (a) XPS survey spectrum of $CQDs_{1.5}$-ZnOVANs(bio)/FTO, and (b), (c) and (d) High-resolution spectra in Zn 2p, O 1s, and C 1s regions of $CQDs_{1.5}$-ZnOVANs(bio)/FTO, respectively.

6.2.2. Electrocatalytic characterizations of working electrodes

6.2.2.1 *Comparison of anodic and cathodic peak currents*

The anodic and cathodic peak currents were recorded using bare/FTO, ZnOVANs(bio)/FTO, $CQDs_{0.5}$-ZnOVANs(bio)/FTO, $CQDs_{1.0}$-ZnOVANs(bio)/FTO, $CQDs_{1.5}$-ZnOVANs(bio)/FTO, and $CQDs_{2.0}$-ZnOVANs(bio)/FTO with 1mM $Ru(NH_3)_6Cl_2$ as the redox-probe in 0.1 M KCl electrolyte at a scan rate of 50 mV/s. The CVs are shown in Fig. 6.7a. $CQDs_{1.5}$-ZnOVANs(bio)/FTO exhibited about 79.1, 60.8, 43.2, 25.0, and 9.9% higher

anodic peak and 77.4, 55.1, 41.9, 23.7, and 8.9% higher cathodic peak currents compared to bare/FTO, ZnOVANs(bio)/FTO, $CQDs_{0.5}$-ZnOVANs(bio)/FTO, $CQDs_{1.0}$-ZnOVANs(bio)/FTO, and $CQDs_{2.0}$-ZnOVANs(bio)/FTO, respectively (Fig. 6.7b). The higher anodic and cathodic peak currents indicate the improved electron transfer kinetics. Therefore, $CQDs_{1.5}$-ZnOVANs(bio)/FTO was employed for further electrocatalytic studies and the detection of NFX.

6.2.2.2 *Electrochemical surface area of working electrodes*

The electrochemical surface area (A_e) of bare/FTO, ZnOVANs(bio)/FTO, and $CQDs_{1.5}$-ZnOVANs(bio)/FTO were evaluated using CVs captured at various scan rates from 5 to 500 mV/s (Figs. 6.7c, 6.7d, and 6.7e). The Randles-Sevcik equation (Eq. 6.4) was employed to calculate A_e (cm^2) working electrodes (Zhang et al., 2023).

$$I_{Pa} = (2.69 \times 10^5)n^{3/2}A_eD^{1/2}\upsilon^{1/2}C_0 \quad (6.4)$$

Where I_{pa}, D, C_0, n, and υ are the anodic peak current (A), diffusion coefficient of redox-probe (8.43×10^{-6} cm^2/s), concentration of redox-probe (mol/cm^3), number of electrons involved in the redox reaction (n = 1), and scan rate (V/s), respectively. Fig. 6.7f confirms the linearity between I_{pa} vs. $\upsilon^{0.5}$ for of bare/FTO, ZnOVANs(bio)/FTO, and $CQDs_{1.5}$-ZnOVANs(bio)/FTO with the slopes of 99.823 (R^2 = 0.996), 124.32 (R^2 = 0.991), and 336.84 (R^2 = 0.994) $\mu A.V^{-1/2}.s^{1/2}$, respectively. A_e of bare/FTO, ZnOVANs(bio)/FTO, and $CQDs_{1.5}$-ZnOVANs(bio)/FTO were 0.128, 0.159, and 0.431 cm^2, respectively. $CQDs_{1.5}$-ZnOVANs(bio)/FTO exhibited the highest A_e. Hence, 3.4- and 2.7-fold higher anodic and cathodic peak currents were noted than bare/FTO and ZnOVANs(bio)/FTO. The significant enhancement in A_e for $CQDs_{1.5}$-ZnOVANs(bio)/FTO could offer more binding sites for electrocatalytic monitoring of NFX (Bhan et al., 2025a).

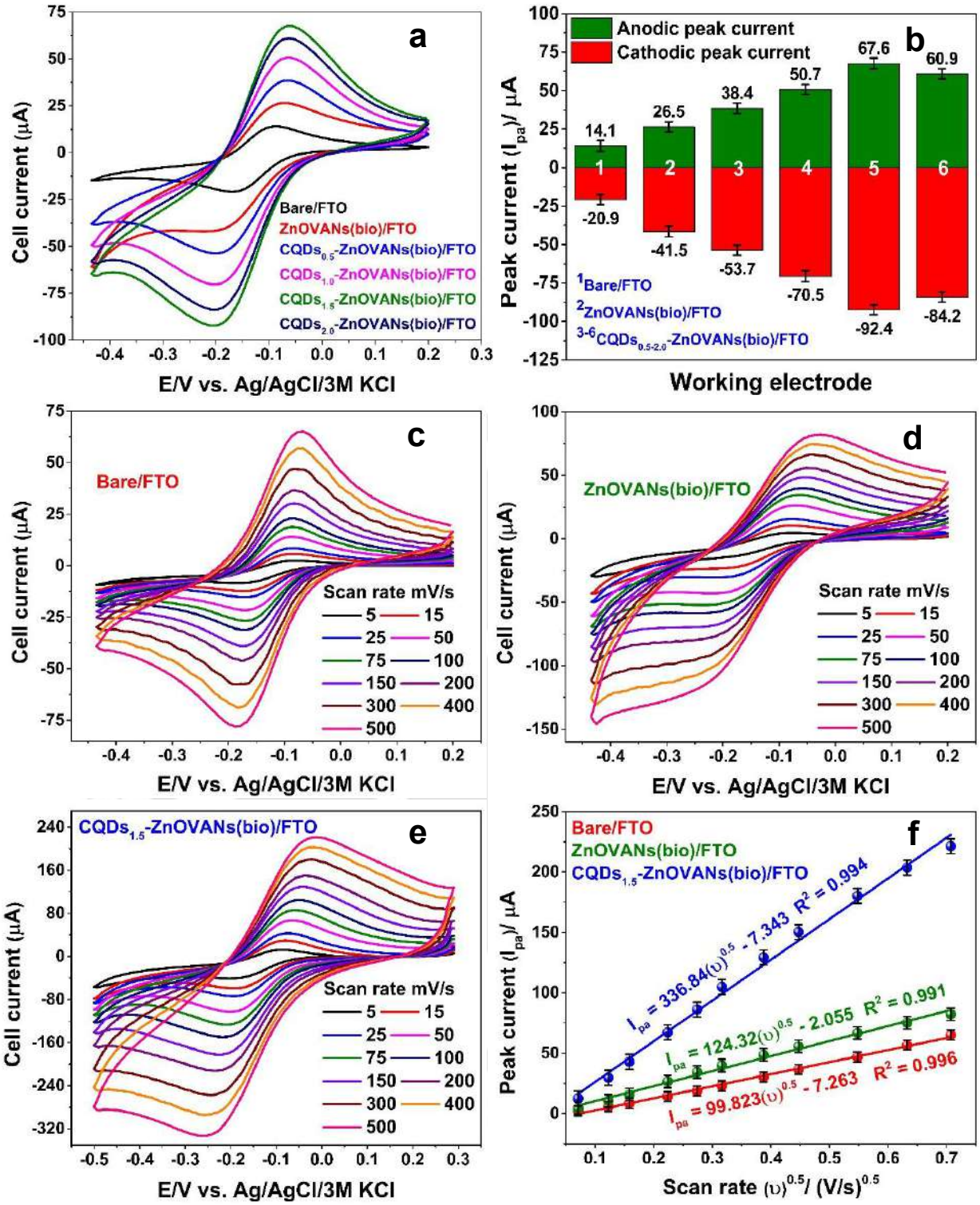

Figure 6.7: (a) CVs and (b) Corresponding anodic/cathodic peak current at bare/FTO, ZnOVANs(bio)/FTO, $CQDs_{0.5}$-ZnOVANs(bio)/FTO, $CQDs_{1.0}$-ZnOVANs(bio)/FTO, $CQDs_{1.5}$-ZnOVANs(bio)/FTO and $CQDs_{2.0}$-ZnOVANs(bio)/FTO, and (c), (d) and (e) CVs of bare/FTO, ZnOVANs(bio)/FTO and $CQDs_{1.5}$-ZnOVANs(bio)/FTO at various scan rates, and (f) I_{pa} vs. $\upsilon^{0.5}$ for bare/FTO, ZnOVANs(bio)/FTO and $CQDs_{1.5}$-ZnOVANs(bio)/FTO.

6.2.2.3 *EIS analyses of working electrodes*

EIS analysis was employed to evaluate the electron transport resistance of bare/FTO, ZnOVANs(bio)/FTO, and $CQDs_{1.5}$-ZnOVANs(bio)/FTO using 1mM $Ru(NH_3)_6Cl_2$ as the redox-probe in a 0.1 M KCl electrolyte over a frequency range of 10^{-2} to 10^5 Hz. The resulting EIS spectrum is presented in Fig. 6.8a, along with the corresponding Randles equivalent circuit in the inset. It illustrates key parameters such as charge transfer resistance (R_p), constant phase element (CPE), and electrolyte resistance (R_s) (Bhan et al., 2025b). The Nyquist plot reveals that the diameter of the semicircle is directly related to R_p, with a larger diameter indicating higher R_p (Kumar and Das, 2023). The EIS parameters are tabulated in Table 6.2. R_p of bare/FTO, ZnOVANs(bio)/FTO, and $CQDs_{1.5}$-ZnOVANs(bio)/FTO were 958, 121, and 79.1 kΩ, respectively. The decrease in R_p for $CQDs_{1.5}$-ZnOVANs(bio)/FTO indicates a significant improvement in charge transfer and electrical conductivity (Teker et al., 2025). R_s of bare/FTO, ZnOVANs(bio)/FTO, and $CQDs_{1.5}$-ZnOVANs(bio)/FTO were 0.081, 0.073, and 0.067 kΩ, respectively. The minor variation in R_s is likely due to slight differences in electrode positioning across different sets of measurements. However, the changes in R_s are negligible compared to R_p values (Kumar and Das, 2024). The variation in CPE may be resulted from the change in conductivity of the working electrode (Bhan and Golder, 2024). The notable improvement in the conductivity of $CQDs_{1.5}$-ZnOVANs(bio)/FTO is attributed to the functionalization of ZnO VANs with CQDs.

Table 6.2: EIS parameters for bare/FTO, ZnOVANs(bio)/FTO, and $CQDs_{1.5}$-ZnOVANs(bio)/FTO.

Working electrodes	R_s (kΩ)	R_p (kΩ)	CPE parameters	
			Y_0 (µMho)	n
Bare/FTO	0.081	958	22.2	0.864
ZnOVANs(bio)/FTO	0.073	121	10.9	0.754
$CQDs_{1.5}$-ZnOVANs(bio)/FTO	0.067	79.1	11.7	0.732

6.2.3. Optimization of NFX detection parameters

6.2.3.1 *Effect of pH*

The effect of electrolyte (0.1 M PBS, 25 °C) pH (2-9) during NFX monitoring was investigated using CV recorded over $CQDs_{1.5}$-ZnOVANs(bio)/FTO at a scan rate of 50 mV/s and NFX concentration of 60 µM (Fig. 6.8b). The anodic peak potential (E_p) shifted towards less positive value as pH was increased from 2 to 9. It signifies that proton was involved in the

electrocatalytic reaction of NFX monitoring (Fig. 6.8b) (Malode et al., 2020). No prominent peak was observed at pH 9, while the highest I_{pa} for NFX sensing was obtained at pH 5. It implies that the electrocatalytic detection of NFX is more favourable at pH 5 (Fig. 6.8c). To assess the ratio of electrons (n) to protons (m) involved in the electrocatalytic reaction of NFX monitoring, the Nernstian equation (eq. 6.5) was utilized (Manivannan et al., 2019).

$$\frac{dE_p}{dpH} = -2.303\frac{mRT}{nF} \quad (6.5)$$

Where F, T, and R represent the Faraday's constant (96,485 C. mol^{-1}), temperature (K), and gas constant (8.314 J. mol^{-1} K^{-1}), respectively. As shown in Fig. 6.8d, a linear correlation was observed between E_p vs. pH, exhibiting a slope of -0.053 V per unit pH and an R^2 value of 0.997. Using the slope value of -0.0503 V per unit pH in Eq. 6.5, the calculated n/m was ~1 (1.12). It suggests that the electrocatalytic monitoring of NFX involves balanced electrons and protons (Bhan et al., 2025b).

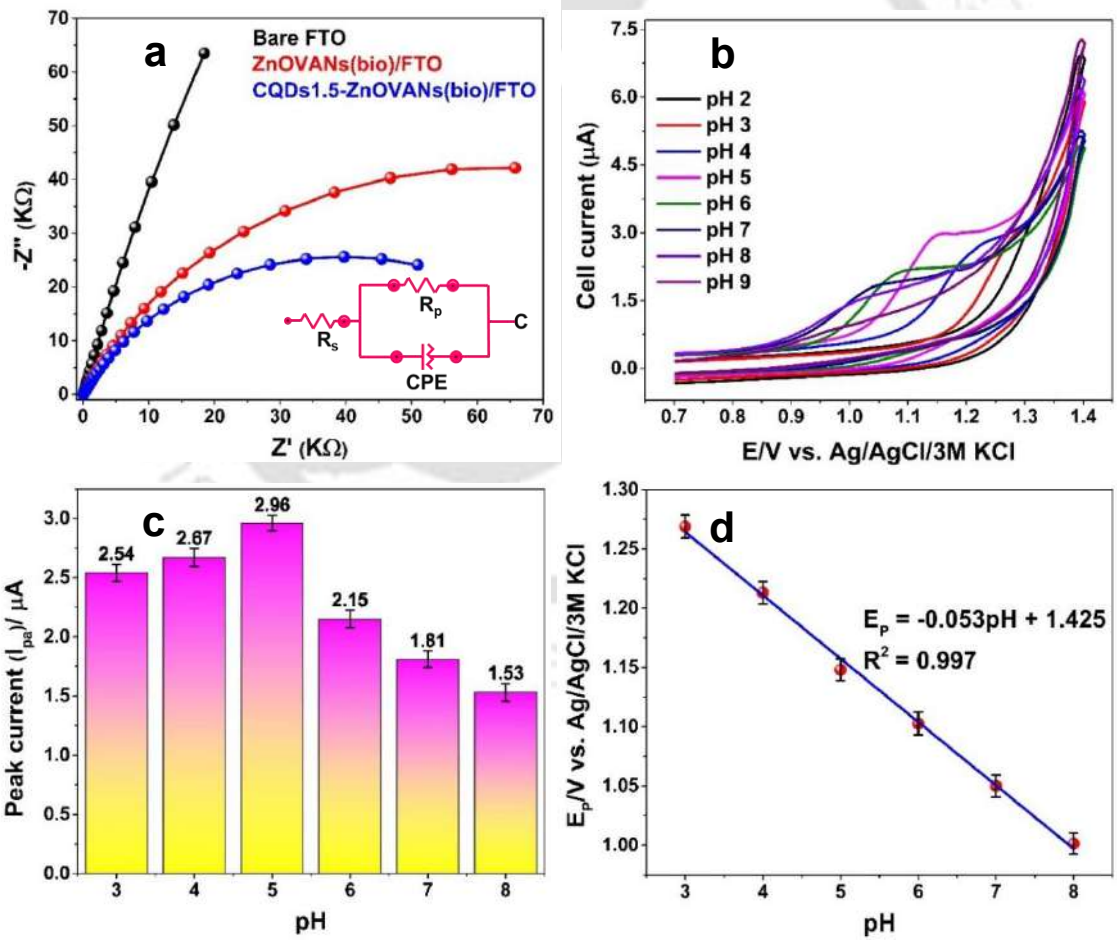

Figure 6.8: (a) EIS spectra for bare/FTO, ZnOVANs(bio)/FTO, $CQDs_{1.5}$-ZnOVANs(bio)/FTO with Randles equivalent circuit (inset), (b) CVs recorded at various pH (2-9) in 0.1 M PBS electrolyte (25 °C) using $CQDs_{1.5}$-ZnOVANs(bio)/FTO, (c) pH vs. I_{pa}, and (d) pH vs. E_P.

6.2.3.2 *Optimization of deposition parameters*

Optimization of deposition parameters such as Dpote, Dtime, and Dtemp was carried out to enhance I_{pa} for NFX monitoring (60 µM) using SWV at CQDs$_{1.5}$-ZnOVANs(bio)/FTO in 0.1 M PBS (pH 5). Fig. 6.9a shows the SWV recorded at various Dpote ranging from 0 to -0.9 V at a Dtime of 80 s and a Dtemp of 25 °C. I_{pa} increased progressively from 0 to -0.7 V, likely due to enhanced accumulation of NFX ions on CQDs$_{1.5}$-ZnOVANs(bio)/FTO surface (Fig. 6.9b) (Bhan et al., 2025b). Beyond, -0.7 V, a decline in I_{pa} was observed, which could be attributed to the evolution of H_2 gas interfering with the deposition process (Gumpu et al., 2017). Moreover, the shift in peak potential toward more positive values may result from the overpotential deposition of NFX ions. It suggests a strong interaction between the analyte and the electrode surface, making it more difficult for NFX ions to detach from the substrate (Bhan and Golder, 2025). Therefore, a Dpote of -0.7 V was selected for the electrocatalytic monitoring of NFX.

Fig. 6.9c exhibits the SWV captured at various Dtime of 20 to 120 s using Dpote of -0.7 V and Dtemp of 25 °C. I_{pa} enhanced steadily from 20 to 80 s, attributed to increased accumulation of NFX ions on the surface of the base electrode (Fig. 6.9d) (Bagheri et al., 2013). Beyond 80 s, only a slight improvement in I_{pa} was observed, likely of NFX ions saturation on the surface of CQDs$_{1.5}$-ZnOVANs(bio)/FTO and/or the equilibrium was achieved between NFX ions in the electrolyte and adsorbed on the electrode (Dash et al., 2020). As a result, Dtime of 80 s was chosen for subsequent experiments.

Fig. 6.9e demonstrates the SWV conducted at different Dtemp ranging from 15 to 45 °C using Dpote of -0.7 V and Dtime of 80 s. I_{pa} increased gradually from 15 to 45 °C, ascribed to accumulation of NFX ions on the surface of CQDs$_{1.5}$-ZnOVANs(bio)/FTO (Fig. 6.9f). Moreover, high temperature facilitates faster diffusion of NFX ions from the electrolyte to the electrode surface (Bhan and Golder, 2025). Beyond 45 °C, only a slight increment in I_{pa} was observed (Bhan and Golder, 2024). Hence, Dtemp of 45 °C was selected for the electrocatalytic detection of NFX as it is unlikely that the ambient temperature would exceed it.

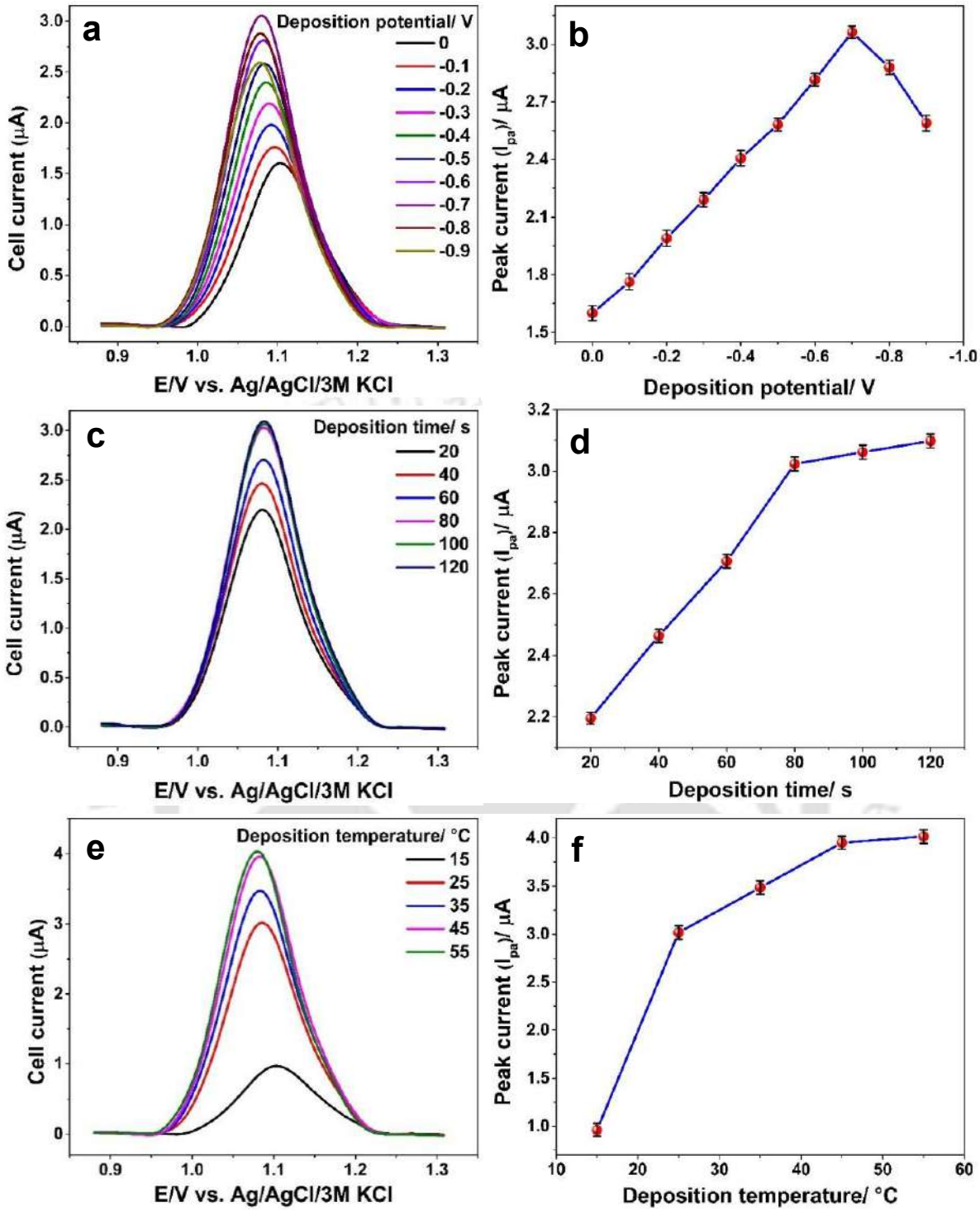

Figure 6.9: (a) SWV of NFX at different Dpote from 0 to -0.9 V vs. Ag/AgCl, Dtime 80 s, and Dtemp 25 °C, (b) Dpote vs. anodic peak current, (c) SWV of NFX recorded at different Dtime from 20 to 120 s, Dpote -0.7 V, and Dtemp 25 °C, (d) Dtime vs. anodic peak current, (e) SWV of NFX performed at different Dtemp from 15 to 55 °C, Dpote -0.7 V, and Dtime 80 s, and (f) Dtemp vs. anodic peak current. Reaction conditions: 60 µM NFX in 0.1 M PBS electrolyte at pH 5.

6.2.4. Electrocatalytic monitoring of NFX at CQDs$_{1.5}$-ZnOVANs(bio)/FTO

6.2.4.1 *Determination of electro-kinetic parameters and surface coverage through NFX*

The electro-kinetic parameters and surface coverage of NFX were evaluated using CV captured using CQDs$_{1.5}$-ZnOVANs(bio)/FTO at various scan rates from 5 to 500 mV/s in 0.1 M PBS (pH 5, 45 °C) with 60 µM NFX (Fig. 6.10a). The linearity between I_{pa} vs. $\upsilon^{0.5}$ (Fig. 6.10b) with a slope of 32.72 µA.V$^{-1/2}$.s$^{1/2}$ (R^2 = 0.985) suggests that the electrochemical reaction of NFX is diffusion-controlled (Dash et al., 2021). Hence, the Laviron equations (Eqs. 6.6 and 6.7) were used to calculate electro-kinetic parameters, namely the number of electrons transferred (n), the standard rate constant (k^0, s^{-1}), and the formal potential (E^0, V), as well as the surface coverage (Γ*, mol cm^{-2}) of NFX for the diffusion-controlled process (Bhan and Kumar Golder, 2023; Elgrishi et al., 2018).

$$E_p = E^0 - \frac{2.303RT}{\alpha nF}\log\frac{RTk^0}{\alpha nF} + \frac{2.303RT}{\alpha nF}\log\upsilon \quad (6.6)$$

$$I_{pa} = \frac{n^2F^2}{4RT}A_e\,\upsilon\,\Gamma^* \quad (6.7)$$

Where α represents the electron transfer coefficient. F, R, T, E_p, A_e, υ, and I_{pa} are previously defined. To determine E^0, the E_p vs. υ plot was extrapolated at υ = 0 (Das et al., 2024), yielding an E^0 of 1.042 V. As shown in Fig. 6.10c, a linear correlation was observed between E_p vs. log υ, with a slope of 0.061 V, an intercept of 1.198 V with a good linearity (R^2 = 0.997). Assuming α = 0.5 and using the obtained values of E^0, the slope, and intercept in Eq. 6.6, n and k^0 were calculated to be 2.07 and 0.105 s^{-1}, respectively. It infers that two electrons are involved in the electrocatalytic monitoring of NFX. Fig. 6.10d shows a linear correlation between I_{pa} vs. υ, with a slope of 41.31 µA.V^{-1}.s (R^2 = 0.986). Using Eq. 6.7 and calculated values of n (2.07), A_e (0.431 cm^2), and slope (41.31 µA.V^{-1}.s), Γ* was found to be 2.54×10^{-11} mol cm^{-2}.

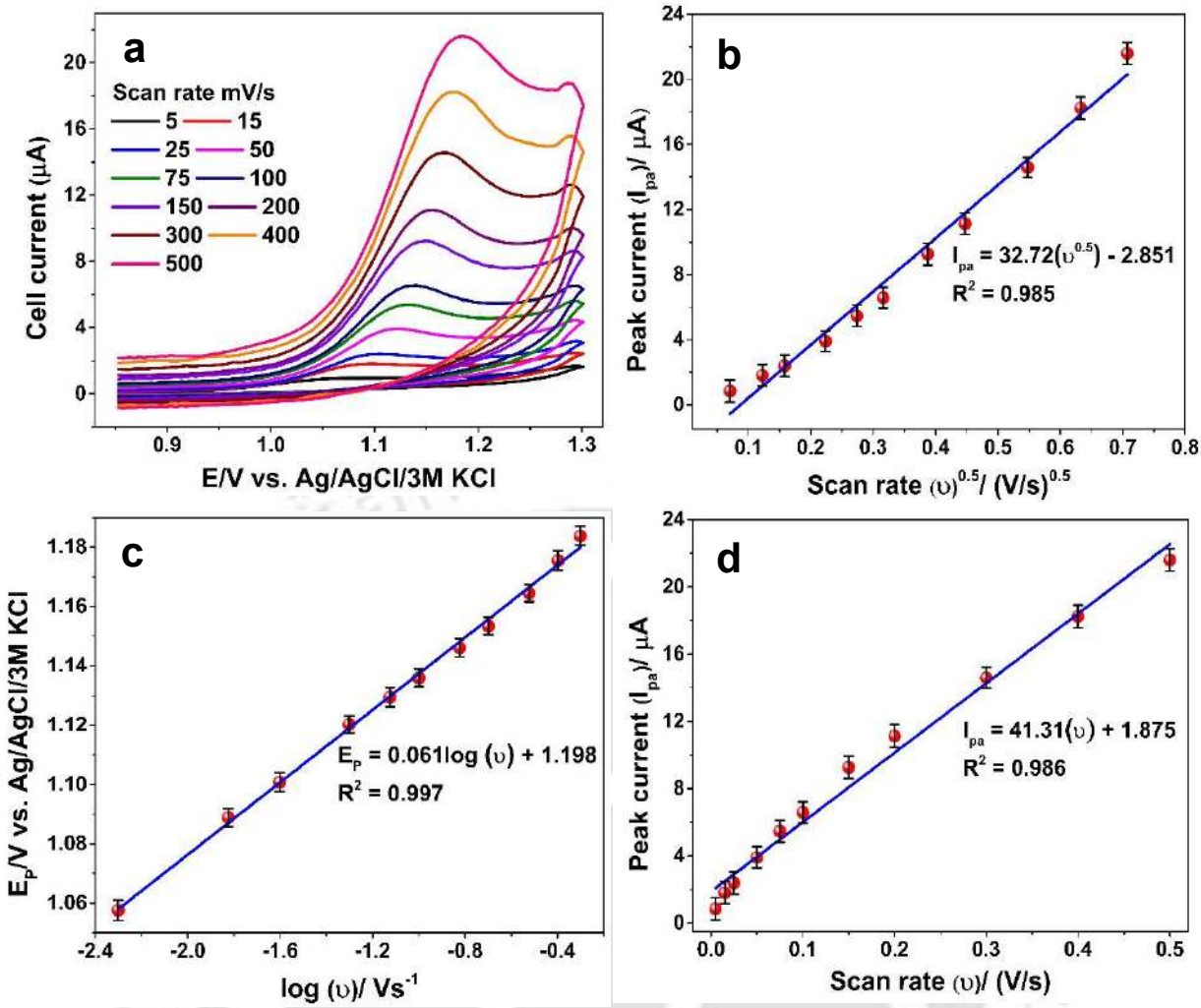

Figure 6.10: (a) CVs captured at various scan rates (5 to 500 mV/s) using 60 µM NFX and $CQDs_{1.5}$-ZnOVANs(bio)/FTO, (b) I_{pa} vs. $\upsilon^{0.5}$, (c) E_p vs. log υ, and (d) I_{pa} vs. υ.

6.2.4.2 *Electrocatalytic detection and quantification of NFX*

Figs. 6.11a and 6.11b represent the SWV and the calibration curve of NFX monitoring using $CQDs_{1.5}$-ZnOVANs(bio)/FTO in 0.1 M PBS (pH 5, 45 °C) at various concentrations of NFX (0.25-300 µM) and optimal deposition parameters. Fig. 6.11b (I_{pa} vs. NFX concentration) displays two linear correlations in the concentration range of 0.25 to 40 and 40 to 300 µM. This is due to the shifting of the NFX monitoring reaction from diffusion-controlled to surface-controlled domains at higher NFX concentrations (Dash et al., 2018). The limit of detection (LOD) and limit of quantification (LOQ) for NFX monitoring were determined using Eqs. 6.8 and 6.9 (Morozov et al., 2025).

$$\mathrm{LOD} = \frac{3S_d}{m} \tag{6.8}$$

$$\mathrm{LOQ} = \frac{10S_d}{m} \tag{6.9}$$

Where m and S_d represent the slope of the calibration plot ($\mu A.\mu M^{-1}$) and standard deviation of blank measurement (0.00018). The linearities with slopes of 0.082 (R^2 = 0.994) and 0.020 (R^2 = 0.995) $\mu A.\mu M^{-1}$ were correlated between NFX concentration ranges of 0.25 to 40 and 40 to 300 µM (Fig. 6.11b). $CQDs_{1.5}$-ZnOVANs(bio)/FTO exhibited LODs of 0.0066 and 0.0270 µM, and LOQs of 0.0220 and 0.0900 µM within 0.25 to 40 and 40 to 300 µM. The sensitivity of the electrode was determined as the ratio of m to A_e (0.431 cm^2) (Bhan et al., 2025b). The sensitivities of the electrode were 0.1903 and 0.0464 $\mu A.\mu M^{-1}$ cm^{-2} within 0.25 to 40 and 40 to 300 µM.

6.2.4.3 *NFX sensing mechanism at $CQDs_{1.5}$-ZnOVANs(bio)/FTO*

Chronoamperometric test was done using $CQDs_{1.5}$-ZnOVANs(bio)/FTO and 200 µM NFX at 1.042 V vs. Ag/AgCl for 2000 s in 0.1 M PBS (pH 5, 45 °C). Subsequently, LC-MS analysis of the same electrolyte was performed before and after the reaction. Figs. 6.11c and 6.11d show the mass spectra of NFX (m/z = 319.13) before and after the oxidation reaction, respectively. A new peak was detected at m/z = 335.13 after the reaction (Fig. 6.11d). This indicates that NFX (m/z = 319.13) is oxidized to NFX radical (m/z = 335.13, 1-ethyl-6-fluoro-7-(4-hydroxypiperazin-1-yl)-4-oxo-1,4-dihydroquinoline-3-carboxylic acid) (Zhou et al., 2024). The reaction of electrocatalytic monitoring of NFX is shown in Fig. 6.11e. It involves the transfer of two electrons (Eq. 6.6) and two protons (Umesh et al., 2021). Thus, the monitoring of NFX primarily involves the detection of the NFX radical.

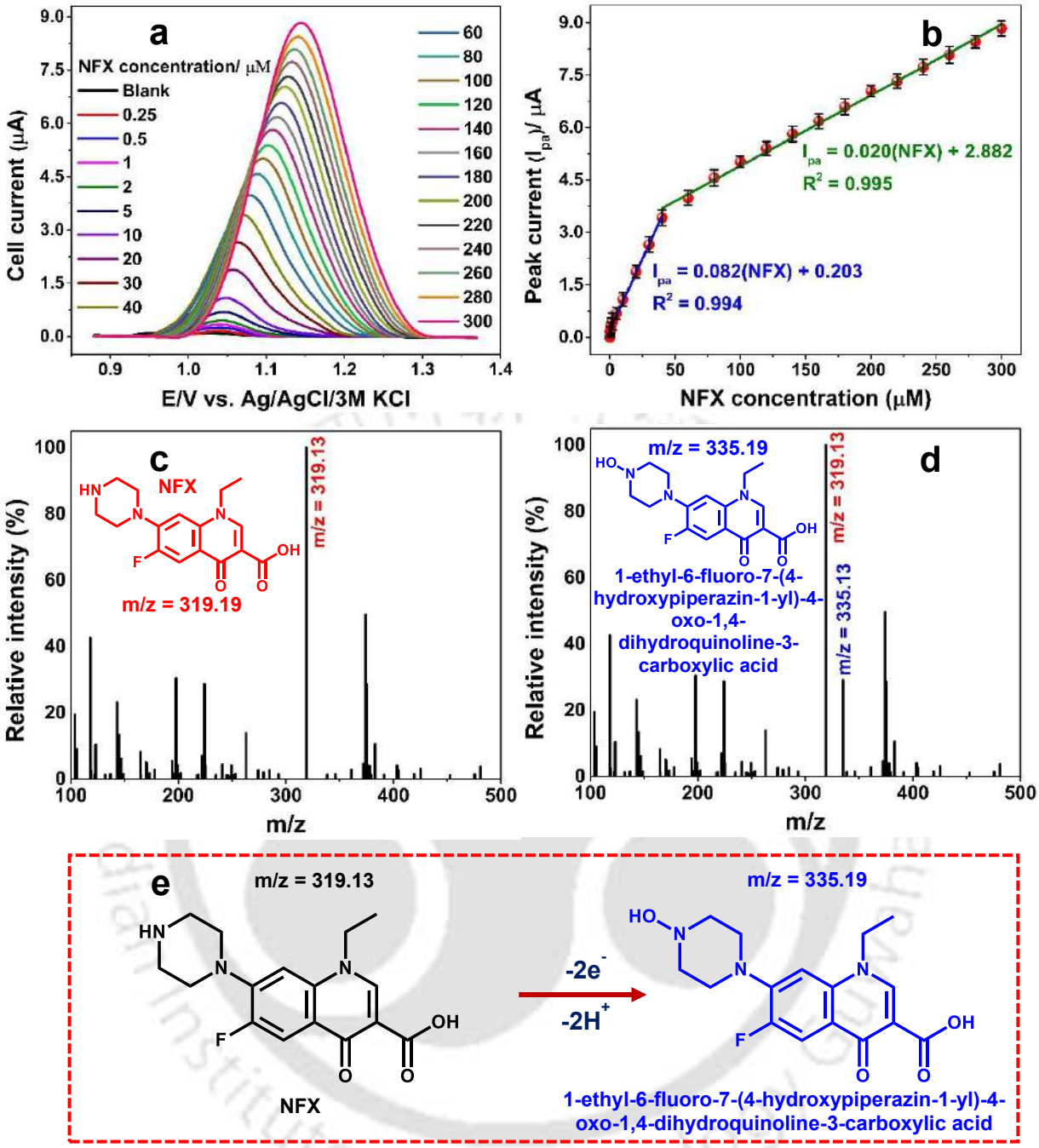

Figure 6.11: (a) SWV captured at various concentrations of NFX (0.25-300 μM) using $CQDs_{1.5}$-ZnOVANs(bio)/FTO, (b) Calibration plot of NFX (NFX concentration vs. I_{pa}), and (c) and (d) LC-MS mass spectra of electrolyte (0.1 M PBS, pH 5) containing 200 μM NFX recorded before and after chronoamperometry test at oxidation potential of 1.042 V vs. Ag/AgCl for 2000 s using $CQDs_{1.5}$-ZnOVANs(bio)/FTO, and (e) Detection mechanism of NFX at $CQDs_{1.5}$-ZnOVANs(bio)/FTO electrode.

6.2.4.4 *Stability and reproducibility of CQDs$_{1.5}$-ZnOVANs(bio)/FTO during NFX monitoring*

The stability and reproducibility tests were conducted using SWV with CQDs$_{1.5}$-ZnOVANs(bio)/FTO in 0.1 M PBS (pH 5, 45 °C) under optimized deposition parameters and 60 µM NFX (Figs. 6.12a and 6.13). For the stability experiment, the same electrode was employed in the same electrolyte solution over 15 consecutive cycles of NFX monitoring. Whereas three freshly fabricated electrodes were tested in fresh separate electrolyte media every time for reproducibility. An insignificant decrement in I_{pa} was observed up to the first five cycles of NFX monitoring. After the 5th cycle of NFX sensing, a slight reduction in I_{pa} was detected. The decrement in I_{pa} is likely due to the accumulation of NFX ions on CQDs$_{1.5}$-ZnOVANs(bio)/FTO surface (Dash et al., 2021). I_{pa} was reduced by only 4.4 and 8.1% after the 10th and 15th cycle of its reuse, which is lower than existing studies (Das et al., 2024). CQDs$_{1.5}$-ZnOVANs(bio)/FTO displayed excellent reproducibility with an acceptable limit of relative standard deviation (RSD) of 2.3% (Fig. 6.13) (Lotfi et al., 2021). The comparison of electrocatalytic monitoring of NFX using CQDs$_{1.5}$-ZnOVANs(bio)/FTO with the recently reported sensor is shown in Table 6.3. The fabricated electrocatalytic monitoring platform exhibited superior stability, reproducibility, and detection of NFX compared to existing sensors.

The stability of CQDs$_{1.5}$-ZnOVANs(bio)/FTO was further tested using FESEM, XRD, and XPS analyses, which were performed after the 15th cycle of NFX monitoring (Figs. 6.12b-6.12f). The FESEM and XRD analyses of CQDs$_{1.5}$-ZnOVANs(bio)/FTO showed insignificant variations in morphology and crystallinity before (Figs. 6.2d and 6.3) and after (Figs. 6.12b and 6.12c) of NFX monitoring. The XPS spectra of Zn, O, and C also display no notable changes in the compositional characterizations of CQDs$_{1.5}$-ZnOVANs(bio)/FTO before (Figs. 6.6b-6.6d) and after (Figs. 6.12d-6.12f) the stability test. Therefore, CQDs$_{1.5}$-ZnOVANs(bio)/FTO maintains its compositional and structural integrity across various cycles of NFX monitoring (Bhan and Kumar Golder, 2023).

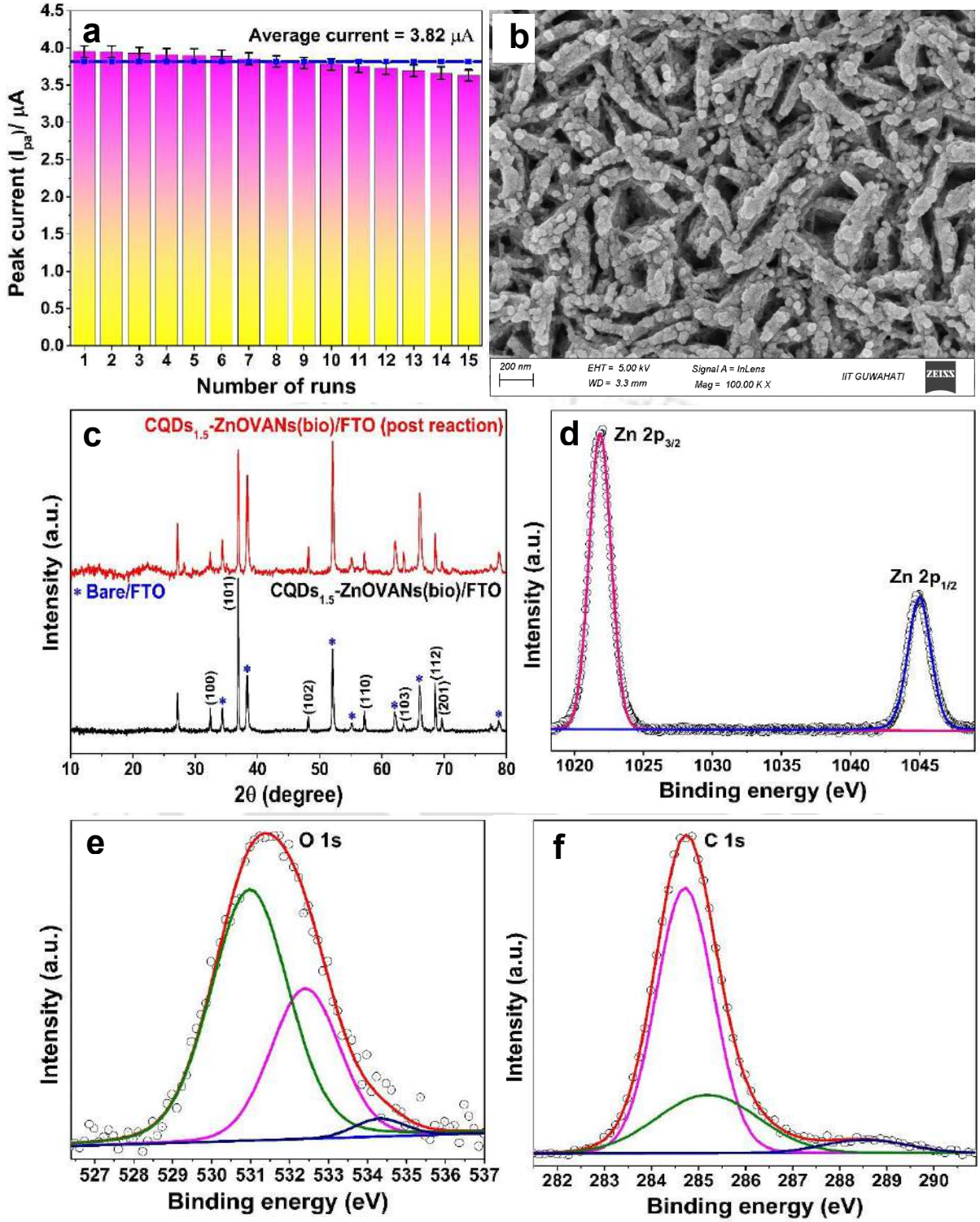

Figure 6.12: (a) Stability of $CQDs_{1.5}$-ZnOVANs(bio)/FTO, (b) FESEM image, (c) XRD pattern, and (d), (e) and (f) XPS spectra in Zn 2p, O 1s, and C 1s regions of $CQDs_{1.5}$-ZnOVANs(bio)/FTO, respectively, after 15 cycles of NFX monitoring.

Table 6.3: Comparison of electrocatalytic performance of $CQDs_{1.5}$-ZnOVANs(bio)/FTO with recently reported sensors for NFX detection.

Working electrodes	Techniques	LOD (µM)	Linear range (µM)	Sources
Bi_2MoO_6/MWCNTs-COOH/GCE	LSV[ɬ]	0.0067	0.03-10	Shi et al., 2024
SPCE	LSV[ɬ]	0.81	3.71-1000	Silva et al., 2024
MIP/MWCNT/GCE	SWV*	0.046	0.1-8	da Silva et al., 2015
Ni/NiO/C/β-CD/RGO	DPV[⁂]	0.01	0.4-80	Cui et al., 2019
APT-BDD	SWASW[ꟾ]	0.04	0.157-12.5	Karahan et al., 2020
CdTe-CB-CTS: EPH/GCE	SWASW[ꟾ]	0.0066	0.2-7.4	Santos et al., 2019
ZnO/GCE	Chronoamperometry	0.41	2-500	Zheng et al., 2019
$CaCuSi_4O_{10}$/GCE	DPV[⁂]	0.0046	0.01-82.1	Muungani and van Zyl, 2023
MIP/Cu-COF/GCE	SWV*	0.0059	0.03-100	Fu et al., 2023
MIP/GCE	SWV*	0.004	0.1-160	Yuan et al., 2022
$CQDs_{1.5}$-ZnOVANs(bio)/FTO	**SWV***	**0.0066**	**0.25-40**	**Present work**
		0.0270	**40-300**	

[ɬ]Linear sweep voltammetry, *Square wave voltammetry, [⁂]Differential pulse voltammetry, [ꟾ]Square wave anodic stripping voltammetry

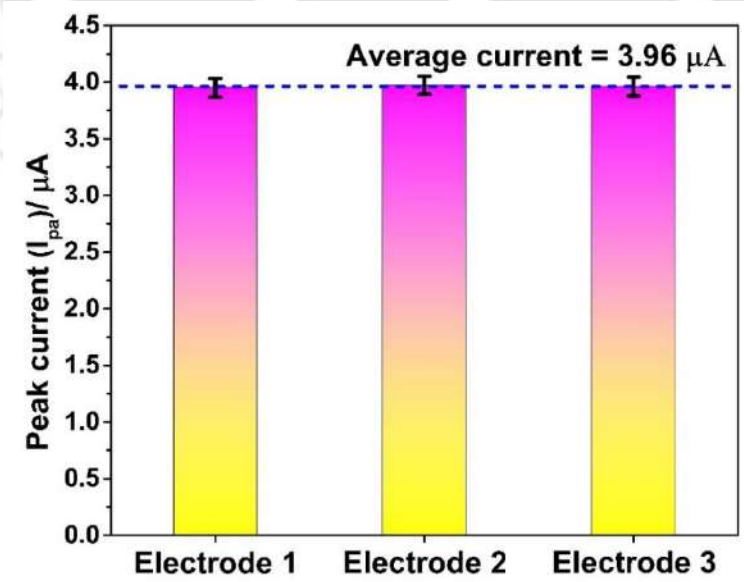

Figure 6.13: Reproducibility of NFX monitoring using three freshly fabricated $CQDs_{1.5}$-ZnOVANs(bio)/FTO electrodes tested in 60 µM NFX. Reaction conditions: Dpote -0.7 V vs. Ag/AgCl, Dtime of 80 s, and Dtemp of 45 °C in 0.1 M PBS electrolyte at pH 5.

6.2.5. Selectivity of NFX monitoring at CQDs$_{1.5}$-ZnOVANs(bio)/FTO

The chronoamperometry was conducted at CQDs$_{1.5}$-ZnOVANs(bio)/FTO with 5, 10 and 30 µM NFX at the beginning with an interval of 20 s (Fig.6.14), followed by the addition of 40 µM of ciprofloxacin, phenylbutazone, and sulfamethoxazole for the selectivity test of NFX monitoring. This test was preceded with 60, 120 and 160 µM NFX in 0.1 M PBS (pH 5, 45 °C) at 1.042 V vs. Ag/AgCl (Fig. 6.14). The changes in I_{pa} were observed with the addition of NFX both at lower (5-30 µM) and higher (60-160 µM) NFX concentrations, and the peak current was stabilized rapidly. Whereas no notable variation in I_{pa} was found with the introduction of potential interfering substances at 1.042 V vs. Ag/AgCl (Bhan et al., 2025b). However, a gradual decrease in current was observed, which could be attributed to the continuous reduction of the analyte concentration as it gets consumed by the oxidation reaction. Hence, the proposed electrocatalytic monitoring platform is almost free from the interference of common drugs (Kabir et al., 2019).

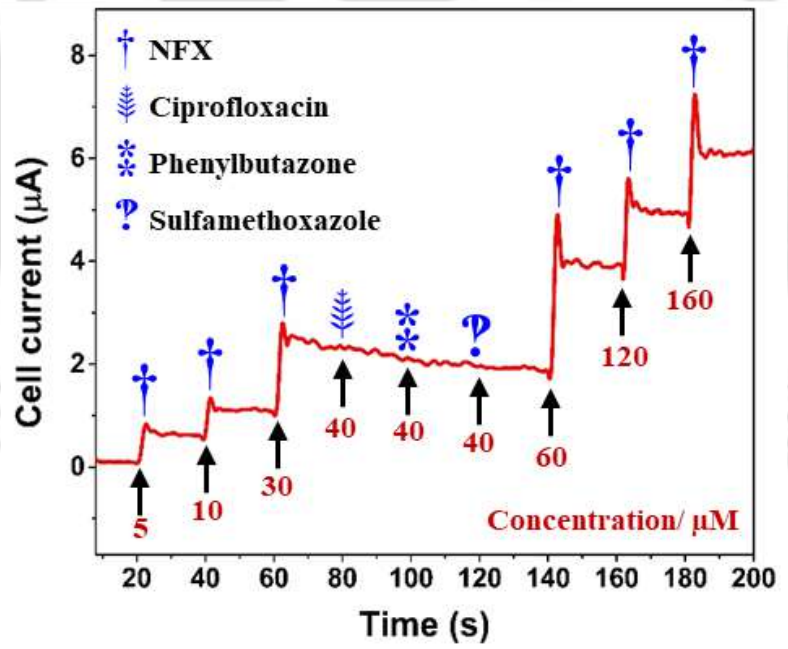

Figure 6.14: Selectivity of CQDs$_{1.5}$-ZnOVANs(bio)/FTO towards NFX monitoring in the presence of common antibiotics, including ciprofloxacin, phenylbutazone, and sulfamethoxazole.

6.2.6. NFX monitoring and quantification in the environmental matrices

The practical applicability of CQDs$_{1.5}$-ZnOVANs(bio)/FTO was tested for NFX monitoring and quantification in tap and river water. SWV was captured using the mixture of

0.1 M PBS (pH 5) and tap/river water (4:1 v/v) with 0-60 µM NFX spiked in it. Tap and river water samples were collected from the domestic supply at IIT Guwahati and the Brahmaputra River. It was then filtered through a 0.2 µm filter paper to remove suspended solids to prevent surface fouling of $CQDs_{1.5}$-ZnOVANs(bio)/FTO (Bhan and Golder, 2024). The monitoring and quantification of NFX was performed at $CQDs_{1.5}$-ZnOVANs(bio)/FTO by determining NFX against the calibration plot shown in Fig. 6.11b, and it was compared with HPLC. The results are summarized in Table 6.4. The recovery of NFX was approximately 100% in both water samples. The maximum RSD and deviation from HPLC analyses were found to be 2.2 and 3.9 % for tap water, and 3.6 and 4.7% for river water. Therefore, the proposed detection platform shows a promising potential for on-site monitoring and quantifying NFX in the environmental matrices.

Table 6.4: Performance of $CQDs_{1.5}$-ZnOVANs(bio)/FTO for monitoring and quantifying NFX in tap and river water samples and its comparison with HPLC.

Sample	NFX spiked (µM)	$CQDs_{1.5}$-ZnOVANs(bio)/FTO			NFX determined using HPLC (µM)	Deviation (%)
		NFX determined (µM)	Recovery (%)	RSD (%)		
Tap water	0	ND	-	-	ND	-
	2	2.05	102.5	2.2	2.13	-3.9
	10	9.91	99.1	2.1	10.19	-2.8
	30	31.09	103.6	1.4	29.96	3.6
	60	61.48	102.5	1.7	60.17	2.1
River water	0	ND	-	-	ND	-
	2	1.97	98.5	3.6	2.06	-4.6
	10	10.45	104.5	3.1	9.96	4.7
	30	30.45	101.5	2.5	31.63	-3.9
	60	60.54	100.9	2.9	61.98	-2.4

6.3. Major findings

We have successfully synthesized 2D ZnO VANs onto FTO using analytes extracted from *Sechium edule* fruit, and it was further functionalized with CQDs derived from carbon-

rich remnant peel for electrocatalytic monitoring of NFX in environmental matrices. Highly crystallinity $CQDs_{1.5}$-ZnOVANs(bio)/FTO grew uniformly in a vertical orientation (length 965.3 nm and thickness 46.3 nm). CQDs particle size was 4.7 nm, exhibiting an amorphous nature. $CQDs_{1.5}$-ZnOVANs(bio)/FTO exhibited 2.6- and 2.7-fold enhancement in I_{pa} and A_e, respectively, along with 1.5-fold reduction in R_p compared to ZnOVANs(bio)/FTO. NFX monitoring was favourable at pH 5 in 0.1 M PBS in which two electrons and two protons were involved in a diffusion-controlled redox reaction with E^0 of 1.042 V, k^0 of 0.105 s^{-1}, and Γ^* of 2.54×10^{-11} mol cm^{-2}. $CQDs_{1.5}$-ZnOVANs(bio)/FTO exhibited LODs of 0.0066 and 0.0270 µM, LOQs of 0.0220 and 0.0900 µM, and sensitivities of 0.1903 and 0.0464 $\mu A.\mu M^{-1}$ cm^{-2} within 0.25 to 40 and 40 to 300 µM NFX. $CQDs_{1.5}$-ZnOVANs(bio)/FTO platform demonstrated excellent stability with only 8.1% reduction in I_{pa} till 15^{th} cycle of NFX monitoring and maintained its uniform morphological and structural attributes. $CQDs_{1.5}$-ZnOVANs(bio)/FTO showed high selectivity towards NFX even in the presence of ciprofloxacin, phenylbutazone, and sulfamethoxazole at 1.042 V vs. Ag/AgCl. NFX monitored at $CQDs_{1.5}$-ZnOVANs(bio)/FTO was well comparable with HPLC, with a maximum RSD of 2.2 and 3.6% for tap and river water, respectively. Therefore, $CQDs_{1.5}$-ZnOVANs(bio)/FTO monitoring platform holds promising potential for the development of a portable sensor for the detection of emerging pollutants in environmental matrices. In the next chapter, the influence of morphological attributes in bio-based VANs from bean-shaped (2D) to rod-shaped (1D) were explored on electrochemical sensing performance.

References

Abbas, M.W., Soomro, R.A., Kalwar, N.H., Zahoor, M., Avci, A., Pehlivan, E., Hallam, K.R., Willander, M., 2019. Carbon quantum dot coated Fe_3O_4 hybrid composites for sensitive electrochemical detection of uric acid. Microchem. J. 146, 517–524. https://doi.org/10.1016/j.microc.2019.01.034

Ahmad, R., Bhat, K.S., Nagal, V., Nakate, U.T., Ahmad, A., Alshammari, M.B., Alam, S., Lee, B.-I., 2024. Surface-engineered vertically-aligned ZnO nanorod for sensitive non-enzymatic electrochemical monitoring of cholesterol. Heliyon 10, e37847. https://doi.org/10.1016/j.heliyon.2024.e37847

Ahmad, R., Lee, B.-I., 2024. Facile fabrication of palm trunk–like ZnO hierarchical nanostructure–based biosensor for wide-range glucose detection. Chem. Eng. J. 492, 152432. https://doi.org/10.1016/j.cej.2024.152432

Ahmad, R., Tripathy, N., Ahn, M.-S., Bhat, K.S., Mahmoudi, T., Wang, Y., Yoo, J.-Y., Kwon, D.-W., Yang, H.-Y., Hahn, Y.-B., 2017. Highly Efficient Non-Enzymatic Glucose Sensor Based on CuO Modified Vertically-Grown ZnO Nanorods on Electrode. Sci. Rep. 7, 5715. https://doi.org/10.1038/s41598-017-06064-8

Arsalan, M., Saddique, I., Baoji, M., Awais, A., Khan, I., Shamseldin, M.A., Mehrez, S., 2022. Novel Synthesis of Sensitive Cu-ZnO Nanorod–Based Sensor for Hydrogen Peroxide Sensing. Front. Chem. 10, 932985. https://doi.org/10.3389/fchem.2022.932985

Awais, A., Arsalan, M., Qiao, X., Yahui, W., Sheng, Q., Yue, T., He, Y., 2021. Facial synthesis of highly efficient non-enzymatic glucose sensor based on vertically aligned Au-ZnO NRs. J. Electroanal. Chem. 895, 115424. https://doi.org/10.1016/j.jelechem.2021.115424

Bagheri, H., Afkhami, A., Khoshsafar, H., Rezaei, M., Shirzadmehr, A., 2013. Simultaneous electrochemical determination of heavy metals using a triphenylphosphine/MWCNTs composite carbon ionic liquid electrode. Sensors Actuators B Chem. 186, 451–460. https://doi.org/10.1016/j.snb.2013.06.051

Bhan, C., Golder, A.K., 2025. Nature-Inspired Vertically Oriented 1D Bi_2S_3 Surface Nanorods for Ultra-Selective Electrochemical Sensing of Mancozeb. Langmuir 41, 15331–15346. https://doi.org/10.1021/acs.langmuir.5c00915

Bhan, C., Golder, A.K., 2024. ZnO Nanorods Aligned in a Vertical Configuration for Targeted Electrochemical Detection of Aniline. ACS Appl. Bio Mater. 7, 7413–7428. https://doi.org/10.1021/acsabm.4c01050

Bhan, C., Kumar Golder, A., 2023. Bio-based hierarchical vertically aligned 2D ZnO nanostructures for ultra selective electrochemical sensing of p-Chloroaniline. Chem. Eng. J. 475, 146122. https://doi.org/10.1016/j.cej.2023.146122

Bhan, C., R, G.S., Golder, A.K., 2025a. A chemo-mimetic approach using bioanalytes for formation of $BiVO_4$ nanostructures for voltammetric detection of bisphenol A. J. Environ. Chem. Eng. 13, 117417. https://doi.org/10.1016/j.jece.2025.117417

Bhan, C., Ravi, R., Golder, A.K., 2025b. Phyto-analytic formation of Ag nanostructures for targeted electrocatalytic sensing of ciprofloxacin. J. Environ. Chem. Eng. 13, 115140. https://doi.org/10.1016/j.jece.2024.115140

Bikesh, S., Dinamani Singh, A., Shougaijam, B., 2024. Development of Ethanol Sensor Based on Vertically Aligned SnO_2/TiO_2 Heterojunction Nanowire Using GLAD Technique. IEEE Trans. Electron Devices 71, 3867–3873. https://doi.org/10.1109/TED.2024.3392173

Chowdhury, A., Bhan, C., Peela, N.R., Golder, A.K., 2022. A tunable bioinspired process of

SnO_2 NPs synthesis for electrochemical CO_2-into-formate conversion. J. CO_2 Util. 66, 102263. https://doi.org/10.1016/j.jcou.2022.102263

Cicek, C., Erdogan, Z.O., 2024. Detection of ciprofloxacin in ear drop using UV spectrophotometric method based on gold nanoparticles as a sensing probe. J. Nanoparticle Res. 26, 121. https://doi.org/10.1007/s11051-024-06027-x

Cui, X., Cao, D., Djellabi, R., Qiao, M., Wang, Y., Zhao, S., Mao, R., Gong, Y., Zhao, X., Yang, B., 2019. Enhancement of Ni/NiO/graphitized carbon and β-Cyclodextrin/reduced graphene oxide for the electrochemical detection of norfloxacin in water sample. J. Electroanal. Chem. 851, 113407. https://doi.org/10.1016/j.jelechem.2019.113407

da Silva, H., Pacheco, J., Silva, J., Viswanathan, S., Delerue-Matos, C., 2015. Molecularly imprinted sensor for voltammetric detection of norfloxacin. Sensors Actuators B Chem. 219, 301–307. https://doi.org/10.1016/j.snb.2015.04.125

Dan, Y., Xu, J., Jian, J., Meng, L., Deng, P., Yan, J., Yuan, Z., Zhang, Y., Zhou, H., 2023. In Situ Decoration of Bi_2S_3 Nanosheets on Zinc Oxide/Cellulose Acetate Composite Films for Photodegradation of Dyes under Visible Light Irradiation. Molecules 28, 6882. https://doi.org/10.3390/molecules28196882

Das, D., Bhan, C., Mukherjee, C., Golder, A.K., 2024. Improved selectivity of electrochemical aniline sensing using one-dimensional silver nanorods with high aspect ratio synthesized by ascorbic acid assisted method. Anal. Chim. Acta 1310, 342697. https://doi.org/10.1016/j.aca.2024.342697

Dash, S.R., Bag, S.S., Golder, A.K., 2021. Bio-inspired PtNPs/Graphene nanocomposite based electrocatalytic sensing of metabolites of dipyrone. Anal. Chim. Acta 1167, 338562. https://doi.org/10.1016/j.aca.2021.338562

Dash, S.R., Bag, S.S., Golder, A.K., 2020. Synthesis of highly structured spherical Ag@Pt core-shell NPs using bio-analytes for electrocatalytic Pb(II) sensing. Sensors Actuators B Chem. 314, 128062. https://doi.org/10.1016/j.snb.2020.128062

Dash, S.R., Bag, S.S., Golder, A.K., 2018. Synergized AgNPs formation using microwave in a bio-mediated route: Studies on particle aggregation and electrocatalytic sensing of ascorbic acid from biological entities. J. Electroanal. Chem. 827, 181–192. https://doi.org/10.1016/j.jelechem.2018.09.023

de Oliveira Morais, C.C., Magalhães, K.F., dos Santos, E.V., Castro, S.S.L., Martínez-Huitle, C.A., 2024. Electrochemically simple, sensitive, and clean method for monitoring norfloxacin in advanced oxidative processes. J. Electroanal. Chem. 974, 118752. https://doi.org/10.1016/j.jelechem.2024.118752

Elgrishi, N., Rountree, K.J., McCarthy, B.D., Rountree, E.S., Eisenhart, T.T., Dempsey, J.L., 2018. A Practical Beginner's Guide to Cyclic Voltammetry. J. Chem. Educ. 95, 197–206. https://doi.org/10.1021/acs.jchemed.7b00361

Elugoke, S.E., Fayemi, O.E., Adekunle, A.S., Mamba, B.B., Nkambule, T.T.I., Ebenso, E.E., 2022. Electrochemical sensor for the detection of dopamine using carbon quantum dots/copper oxide nanocomposite modified electrode. FlatChem 33, 100372. https://doi.org/10.1016/j.flatc.2022.100372

Espinosa-Mansilla, A., Peña, A.M. de la, Gómez, D.G., Salinas, F., 2005. HPLC determination of enoxacin, ciprofloxacin, norfloxacin and ofloxacin with photoinduced fluorimetric (PIF) detection and multiemission scanning. J. Chromatogr. B 822, 185–193. https://doi.org/10.1016/j.jchromb.2005.05.045

Fu, Y., Xie, Y., Shi, H., Zhang, G., Zhang, H., Feng, S., 2023. Molecularly imprinted electrochemical sensor based on metal-covalent organic framework for specifically recognizing norfloxacin from unpretreated milk. Food Chem. 429, 136921. https://doi.org/10.1016/j.foodchem.2023.136921

Gawal, P.M., Golder, A.K., 2024. Vegetal route for synthesis of CQDs/CdS nanocomposites for photocatalytic reduction of CO_2 to methanol under visible light. Colloids Surfaces A Physicochem. Eng. Asp. 683, 133068. https://doi.org/10.1016/j.colsurfa.2023.133068

Gawal, P.M., Ishrat, J., Bhattacharyya, K., Golder, A.K., 2025. Experimental and Theoretical Studies on Photocatalytic CO_2 Reduction to HCOOH by Biomass-Derived Carbon Dots Embedded Phytochemical-Based CdS Quantum Dots. Langmuir 41, 11161–11172. https://doi.org/10.1021/acs.langmuir.5c01002

Gumpu, M.B., Veerapandian, M., Krishnan, U.M., Rayappan, J.B.B., 2017. Simultaneous electrochemical detection of Cd(II), Pb(II), As(III) and Hg(II) ions using ruthenium(II)-textured graphene oxide nanocomposite. Talanta 162, 574–582. https://doi.org/10.1016/j.talanta.2016.10.076

Jung, H., Sapner, V.S., Adhikari, A., Sathe, B.R., Patel, R., 2022. Recent Progress on Carbon Quantum Dots Based Photocatalysis. Front. Chem. 10, 1–28. https://doi.org/10.3389/fchem.2022.881495

Kabir, H., Ma, P.Y., Renn, N., Nicholas, N.W., Cheng, I.F., 2019. Electrochemical determination of free chlorine on pseudo-graphite electrode. Talanta 205, 120101. https://doi.org/10.1016/j.talanta.2019.06.101

Karahan, F., Başı, Z., Keskin, E., Pınar, P.T., Yardım, Y., Şentürk, Z., 2020. Electrochemical Determination of Fluoroquinolone Antibiotic Norfloxacin in the Presence of Anionic

Surfactant Using the Anodically Pretreated Boron-Doped Diamond Electrode. ChemistrySelect 5, 12862–12868. https://doi.org/10.1002/slct.202002921

Kumar, A., Das, C., 2025. Anticorrosive Behavior of a Novel Ternary RGO–ZnO–PANI Nanocomposite-Reinforced Epoxy Coating on Mild Steel in Marine Environment. Adv. Eng. Mater. 2500949, 1–17. https://doi.org/10.1002/adem.202500949

Kumar, A., Das, C., 2024. Corrosion inhibition of mild steel by Praecitrullus fistulosus (tinda fruit and peel) extracts. Sci. Total Environ. 929, 172569. https://doi.org/10.1016/j.scitotenv.2024.172569

Kumar, A., Das, C., 2023. A novel eco-friendly inhibitor of chayote fruit extract for mild steel corrosion in 1 M HCl: Electrochemical, weight loss studies, and the effect of temperature. Sustain. Chem. Pharm. 36, 101261. https://doi.org/10.1016/j.scp.2023.101261

Liu, Z., Jin, M., Cao, J., Wang, J., Wang, X., Zhou, G., van den Berg, A., Shui, L., 2018. High-sensitive electrochemical sensor for determination of Norfloxacin and its metabolism using MWCNT-CPE/pRGO-ANSA/Au. Sensors Actuators B Chem. 257, 1065–1075. https://doi.org/10.1016/j.snb.2017.11.052

Liu, Z., Jin, M., Lu, H., Yao, J., Wang, X., Zhou, G., Shui, L., 2019. Molecularly imprinted polymer decorated 3D-framework of functionalized multi-walled carbon nanotubes for ultrasensitive electrochemical sensing of Norfloxacin in pharmaceutical formulations and rat plasma. Sensors Actuators B Chem. 288, 363–372. https://doi.org/10.1016/j.snb.2019.02.097

Lotfi, S., Veisi, H., Karmakar, B., 2021. A convenient strategy for the electrochemical evaluation of acetaminophen and caffeine in combined drugs and biological samples over TiO_2@polymethyldopa/Pd nanocomposite functionalized glassy carbon electrodes. Measurement 186, 110156. https://doi.org/10.1016/j.measurement.2021.110156

Lv, Z., Ma, Y., Wang, J., Wu, H., Zhao, Q., Chen, J., Qiao, Z., Men, J., 2025. Construction of an electrochemical sensor for sensitive detection of norfloxacin based on DFT and surface molecular imprinting technology. Colloids Surfaces A Physicochem. Eng. Asp. 716, 136675. https://doi.org/10.1016/j.colsurfa.2025.136675

Malode, S.J., Keerthi, P.K., Shetti, N.P., Kulkarni, R.M., 2020. Electroanalysis of Carbendazim using MWCNT/Ca-ZnO Modified Electrode. Electroanalysis 32, 1590–1599. https://doi.org/10.1002/elan.201900776

Manivannan, K., Sivakumar, M., Cheng, C.-C., Lu, C.-H., Chen, J.-K., 2019. An effective electrochemical detection of chlorogenic acid in real samples: Flower-like ZnO surface covered on PEDOT:PSS composites modified glassy carbon electrode. Sensors Actuators

B Chem. 301, 127002. https://doi.org/10.1016/j.snb.2019.127002

Mao, Z., Zhu, H., Peng, X., Chen, J., Chen, Q., Chen, X., Hu, X., Chen, H., 2022. In situ vertical alignment of 2D MoS_2 layers on GO film: enhanced electrochemical properties for PD-L1 sensing. Microchim. Acta 189, 155. https://doi.org/10.1007/s00604-022-05269-7

Meireles, L.M., Silva, R.M., da Silva, R.C., Okumura, L.L., Moreira, R.P.L., Silva, T.A., 2024. Low-cost electrochemical sensor for ciprofloxacin antibiotic based on green-synthesized silver nanoparticles and carbon black. J. Solid State Electrochem. https://doi.org/10.1007/s10008-024-06033-y

Morozov, R., Avdin, V., Lychkin, G., Uchaev, D., Vakhitov, I., Stanković, D., 2025. Facile prepared high purity Cerium vanadate for simultaneous electrochemical detection of p-nitrophenol and 2,4,6-trichlorophenol. J. Phys. Chem. Solids 196, 112355. https://doi.org/10.1016/j.jpcs.2024.112355

Muungani, G., van Zyl, W.E., 2023. A $CaCuSi_4O_{10}$/GCE electrochemical sensor for detection of norfloxacin in pharmaceutical formulations. RSC Adv. 13, 12799–12808. https://doi.org/10.1039/D3RA01702H

Ordonez, A., Gomez, J., Vattuone, M., Lsla, M., 2006. Antioxidant activities of *Sechium edule* (Jacq.) Swartz extracts. Food Chem. 97, 452–458. https://doi.org/10.1016/j.foodchem.2005.05.024

Patra, S., Golder, A.K., Uppaluri, R.V.S., 2024. Green synthesis of carbon dots from mature green tea leaves for label-free fluorescence sensing of chromium(VI). Opt. Mater. (Amst). 154, 115767. https://doi.org/10.1016/j.optmat.2024.115767

Pino, F., Mayorga-Martinez, C.C., Merkoçi, A., 2016. High-performance sensor based on copper oxide nanoparticles for dual detection of phenolic compounds and a pesticide. Electrochem. commun. 71, 33–37. https://doi.org/10.1016/j.elecom.2016.08.001

Rafaie, H.A., Samat, N.A., Nor, R.M., 2014. Effect of pH on the growth of zinc oxide nanorods using Citrus aurantifolia extracts. Mater. Lett. 137, 297–299. https://doi.org/10.1016/j.matlet.2014.09.033

Ravi, R., Golder, A.K., 2025. Bio-based synthesis of oxygen-deficient Ni-doped TiO_2 using waste pineapple peel: Density functional theory studies and photocatalytic degradation of furazolidone. J. Environ. Chem. Eng. 13, 116198. https://doi.org/10.1016/j.jece.2025.116198

Ravi, R., Golder, A.K., 2023a. Bio-based Au Doping with Dominant Oxygen Vacancies and Ti^{3+} Defects on Photocatalytic Functionalities of TiO_2. Ind. Eng. Chem. Res. 62, 20702–20715. https://doi.org/10.1021/acs.iecr.3c02850

Ravi, R., Golder, A.K., 2023b. A tuneable bioinspired process of Pt-doping in TiO_2 for improved photoelectrochemical and photocatalytic functionalities. Colloids Surfaces A Physicochem. Eng. Asp. 663, 131034. https://doi.org/10.1016/j.colsurfa.2023.131034

Santos, A.M., Wong, A., Cincotto, F.H., Moraes, F.C., Fatibello-Filho, O., 2019. Square-wave adsorptive anodic stripping voltammetric determination of norfloxacin using a glassy carbon electrode modified with carbon black and CdTe quantum dots in a chitosan film. Microchim. Acta 186. https://doi.org/10.1007/s00604-019-3268-1

Shi, S., Zhou, C., Chen, A., Tang, N., Wan, K., Jiang, Y., Liu, J., He, Q., Cao, L., 2024. Bi_2MoO_6/MWCNTs-COOH/GCE electrochemical probe for ultrasensitively and selectively detecting antibiotic norfloxacin. Chemosphere 364, 143139. https://doi.org/10.1016/j.chemosphere.2024.143139

Silva, L.R.G., Stefano, J.S., de Lourdes Soprani Vasconcellos, M., de Queiroz Ferreira, R., 2024. Portable and sustainable electrochemical platform for the sub-minute detection of norfloxacin in organic fertilizers. Ionics (Kiel). 30, 563–570. https://doi.org/10.1007/s11581-023-05289-0

Teker, T., Bağdiken, F.N., Aslanoglu, M., 2025. Ultrasonic-assisted development of a high-sensitivity voltammetric sensor based on graphene nanoplatelets and hafnium oxide nanomaterials for paracetamol detection. Microchem. J. 213, 113862. https://doi.org/10.1016/j.microc.2025.113862

Umesh, N., Antolin Jesila, J., Wang, S.-F., Vishnu, N., Yang, Y.-J., 2021. Novel voltammetric detection of norfloxacin in urine and blood serum using a flexible Ni foam based Ni-Co-MOF ultrathin nanosheets derived from Ni-Co-LDH. Microchem. J. 160, 105747. https://doi.org/10.1016/j.microc.2020.105747

Verma, S., Sen, A., Dutta, N., Sengupta, P., Chakraborty, P., Dutta, G., 2024. Highly Specific Non-Enzymatic Electrochemical Sensor for the Detection of Uric Acid Using Carboxylated Multiwalled Carbon Nanotubes Intertwined with GdS-Gd_2O_3 Nanoplates in Human Urine and Serum. Langmuir 40, 21427–21441. https://doi.org/10.1021/acs.langmuir.4c02233

Vu, O.T., Nguyen, Q.H., Nguy Phan, T., Luong, T.T., Eersels, K., Wagner, P., Truong, L.T.N., 2023. Highly Sensitive Molecularly Imprinted Polymer-Based Electrochemical Sensors Enhanced by Gold Nanoparticles for Norfloxacin Detection in Aquaculture Water. ACS Omega 8, 2887–2896. https://doi.org/10.1021/acsomega.2c04414

Wahab, R., Ansari, S.G., Kim, Y.S., Song, M., Shin, H.-S., 2009. The role of pH variation on the growth of zinc oxide nanostructures. Appl. Surf. Sci. 255, 4891–4896.

https://doi.org/10.1016/j.apsusc.2008.12.037

Wang, M., Wang, Q., Wang, X., Wang, S., 2024. Nitrogen doped biomass derived carbon and $BiVO_4$ composite for simultaneous detection of furazolidone and chloramphenicol. Microchem. J. 197, 109810. https://doi.org/10.1016/j.microc.2023.109810

Wang, W., Gong, Z., Yang, S., Xiong, T., Wang, D., Fan, M., 2020. Fluorescent and visual detection of norfloxacin in aqueous solutions with a molecularly imprinted polymer coated paper sensor. Talanta 208, 120435. https://doi.org/10.1016/j.talanta.2019.120435

Xu, J.-T., Hu, H.-T., Chen, Z., Feng, X.-Z., Han, G.-C., Kraatz, H.-B., 2024. One-step construction of MWCNTs@MoS_2@Chitosan film for ciprofloxacin sensing and its oxidation mechanism. Microchem. J. 205, 111184. https://doi.org/10.1016/j.microc.2024.111184

Yuan, J., Zhang, H., Shi, H., Zhang, G., Feng, S., 2022. Molecularly Imprinted Polymer Modified Electrode Prepared by In Situ Polymerization for Specific Determination of Norfloxacin. J. Electrochem. Soc. 169, 117509. https://doi.org/10.1149/1945-7111/aca0c6

Zhang, S., Ling, P., Chen, Y., Liu, J., Yang, C., 2023. 2D/2D porous Co_3O_4/rGO nanosheets act as an electrochemical sensor for voltammetric tryptophan detection. Diam. Relat. Mater. 135, 109811. https://doi.org/10.1016/j.diamond.2023.109811

Zhang, Z., Zuo, Y., Fan, Y., Wang, X., Wang, C., Yang, S., Zhao, X., Wang, M., Xu, R., 2024. In situ fabrication of Ag nanoparticles modified vertically-grown ZnO nanorods on carbon fiber paper electrode for simultaneous detection of luteolin, daidzein and baicalein. Colloids Surfaces A Physicochem. Eng. Asp. 694, 134118. https://doi.org/10.1016/j.colsurfa.2024.134118

Zheng, Y., Huang, Y., Shi, H., Fu, L., 2019. Green biosynthesis of ZnO nanoparticles by plectranthus amboinicus leaf extract and their application for electrochemical determination of norfloxacin. Inorg. Nano-Metal Chem. 49, 277–282. https://doi.org/10.1080/24701556.2019.1661441

Zhou, Y., Abdurexit, A., Jamal, R., Abdiryim, T., Liu, X., Liu, F., Xu, F., Zhang, Y., Wang, Z., 2024. Highly sensitive electrochemical sensing of norfloxacin by molecularly imprinted composite hollow spheres. Biosens. Bioelectron. 251, 116119. https://doi.org/10.1016/j.bios.2024.116119

CHAPTER 7

Nature-inspired Vertically Oriented 1D Bi_2S_3 Surface Nanorods for Ultra Selective Electrochemical Sensing of Mancozeb

This chapter introduce the development of nature-inspired 1D surface vertically oriented nanostructures (VONs) of Bi_2S_3 on the surface of FTO using bio-extract of Sechium edule for highly selective electrochemical detection and determination of mancozeb (MCZ) by SWV. This study also aims to address the shortcoming of the rapid detachment of nanomaterials from the surface of kinetic electrodes by optimizing Bi_2S_3 VONs synthesis and electrochemical sensing parameters to maintain consistent sensitivity and selectivity. Moreover, the high surface area and unimpeded charge transfer characteristics of the VONs significantly contribute to enhancing the sensor's sensitivity and selectivity. The practical applicability of the proposed sensing platform for MCZ detection and quantification was examined using tap water, river water, agricultural runoff, and wastewater and compared with the HPLC.

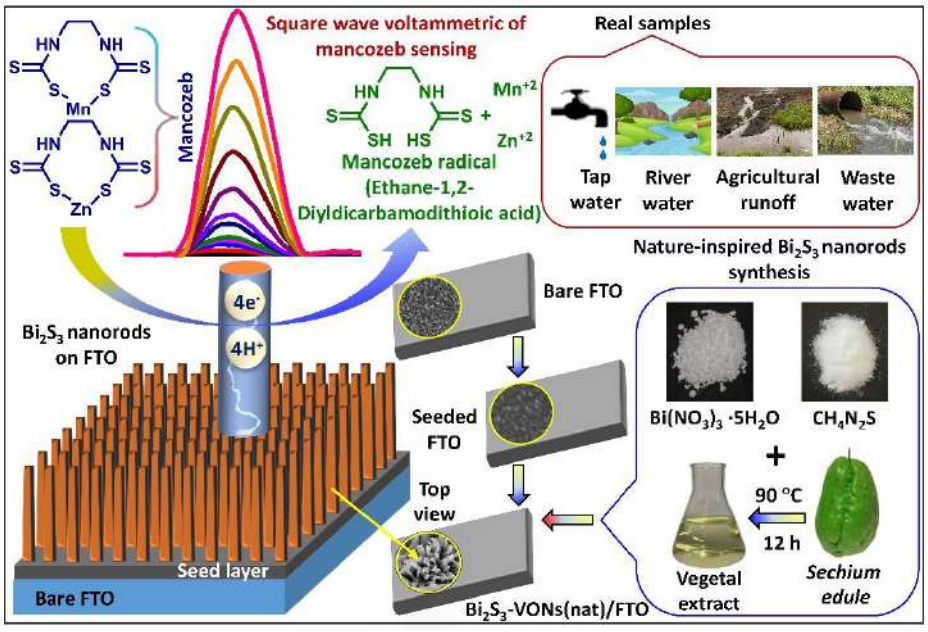

Chapter highlights

- Nature-inspired development of vertically oriented nanostructures of 1D Bi_2S_3
- Bi_2S_3-VONs(nat)/FTO catalyzed mancozeb sensing by square wave voltammetry
- Mancozeb sensing involves four electrons and four protons transfer reaction
- Mancozeb detection limit of 0.0085 µM and sensitivity of 0.1578 µA. $\mu M^{-1}.cm^{-2}$
- Mancozeb sensing highly selective against common pesticides and ionic interferants

7.1. Background and executive motivation

The rapid growth of industrial and agricultural activities has augmented the need for effective environmental monitoring and pollution control. The existence of pesticide residues in the environment is a major concern among the various pollutants that pose a significant threat to our ecosystems and human health (Guo et al., 2025). Mancozeb (MCZ), a widely used ethylene bisdithiocarbamate fungicide, is infamous for its extensive application in agriculture to combat fungal diseases in crops. Due to its low cost, MCZ accounts for 20% of the worldwide fungicide market (Bao et al., 2022). India represents 28% of the global MCZ market. Pacific Asia and Europe account for 85% of sales, and the United States contributes 4% (Cocco, 2022). Despite its efficacy in enhancing crop yields, MCZ poses significant environmental and health risks due to its persistence and potential to accumulate in the food chain (Buledi et al., 2022). Human exposure to MCZ can occur through skin contact, inhalation or ingestion, leading to immediate health issues such as headaches, nausea, and irritation of the skin and eyes. Prolonged exposure may have more severe effects, impacting the thyroid gland and impairing the nervous system (Slathia et al., 2024). Consequently, there is a high need for advanced detection methods capable of detecting trace levels of pesticide residue with high sensitivity and specificity.

Analytical methods, such as chromatographic and spectroscopic are efficient for monitoring and determining pesticide residue in environmental matrix (Armenta et al., 2006; Petha et al., 2017). These techniques require adept personnel, arduous procedures, costly reagents, and extended sample preparation (Musarurwa and Tawanda Tavengwa, 2021). Therefore, the development of an alternative cost-effectiveness electrochemical sensing platform is highly warranted for detecting and determining pesticide residues in environmental matrices.

Electrochemical sensors have emerged as a promising technique for sensing and quantification of environmental contaminants, including pesticides, pharmaceuticals, and heavy metals, owing to high sensitivity and selectivity, low cost, simple sample preparation, and potential for real-time monitoring of target analytes (Bhan et al., 2025; Bhan and Golder, 2024; Chen et al., 2024). Furthermore, functionalizing the kinetic electrode (e.g., fluorine-/indium-doped tin oxide (FTO/ITO), glassy carbon electrode (GCE), Pt, and Au) surface by nanoparticles (NPs), such as AuNPs, AgNPs, Co_2O_4, V_2O_5, $BiVO_4$, Bi_2S_3, ZnS, etc., using a binding agent (Nafion, polyurethane, polypyrrole, and polyethylene glycol) could enhance the performance of electrochemical sensing platform due to increase in chemical stability and

adsorption sites for target analytes (Ali and El-Wekil, 2023; Chi et al., 2023; Maji et al., 2023). However, the rapid detachment of nanomaterials embedded at the kinetic electrode surface is a significant impediment during the course of electrochemical measurement, and the binding agent could interfere with the electrochemical reactions or introduce noise into the signal, potentially reducing sensor stability, sensitivity, and selectivity. Moreover, the complexity of integrating and optimizing binder materials can complicate the sensor design and manufacturing process, increasing its fabrication time and cost. In previous studies, binder-based sensors, such as PtNPs/graphene/GCE and AgNRs/GCE, demonstrated 20 and 26% decrease in anodic peak current up to the 10^{th} cycle when the same sensing platform was reused for sensing of dipyrone and aniline, respectively (Das et al., 2024; Dash et al., 2021). Therefore, the growing nanomaterials in vertical configuration directly on the surface of the kinetic electrode could eliminate the need for surface coating, reduce cost, and enhance the life of the sensors by mitigating the possibility of delamination of catalysts (Bhan and Golder, 2024; Weng et al., 2024).

Recent studies have shown growing vertically oriented nanostructures (VONs) of ZnO, SnO_2, TiO_2, WO_3, Bi_2S_3, MoS_2, etc., on the kinetic electrode's surface (FTO/ITO) could significantly boost the sensor's performance (Ahmad et al., 2024; Bikesh et al., 2024; Malik et al., 2024; Mao et al., 2022). VONs exhibit a high surface-to-volume ratio, providing more surface area for increased interaction with analytes and minimizing background interference, resulting in improved selectivity, stability, and sensitivity (Ahmad and Lee, 2024; Arsalan et al., 2022; Awais et al., 2021; Zhang, 2024). The VONs could also improve charge transport efficiency, increase surface roughness, and reduce electron scattering, leading to better electrical conductivity and faster response times. It also facilitates effective contact with electrolyte solutions, which is crucial for accurate and stable sensor performance with greater chemical stability (Hideshima et al., 2024; Kumar and Kumar Sinha, 2024; Zhang et al., 2024). In our previous study, the growth of ZnO in vertical configuration on the surface of FTO (binder-free sensor) showed only a 11.97% decrease in the anodic peak current when the same electrode was reused for aniline sensing (Bhan and Golder, 2024). However, the methods described for the development of VONs typically involve chemical-intensive processes.

On the other hand, sulfide nanostructures, namely Bi_2S_3, MoS_2, CdS, and ZnS, have drawn substantial research attention due to their promising applications in various catalytic processes, such as electrochemical monitoring, wastewater treatment, CO_2 conversion by photo and electrochemical method, etc. (Ejeromedoghene et al., 2024; Ganesamurthi et al., 2024; Gawal and Golder, 2024; Ravi and Golder, 2025a; Younis et al., 2024). Among them, Bi_2S_3

has garnered significant attention due to their exceptional electronic, optical, and chemical properties. Its tunable bandgap (between 1.3-1.7 eV), high electrical conductivity (range from 10^{-6}-10^{-7} Ω^{-1} cm^{-1}), and large surface area contribute to its efficiency in catalytic applications (Ajiboye and Onwudiwe, 2021; Godzierz et al., 2024; Khadka et al., 2024). Moreover, Bi_2S_3 nanostructures synthesized into vertical configuration exhibit an even greater surface area and improved electron transport, which are critical factors for developing high-performance electrochemical sensors (Tang et al., 2016).

In this study, a nature-inspired methodology is presented for the development of Bi_2S_3 VONs on FTO. The selection of bio-extract for developing nature-inspired VONs was largely based on its content of reducing agents. In our previous studies, we have developed bio-inspired VONs of ZnO over FTO glass surface using *Sechium edule* extract for electrochemical detection of p-Chloroaniline (Bhan and Kumar Golder, 2023). *Sechium edule* fruit contains ascorbic acid (AA), flavonoids, and amino acids of 0.294, 19.3, and 12.9 mg/g on a dry basis, respectively (Flick et al., 1978; Ordonez et al., 2006; Rao and Golder, 2016; Ravi and Golder, 2023a, 2023b). The phytoconstituents in the *Sechium edule* extract have been used to leverage its potential for the growth of VONs of Bi_2S_3 onto the FTO surface.

Herein, nature-inspired 1D surface VONs of Bi_2S_3 have been developed on the surface of FTO using bio-extract of *Sechium edule* for highly selective electrochemical detection and determination of MCZ by square wave voltammetry (SWV). This study also aims to address the shortcoming of the rapid detachment of nanomaterials from the surface of kinetic electrodes by optimizing Bi_2S_3 VONs synthesis and electrochemical sensing parameters to maintain consistent sensitivity and selectivity. Moreover, the high surface area and unimpeded charge transfer characteristics of the VONs significantly contribute to enhancing the sensor's sensitivity and selectivity. The selectivity of the developed sensor was investigated in the presence of potential interferants, including chlorpyrifos, carbendazim, malathion, thiram, ziram, and profenofos. The practical applicability of the proposed sensing platform for MCZ detection and quantification was examined using tap water, river water, agricultural runoff, and wastewater and compared with the HPLC. To our knowledge, the introduction of nature-inspired VONs of Bi_2S_3 into the development of electrochemical sensing platforms represents a novel approach for the detection of MCZ.

7.2. Results and discussion

7.2.1. Bi_2S_3-VONs(nat)/FTO

7.2.1.1 *FESEM analysis*

Fig. 7.1 illustrates the top view FESEM micrographs of (a) bare FTO (FTO(bare)), (b) Bi_2S_3@seed/FTO, (c) 2.3Bi_2S_3-VONs(nat)/FTO@pH2, (d) 2.3Bi_2S_3-VONs(nat)/FTO@pH3 (e) 2.3Bi_2S_3-VONs(nat)/FTO@pH4, and (f) 2.3Bi_2S_3-VONs(nat)/FTO@pH5. The surface of FTO(bare) is found to be uneven (Fig. 7.1a.). Whereas, Bi_2S_3@seed/FTO exhibited improved smoothness (Fig. 7.1b), and its surface roughness was reduced by around 40.5% compared to FTO(bare) (Fig. 7.7b). 2.3Bi_2S_3-VONs(nat)/FTO@pH2 (Fig. 7.1c) was less densed compared to 2.3Bi_2S_3-VONs(nat)/FTO@pH3 (Fig. 7.1d). As pH increased from 3 to 5, the formation of Bi_2S_3 nanostructures over FTO was grown in a random manner with agglomerated particles of variant morphologies instead of its growth in vertical configuration (Figs. 7.1e and 7.1f). Figs. 7.1g, 7.1h, 7.1i, and 7.1j display the FESEM images of 1.0Bi_2S_3-VONs(nat)/FTO@pH3, 1.5Bi_2S_3-VONs(nat)/FTO@pH3, 2.0Bi_2S_3-VONs(nat)/FTO@pH3, and 2.5Bi_2S_3-VONs(nat)/FTO@pH3 at fixed pH of 3 and different precursor ($Bi(NO_3)_3 \cdot 5H_2O$) loading of 1.0, 1.5, 2, and 2.5 g, respectively. Interlinked flake-like nanostructures of Bi_2S_3 were formed with an increase in precursor amount from 1.0 to 2.0 g ((1.0-2.0)Bi_2S_3-VONs(nat)/FTO@pH3, Figs. 7.1g, 7.1h, and 7.1i). Well-defined Bi_2S_3 VONs were formed at a precursor amount of 2.3 g and pH 3 (2.3Bi_2S_3-VONs(nat)/FTO@pH3, Fig. 7.1d). At the 2.5 g of precursor loading and pH 3, Bi_2S_3 demonstrates a flower shaped morphology (Fig. 7.1j). 2.3Bi_2S_3-VONs(nat)/FTO@pH3 demonstrates surface roughness about 67.5 and 80.7% higher than FTO(bare) and Bi_2S_3@seed/FTO, respectively (Fig. 7.7c). The control synthesis of Bi_2S_3 nanostructures (2.3Bi_2S_3-H_2O(control)/FTO@pH3, Fig. 7.1k) was conducted by substituting the bio-extract with an equivalent volume of DI water at the optimum parameters (pH 3 and precursor amount of 2.3 g) under identical experimental condition. The formation of loosely arranged Bi_2S_3 nanostructures was observed. Additionally, the surface roughness of 2.3Bi_2S_3-VONs(nat)/FTO@pH3 was 69.9% greater than the 2.3Bi_2S_3-H_2O(control)/FTO@pH3. Fig. 7.1l shows the cross-sectional image of 2.3Bi_2S_3-VONs(nat)/FTO@pH3 with an average height of ~1.74 ± 0.09 μm. 2.3Bi_2S_3-VONs(nat)/FTO@pH3 displayed consistent morphology across the three batches of nanorods synthesis (Fig. 7.2). The influence of pH and precursor amount on the morphology of Bi_2S_3 nanostructures has been documented in prior studies as well (Chowdhury et al., 2023; Ma et al., 2011; Xing et al., 2012).

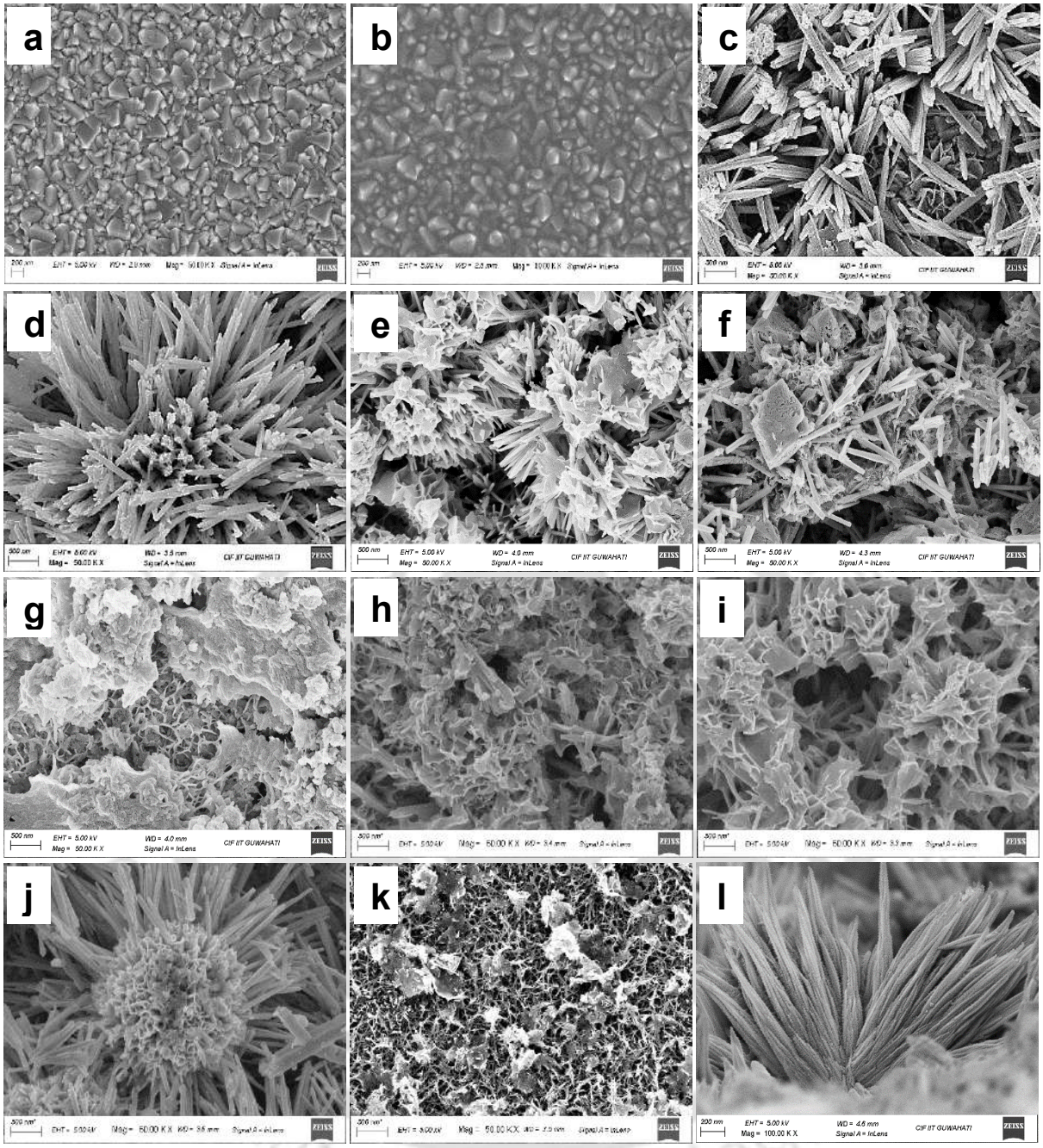

Figure 7.1: FESEM images (top view) of (a) FTO(bare), (b) Bi_2S_3@seed/FTO, (c) 2.3Bi_2S_3-VONs(nat)/FTO@pH2, (d) 2.3Bi_2S_3-VONs(nat)/FTO@pH3, (e) 2.3Bi_2S_3-VONs(nat)/FTO@pH4, (f) 2.3Bi_2S_3-VONs(nat)/FTO@pH5, (g) 1.0Bi_2S_3-VONs(nat)/FTO@pH3, (h) 1.5Bi_2S_3-VONs(nat)/FTO@pH3, (i) 2.0Bi_2S_3-VONs(nat)/FTO@pH3, (j) 2.5Bi_2S_3-VONs(nat)/FTO@pH3, (k) 2.3Bi_2S_3-H_2O(control)/FTO@pH3, and (l) cross-sectional view of 2.3Bi_2S_3-VONs(nat)/FTO@pH3.

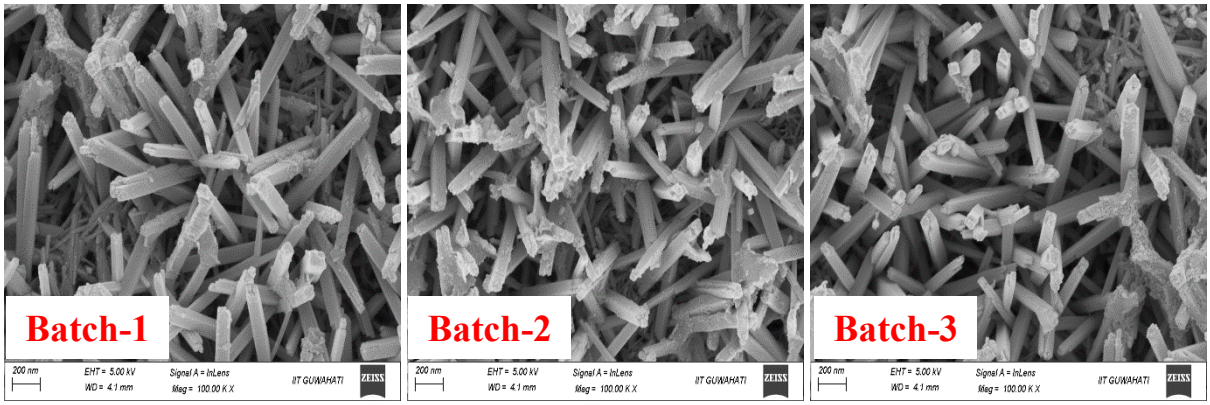

Figure 7.2: Reproducibility of 2.3Bi_2S_3-VONs(nat)/FTO@pH3 formation in three different batches under identical synthesis conditions.

7.2.1.2 *XRD analysis*

Fig. 7.3 represents the XRD patterns of FTO(bare), Bi_2S_3@seed/FTO, 2.3Bi_2S_3-VONs(nat)/FTO@pH2, 2.3Bi_2S_3-VONs(nat)/FTO@pH3, 2.3Bi_2S_3-VONs(nat)/FTO@pH4, 2.3Bi_2S_3-VONs(nat)/FTO@pH5, 1.0Bi_2S_3-VONs(nat)/FTO@pH3, 1.5Bi_2S_3-VONs(nat)/FTO@pH3, 2.0Bi_2S_3-VONs(nat)/FTO@pH3, 2.5Bi_2S_3-VONs(nat)/FTO@pH3, and 2.3Bi_2S_3-H_2O(control)/FTO@pH3. The peak positions at 2θ=27.19(220), 34.40(002), 38.42(200), 52.16(102), 55.16(110), 62.15(103), 66.11°(200), and 78.75°(202) illustrate different phases of FTO(bare) (JCPDS, file No. 00-001-0657 and 01-083-7977). No new peaks were observed after seed layer coating of Bi_2S_3 precursors on FTO due to deficient concentration. Additionally, peaks at 2θ=23.07(220), 25.55(111), 29.23(211), 32.35(221), 33.53(212), 36.16(231), 46.03(205), and 53.16°(222) in 2.3Bi_2S_3-VONs(nat)/FTO@pH3 representing Bi_2S_3 nanostructures, indicating its formation in 2.3Bi_2S_3-VONs(nat)/FTO@pH3 (JCPDS, file No. 01-074-9443 and 01-089-8963). After the formation of VONs of Bi_2S_3, FTO peaks were shifted and dissolved due to merging with Bi_2S_3 peaks and covering the FTO surface. However, all these peaks were slightly shifted from 0.001 to 0.130° corresponding to FTO(bare) at 2θ=52.16°(102), as displayed in Fig. 7.4. The XRD pattern of 2.3Bi_2S_3-VONs(nat)/FTO@pH3 showed Bi_2S_3 peaks with a uniform intensity than that of synthesized at other pH and precursor amounts, which is also supported by FESEM analysis (Chowdhury et al., 2023).

The lattice parameters such as crystallite size (nm), lattice strain (ε), and dislocation densities (Lines/nm^2) were premeditated to analyze the effect of pH and precursor amount on lattice structure after the formation of Bi_2S_3 nanostructures. These parameters were calculated

at 2θ=25.08° using the following relations (Eqs. 7.1-7.3) (Ravi et al., 2025; Ravi and Golder, 2025b).

$$d = \frac{k\lambda}{\beta\cos\theta_B} \quad (7.1)$$

$$\varepsilon = \frac{\beta}{4\mathrm{Tan}\theta_B} \quad (7.2)$$

$$\delta = \frac{1}{d^2} \quad (7.3)$$

Where d, k, λ, ε, θ_B, β, and δ are the crystallite size (nm), 0.94 nm, 0.154 nm, lattice strain, Bragg angle, FWHM of diffraction peak, and dislocation density (lines/nm^2), respectively.

The crystallite size (d) of Bi_2S_3 VONs was determined using Eq. 7.1, and the calculated parameters are presented in Table 7.1. 2.3Bi_2S_3-VONs(nat)/FTO@pH3 exhibited less crystallite size and higher lattice strain and dislocation density than Bi_2S_3 synthesized at different experimental condition. Additionally, higher lattice strain and dislocation density of 2.3Bi_2S_3-VONs(nat)/FTO@pH3 indicate more lattice defects in Bi_2S_3 nanostructures (Bhan and Golder, 2024). A slight variation in d-spacing values was observed, revealing different orientations of lattice structures at different pH levels (Bhan and Kumar Golder, 2023).

Table 7.1: XRD diffraction parameters of FTO(bare), Bi_2S_3@seed/FTO, (1.0-2.5)Bi_2S_3-VONs(nat)/FTO@pH(2-5), and 2.3Bi_2S_3-H_2O(control)/FTO@pH3.

Sample code	Crystallite size (nm)	d-spacing (nm)	Lattice strain (ε)	Dislocation densities (Lines/nm^2)
FTO(bare)	57.03	0.1756	1.45 ×10^{-3}	3.07 ×10^{-4}
Bi_2S_3@seed/FTO	56.98	0.1753	1.45 ×10^{-3}	3.08 ×10^{-4}
2.3Bi_2S_3-VONs(nat)/FTO@pH2	55.03	0.1756	1.50 ×10^{-3}	3.30 ×10^{-4}
2.3Bi_2S_3-VONs(nat)/FTO@pH3	51.15	0.1755	1.61 ×10^{-3}	3.82 ×10^{-4}
2.3Bi_2S_3-VONs(nat)/FTO@pH4	55.66	0.1756	1.48 ×10^{-3}	3.23 ×10^{-4}
2.3Bi_2S_3-VONs(nat)/FTO@pH5	53.02	0.1753	1.55 ×10^{-3}	3.56 ×10^{-4}
1.0Bi_2S_3-VONs(nat)/FTO@pH3	52.82	0.1756	1.56 ×10^{-3}	3.58 ×10^{-4}
1.5Bi_2S_3-VONs(nat)/FTO@pH3	57.62	0.1753	1.43 ×10^{-3}	3.01 ×10^{-4}
2.0Bi_2S_3-VONs(nat)/FTO@pH3	57.59	0.1752	1.43 ×10^{-3}	3.01 ×10^{-4}
2.5Bi_2S_3-VONs(nat)/FTO@pH3	57.41	0.1753	1.44 ×10^{-3}	3.03 ×10^{-4}
2.3Bi_2S_3-H_2O(control)/FTO@pH3	57.14	0.1756	1.44 ×10^{-3}	3.06 ×10^{-4}

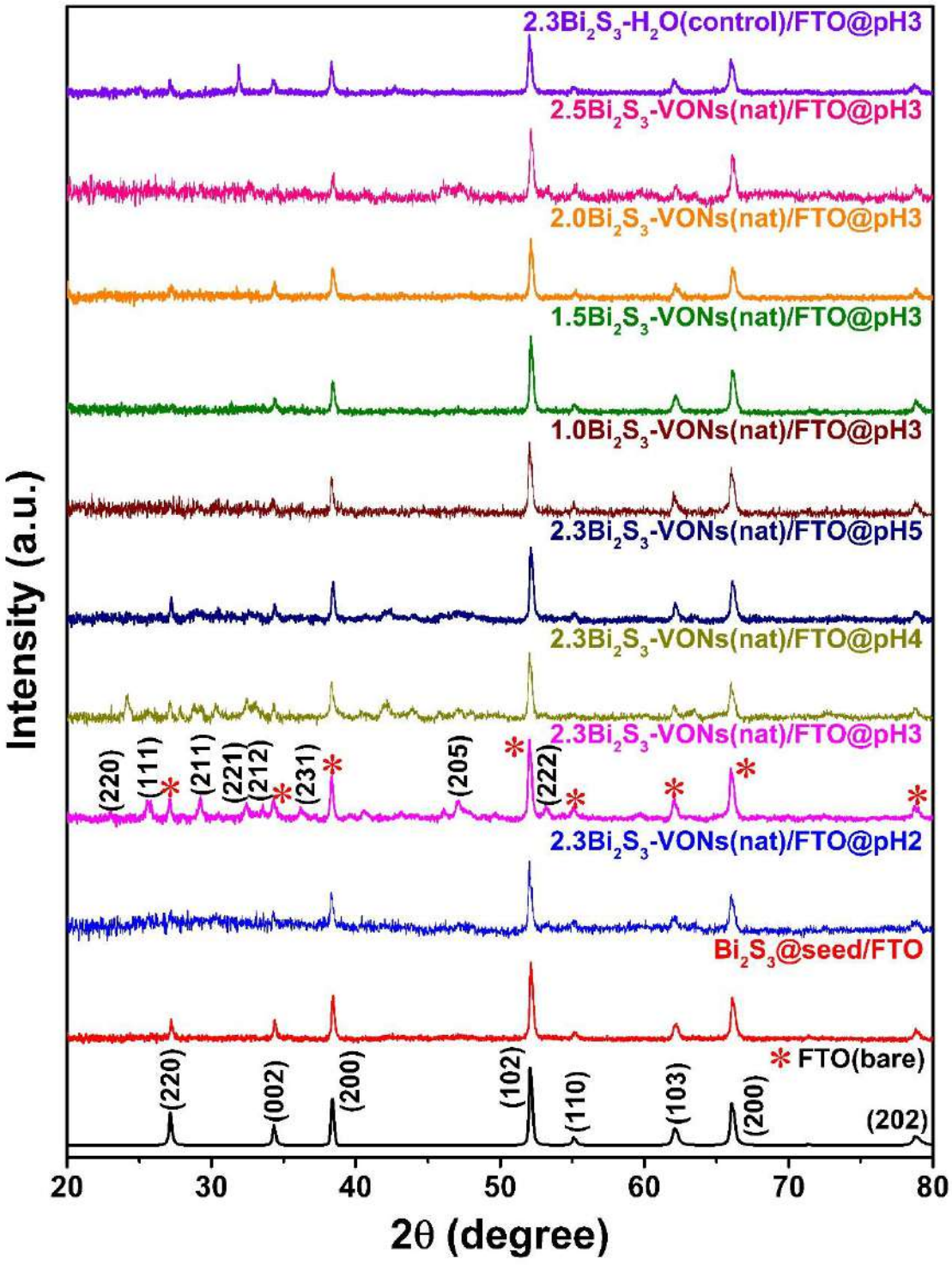

Figure 7.3: XRD patterns of FTO(bare), Bi_2S_3@seed/FTO, 2.3Bi_2S_3-VONs(nat)/FTO@pH2, 2.3Bi_2S_3-VONs(nat)/FTO@pH3, 2.3Bi_2S_3-VONs(nat)/FTO@pH4, 2.3Bi_2S_3-VONs(nat)/FTO@pH5, 1.0Bi_2S_3-VONs(nat)/FTO@pH3, 1.5Bi_2S_3-VONs(nat)/FTO@pH3, 2.0Bi_2S_3-VONs(nat)/FTO@pH3, 2.5Bi_2S_3-VONs(nat)/FTO@pH3, and 2.3Bi_2S_3-H_2O(control)/FTO@pH3.

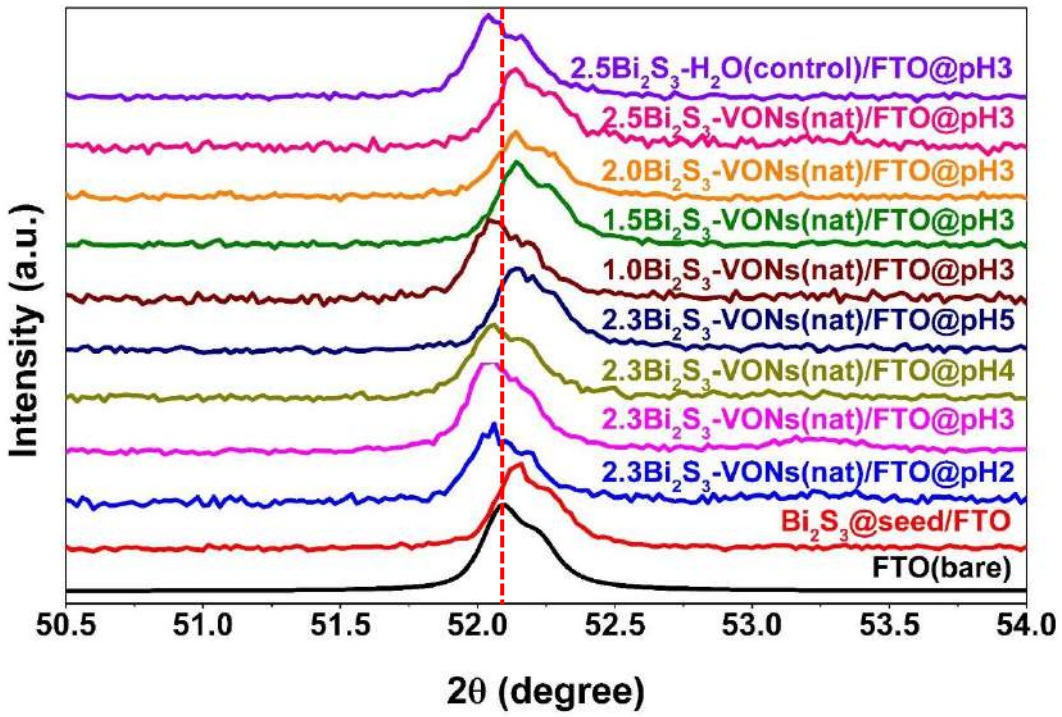

Figure 7.4: A slight peak shifting in XRD patterns of all Bi_2S_3 modified FTOs at 2θ = 52.16° (102), corresponding to FTO(bare).

7.2.1.3 *Raman analysis*

Fig. 7.5a presents the Raman spectra of FTO(bare), Bi_2S_3@seed/FTO, 2.3Bi_2S_3-VONs(nat)/FTO@pH3, and 2.3Bi_2S_3-H_2O(control)/FTO@pH3. In FTO(bare), two prominent peaks appear at ~558.4 and ~1091.7 cm^{-1}, corresponding to the stretching vibrations of Sn-O and O-Sn-O bonds, respectively, associated with the SiO_2 layer (Hvojnik et al., 2021). For Bi_2S_3@seed/FTO, characteristic peaks at 73.7 and 94.8 cm^{-1} were attributed to the B_{1g} and A_g vibrational modes of Bi_2S_3, respectively, along with an additional A_g mode observed at 46.1 cm^{-1}. The 2.3Bi_2S_3-VONs(nat)/FTO@pH3 exhibits two intense peaks at 236.8 cm^{-1} (A_g mode) and 260.7 cm^{-1} (B_{1g} mode), which are also detected in the seed-layered and control samples, albeit with significantly lower intensities (Koh et al., 2003; Zhao et al., 2011). The absence of FTO peaks in the Bi_2S_3 modified FTO samples indicates complete surface coverage by the Bi_2S_3 VONs. In contrast, the control sample shows additional peaks beyond 550 cm^{-1} attributable to FTO, suggesting non-uniform Bi_2S_3 growth in the absence of the bio-extract. The presence of both A_g and B_{1g} modes confirms the existence of symmetric and antisymmetric geometry within the Bi_2S_3 crystal structure. Furthermore, Bi_2S_3 modified FTO samples synthesized under varying pH conditions (2.3Bi_2S_3-VONs(nat)/FTO@pH2-5) exhibit nearly identical Raman attributes (Fig. 7.5b), indicating consistent nanostructure formation. Similarly,

Bi_2S_3 growth on FTO using varying precursor concentrations (1.0-2.5Bi_2S_3-VONs(nat)/FTO@pH3) display comparable spectral profiles (Fig. 7.5c).

7.2.1.4 *FTIR analysis*

The FTIR spectra of FTO(bare), Bi_2S_3@seed/FTO, 2.3Bi_2S_3-VONs(nat)/FTO@pH2, 2.3Bi_2S_3-VONs(nat)/FTO@pH3, 2.3Bi_2S_3-VONs(nat)/FTO@pH4, 2.3Bi_2S_3-VONs(nat)/FTO@pH5, 1.0Bi_2S_3-VONs(nat)/FTO@pH3, 1.5Bi_2S_3-VONs(nat)/FTO@pH3, 2.0Bi_2S_3-VONs(nat)/FTO@pH3, 2.5Bi_2S_3-VONs(nat)/FTO@pH3, and 2.3Bi_2S_3-H_2O(control)/FTO@pH3, are presented in Figs. 7.5d-7.5f. In FTO(bare), the peaks observed around 597 and 743 cm^{-1} correspond to the Sn-O and Sn-O-Sn vibrations of SnO_2, respectively (Fig. 7.5d) (Bhan and Golder, 2024). In all the Bi_2S_3 modified FTO, the Sn-O and Sn-O-Sn peaks disappeared due to the growth of Bi_2S_3 VONs on the FTO surface. The peak around 1615 cm^{-1}, attributed to the C=O bending modes, could be due to the surface-adsorbed CO_2 or precursors used during the synthesis of Bi_2S_3 VONs on FTO. The peak at approximately 1280 cm^{-1} is associated with C-O stretching vibration (Arumugam et al., 2017). Notably, the distinct peaks at around 554 and 1025 cm^{-1} are attributed to the stretching vibrations of Bi-S bonds, confirming the formation of Bi_2S_3 VONs (Figs. 7.5d-7.5f) (Dawi et al., 2023). Additionally, the shift in the Bi-S bond could be due to the variations in the crystallinity of Bi_2S_3 VONs synthesized under different conditions.

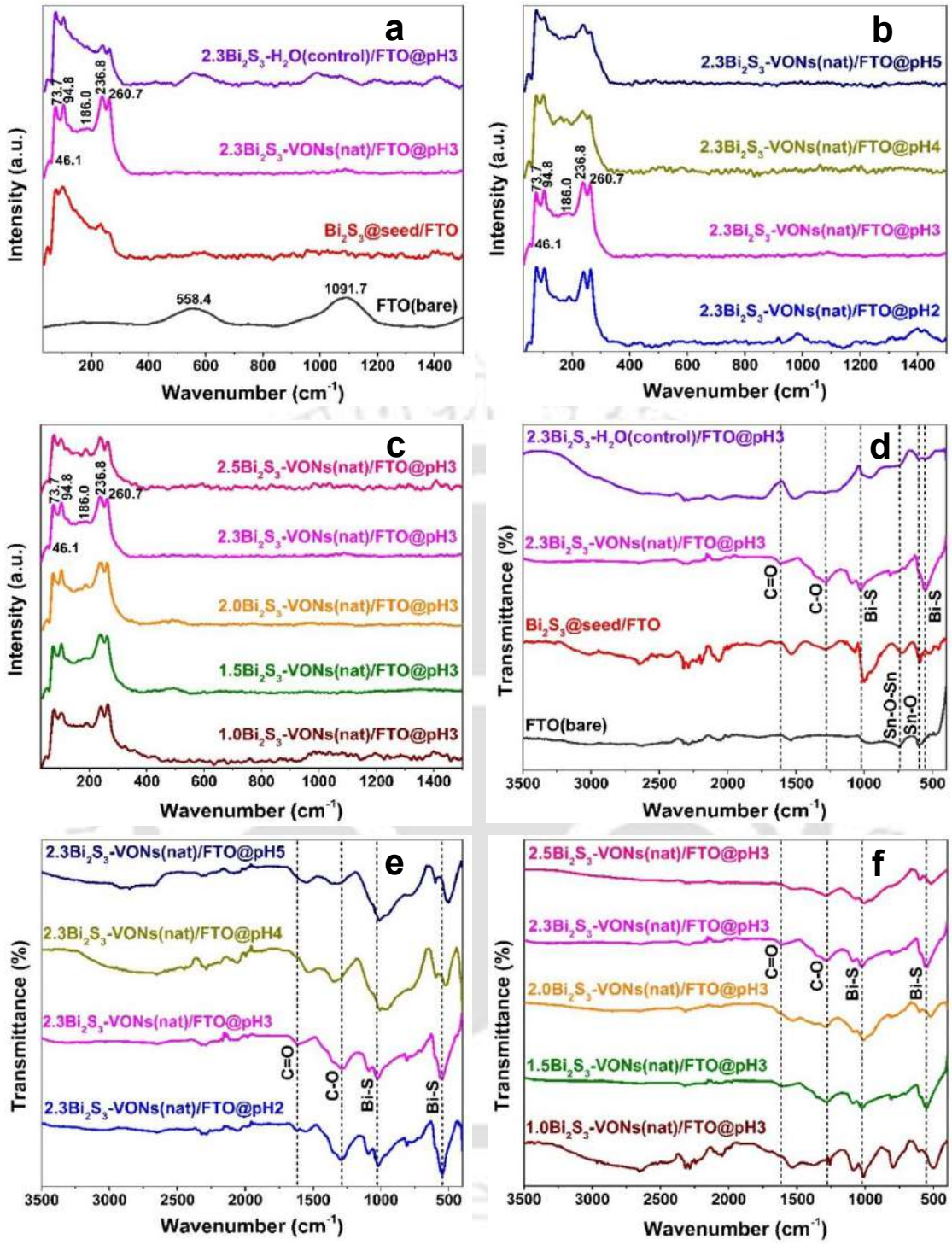

Figure 7.5: (a-c) Raman spectra and (d-f) FTIR spectra of FTO(bare), Bi_2S_3@seed/FTO, 2.3Bi_2S_3-VONs(nat)/FTO@pH2, 2.3Bi_2S_3-VONs(nat)/FTO@pH3, 2.3Bi_2S_3-VONs(nat)/FTO@pH4, 2.3Bi_2S_3-VONs(nat)/FTO@pH5, 1.0Bi_2S_3-VONs(nat)/FTO@pH3, 1.5Bi_2S_3-VONs(nat)/FTO@pH3, 2.0Bi_2S_3-VONs(nat)/FTO@pH3, 2.5Bi_2S_3-VONs(nat)/FTO@pH3, and 2.3Bi_2S_3-H_2O(control)/FTO@pH3.

7.2.1.5 *AFM analysis*

AFM analysis was performed in the scan area of 5 × 5 μm^2 (Figs. 7.7a-7.7d). FTO(bare) (Fig. 7.7a), Bi_2S_3@seed/FTO (Fig. 7.7b), 2.3Bi_2S_3-VONs(nat)/FTO@pH3 (Fig. 7.7c), and 2.3Bi_2S_3-H_2O(control)/FTO@pH3 (Fig. 7.7d) demonstrate the root-mean-square (RMS) value of 32.52, 19.36, 100.1, and 30.09 nm, respectively. The RMS value of 2.3Bi_2S_3-VONs(nat)/FTO@pH3 is about 3.1-, 5.2-, and 3.3-fold higher compared to FTO(bare), Bi_2S_3@seed/FTO, and 2.3Bi_2S_3-H_2O(control)/FTO@pH3, respectively. Additionally, 2.3Bi_2S_3-VONs(nat)/FTO@pH3 showed uniform growth of nanostructures in comparison to 2.3Bi_2S_3-H_2O(control)/FTO@pH3. Therefore, the higher surface roughness of the kinetic electrode could provide maximum nucleation and adsorption sites for the targeted analytes, which could enhance the performance of electrochemical sensors (Bhan and Kumar Golder, 2023).

7.2.1.6 *FETEM analysis*

FETEM analysis of 2.3Bi_2S_3-VONs(nat)/FTO@pH3 was performed by disintegrating the Bi_2S_3 VONs onto the FTO glass surface. This was achieved using an ultrasonic bath, where the fabricated electrode was immersed in ethanol for 1 h to facilitate detachment of the Bi_2S_3 nanorods onto the FTO glass surface (Bhan and Kumar Golder, 2023). Figs. 7.7e, 7.7f, and 7.7g show the FETEM micrograph, HRTEM image, and SAED pattern, respectively. The FETEM micrograph revealed the rod-shaped morphology of Bi_2S_3 nanoparticles with an average length of 502.63 nm (horizontally placed in Fig. 7.7e), which aligns with the FESEM analysis. The average length of Bi_2S_3 nanorods in FETEM analysis could differ from FESEM analysis due to the crumbling of nanorods during its peeling from the FTO glass surface. The d-spacing value of 2.3Bi_2S_3-VONs(nat)/FTO@pH3 was found to be 0.176 nm, corresponding to the (111) phase of Bi_2S_3 (Fig. 7.7f). SAED pattern revealed the polycrystalline nature of Bi_2S_3 nanorods, which is in line with the XRD analysis (Fig. 7.7g) (Chowdhury et al., 2023).

7.2.1.7 *EDX analysis*

The weight percentage (w/w %) of the elements with image mapping of FTO(bare) and 2.3Bi_2S_3-VONs(nat)/FTO@pH3 was performed via EDX (Fig. 7.6). The w/w % was determined by omitting the peaks of Au (~2.0 keV) ascribed to Au coating before analysis. The w/w % of Sn, O, and F in FTO(bare) were 71.7, 28.0, and 0.3 %, respectively (Fig. 7.6a). In 2.3Bi_2S_3-VONs(nat)/FTO@pH3, Sn, O, F, Bi, and S were found to be 3.4, 1.4,0.1, 76.7, and 18.4 %, respectively (Fig. 7.6b). The image mapping of elements highlighted the uniform

distribution of all the elements in the FTO(bare) and 2.3Bi_2S_3-VONs(nat)/FTO@pH3 (Figs. 7.6c and 7.6d). It indicates that Bi_2S_3 VONs were synthesized without impurities.

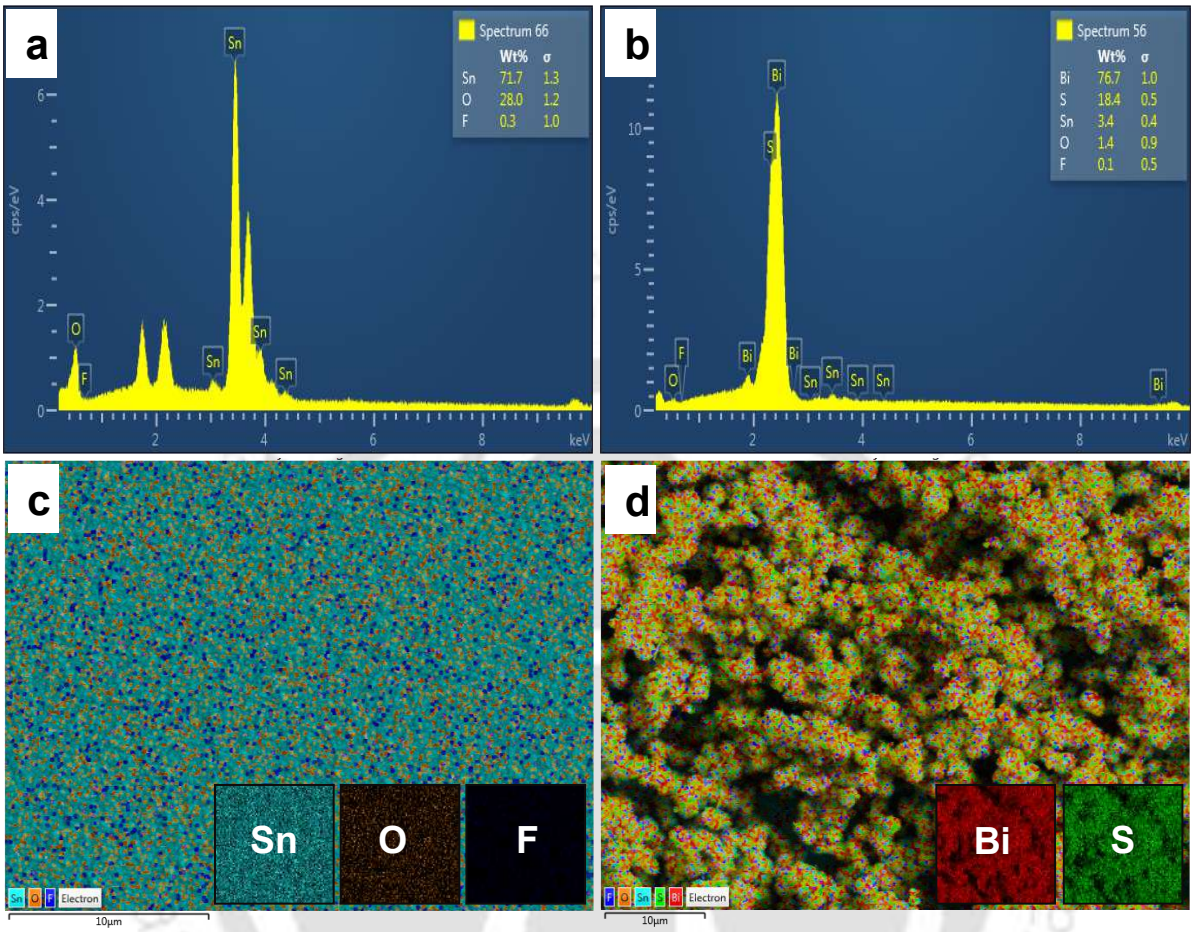

Figure 7.6: EDX elemental spectrum of (a) FTO(bare), (b) 2.3Bi_2S_3-VONs(nat)/FTO@pH3; and EDX image mapping of (c) FTO(bare), and (d) 2.3Bi_2S_3-VONs(nat)/FTO@pH3.

7.2.1.8 *XPS analysis*

Fig. 7.7h displays the XPS survey spectrum of 2.3Bi_2S_3-VONs(nat)/FTO@pH3, indicating the presence of Bi, S, Sn, O, and C. The existence of C and O can be ascribed to the adsorption of atmospheric gases (CO_2 and O_2) on the surface of Bi_2S_3 VONs and the reaction precursors, including $C_4H_{11}NO_2$ (used for seed layer coating), $Bi(NO_3)_3{\cdot}5H_2O$ (Bi source), and CH_4N_2S (S source). Additionally, the presence of Sn is due to the FTO glass substrate. The high-resolution spectrum of Bi_2S_3 VONs in Bi 4f and S 2p region was studied to examine the chemical state of Bi_2S_3 (Fig. 7.7i). The Bi 4f spectrum of Bi_2S_3 VONs displays two prominent peaks at 163.94 and 158.82 eV, ascribed to the spin-orbital splitting of Bi $4f_{5/2}$ and $4f_{7/2}$, respectively, and are indicative of the Bi^{3+} oxidation state in Bi_2S_3 (Chowdhury et al., 2023).

Moreover, two additional peaks in the Bi 4f region at 164.32 and 159.07 eV were attributed to bismuth oxide, which could be due to the calcination of seed layer coated FTO at 400 °C before the growth of VONs of Bi_2S_3 (Moyseowicz, 2019). The peaks observed at 162.32 and 160.57 eV are attributed to the divalent of the S 2p region, representing the spin states of S $2p_{1/2}$ and S $2p_{3/2}$, respectively. The doublet signal of S 2p indicates that sulfur is predominantly in the S^{2-} valence state of Bi_2S_3 (Vattikuti et al., 2019).

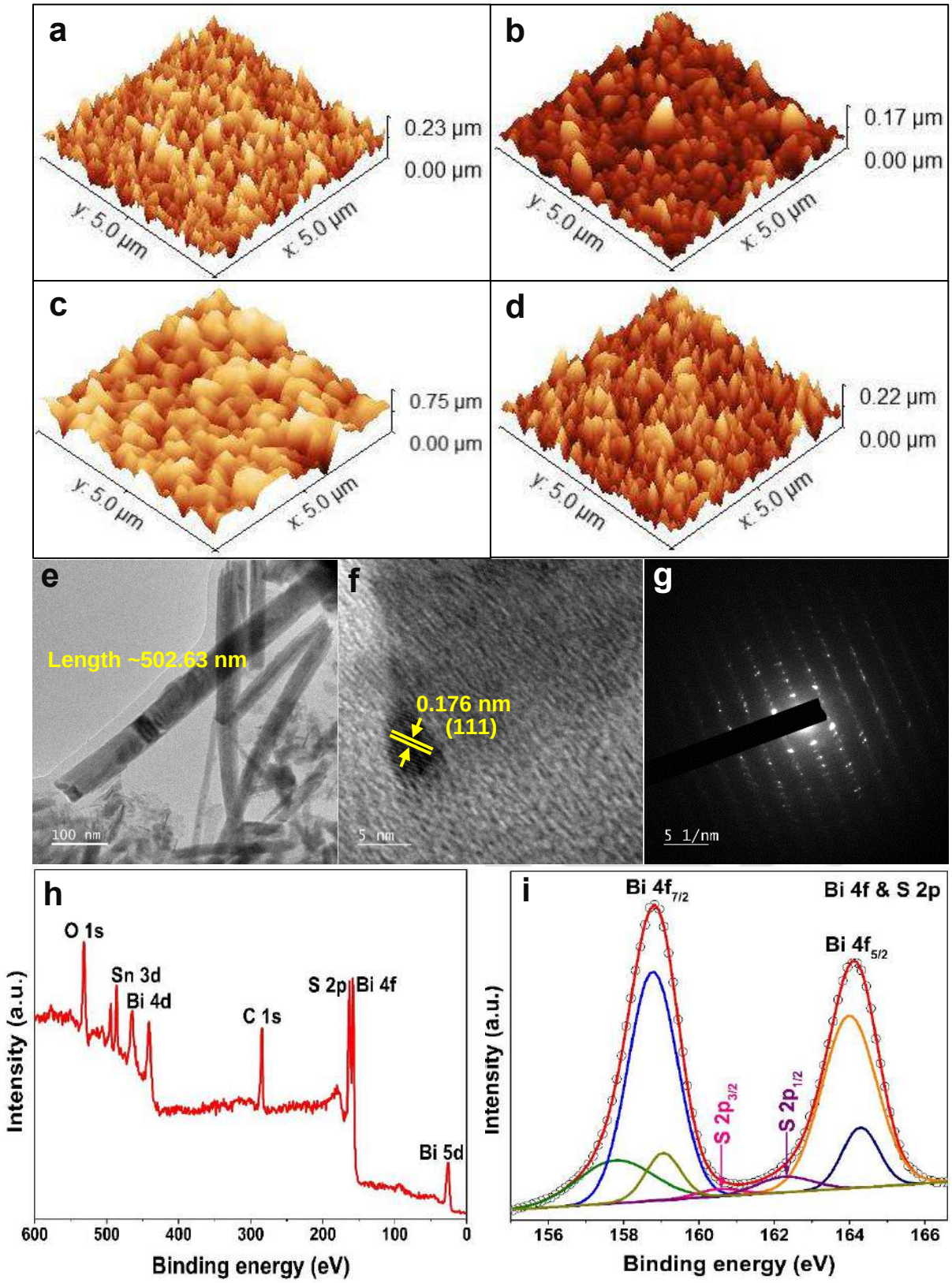

Figure 7.7: AFM micrographs of (a) FTO(bare), (b) Bi_2S_3@seed/FTO, (c) 2.3Bi_2S_3-VONs(nat)/FTO@pH3, and (d) 2.3Bi_2S_3-H_2O(control)/FTO@pH3 in a 5×5 μm^2 scan area. TEM analysis of 2.3Bi_2S_3-VONs(nat)/FTO@pH3, including (e) FETEM micrograph, (f) HRTEM micrograph, and (g) SAED pattern (nanorods of Bi_2S_3 were delaminated from the

FTO glass surface using an ultrasonic bath in ethanol for 1 h). XPS analysis of 2.3Bi_2S_3-VONs(nat)/FTO@pH3, showing (h) Survey spectra and (i) High-resolution spectrum for Bi 4f and S 2p.

7.2.2. Growth mechanism of Bi_2S_3-VONs(nat)/FTO

The proposed mechanism for the development of Bi_2S_3 nanostructures in the absence and presence of *Sechium edule* extract is described through the following reaction pathways (Eqs. 7.4-7.9). The anisotropic fabrication of nanostructures is promoted via the internal dipole moment that aligns with the prime axis of the crystal lattice. The polar and anisotropic characteristics of the Bi_2S_3 crystal facilitate the development of nanoparticles along a specific crystallographic (0001) plan, being the most prominent polar surface due to the positively charged Bi^{3+} ions and oppositely charged S^{2-} ions (Bhan and Kumar Golder, 2023). In the absence of bio-extract, $Bi(NO_3)_3{\cdot}5H_2O$ dissociates into Bi^{3+} and NO_3^- ions in aqueous solution, as shown in Eq. 7.4. Simultaneously, CH_4N_2S decomposes into CO_2, NH_3, and H_2S in acidic solutions (Eqs. 7.5-7.7), and H_2S readily ionizes to H^+ and S^{2-} ions (Eq. 7.8). Finally, Bi^{3+} ions react with S^{2-} ions to form Bi_2S_3 nanostructures (Eq. 7.9) (Ramos Reynoso et al., 2018). In the presence of *Sechium edule* extract, the hydrogen of the -OH group in AA from bio-extract binds with the unsaturated sulfur of Bi_2S_3 (Chowdhury et al., 2023). Additionally, the deposition of the oxidized form of AA (dehydro-AA, acting as a capping agent) onto non-polar crystal faces, specifically $(0\bar{1}10)$, $(1\bar{1}00)$, $(10\bar{1}0)$, $(\bar{1}100)$, $(1\bar{1}00)$, and $(01\bar{1}0)$, restricting the lateral growth of Bi_2S_3 nanostructures in these directions and encouraging the nanostructures to grow preferentially along the (0001) and $(000\bar{1})$ directions (Fig. 7.8) (Bhan and Golder, 2024; Bhan and Kumar Golder, 2023). However, the development of Bi_2S_3 nanorods is hindered in $(000\bar{1})$ direction due to the surface of FTO(bare). Therefore, the Bi_2S_3 nanorods grow predominantly in the (0001) direction, resulting in 1D surface Bi_2S_3 nanorods oriented in vertical configuration.

$$Bi(NO_3)_3 \cdot 5H_2O \rightarrow Bi^{3+} + 3NO_3^- + 5H_2O \quad (7.4)$$

$$CH_4N_2S \leftrightarrow CH_2N_2 + H_2S \quad (7.5)$$

$$CH_2N_2 + H_2O \leftrightarrow CO_2 + NH_3 \quad (7.6)$$

$$CH_4N_2S + 2H_2O \rightarrow 2NH_3 + H_2S + CO_2 \quad (7.7)$$

$$H_2S \rightarrow 2H^+ + S^{2-} \quad (7.8)$$

$$2Bi^{3+} + 3S^{2-} \rightarrow 2Bi_2S_3 \quad (7.9)$$

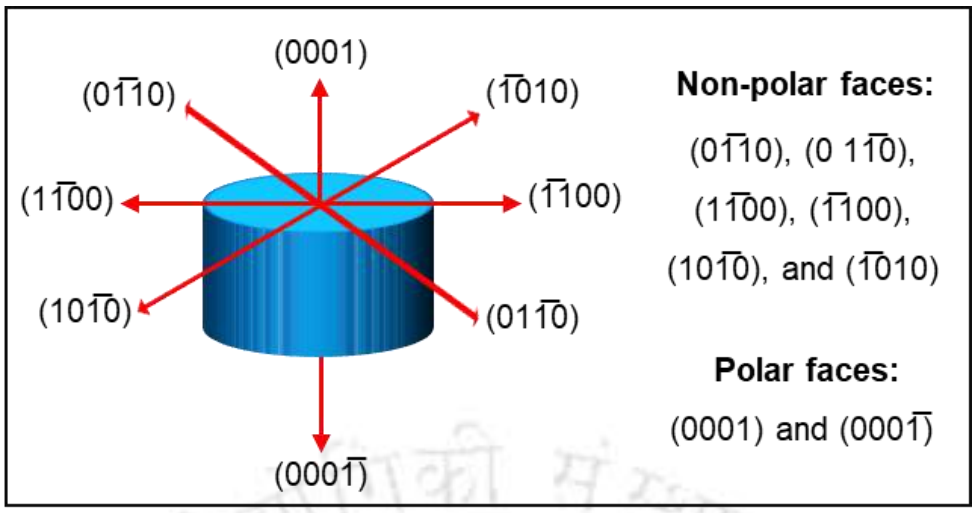

Figure 7.8: Pictorial view of Bi_2S_3VONs with the polar and non-polar faces.

7.2.3. Electrochemical studies of FTO(bare) and 2.3Bi_2S_3-VONs(nat)/FTO@pH3

7.2.3.1 *EIS analysis*

To investigate the electron transport resistance of FTO(bare) and 2.3Bi_2S_3-VONs(nat)/FTO@pH3, EIS analysis was performed using a standard analyte (1 mM $Ru(NH_3)_6Cl_2$) in 0.1 M KCl as the electrolyte within a frequency range of 10^{-2}-10^5 Hz at 25 °C. Fig. 7.9a displays the EIS spectra of the kinetic electrodes, along with the corresponding Randles equivalent circuit (inset), with key electro-kinetic parameters such as charge transfer resistance (R_p), constant phase elements (CPE), and electrolyte resistance (R_s) (Bhan et al., 2025). The diameter of the semicircle in the Nyquist plot directly correlates with R_p, where a large diameter of a semicircle indicates a high R_p (Kumar and Das, 2023). The R_p value of FTO(bare) was found to be 953 kΩ. It significantly decreased to 103 kΩ in the case of 2.3Bi_2S_3-VONs(nat)/FTO@pH3 (Kunpatee et al., 2022). The value of R_s for FTO(bare) and 2.3Bi_2S_3-VONs(nat)/FTO@pH3 were found to be 0.082 and 0.077 kΩ, respectively. The slight fluctuation in R_s value may be ascribed to the minor changes in electrode spacing during different sets of experimentation. However, the change in R_s is insignificant compared to R_p (Kumar and Das, 2024). Furthermore, the changes in CPE values could be due to the variations in the conductivity of kinetic electrodes (Bhan and Golder, 2024). Table 7.2 summarises the EIS parameters of FTO(bare) and 2.3Bi_2S_3-VONs(nat)/FTO@pH3. It implies significant improvements in conductivity due to the formation of Bi_2S_3 VONs on the surface of the FTO(bare).

Table 7.2: Nyquist's plot fitting parameters for FTO(bare) and 2.3Bi_2S_3-VONs(nat)/FTO@pH3.

Working electrode	R_s (kΩ)	R_p (kΩ)	CPE parameters	
			Y_0 (µMho)	n
FTO(bare)	0.082 ± 0.001	953 ± 3.54	22.1 ± 0.10	0.852 ± 0.002
2.3Bi_2S_3-VONs(nat)/FTO@pH3	0.077 ± 0.002	103 ± 0.69	11.0 ± 0.08	0.744 ± 0.001

7.2.3.2 *Electroactive surface area of FTO(bare) and 2.3Bi_2S_3-VONs(nat)/FTO@pH3*

CV was conducted to determine the electrochemical surface area (A_e) of kinetic electrodes, using a standard analyte (1 mM $Ru(NH_3)_6Cl_2$) in 0.1 M KCl electrolyte at various scan speeds (5-500 mV/s) and 25 °C (Figs. 7.9b and 7.9c.) The Randles-Sevcik equation (Eq. 7.10) was employed to calculate A_e (cm^2) for the kinetic electrodes (Stanley et al., 2024).

$$I_{Pa} = (2.69 \times 10^5)n^{3/2}A_eD^{1/2}\upsilon^{1/2}C_0 \quad (7.10)$$

Where I_{pa}, n, D, υ, and C_0 are the anodic peak response (A), number of electrons involved in the redox process (n = 1), diffusion coefficient (8.43×10^{-6} cm^2/s), scan rate (V/s), and concentration of analyte (mol/cm^3), respectively. The plot of I_{pa} vs $\upsilon^{0.5}$ was linear with slopes of 117.57 (R^2 = 0.998) and 331.41 (R^2 = 0.983) µA. $V^{-1/2}.s^{1/2}$ for FTO(bare) and 2.3Bi_2S_3-VONs(nat)/FTO@pH3, respectively (Fig. 7.9d). To determine the A_e of kinetic electrodes, the slope of the linear plots of I_{pa} vs $\upsilon^{0.5}$ was substituted into Eq. 7.10. A_e of FTO(bare) and 2.3Bi_2S_3-VONs(nat)/FTO@pH3 were calculated to be 0.151 and 0.424 cm^2, respectively. The growth of VONs of Bi_2S_3 over FTO glass resulted in a significant increment (64.4%) in A_e compared to FTO(bare), thereby enhancing the number of docking sites for MCZ and improving the sensing performance of the developed electrode (Bhan and Kumar Golder, 2023).

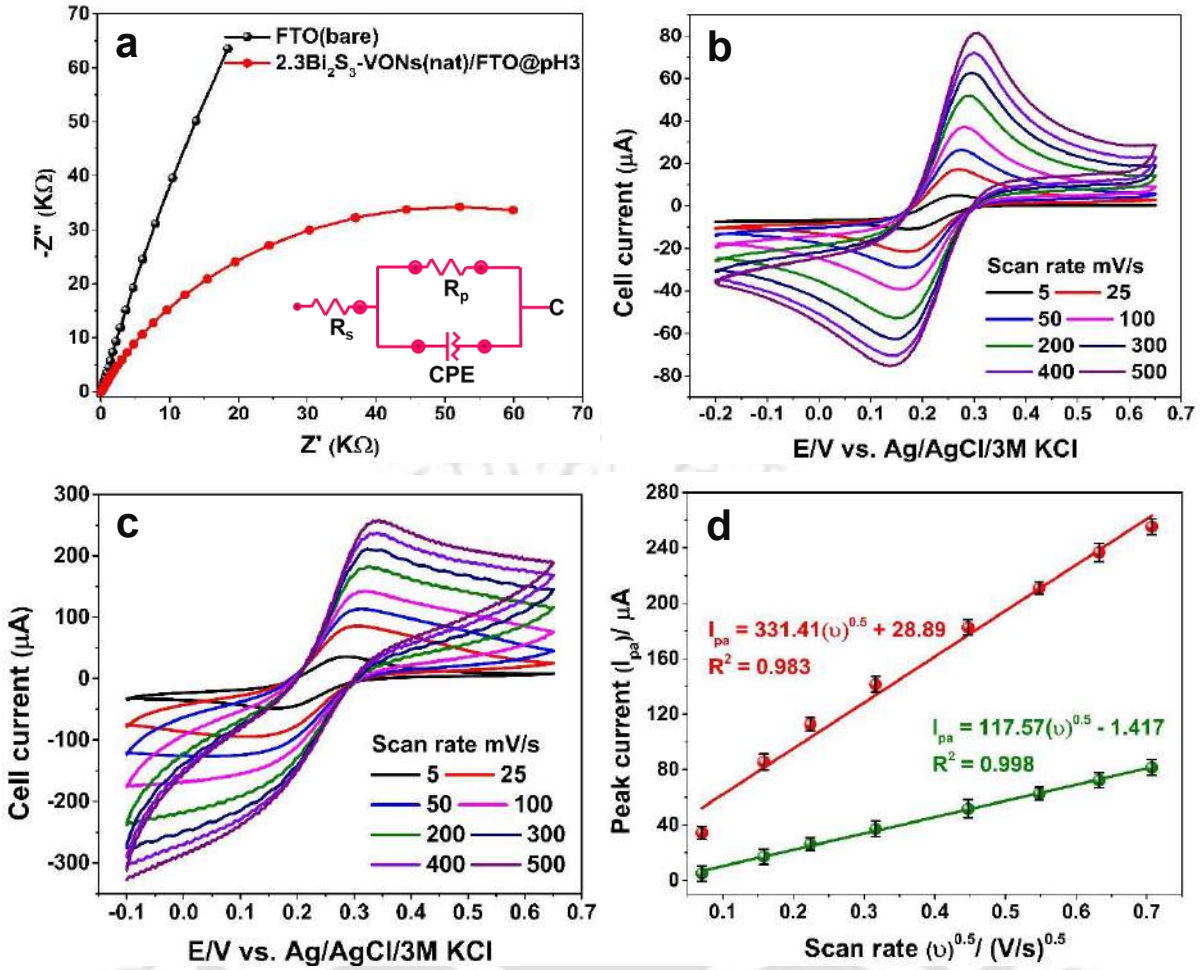

Figure 7.9: (a) EIS analysis for determining the electron transport resistance of FTO(bare) and 2.3Bi_2S_3-VONs(nat)/FTO@pH3 with the Randles equivalent circuit (inset), (b) and (c) CVs of FTO(bare) and 2.3Bi_2S_3-VONs(nat)/FTO@pH3 electrode captured at various scan speeds (5-500 mV/s), and (d) I_{pa} vs. $\upsilon^{0.5}$ for FTO(bare) and 2.3Bi_2S_3-VONs(nat)/FTO@pH3 electrodes.

7.2.4. Optimization of parameters for MCZ detection

7.2.4.1 *Effect of pH*

To examine the effect of pH on electrochemical detection of MCZ, CV was conducted using 2.3Bi_2S_3-VONs(nat)/FTO@pH3 at various pH (3-9) in 0.04 M BR buffer containing 40 µM of MCZ at a scan speed of 50 mV/s and 25 °C (Fig. 7.10a).With the increase in pH from 3 to 8, the anodic peak potential (E_p) of MCZ shifted towards less positive potential, signifying the participation of H^+ in the redox process of MCZ sensing (Malode et al., 2020). At pH 9, no notable peak was observed (Fig. 7.10a). The highest anodic peak current was recorded at pH 7 in 0.04 M BR buffer, suggesting that the electrochemical detection of MCZ is most optimal in a neutral media (Fig. 7.10b). Therefore, 0.04 M BR buffer (pH 7) was utilized for subsequent experiments. The Nernstian equation (Eq. 7.11) was employed to investigate the ratio of

electrons (n) to protons (m) participating in the MCZ detection reaction (Manivannan et al., 2019).

$$\frac{dE_p}{dpH} = -2.303\frac{mRT}{nF} \quad (7.11)$$

Where T, R, and F represent the temperature (K), the gas constant (8.314 J/mol.K), and Faraday's constant (96485 C/mol), respectively. Fig. 7.10c demonstrates the linear relationship between E_p vs pH with a slope of -0.0508 per unit pH and intercept of 1.493 V (R^2 = 0.994). By substituting the slope of -0.0508 per unit pH in Eq. 7.11, the ratio of $\frac{n}{m}$ was found to be 1.16 (~1), indicating that the electrochemical reaction of MCZ sensing involves an equal number of electrons and protons (Bhan et al., 2025). Fig. 7.10d showed the CV of MCZ sensing to compare anodic peak current using FTO(bare) and 2.3Bi_2S_3-VONs(nat)/FTO@pH3 in 0.04 M BR buffer (pH 7, 25 °C) containing 40 µM MCZ, under identical conditions (scan speed of 50 mV/s). 2.3Bi_2S_3-VONs(nat)/FTO@pH3 electrode showed a 68.7% rise in the anodic peak response for MCZ detection in comparison to FTO(bare).

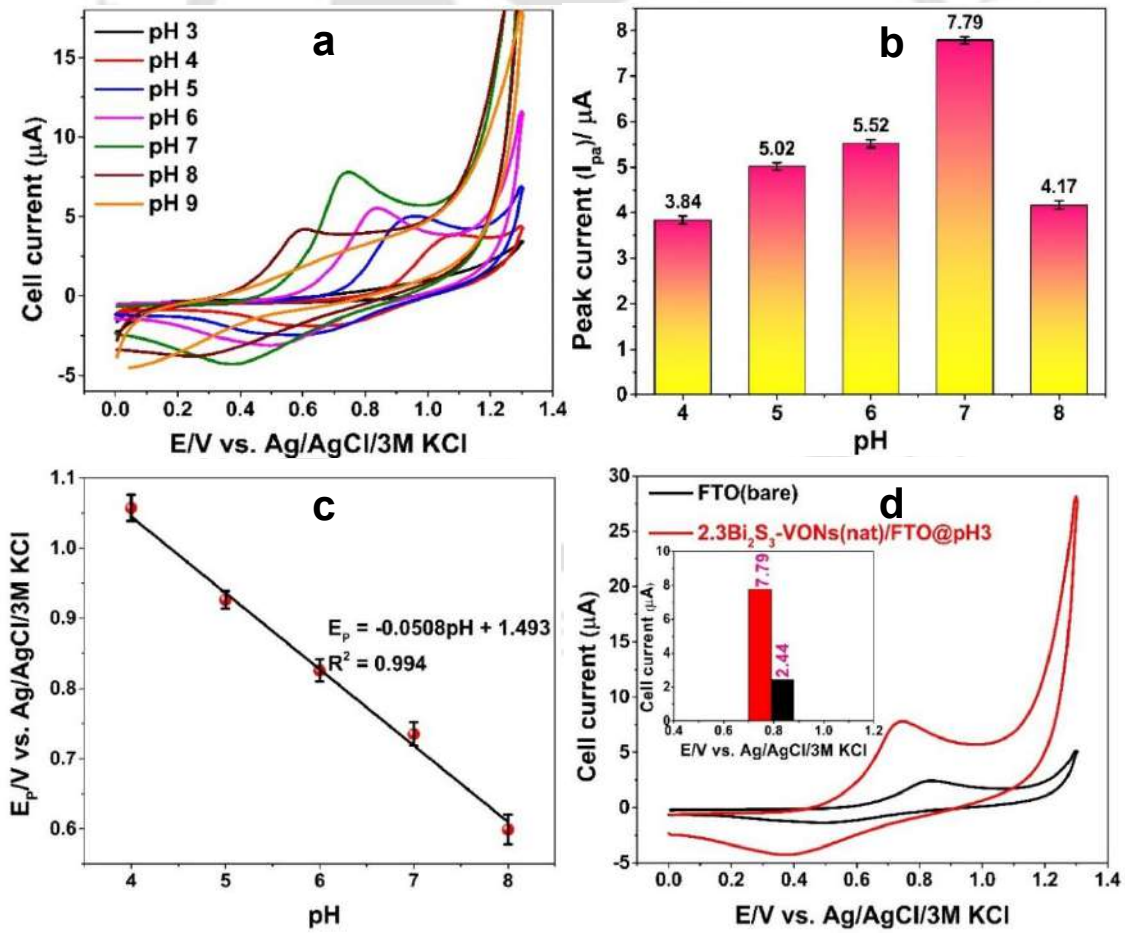

Figure 7.10: (a) CV of MCZ (40 µM) at various pH (3-9) of 0.04 M BR buffer (25 °C) using 2.3Bi_2S_3-VONs(nat)/FTO@pH3 at a scan speed of 50 mV/s, (b) I_{pa} vs. pH, (c) E_p vs. pH, and

(d) CV of MCZ (40 µM) using FTO(bare) and 2.3Bi_2S_3-VONs(nat)/FTO@pH3 electrodes, with the comparison of anodic peak current (inset) in 0.04 M BR buffer (pH 7, 25 °C) at a scan rate of 50 mV/s.

7.2.4.2 *Effect of deposition parameters*

To study the effect of Dpote, Dtime, and Dtemp on the detection of MCZ, SWV was conducted in a 0.04 M BR buffer (pH 7) containing 40 µM of MCZ using a 2.3Bi_2S_3-VONs(nat)/FTO@pH3 electrode (Fig. 7.11). Dpote significantly influences the sensitivity of the kinetic electrode during MCZ sensing, and it was varied from 0 to -0.6 V in 0.04 M BR buffer (pH 7) at Dtime of 60 s and Dtemp of 25 °C (Fig. 7.11a). The anodic peak current of MCZ gradually increased as the Dpote varied from 0 to -0.4 V, likely due to the deposition of MCZ ions over the surface of VONs of Bi_2S_3 (Fig. 7.11b). However, a decrease in the anodic peak current of MCZ sensing was observed from Dpote -0.5 to -0.6 V, which could be attributed to the evolution of H_2 gas at high overpotential (Gumpu et al., 2017). It indicates a strong interaction between MCZ and kinetic electrode, making it difficult for MCZ ions to get desorbed from the surface (Dash et al., 2020). As a result, a Dpote of -0.4 V vs. Ag/AgCl was selected for further experiments.

Figs. 7.11c and 7.11d illustrate the effect of Dtime on the anodic peak current of MCZ at a developed electrode. Dtime considerably impacts the anodic peak current of MCZ sensing at 2.3Bi_2S_3-VONs(nat)/FTO@pH3, and it was varied from 0 to 120 s in a 0.04 M BR buffer (pH 7) at a Dpote of -0.4 V vs. Ag/AgCl and Dtemp of 25 °C (Fig. 7.11c). The anodic peak response increases gradually from Dtime of 0 to 60 s, which could be of MCZ accumulation ions onto the surface of Bi_2S_3 VONs (Bagheri et al., 2013). After 60 s of Dtime, the anodic peak response of MCZ slightly increased, which could be of MCZ ions saturation over the surface or equilibrium among the MCZ ions onto the surface of the electrode and in the supporting electrolyte (Fig. 7.11d). A fewer MCZ ions also could be available for the redox process, as a MCZ concentration was fixed at 40 µM in a 0.04 M BR buffer (pH 7) during the optimization of Dtime (Dash et al., 2020). Therefore, a Dtime of 60 s was selected for further experiments.

Figs. 7.11e and 7.11f demonstrate the influence of Dtemp on the anodic peak response of MCZ detection using 2.3Bi_2S_3-VONs(nat)/FTO@pH3 in a 0.04 M BR buffer (pH 7) at a Dpote of -0.4 V vs. Ag/AgCl and Dtime of 60 s. As the Dtemp increases from 15 to 45 °C, a noticeable increase in the peak current was observed owing to the deposition of MCZ ions on the surface of the fabricated electrode (Fig. 7.11e). Alternatively, higher temperatures promote fast diffusion of MCZ ions from the supporting electrolyte to the electrode surface. After

Dtemp >45 °C, only a slight increase in anodic peak current was noted (Fig. 7.11f). Furthermore, the maximum temperature in field applications is typically around 45 °C. Therefore, the Dtemp of 45 °C was chosen for the subsequent experiments. The effect of deposition parameters on the electrochemical sensing of organic analytes has also been documented in previous studies (Bhan and Golder, 2024; Bhan and Kumar Golder, 2023).

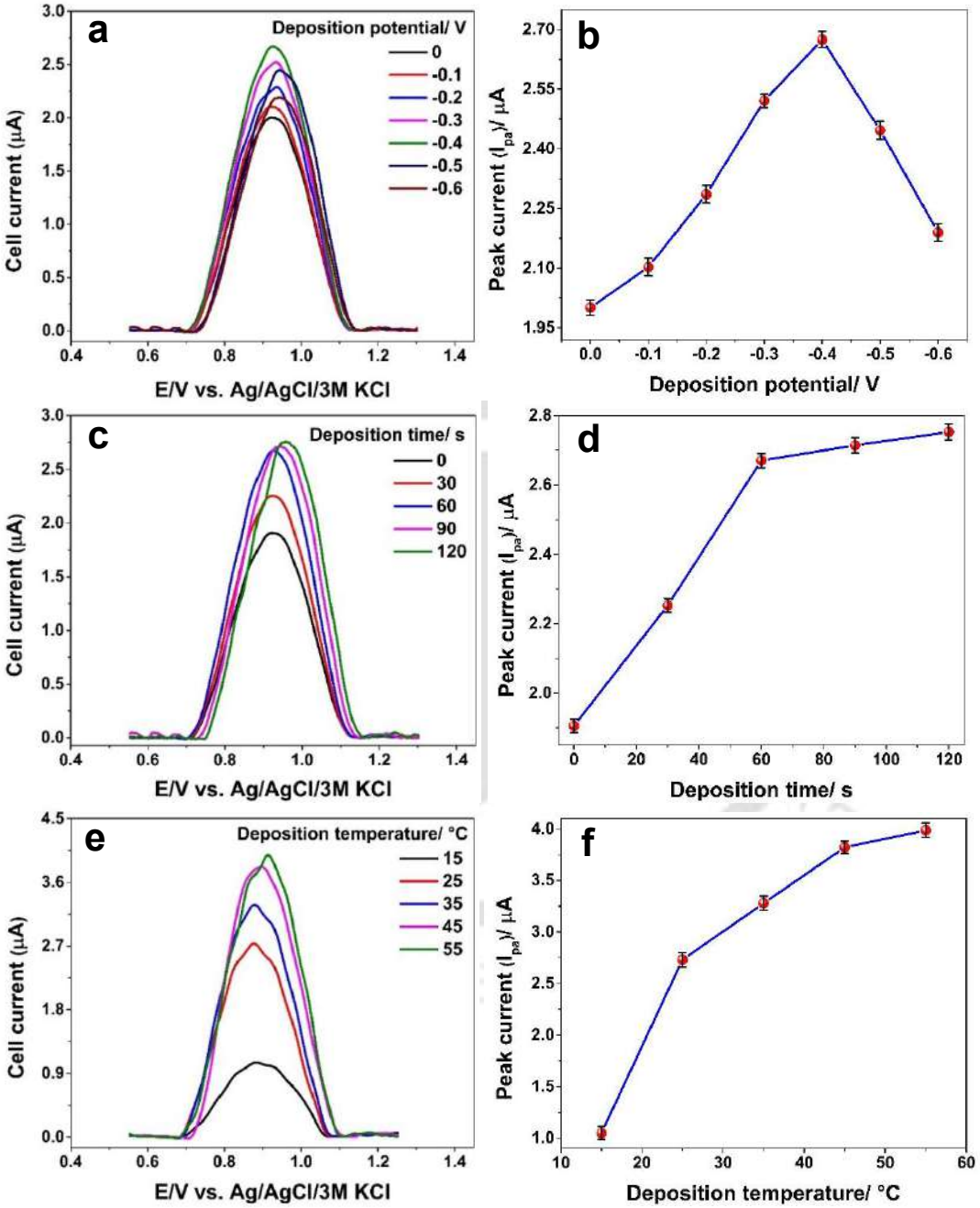

Figure 1.11: (a) SWV of MCZ conducted at different Dpote from 0 to -0.6 V vs. Ag/AgCl, Dtime 60 s, and Dtemp 25 °C, (b) Dpote vs. Anodic peak current (I_{pa}), (c) SWV of MCZ recorded at different Dtime from 0 to 120 s, Dpote -0.4 V, and Dtemp 25 °C, (d) Dtime vs. I_{pa},

(e) SWV of MCZ performed at different Dtemp from 15 to 55 °C, Dpote -0.4 V, and Dtime 60 s, and (f) Dtemp vs. I_{pa}. Reaction conditions: 40 µM MCZ in 0.04 M BR buffer at pH 7.

7.2.5. Electrochemical MCZ detection at 2.3Bi_2S_3-VONs(nat)/FTO@pH3

7.2.5.1 *Calculation of electrokinetic parameters and surface coverage of MCZ*

To determine the number of electrons involved in the oxidation event (n), reaction rate constant (k^0, s^{-1}), and formal standard potential (E^0, V), and surface coverage of MCZ ions (Γ*, mol cm^{-2}), CV was conducted at different scan speeds (5-500 mV/s) using 2.3Bi_2S_3-VONs(nat)/FTO@pH3 in 0.04 M BR buffer (pH 7, 45 °C) containing 40 µM of MCZ (Fig. 7.12a). A linear trend was observed between I_{pa} vs. $\upsilon^{0.5}$ (Fig. 7.12b) with a slope of 47.202 µA.$V^{-1/2}$.$s^{1/2}$ (R^2 = 0.988), indicating that the electrochemical reaction of MCZ is diffusion-controlled (Dash et al., 2021). Therefore, Eqs. 7.12 (Laviron equation) and 7.13 were employed to determine the electrokinetic parameters (n, k^0, and E^0) and adsorption of MCZ (Γ*) for the diffusion-controlled reaction, respectively (Bhan and Kumar Golder, 2023; Elgrishi et al., 2018).

$$E_p = E^0 - \frac{2.303RT}{\alpha nF}\log\frac{RTk^0}{\alpha nF} + \frac{2.303RT}{\alpha nF}\log\upsilon \quad (7.12)$$

$$I_{pa} = \frac{n^2F^2}{4RT}A_e\,\upsilon\,\Gamma^* \quad (7.13)$$

Where α is the charge transfer coefficient, and E_p, R, T, F, υ, I_{pa}, and A_e are the same as defined before. Firstly, the value of E^0 was found by the extrapolation of the plot between E_p vs. υ at υ = 0 (Das et al., 2024), resulting in E^0 = 0.655 V. Fig. 7.12c displays the linear relationship between E_p vs. log υ with a slope of 0.0339 V and an intercept of 0.8841 V (R^2 = 0.993). By considering α = 0.5 and substituting the value of E^0 (0.655 V), slope (0.0339 V), and intercept (0.8841 V) into Eq. 7.12, the n and k^0 were calculated to be 3.72 and 0.011 s^{-1}, respectively. It implies that four electrons participate in the electrochemical reaction of MCZ sensing. Fig. 7.12d reveals the linear trend between the I_{pa} vs. υ with a slope of 58.132 µA.V^{-1}.s (R^2 = 0.983). The value of Γ* was found by substituting the value of n (3.72), A_e (0.424 cm^2, obtained from Eq. 7.10), and slope (58.132 µA.V^{-1}.s) in Eq. 7.13. The value of Γ* was 1.126 × 10^{-11} mol cm^{-2}.

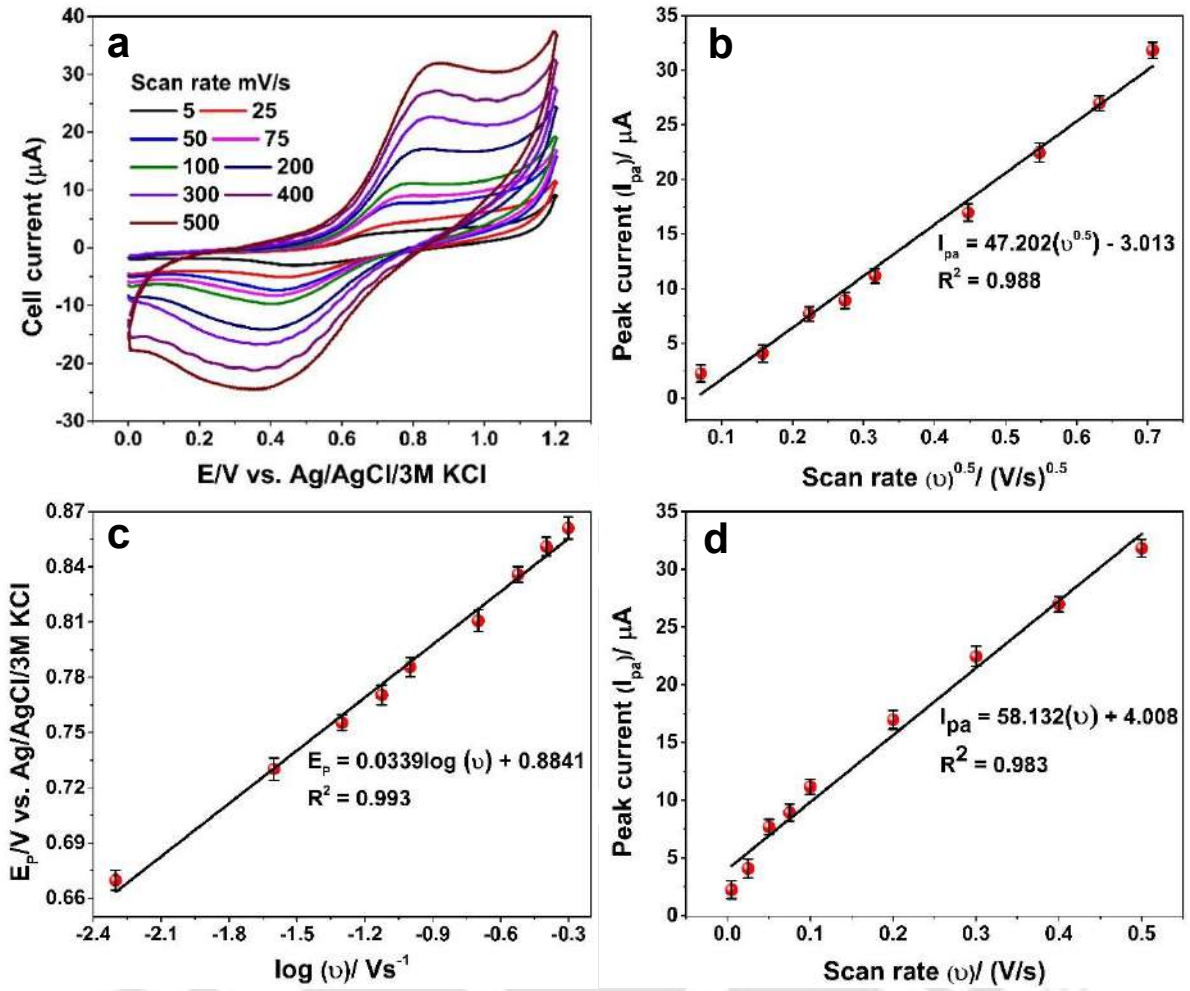

Figure 7.12: (a) CV was conducted at different scan speeds (5-500 mV/s) for determining electrokinetic parameters and surface coverage by adsorption of MCZ, (b) I_{pa} vs. $\upsilon^{0.5}$, (c) E_p vs. log υ, and (d) I_{pa} vs. υ.

7.2.5.2 *Electrochemical MCZ sensing at 2.3Bi_2S_3-VONs(nat)/FTO@pH3*

To develop the calibration curve of MCZ sensing, SWV was performed using 2.3Bi_2S_3-VONs(nat)/FTO@pH3 electrode at various MCZ concentrations (0-200 µM) in a 0.04 M BR buffer (pH7) at selected Dpote of -0.4 V, Dtime of 60 s, and Dtemp of 45 °C (Fig. 7.13a). The plot of I_{pa} vs. MCZ concentration varied linearly with the slope of 0.0669 µA.µM^{-1} (R^2 = 0.995) between the MCZ concentration window of 0-200 µM (Fig. 7.13b). The LOD and LOQ for MCZ detection were calculated using Eqs. 7.14 and 7.15, respectively (Das et al., 2024).

$$\text{LOD} = \frac{3S_d}{m} \tag{7.14}$$

$$\text{LOQ} = \frac{10S_d}{m} \tag{7.15}$$

Where m and S_d represent the slope of the calibration plot (0.0669 µA.µM^{-1}, Fig. 7.13b) and the standard deviation of blank analysis (0.00019), respectively. 2.3Bi_2S_3-

VONs(nat)/FTO@pH3 electrode exhibited LOD of 0.0085 µM and LOQ of 0.0284 µM within the concentration range of 0-200 µM MCZ. The sensitivity of the developed electrode calculated by dividing m (0.0669 $\mu A.\mu M^{-1}$) by A_e (0.424 cm^2, obtained from Eq. 7.10), was 0.1578 $\mu A.\ \mu M^{-1}.cm^{-2}$ (Bhan et al., 2025).

7.2.5.3 *MCZ reaction at 2.3Bi_2S_3-VONs(nat)/FTO@pH3 and detection mechanism*

The formation of reaction products of MCZ detection was analysed following the chronoamperometry using 2.3Bi_2S_3-VONs(nat)/FTO@pH3 in a 0.04 M BR buffer (pH 7, 45 °C) containing 200 µM MCZ at a potential of 0.655 V for 1800 s followed by HPLC and LC-MS analyses of the same electrolyte before and after the test. Fig. 7.14 demonstrates the HPLC analysis of 0.04 M BR buffer (pH 7, 45 °C) containing 200 µM MCZ. The sharp peaks at the retention time of 4.342 and 4.291 min before (Fig. 7.14a) and after (Fig. 7.14b) the redox process were detected. Additionally, a new peak appeared at a retention time of 4.450 min in Fig. 7.14b. Figs. 7.13c and 7.13d present the mass spectra of MCZ (peaks at m/z = 266.88 and 279.86 in both spectra) before and after the test. A new peak at m/z of 211.96 was identified, which is attributed to the redox reaction of MCZ. Consequently, after the redox reaction, MCZ (m/z = 266.88 and 279.86) is converted into the MCZ radical (ethane-1,2-diyldicarbamodithioic acid, m/z =211.96) (Swarupa, C; Siva Prasad, M; Dhananjayulu, M; Sreedhar, 2013). The highest intensity peak at m/z of 142.95 was observed from the supporting electrolyte (0.04 M BR buffer at pH 7) without adding MCZ (Fig. 7.15). Based on the HPLC and LCMS analyses, the sensing mechanism of MCZ is depicted in Fig. 7.13e, involving four electrons and four protons (Eq. 7.12). Therefore, the sensing of MCZ essentially involves the sensing of MCZ radical (ethane-1,2-diyldicarbamodithioic acid).

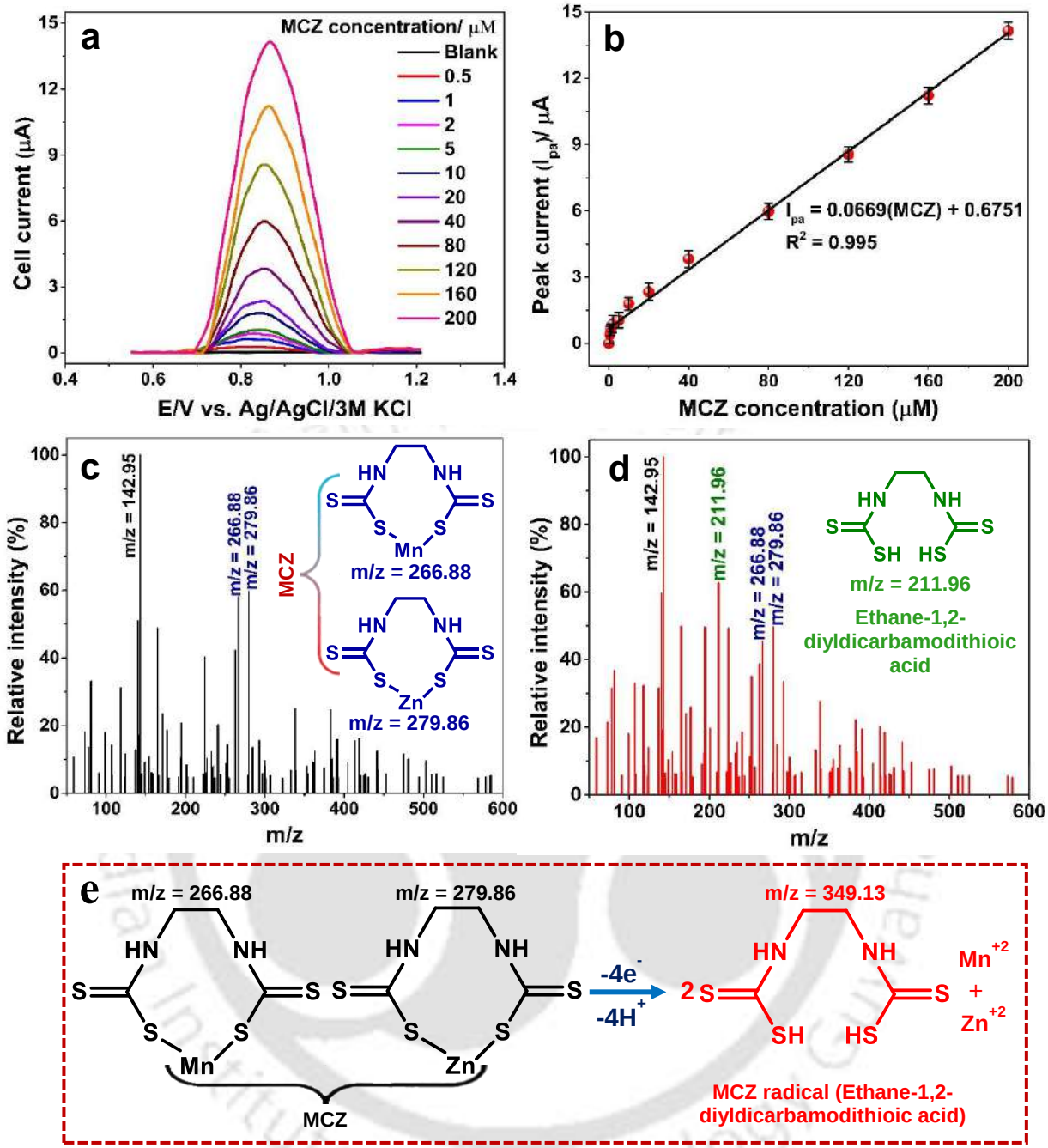

Figure 7.13: (a) SWV conducted at various concentrations of MCZ (0-200 µM) at 2.3Bi_2S_3-VONs(nat)/FTO@pH3 electrode under optimized Dpote of -0.4 V, Dtime of 60 s, and Dtemp of 45 °C, (b) Calibration curve for MCZ determination (MCZ concentration vs. I_{pa}), (c and d) Mass spectra obtained from LC-MS analysis of MCZ solution before and after the chronoamperometry at 0.655 V vs. Ag/AgCl for 1800 s using 2.3Bi_2S_3-VONs(nat)/FTO@pH3 electrode, and (e) Reaction mechanism for MCZ sensing on the 2.3Bi_2S_3-VONs(nat)/FTO@pH3 electrode.

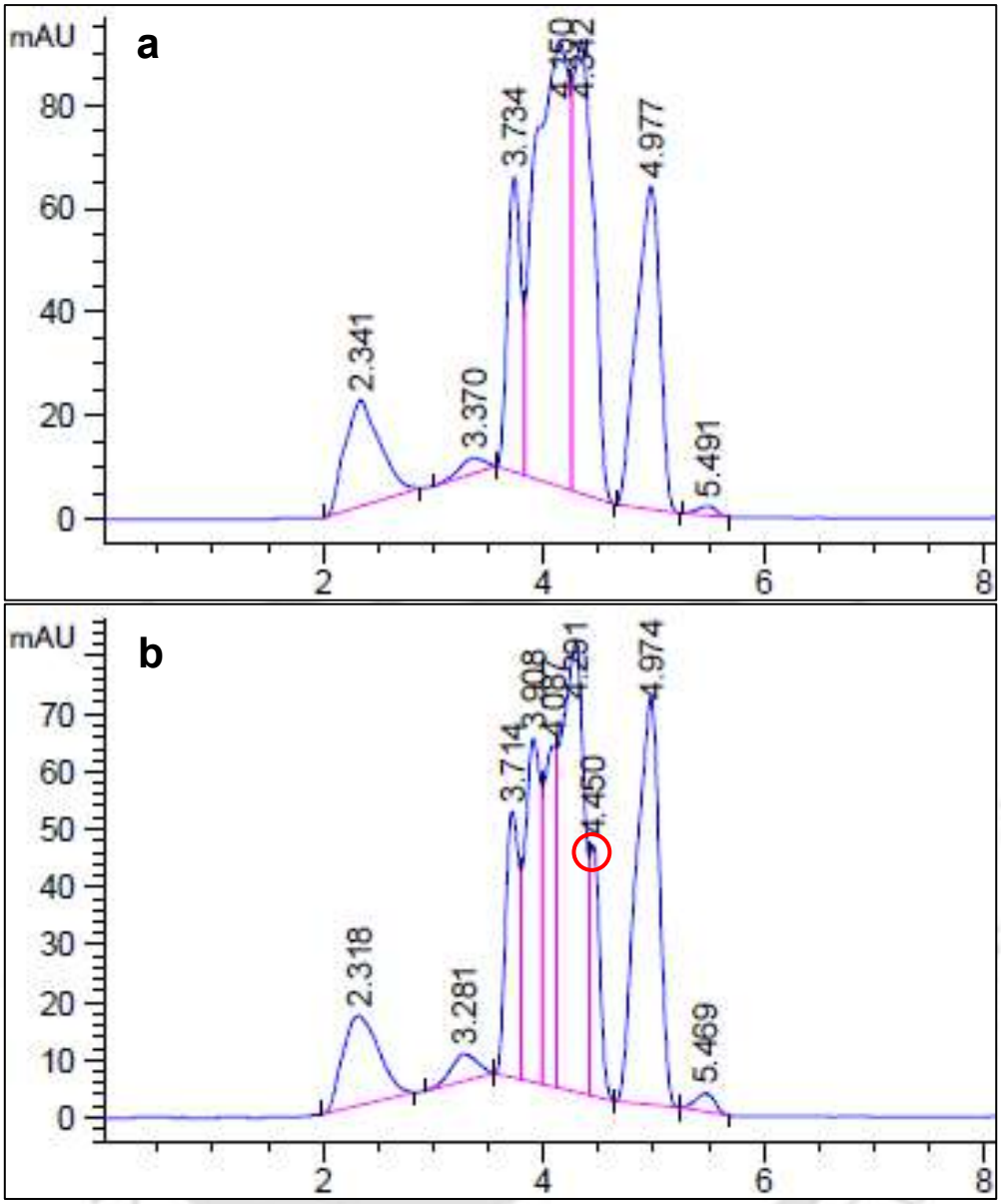

Figure 7.14: HPLC chromatograms of MCZ solution (a) before (retention time: 4.342 min) and (b) after (retention time: 4.291 min) the chronoamperometric test conducted at 0.655 V vs. Ag/AgCl for 1800 s using 2.3Bi_2S_3-VONs(nat)/FTO@pH3 electrode. HPLC was equipped with an ultra C18 column (UMISil C18(3), 250×4.6 mm, 5 µm particle size, Thermoscientific). The mobile phase consisted of 90% acetonitrile and 10% water, and MCZ was detected using a UV detector at a fixed wavelength of 230 nm.

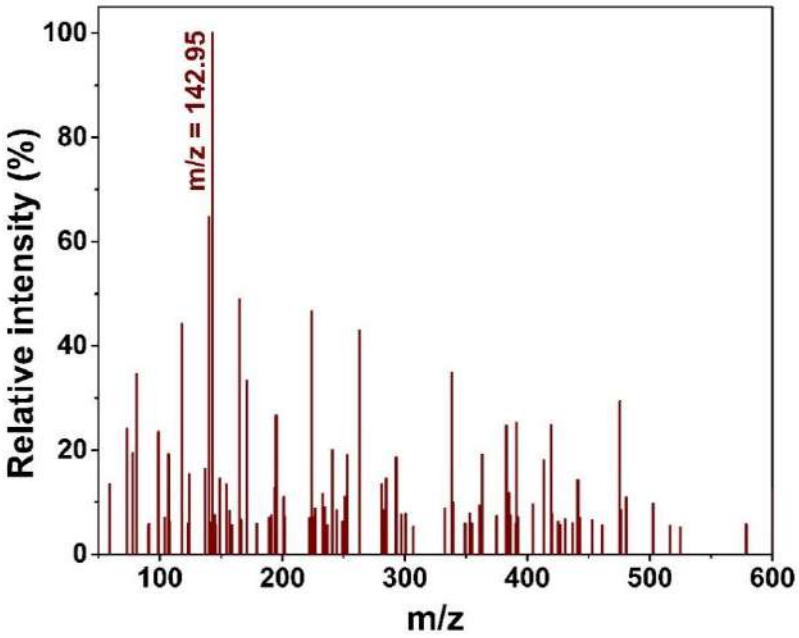

Figure 7.15: Mass spectrum obtained from LC-MS analysis of the supporting electrolyte (0.04 M BR buffer at pH 7) without adding MCZ.

7.2.5.4 *Stability, reproducibility, and long-term stability of 2.3Bi_2S_3-VONs(nat)/FTO@pH3*

The stability of 2.3Bi_2S_3-VONs(nat)/FTO@pH3 during MCZ sensing was determined using SWV conducted in a 0.04 M BR buffer (pH 7) containing 40 µM MCZ, with the same electrode reused for 15 cycles in the same electrolyte under optimized Dpote of -0.4 V, Dtime of 60 s, and Dtemp of 45 °C (Fig. 7.19a). No notable decrease in anodic peak response was identified up to first five cycles. After that, a slight decrease in the anodic peak current was noted with each MCZ sensing cycle (Dash et al., 2021). The decrease in anodic peak response was identified as 3.6 and 7.1% after the 10 and 15th cycles of MCZ sensing, respectively. Furthermore, an extended stability analysis of the developed electrode up to 30 cycles of MCZ sensing under identical experimental conditions is presented in Fig. 7.16a. A decrease in the anodic peak current was observed at about 10.9, 13.3, and 16.4% after the 20, 25, and 30th cycles of MCZ sensing, respectively. Considering the highest reduction in anodic peak current across all MCZ concentrations in the calibration curve, the slope of the calibration curve (Fig. 7.13b) also decreased by ~16.4%. The sensitivity and LOD also varied accordingly to the same extent after 30 cycles of MCZ sensing. The reproducibility of the fabricated electrode was investigated using SWV with three freshly prepared electrodes in three different 0.04 M BR buffers (pH 7, 45 °C) (Fig. 7.19b). 2.3Bi_2S_3-VONs(nat)/FTO@pH3 exhibited excellent reproducibility for MCZ sensing with a relative standard deviation (RSD) of only 2.45%, which

is within the acceptable range (Lotfi et al., 2021). Furthermore, the long-term stability of the developed electrode was evaluated up to 90 days after its fabrication using SWV in a 0.04 M BR buffer (pH 7) containing 40 µM MCZ under identical experimental conditions (Fig. 7.16b). After 90 days of storage at room temperature, the fabricated electrode showed only a 4.8% decrease in anodic peak current compared to a freshly prepared electrode under the same experimental conditions. Therefore, the developed sensing platform exhibited superior stability, reproducibility, and long-term stability during MCZ sensing.

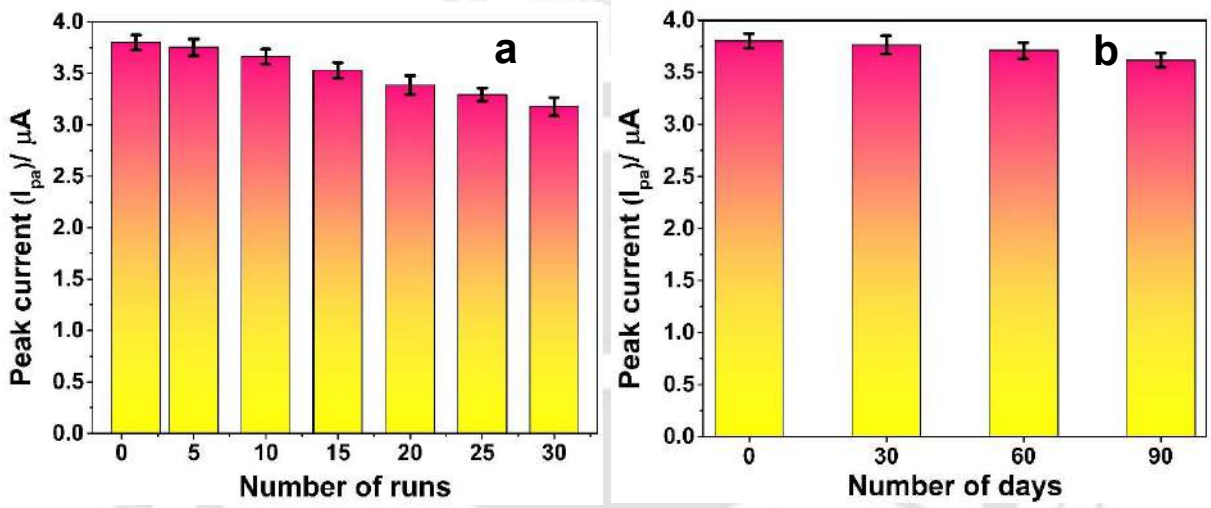

Figure 7.16: (a) Stability of the same 2.3Bi_2S_3-VONs(nat)/FTO@pH3 electrode tested up to 30th cycles using SWV in 0.04 M BR buffer (pH 7) containing 40 µM MCZ and (b) Long-term stability of the developed electrode after storage at room temperature for up to 90 days, evaluated by SWV in 0.04 M BR buffer (pH 7) with 40 µM MCZ concentration. Reaction condition: Dpote of -0.4 V vs. Ag/AgCl, Dtime of 60 s, and Dtemp of 45 °C.

To further confirm the stability of 2.3Bi_2S_3-VONs(nat)/FTO@pH3 electrode, FESEM, XRD, and XPS analyses were performed after the 15th cycle of MCZ sensing (Figs. 7.19c-7.19e). The FESEM images of the 2.3Bi_2S_3-VONs(nat)/FTO@pH3 electrode before (Fig. 7.1d) and after (Fig. 7.19c) the 15th cycle of MCZ sensing show negligible changes in morphology. Similarly, the XRD patterns indicate no significant changes in crystallinity after the 15th cycle of MCZ detection (Fig. 7.19d), compared to the fresh electrode (Fig. 7.3). The XPS analysis also reveals insignificant variations in the compositional attributes of the fabricated electrode before (Fig. 7.7i) and after (Fig. 7.19e) MCZ adsorption. Therefore, 2.3Bi_2S_3-VONs(nat)/FTO@pH3 electrode could retain its structural and compositional stability during electrochemical sensing of MCZ (Bhan and Kumar Golder, 2023).

FTIR analysis was used to investigate the surface chemistry of the 2.3Bi_2S_3-VONs(nat)/FTO@pH3 electrode before and after the 15th cycle of MCZ detection (Fig. 7.17). The fabricated electrode exhibited characteristic peaks at around 1615, 1280, 1025, and 554 cm^{-1}, corresponding to the stretching vibrations of C=O, C-O, Bi-S, and Bi-S bonds, respectively (Arumugam et al., 2017; Dawi et al., 2023). Additional peaks and peak shifting were observed after the 15th cycle of MCZ detection. The distinct peaks at around 3283, 2856, 1361, 1025, and 665 cm^{-1} were attributed to the stretching vibrations of N-H, C-H, C-H, C=S, and S-S bonds, respectively. Notably, the appearance of a band approximately 1531 cm^{-1}, ascribed to the N-H bending modes, resulted from MCZ surface adsorption (Daqa et al., 2022). The peak at 1025 cm^{-1}, associated with both Bi-S and C=S stretching, indicates the interaction of the thiocarbamate moiety of MCZ with Bi_2S_3.

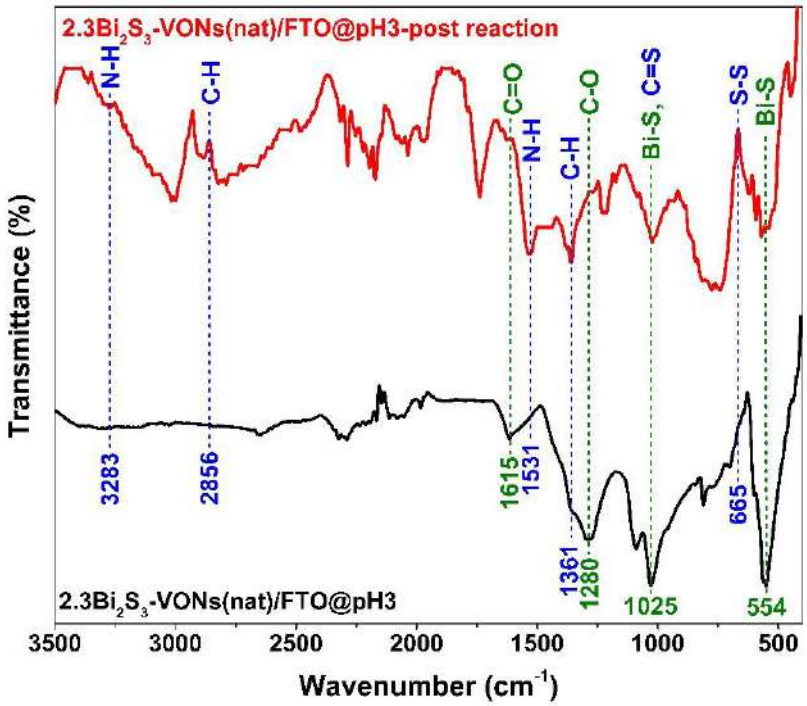

Figure 7.17: FTIR spectra of the 2.3Bi_2S_3-VONs(nat)/FTO@pH3 electrode before and after the 15th cycle of MCZ sensing.

Table 7.3 demonstrates the comparison of the sensing parameters (LOD, sensitivity, and linear concentration range) of 2.3Bi_2S_3-VONs(nat)/FTO@pH3 electrode for MCZ detection using SWV with the reported electrochemical sensors. The proposed MCZ detection platform showed significant enhancement in the sensing parameters compared to previously reported sensors.

Table 7.3: Performance of 2.3Bi_2S_3-VONs(nat)/FTO@pH3 in electrochemical sensing of MCZ and its comparison with the recently reported sensors.

Working electrodes	Technique	LOD (µM)	Linear range (µM)	Source
SQDs/GCE	⁂DPV	0.4327	3-1000	Guo et al., 2025
BC700-CPE	⁜DP-AdSV	0.028	0.09-10.25	Mutić et al., 2025
PEDOT/MWCNT/AuNPs	⁑CV	5.0	5-100	Zamora-Sequeira et al., 2019
WO_3/rGO/GCE	⁂DPV	0.0038	0.05-70	Buledi et al., 2022
PANI/GCE	⁂DPV	0.026	0.45-10000	Swarupa et al., 2013
GCE	*SWASV	7.0	10-90	López-Fernández et al., 2015
PEDOT/MWCNT	⁑CV	10	25-150	Zamora et al., 2018
MISP-modified PGEs	⁋SWV	0.0018	0.011-0.475	Kumar et al., 2016
BDD	†AMP	0.514	40-650	Silva et al., 2014
2D $CoTe_2$/GCE	⁑CV	0.18	18.48-184	Slathia et al., 2024
2.3Bi_2S_3-VONs(nat)/FTO@pH3	**⁋SWV**	**0.0085**	**0-200**	**Present work**

*Square wave anodic stripping voltammetry, ⁋Square wave voltammetry, †Amperometry, ⁑Cyclic voltammetry, ⁂Differential pulse voltammetry, ⁜Differential pulse adsorptive stripping voltammetry

7.2.6. Selectivity of MCZ sensing using 2.3Bi_2S_3-VONs(nat)/FTO@pH3

The selectivity of MCZ sensing was tested using chronoamperometry over 2.3Bi_2S_3-VONs(nat)/FTO@pH3 electrode with the addition of interferents (20 µM each), such as chlorpyrifos, carbendazim, and malathion followed by MCZ (5-20 µM), then interferents at higher concentration (40 µM each), and finally MCZ (60-90 µM) in a 0.04 M BR buffer (pH 7, 45 °C), as shown in Fig. 7.19f. Furthermore, the MCZ selectivity was evaluated by introducing MCZ at different concentrations in the presence of potential interferents, including thiram, ziram, and profenofos under identical experimental conditions (Fig. 7.18). The cell current was measured at a redox potential of 0.655 V vs. Ag/AgCl and an interval of 20 s (Figs. 7.18 and 7.19). The variations in the cell current were noted after the addition of MCZ at 0.655 V, and it stabilized rapidly. However, the addition of interferents didn't alter the cell current at this potential (Bhan et al., 2025). Therefore, the developed sensing platform demonstrated unprecedented selectivity towards MCZ sensing, even in the presence of common agriculture pesticides at the redox potential of 0.655 V vs. Ag/AgCl (Kabir et al., 2019).

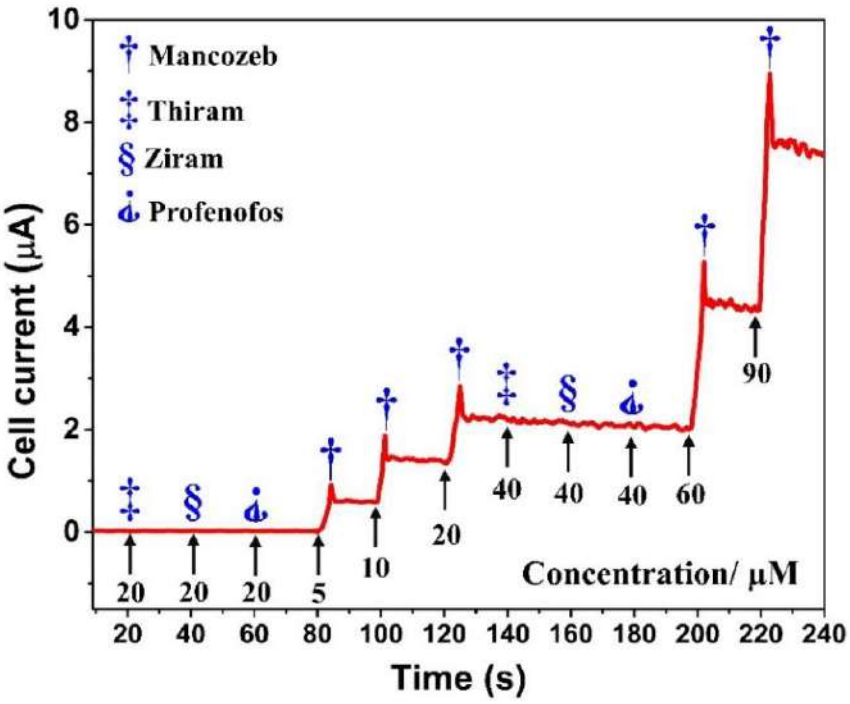

Figure 7.18: Chronoamperometric profile recorded using the 2.3Bi_2S_3-VONs(nat)/FTO@pH3 electrode in a 0.04 M BR buffer (pH 7, 45 °C) at a redox potential of 0.655 V vs. Ag/AgCl, with successive addition of interferents (20 µM each), including thiram, ziram, and profenofos, followed by MCZ (5-20 µM), again interferents (40 µM each), and finally MCZ (60-90 µM) at 20 s intervals.

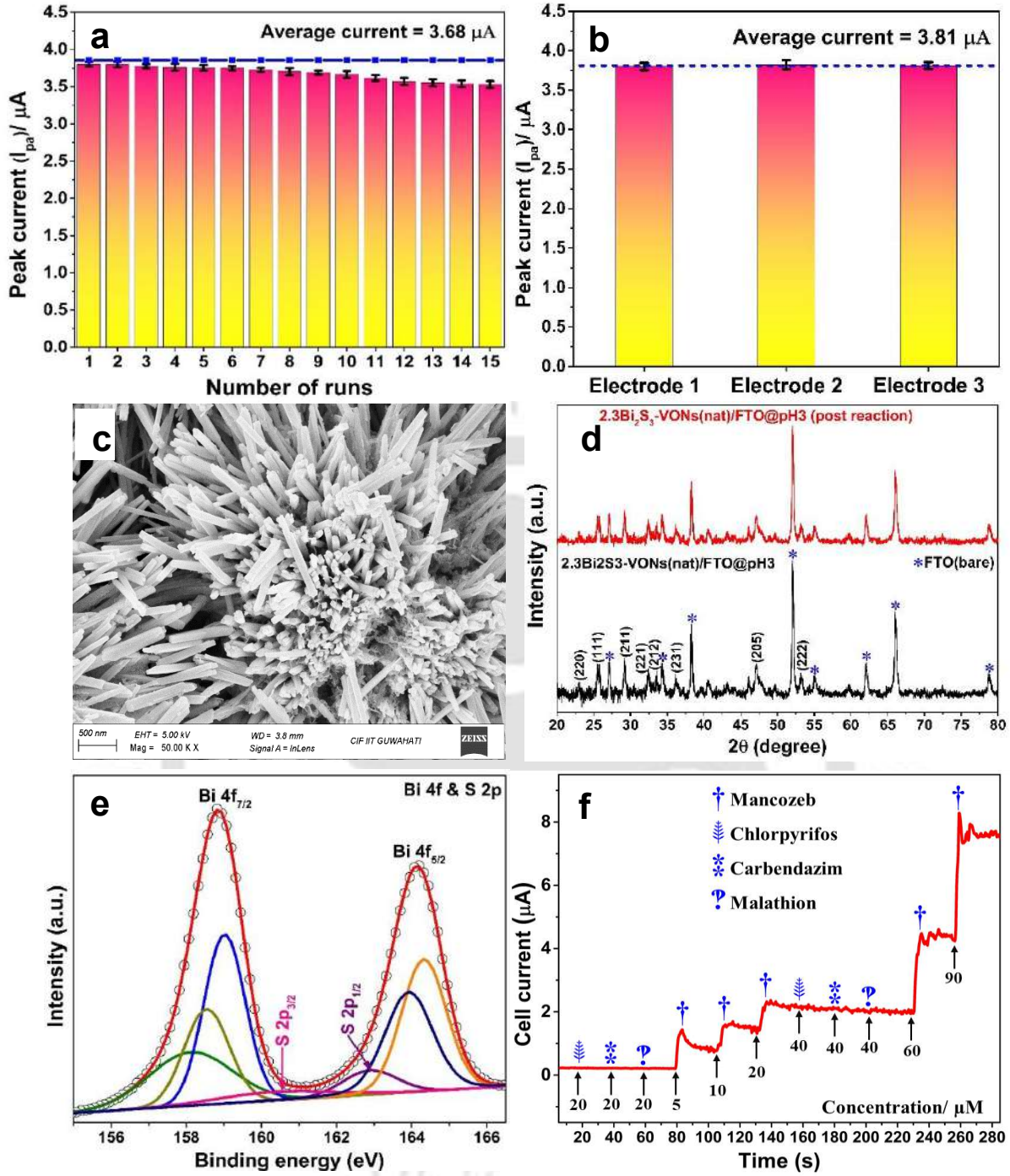

Figure 7.19: (a) Stability of $2.3Bi_2S_3$-VONs(nat)/FTO@pH3 electrode, (b) Reproducibility of $2.3Bi_2S_3$-VONs(nat)/FTO@pH3 electrode during MCZ sensing, (c) FESEM micrograph, (d) XRD patterns, (e) XPS spectra of $2.3Bi_2S_3$-VONs(nat)/FTO@pH3 after the 15th run of MCZ sensing (post reaction), and (f) Chronoamperometric profile recorded using $2.3Bi_2S_3$-VONs(nat)/FTO@pH3 electrode in a 0.04 M BR buffer (pH 7, 45 °C) at a redox potential of 0.655 V vs. Ag/AgCl, with sequential addition of interferents (20 µM each), namely, chlorpyrifos, carbendazim, and malathion, followed by MCZ (5-20 µM), again interferents (40 µM each), and finally MCZ (60-90 µM) at 20 s intervals.

7.2.7. MCZ sensing and quantification in environmental matrix

To determine the practical feasibility of 2.3Bi_2S_3-VONs(nat)/FTO@pH3 electrode for sensing and quantification of MCZ in environmental matrices (tap water, river water, agricultural runoff, and wastewater), SWV was conducted in a mixture of 0.04 M BR buffer (pH 7) and water samples (4:1 v/v) with MCZ spiked at different concentration (0-80 µM) at the optimized Dpote of -0.4 V, Dtime of 60 s, and Dtemp of 45 °C. Tap water, river water, agricultural runoff, and wastewater samples were obtained from the tap water supply at IIT Guwahati, the Brahmaputra River, a nearby village, and the wastewater treatment plant at IIT Guwahati, Assam, India, respectively. These samples were then filtered through 0.2 µm filter paper to eliminate any suspended contaminants and to avoid surface fouling of the kinetic electrode (Bhan and Golder, 2024). After the filtration, water samples underwent specific assays (Tables 7.4 and 7.5). Moreover, tap water, river water, agricultural runoff, and wastewater contained several background ions, such as fluoride, sulphate, nitrate, chloride, phosphate, and bromide (Fig. 7.20) (Bhan and Kumar Golder, 2023). The sensing and quantification of MCZ on 2.3Bi_2S_3-VONs(nat)/FTO@pH3 electrode were carried out by measuring MCZ against the calibration curve in Fig. 7.13b. The results were compared with HPLC. Table 7.6 summarizes the performance of the fabricated electrode for the determination of MCZ in environmental matrices and compares it with HPLC. The recovery of MCZ was about 100% in tap water, river water, agricultural runoff, and wastewater, with the maximum deviation from HPLC of 4.1% in tap water, 4.9% in river water, 7.1 % in agricultural runoff, 9.7% in wastewater, even in the presence of background ions and organic residues (Tables 7.4 and 7.5). Furthermore, the maximum RSD observed were 2.3, 3.8, 6.2, and 7.4% for tap water, river water, agricultural runoff, and wastewater, respectively. Therefore, the developed sensing platform holds significant potential for in-site detection and determination of MCZ in the environmental matrices.

Table 7.4: Anions concentrations in tap water, river water, agricultural runoff, and wastewater used for MCZ spiking for its electrochemical sensing.

Anions	Tap water (mg/L)	River water (mg/L)	Agricultural runoff (mg/L)	Wastewater (mg/L)
Fluoride	0.05	0.16	0.51	0.29
Chloride	0.84	0.79	22.2	66.9
Nitrate	0.87	1.25	0.85	-
Phosphate	0.45	-	24.9	-
Sulphate	28.1	48.1	63.5	67.9
Bromide	-	-	0.44	1.56

Table 7.5: Tap water, river water, agricultural runoff, and wastewater characterizations used for MCZ spiking for its electrochemical sensing.

Parameters	Tap water	River water	Agricultural runoff	Wastewater
pH	6.29	6.68	7.75	7.78
Conductivity (µS)	281	258	410	1023
TDS (mg/L)	53	51	85	222
TOC (mg/L)	0	3.85	13.3	42.5
TIC (mg/L)	8.26	1.89	1.83	6.83
TN (mg/L)	0.86	1.95	1.88	36.6

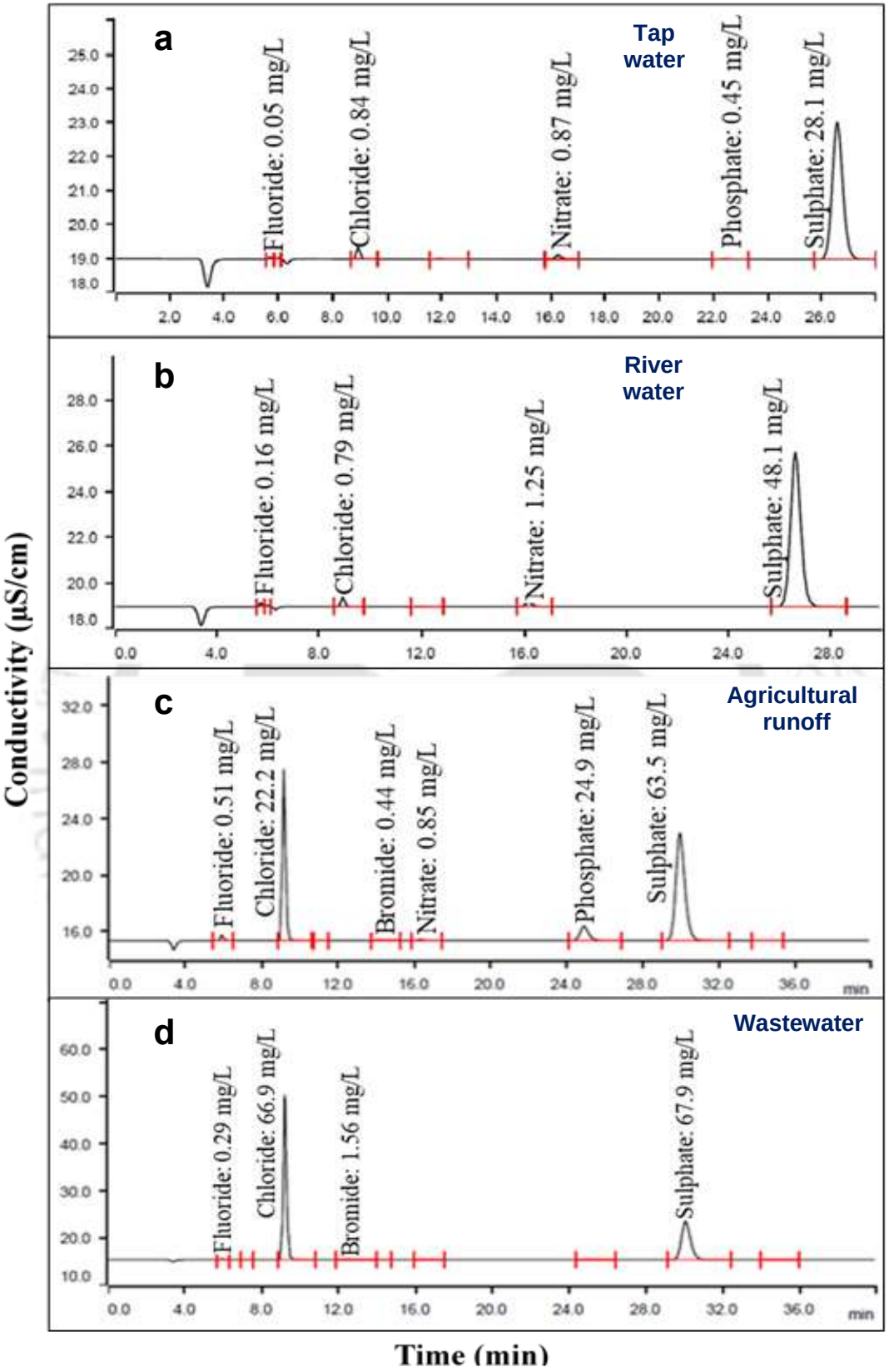

Figure 7.20: Anions concentration in (a) tap water, (b) river water, (c) agricultural runoff, and (d) wastewater used for MCZ spiking for its electrochemical sensing.

Table 7.6: Performance of 2.3Bi_2S_3-VONs(nat)/FTO@pH3 electrode for MCZ detection and determination from environmental matrices and its comparison with HPLC. ANOVA (Single Factor) test results.

Sample	MCZ spiked (µM)	Performance of 2.3Bi_2S_3-VONs(nat)/FTO@pH3				MCZ determination using HPLC (µM)	Deviation (%)
		MCZ determination (µM)	Recovery (%)	RSD (%)	p-value		
Tap water	0	ND	-	-	-	ND	-
	2	2.06	102.9	2.3	2.13×10^{-15}	2.14	-4.1
	10	9.99	99.9	2.1		10.27	-2.9
	40	40.69	101.7	0.7		39.96	1.8
	80	80.60	100.7	0.6		80.17	0.5
River water	0	ND	-	-	-	ND	-
	2	1.99	99.4	3.8	2.27×10^{-13}	2.08	-4.8
	10	10.47	104.7	3.3		9.95	4.9
	40	40.52	101.3	1.6		40.10	1.1
	80	80.69	100.9	1.1		79.93	1.0
Agricultural runoff	0	ND	-	-	-	ND	-
	2	2.12	106.0	6.2	7.84×10^{-11}	2.27	-7.1
	10	9.91	99.1	5.1		10.43	-5.2
	40	40.82	102.1	3.4		39.17	4.0
	80	82.86	103.6	2.6		80.85	2.4
Wastewater	0	ND	-	-	-	ND	-
	2	2.17	108.5	7.4	6.09×10^{-10}	1.96	9.7
	10	10.42	104.2	6.6		9.82	5.8
	40	39.45	98.6	4.8		41.87	-6.1
	80	78.97	98.7	3.2		82.28	-4.2

*$p \leq 0.0001$ indicates the reliability of the data obtained from triplicate experiments at a confidence interval of 99.99%.

7.3. Major findings

We have successfully developed a nature-inspired methodology for synthesizing 1D VONs of Bi_2S_3 on FTO using the *Sechium edule* extract for the electrochemical sensing of

MCZ in tap water, river water, agricultural runoff, and wastewater samples. The growth of Bi_2S_3 nanostructures was highly dependent on pH and Bi precursor loading, significantly influencing the morphology, size, growth mechanism, and self-stabilization of VONs. 2.3Bi_2S_3-VONs(nat)/FTO@pH3 were uniformly grown in a vertical configuration up to 1.74 ± 0.09 µm in length with high crystallinity and surface roughness of 3.1-, 5.2-, and 3.3-fold higher compared to FTO(bare), Bi_2S_3@seed/FTO, and 2.3Bi_2S_3-H_2O(control)/FTO@pH3, respectively. R_p was decreased by 9.3-fold, A_e was increased by 2.8-fold, and I_{pa} was enhanced by 3.2-fold for 2.3Bi_2S_3-VONs(nat)/FTO@pH3 electrode compared to the FTO(bare). The highest anodic peak current for MCZ was observed at pH 7 in a 0.04 M BR buffer. Dpote of -0.4 V vs. Ag/AgCl, Dtime of 60 s, and Dtemp of 45 °C were favourable for MCZ deposition in 0.04 M BR buffer at pH 7. The redox reaction of MCZ detection at 2.3Bi_2S_3-VONs(nat)/FTO@pH3 electrode involved a four-electron diffusion-controlled process with E^0 of 0.655 V vs. Ag/AgCl, k^0 of 0.011 s^{-1}, and Γ* of 1.126 × 10^{-11} mol cm^{-2}. The developed sensing platform exhibited LOD of 0.0085 µM, LOQ of 0.0284 µM, and sensitivity of 0.1578 µA. μM^{-1} .cm^{-2} within a linear MCZ concentration range of 0-200 µM. The proposed sensor demonstrated superior sensing performance for MCZ compared to previously reported electrochemical sensors. A minimal decrease of 7.1 and 16.4% in I_{pa} was noted up to the 15 and 30th runs of MCZ sensing, respectively. The negligible changes in the morphology, crystallinity, and compositional characteristics of the fabricated electrode were observed after the 15th cycle of MCZ detection. The coexistent interferants, including chlorpyrifos, carbendazim, malathion, thiram, ziram, and profenofos, could not interfere with MCZ detection at the redox potential of 0.655 V vs. Ag/AgCl, even in the presence of common background ions. The quantification of MCZ spiked in water samples was comparable to HPLC, with a maximum deviation of 4.1, 4.9, 7.1, and 9.7% observed for tap water, river water, agricultural runoff, and wastewater, respectively. Moreover, integrating an FTO-based electrode into a portable device could be a potential step toward commercialization. However, FTO glass is inherently rigid and does not naturally integrate with the flexible miniaturized device, requiring additional engineering efforts to ensure a seamless integration. Environmental matrices often contain multiple coexisting pollutants, making simultaneous detection very imperative. This approach demonstrates the sensor's ability to resolve overlapping signals and quantify multiple analytes in a single run. The transition from individual to simultaneous sensing highlights the sensor's adaptability, enhances real-time data integration, and could reduce costs by eliminating the need of multiple sensors.

References

Ahmad, R., Bhat, K.S., Nagal, V., Nakate, U.T., Ahmad, A., Alshammari, M.B., Alam, S., Lee, B.-I., 2024. Surface-engineered vertically-aligned ZnO nanorod for sensitive non-enzymatic electrochemical monitoring of cholesterol. Heliyon 10, e37847. https://doi.org/10.1016/j.heliyon.2024.e37847

Ahmad, R., Lee, B.-I., 2024. Facile fabrication of palm trunk–like ZnO hierarchical nanostructure–based biosensor for wide-range glucose detection. Chem. Eng. J. 492, 152432. https://doi.org/10.1016/j.cej.2024.152432

Ajiboye, T.O., Onwudiwe, D.C., 2021. Bismuth sulfide based compounds: Properties, synthesis and applications. Results Chem. 3, 100151. https://doi.org/10.1016/j.rechem.2021.100151

Ali, R., El-Wekil, M.M., 2023. Construction of MIP/Bi_2S_3 nanoparticles/rGO nanoprobe for simultaneous electrochemical determination of amoxicillin and clavulanic acid. J. Alloys Compd. 962, 171180. https://doi.org/10.1016/j.jallcom.2023.171180

Armenta, S., Moros, J., Garrigues, S., de la Guardia, M., 2006. Direct determination of Mancozeb by photoacoustic spectrometry. Anal. Chim. Acta 567, 255–261. https://doi.org/10.1016/j.aca.2006.03.031

Arsalan, M., Saddique, I., Baoji, M., Awais, A., Khan, I., Shamseldin, M.A., Mehrez, S., 2022. Novel Synthesis of Sensitive Cu-ZnO Nanorod–Based Sensor for Hydrogen Peroxide Sensing. Front. Chem. 10, 932985. https://doi.org/10.3389/fchem.2022.932985

Arumugam, J., Dhayal Raj, A., Albert Irudayaraj, A., 2017. Solvent effects on the properties of Bi_2S_3 nanoparticles: photocatalytic application. J. Mater. Sci. Mater. Electron. 28, 3487–3494. https://doi.org/10.1007/s10854-016-5947-6

Awais, A., Arsalan, M., Qiao, X., Yahui, W., Sheng, Q., Yue, T., He, Y., 2021. Facial synthesis of highly efficient non-enzymatic glucose sensor based on vertically aligned Au-ZnO NRs. J. Electroanal. Chem. 895, 115424. https://doi.org/10.1016/j.jelechem.2021.115424

Bagheri, H., Afkhami, A., Khoshsafar, H., Rezaei, M., Shirzadmehr, A., 2013. Simultaneous electrochemical determination of heavy metals using a triphenylphosphine/MWCNTs composite carbon ionic liquid electrode. Sensors Actuators B Chem. 186, 451–460. https://doi.org/10.1016/j.snb.2013.06.051

Bao, J., Zhang, Y., Wen, R., Zhang, L., Wang, X., 2022. Low level of mancozeb exposure affects ovary in mice. Ecotoxicol. Environ. Saf. 239, 113670. https://doi.org/10.1016/j.ecoenv.2022.113670

Bhan, C., Golder, A.K., 2024. ZnO Nanorods Aligned in a Vertical Configuration for Targeted Electrochemical Detection of Aniline. ACS Appl. Bio Mater. 7, 7413–7428. https://doi.org/10.1021/acsabm.4c01050

Bhan, C., Kumar Golder, A., 2023. Bio-based hierarchical vertically aligned 2D ZnO nanostructures for ultra selective electrochemical sensing of p-Chloroaniline. Chem. Eng. J. 475, 146122. https://doi.org/10.1016/j.cej.2023.146122

Bhan, C., Ravi, R., Golder, A.K., 2025. Phyto-analytic formation of Ag nanostructures for targeted electrocatalytic sensing of ciprofloxacin. J. Environ. Chem. Eng. 13, 115140. https://doi.org/10.1016/j.jece.2024.115140

Bikesh, S., Dinamani Singh, A., Shougaijam, B., 2024. Development of Ethanol Sensor Based on Vertically Aligned SnO_2/TiO_2 Heterojunction Nanowire Using GLAD Technique. IEEE Trans. Electron Devices 71, 3867–3873. https://doi.org/10.1109/TED.2024.3392173

Buledi, J.A., Mahar, N., Mallah, A., Solangi, A.R., Palabiyik, I.M., Qambrani, N., Karimi, F., Vasseghian, Y., Karimi-Maleh, H., 2022. Electrochemical quantification of mancozeb through tungsten oxide/reduced graphene oxide nanocomposite: A potential method for environmental remediation. Food Chem. Toxicol. 161, 112843. https://doi.org/10.1016/j.fct.2022.112843

Chen, P., Wang, H., Li, H., Niu, B., Guo, H., Chen, Z., 2024. A high-activity Fe-based MOFs fabricated through ultrasound strategy for electrochemical sensor of heavy metal ions and dopamine. J. Electroanal. Chem. 957, 118129. https://doi.org/10.1016/j.jelechem.2024.118129

Chi, C.-Y., Hsiao, T.-H., Wu, T., Yeh, C.-H., Chou, J.-P., Hsiao, F.-L., Ko, T.-S., Lin, Y.-W., 2023. Nafion/Silver Nanoparticles as an Electrochemically Sensitive Interface for the Detection of Ractopamine in Pork Liver. ACS Omega 8, 46252–46260. https://doi.org/10.1021/acsomega.3c07588

Chowdhury, A., Bhan, C., Rao Peela, N., Kumar Golder, A., 2023. A simple template-free bioinspired route of 1D Bi_2S_3 nanorods synthesis for electrochemical CO_2 reduction to formate. J. Ind. Eng. Chem. 127, 138–148. https://doi.org/10.1016/j.jiec.2023.06.055

Cocco, P., 2022. Time for Re-Evaluating the Human Carcinogenicity of Ethylenedithiocarbamate Fungicides? A Systematic Review. Int. J. Environ. Res. Public Health 19, 2632. https://doi.org/10.3390/ijerph19052632

Daqa, W.M., Alshoaibi, A., Ahmed, F., Rao, T.N., 2022. Synthesis and Characterization of Nanoformulation of the Broad-Spectrum Enzyme Inhibitor Mancozeb by Polyethylene

Glycol Capping and Its Dissipation Kinetics in Water Using TiO_2 Nanoparticles. Processes 10, 2733. https://doi.org/10.3390/pr10122733

Das, D., Bhan, C., Mukherjee, C., Golder, A.K., 2024. Improved selectivity of electrochemical aniline sensing using one-dimensional silver nanorods with high aspect ratio synthesized by ascorbic acid assisted method. Anal. Chim. Acta 1310, 342697. https://doi.org/10.1016/j.aca.2024.342697

Dash, S.R., Bag, S.S., Golder, A.K., 2021. Bio-inspired PtNPs/Graphene nanocomposite based electrocatalytic sensing of metabolites of dipyrone. Anal. Chim. Acta 1167, 338562. https://doi.org/10.1016/j.aca.2021.338562

Dash, S.R., Bag, S.S., Golder, A.K., 2020. Synthesis of highly structured spherical Ag@Pt core-shell NPs using bio-analytes for electrocatalytic Pb(II) sensing. Sensors Actuators B Chem. 314, 128062. https://doi.org/10.1016/j.snb.2020.128062

Dawi, E.A., Padervand, M., Bargahi, A., Eftekhari-Sis, B., Bahrami, M.K., Abdelkader, A., 2023. Efficient visible-light-driven photocatalytic removal of Acid Blue 92, E. coli, and S. aureus over Ag-AgCl nanoparticles-decorated bismuth sulfide microparticles. Mater. Res. Express 10, 105008. https://doi.org/10.1088/2053-1591/ad0288

Ejeromedoghene, O., Abdulwahab, K.O., Udofia, I.A., Kumi, M., Nejo, A.O., 2024. Evaluation of zinc sulfide heterostructures as catalysts for the transformation of CO_2 into valuable chemicals and clean energy generation. Energy Adv. 3, 1196–1221. https://doi.org/10.1039/D4YA00202D

Elgrishi, N., Rountree, K.J., McCarthy, B.D., Rountree, E.S., Eisenhart, T.T., Dempsey, J.L., 2018. A Practical Beginner's Guide to Cyclic Voltammetry. J. Chem. Educ. 95, 197–206. https://doi.org/10.1021/acs.jchemed.7b00361

Flick, G.J., Burnette, F.S., Aung, L.H., Ory, R.L., St. Angelo, A.J., 1978. Chemical composition and biochemical properties of mirlitons (*Sechium edule*) and purple, green, and white eggplants (*Solanum melongena*). J. Agric. Food Chem. 26, 1000–1005. https://doi.org/10.1021/jf60219a045

Ganesamurthi, J., Veerakumar, P., Liu, T.-Y., Juang, R.-S., 2024. Electrochemical detection and photodegradation of antihistamine promethazine hydrochloride in water using nanostructured Bi_2S_3 catalysts. J. Environ. Chem. Eng. 12, 111962. https://doi.org/10.1016/j.jece.2024.111962

Gawal, P.M., Golder, A.K., 2024. Plant-Based Phytochemicals for Synthesis of Z-Scheme In_2O_3/CdS Heterostructures: DFT Analysis and Photocatalytic CO_2 Reduction to HCOOH and CO. Langmuir 40, 13538–13549. https://doi.org/10.1021/acs.langmuir.4c01015

Godzierz, M., Mistewicz, K., Gawron, A., Kurtyka, K., Otulakowski, Ł., Kanti Das, T., 2024. Visible light photodetectors based on the Bi_2S_3 flower-like 3D microrods with Schottky emission. J. Alloys Compd. 1008, 176820. https://doi.org/10.1016/j.jallcom.2024.176820

Gumpu, M.B., Veerapandian, M., Krishnan, U.M., Rayappan, J.B.B., 2017. Simultaneous electrochemical detection of Cd(II), Pb(II), As(III) and Hg(II) ions using ruthenium(II)-textured graphene oxide nanocomposite. Talanta 162, 574–582. https://doi.org/10.1016/j.talanta.2016.10.076

Guo, T., Qu, Y., Ning, B., Song, Q., Wan, J., Lin, X., Zhuang, S., Lin, P., Yang, J., Huang, G., 2025. A novel sulfur quantum dots-based electrochemical sensor for highly sensitive and specific detection of mancozeb. Microchem. J. 209, 112642. https://doi.org/10.1016/j.microc.2024.112642

Hideshima, S., Ogata, Y., Takimoto, D., Gogotsi, Y., Sugimoto, W., 2024. Vertically aligned MXene bioelectrode prepared by freeze-drying assisted electrophoretic deposition for sensitive electrochemical protein detection. Biosens. Bioelectron. 250, 116036. https://doi.org/10.1016/j.bios.2024.116036

Hvojnik, M., Vida, J., Homola, T., Pavličková, M., Hatala, M., Tomanová, K., Mikula, M., Gemeiner, P., 2021. The effect of rapid atmospheric plasma treatment of FTO substrates on the quality of TiO_2 blocking layers for printed perovskite solar cells. Mater. Sci. Semicond. Process. 131, 105850. https://doi.org/10.1016/j.mssp.2021.105850

Kabir, H., Ma, P.Y., Renn, N., Nicholas, N.W., Cheng, I.F., 2019. Electrochemical determination of free chlorine on pseudo-graphite electrode. Talanta 205, 120101. https://doi.org/10.1016/j.talanta.2019.06.101

Khadka, D.B., Islam, M.A., Kato, S., Soga, T., 2024. Fabrication and Properties of Bi_2S_3 Nanowire Thin Film Solar Cells by Spin Coating with Varying Sulfur Concentrations in the Precursor. J. Electron. Mater. 53, 4224–4235. https://doi.org/10.1007/s11664-024-11129-2

Koh, Y.W., Lai, C.S., Du, A.Y., Tiekink, E.R.T., Loh, K.P., 2003. Growth of Bismuth Sulfide Nanowire Using Bismuth Trisxanthate Single Source Precursors. Chem. Mater. 15, 4544–4554. https://doi.org/10.1021/cm021813k

Kumar, A., Das, C., 2024. Corrosion inhibition of mild steel by Praecitrullus fistulosus (tinda fruit and peel) extracts. Sci. Total Environ. 929, 172569. https://doi.org/10.1016/j.scitotenv.2024.172569

Kumar, A., Das, C., 2023. A novel eco-friendly inhibitor of chayote fruit extract for mild steel corrosion in 1 M HCl: Electrochemical, weight loss studies, and the effect of temperature.

Sustain. Chem. Pharm. 36, 101261. https://doi.org/10.1016/j.scp.2023.101261

Kumar, B., Kumar Sinha, S., 2024. Development of a highly sensitive non-enzymatic electrochemical cholesterol biosensor based on Ag with Cu_2O nanomaterial deposited on TiO_2 nanotubes. Measurement 232, 114707. https://doi.org/10.1016/j.measurement.2024.114707

Kumar, S., Karfa, P., Patra, S., Madhuri, R., Sharma, P.K., 2016. Molecularly imprinted star polymer-modified superparamagnetic iron oxide nanoparticle for trace level sensing and separation of mancozeb. RSC Adv. 6, 36751–36760. https://doi.org/10.1039/c6ra03204d

Kunpatee, K., Kaewdorn, K., Duangtong, J., Chaiyo, S., Chailapakul, O., Kalcher, K., Kerr, M., Samphao, A., 2022. A new disposable electrochemical sensor for the individual and simultaneous determination of carbamate pesticides using a nanocomposite modified screen-printed electrode. Microchem. J. 177. https://doi.org/10.1016/j.microc.2022.107318

López-Fernández, O., Barroso, M.F., Fernandes, D.M., Rial-Otero, R., Simal-Gándara, J., Morais, S., Nouws, H.P.A., Freire, C., Delerue-Matos, C., 2015. Voltammetric analysis of mancozeb and its degradation product ethylenethiourea. J. Electroanal. Chem. 758, 54–58. https://doi.org/10.1016/j.jelechem.2015.08.030

Lotfi, S., Veisi, H., Karmakar, B., 2021. A convenient strategy for the electrochemical evaluation of acetaminophen and caffeine in combined drugs and biological samples over TiO_2@polymethyldopa/Pd nanocomposite functionalized glassy carbon electrodes. Measurement 186, 110156. https://doi.org/10.1016/j.measurement.2021.110156

Ma, J., Yang, J., Jiao, L., Wang, T., Lian, J., Duan, X., Zheng, W., 2011. Bi_2S_3 nanomaterials: morphology manipulation and related properties. Dalt. Trans. 40, 10100. https://doi.org/10.1039/c1dt10846h

Maji, B., Sahoo, S.J., Rout, V., Barik, B., Behera, N., Dash, P., 2023. Highly Sensitive and Selective Nonenzymatic Sensing of Glyphosate Using FTO-Modified MOF-Derived $CuCo_2O_4$ Nanostructures Intercalated in Protonated-g-C_3N_4 and 3D-Graphene Oxide Sheets. Ind. Eng. Chem. Res. 62, 3477–3491. https://doi.org/10.1021/acs.iecr.2c04426

Malik, S.B., Mejia-Centeno, K. V., Martínez-Alanis, P.R., Cabot, A., Güell, F., Annanouch, F.E., Llobet, E., 2024. Synergistic effect of CeO_2 nanoparticles and WO_3 nanowires in gas sensing applications. Sensors Actuators B Chem. 400, 134879. https://doi.org/10.1016/j.snb.2023.134879

Malode, S.J., Keerthi, P.K., Shetti, N.P., Kulkarni, R.M., 2020. Electroanalysis of Carbendazim using MWCNT/Ca-ZnO Modified Electrode. Electroanalysis 32, 1590–1599.

https://doi.org/10.1002/elan.201900776

Manivannan, K., Sivakumar, M., Cheng, C.-C., Lu, C.-H., Chen, J.-K., 2019. An effective electrochemical detection of chlorogenic acid in real samples: Flower-like ZnO surface covered on PEDOT:PSS composites modified glassy carbon electrode. Sensors Actuators B Chem. 301, 127002. https://doi.org/10.1016/j.snb.2019.127002

Mao, Z., Zhu, H., Peng, X., Chen, J., Chen, Q., Chen, X., Hu, X., Chen, H., 2022. In situ vertical alignment of 2D MoS_2 layers on GO film: enhanced electrochemical properties for PD-L1 sensing. Microchim. Acta 189, 155. https://doi.org/10.1007/s00604-022-05269-7

Moyseowicz, A., 2019. Scalable one-pot synthesis of bismuth sulfide nanorods as an electrode active material for energy storage applications. J. Solid State Electrochem. 23. https://doi.org/10.1007/s10008-019-04215-7

Musarurwa, H., Tawanda Tavengwa, N., 2021. Extraction and electrochemical sensing of pesticides in food and environmental samples by use of polydopamine-based materials. Chemosphere 266, 129222. https://doi.org/10.1016/j.chemosphere.2020.129222

Mutić, S., Anojčić, J., Đukanović, N., Apostolović, T., Simetić, T., Petrović, J., Beljin, J., 2025. Exploring wood-derived biochar potential for electrochemical sensing of fungicides mancozeb and maneb in environmental water samples. Talanta 287, 127648. https://doi.org/10.1016/j.talanta.2025.127648

Ordonez, A., Gomez, J., Vattuone, M., Lsla, M., 2006. Antioxidant activities of *Sechium edule* (Jacq.) Swartz extracts. Food Chem. 97, 452–458. https://doi.org/10.1016/j.foodchem.2005.05.024

Petha, N.H., Lokhande, R.S., Seshadri, D.T., Patil, R.M., Bhagat, T.S., Patil, J.G., 2017. A simple pre-column derivatization method for the determination of mancozeb technical (fungicide) by reverse phase HPLC-UV. Anal. Methods 9, 4702–4708. https://doi.org/10.1039/C7AY00830A

Ramos Reynoso, Y., Martinez-Ayala, A., Pal, M., Paraguay-Delgado, F., Mathews, N.R., 2018. Bi_2S_3 nanoparticles by facile chemical synthesis: Role of pH on growth and physical properties. Adv. Powder Technol. 29, 3561–3568. https://doi.org/10.1016/j.apt.2018.09.037

Rao, C.V., Golder, A.K., 2016. Development of a bio-mediated technique of silver-doping on titania. Colloids Surfaces A Physicochem. Eng. Asp. 506, 557–565. https://doi.org/10.1016/j.colsurfa.2016.07.031

Ravi, R., Bhan, C., Golder, A.K., 2025. Bio-analytic synthesis of Cu-doped TiO_2 for photocatalytic degradation of ciprofloxacin under visible light. Opt. Mater. (Amst). 159,

116577. https://doi.org/10.1016/j.optmat.2024.116577

Ravi, R., Golder, A.K., 2025a. Photocatalytic and biological degradation processes to mineralize pharmaceutically active compounds and catalyst recovery: A review. Coord. Chem. Rev. 523, 216267. https://doi.org/10.1016/j.ccr.2024.216267

Ravi, R., Golder, A.K., 2025b. Bio-based synthesis of oxygen-deficient Ni-doped TiO_2 using waste pineapple peel: Density functional theory studies and photocatalytic degradation of furazolidone. J. Environ. Chem. Eng. 13, 116198. https://doi.org/10.1016/j.jece.2025.116198

Ravi, R., Golder, A.K., 2023a. A tuneable bioinspired process of Pt-doping in TiO_2 for improved photoelectrochemical and photocatalytic functionalities. Colloids Surfaces A Physicochem. Eng. Asp. 663, 131034. https://doi.org/10.1016/j.colsurfa.2023.131034

Ravi, R., Golder, A.K., 2023b. Bio-based Au Doping with Dominant Oxygen Vacancies and Ti^{3+} Defects on Photocatalytic Functionalities of TiO_2. Ind. Eng. Chem. Res. 62, 20702–20715. https://doi.org/10.1021/acs.iecr.3c02850

Silva, R.A.G., Silva, L.A.J., Munoz, R.A.A., Richter, E.M., Oliveira, A.C., 2014. Fast and direct determination of mancozeb through batch injection analysis with amperometric detection on boron-doped diamond electrodes. J. Electroanal. Chem. 733, 85–90. https://doi.org/10.1016/j.jelechem.2014.09.025

Slathia, S., Ipaves, B., Campos de Oliveira, C., Negedu, S.D., Sarkar, S., Autreto, P.A.S., Tiwary, C.S., 2024. Ultralow Detection of Mancozeb Using Two-Dimensional Cobalt Telluride ($CoTe_2$). Langmuir. https://doi.org/10.1021/acs.langmuir.4c01549

Stanley, M.M., Sriram, B., Wang, S.-F., Sherlin, A., Kogularasu, S., Lee, Y.-Y., George, M., 2024. Rational confinement of ternary layered double hydroxide within three-dimensional graphene aerogel: An electrochemical tool for propyl gallate sensing. Chem. Eng. J. 485, 149682. https://doi.org/10.1016/j.cej.2024.149682

Swarupa, C; Siva Prasad, M; Dhananjayulu, M; Sreedhar, N., 2013. Electrochemical determination and reduction behaviour of mancozeb at glassy carbon electrode modified with polyaniline based nanosensors. Int. J. Sci. Eng. Res. 4, 1234–1241.

Tang, C., Zhang, Y., Su, J., Wang, C., Sun, R., Zhang, J., Li, G., 2016. Synthesis and photocatalytic properties of vertically aligned Bi_2S_3 platelets. Solid State Sci. 51, 24–29. https://doi.org/10.1016/j.solidstatesciences.2015.11.004

Vattikuti, S.V.P., Nagajyothi, P.C., Shim, J., 2019. Fabrication of CdS quantum dot/Bi_2S_3 nanocomposite photocatalysts for enhanced H_2 production under simulated solar light. J. Mater. Sci. Mater. Electron. 30, 5681–5690. https://doi.org/10.1007/s10854-019-00861-9

Weng, N., Peng, H., Sun, F., Zhang, Y., Li, B., Li, R., Gong, Y., Zheng, F., Wang, M., Sun, P., 2024. Vertically well-aligned ZnO nanorods based biosensor for determination of paeoniflorin as an antidepressant medicine. Alexandria Eng. J. 86, 471–480. https://doi.org/10.1016/j.aej.2023.11.033

Xing, R., Li, D., An, C., Zhang, L., Li, Q., Liu, S., 2012. Single-Crystalline Bi_2S_3 Nanobelts: Hydrothermal Synthesis and Growth Mechanism. J. Nanosci. Nanotechnol. 12, 8029–8033. https://doi.org/10.1166/jnn.2012.6657

Younis, A., Sehar, S., Guan, X., Aftab, S., Manaa, H., Mahmood, T., Iqbal, J., Akram, F., Ali, N., Wu, T., 2024. Four-in-one strategy to boost the performance of 3-dimensional MoS_2 nanostructures for industrial effluent treatment and hydrogen evolution reactions. J. Alloys Compd. 976, 173104. https://doi.org/10.1016/j.jallcom.2023.173104

Zamora-Sequeira, R., Alvarado-Hidalgo, F., Robles-Chaves, D., Sáenz-Arce, G., Avendano-Soto, E.D., Sánchez-Kopper, A., Starbird-Perez, R., 2019. Electrochemical characterization of mancozeb degradation for wastewater treatment using a sensor based on poly (3,4-ethylenedioxythiophene) (PEDOT) modified with carbon nanotubes and gold nanoparticles. Polymers (Basel). 11. https://doi.org/10.3390/polym11091449

Zamora, R., Masís-Meléndez, F., Phillips, H., Alvarado-Marchena, L.A., Starbird, R., 2018. Development of Poly(3,4-ethylenedioxythiophene(PEDOT)/carbon nanotube electrodes for electrochemical detection of Mancozeb in water. Int. J. Electrochem. Sci. 13, 1931–1944. https://doi.org/10.20964/2018.02.20

Zhang, C., 2024. Monitoring athlete health and performance using an electrochemical sensor based on zinc oxide nanorods. Alexandria Eng. J. 92, 221–230. https://doi.org/10.1016/j.aej.2024.02.056

Zhang, Z., Zuo, Y., Fan, Y., Wang, X., Wang, C., Yang, S., Zhao, X., Wang, M., Xu, R., 2024. In situ fabrication of Ag nanoparticles modified vertically-grown ZnO nanorods on carbon fiber paper electrode for simultaneous detection of luteolin, daidzein and baicalein. Colloids Surfaces A Physicochem. Eng. Asp. 694, 134118. https://doi.org/10.1016/j.colsurfa.2024.134118

Zhao, Y., Chua, K.T.E., Gan, C.K., Zhang, J., Peng, B., Peng, Z., Xiong, Q., 2011. Phonons in Bi_2S_3 nanostructures: Raman scattering and first-principles studies. Phys. Rev. B 84, 205330. https://doi.org/10.1103/PhysRevB.84.205330

CHAPTER 8

Dual-Analyte Selective Electrochemical Detection of Phenylbutazone and Sulfamethoxazole using Bio-Engineered Bi_2S_3-ZnO Nanocomposites

This chapter reports on synthesis of bio-based Bi_2S_3-ZnO nanocomposite using the phytochemicals present in the bio-extract of Sechium edule fruit. These phytochemicals could facilitate the development of stable Bi_2S_3-ZnO nanocomposite. Subsequently, the bio-based synthesized Bi_2S_3-ZnO nanocomposite was functionalized onto GCE using Nafion as a binder for the selective and simultaneous sensing of phenylbutazone (PBZ) and sulfamethoxazole (SMZ) through the SWV. The practical applicability of the proposed simultaneous sensing platform was tested in the tap and river water samples. It also serves as a platform to compare and explore the performance of binder-free sensors reported in Chapters 4-7.

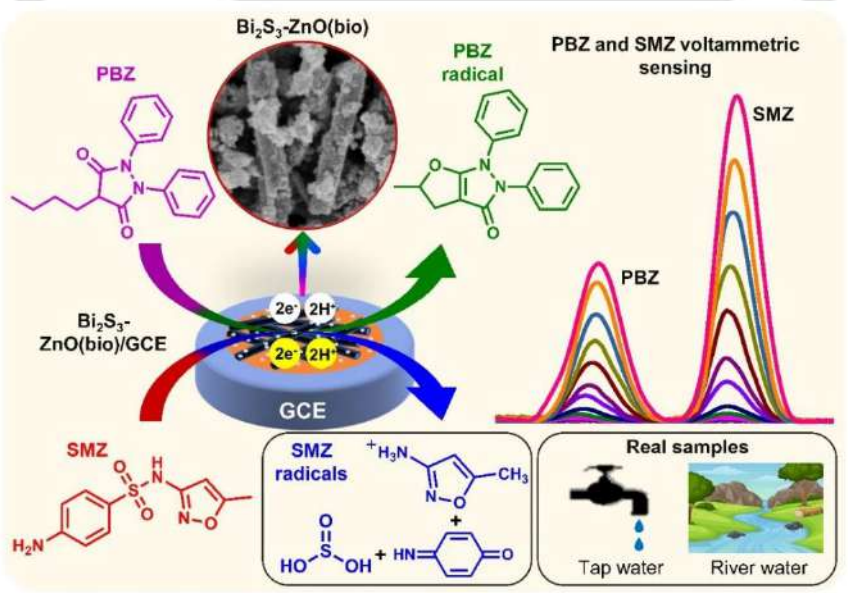

Chapter highlights

- Bio-engineered development of Bi_2S_3-ZnO nanocomposites using *Sechium edule* extract
- Bi_2S_3-ZnO(bio)/GCE catalyzed selective sensing of phenylbutazone and sulfamethoxazole
- Phenylbutazone and sulfamethoxazole sensing involve equal electron and proton transfer
- Developed sensing platform exhibited excellent sensitivity and selectivity
- Phenylbutazone and sulfamethoxazole detection limit of 0.222 and 0.089 µM

8.1. Background and executive motivation

The increasing presence of pharmaceutically active compounds (PhACs) in the environment is an emerging global concern due to their potential impact on human health and ecosystems. Among the various PhACs, phenylbutazone (PBZ) and sulfamethoxazole (SMZ) are two commonly used drugs that have been found in water bodies and food supplies (Kaczala and E. Blum, 2016; Worboys and Toon, 2018). PBZ is a nonsteroidal anti-inflammatory drug extensively used for its anti-inflammatory and analgesic properties in human and veterinary medicine (Tesena et al., 2024). SMZ is a broad-spectrum antimicrobial agent frequently used to treat bacterial infections. Despite their beneficial advantages, PBZ and SMZ have been found in aquatic environments, posing risks to aquatic organisms and potentially leading to the growth of drug-resistant bacteria. The prolonged presence of both PBZ and SMZ in the environment, even at low concentrations, can lead to significant effects on human health, such as kidney damage, rashes, nausea, leukopenia, agranulocytosis, blood disorders, thrombocytopenia, gastrointestinal issues, and exacerbate blood cell reduction (Borges et al., 2019; Pan et al., 2023). Therefore, detecting and determining PhACs in the environmental matrices due to their widespread use and environmental persistence is highly warranted.

Traditional detection methods, such as mass spectrometry and liquid chromatography, are effective for detecting and determining PhACs in environmental matrices (Haque and Stewart, 1997; Sun et al., 2009; Zaky and Fadel Osman, 2022). However, these traditional techniques required expensive instruments, complex sample preparation, extended analysis times, and proficient workmanship, triggering high analysis costs. As a result, there is an urgent need for a bio-based, rapid, cost-effective, and efficient sensing platform for the selective and simultaneous monitoring and quantification of PhACs in environmental matrices.

Electrochemical sensors have emerged as promising alternatives for monitoring PhACs due to their easy-working electrode modification, low cost, ease of use, high sensitivity, and selectivity (Y. Li et al., 2025; Zhang et al., 2025). Simultaneous electrochemical sensing of PhACs enables the detection of multiple drugs in a single analysis, compared to sensing each drug individually. This approach allows for enhanced data integration and the ability to correlate variables in real-time (S.-N. Li et al., 2025; Li et al., 2020). Additionally, simultaneous analyte sensing is cost-effective, eliminating the need for multiple electrochemical sensors, thereby reducing equipment and maintenance costs.

Simultaneously, engineered metal sulphide/oxides nanoparticles (NPs), including Bi_2S_3, CdS, ZnS, CuS, ZnO, SnO_2, Fe_3O_4, and $CeVO_4$ immobilized onto the working electrode

surface could significantly enhance the detection parameters of the electrochemical sensors due to the unique characteristics of nanostructures, for instance high surface area, tuneable electronic characteristics, and excellent catalytic activity (Morozov et al., 2025; Ouyang et al., 2025; Savari et al., 2025). Particularly, Bi_2S_3 and ZnO nanomaterials exhibit remarkable electrocatalytic characteristics, including strong electrocatalytic functionalities, high electrical conductivity, a wide electrochemical window, and an ability to efficiently interact with target analytes (Bhan and Golder, 2024; Nehru et al., 2024). When ZnO is embedded into Bi_2S_3, the resulting Bi_2S_3-ZnO nanocomposites exhibit enhanced characteristics, including improved charge transfer, increased electron conductivity, excellent biocompatibility, and superior stability due to their synergistic effects for individual and simultaneous electrochemical sensing of PBZ and SMZ. Furthermore, recently reported studies have shown innovative applications of the Bi_2S_3-ZnO nanocomposites across numerous fields, including gas sensors, photocatalytic degradation of antibiotics, organic dye degradation, photoelectrochemical performance, and water splitting (Mohammed and Ali, 2023; Palma Soto et al., 2024; Sadhasivam et al., 2024; Yao et al., 2024). However, the reported synthesis of the Bi_2S_3-ZnO nanocomposites utilizes environmentally intensive chemicals.

In recent years, the synthesis of bio-based nanocomposites using bio-extracts of plants and their derivatives has attracted increasing attention as an environmentally friendly alternative to conventional methods (Gawal and Golder, 2025). The phytochemicals present in the plant extracts could be exploited for the synthesis of stable and tailor-made nanostructures (Bhan and Kumar Golder, 2023). Additionally, using plant extracts could reduce the synthesis cost of nanocomposites and eliminate the use of environmentally intensive chemicals compared to conventional synthesis methods (Nadar and Sellappan, 2025). Moreover, the Bi_2S_3-ZnO nanocomposites synthesized using a bio-based route for the individual and simultaneous sensing of PBZ and SMZ exhibited several advantages, including a reduced environmental impact, enhanced sustainability, and improved biocompatibility and hydrophilicity.

Herein, we have synthesized bio-based Bi_2S_3-ZnO nanocomposites using the phytochemicals derived from *Sechium edule* fruit extract. These phytochemicals could facilitate the development of stable Bi_2S_3-ZnO nanocomposites. Subsequently, the bio-based synthesized Bi_2S_3-ZnO nanocomposites were functionalized onto a glassy carbon electrode (GCE) using a Nafion binding agent for the dual-analyte selective and simultaneous electrocatalytic sensing of PBZ and SMZ through the square wave voltammetry (SWV) technique. The proposed simultaneous detection platform was tested in environmental matrices to evaluate its practical implementation. The bio-based synthesis and comprehensive

characterizations of the Bi_2S_3-ZnO nanocomposites, along with its utilization as an electrocatalyst for the selective and simultaneous sensing of PBZ and SMZ using SWV, are documented for the first time. Additionally, this is the first study to report the simultaneous electrochemical sensing of PBZ and SMZ.

8.2. Result and discussions

8.2.1. Characterizations of ZnO(bio), Bi_2S_3(bio), and Bi_2S_3-ZnO(bio)

8.2.1.1 *Morphology and elemental analyses*

Figs. 8.1a, 8.1b, and 8.1c show the FESEM images of Bi_2S_3(bio), ZnO(bio), and Bi_2S_3-ZnO(bio), respectively. The control synthesis of Bi_2S_3(bio) and ZnO(bio) nanostructures were done with DI water instead of bio-extract under similar conditions and are denoted as Bi_2S_3(control) (Fig. 8.1d) and ZnO(control) (Fig. 8.1e), respectively. The Bi_2S_3(bio) and ZnO(bio) exhibited distinct rod- and nearly spherical-shaped morphology with an average rod length of 1267.8 nm and particle size of 54.9 nm, respectively. Bi_2S_3-ZnO(bio) demonstrates the ZnO(bio) embedded on ~1409.7 nm Bi_2S_3(bio) nanorods. Figs. 8.1d and 8.1e show the FESEM images of Bi_2S_3(bio) and ZnO(bio), respectively, clearly illustrating the role of the bio-extract (Chowdhury et al., 2023; Elavarasan et al., 2017).

Figs. 8.1f and 8.1g display the FETEM and HRTEM (inset SAED pattern and magnified image of HRTEM) micrographs of Bi_2S_3-ZnO(bio), respectively. The FETEM micrograph reveals ZnO(bio) nanostructures embedded on the Bi_2S_3(bio) nanorods, consistent with the FESEM image of Bi_2S_3-ZnO(bio) (Fig. 8.1c). The HRTEM image of Bi_2S_3-ZnO(bio) illustrates the lattice-fringes with a d-spacing of 0.281 nm, corresponding to (221) and (100) planes of Bi_2S_3(bio) and ZnO(bio), respectively. Furthermore, the SAED pattern (as shown in the inset of Fig. 8.1g) shows the polycrystalline nature of Bi_2S_3-ZnO(bio), which aligns with the XRD analysis (AL-Zahrani et al., 2020).

Fig. 8.1h presents the elemental study of Bi_2S_3-ZnO(bio), with the weight% of Bi, S, Zn, and O determined to be 50.37, 10.78, 11.70, and 27.15%, respectively. Similarly, the atomic% of Bi, S, Zn, and O were 9.83, 13.70, 7.29, and 69.18%, respectively (inset of Fig. 8.1h).

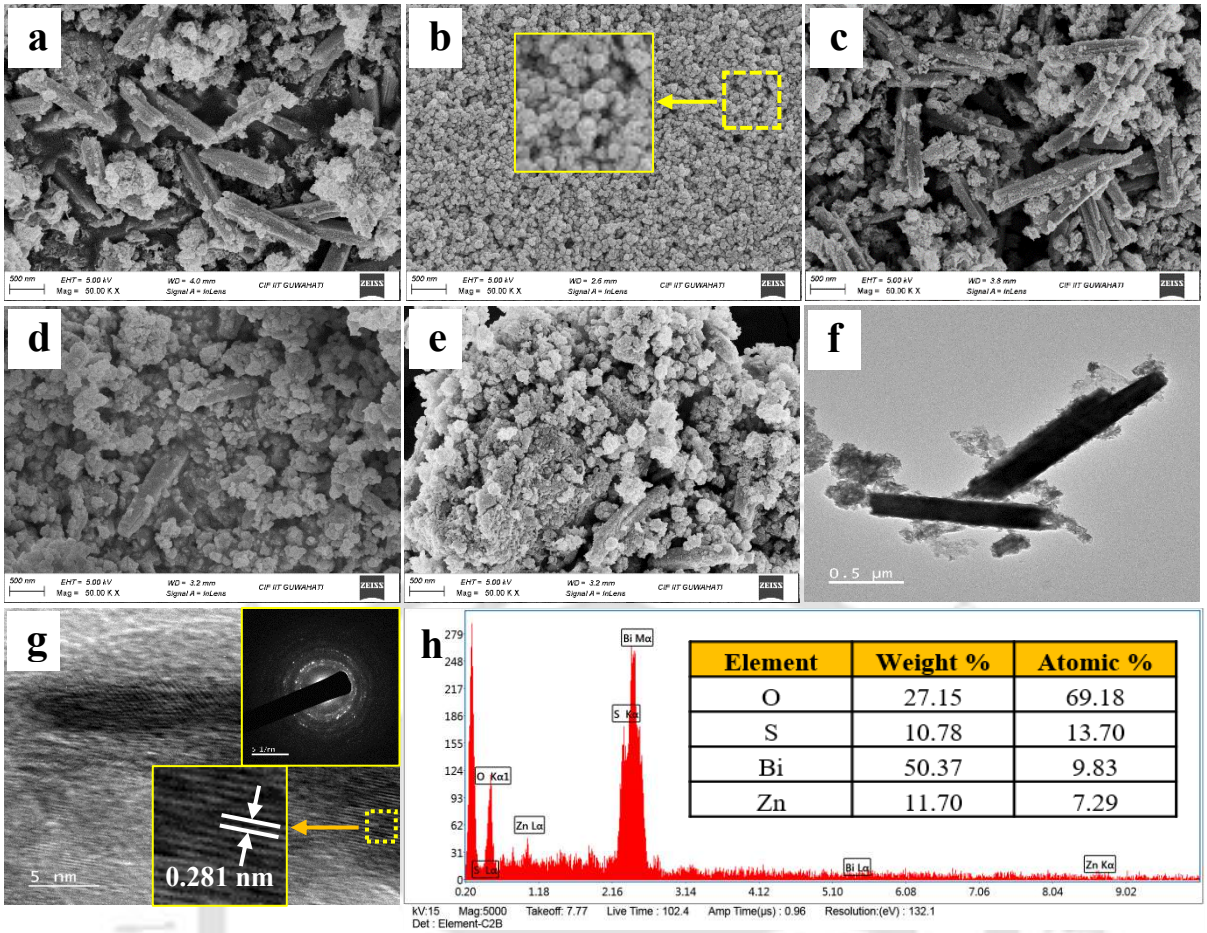

Element	Weight %	Atomic %
O	27.15	69.18
S	10.78	13.70
Bi	50.37	9.83
Zn	11.70	7.29

Figure 8.1: FESEM images of (a) Bi_2S_3(bio), (b) ZnO(bio) (inset magnified image), (c) Bi_2S_3-ZnO(bio), (d) Bi_2S_3(control), and (e) ZnO(control). (f) and (g) FETEM and HRTEM (inset SAED pattern with magnified image of HRTEM) micrographs of Bi_2S_3-ZnO(bio), respectively. (h) Elemental analysis of Bi_2S_3-ZnO(bio).

8.2.1.2 *XRD analysis*

Fig. 8.2 shows the XRD patterns of Bi_2S_3(bio), ZnO(bio), Bi_2S_3-ZnO(bio), Bi_2S_3(control), and ZnO(control), along with the JCPDS patterns of Bi_2S_3 and ZnO. The characteristics peaks observed at 2θ = 25.9° (310), 28.6° (230), 31.9° (221), 41.4° (510), 45.8° (002), 53.4° (531), and 67.1° (470) correspond to the crystalline phases of Bi_2S_3(bio) (JCPDS Card No. 01-089-8963). Similarly, the peaks at 2θ = 31.6° (100), 34.3° (002), 36.1° (101), 47.4° (102), 56.4° (110), 62.8° (103), 66.3° (200), 67.8° (112), and 68.9° (201) confirm the phases of ZnO(bio) (JCPDS Card No. 00-005-0664). Eqs. 8.1-8.3 were employed to determine the crystal size (d, nm), lattice strain (ε), and dislocation density (δ, lines/nm^2) (Kumar and Das, 2025; Ravi and Golder, 2025, 2023a).

$$d = \frac{k\lambda}{\beta \cos\theta_B} \quad (8.1)$$

$$\varepsilon = \frac{\beta}{4\mathrm{Tan}\theta_B} \tag{8.2}$$

$$\delta = \frac{1}{d^2} \tag{8.3}$$

Where β, θ_B, λ, and k are the full width at half maximum (FWHM), Bragg angle, the X-ray wavelength (0.154 nm), and the shape factor (0.94), respectively. The XRD diffraction parameters, including crystal size, dislocation density, and lattice strain of Bi_2S_3(bio), ZnO(bio), Bi_2S_3-ZnO(bio), Bi_2S_3(control), and ZnO(control) were determined corresponding to the diffraction peaks at 2θ = 31.9° (221) for Bi_2S_3 and 2θ = 31.6° (100) for ZnO, as summarized in Table 8.1. Bi_2S_3-ZnO(bio) exhibited a decrease in the crystallite size and an increase in dislocation density and lattice strain compared to other synthesized nanostructures. The crystal size of Bi_2S_3-ZnO(bio) decreased, attributed to the peak broadening, which originated from ZnO and Bi_2S_3 peak merging. The increase in dislocation density and lattice strain is ascribed to generating more defects and lattice mismatch (creating interfacial strain) between ZnO and Bi_2S_3, respectively (Bhan and Golder, 2024). Therefore, the smaller crystal size provided more active sites and a larger surface area, whereas higher lattice strain and dislocation density facilitated enhanced charge transport kinetics, resulting in the increased sensitivity of the proposed sensing platform (Bhan and Kumar Golder, 2023).

Table 8.1: XRD crystallographic parameters of Bi_2S_3(bio), ZnO(bio), Bi_2S_3-ZnO(bio), Bi_2S_3(control), and ZnO(control).

Sample code	Peak position (2θ, degree)	Crystal size (nm)	d-spacing (Å)	Lattice strain (ε)	Dislocation density (Lines/nm^2)
Bi_2S_3(bio)	31.94	18.35	2.80	7.16×10^{-3}	2.97×10^{-3}
ZnO(bio)	31.60	75.58	2.83	1.76×10^{-3}	0.18×10^{-3}
Bi_2S_3-ZnO(bio)	31.86	14.43	2.81	9.14×10^{-3}	4.80×10^{-3}
Bi_2S_3(control)	31.77	42.83	2.81	3.09×10^{-3}	0.55×10^{-3}
ZnO(control)	31.69	55.83	2.82	2.38×10^{-3}	0.32×10^{-3}

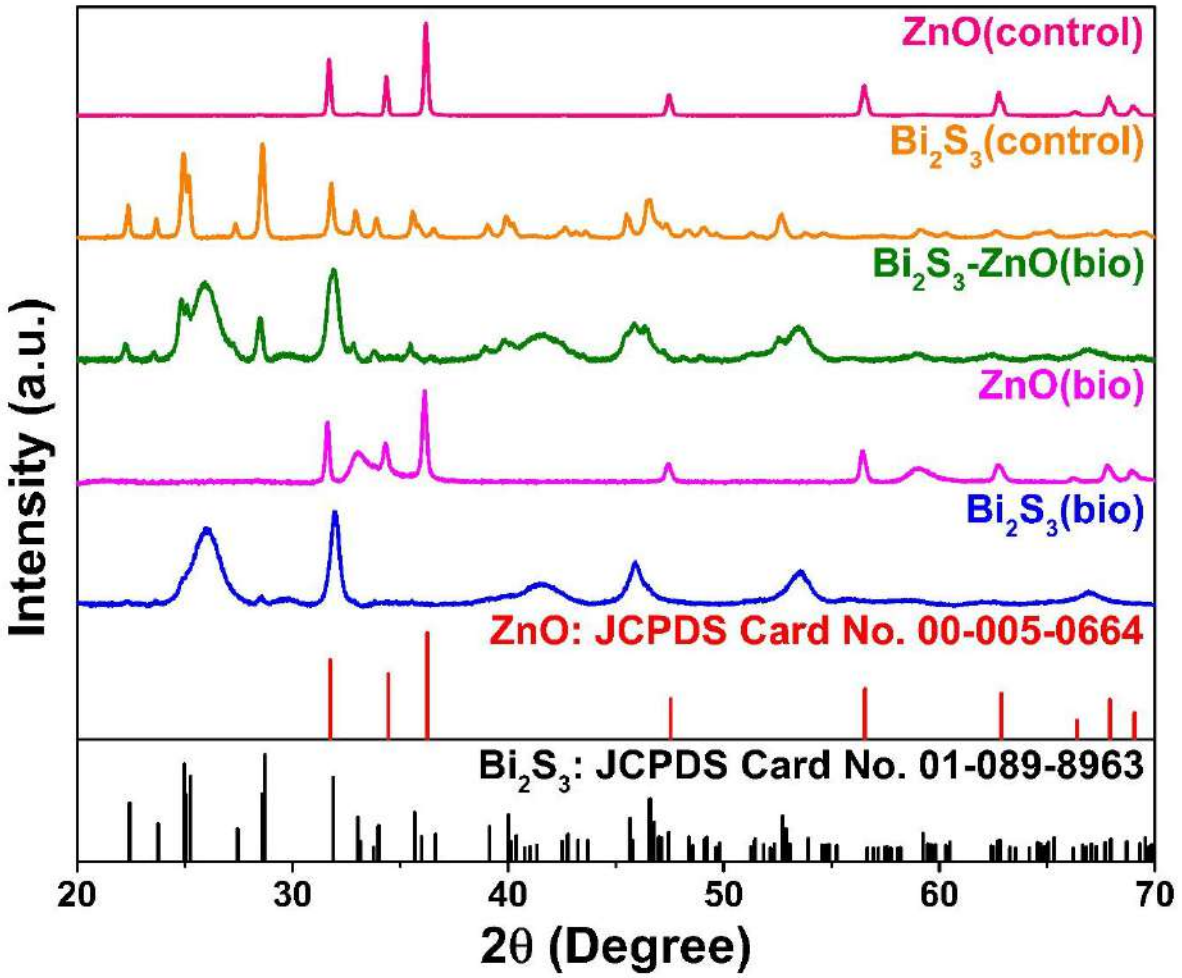

Figure 8.2: XRD patterns of Bi_2S_3(bio), ZnO(bio), Bi_2S_3-ZnO(bio), Bi_2S_3(control), and ZnO(control), along with the corresponding JCPDS patterns of Bi_2S_3 and ZnO.

8.2.1.3 *XPS analysis*

The XPS survey spectrum (Fig. 8.3a) of Bi_2S_3-ZnO(bio) indicates the existence of Bi, S, Zn, O, and C. The presence of C could be attributed the reaction precursors used during the synthesis process and adsorption of surrounding gases, which not detect in EDX study (Fig. 8.1h). The high-resolution spectra of Bi_2S_3-ZnO(bio) in the Zn 2p, O 1s, Bi 4f and S 2p region were analyzed to investigate the chemical state of ZnO and Bi_2S_3 (Figs. 8.3b-8.3d). The Bi 4f spectra of Bi_2S_3-ZnO(bio) reveal two prominent peaks at 158.35 and 163.71 eV, corresponding to the Bi $4f_{7/2}$ and $4f_{5/2}$ chemical states, respectively (Fig. 8.3b), indicating the presence of Bi^{3+} in Bi_2S_3 (AL-Zahrani et al., 2020). In the Bi 4f and S 2p regions, the peaks at 159.17 and 160.96 are credited to the chemical states of S $2p_{3/2}$ and S $2p_{1/2}$, respectively (Fig. 8.3b), revealing the existence of S^{2-} in Bi_2S_3 (Al-Zahrani et al., 2020). Similarly, the Zn 2p spectrum of Bi_2S_3-ZnO(bio) showed two prominent peaks at 1021.41 and 1044.51 eV, attributed to the spin-

orbital interaction causing the separation of Zn $2p_{3/2}$ and $2p_{1/2}$, respectively (Fig. 8.3c), confirming the presence of Zn^{2+} in ZnO (Dan et al., 2023). The predominant peak at 530.57 eV corresponds to the O 1s regime, as shown in Fig. 8.3d. In the O 1s spectrum, the peaks at 530.47 eV representing lattice oxygen, while the peak at 531.78 eV is attributed to the surface-adsorbed oxygen, respectively. The presence of an additional peak at 533.41 eV could be due to bio-analyte adsorption during the synthesis process (Ravi and Golder, 2023b). Therefore, the increase in the surface-adsorbed oxygen in Bi_2S_3-ZnO(bio) enhances the sensitivity of the developed sensing platform by improving the adsorption of target analyte molecules (Bhan and Kumar Golder, 2023).

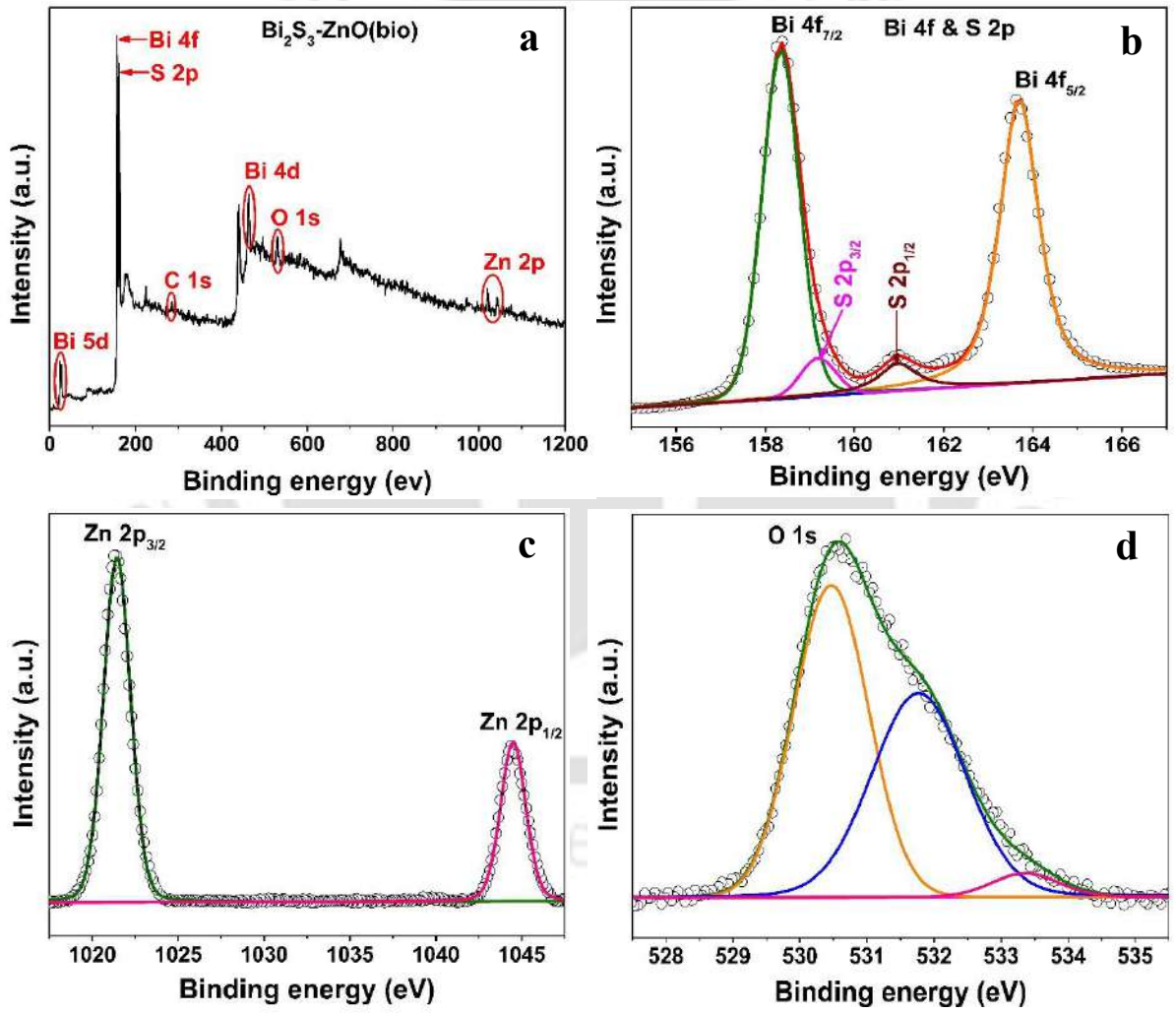

Figure 8.3: XPS survey spectrum of (a) Bi_2S_3-ZnO(bio) and High-resolution spectra in (b) Bi 4f and S 2p, (c) Zn 2p, and (d) O 1s region of Bi_2S_3-ZnO(bio).

8.2.2. Electrochemical studies of kinetic electrodes

8.2.2.1 *EIS analysis*

To investigate the electron transport resistance of kinetic electrodes, including bare/GCE, Bi_2S_3(bio)/GCE, ZnO(bio)/GCE, and Bi_2S_3-ZnO(bio)/GCE, EIS analysis was conducted using 1mM $Ru(NH_3)_6Cl_2$ as a standard probe in a 0.1 M KCl electrolyte with a frequency range from 10^{-2} to 10^5 Hz and 25 °C (Fig. 8.4a). The electron transfer resistance (R_p), electrolyte resistance (R_s), and constant phase element (CPE) were determined by the fitting and simulating the data obtained from the Nyquist plot in the Randle's equivalent circuit (inset in Fig. 8.4a) (Bhan et al., 2025b). The parameters obtained from the Nyquist plot are tabulated in Table 8.2. The diameter of the truncated semicircle in the Nyquist plot is directly related to the R_p, with a larger semicircle diameter indicating a higher R_p of the kinetic electrode (Kumar et al., 2025; Kumar and Das, 2023). The R_p values for bare/GCE, Bi_2S_3(bio)/GCE, ZnO(bio)/GCE, and Bi_2S_3-ZnO(bio)/GCE were 3190, 318, 604, and 173 kΩ, respectively. A significant decrease in R_p was observed for Bi_2S_3-ZnO(bio)/GCE, showing a 94.6, 45.6, and 71.4% reduction compared to bare/GCE, Bi_2S_3(bio)/GCE, and ZnO(bio)/GCE, respectively. The reduction in R_p indicates improved interaction of the Bi_2S_3-ZnO(bio) nanocomposites with the targeted analyte at the electrode-electrolyte interface, faster charge transport kinetics, and higher conductivity of the kinetic electrode (Teker et al., 2025). The values of R_s for bare/GCE, Bi_2S_3(bio)/GCE, ZnO(bio)/GCE, and Bi_2S_3-ZnO(bio)/GCE were determined to be 0.130, 0.141, 0.142, and 0.136 kΩ, respectively. The change in R_s values compared to the R_p values of the kinetic electrodes was insignificant (Kumar and Das, 2024). A slight variation in the CPE of the kinetic electrodes was observed, which could be due to the variations in the conductivity of the kinetic electrodes (Bhan and Golder, 2024).

The apparent rate constant (K_{app}, cm/s) of the kinetic electrodes, such as bare/GCE, Bi_2S_3(bio)/GCE, ZnO(bio)/GCE, and Bi_2S_3-ZnO(bio)/GCE, was calculated using Eq. 8.4 (Lazanas and Prodromidis, 2023).

$$K_{app} = \frac{RT}{n^2F^2A_eR_pC_0} \tag{8.4}$$

Where R, T, n, F, A_e, R_p, and C_0 represents the gas constant (8.314 J/mol.K), the reaction temperature (K), the number of electrons participated in the redox event (n=1), Faraday's constant (96485 C/mol), electroactive surface area (cm^2), electron transfer resistance (Ω), and concentration of the redox specie (mol/cm^3), respectively. K_{app} for bare/GCE, Bi_2S_3(bio)/GCE, ZnO(bio)/GCE, and Bi_2S_3-ZnO(bio)/GCE were found to be 2.14×10^{-6}, 9.85×10^{-6}, 5.80×10^{-6}, and 1.45×10^{-5} cm/s, respectively, as presented in Table 8.2. Bi_2S_3-ZnO(bio)/GCE exhibited

6.8-, 1.5-, and 2.5-folds higher K_{app} compared to bare/GCE, Bi_2S_3(bio)/GCE, and ZnO(bio)/GCE, respectively. Furthermore, Bi_2S_3-ZnO(bio)/GCE achieved the highest K_{app} (1.45×10^{-5} cm/s), corresponding to the lowest R_p (173 kΩ) and the largest A_e (0.106 cm^2), indicating its superior electron-transfer kinetics compared to the bare/GCE, Bi_2S_3(bio)/GCE, and ZnO(bio)/GCE.

8.2.2.2 *Electroactive surface area of kinetic electrodes*

To determine the electroactive surface area (A_e) of the bare/GCE, Bi_2S_3(bio)/GCE, ZnO(bio)/GCE, and Bi_2S_3-ZnO(bio)/GCE, CV was conducted using 1mM $Ru(NH_3)_6Cl_2$ as a standard probe in a 0.1 M KCl electrolyte at varying scan rates (5-500 mV/s) and 25 °C, as shown in Figs. 8.4b, 8.4c, 8.4d, and 8.4e. The A_e (cm^2) of the kinetic electrodes were investigated thru the Randles-Sevcik equation (Eq. 8.5) (Zhang et al., 2023).

$$I_{Pa} = (2.69 \times 10^5)n^{3/2}A_eD^{1/2}\upsilon^{1/2}C_0 \quad (8.5)$$

Where I_{pa}, C_0, υ, D, and n represent the anodic peak response (A), the concentration of the standard probe (mol/cm^3), scan rate (V/s), the diffusion coefficient of the standard probe (8.43×10^{-6} cm^2/s), and the number of electrons participated in the redox reaction (n=1), respectively. The slopes of the linear plots between I_{pa} vs. $\upsilon^{0.5}$ for the bare/GCE, Bi_2S_3(bio)/GCE, ZnO(bio)/GCE, and Bi_2S_3-ZnO(bio)/GCE were determined to be 30.573 (R^2 = 0.992), 66.356 (R^2 = 0.999), 59.161 (R^2 = 0.995), and 83.123 $\mu A.V^{-1/2}.s^{1/2}$ (R^2 =0.991), respectively (Fig. 8.4f). The A_e for the bare/GCE, Bi_2S_3(bio)/GCE, ZnO(bio)/GCE, and Bi_2S_3-ZnO(bio)/GCE were 0.039, 0.085, 0.076, 0.106 cm^2, respectively (Table 8.2). Therefore, the bio-based synthesis of Bi_2S_3-ZnO(bio)/GCE exhibited a higher A_e for the selective and simultaneous electrocatalytic detection of PBZ and SMZ, which is about 2.7-, 1.2-, and 1.4-folds higher compared to the bare/GCE, Bi_2S_3(bio)/GCE, ZnO(bio)/GCE, respectively. The increased A_e for Bi_2S_3-ZnO(bio)/GCE provides more binding sites for the sensing of PBZ and SMZ, which could enhance the sensor's sensitivity (Bhan and Kumar Golder, 2023).

Table 8.2: EIS parameters and electroactive surface area of kinetic electrodes.

Working electrodes	R_s (kΩ)	R_p (kΩ)	CPE (μMho)	Chi-square of fitting (χ^2) × 10^3	$K_{app}\times10^5$ (cm/s)	A_e (cm^2)
Bare/GCE	0.130	3190	14.2	1.31	0.214	0.039
Bi_2S_3(bio)/GCE	0.141	318	21.7	3.46	0.985	0.085
ZnO(bio)/GCE	0.142	604	22.9	2.15	0.580	0.076
Bi_2S_3-ZnO(bio)/GCE	0.136	173	23.3	1.63	1.452	0.106

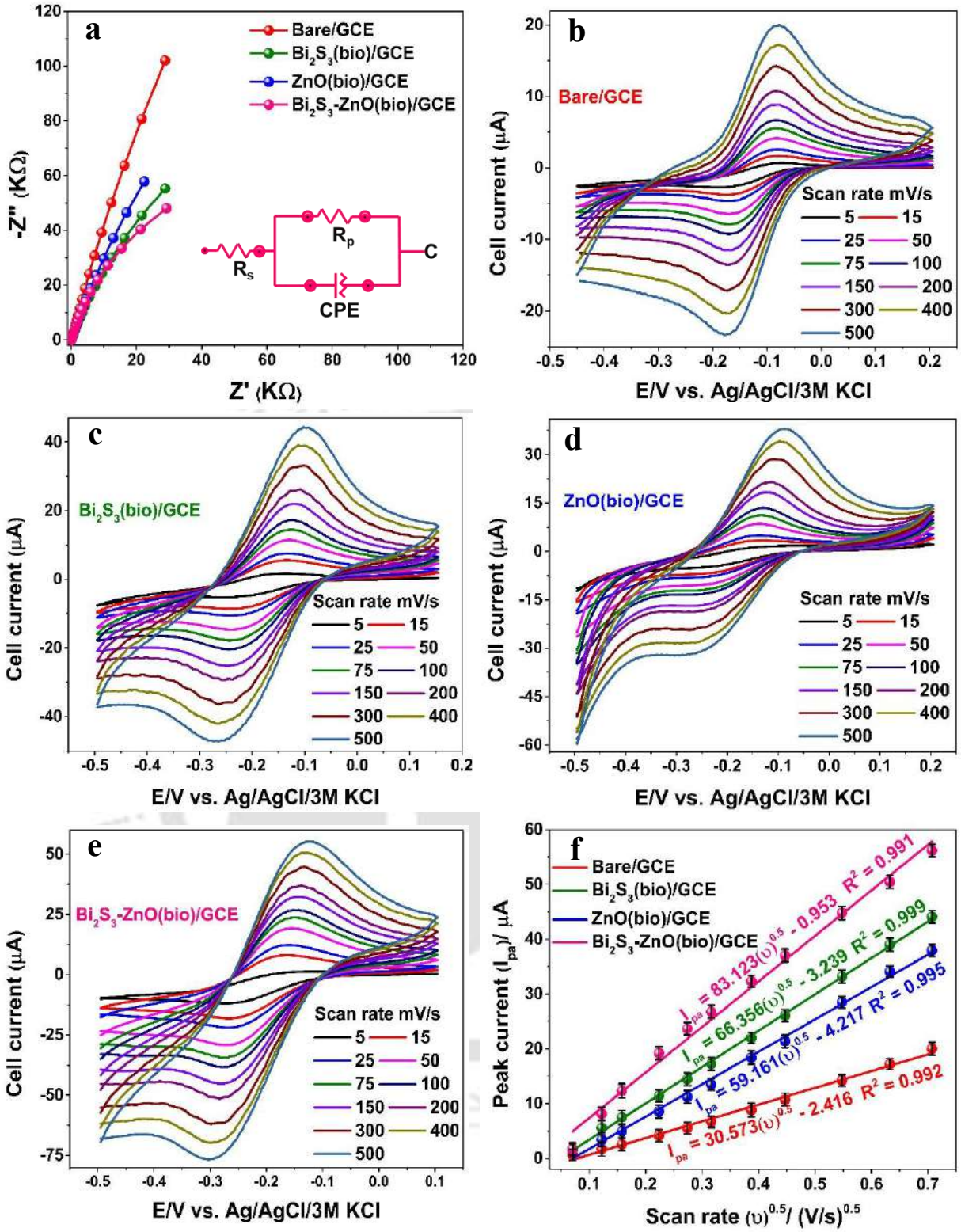

Figure 8.4: (a) EIS spectra for investigating the electron transport resistance of bare/GCE, Bi_2S_3(bio)/GCE, ZnO(bio)/GCE, and Bi_2S_3-ZnO(bio)/GCE with the Randles equivalent circuit (inset), (b), (c), (d), and (e) CVs of bare/GCE, Bi_2S_3(bio)/GCE, ZnO(bio)/GCE, and Bi_2S_3-ZnO(bio)/GCE recorded at various scan rates (5-500 mV/s), and (f) I_{pa} vs. $\upsilon^{0.5}$ for bare/GCE,

Bi_2S_3(bio)/GCE, ZnO(bio)/GCE, and Bi_2S_3-ZnO(bio)/GCE. Reaction conditions: 1 mM $Ru(NH_3)_6Cl_2$ was used as a standard probe in 0.1 M KCl electrolyte at 25 °C.

8.2.2.3 *Comparison of anodic and cathodic peak currents using different kinetic electrodes*

To compare the anodic and cathodic peak currents obtained using various kinetic electrodes, namely Bare/GCE, Bi_2S_3(bio)/GCE, ZnO(bio)/GCE, and Bi_2S_3-ZnO(bio)/GCE, CV was performed with 1mM $Ru(NH_3)_6Cl_2$ as a standard probe in a KCl electrolyte (0.1 M, 25 °C) and a fixed scan rate of 50 mV/s (Fig. 8.5a). The cathodic peak current (I_{pc}) for the kinetic electrodes increases more than the anodic peak current (Fig. 8.5b), leading to a deviation from the reversibility (I_{pa}/I_{pc} = 1). It could be attributed to enhanced electron-transfer kinetics and improved electrocatalytic activity provided by catalyst particles. The anodic peak current of Bi_2S_3-ZnO(bio)/GCE was about 76.5, 39.8, and 59.1% higher than that of bare/GCE, Bi_2S_3(bio)/GCE, ZnO(bio)/GCE, respectively. Similarly, the cathodic peak current of Bi_2S_3-ZnO(bio)/GCE was almost 79.3, 49.2, and 68.5% higher than that of bare/GCE, Bi_2S_3(bio)/GCE, ZnO(bio)/GCE, respectively (Fig. 8.5b). The synergistic integration of Bi_2S_3(bio) and ZnO(bio) in Bi_2S_3-ZnO(bio)/GCE enhances the charge transfer characteristics, surface area, density of active sites, and facilitates adsorption of the redox species, thereby promoting the cathodic process more efficiently than the anodic process. It results in a higher cathodic peak current. Furthermore, the deviation from the reversibility is more in the case of Bi_2S_3-ZnO(bio)/GCE due to the smallest charge transfer resistance, highest conductivity, and largest electroactive surface area as compared to bare/GCE, Bi_2S_3(bio)/GCE, and ZnO(bio)/GCE. Therefore, Bi_2S_3-ZnO(bio)/GCE was selected for further electrochemical studies. Such asymmetry in peak currents is commonly observed in surface-modified electrodes and is associated with kinetically favoured redox events (Lei et al., 2024; Xin et al., 2020).

8.2.3. Optimization of PBZ and SMZ sensing parameters

8.2.3.1 *Effect of pH*

To study the effect of the supporting electrolyte pH (0.1 M PBS) during the electrochemical monitoring of PBZ/SMZ, CV was performed using Bi_2S_3-ZnO(bio)/GCE at varying pH (3-9) of 0.1 M PBS (25 °C) with a 40 µM concentration of PBZ/SMZ and a scan speed of 50 mV/s. Figs. 8.5c and 8.5d demonstrate a reduction in the anodic peak potential (E_p) with an increase in pH from 3-9, indicating the involvement of protons during the PBZ and SMZ sensing reaction (Malode et al., 2020). The Nernstian equation (Eq. 8.6) was employed

to determine the ratio of electrons to protons (n/m) involved in the electrochemical sensing of PBZ and SMZ (Manivannan et al., 2019).

$$\frac{dE_p}{dpH} = -2.303\frac{mRT}{nF} \quad (8.6)$$

Where R, F, and T represent the gas constant (8.314 J/mol.K), Faraday's constant (96485 C/mol), and the reaction temperature (K), respectively. The slopes of the linear plots between E_p vs. pH for PBZ and SMZ detection were found to be -0.047 and -0.049 V per unit pH, respectively (Fig. 8.5e). The n/m ratio was determined by substituting the slope values into Eq. 8.6. The n/m for PBZ and SMZ were found to be 1.26 and 1.21, respectively, both approximately equal to 1, indicating an equivalent number of electrons and protons involved in PBZ and SMZ sensing reactions (Bhan et al., 2025b). Furthermore, at pH 5, the anodic peak current for PBZ and SMZ was observed to be maximum, indicating that the sensing of PBZ and SMZ is most suitable in an acidic medium (Fig. 8.5f). Therefore, pH 5 was selected for subsequent experiments.

8.2.3.2 *Optimization of deposition parameters*

To examine the effect of D_P and D_T for electrochemical sensing of PBZ and SMZ, SWV was performed using Bi_2S_3-ZnO(bio)/GCE in 0.1 M PBS (pH 5) at a fixed concentration (40 µM) of PBZ/SMZ (Figs. 8.6a-8.6d). The optimized D_P and D_T could significantly enhance the sensitivity of the Bi_2S_3-ZnO(bio)/GCE for individual and simultaneous PBZ and SMZ sensing. It was observed that the peak response of PBZ and SMZ steadily risen from D_P of 0 to -0.4 V at D_T of 60 s, which could be due to the accumulation of PBZ/SMZ ions at the Bi_2S_3-ZnO(bio)/GCE surface (Bhan et al., 2025b). After D_P of -0.4 V, the anodic peak current was decreased, which was owing to the H_2 gas evaluation (Fig. 8.6e) (Gumpu et al., 2017). Therefore, a D_P of -0.4 V was selected for electrochemical detection of PBZ and SMZ.

Figs. 8.6c and 8.6d illustrate the effect of D_T on the peak response of PBZ and SMZ using a Bi_2S_3-ZnO(bio)/GCE at a D_P of -0.4 V. The anodic peak response for both PBZ and SMZ gradually improved as the D_T risen from 20 to 60 s, credited to the accumulation of PBZ/SMZ ions over the Bi_2S_3-ZnO(bio)/GCE surface (Bagheri et al., 2013). Beyond a D_T of 60 s, the anodic peak response was slightly boosted, likely due to the surface saturation of the Bi_2S_3-ZnO(bio)/GCE with PBZ/SMZ ions or the establishment of an equilibrium between the PBZ/SMZ ions on the surface of Bi_2S_3-ZnO(bio)/GCE and those in the 0.1 M PBS at pH 5 (Fig. 8.6f) (Dash et al., 2020). As a result, a D_T of 60 s was selected for PBZ and SMZ sensing for ongoing experiments.

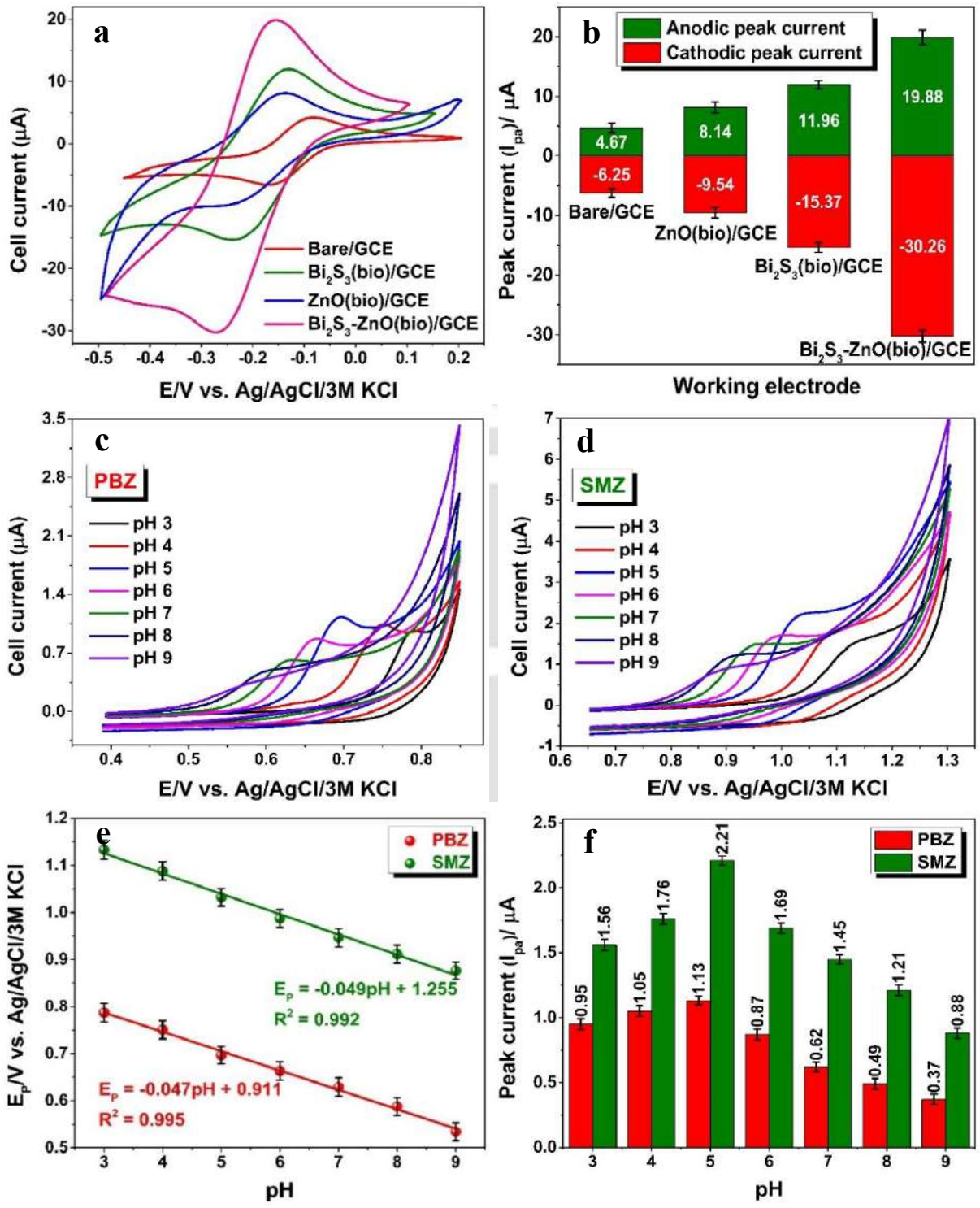

Figure 8.5: (a) CVs and (b) comparison of anodic and cathodic peak responses for bare/GCE, Bi_2S_3(bio)/GCE, ZnO(bio)/GCE, and Bi_2S_3-ZnO(bio)/GCE using 1mM $Ru(NH_3)_6Cl_2$ as a standard probe in 0.1 M KCl electrolyte (25 °C) with a fixed scan rate of 50 mV/s. CVs of (c) PBZ and (d) SMZ captured at various pH (3-9) in 0.1 M PBS (25 °C) with a fixed concentration of PBZ/SMZ (40 μM) and a scan speed of 50 mV/s using Bi_2S_3-ZnO(bio)/GCE. (e) pH vs. E_P and (f) pH vs. I_{pa}.

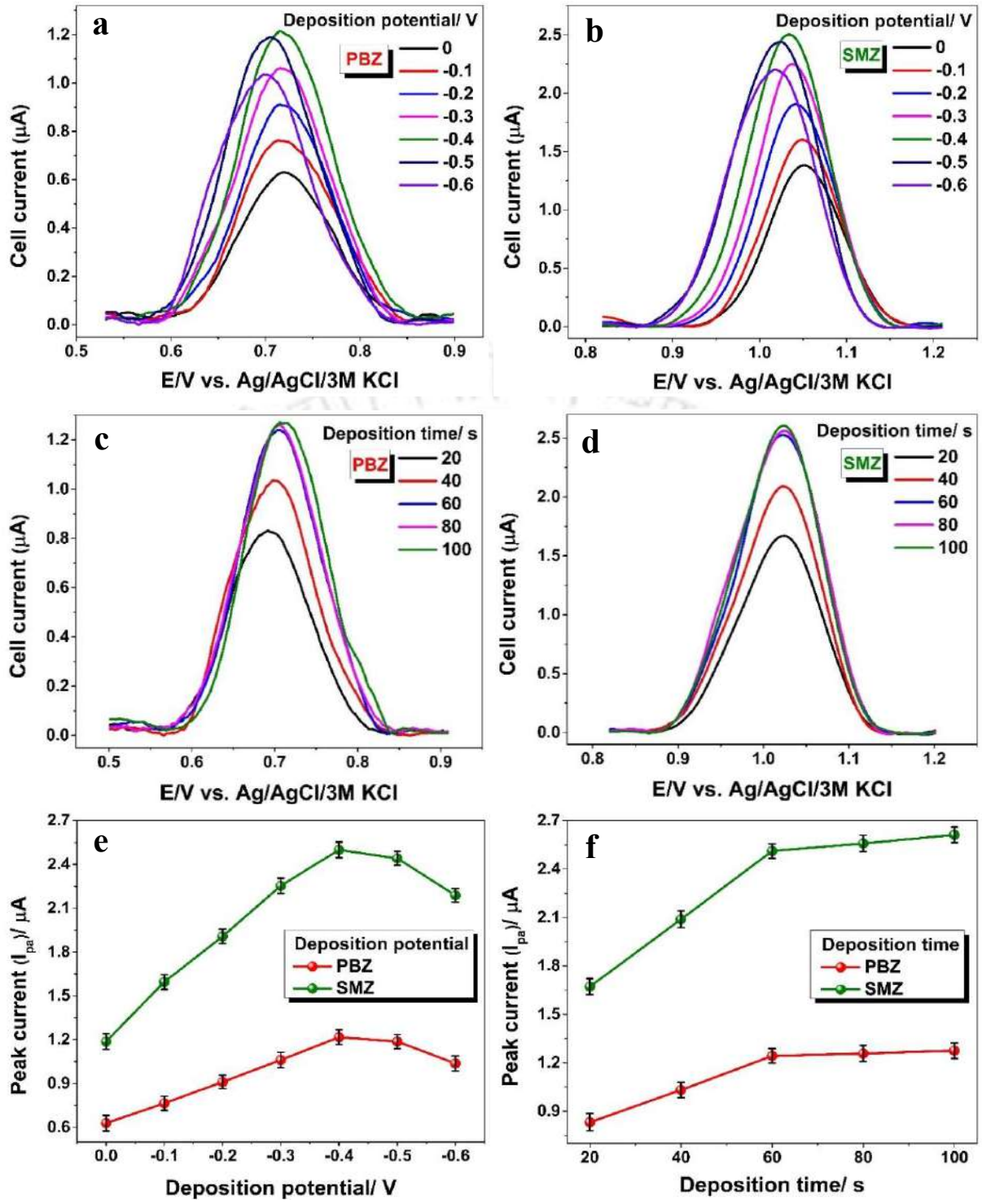

Figure 8.6: SWV of (a) PBZ and (b) SMZ conducted at various D_P from 0 to -0.6 V vs. Ag/AgCl with a D_T of 60 s. SWV of (c) PBZ and (d) SMZ was recorded at different D_T from 20 to 100 s, with D_P of -0.4 V vs. Ag/AgCl. (e) D_P vs. Anodic peak current, and (f) D_T vs. Anodic peak current. Reaction conditions: Bi_2S_3-ZnO(bio)/GCE employed as a kinetic electrode in 0.1 M PBS electrolyte at pH 5 (25 °C) containing a fixed concentration of PBZ/SMZ (40 μM).

8.2.4. Electrochemical PBZ and SMZ sensing at Bi_2S_3-ZnO(bio)/GCE

8.2.4.1 *Determination of electrokinetic parameters and surface coverage by adsorption*

CV was conducted to obtain the electrokinetic parameters and surface coverage through the PMZ (Fig. 8.7a) and SMZ (Fig. 8.7b) adsorption at various scan rates from 5-500 mV/s in 0.1 M PBS (pH 5, 25 °C) using Bi_2S_3-ZnO(bio)/GCE. Fig. 8.7c demonstrates the linear plots of I_{pa} vs. $\upsilon^{0.5}$ with slopes of 9.659 $\mu A.V^{-1/2}.s^{1/2}$ (R^2 = 0.981) for PMZ and 18.435 $\mu A.V^{-1/2}.s^{1/2}$ (R^2 = 0.982) for SMZ, respectively. This indicates the electrocatalytic detection reaction is diffusion-controlled (Dash et al., 2021). Thus, the Laviron equation (Eq. 8.7) was used to obtain electrokinetic parameters, such as the number of electrons that participated in the electrochemical sensing reaction (n) and the reaction rate constant (k^0, s^{-1}) for the diffusion-controlled event (Bhan and Kumar Golder, 2023).

$$E_p = E^0 - \frac{2.303RT}{\alpha nF}\log\frac{RTk^0}{\alpha nF} + \frac{2.303RT}{\alpha nF}\log\upsilon \quad (8.7)$$

Where E_p, E^0, and α represent the anodic peak potential (V), the standard formal potential (V), and the charge transfer coefficient (α=0.5), respectively. R, T, F, n, k^0 and υ have the same meaning as mentioned above. The E^0 was calculated by extrapolating the plot of E_p vs. υ at υ=0 using Origin software (Bhan et al., 2025a). The obtained values of E^0 were 0.655 V for PBZ and 1.015 V for SMZ. For the determination of the values of n and k^0 for PBZ and SMZ sensing, the slopes and intercepts of the E_p vs. log υ plots were equalized with Eq. 8.7. From the E_p vs. log υ plot of PBZ (Fig. 8.7d), the slope and intercept were 0.049 and 0.739 V (R^2 = 0.995), respectively. For SMZ (Fig. 8.7e), the slope and intercept were 0.052 and 1.108 V, respectively. By considering α = 0.5 and using an E^0 value of 0.655 V for PBZ sensing, the n and k^0 were calculated to be 2.41 (demonstrating the involvement of two electrons in the electrocatalytic reaction) and 0.907 s^{-1}, respectively. For SMZ detection at E^0 = 1.015 V, n and k^0 were 2.28 (representing the participation of two electrons in the reaction) and 0.721 s^{-1}, respectively.

To study the surface coverage thru the PBZ and SMZ adsorption over the surface of Bi_2S_3-ZnO(bio)/GCE, Eq. 8.8 was used (Elgrishi et al., 2018).

$$I_{pa} = \frac{n^2F^2}{4RT}A_e\,\upsilon\,\Gamma^* \quad (8.8)$$

Where Γ* represents the surface coverage through the adsorption ($mol\cdot cm^{-2}$). Γ* was obtained by equating the slopes of the I_{pa} vs. υ plot (Fig. 8.7f) with Eq. 8.8. The slopes of the linear plots (I_{pa} vs. υ) were 12.241 (R^2 = 0.989) and 23.329 $\mu A.V^{-1}.s$ (R^2 = 0.988) for PBZ and SMZ, respectively. Using A_e = 0.106 cm^2 (obtained from Eq. 8.5 and Fig. 8.4e), the values of Γ* were 2.118×10^{-11} $mol.cm^{-2}$ at n = 2.41 for PBZ and 4.509×10^{-11} $mol.cm^{-2}$ at n = 2.28 for SMZ. The obtained parameters for the sensing of PBZ and SMZ are presented in Table 8.3.

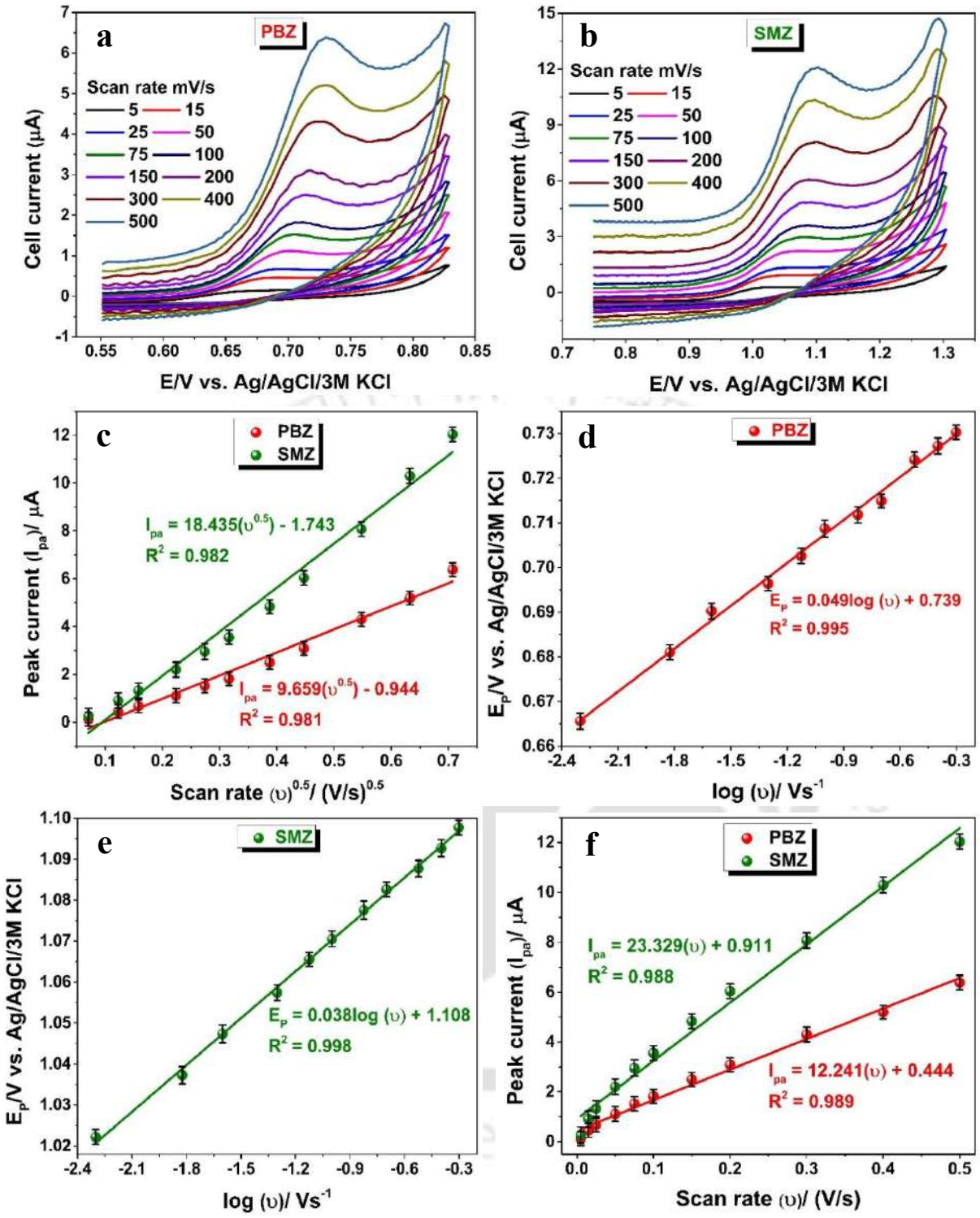

Figure 8.7: CVs of (a) PBZ and (b) SMZ at various scan speeds of (5-500 mV/s). (c) I_{pa} vs. $\upsilon^{0.5}$ for PBZ and SMZ, (d) E_p vs. log υ for PBZ, (e) E_p vs. log υ for SMZ, and (f) I_{pa} vs. υ for PBZ and SMZ. Reaction conditions: Bi_2S_3-ZnO(bio)/GCE utilized as the kinetic electrode in a 0.1 M PBS electrolyte (pH 5, 25 °C) with a fixed PBZ/SMZ concentration of 40 µM.

Table 8.3: Electrokinetic parameters and the surface coverage through the adsorption of PMZ and SMZ.

Analyte	E^0 (V)	n	k (s^{-1})	Γ* ($mol.cm^{-2}$)
PBZ	0.655	2.41	0.907	2.118×10^{-11}
SMZ	1.015	2.28	0.721	4.509×10^{-11}

8.2.4.2 *Individual and simultaneous PBZ and SMZ sensing at Bi_2S_3-ZnO(bio)/GCE*

SWV was captured using a Bi_2S_3-ZnO(bio)/GCE in 0.1 M PBS (25 °C, pH 5) across a concentration range of 0.25-120 µM for PBZ and/or SMZ at a selected D_P of -0.4 V and a D_T of 60 s, to establish the calibration curve for determine LOD, LOQ, and sensitivity. The LOD and LOQ of the fabricated Bi_2S_3-ZnO(bio)/GCE for the selective and simultaneous electrocatalytic monitoring of PBZ and SMZ were determined through Eqs. 8.9 and 8.10, respectively (Morozov et al., 2025).

$$\mathrm{LOD} = \frac{3S_d}{m} \tag{8.9}$$

$$\mathrm{LOQ} = \frac{10S_d}{m} \tag{8.10}$$

Where m and S_d are the slope of the calibration graph and blank run standard deviation. The sensitivity of the Bi_2S_3-ZnO(bio)/GCE for sensing the targeted analytes is defined as the ratio of the m to A_e (obtained from Eq. 8.5) within the concentration range of 0.25-120 µM (Bhan et al., 2025b).

Figs. 8.8a and 8.8b show the SWV of PBZ and the corresponding calibration curve at varying concentrations (0.25-120 µM). Fig. 8.8b demonstrates a linear trend between I_{pa} vs. PBZ concentration with a slope of 0.0279 $\mu A.\mu M^{-1}$ (R^2 = 0.996). For PBZ detection, the developed Bi_2S_3-ZnO(bio)/GCE displayed the LOD, LOQ, and sensitivity of 0.098 µM, 0.326 µM, and 0.263 µA. $\mu M^{-1}.cm^{-2}$ within the linear range of 0.25-120 µM.

Figs. 8.8c and 8.8d exhibit the SWV of SMZ and the associated calibration curve at different concentrations from 0.25 to 120 µM. Fig. 8.8d demonstrates a linear relationship between I_{pa} vs. SMZ concentration with a slope of 0.0526 $\mu A.\mu M^{-1}$ (R^2 = 0.995). The LOD, LOQ, and sensitivity of the Bi_2S_3-ZnO(bio)/GCE for SMZ sensing were 0.042 µM, 0.139 µM, and 0.496 µA. $\mu M^{-1}.cm^{-2}$, respectively, within the concentration range of 0.25-120 µM.

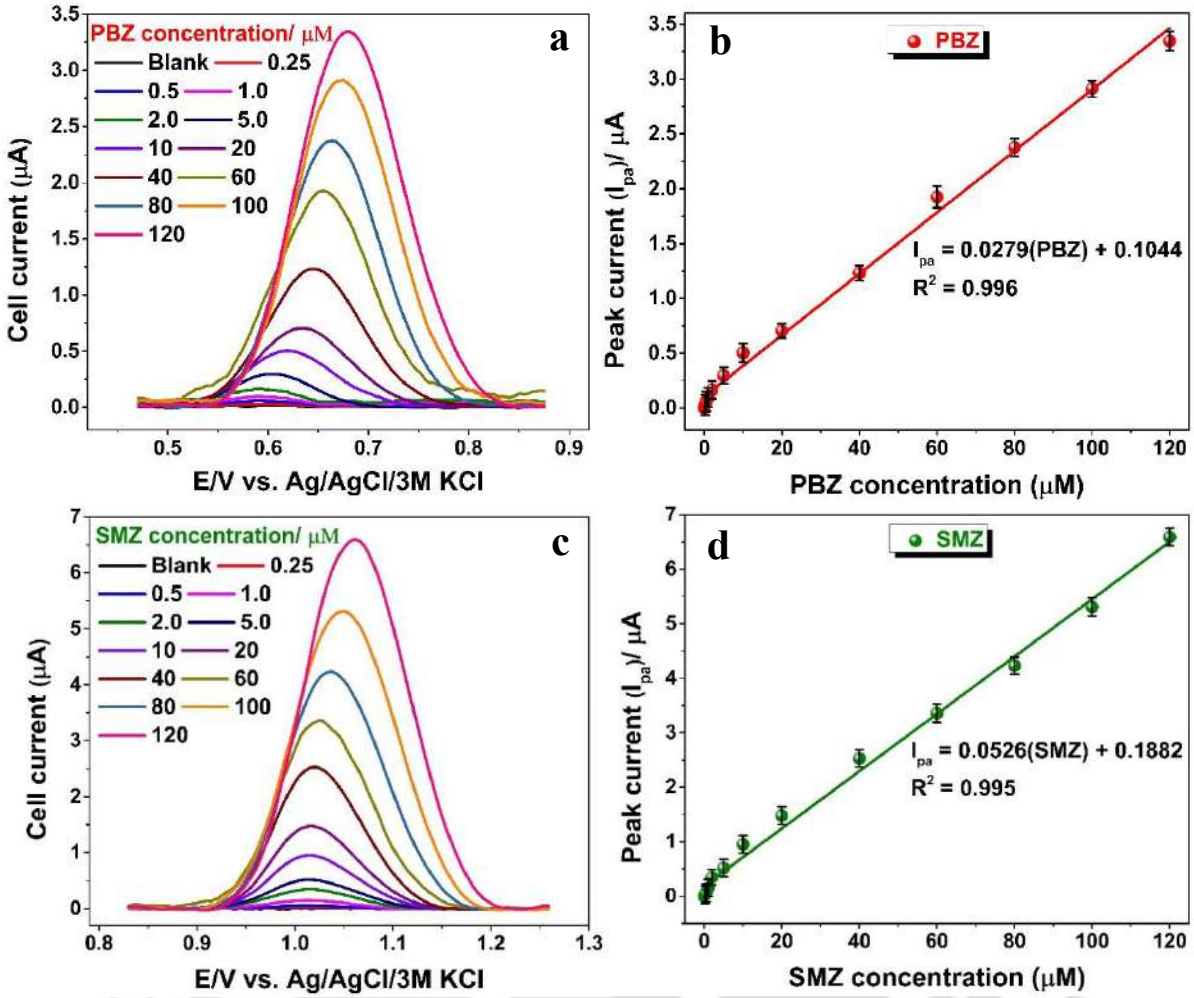

Figure 8.8: (a) SWV captured at different concentrations of PBZ (0.25-120 µM), (b) Calibration curve for PBZ determination (PBZ concentration vs. I_{pa}), (c) SWV recorded at various concentrations of SMZ (0.25-120 µM), and (d) SMZ concentration vs. I_{pa}. Reaction conditions: Bi_2S_3-ZnO(bio)/GCE employed as the kinetic electrode in a 0.1 M PBS electrolyte (pH 5, 25 °C) under optimized deposition parameters.

Fig. 8.9a demonstrates the SWV of the simultaneous electrocatalytic monitoring of PBZ and SMZ using a Bi_2S_3-ZnO(bio)/GCE in 0.1 M PBS (pH 5, 25 °C) with varying concentrations of PBZ (0.25-120 µM) and a fixed concentration of SMZ (20 µM) at optimized deposition parameters. The calibration curve for PBZ at the fixed concentration of SMZ (I_{pa} vs. PBZ concentration, Fig. 8.9b) exhibited a linear relationship with a slope of 0.0268 $\mu A.\mu M^{-1}$ (R^2 = 0.995). For PBZ detection, Bi_2S_3-ZnO(bio)/GCE displayed the LOD, LOQ, and sensitivity of 0.102 µM, 0.340 µM, and 0.253 $\mu A.\ \mu M^{-1}.cm^{-2}$ within the 0.25-120 µM linear trend at a fixed SMZ concentration.

Fig. 8.9c illustrates the SWV of the simultaneous sensing of PBZ and SMZ using a Bi_2S_3-ZnO(bio)/GCE at a fixed concentration of PBZ (40 µM) and varying concentration of SMZ (0.25-120 µM) under identical conditions. Fig. 8.9d displayed the calibration curve for SMZ at the fixed concentration of PBZ (I_{pa} vs. SMZ concentration) with a slope of 0.0446 $\mu A.\mu M^{-1}$ (R^2 = 0.994). The Bi_2S_3-ZnO(bio)/GCE revealed the LOD of 0.049 µM, LOQ of 0.164 µM, and a sensitivity of 0.421 $\mu A.\ \mu M^{-1}.cm^{-2}$ for SMZ within the linear trend at a fixed PBZ concentration.

Fig. 8.9e displays the SWV of the simultaneous electrocatalytic detection of both PBZ and SMZ using a Bi_2S_3-ZnO(bio)/GCE with varying concentrations of both PBZ and SMZ (0.25-120 µM) in 0.1 M PBS (pH 5, 25 ℃) at selected deposition parameters. The corresponding calibration plot (Fig. 8.9f) demonstrates strong linearity for both PBZ (I_{pa} vs. PBZ concentration) and SMZ (I_{pa} vs. SMZ concentration) with slopes of 0.0123 $\mu A.\mu M^{-1}$ (R^2 = 0.995) and 0.0247 $\mu A.\mu M^{-1}$ (R^2 = 0.998), respectively. The Bi_2S_3-ZnO(bio)/GCE revealed the LOD of 0.222 µM and LOQ of 0.740 µM for PBZ and LOD of 0.089 µM and LOQ of 0.296 µM for SMZ within the linear trend of 0.25-120 µM. The sensitivities were 0.116 and 0.233 $\mu A.\ \mu M^{-1}.cm^{-2}$ for PBZ and SMZ, respectively. The obtained LOD, LOQ, and sensitivity for both individual and simultaneous detection of PBZ and SMZ are summarized in Table 8.4, highlighting the excellent sensing capability of the Bi_2S_3-ZnO(bio)/GCE.

These results are attributed to the superior properties of the Bi_2S_3-ZnO(bio) nanocomposite, which arises from the synergistic integration of ZnO into Bi_2S_3. ZnO, a wide bandgap (~3.2 eV) n-type semiconductor (Kumar Jangir et al., 2017), and Bi_2S_3, a narrow bandgap (~1.3 eV) n-type/p-type semiconductor (Chowdhury et al., 2023), form a nanocomposite with favourable band alignment that facilitates efficient and directional charge transfer. ZnO contributes high catalytic activity and abundant active sites, enhancing the adsorption of target analytes, while Bi_2S_3 offers high electrical conductivity and promotes redox reactions. Therefore, the integration of the catalytic properties of ZnO(bio) with the unimpeded charge transfer characteristics of Bi_2S_3(bio) in the Bi_2S_3-ZnO(bio) nanocomposites significantly enhances the electrode surface area, charge transfer efficiency, current response, sensitivity, while also reducing the overpotential required for drug detection and enabling better peak separation for simultaneous PBZ and SMZ detection (Yuan et al., 2019).

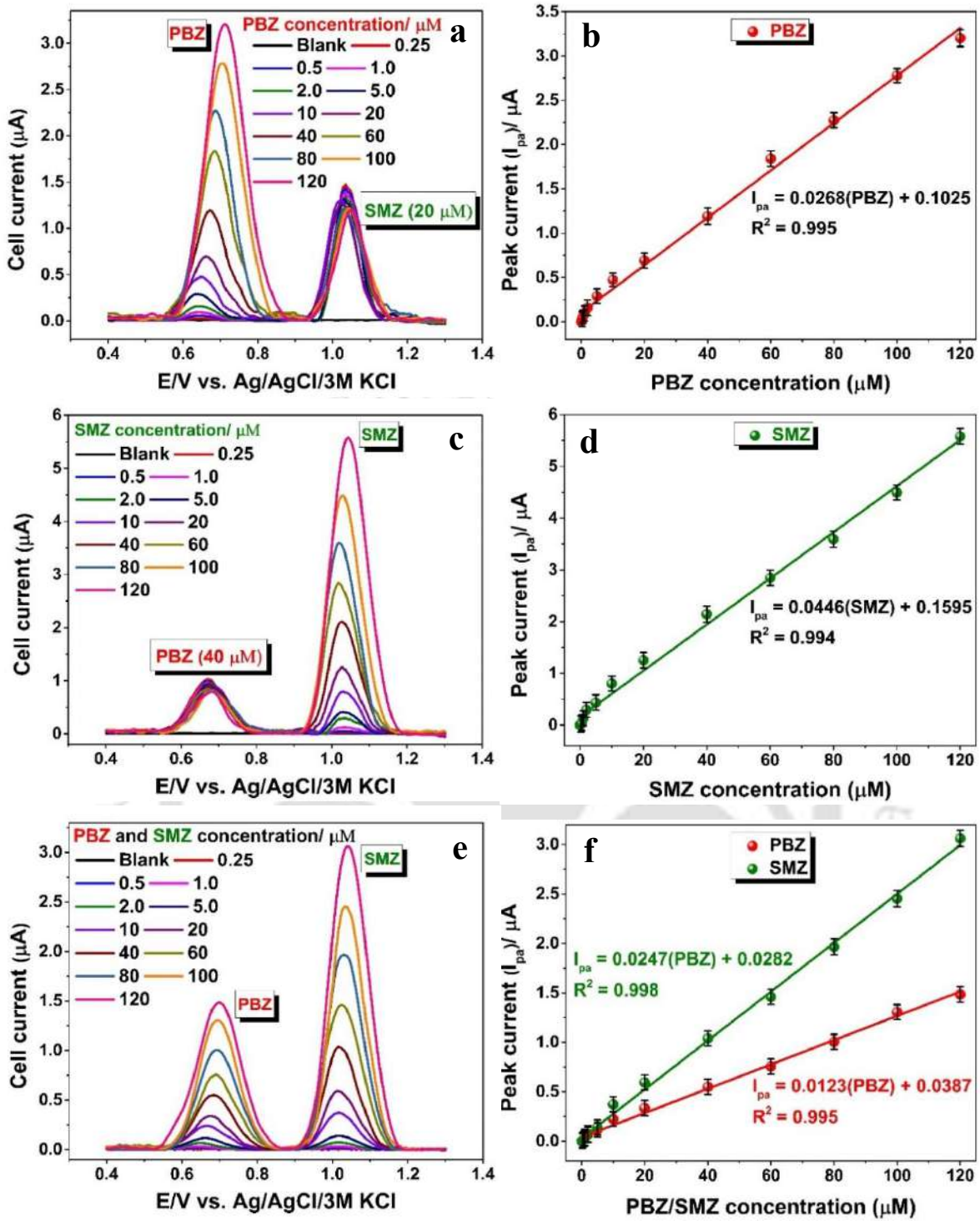

Figure 8.9: (a) SWV recorded at varying concentrations of PBZ (0.25-120 µM) in the presence of a fixed SMZ concentration (20 µM), (b) PBZ concentration vs. I_{pa}, (c) SWV conducted at different concentrations of SMZ (0.25-120 µM) in the presence of a fixed PBZ concentration (40 µM), (d) SMZ concentration vs. I_{pa}, (e) SWV captured for simultaneous electrochemical detection of PBZ and SMZ at varying concentrations (0.25-120 µM each), and (f) PBZ and SMZ concentration vs. I_{pa} Reaction conditions: Bi_2S_3-ZnO(bio)/GCE used as the kinetic electrode in a 0.1 M PBS electrolyte (pH 5, 25 °C) under optimized deposition parameters.

Table 8.4: Electrochemical sensing parameters for individual and simultaneous monitoring of PBZ and SMZ using Bi_2S_3-ZnO(bio)/GCE.

Sensing type		LOD (µM)	LOQ (µM)	Sensitivity (µA $µM^{-1}$ cm^{-2})	Linear range (µM)
Individual PBZ		0.098	0.326	0.263	0.25-120
Individual SMZ		0.042	0.139	0.496	
Varying PBZ & fixed SMZ		0.102	0.340	0.253	
Fixed PBZ & varying SMZ		0.049	0.164	0.421	
Simultaneous PBZ & SMZ	PBZ	0.222	0.740	0.116	
	SMZ	0.089	0.296	0.233	

8.2.4.3 *Detection mechanism of PBZ and SMZ and sensing reaction at Bi_2S_3-ZnO(bio)/GCE*

To recognize the oxidation products of PBZ and SMZ, chronoamperometry was performed using the Bi_2S_3-ZnO(bio)/GCE in a 0.1 M PBS (pH 5, 25 ℃) containing 120 µM PBZ/SMZ at 0.655 V/1.015 V for 2000 s, subsequently subjected to LC-MS analyses of the same supporting electrolyte containing PBZ/SMZ that was used during the chronoamperometry. Figs. 8.10a and 8.10b demonstrate the mass spectra obtained from LC-MS analysis of 0.1 M PBS (pH 5, 25 ℃) with 120 µM PBZ prior to and following the chronoamperometry test, respectively. Similarly, Figs. 8.10c and 8.10d illustrate the mass spectra obtained from LC-MS analyses of the supporting electrolyte with 120 µM SMZ prior to and after the electrochemical detection. These mass spectra's provided insight into the sensing mechanisms of PBZ and SMZ. The oxidation of PBZ (m/z = 309.16) generated the PBZ radical (5-methyl-1,2-diphenyl-4,5-dihydro-1H-furo[2,3-c]pyrazol-3(2H)-one, m/z = 292.13) through the involvement of two electrons and two protons (Fig. 8.10e) (Megalamani et al., 2023). Similarly, the oxidation of SMZ (m/z = 254.06) leads to the formation of the SMZ radicals, including 4-iminocyclohexa-2,5-dienone (m/z = 108.06), 5-methylisoxazol-3-aminium (m/z = 100.07), and sulfurous acid (m/z = 81.97), accompanied by the transfer of two electrons and two protons (Fig. 8.10f) (Shi et al., 2024). The number of electrons participated in the electrochemical reaction of PBZ and SMZ aligned with those obtained from the Laviron equation (Eq. 8.7). The oxidation of PBZ and SMZ at Bi_2S_3-ZnO(bio)/GCE in a 0.1 M PBS (pH 5, 25 ℃) was further confirmed by the identified m/z value of PBZ and SMZ radicals. Thus, the detection of PBZ and SMZ essentially involves the detection of the PBZ and SMZ radicals, respectively.

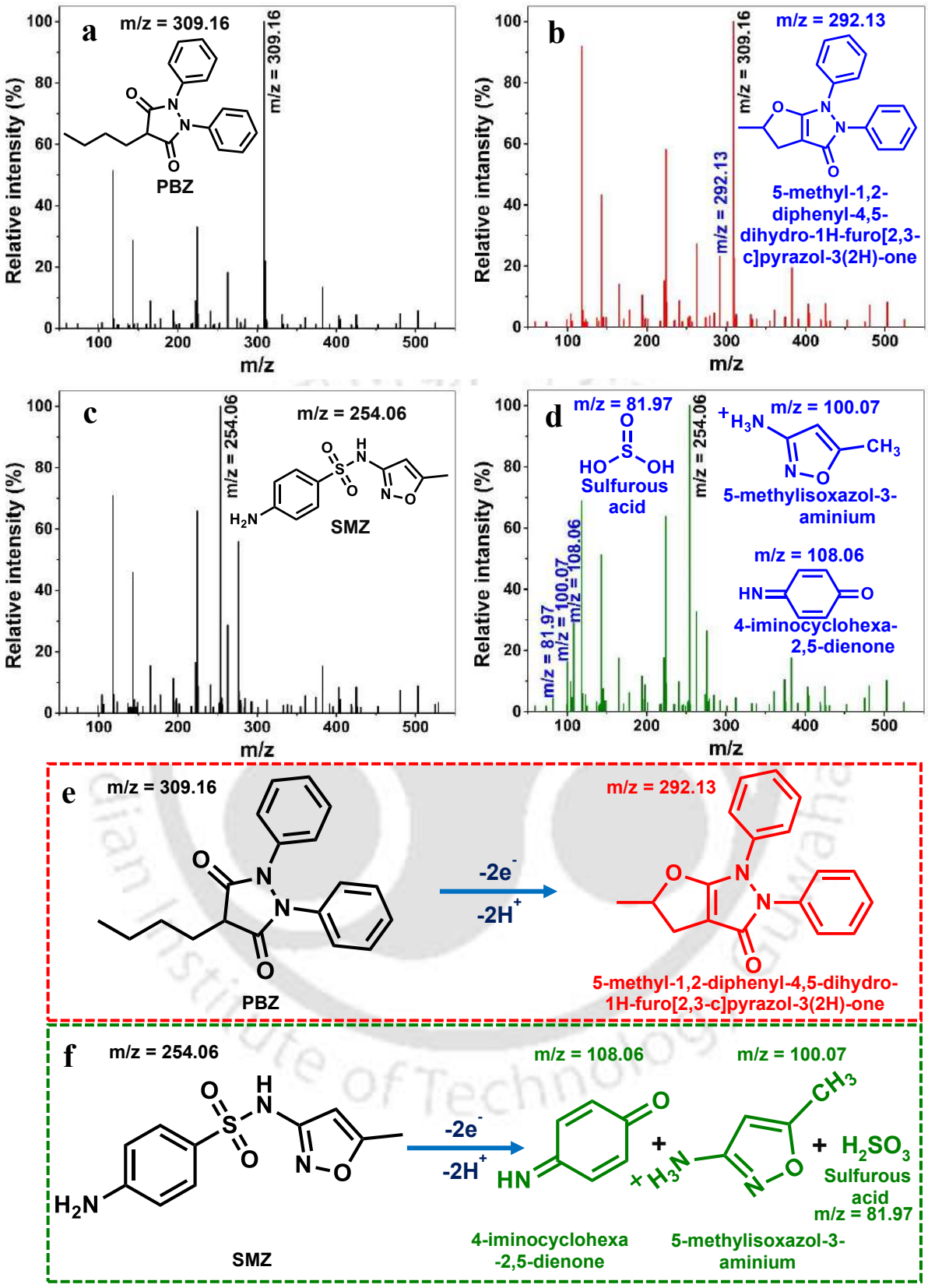

Figure 8.10: Mass spectra of PBZ solution (a) before and (b) after the chronoamperometry at 0.655 V, and SMZ solution (c) before and (d) after the chronoamperometry at 1.015 V for 2000

s using Bi_2S_3-ZnO(bio)/GCE. Reaction mechanism for (e) PBZ and (f) SMZ sensing on the Bi_2S_3-ZnO(bio)/GCE.

8.2.4.4 *Stability and reproducibility of Bi_2S_3-ZnO(bio)/GCE for PBZ and SMZ detection*

To evaluate the stability and reproducibility of the Bi_2S_3-ZnO(bio)/GCE for simultaneous electrochemical sensing of PBZ and SMZ, SWV was conducted in a 0.1 M PBS (pH 5, 25 ℃) with a fixed concentration of PBZ and SMZ (40 µM each) using selected deposition parameters. For the stability analysis, the same Bi_2S_3-ZnO(bio)/GCE was used in the same supporting electrolyte for 10 consecutive cycles, and for the reproducibility analysis, four new Bi_2S_3-ZnO(bio)/GCE were tested in four different supporting electrolytes. Fig. 8.11a displays a slight decrease in the anodic peak current of PBZ and SMZ after each cycle, likely due to the accumulation of PBZ and SMZ ions at the Bi_2S_3-ZnO(bio)/GCE surface (Dash et al., 2021). The decrement in the anodic peak response was 12.9% for PBZ and 11.8% for SMZ after the 10 reuse cycles, which is less than that reported in previous studies (Das et al., 2024). Fig. 8.11b demonstrates the reproducibility of the Bi_2S_3-ZnO(bio)/GCE for PBZ and SMZ sensing, with a relative standard deviation (RSD) of 4.3 and 3.9%, respectively. The RSD of the Bi_2S_3-ZnO(bio)/GCE for detecting PBZ and SMZ are under the acceptable range (Lotfi et al., 2021). Table 8.5 exhibited the electrocatalytic activity of the Bi_2S_3-ZnO(bio)/GCE for the simultaneous detection of PBZ and SMZ compared to recently reported sensors for various simultaneous analyte detection. The developed sensing platform significantly enhances the performance for simultaneous PBZ and SMZ monitoring compared to previous studies.

Table 8.5: Electrocatalytic activity of Bi_2S_3-ZnO(bio)/GCE for simultaneous detection of PBZ and SMZ and its comparison with recently reported sensors for various simultaneous analytes detection.

SI. No.	Working electrodes	Techniques	Analytes	LOD (µM)	Linear range (µM)	Sources
1.	CoV/MWCNTs-COOH/GCE	DPV	Ascorbic acid	0.4	1-100	S.-N. Li et al., 2025
			Dopamine	0.03		
			Uric acid	0.1		
2.	GC/$CeVO_4$	SWV	p-nitrophenol	0.091	0.2-60	Morozov et al., 2025
			2,4,6-trichlorophenol	0.151		
3.	Fe_3O_4/Ni@NPC/CP	DPV	Dopamine	0.165	0.5-200	Huang et al., 2025
			5-hydroxytryptamine	0.327		

4.	Cu-BTC/CPE	DPV	Dopamine	0.03	0.05-500	Azizpour Moallem & Beitollahi, 2022
			Uric acid	0.2	0.5-600	
5.	Au@Cu-MOF/SPCE	DPV	Dopamine	3.40	10-1000	Zhou et al., 2024
			Uric acid	10.36		
6.	MWCNTs-Nafion/GCE	DPV	Levodapa	0.6	2-300	Li et al., 2020
			Paracetamol	0.5	2-180	
			L-tyrosine	0.8	2-120	
7.	Au-CNFs/SPE	DPV	Ascorbic acid	0.9	5-40	Sakthivel et al., 2024
			Dopamine	0.4	2-16	
			Uric acid	0.3	2-16	
8.	C-SPE/CNF-COOH	SWV	Paracetamol	2	2.5-50	Fdez-Sanromán et al., 2025
			4-aminophenol	7		
9.	HOOC-MWCNT/GCE	DPV	SO_3^{2-}	0.215	400-2800	Sudha et al., 2018
			NO_2^-	0.565	100-700	
10.	**Bi_2S_3-ZnO(bio)/GCE**	**SWV**	**PBZ**	**0.098**	**0.25-120**	**This work**
			SMZ	**0.042**		

#DPV: Differential pulse voltammetry; SWV: Square wave voltammetry

8.2.5. Selectivity of PBZ and SMZ monitoring at Bi_2S_3-ZnO(bio)/GCE

The selectivity of the PBZ and SMZ sensing was evaluated by chronoamperometry using Bi_2S_3-ZnO(bio)/GCE in 0.1 M PBS (pH 5) at the redox potentials of 0.655 and 1.015 V, respectively. Interferants, such as SMZ, ciprofloxacin, and norfloxacin, were used to examine the selectivity for PBZ (Fig. 8.11c), whereas PBZ, ciprofloxacin, and norfloxacin were utilized to determine the selectivity for SMZ (Fig. 8.11d). The variation in the anodic peak response was observed upon the sequential addition of PBZ (5-40 µM), subsequent introduction of interfering species (40 µM each), and final addition of PBZ (60-100 µM) in the interval of 20 s. The significant increases in the peak response were noted after each addition of PBZ (Fig. 8.11c). Similarly, the changes in the anodic peak response were detected by introducing SMZ (5-40 µM), then interference (40 µM each) and finally SMZ (60-100 µM) in the interval of 20 s. The anodic peak response increased after each addition of SMZ, and the cell current quickly stabilized (Fig. 8.11d). However, insignificant changes were observed in the anodic peak current after the addition of SMZ and PBZ at the redox potentials of 0.655 and 1.015 V, respectively. Furthermore, no significant variations in the anodic peak current were detected

after the addition of interferents, which could be attributed to the different redox potentials of the interferents (Bhan and Golder, 2024). The Bi_2S_3-ZnO(bio)/GCE illustrated excellent selectivity for the electrochemical sensing of PBZ and SMZ in the existence of interfering substances at the redox potential of 0.655 and 1.015 V, respectively (Bhan et al., 2025b). Furthermore, the co-existence of interferents could not affect the redox potential of PBZ and SMZ sensing. Thus, the fabricated sensing platform exhibited exceptional selectivity for the electrochemical sensing of PBZ and SMZ.

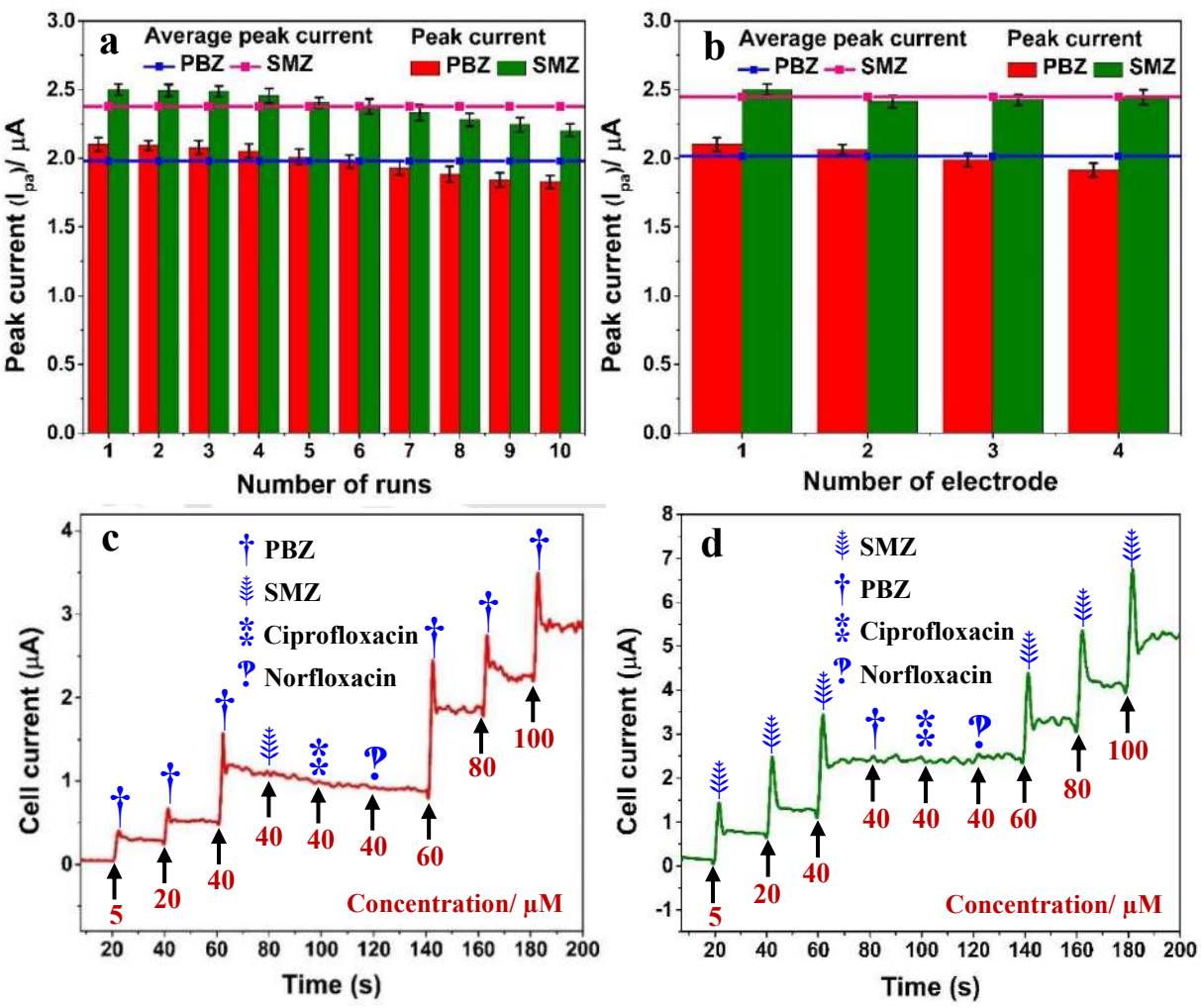

Figure 8.11: (a) Stability of the Bi_2S_3-ZnO(bio)/GCE for the simultaneous monitoring of PBZ and SMZ, (b) Reproducibility of the Bi_2S_3-ZnO(bio)/GCE for the simultaneous sensing of PBZ and SMZ, (c) Chronoamperometric captured using Bi_2S_3-ZnO(bio)/GCE in a 0.1 M PBS electrolyte (pH 5) at a redox potential of 0.655 V vs. Ag/AgCl, with sequential addition of PBZ (5-40 µM) then interferents, such as SMZ, ciprofloxacin, and norfloxacin, and again PBZ (60-100 µM), and (d) Chronoamperometric recorded using Bi_2S_3-ZnO(bio)/GCE in a 0.1 M PBS electrolyte (pH 5) at a redox potential of 1.015 V vs. Ag/AgCl, with sequential addition of SMZ

(5-40 µM) followed by interferents, including PBZ, ciprofloxacin, and norfloxacin, and finally PBZ (60-100 µM). Reaction conditions: all experiments were conducted in 0.1 M PBS electrolyte (pH 5) at 25 °C.

8.2.6. Simultaneous PBZ and SMZ sensing in environmental matrices

To study the practical applicability of Bi_2S_3-ZnO(bio)/GCE for the simultaneous electrochemical sensing and quantification of PBZ and SMZ in environmental matrices, SWV was conducted in a mixture of 0.1 M PBS (pH 5) and tap/river water (4:1 v/v) spiked with PBZ and SMZ at concentrations ranging from 0 to 80 µM using optimized deposition parameters. River and tap water samples were collected from the Brahmaputra River and the domestic water supply of IIT Guwahati, India, respectively. The collected samples were then filtered using a 0.2 µm membrane filter to eliminate suspended solids and prevent the Bi_2S_3-ZnO(bio)/GCE surface blockage, which could affect the sensor's performance (Bhan and Golder, 2024). The practical applicability of the Bi_2S_3-ZnO(bio)/GCE was investigated by determining PBZ and SMZ concentrations in environmental matrices using the calibration curve (Fig. 8.9f), and the obtained results are presented in Table 8.6. In both water samples, the recovery of PBZ and SMZ was ~100% noted. The maximum RSD for PBZ and SMZ in tap water was 6.6 and 6.1%, respectively, while in river water, the RSD was 7.8% for PBZ and 6.7% for SMZ. Therefore, the results presented in Table 8.6 indicate that the developed Bi_2S_3-ZnO(bio)/GCE has the potential for in-situ, simultaneous detection and quantification of PBZ and SMZ in environmental matrices.

Table 8.6: Performance of Bi_2S_3-ZnO(bio)/GCE for simultaneous monitoring of PBZ and SMZ in tap and river water samples.

Real samples	Spiked (µM)		Performance of Bi_2S_3-ZnO(bio)/GCE					
	PBZ	SMZ	Determination (µM)		Recovery (%)		RSD (%)	
			PBZ	SMZ	PBZ	SMZ	PBZ	SMZ
Tap water	0	0	ND	ND	-	-	-	-
	2	2	2.11	2.09	105.5	104.5	6.6	6.1
	10	10	10.47	9.94	104.7	99.4	4.9	3.9
	40	40	39.52	39.62	98.8	99.1	4.1	4.5
	80	80	80.52	80.42	100.7	100.5	3.5	2.8

River water	0	0	ND	ND	-	-	-	-
	2	2	2.15	2.12	107.5	106.0	7.8	6.7
	10	10	9.95	10.45	99.5	104.5	5.2	4.8
	40	40	40.23	39.71	100.6	99.3	3.8	4.2
	80	80	80.86	80.97	101.1	101.2	4.3	3.5

8.3. Major findings

We have successfully synthesized a Bi_2S_3-ZnO(bio) nanocomposite via a bio-engineered protocol using *Sechium edule* fruit extract for individual and simultaneous electrocatalytic monitoring of PBZ and SMZ by SWV techniques in tap and river waters. The Bi_2S_3-ZnO(bio) displayed ZnO(bio) nanostructures embedded on the Bi_2S_3(bio) nanorods with an average rod length of 1409.7 nm. The structural characteristics of Bi_2S_3-ZnO(bio) nanocomposites revealed a reduction in the crystal size to 14.43 nm, an increase in lattice strain to 9.14×10^{-3}, and a higher dislocation density of 4.80×10^{-3} Lines/nm^2. Bi_2S_3-ZnO(bio)/GCE demonstrated an 18.4-, 1.8-, 3.5-folds decrease in electron transfer resistance and a 2.7-, 1.2-, 1.4-folds increase in electrochemical surface area with 76.5, 39.8, and 59.1% boost in anodic peak current compare to the bare/GCE, Bi_2S_3(bio)/GCE, ZnO(bio)/GCE, respectively. The oxidation event of PBZ and SMZ involved a two-electron diffusion-controlled process with E^0 values of 0.655 and 1.015 V, k^0 of 0.907 and 0.721 s^{-1}, and Γ^* of 2.118×10^{-11} and 4.509×10^{-11} mol cm^{-2}, respectively. For individual sensing, Bi_2S_3-ZnO(bio)/GCE exhibited LODs of 0.098 and 0.042 µM, LOQs of 0.326 and 0.139 µM, and sensitivities of 0.263 and 0.496 µA μM^{-1} cm^{-2} for PBZ and SMZ detection, respectively, within a linear trend of 0.25-120 µM for each. Similarly, for the simultaneous monitoring of PBZ and SMZ, the developed sensing platform exhibited LODs of 0.222 and 0.089 µM, LOQs of 0.740 and 0.296 µM, and sensitivities of 0.116 and 0.233 µA μM^{-1} cm^{-2} for PBZ and SMZ, respectively, within a linear range of 0.25-120 µM. Bi_2S_3-ZnO(bio)/GCE exhibited a minimal reduction in the anodic peak response of 12.9% for PBZ and 11.8% for SMZ after 10 reuse cycles during the simultaneous monitoring. The presence of interference, such as SMZ, ciprofloxacin, and norfloxacin for PBZ detection, and PBZ, ciprofloxacin, and norfloxacin for SMZ detection, could not interfere with the electrochemical sensing of PBZ and SMZ at their respective oxidation potential of 0.655 and 1.015 V. The simultaneous monitoring of PBZ and SMZ spiked in water samples exhibited maximum RSD of 6.6 and 7.8% for PBZ and 6.1 and 6.7% for SMZ in tap water and river water, respectively. Therefore, the proposed bio-engineered monitoring platforms with enhanced detection

parameters has the potential for in-situ detection and quantification of PhACs in environmental matrices.

References

AL-Zahrani, A.A., Zainal, Z., Talib, Z.A., Lim, H.N., Holi, A.M., 2020. Bismuth sulphide decorated ZnO nanorods heterostructure assembly via controlled SILAR cationic concentration for enhanced photoelectrochemical cells. Mater. Res. Express 7, 025510. https://doi.org/10.1088/2053-1591/ab6e2e

Al-Zahrani, A.A., Zainal, Z., Talib, Z.A., Lim, H.N., Holi, A.M., Bahrudin, N.N., 2020. Enhanced photoelectrochemical performance of Bi_2S_3/Ag_2S/ZnO novel ternary heterostructure nanorods. Arab. J. Chem. 13, 9166–9178. https://doi.org/10.1016/j.arabjc.2020.10.040

Azizpour Moallem, Q., Beitollahi, H., 2022. Electrochemical sensor for simultaneous detection of dopamine and uric acid based on a carbon paste electrode modified with nanostructured Cu-based metal-organic frameworks. Microchem. J. 177, 107261. https://doi.org/10.1016/j.microc.2022.107261

Bagheri, H., Afkhami, A., Khoshsafar, H., Rezaei, M., Shirzadmehr, A., 2013. Simultaneous electrochemical determination of heavy metals using a triphenylphosphine/MWCNTs composite carbon ionic liquid electrode. Sensors Actuators B Chem. 186, 451–460. https://doi.org/10.1016/j.snb.2013.06.051

Bhan, C., Golder, A.K., 2024. ZnO Nanorods Aligned in a Vertical Configuration for Targeted Electrochemical Detection of Aniline. ACS Appl. Bio Mater. 7, 7413–7428. https://doi.org/10.1021/acsabm.4c01050

Bhan, C., Kumar Golder, A., 2023. Bio-based hierarchical vertically aligned 2D ZnO nanostructures for ultra selective electrochemical sensing of p-Chloroaniline. Chem. Eng. J. 475, 146122. https://doi.org/10.1016/j.cej.2023.146122

Bhan, C., R, G.S., Golder, A.K., 2025a. A chemo-mimetic approach using bioanalytes for formation of $BiVO_4$ nanostructures for voltammetric detection of bisphenol A. J. Environ. Chem. Eng. 13, 117417. https://doi.org/10.1016/j.jece.2025.117417

Bhan, C., Ravi, R., Golder, A.K., 2025b. Phyto-analytic formation of Ag nanostructures for targeted electrocatalytic sensing of ciprofloxacin. J. Environ. Chem. Eng. 13, 115140. https://doi.org/10.1016/j.jece.2024.115140

Borges, R.S., Palheta, I.C., Ota, S.S.B., Morais, R.B., Barros, V.A., Ramos, R.S., Silva, R.C.,

Costa, J. da S., Silva, C.H.T.P., Campos, J.M., Santos, C.B.R., 2019. Toward of Safer Phenylbutazone Derivatives by Exploration of Toxicity Mechanism. Molecules 24, 143. https://doi.org/10.3390/molecules24010143

Chowdhury, A., Bhan, C., Rao Peela, N., Kumar Golder, A., 2023. A simple template-free bioinspired route of 1D Bi_2S_3 nanorods synthesis for electrochemical CO_2 reduction to formate. J. Ind. Eng. Chem. 127, 138–148. https://doi.org/10.1016/j.jiec.2023.06.055

Dan, Y., Xu, J., Jian, J., Meng, L., Deng, P., Yan, J., Yuan, Z., Zhang, Y., Zhou, H., 2023. In Situ Decoration of Bi_2S_3 Nanosheets on Zinc Oxide/Cellulose Acetate Composite Films for Photodegradation of Dyes under Visible Light Irradiation. Molecules 28, 6882. https://doi.org/10.3390/molecules28196882

Das, D., Bhan, C., Mukherjee, C., Golder, A.K., 2024. Improved selectivity of electrochemical aniline sensing using one-dimensional silver nanorods with high aspect ratio synthesized by ascorbic acid assisted method. Anal. Chim. Acta 1310, 342697. https://doi.org/10.1016/j.aca.2024.342697

Dash, S.R., Bag, S.S., Golder, A.K., 2021. Bio-inspired PtNPs/Graphene nanocomposite based electrocatalytic sensing of metabolites of dipyrone. Anal. Chim. Acta 1167, 338562. https://doi.org/10.1016/j.aca.2021.338562

Dash, S.R., Bag, S.S., Golder, A.K., 2020. Synthesis of highly structured spherical Ag@Pt core-shell NPs using bio-analytes for electrocatalytic Pb(II) sensing. Sensors Actuators B Chem. 314, 128062. https://doi.org/10.1016/j.snb.2020.128062

Elavarasan, N., Kokila, K., Inbasekar, G., Sujatha, V., 2017. Evaluation of photocatalytic activity, antibacterial and cytotoxic effects of green synthesized ZnO nanoparticles by *Sechium edule* leaf extract. Res. Chem. Intermed. 43, 3361–3376. https://doi.org/10.1007/s11164-016-2830-2

Elgrishi, N., Rountree, K.J., McCarthy, B.D., Rountree, E.S., Eisenhart, T.T., Dempsey, J.L., 2018. A Practical Beginner's Guide to Cyclic Voltammetry. J. Chem. Educ. 95, 197–206. https://doi.org/10.1021/acs.jchemed.7b00361

Fdez-Sanromán, A., Ben Messaoud, N., Pazos, M., Rosales, E., Barbosa Queirós, R., 2025. Development of eco-friendly and cost-effective electrochemical sensor for the simultaneous detection of 4-aminophenol and paracetamol in water. Sens. Bio-Sensing Res. 48, 100782. https://doi.org/10.1016/j.sbsr.2025.100782

Gawal, P.M., Golder, A.K., 2025. Plant-Derived Phytochemicals for the Synthesis of p–n Junction CuO/CdS Heterostructures for Photocatalytic Carbon Dioxide Reduction to Ethanol and Carbon Monoxide. ACS Appl. Energy Mater. 8, 6087–6099.

https://doi.org/10.1021/acsaem.5c00497

Gumpu, M.B., Veerapandian, M., Krishnan, U.M., Rayappan, J.B.B., 2017. Simultaneous electrochemical detection of Cd(II), Pb(II), As(III) and Hg(II) ions using ruthenium(II)-textured graphene oxide nanocomposite. Talanta 162, 574–582. https://doi.org/10.1016/j.talanta.2016.10.076

Haque, A., Stewart, J.T., 1997. Direct injection HPLC method for the determination of phenylbutazone and oxyphenylbutazone in serum using a semipermeable surface column. J. Pharm. Biomed. Anal. 16, 287–293. https://doi.org/10.1016/S0731-7085(97)00041-1

Huang, Z., Lu, H., Dong, H., Chen, Z., Lu, R., Zhao, Y., Du, Y., Liu, Y., Wu, Y., Xu, M., Bi, Y., Zhou, Y., 2025. Fe_3O_4/Ni nanoparticles anchored nitrogen-doped porous carbon derived from core-shell MOF for simultaneous electrochemical detection of dopamine and 5-hydroxytryptamine. Talanta 286, 127522. https://doi.org/10.1016/j.talanta.2025.127522

Kaczala, F., E. Blum, S., 2016. The Occurrence of Veterinary Pharmaceuticals in the Environment: A Review. Curr. Anal. Chem. 12, 169–182. https://doi.org/10.2174/1573411012666151009193108

Kumar, A., Bhattacharya, B., Das, C., 2025. Studies on the inhibitive effect of ferrozine on the corrosion of mild steel in hydrochloric acid. J. Taiwan Inst. Chem. Eng. 174, 106221. https://doi.org/10.1016/j.jtice.2025.106221

Kumar, A., Das, C., 2025. Anticorrosive Behavior of a Novel Ternary RGO–ZnO–PANI Nanocomposite-Reinforced Epoxy Coating on Mild Steel in Marine Environment. Adv. Eng. Mater. 2500949, 1–17. https://doi.org/10.1002/adem.202500949

Kumar, A., Das, C., 2024. Corrosion inhibition of mild steel by Praecitrullus fistulosus (tinda fruit and peel) extracts. Sci. Total Environ. 929, 172569. https://doi.org/10.1016/j.scitotenv.2024.172569

Kumar, A., Das, C., 2023. A novel eco-friendly inhibitor of chayote fruit extract for mild steel corrosion in 1 M HCl: Electrochemical, weight loss studies, and the effect of temperature. Sustain. Chem. Pharm. 36, 101261. https://doi.org/10.1016/j.scp.2023.101261

Kumar Jangir, L., Kumari, Y., Kumar, A., Kumar, M., Awasthi, K., 2017. Investigation of luminescence and structural properties of ZnO nanoparticles, synthesized with different precursors. Mater. Chem. Front. 1, 1413–1421. https://doi.org/10.1039/C7QM00058H

Lazanas, A.C., Prodromidis, M.I., 2023. Electrochemical Impedance Spectroscopy─A Tutorial. ACS Meas. Sci. Au 3, 162–193. https://doi.org/10.1021/acsmeasuresciau.2c00070

Lei, P., Zhao, S., Asif, M., Aziz, A., Zhou, Y., Dong, C., Li, M., Shuang, S., 2024. Bovine Serum Albumin Template-Mediated Fabrication of Ruthenium Dioxide/Multiwalled Carbon Nanotubes: High-Performance Electrochemical Dopamine Biosensing in Human Serum. Langmuir 40, 11635–11641. https://doi.org/10.1021/acs.langmuir.4c00898

Li, S.-N., Zhang, J., Liu, Y.-Q., Zhou, K.-P., Jiang, X.-Y., Yu, J.-G., 2025. Cobalt vanadate intertwined in carboxylated multiple-walled carbon nanotubes for simultaneous electrochemical detection of ascorbic acid, dopamine and uric acid. Talanta 282, 127038. https://doi.org/10.1016/j.talanta.2024.127038

Li, Y., Ren, F., Li, J., Chen, Y., Liu, J., Yang, C., 2025. 1D/2D SnO_2/rGO composites-modified GCE for highly sensitive nonenzymatic electrochemical determination of chloramphenicol. J. Alloys Compd. 1014, 178637. https://doi.org/10.1016/j.jallcom.2025.178637

Li, Z.-Y., Gao, D.-Y., Wu, Z.-Y., Zhao, S., 2020. Simultaneous electrochemical detection of levodapa, paracetamol and L-tyrosine based on multi-walled carbon nanotubes. RSC Adv. 10, 14218–14224. https://doi.org/10.1039/D0RA00290A

Lotfi, S., Veisi, H., Karmakar, B., 2021. A convenient strategy for the electrochemical evaluation of acetaminophen and caffeine in combined drugs and biological samples over TiO_2@polymethyldopa/Pd nanocomposite functionalized glassy carbon electrodes. Measurement 186, 110156. https://doi.org/10.1016/j.measurement.2021.110156

Malode, S.J., Keerthi, P.K., Shetti, N.P., Kulkarni, R.M., 2020. Electroanalysis of Carbendazim using MWCNT/Ca-ZnO Modified Electrode. Electroanalysis 32, 1590–1599. https://doi.org/10.1002/elan.201900776

Manivannan, K., Sivakumar, M., Cheng, C.-C., Lu, C.-H., Chen, J.-K., 2019. An effective electrochemical detection of chlorogenic acid in real samples: Flower-like ZnO surface covered on PEDOT:PSS composites modified glassy carbon electrode. Sensors Actuators B Chem. 301, 127002. https://doi.org/10.1016/j.snb.2019.127002

Megalamani, M.B., Patil, Y.N., Nandibewoor, S.T., 2023. A novel CTN-Fe_3O_4/g-C_3N_4 modified green synthetic sensor for electro-sensing of phenylbutazone. Mater. Sci. Semicond. Process. 166, 107750. https://doi.org/10.1016/j.mssp.2023.107750

Mohammed, R., Ali, M.E.M., 2023. Decorated ZnO nanorods with Bi_2S_3 nanosheets for enhanced photocatalytic removal of antibiotics and analgesics: Degradation mechanism and pathway. Environ. Nanotechnology, Monit. Manag. 20, 100885. https://doi.org/10.1016/j.enmm.2023.100885

Morozov, R., Avdin, V., Lychkin, G., Uchaev, D., Vakhitov, I., Stanković, D., 2025. Facile

prepared high purity Cerium vanadate for simultaneous electrochemical detection of p-nitrophenol and 2,4,6-trichlorophenol. J. Phys. Chem. Solids 196, 112355. https://doi.org/10.1016/j.jpcs.2024.112355

Nadar, A.P., Sellappan, K., 2025. Bio-inspired Synthesis of Silver and Zinc Oxide Nanoparticles Using Syzygium salicifolium: Unveiling Versatile In Vitro Biomedical and Photocatalytic Applications. J. Clust. Sci. 36, 106. https://doi.org/10.1007/s10876-025-02823-0

Nehru, R., Senthil Kumar, B., Chen, C.-W., Dong, C.-D., 2024. Surface modification of Au nanoparticles with porous carbon microsheets/Bi_2S_3 for enhanced electrochemical monitoring of hazardous sulfamethoxazole. J. Environ. Chem. Eng. 12, 114814. https://doi.org/10.1016/j.jece.2024.114814

Ouyang, R., Ma, Y., Jiang, L., Zhang, X., Liu, X., Wang, Y., Huang, Y., Zhao, Y., Jiang, Y., Miao, Y., Liu, B., 2025. Cocatalysis of catalytic hairpin assembly and ternary heterojunction Bi_2S_3@MoS_2@Bi_2MoO_6 promotes ultra-sensitive electrochemical of detection MiRNA-21. Microchim. Acta 192, 115. https://doi.org/10.1007/s00604-025-06977-6

Palma Soto, E., Rodriguez Gonzalez, C.A., Luque Morales, P.A., Reyes Blas, H., Carrillo Castillo, A., 2024. Degradation of Organic Dye Congo Red by Heterogeneous Solar Photocatalysis with Bi_2S_3, Bi_2S_3/TiO_2, and Bi_2S_3/ZnO Thin Films. Catalysts 14, 589. https://doi.org/10.3390/catal14090589

Pan, Z., Wei, Y., Guo, H., Liu, B., Sun, L., Lu, Z., Wei, X., Zhang, H., Chen, Y., Yang, W., 2023. Sensitive detection of sulfamethoxazole by an electrochemical sensing platform with a covalent organic framework in situ grown on polyaniline. Microporous Mesoporous Mater. 348, 112409. https://doi.org/10.1016/j.micromeso.2022.112409

Ravi, R., Golder, A.K., 2025. Bio-based synthesis of oxygen-deficient Ni-doped TiO_2 using waste pineapple peel: Density functional theory studies and photocatalytic degradation of furazolidone. J. Environ. Chem. Eng. 13, 116198. https://doi.org/10.1016/j.jece.2025.116198

Ravi, R., Golder, A.K., 2023a. Bio-based Au Doping with Dominant Oxygen Vacancies and Ti^{3+} Defects on Photocatalytic Functionalities of TiO_2. Ind. Eng. Chem. Res. 62, 20702–20715. https://doi.org/10.1021/acs.iecr.3c02850

Ravi, R., Golder, A.K., 2023b. A tuneable bioinspired process of Pt-doping in TiO_2 for improved photoelectrochemical and photocatalytic functionalities. Colloids Surfaces A Physicochem. Eng. Asp. 663, 131034. https://doi.org/10.1016/j.colsurfa.2023.131034

Sadhasivam, S., Sadhasivam, T., Selvakumar, K., Oh, T.H., 2024. Hierarchical Bi_2S_3 nanothorn on ZnO core-branch photoelectrode: A promising heterostructure for enhanced photoelectrochemical water splitting. Curr. Appl. Phys. 68, 257–266. https://doi.org/10.1016/j.cap.2024.10.009

Sakthivel, P., Ramachandran, K., Maheshvaran, K., Senthil, T.S., Manivel, P., 2024. Simultaneous electrochemical detection of ascorbic acid, dopamine and uric acid using Au decorated carbon nanofibers modified screen printed electrode. Carbon Lett. 34, 2325–2341. https://doi.org/10.1007/s42823-024-00759-5

Savari, R., Fakhar, O., Rouhi, J., 2025. An electrochemical sensor based on ZnO–CuO nanocomposites for vancomycin detection in food samples. Ceram. Int. https://doi.org/10.1016/j.ceramint.2025.02.388

Shi, M., Shi, P., Yang, X., Zhao, N., Wu, M., Li, J., Ye, C., Li, H., Jiang, N., Li, X., Lai, G., Xie, W.-F., Fu, L., Wang, G., Zhu, Y., Tsai, H.-S., Lin, C.-T., 2024. A promising electrochemical sensor based on PVP-induced shape control of a hydrothermally synthesized layered structured vanadium disulfide for the sensitive detection of a sulfamethoxazole antibiotic. Analyst 149, 386–394. https://doi.org/10.1039/D3AN01355C

Sudha, V., Senthil Kumar, S.M., Thangamuthu, R., 2018. Simultaneous electrochemical sensing of sulphite and nitrite on acid-functionalized multi-walled carbon nanotubes modified electrodes. J. Alloys Compd. 749, 990–999. https://doi.org/10.1016/j.jallcom.2018.03.287

Sun, L., Chen, L., Sun, X., Du, X., Yue, Y., He, D., Xu, H., Zeng, Q., Wang, H., Ding, L., 2009. Analysis of sulfonamides in environmental water samples based on magnetic mixed hemimicelles solid-phase extraction coupled with HPLC–UV detection. Chemosphere 77, 1306–1312. https://doi.org/10.1016/j.chemosphere.2009.09.049

Teker, T., Bağdiken, F.N., Aslanoglu, M., 2025. Ultrasonic-assisted development of a high-sensitivity voltammetric sensor based on graphene nanoplatelets and hafnium oxide nanomaterials for paracetamol detection. Microchem. J. 213, 113862. https://doi.org/10.1016/j.microc.2025.113862

Tesena, P., Vinijkumthorn, R., Preuksathaporn, T., Piyakul, P., Chotikaprakal, T., Sirireugwipas, R., Wong-aree, K., Prapaiwan, N., 2024. Evaluation of gastrointestinal tract lesions and serum malondialdehyde levels after repeated oral administration of phenylbutazone in horses. Vet. Res. Commun. 48, 2343–2355. https://doi.org/10.1007/s11259-024-10415-y

Worboys, M., Toon, E., 2018. Phenylbutazone (Bute, PBZ, EPZ): one drug across two species. Hist. Philos. Life Sci. 40, 27. https://doi.org/10.1007/s40656-018-0191-4

Xin, X., Sun, S., Wang, M., Jia, R., 2020. Sensitive detection of estriol with an electrochemical sensor based on core-shell N-MWCNT/GONR-imprinted electrode. Ionics (Kiel). 26, 2633–2641. https://doi.org/10.1007/s11581-019-03377-8

Yao, L., Zhao, Z., Chen, C., Shao, Z., Wu, L., 2024. Fabrication of Bi_2S_3/ZnO nanocomposites for TEA gas sensors operating at room temperature: Towards seafood freshness detection during storage. Microchem. J. 207, 112239. https://doi.org/10.1016/j.microc.2024.112239

Yuan, X., Wu, X., Feng, Z., Jia, W., Zheng, X., Li, C., 2019. Facile Synthesis of Heterojunctioned ZnO/Bi_2S_3 Nanocomposites for Enhanced Photocatalytic Reduction of Aqueous Cr(VI) under Visible-Light Irradiation. Catalysts 9, 624. https://doi.org/10.3390/catal9070624

Zaky, M., Fadel Osman, S.F., 2022. Rapid HPLC Determination of Ciprofloxacin, Ofloxacin, and, Marbofloxacin Alone or in a Mixture. SSRN Electron. J. https://doi.org/10.2139/ssrn.4178998

Zhang, S., Ling, P., Chen, Y., Liu, J., Yang, C., 2023. 2D/2D porous Co_3O_4/rGO nanosheets act as an electrochemical sensor for voltammetric tryptophan detection. Diam. Relat. Mater. 135, 109811. https://doi.org/10.1016/j.diamond.2023.109811

Zhang, X., Min, T., Zhang, J., Liang, B., Li, X., Xu, T., Xing, S., Liang, S.-X., 2025. Electrochemical determination of sulfamethoxazole in body-fluids and foods using MIL-101(Fe)-doped N-Cu-MOF modified electrode. Microchem. J. 210, 113022. https://doi.org/10.1016/j.microc.2025.113022

Zhou, F., Lim, H.N., Ibrahim, I., Endot, N.A., Malek, E.A., Gowthaman, N.S.K., 2024. Simultaneous Electrochemical Detection of Dopamine and Uric Acid via Au@Cu-Metal Organic Framework. Chempluschem 89. https://doi.org/10.1002/cplu.202300686

CHAPTER 9

Conclusions and Scopes for Future Studies

This chapter highlights the key findings of the doctoral work and presents their overall significance. In addition, the suggestions and recommendations for future research directions are provided, drawn from the insights and experience gained in the present study.

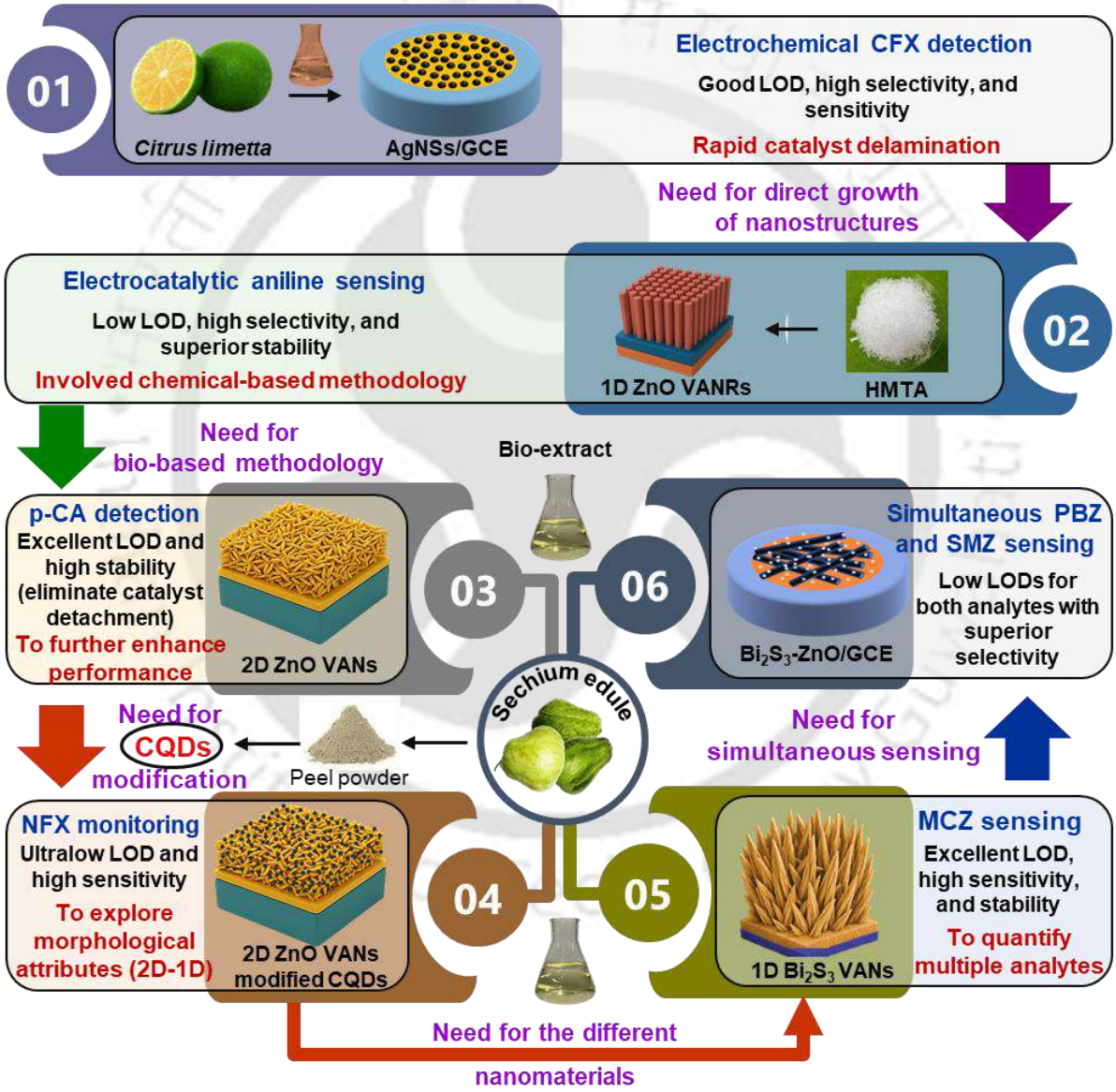

9.1. Overall conclusions

In the course of this doctoral work, binder-based and binder-free electrochemical sensing platforms were successfully developed for the detection and determination of CFX, aniline, p-CA, NFX, MCZ, PBZ, and SMZ using SWV technique in the environmental matrices. The major outcomes are summarized below in accordance with the research objectives.

1. Phyto-analytic formation of AgNSs for CFX sensing (Chapter 3):

Phyto-analytic AgNSs were synthesized using *Citrus limetta* fruit extract and immobilized on GCE using Nafion binder for CFX detection. AgNSs/GCE exhibited enhanced electrocatalytic activity with 93.13% reduction in charge-transfer resistance, 61.22% increase in active surface area, and improved current density compared to bare GCE. The sensor achieved a low detection limit (0.199 µM), excellent selectivity against common interferents, and reliable recovery (~100%) in real water samples when validated against HPLC. A 16.27% decrease in the anodic peak current was observed up to the 15th cycle, when the same sensing platform was reused. However, partial catalyst delamination remained a limitation, highlighting the importance of binder-free strategies for enhanced performance of the electrochemical detection platform.

2. Synthesis of vertically aligned ZnO nanorods for aniline detection (Chapter 4):

Vertically aligned ZnO nanorods were fabricated on an FTO substrate using a chemical method, yielding high crystallinity and significantly increased surface roughness (2.4-fold higher than bare FTO). ZnO-VANRs/FTO electrode exhibited 2.5-fold higher effective surface area, 86.85% lower charge-transfer resistance, and well-defined redox peaks with enhanced current response. The platform achieved an outstanding LOD of 0.193 µM with high sensitivity, excellent stability (only 2.63% decrease in anodic peak current up to 6 reused cycles), and strong selectivity against potential interferents. Electrochemical determination of aniline spiked in tap and river water was well comparable with HPLC, demonstrating the practical applicability potential of the sensor. While the chemical route proved effective, bio-based synthesis of ZnO VANRs on FTO remains challenging for future exploration.

3. Development of bio-based hierarchical 2D ZnO VANs for p-CA sensing (Chapter 5):

A new bioinspired methodology was successfully developed for synthesising 2D ZnO VANs onto the FTO glass surface using *Sechium edule* fruit extract. The synthesis process was

strongly pH dependent, which in turn affects the shape, size, mechanism of formation, and VANs self-stabilization. ZnO-VANs(bio)/FTO@pH7 electrode exhibited high crystallinity, 61.18% lower charge transfer resistance, and increased effective surface area compared to bare FTO. The developed platform achieved an excellent LOD of 0.021 µM with high sensitivity, superior stability (only 4.7% reduction in anodic peak current up to 9 cycles), and excellent selectivity in the presence of potential interferents. The detection and quantification of p-CA spiked in environmental samples was consistent and comparable with HPLC, demonstrating the strong potential of this binder-free, bio-based approach for environmental emerging pollutant monitoring. This bio-based reusable sensor minimizes the problem associated with the quick catalyst delamination from the electrode surface. Furthermore, the modification of these ZnO-VANs with CQDs derived from biomass was explored in the next chapter to further enhance electrochemical sensor performance.

4. Bioinspired 2D ZnO VANs modified with CQDs for NFX monitoring (Chapter 6):

In this study, bio-based 2D ZnO VANs were functionalized with CQDs derived from the carbon-rich remnant peel of *Sechium edule* fruit. $CQDs_{1.5}$-ZnOVANs(bio)/FTO displayed uniform vertical growth, 2.7-fold increase in electroactive surface area, and 1.5-fold reduction in charge transfer resistance compared to unmodified ZnO-VANs(bio)/FTO. The platform achieved ultralow detection limits (0.0066 µM) with wide linear ranges, high stability (only 8.1% reduction in anodic peak current till the 15^{th} cycle of NFX monitoring), and strong selectivity against common antibiotics. NFX quantification in environmental samples was well comparable with HPLC with minimal deviation. Therefore, CQDs-modified ZnO VANs is proven as robust platforms for environmental monitoring. The influence of morphological attributes from 2D (bean-shaped) to 1D (rod-shaped) was investigated to assess their impact on sensing performance in the next chapter.

5. Development of vertically oriented 1D Bi_2S_3 nanorods for MCZ sensing (Chapter 7):

In Chapter 7, a novel nature-inspired route was successfully developed to grow 1D Bi_2S_3 surface nanorods in the vertical configuration onto FTO substrate using the bio-extract of *Sechium edule* fruit. The morphology and electrocatalytic efficiency were strongly dependent on precursor loading and pH, resulting in highly crystalline, vertically oriented nanostructures with enhanced surface roughness (3.1-fold), significantly reduced charge transfer resistance (9.3-fold), and improved electrochemical surface area (2.8-fold) compared to bare FTO. The developed electrochemical detection platform displayed excellent detection limits (0.0085

μM), high stability (a minimal 7.1% decrease in anodic peak response was noted up to the 15th runs of MCZ sensing), and strong anti-interference ability even in the presence of pesticides and common background ions. Its performance in spiked water samples was similar to that of HPLC with minimal deviation. However, environmental matrices often contain multiple coexisting pollutants, making simultaneous detection very imperative.

6. Bi_2S_3-ZnO nanocomposites for dual-analyte selective detection (Chapter 8):

A bio-engineered Bi_2S_3-ZnO nanocomposite was successfully synthesized using *Sechium edule* extract for individual and simultaneous monitoring of PBZ and SMZ. The nanocomposites exhibited reduced crystallite size, higher lattice strain, and enhanced electrochemical activity with 18.4-fold reduction in charge-transfer resistance and 2.7-fold increase in electroactive area compared to bare GCE. Bi_2S_3-ZnO(bio)/GCE achieved low detection limits (0.098 μM PBZ, 0.042 μM SMZ individually; 0.222 μM PBZ, 0.089 μM SMZ simultaneously) within a wide linear range and high selectivity against common antibiotics. A minimal reduction in the anodic peak response of 12.9% for PBZ and 11.8% for SMZ after 10 reuse cycles was observed using Bi_2S_3-ZnO(bio)/GCE during the simultaneous monitoring. The developed simultaneous sensing platform could efficiently detect and quantify PBZ and SMZ in real water samples, achieving about 100% recovery. Therefore, Bi_2S_3-ZnO(bio)/GCE is a robust bio-engineered platform for in-situ PhAC detection in environmental samples.

Overall, a new bioinspired methodology was successfully developed for the synthesis of ZnO and Bi_2S_3 VANs using *Sechium edule* fruit extract. Functionalizing bio-based ZnO VANs with CQDs derived from the carbon-rich remnant peel of *Sechium edule* fruit significantly enhanced the electrochemical sensing performance. The binder-free bioinspired sensors demonstrated superior stability compared to binder-based sensors, as they effectively addressed the catalyst delamination problem and maintained a higher anodic peak current upon repeated use. A plausible sensing mechanism for each target analyte was proposed based on LC-MS studies and further supported by the number of electrons transfer determined from the Laviron equation. The fabricated sensors demonstrated high selectivity and sensitivity toward emerging pollutants, including CFX, aniline, p-CA, NFX, MCZ, PBZ, and SMZ. Notably, bio-based ZnO VANs exhibited superior sensing performance over chemically synthesized counterparts, while CQD-functionalized bioinspired 2D ZnO VANs achieved an exceptionally low detection limit for NFX sensing compared to other fabricated sensors. Finally, the practical applicability of the developed sensing platforms was tested for the analysis of environmental water samples and confirming their potential for real-world environmental monitoring.

9.2. Scopes for future studies

The present work has demonstrated the potential of bio-based electrocatalytic platforms for sensing emerging pollutants, there is still considerable scope for further studies. Based on the findings of this work, future studies may focus on improving material design, exploring advanced sensing strategies, and expanding real-world applications. Furthermore, bridging the gap between laboratory-scale electrochemical sensors and their deployment in real-world analytical applications represents one of the most pressing future directions in electrochemical research. A successful convergence of these domains would unlock the full potential of electrochemical sensors for real-time, on-site environmental monitoring, particularly in detecting emerging pollutants. The key directions are highlighted below.

- The present work reports on bioinspired synthesis of nanostructures using a mixture of functional bio-analytes together however, the contribution of the individual analyte is yet to be determined.
- The selectivity study may include structurally similar antibiotics interferants, such as ofloxacin, levofloxacin, enrofloxacin, moxifloxacin, and sparfloxacin.
- The stability test for a longer period of analysis beyond 10 cycles should be under taken, and the morphological and structural changes should be considered as a future scope of the work.
- The investigation on fouling characteristics and long-term operational stability of CQD-modified electrodes under real environmental conditions over multiple cycles needs proper and systematic investigations.
- The performance of the sensor in complex environmental matrices containing multiple aromatic amines and other potential interfering species may be taken up as a future scope of work.
- The influence of band structures of ZnO and Bi_2S_3, and their correlation with growth mechanisms and sensor performance, to gain deeper insight into their material properties and electrocatalytic behaviour, is an area of future research.
- A transformative direction in this field lies in the integration of bio-synthesized VANs into miniaturized, smartphone-compatible electrochemical platforms. As a proof of concept, we propose a patterned FTO-based substrate designed for a compact three-electrode assembly comprising a bio-based VAN working electrode, a reference electrode fabricated via Ag/AgCl ink deposition, and a counter electrode from the uncoated section of FTO (Fig. 9.1). This device can be seamlessly integrated with

smartphone-based electrochemical interfaces to facilitate portable, real-time, and in-situ detection of emerging contaminants and their intermediates at the point of use.

- ❖ Despite the advantages of nanostructures, the increased surface area may inadvertently promote surface fouling and non-specific adsorption, leading to background noise and false signals. Future advancements must therefore prioritize antifouling strategies, selective surface functionalization, and signal enhancement approaches to improve signal-to-noise ratios and charge transfer kinetics.
- ❖ Simultaneously, efforts must be directed toward scaling up bio-based synthesis methods, assessing long-term environmental stability, and evaluating the toxicity and biodegradability of nanomaterials to ensure safe and sustainable sensor deployment.

In nutshell, the bio-based fabrication of vertically aligned nanostructures on electrode surfaces offers a scalable, eco-friendly, and high-performance approach to next-generation electrochemical sensors. Their integration into portable, digital platforms paves the way for decentralized environmental diagnostics, with far-reaching implications for emerging pollutant monitoring, food safety, and public health.

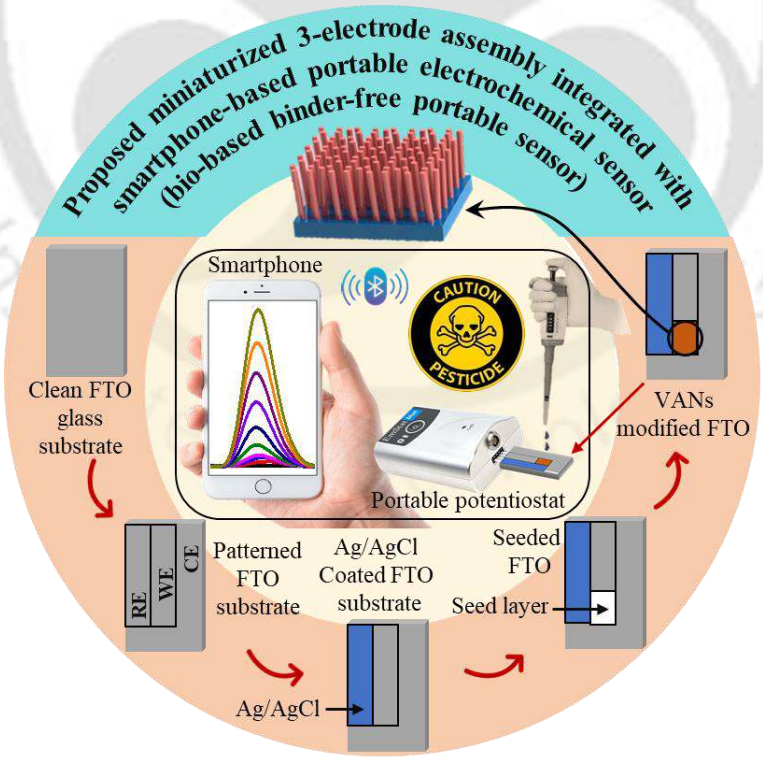

Figure 9.1: Proposed miniaturized three-electrode system integrated with a smartphone-based portable electrochemical sensor featuring bio-based VANs over FTO glass substrate for sensing environmental emerging pollutants.

Research Outcomes

Journal papers (thesis)

1. **C. Bhan**, A.K. Golder, Nature-inspired vertically oriented 1D Bi_2S_3 surface nanorods for ultra-selective electrochemical sensing of mancozeb, ***Langmuir*** 41, 2025, 15331–15346. https://doi.org/10.1021/acs.langmuir.5c00915.
2. **C. Bhan**, A.K. Golder, Dual-analyte selective electrochemical detection of phenylbutazone and sulfamethoxazole using bio-engineered Bi_2S_3-ZnO nanocomposites, ***Langmuir***, 41, 2025, 25464–25480. https://doi.org/10.1021/acs.langmuir.5c03259.
3. **C. Bhan**, A.K. Golder, Advances in smart electrocatalytic sensors based on vertically aligned nanostructures for agricultural pesticide monitoring, ***ACS Agric. Sci. Technol.***, 2025, https://doi.org/10.1021/acsagscitech.5c00770.
4. **C. Bhan**, R. Ravi, A.K. Golder, Phyto-analytic formation of Ag nanostructures for targeted electrocatalytic sensing of ciprofloxacin, ***J. Environ. Chem. Eng.*** 13, 2025, 115140. https://doi.org/10.1016/j.jece.2024.115140.
5. **C. Bhan**, A.K. Golder, ZnO nanorods aligned in a vertical configuration for targeted electrochemical detection of aniline, ***ACS Appl. Bio Mater.*** 7, 2024, 7413–7428. https://doi.org/10.1021/acsabm.4c01050.
6. **C. Bhan**, A.K. Golder, Bio-based hierarchical vertically aligned 2D ZnO nanostructures for ultra selective electrochemical sensing of p-Chloroaniline, ***Chem. Eng. J.*** 475, 2023, 146122. https://doi.org/10.1016/j.cej.2023.146122.
7. **C. Bhan**, A.K. Golder, Bioinspired synthesis of vertically aligned 2D ZnO surface nanostructures functionalized with carbon quantum dots for electrocatalytic monitoring of norfloxacin, ***ACS Appl. Electron. Mater.*** (**Revision submitted**)

Journal papers (others)

1. **C. Bhan**, G.S. R, A.K. Golder, A chemo-mimetic approach using bioanalytes for formation of $BiVO_4$ nanostructures for voltammetric detection of bisphenol A, ***J. Environ. Chem. Eng.*** 13, 2025, 117417. https://doi.org/10.1016/j.jece.2025.117417.
2. R. Ravi, **C. Bhan**, A.K. Golder, Bio-analytic synthesis of Cu-doped TiO_2 for photocatalytic degradation of ciprofloxacin under visible light, ***Opt. Mater.*** 159, 2025, 116577. https://doi.org/10.1016/j.optmat.2024.116577.
3. D. Das, **C. Bhan**, C. Mukherjee, A.K. Golder, Improved selectivity of electrochemical aniline sensing using one-dimensional silver nanorods with high aspect ratio synthesized

by ascorbic acid assisted method, ***Anal. Chim. Acta*** 1310, 2024, 342697. https://doi.org/10.1016/j.aca.2024.342697.

4. **C. Bhan**, A.K. Golder, Utilizing bioinspired AgNPs as an antibacterial agent to enhance ceramic membrane performance, ***J. Environ. Chem. Eng.*** 11, 2023, 110283. https://doi.org/10.1016/j.jece.2023.110283.
5. A. Chowdhury, **C. Bhan**, N.R. Peela, A.K. Golder, A tunable bioinspired process of SnO_2 NPs synthesis for electrochemical CO_2-into-formate conversion, ***J. CO_2 Util.*** 66, 2022, 102263. https://doi.org/10.1016/j.jcou.2022.102263.
6. A. Chowdhury, **C. Bhan**, N. Rao Peela, A. Kumar Golder, A simple template-free bioinspired route of 1D Bi_2S_3 nanorods synthesis for electrochemical CO_2 reduction to formate, ***J. Ind. Eng. Chem.*** 127, 2023, 138–148. https://doi.org/10.1016/j.jiec.2023.06.055.
7. **C. Bhan**, A.K. Golder, Bio-based development of 1D Bi_2S_3 surface nanorods modified with carbon dots for electrochemical detection of 4-chloroaniline (**Under preparation**)
8. **C. Bhan**, A.K. Golder, Facile synthesis of V_2O_5/GO nanocomposites for ultrasensitive electrochemical detection of furazolidone (**Under preparation**)
9. **C. Bhan**, A.K. Golder, Synergistic SnO_2/rGO nanocomposites for selective electrochemical sensing of carbendazim (**Under preparation**)

Book chapters

1. **C. Bhan**, R. Ravi, A.K. Golder, Recent advancement in monitoring of environmental pollutants using structured nano-catalyst integrated electrochemical sensing technique: A review, **Research and Industrial Conclave-Integration'-2024** (**Accepted**)
2. **C. Bhan**, S.R. Dash, A.K. Golder, Natural analytes for formation of silver nanostructures for electrocatalytic sensing of carbendazim, **Research and Industrial Conclave-Integration'-2024** (**Accepted**)
3. R. Ravi, **C. Bhan**, A.K. Golder, Recent advances in bio-based synthesis of nanomaterials for photocatalytic applications, **Research and Industrial Conclave-Integration'-2024** (**Accepted**)

Conferences attended

1. **C. Bhan**, A.K. Golder, Bioinspired synthesis of vertically aligned ZnO nanomaterials for electrochemical sensing of agriculture pesticides, North East Research Conclave (NERC) - 2022, 20-23th Jan 2022, held at IIT Guwahati, Guwahati, Assam, India (**Poster Presentation**)
2. **C. Bhan**, A.K. Golder, Bioinspired AgNPs for the fabrication of modified ceramic membrane, Biotechnology for Sustainable Bioresources and Bioeconomy (BSBB)-2022, 7-11th Dec 2022 held at IIT Guwahati, Guwahati, Assam, India (**Flash and Poster Presentation**)
3. D. Das, **C. Bhan**, A.K. Golder, Synthesis of silver nanorod structures by ascorbic acid assisted chemical method, Biotechnology for Sustainable Bioresources and Bioeconomy (BSBB)-2022, 7-11th Dec 2022 held at IIT Guwahati, Guwahati, Assam, India (**Flash and Poster Presentation**)
4. **C. Bhan**, A.K. Golder, Vertically aligned 1D surface ZnO nanorods for electrochemical sensing of agriculture pesticides, Research and Industrial Conclave (RIC)-Integration'-2023, 14-16th May 2023, held at IIT Guwahati, Guwahati, Assam, India (**Poster Presentation**)
5. **C. Bhan**, A.K. Golder, Bio-based formation of 1D surface vertically aligned Bi_2S_3 nanorods for electrochemical sensing of agriculture pesticides, IIChE - CHEMCON 2023, 27-30th Dec 2023 held at Heritage Institute of Technology, Kolkata, India (**Oral Presentation**)
6. **C. Bhan**, R. Ravi, A.K. Golder, Recent advancement in monitoring of environmental pollutants using structured nano-catalyst integrated electrochemical sensing technique: A review, Research and Industrial Conclave (RIC)-Integration'-2024, 09-11th Aug 2024 held at IIT Guwahati, Guwahati, Assam, India (**Oral Presentation**)
7. **C. Bhan**, S.R. Dash, A.K. Golder, Natural analytes for formation of silver nanostructures for electrocatalytic sensing of carbendazim, Research and Industrial Conclave (RIC)-Integration'-2024, 09-11th Aug 2024 held at IIT Guwahati, Guwahati, Assam, India (**Oral Presentation**)
8. R. Ravi, **C. Bhan**, A.K. Golder, Recent advances in bio-based synthesis of nanomaterials for photocatalytic applications, Research and Industrial Conclave (RIC)-Integration'-2024, 09-11th Aug 2024 held at IIT Guwahati, Guwahati, Assam, India (**Oral Presentation**)

9. **C. Bhan**, A.K. Golder, Phyto-analytic development of V_2O_5 nanostructures for ultra-selective electrochemical detection of phenylbutazone, Environment 2024, 09-11th Dec 2024 held at Centre for the Environment, IIT Guwahati, Assam, India (**Oral Presentation**)
10. **C. Bhan**, A.K. Golder, Bioinspired vertically aligned 2D ZnO surface nanostructures functionalized with carbon quantum dots for electrocatalytic monitoring of norfloxacin, Research and Industrial Conclave (RIC)-Synergy'25, IIT Guwahati, India, 10-12th Oct 2025 (**Poster Presentation**)

Symposium attended

1. **C. Bhan**, A.K. Golder, Studies on the Role of Bio-inspired AgNPs for the Fabrication of Modified Ceramic Membrane, Workshop cum Symposium on Bio-inspired Nanomaterials for Environmental Application, 12-13th Feb 2020 held at IIT Guwahati, Guwahati, Assam, India (**Poster presentation**)
2. G.S. R, **C. Bhan**, A.K. Golder, Nature-inspired $BiVO_4$ nanospheres for sensitive voltammetric determination of bisphenol A, Symposium on environmental challenges, opportunities and sustainable solutions, 5th June 2024, organized by Centre for the Environment, IIT Guwahati, Assam, India (**Poster Presentation**)
3. **C. Bhan**, A.K. Golder, Nature-inspired vertically oriented 1D Bi_2S_3 surface nanorods for electrochemical sensing of mancozeb, Symposium on ending plastic pollution, 5th June 2025, organized by Centre for the Environment, IIT Guwahati, Assam, India (**Poster Presentation**)

Awards

1. **Best Flash and Poster Presentation Award** for "**C. Bhan**, A.K. Golder, Bioinspired AgNPs for the fabrication of modified ceramic membrane, Biotechnology for Sustainable Bioresources and Bioeconomy (BSBB)-2022, 7-11th Dec 2022 held at IIT Guwahati, Guwahati, Assam, India (**Flash and Poster Presentation**)"
2. **Best Oral Presentation Award** for "**C. Bhan**, S.R. Dash, A.K. Golder, Natural analytes for formation of silver nanostructures for electrocatalytic sensing of carbendazim, Research and Industrial Conclave (RIC)-Integration'-2024, 09-11th Aug 2024 held at IIT Guwahati, Guwahati, Assam, India (**Oral Presentation**)"
3. **Best Poster Presentation Award** for "**C. Bhan**, A.K. Golder, Nature-inspired vertically oriented 1D Bi_2S_3 surface nanorods for electrochemical sensing of mancozeb, Symposium on ending plastic pollution, 5th June 2025, organized by Centre for the Environment, IIT Guwahati, Assam, India (**Poster Presentation**)"

Chandra Bhan

Roll Number: 196107104
PhD - Chemical Engineering
Indian Institute of Technology Guwahati

+91-8433017724
bchandra@iitg.ac.in
chandrabhan.research@gmail.com
linkedin.com/in/chandra-bhan-780764195

Education

Year	Degree / Certificate	Institute / Board	CGPA/Percentage
2019 - 2025	PhD	Indian Institute of Technology Guwahati	-
2017 - 2019	M.Tech	Indian Institute of Technology Guwahati	8.06
2011 - 2015	B.Tech	BBDNITM, Lucknow	72.76%
2009	Senior Secondary	UP Board	76.60%
2007	Secondary	UP Board	73.83%

Publications

- Nature-inspired vertically oriented 1D Bi_2S_3 surface nanorods for ultra-selective electrochemical sensing of mancozeb, ***Langmuir*** 41, 2025, 15331–15346
  C. Bhan *and A.K. Golder* *https://doi.org/10.1021/acs.langmuir.5c00915*
- Dual-analyte selective electrochemical detection of phenylbutazone and sulfamethoxazole using bio-engineered Bi_2S_3-ZnO nanocomposites, ***Langmuir*** 41, 2025, 25464-25480
  C. Bhan *and A.K. Golder* *https://doi.org/10.1021/acs.langmuir.5c03259*
- Advances in smart electrocatalytic sensors based on vertically aligned nanostructures for agricultural pesticide monitoring, ***ACS Agric. Sci. Technol.***, 2025
  C. Bhan *and A.K. Golder* *https://doi.org/10.1021/acsagscitech.5c00770*
- Phyto-analytic formation of Ag nanostructures for targeted electrocatalytic sensing of ciprofloxacin, ***J. Environ. Chem. Eng.*** 13, 2025, 115140
  C. Bhan*, R. Ravi, and A.K. Golder* https://doi.org/10.1016/j.jece.2024.115140
- A chemo-mimetic approach using bioanalytes for formation of $BiVO_4$ nanostructures for voltammetric detection of bisphenol A, ***J. Environ. Chem. Eng.*** 13, 2025, 117417
  C. Bhan*, G.S. R, and A.K. Golder* https://doi.org/10.1016/j.jece.2025.117417
- ZnO nanorods aligned in a vertical configuration for targeted electrochemical detection of aniline, ***ACS Appl. Bio Mater.*** 7, 2024, 7413–7428
  C. Bhan *and A.K. Golder* https://doi.org/10.1021/acsabm.4c01050
- Bio-based hierarchical vertically aligned 2D ZnO nanostructures for ultra selective electrochemical sensing of p-Chloroaniline, ***Chem. Eng. J.*** 475, 2023, 146122
  C. Bhan *and A.K. Golder* https://doi.org/10.1016/j.cej.2023.146122
- Utilizing bioinspired AgNPs as an antibacterial agent to enhance ceramic membrane performance, ***J. Environ. Chem. Eng.*** 11, 2023, 110283
  C. Bhan *and A.K. Golder* https://doi.org/10.1016/j.jece.2023.110283
- Bio-analytic synthesis of Cu-doped TiO_2 for photocatalytic degradation of ciprofloxacin under visible light, ***Opt. Mater.*** 159, 2025, 116577
  R. Ravi, ***C. Bhan****, and A.K. Golder* https://doi.org/10.1016/j.optmat.2024.116577
- Improved selectivity of electrochemical aniline sensing using one-dimensional silver nanorods with high aspect ratio synthesized by ascorbic acid assisted method, ***Anal. Chim. Acta.*** 1310, 2024, 342697
  D. Das, ***C. Bhan****, C. Mukherjee, and A.K. Golder* https://doi.org/10.1016/j.aca.2024.342697
- A simple template-free bioinspired route of 1D Bi_2S_3 nanorods synthesis for electrochemical CO_2 reduction to formate, ***J. Ind. Eng. Chem.*** 127, 2023, 138–148
  A. Chowdhury, ***C. Bhan****, N.R. Peela, and A.K. Golder* https://doi.org/10.1016/j.jiec.2023.06.055
- A tunable bioinspired process of SnO_2 NPs synthesis for electrochemical CO_2-into-formate conversion, ***J. CO_2 Util.*** 66, 2022, 102263

*A. Chowdhury, **C. Bhan**, N.R. Peela, and A.K. Golder* https://doi.org/10.1016/j.jcou.2022.102263

- Bioinspired vertically aligned 2D ZnO surface nanostructures functionalized with carbon quantum dots for electrocatalytic monitoring of norfloxacin, ***ACS Appl. Electron. Mater.***
  ***C. Bhan** and A.K. Golder* *Revision submitted*
- Bio-based development of 1D Bi_2S_3 surface nanorods modified with carbon dots for electrochemical detection of 4-chloroaniline
  ***C. Bhan** and A.K. Golder* *Under preparation*
- Facile synthesis of V_2O_5/GO nanocomposites for ultrasensitive electrochemical detection of furazolidone
  ***C. Bhan** and A.K. Golder* *Under preparation*
- Synergistic SnO_2/rGO nanocomposites for selective electrochemical sensing of carbendazim
  ***C. Bhan** and A.K. Golder* *Under preparation*

Book chapters

- Recent advancement in monitoring of environmental pollutants using structured nano-catalyst integrated electrochemical sensing technique: A review, ***Current Progress in Engineering Sciences*** 1, 2024
  ***C. Bhan,** R. Ravi, and A.K. Golder* *Accepted*
- Natural analytes for formation of silver nanostructures for electrocatalytic sensing of carbendazim, ***Current Progress in Engineering Sciences 1***, 2024
  ***C. Bhan,** S.R. Dash, and A.K. Golder* *Accepted*
- Recent advances in bio-based synthesis of nanomaterials for photocatalytic applications, ***Current Progress in Engineering Sciences*** 1, 2024
  *R. Ravi, **C. Bhan,** and A.K. Golder* *Accepted*

Projects

- **Advanced electrochemical platforms for selective and simultaneous detection of emerging pollutants** ***Dec 2025***
  Prof. Animes Kumar Golder, Dept. of Chemical Engg., IIT Guwahati
- **Studies on the role of bio-inspired AgNPs for the fabrication of modified ceramic membrane** ***July 2019***
  Prof. Animes Kumar Golder, Dept. of Chemical Engg., IIT Guwahati
- **Production of biodiesel by transesterification of different plant oils** ***May 2015***
  Assistant Prof. Amit Kumar Gupta, Dept. of Chemical Engg., BBDNITM, Lucknow

Technical skills

- **Writing:** Academic publications, Scientific writing, and Project proposal
- **Instruments:** Potentiostat, FESEM, FETEM, EDX, AFM, XRD, XPS, UV-Vis, Spin coater, BET, LCMS, FTIR, HPLC, NMR, TGA, Raman, and Microwave reactor
- **Electrochemical techniques:** EIS, CV, SWV, DPV, LSV, and Chronoamperometry
- **Software:** Microsoft Office, Origin, Nova, Gwyddion, ImageJ, ChemDraw, XPS peak fit, Mendeley, Mass Hunter, and Aspen HYSIS
- **Miscellaneous:** Nanomaterial synthesis, Electrochemical sensing, Electrocatalytic CO_2 reduction, Ceramic membrane fabrication, Photocatalysis, Wastewater treatment, Surface functionalization, and Photoelectrochemical catalyst study

Conferences/Symposiums

- Bioinspired synthesis of vertically aligned ZnO nanomaterials for electrochemical sensing of agriculture pesticides, ***North East Research Conclave (NERC)***-2022, IIT Guwahati, 20-23 Jan 2022
  C. Bhan** and A.K. Golder* ***Poster presentation
- Bioinspired AgNPs for the fabrication of modified ceramic membrane, ***Biotechnology for Sustainable Bioresources and Bioeconomy (BSBB)***-2022, IIT Guwahati, 7-11 Dec 2022
  C. Bhan** and A.K. Golder* ***Flash and poster presentation
- Synthesis of silver nanorod structures by ascorbic acid assisted chemical method, ***Biotechnology for Sustainable***

Bioresources and Bioeconomy (BSBB)-2022, IIT Guwahati, 7-11 Dec 2022
D. Das, ***C. Bhan*** *and A.K. Golder* ***Flash and poster presentation***

- Vertically aligned 1D surface ZnO nanorods for electrochemical sensing of agriculture pesticides, ***Research and Industrial Conclave (RIC)***-Integration'-2023, IIT Guwahati, 14-16 May 2023
  C. Bhan *and A.K. Golder* ***Poster presentation***
- Bio-based formation of 1D surface vertically aligned Bi_2S_3 nanorods for electrochemical sensing of agriculture pesticides, ***IIChE - CHEMCON*** 2023, Heritage Institute of Technology, Kolkata, 27-30 Dec 2023
  C. Bhan *and A.K. Golder* ***Oral presentation***
- Recent advancement in monitoring of environmental pollutants using structured nano-catalyst integrated electrochemical sensing technique: A review, ***Research and Industrial Conclave (RIC)***-Integration'-2024, IIT Guwahati, 09-11 Aug 2024
  C. Bhan, *R. Ravi, and A.K. Golder* ***Oral presentation***
- Natural analytes for formation of silver nanostructures for electrocatalytic sensing of carbendazim, ***Research and Industrial Conclave (RIC)***-Integration'-2024, IIT Guwahati, 09-11 Aug 2024
  C. Bhan, *S.R. Dash, and A.K. Golder* ***Oral presentation***
- Recent advances in bio-based synthesis of nanomaterials for photocatalytic applications, ***Research and Industrial Conclave (RIC)***-Integration'-2024, IIT Guwahati, 09-11 Aug 2024
  R. Ravi, ***C. Bhan*** *and A.K. Golder* ***Oral presentation***
- Phyto-analytic development of V_2O_5 nanostructures for ultra-selective electrochemical detection of phenylbutazone, ***Environment*** 2024, IIT Guwahati, 09-11 Dec 2024
  C. Bhan *and A.K. Golder* ***Oral presentation***
- Studies on the role of bio-inspired AgNPs for the fabrication of modified ceramic membrane, ***Workshop Cum Symposium on Bio-inspired Nanomaterials for Environmental Application,*** *IIT Guwahati*, 12-13 Feb 2020
  C. Bhan *and A.K. Golder* ***Poster presentation***
- Nature-inspired $BiVO_4$ nanospheres for sensitive voltammetric determination of bisphenol A, ***Symposium on Environmental Challenges***, Opportunities and Sustainable Solutions, IIT Guwahati, 5 Jun 2024
  G.S. R, ***C. Bhan*** *and A.K. Golder* ***Poster presentation***
- Nature-inspired vertically oriented 1D Bi_2S_3 surface nanorods for electrochemical sensing of mancozeb, ***Symposium on Ending Plastic Pollution***, IIT Guwahati, 5 Jun 2025
  C. Bhan *and A.K. Golder* ***Poster presentation***
- Bioinspired vertically aligned 2D ZnO surface nanostructures functionalized with carbon quantum dots for electrocatalytic monitoring for norfloxacin, ***Research and Industrial Conclave (RIC)***-Synergy'-2025, IIT Guwahati, 10-12 Oct 2025
  C. Bhan *and A.K. Golder* ***Poster presentation***

Positions of Responsibility

- **Organizing Committee Member,** One-Day Symposium on Ending Plastic Pollution, IIT Guwahati, World Environment Day 2025
- **Organizing Committee Member,** ENVIRONMENT 2024 - An International Conference on Environmental Challenges, Opportunities and Sustainable Solutions, Dec 2024
- **Volunteer,** Workshop-cum Symposium on Bio-inspired Nanomaterials for Environmental Applications, IIT Guwahati, Feb 2020
- **Volunteer,** Symposium on Recent Advances in Bio-inspired Nanomaterials for Environmental Applications, IIT Guwahati, 2018

Achievements

- **Graduate Aptitude Test in Engineering (GATE):** Qualified 2016 and 2017
- **Best Flash and Poster Presentation Award,** Biotechnology for Sustainable Bioresources and Bioeconomy (BSBB)-2022, IIT Guwahati, 7-11 Dec 2022

- **Best Oral Presentation Award**, Research and Industrial Conclave (RIC)-Integration'-2024, IIT Guwahati, 09-11 Aug 2024
- **Best Poster Presentation Award**, Symposium on Ending Plastic Pollution, IIT Guwahati, 5 Jun 2025
- **MHRD Doctoral Fellowship**, Government of India, 2020

Key courses taken

- Chemical Reaction Engineering
- Mechanical Operation
- Heat Transfer
- Fluid Mechanics
- Mass Transfer
- Characterization of Materials
- Process Control
- Chemical Thermodynamics

Experience

- Training at ***'Indian Oil Corporation Limited,*** Mathura *July 2014*

Extracurriculars

- **Peer Reviewer,** Journal of Colloid and Interface Science – Reviewed research manuscript for publication
- **Participant,** One-Day Workshop on Fuel Cell Technology: Advancements and Applications, Department of Chemical Engineering, IIT Guwahati, 17 Mar 2025
- **Participant,** Plastic Collection Drive, jointly organized by the Centre for the Environment, Hostel Affairs Board and NSS, IIT Guwahati, 04 Jun 2025
- **Participant,** Workshop on Recent Advances on Bio-inspired Nanomaterials for Environmental Applications, IIT Guwahati, 18 Dec 2018
- **Certification,** Chemical Process Simulation using Aspen HYSIS' (15-20 Apr 2013) & (Sep 2013 - Apr 2014) - Completed training on process modelling and simulation

---

References

- **Dr. Animes Kumar Golder** (PhD Supervisor)
  Professor, Department of Chemical Engineering, Indian Institute of Technology Guwahati, Assam-781039, India
  Email: animes@iitg.ac.in
  Google scholar: https://scholar.google.com/citations?user=6VCZydkAAAAJ&hl=en
- **Dr. Bishnupada Mandal** (Doctoral Committee Chairman)
  Professor, Department of Chemical Engineering, Indian Institute of Technology Guwahati, Assam-781039, India
  Email: bpmandal@iitg.ac.in
  Google scholar: https://scholar.google.com/citations?user=2zTissgAAAAJ&hl=en
- **Dr. Chandan Das** (Lab Collaboration)
  Professor, Department of Chemical Engineering, Indian Institute of Technology Guwahati, Assam-781039, India
  Email: cdas@iitg.ac.in
  Google scholar: https://scholar.google.co.in/citations?user=HB_fCMoAAAAJ&hl=en

---

Declaration

I hereby declare that the above information is true and correct to the best of my knowledge.

Date: 29 Dec 2025
Place: IIT Guwahati

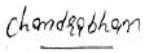

Signature